frontiers | Research Topics

Methods in molecular innate immunity 2022

Edited by
Carrie Ambler, Jorg Hermann Fritz and Thomas A. Kufer

Published in
Frontiers in Immunology

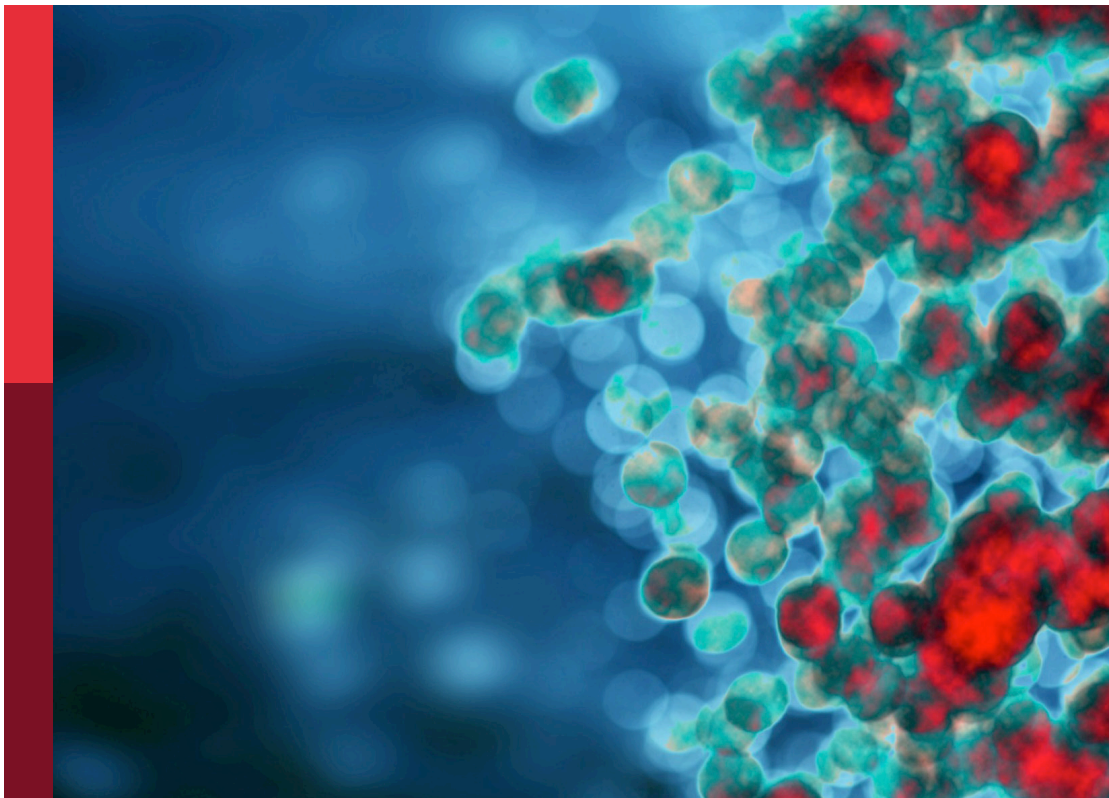

ISSN 1664-8714
ISBN 978-2-8325-6121-8
DOI 10.3389/978-2-8325-6121-8

About Frontiers

Frontiers is more than just an open access publisher of scholarly articles: it is a pioneering approach to the world of academia, radically improving the way scholarly research is managed. The grand vision of Frontiers is a world where all people have an equal opportunity to seek, share and generate knowledge. Frontiers provides immediate and permanent online open access to all its publications, but this alone is not enough to realize our grand goals.

Frontiers journal series

The Frontiers journal series is a multi-tier and interdisciplinary set of open-access, online journals, promising a paradigm shift from the current review, selection and dissemination processes in academic publishing. All Frontiers journals are driven by researchers for researchers; therefore, they constitute a service to the scholarly community. At the same time, the *Frontiers journal series* operates on a revolutionary invention, the tiered publishing system, initially addressing specific communities of scholars, and gradually climbing up to broader public understanding, thus serving the interests of the lay society, too.

Dedication to quality

Each Frontiers article is a landmark of the highest quality, thanks to genuinely collaborative interactions between authors and review editors, who include some of the world's best academicians. Research must be certified by peers before entering a stream of knowledge that may eventually reach the public - and shape society; therefore, Frontiers only applies the most rigorous and unbiased reviews. Frontiers revolutionizes research publishing by freely delivering the most outstanding research, evaluated with no bias from both the academic and social point of view. By applying the most advanced information technologies, Frontiers is catapulting scholarly publishing into a new generation.

What are Frontiers Research Topics?

Frontiers Research Topics are very popular trademarks of the *Frontiers journals series*: they are collections of at least ten articles, all centered on a particular subject. With their unique mix of varied contributions from Original Research to Review Articles, Frontiers Research Topics unify the most influential researchers, the latest key findings and historical advances in a hot research area.

Find out more on how to host your own Frontiers Research Topic or contribute to one as an author by contacting the Frontiers editorial office: frontiersin.org/about/contact

Methods in molecular innate immunity: 2022

Topic editors

Carrie Ambler — Durham University, United Kingdom

Jorg Hermann Fritz — McGill University, Canada

Thomas A. Kufer — University of Hohenheim, Germany

Citation

Ambler, C., Fritz, J. H., Kufer, T. A., eds. (2025). *Methods in molecular innate immunity: 2022*. Lausanne: Frontiers Media SA. doi: 10.3389/978-2-8325-6121-8

Table of contents

frontiers | Frontiers in Immunology

TYPE Editorial
PUBLISHED 28 February 2025
DOI 10.3389/fimmu.2025.1576957

OPEN ACCESS

EDITED AND REVIEWED BY
Francesca Granucci,
University of Milano-Bicocca, Italy

*CORRESPONDENCE
Jörg H. Fritz
jorg.fritz@mcgill.ca

RECEIVED 14 February 2025
ACCEPTED 17 February 2025
PUBLISHED 28 February 2025

CITATION
Fritz JH and Kufer TA (2025)
Editorial: Methods in molecular
innate immunity: 2022.
Front. Immunol. 16:1576957.
doi: 10.3389/fimmu.2025.1576957

Editorial: Methods in molecular innate immunity: 2022

Jörg H. Fritz[1,2,3]* and Thomas A. Kufer[4]

[1]Department of Microbiology and Immunology, McGill University, Montréal, QC, Canada, [2]McGill University Research Center on Complex Traits (MRCCT), McGill University, Montréal, QC, Canada, [3]Dahdaleh Institute of Genomic Medicine (DIgM), McGill University, Montréal, QC, Canada, [4]Department of Immunology, Institute for Nutritional Medicine, University of Hohenheim, Stuttgart, Germany

KEYWORDS

innate immunity, inflammation, methods, innate lymphoid cells, myeloid cells

Editorial on the Research Topic
Methods in molecular innate immunity: 2022

Advances in immunology are inherently linked to progress in implementing novel methods as best illustrated by the development of the cre-lox technique that allows to analyse the effect of single genes on lymphocyte development and function by the generation of "conditional" knock-out mice (1). Development of novel as well as the optimization of existing technologies and methods furthers constant progress in biomedical research. The most recent game changer being the development of the bacterial immune system CRISPR-Cas9 into a universal tool for gene and genome editing (2).

Here in this Research Topic on "*Methods in Molecular Innate Immunity: 2022*" we provide a brief collection of state-of the art methods and protocols to enable in-depth studies of innate immune responses in *in vitro* cell culture systems as well as in *in vivo* models.

The identification of innate lymphoid cells (ILCs) and the rapid progress made in this field showed that ILCs exert essential roles in immune responses and tissue homeostasis (3). Four detailed protocols deal with the characterization of ILCs, their genetic manipulation, as well as the analysis of their metabolic states, respectively. Audouze-Chaud et al. provide a novel CRISPR/Cas9 protocol for efficient genetic knockout in human group 2 innate lymphoid cells (ILC2s) and discuss challenges and solutions. Sadeghalvad et al. present a detailed protocol for cytometric analysis of ILCs and provide tips for its successful implementation. Roy-Dorval et al. detail approaches for analysis of lipid uptake, storage, and fatty acid oxidation by ILC2s, while Krisna et al. provide a comprehensive framework for the immunometabolic analysis of primary murine ILC2s.

In vivo analysis of the distribution of immune cell subsets and their activation status was boosted by the development of single cell sequencing techniques, primarily single-cell RNA sequencing (4). Mindt et al. present a protocol to allow for spatial differentiation in single-cell RNA sequencing by using barcoded antibodies.

Macrophages and neutrophils are the first line of the innate immune defence. While macrophages emerged as key instruments to study innate immune responses due to their easy differentiation *in vitro* and their robustness in cell culture (5), neutrophils are extremely short-lived and isolation strategies for *in vitro* assays were only recently developed (6). In addition to its central role in host defence upon microbial challenge,

the immune system is increasingly recognized as an integral part of fundamental physiological processes such as development, reproduction and wound healing, which involves a very close crosstalk with other body systems such as metabolism, the central nervous system and the cardiovascular system is evident (7). One prominent example being the discovery that TNFα is secreted from adipose tissue in obese mice and drives insulin resistance, highlighting that metabolic disorders are intimately linked to dysregulated immune responses (8). In an original research article, Iovino et al. present novel insights into the link of macrophage activation by saturated fatty acids and IRE1 RNase in metabolic reprogramming. Their work highlights a key role of IRE1α in HIF-1α-mediated glycolysis in macrophages independent of XBP1s.

Immune cell activation is tightly linked to changes in the metabolic wiring and mitochondrial activity. The development of devices to measure extracellular flux by redox potential changes in small volumes generated the basis to study cellular metabolic changes upon immune cell activation in great detail (9). Grudzinska et al. provide a protocol that exemplifies how extracellular flux (XF) analysis can be used to measure metabolism and oxidate burst in activated neutrophils.

The core function of innate immunity is the quick and often cell intrinsic reaction towards pathogen challenge (10). Zhi et al. detail investigations of the cGAS-STING signaling pathway and its modulation by traditional Chinese medicines. Furthermore, detailed studies of host-pathogen interactions at a time-resolved and molecular level are providing exiting new insights into the function of innate immune responses. Using a GFP fluorophore that is quenched when exposed to reactive oxygen species combined with a stable secondary fluorescent marker Hinman et al. provide a useful protocol to analyse killing of the human pathogen *Staphyococcus aureus* and neutrophil function in murine disease models.

We are living in an environment that is more and more polluted with chemicals that can affect the innate immune response. Plastic- and environment-derived bisphenol A (BPA) for example can accumulate in the human body and acts as an endocrine-disrupting compound. Dallio et al. analysed BPA levels in individuals and stimulated monocytes with BPA to assess metabolic and cytokine profiling.

This brief Research Topic will be helpful for research professional and trainees to implement novel methodologies to further detail the wealth of functions of the innate immune system upon microbial challenge and during inflammatory processes.

Author contributions

JF: Writing – original draft, Writing – review & editing. TK: Writing – original draft, Writing – review & editing.

Conflict of interest

The authors declare that the research was conducted in the absence of any commercial or financial relationships that could be construed as a potential conflict of interest.

The author(s) declared that they were an editorial board member of Frontiers, at the time of submission. This had no impact on the peer review process and the final decision.

Generative AI statement

The author(s) declare that no Generative AI was used in the creation of this manuscript.

Publisher's note

References

1. Rajewsky K. From a dream to reality. *Eur J Immunol.* (2007) 37 Suppl 1:S134–7. doi: 10.1002/eji.200737819

2. Doudna JA, Charpentier E. Genome editing. The new frontier of genome engineering with crispr-cas9. *Science*. (2014) 346:1258096. doi: 10.1126/science.1258096

3. Diefenbach A, Colonna M, Koyasu S. Development, differentiation, and diversity of innate lymphoid cells. *Immunity*. (2014) 41:354–65. doi: 10.1016/j.immuni.2014.09.005

4. Stark R, Grzelak M, Hadfield J. Rna sequencing: the teenage years. *Nat Rev Genet.* (2019) 20:631–56. doi: 10.1038/s41576-019-0150-2

5. Luque-Martin R, Mander PK, Leenen PJM, Winther MPJ. Classic and new mediators for *in vitro* modelling of human macrophages. *J Leukoc Biol.* (2021) 109:549–60. doi: 10.1002/JLB.1RU0620-018R

6. Monceaux V, Chiche-Lapierre C, Chaput C, Witko-Sarsat V, Prevost MC, Taylor CT, et al. Anoxia and glucose supplementation preserve neutrophil viability and function. *Blood.* (2016) 128:993–1002. doi: 10.1182/blood-2015-11-680918

7. Sattler S. The role of the immune system beyond the fight against infection. *Adv Exp Med Biol.* (2017) 1003:3–14. doi: 10.1007/978-3-319-57613-8_1

8. Hotamisligil GS. Inflammation and metabolic disorders. *Nature.* (2006) 444:860–7. doi: 10.1038/nature05485

9. Ferrick DA, Neilson A, Beeson C. Advances in measuring cellular bioenergetics using extracellular flux. *Drug Discov Today*. (2008) 13:268–74. doi: 10.1016/j.drudis.2007.12.008

10. Kufer TA, Creagh EM, Bryant CE. Guardians of the cell: effector-triggered immunity steers mammalian immune defense. *Trends Immunol.* (2019) 40:939–51. doi: 10.1016/j.it.2019.08.001

frontiers | Frontiers in Immunology

TYPE Original Research
PUBLISHED 23 January 2023
DOI 10.3389/fimmu.2023.1089111

OPEN ACCESS

EDITED BY
Carrie Ambler,
Durham University, United Kingdom

REVIEWED BY
Tamás Laskay,
University of Lübeck, Germany
Kristian Juul-Madsen,
Aarhus University, Denmark

*CORRESPONDENCE
Craig T. Lefort
craig_lefort@brown.edu

SPECIALTY SECTION
This article was submitted to Molecular Innate Immunity, a section of the journal Frontiers in Immunology

RECEIVED 03 November 2022
ACCEPTED 03 January 2023
PUBLISHED 23 January 2023

CITATION
Hinman KD, Laforce-Nesbitt SS, Cohen JT, Mundy M, Bliss JM, Horswill AR and Lefort CT (2023) Bi-fluorescent *Staphylococcus aureus* infection enables single-cell analysis of intracellular killing *in vivo*. *Front. Immunol.* 14:1089111. doi: 10.3389/fimmu.2023.1089111

Bi-fluorescent *Staphylococcus aureus* infection enables single-cell analysis of intracellular killing *in vivo*

Kristina D. Hinman[1,2,3], Sonia S. Laforce-Nesbitt[4], Joshua T. Cohen[1], Miles Mundy[3], Joseph M. Bliss[2,4], Alexander R. Horswill[5] and Craig T. Lefort[1,2]*

[1]Division of Surgical Research, Department of Surgery, Rhode Island Hospital, Providence, RI, United States, [2]Warren Alpert Medical School, Brown University, Providence, RI, United States, [3]Graduate Program in Pathobiology, Brown University, Providence, RI, United States, [4]Department of Pediatrics, Women and Infants Hospital, Providence, RI, United States, [5]Department of Immunology and Microbiology, University of Colorado School of Medicine, Aurora, CO, United States

Techniques for studying the clearance of bacterial infections are critical for advances in understanding disease states, immune cell effector functions, and novel antimicrobial therapeutics. Intracellular killing of *Staphylococcus aureus* by neutrophils can be monitored using a *S. aureus* strain stably expressing GFP, a fluorophore that is quenched when exposed to the reactive oxygen species (ROS) present in the phagolysosome. Here, we expand upon this method by developing a bi-fluorescent *S. aureus* killing assay for use *in vivo*. Conjugating *S. aureus* with a stable secondary fluorescent marker enables the separation of infected cell samples into three populations: cells that have not engaged in phagocytosis, cells that have engulfed and killed *S. aureus*, and cells that have viable internalized *S. aureus*. We identified ATTO647N-NHS Ester as a favorable dye conjugate for generating bi-fluorescent *S. aureus* due to its stability over time and invariant signal within the neutrophil phagolysosome. To resolve the *in vivo* utility of ATTO647N/GFP bi-fluorescent *S. aureus*, we evaluated neutrophil function in a murine model of chronic granulomatous disease (CGD) known to have impaired clearance of *S. aureus* infection. Analysis of bronchoalveolar lavage (BAL) from animals subjected to pulmonary infection with bi-fluorescent *S. aureus* demonstrated differences in neutrophil antimicrobial function consistent with the established phenotype of CGD.

KEYWORDS

infection, Staphylococcus aureus, phagocytosis, reactive oxygen species, neutrophil, flow cytometry

Introduction

The inflammatory response to infection is a dynamic process with tissue-specific variability: leukocytes are recruited to cross endothelial barriers at different times, with specificity dependent on the cytokine environment and cellular affinity for endothelial adhesion receptors (1, 2). In response to the initial insult, resident cells such as macrophages or natural killer cells recruit innate immune cells as the first line of defense (3–5). In the acute phase, neutrophils are the most abundant infiltrating leukocyte in response to bacterial infections. This recruitment is self-amplified by neutrophil-derived signals such as interleukin-8 (IL-8) and leukotriene B4 (LTB4) (3, 6). Tight regulation over recruitment is crucial as neutrophil depletion is often fatal while overactivation leads to enzymatic and oxidative damage to the tissues involved (4, 7).

Neutrophils clear bacterial infections through numerous intra- and extracellular effector functions, depending on the species of bacteria. *Staphylococcus aureus* is one species of interest due to its prevalence, ability to evade the immune system, and increasing resistance to pharmaceutical anti-microbial agents. As of 2018, methicillin-resistant *S. aureus* (MRSA) was the leading cause of death resulting from an antibiotic-resistant pathogen (8). Neutrophils predominantly kill *S. aureus via* internalization into a phagolysosome (5). Within the phagolysosome, the nicotinamide adenine dinucleotide phosphate (NADPH) oxidase complex generates reactive oxygen species (ROS) *via* a series of reactions referred to as the oxidative burst (7, 9). The proposed mechanisms of bacterial killing by ROS include oxidative damage of the microbe membrane, DNA, and other cellular components (7, 10, 11). In addition, NADPH oxidase activity may modulate the potency of proteolytic enzymes that are delivered to the phagosome and contribute to microbicidal activities (10, 12).

Numerous pathologies affect the neutrophil-dependent clearance of bacteria. An impaired neutrophilic response may be the result of depleted cell counts (neutropenia), the inability to recruit cells to inflamed tissue sites, or loss of effector functions (13). Neutrophil dysfunction can be caused by a primary immunodeficiency or can occur secondary to a disease state, such as sepsis or cancer (5, 9, 14). There are sufficient experimental methods for quantifying neutrophil counts to evaluate defects in production or tissue-specific recruitment, including the characterization of surface markers by flow cytometry or morphology by cytospin. However, methods for evaluating microbe killing on a single cell level *in vivo* are relatively limited. Current methods depend on comparing pathogen clearance through plating tissue homogenates and counting colony forming units (CFU) *ex vivo*. This method is limited as it is non-specific, only providing insight into overall host defense discrepancies without identifying the specific effector cell(s) responsible for observed differences. *In vitro* experiments may implicate cellular function more specifically but exclude the influence of host extracellular factors and proteins that aid in the clearance of *S. aureus* (15). Alternatives based on live *in vivo* imaging require advanced technology which is expensive, time-consuming, and limited by the target tissue location (16). Therefore, we sought to develop a fluorescence-based assay to quantify *in vivo* neutrophil antimicrobial function on a single cell level.

Previous work by Schwartz, et al. has demonstrated *in vitro* that the fluorescent signal from a GFP-producing *S. aureus* is quenched in a ROS-dependent manner over time (17, 18). This loss of fluorescence is correlated with intracellular *S. aureus* viability. The mechanism of GFP bleaching is attributed to the HOCl in the phagosome, likely *via* chlorination of the tyrosine 66 residue in GFP (19). For a single point in time, the GFP signal alone is insufficient to distinguish cells that have not undergone phagocytosis of *S. aureus* from cells that have bleached the GFP fluorescent signal in conjunction with eradicating internalized *S. aureus*. Therefore, we screened for a secondary fluorescent dye capable of maintaining a robust fluorescent signal over time, independent of ROS production, phagolysosome activity, or *S. aureus* viability. We generated bi-fluorescent *S. aureus* by conjugating a far-red fluorescent dye to a GFP-producing USA300 *S. aureus*. In our study, we extensively characterize neutrophil intracellular killing of bi-fluorescent *S. aureus* to demonstrate the fidelity and utility of the assay for evaluating neutrophil antimicrobial function or dysfunction *in vivo*.

Materials and methods

Staphylococcus aureus culture and staining

Glycerol stocks of the superfolded GFP-producing USA300 strain of *S. aureus* were provided by Alexander Horswill and have been described (18). Liquid cultures were grown in tryptic soy broth (TSB, Sigma-Aldrich, St. Louis, MO) from the glycerol stock by incubating at 37C, shaking at 250 rpm, overnight. Before experimentation, overnight cultures were diluted and allowed to grow to the exponential phase. For staining, cultures were washed 2x in phosphate-buffered saline, pH=7.4 (PBS, Gibco, Dun Laoghaire, Co Dublin, Ireland), and brought to a concentration of $4x10^8$ CFU/mL. *S. aureus* was stained for 30 minutes in the dark at a final concentration of 0.5ug/mL of ATTO647N-NHS ester (Sigma-Aldrich). To pellet, cultures were centrifuged for 5 minutes at 3000 RPM. After staining, *S. aureus* was washed 2x in assay buffer (Hank's balanced salt solution/10% fetal bovine serum/20 mM HEPES). Before use *in vitro*, *S. aureus* was opsonized by incubating at 37C and shaking for 5-10 minutes in assay buffer.

Growth curves were generated by bringing bi-fluorescent or GFP *S. aureus* to OD_{600} = 0.1 in TSB. OD was measured using SmartSpec 3000 (Bio-Rad, Hercules, CA). Cultures were grown for four and a half hours, with a sample drawn every 30 minutes for the first 2 hours and then at 3 hours and 4.5 hours. At each time point, the OD_{600} was measured and the fluorescence of the *S. aureus* particles was measured using a MACSQuant Analyzer 10 flow cytometer (Miltenyi).

HoxB8 conditionally immortalized progenitor derivation, culture, and differentiation

HoxB8 conditionally immortalized neutrophil progenitors were generated as previously described (20–22). Briefly, C57BL/6 mouse bone marrow was isolated, cultured, and transduced with a

tamoxifen-inducible *Hoxb8* transgene. All cells were grown in Opti-Mem media supplemented with GlutaMax (Gibco), 30uM beta-mercaptoethanol (Sigma-Aldrich), 10% fetal bovine serum (Gemini Bio-Products, West Sacramento, CA), 1x penicillin/streptomycin (Gibco), 1x non-essential amino acids (Gibco) at a density of ~10^6 cells/mL. The progenitor cell culture was supplemented with stem cell factor (SCF) and 100nM Z-4-hydroxytamoxifen (Tocris Bioscience, Bristol, UK) to induce *Hoxb8* expression. SCF was derived from the supernatant of CHO cells that secrete recombinant murine SCF (a gift from Patrice Dubreuil, Centre de Recherche en Cancérologie de Marseille). For differentiation, cells were washed 3x in PBS to remove Z-4-hydroxytamoxifen induction. Cells were pelleted by centrifugation at 400xg for 3 minutes. The differentiation culture was supplemented with SCF and 20 ng/mL G-CSF (BioLegend) for 2-3 days, and then just G-CSF until use on days 5-7.

In vitro killing assay

Differentiated *Hoxb8* progenitor-derived neutrophils were suspended in assay buffer at a density of 1x10^7 cells/mL. Samples treated with diphenyleneiodonium (DPI; Selleck Chemicals, Houston, TX) or cytochalasin D (Sigma-Aldrich) were incubated at 37°C for 20 minutes before infection. For each sample, one million cells were inoculated with 25µL of OD=0.5 *S. aureus* for an MOI of 20:1 for 15 minutes. Cells were then washed with warm lysostaphin 200ng/mL followed by assay buffer 1x. Cells were suspended in a final volume of 100µL of assay buffer. For killing assays, this was considered time zero. For experiments determining fluorescent intensity over time, every 20 minutes 10µL of the sample was plated in 200µL of cold PBS/1% FBS and kept on ice until analysis by the MACSQuant.

Dead *S. aureus* phagocytosis assay

Bi-fluorescent *S. aureus* was heat-inactivated at 60C for 30 minutes. To evaluate the phagocytosis of dead *S. aureus*, cells were inoculated and washed using the same protocol as the live *S. aureus* killing assay. Cells were analyzed at time zero (after lysostaphin wash) to evaluate the internalization of the heat-killed *S. aureus*.

Animal care and breeding

All studies were performed under the approval of the Lifespan Animal Welfare Committee (Protocol number 5017-19, Office of Laboratory Animal Welfare Assurance #A3922-01). These studies follow Public Health Service guidelines for animal care and use. The CGD mouse model was acquired from Jackson Laboratories (Bar Harbor, ME), strain B6.129S-Cybb^{tm1Din}/J for in-house breeding. This strain was originally developed by knocking out the *Cybb* gene (gp91phox) to recapitulate the CGD phenotype. Female mice heterozygous for the knocked out *Cybb* gene (x-linked) were bred with wild-type males to yield hemizygous wild-type (WT) or knockout male progeny used in this study. Animals were housed in sterile caging until infection at 6-10 weeks old and provided access to water and standard chow *ad libitum*.

S. aureus pulmonary infection

S. aureus was stained as previously described and brought to an OD_{600} = 0.5 or 2x10^8 CFU/mL. One mL of *S. aureus* was pelleted and suspended in 100µL of normal saline for a working solution. The inoculum was further diluted to provide a bolus of 6x10^7CFU or 8x10^7CFU in 40µL. Animals were anesthetized with vaporized isoflurane (Braintree Scientific, Braintree, MA) before oropharyngeal inhalation of the inoculum.

In vivo killing assay

Twelve hours post pulmonary infection, mice were euthanized by Fatalplus (Vortech Pharmaceuticals, Dearborn, MI) and cervical dislocation. Bronchoalveolar lavage (BAL) was collected by pushing and withdrawing 1mL cold 1% FBS/PBS into the lungs *via* an angiocatheter (performed 3x) and then passed through a 70-micron filter (Falcon, Corning, NY). Cells were pelleted and resuspended in 2mL lysostaphin and then washed twice in 1% FBS/PBS. To determine total cell counts, the pellet was brought to 1mL before analysis. Cells were stained with PE anti-Ly6G (BioLegend) in 1% FBS/PBS for 30 minutes. Before analysis by flow cytometry, samples were washed 3x in 1%FBS/PBS. Samples were analyzed on a MACSQuant and data were analyzed with FlowJo software to determine fluorescent intensities, population percentages, and total counts.

Colony forming units assays

BAL samples were stained with PE anti-Ly6G (BioLegend) and sorted into three populations: $Ly6G^+ATTO647N^+GFP^+$, $Ly6G^+ATTO647N^+GFP^-$, and $Ly6G^+ATTO647N^-GFP^-$. Cell sorting was performed using a FACSAria (BD). *In vitro* assay samples omitted the PE anti-Ly6G stain and were sorted based on ATTO647N and GFP expression. Samples were pelleted and resuspended in 1mL of pH=11 H_2O. Cells were lysed by incubating and vortexing for ~5 minutes (23). Lysates were serially diluted at 1:10 and plated, 3x10µL drops per dilution onto TSB agar plates. Plates were incubated at 37C overnight. Colonies were counted and the total CFU burden of the sorted cells was determined. CFU burden was normalized to the total events sorted in each population.

Imaging

For imaging analysis of cell suspensions, cells were spun at 1500 RPM onto a superfrost plus glass slide (Fisher Scientific, Pittsburgh, PA) after phagocytosis and killing *in vitro*. *Ex vivo* analysis of lung tissue was performed through frozen sectioning of infected animals. WT animals were infected and euthanized twelve hours post-infection. The lungs were carefully removed avoiding puncture and inflated through the trachea with 0.8mL of a 2:1 mixture of optimal cutting temperature compound (OCT):PBS. The trachea was tied with a suture and the lungs were immediately frozen in liquid nitrogen. Once frozen, the tissue was then embedded in a mold

with OCT (Sakura Finetek, Torrance, CA) on dry ice. Samples were sliced in a cryostat microtome at a thickness of 5-7 μm and adhered to superfrost plus glass slides. Prior to imaging, slides were fixed in cold acetone for 2 minutes and allowed to dry at room temperature.

For both types of imaging experiments, coverslips were applied with antifade mounting medium with DAPI (Vectashield, Newark, CA) and immediately imaged. Slides were imaged using a Nikon Eclipse 80i, with light provided by an X-Cite 120 lamp (Excelitas Technologies). Images were captured with a Retiga EXi Fast 1394 camera (QImaging, Burnaby, BC, Canada). Post-imaging analyses to merge images, analyze colocalization, and include scale bars were done using ImageJ.

In order to measure the colocalization of the GFP and ATTO647N fluorescence in the lung tissue, 11 images from distinct sections of lung tissue were analyzed (20x magnification). Images were collected by sectioning lungs from 3 separate animals. First, the background signal was subtracted from the GFP and ATTO647N images. The two images were compared with the "colocalization threshold" and "colocalization test" functions. Since we do not expect a relationship between the fluorescent intensity of the ATTO647N and GFP signal but do expect spatial correlation, we report Mander's Coefficient for the GFP and ATTO647N channels relative to one another. The colocalization test was run with Costes approximation and 25 iterations of randomized pixels.

Human neutrophil infections

Human cord blood was collected following approval of the Care New England Women & Infants Hospital IRB, Project number 04-0061. To isolate white blood cells, 4mL of cord blood was lysed with red blood cell lysis buffer (BioLegend) in the dark for 20 minutes. Cells were then washed 2x in assay buffer. Cells were suspended in 1.20mL of assay buffer and 100μLwas used per sample. Samples were inoculated with 15μL of bi-fluorescent *S. aureus* prepared as described above. Cells were incubated for 15 minutes at 37C, washed with warm lysostaphin, and brought to a final volume of 100uL. At the given time points (0, 30, 60, and 120 minutes) 10μL of the sample was plated into 200μL of cold PBS/FBS for analysis using a MACSQuant flow cytometer.

Statistical analysis

Graphical depictions of the data represent group means and standard deviations (SD) generated using Prism 9 (GraphPad). The SD represents biological replicates across all figures except Figure 3C, in which the SD is representative of technical replicates calculating the CFU from one sample lysate for the distinct samples represented by each point on the plot. Where indicated, statistical analysis was conducted to compare groups. First, significance was calculated by the Prism 9 ordinary one-way ANOVA test. A p-value threshold of 0.05 indicated a significant difference when comparing the four groups (WT low, WT high, CGD low, CGD high) to one another using Tukey's multiple comparisons tests. When there was no significant difference between the low and high dose for the same genotype but there was a significant difference between genotypes for each dose, this was represented graphically by grouping the genotypes under one line and indicating the asterisk for the highest multiple comparisons p-value determined by Tukey's test. Asterisks indicate significance as follows: "ns" (not significant) for $p>0.05$, * for $p<0.05$, ** for $p<0.01$, *** $p<0.001$, and **** for $p<0.0001$.

Results

ATTO647N-NHS Ester fluorescently labels *S. aureus*

We found that staining superfolded GFP-producing *S. aureus* (18) with a low concentration of ATTO647N-NHS Ester generated a pure population of ATTO647N$^+$GFP$^+$ bi-fluorescent particles (Figure 1A). The stain did not affect *S. aureus* viability as the growth rate in culture was comparable to the unstained GFP-fluorescing *S. aureus* (Figure 1B). We predicted that with bacterial cell division, the ATTO647N mean fluorescent intensity (MFI) would decrease due to the dilution of the intracellular concentration of the dye. To determine the change in fluorescent intensity with proliferation, bi-fluorescent and GFP-fluorescent *S. aureus* cultures were grown from an initial optical density (OD) of 0.1. As expected, *S. aureus* stably expressing GFP maintained a detectable signal with culture growth, as particles remained nearly 100% GFP$^+$ compared to a non-fluorescing, unstained *S. aureus* control (Figure 1C). The GFP MFI also remained robust with culture growth and was comparable between the bi-fluorescent and GFP-fluorescent groups (Figure 1D). The ATTO647N MFI began to decrease with growth in culture as the OD increased (Figure 1D). However, with the bacterial proliferation, the ATTO647N signal remained high enough to differentiate between stained and unstained *S. aureus* until an OD of 1.0 when the population begins to overlap with the unstained control (Figure 1E). Overall, the ATTO647N signal of conjugated *S. aureus* remains detectable after a substantial level of bacterial replication, without affecting *S. aureus* growth, making it an optimal candidate as a secondary marker for the assessment of bacterial killing by leukocytes.

ATTO647N-NHS ester fluorescence is resistant to intraphagosomal bleaching

Conditional ectopic expression of transcription factor *Hoxb8* in murine bone marrow stem cells produces a progenitor cell line capable of exponential expansion while *Hoxb8* is induced or neutrophil differentiation through *Hoxb8* withdrawal (22). Differentiation of *Hoxb8* progenitors derived from a wild-type (WT) C57BL/6 mouse into mature neutrophils (HB8 neutrophils) was confirmed through characterization of surface markers. Differentiation of progenitors into neutrophils was confirmed by increased Ly6G expression and loss of cKit expression by HB8 neutrophils (Supplemental Figures 1A, B). HB8 neutrophils produce ROS and have microbial killing capacity *in vitro* (20), making them a useful screening tool for the effects of phagocytosis and intracellular killing of the bi-fluorescent *S. aureus*. For preliminary experiments, the bi-fluorescent *S. aureus* was phagocytosed by HB8 neutrophils *in vitro*, treated with lysostaphin

10.3389/fimmu.2023.1089111

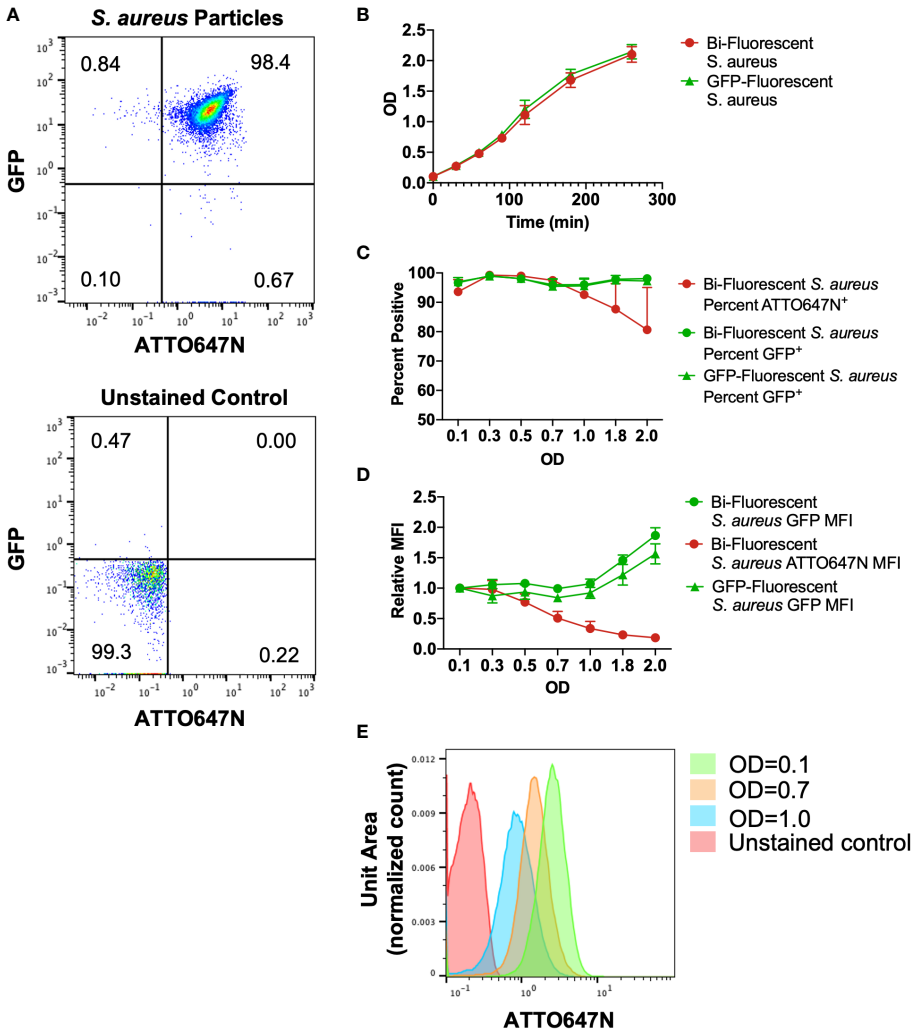

FIGURE 1
Characterization of cultured bi-fluorescent *S. aureus*. **(A)** Staining GFP-*S. aureus* with 200ng/mL ATTO647N-NHS Ester generates a pure population of bi-fluorescent *S. aureus* detectable by flow cytometry. **(B)** The growth curve of S. aureus with or without secondary ATTO647N-NHS Ester stain was indistinguishable. **(C)** The percent of particles gated as GFP^+ or $ATTO647N^+$ relative to unstained control demonstrates a loss of detection of the ATTO647N signal with bacterial replication. **(D)** Geometric mean fluorescent intensity (MFI) of GFP or ATTO647N signal relative to the signal at the start of growth in culture demonstrates robust GFP MFI and loss of ATTO647N signal with bacterial replication (n=3, performed across three independent experiments). **(E)** Representative shifts in the ATTO647N fluorescent intensity towards the unstained control with increasing OD, with overlap visualized at OD=1.0.

to remove residual extracellular *S. aureus* (24), and changes in fluorescence were monitored over time as intracellular killing occurred (Figure 2A). Treating cells with cytochalasin D before inoculation to prevent phagocytosis by disrupting the actin cytoskeleton blocked neutrophils from acquiring the GFP and the ATTO647N signal, confirming that the detected fluorescence is predominantly acquired by internalizing *S. aureus* (Supplemental Figures 2A, B).

At the initial time point following phagocytosis, the HB8 neutrophils with engulfed *S. aureus* acquired the bi-fluorescent properties, as measured by flow cytometry (Figure 2B). The percentage of $ATTO647N^+$ events was stable over time despite changes in the percentage of GFP^+ events (Figure 2C). As expected, the percentage of GFP^+ events and GFP MFI decreased over time in HB8 neutrophils, suggesting successful intracellular *S. aureus* killing (Figure 2D). Importantly, these metrics remained the same over time in the ATTO647N channel (Figure 2D). HB8 neutrophils treated with diphenyleneiodonium (DPI), to inhibit the generation of ROS, exhibit a robust GFP signal that is maintained over time (Figures 2B–D). The bleaching of the GFP signal, but not the ATTO647N signal, suggests that the latter fluorophore is resistant to quenching by neutrophils and remains stable in the conditions of the active phagosome.

Taken together, these results suggest that ATTO647N fluorescence identifies the population of cells that have undergone phagocytosis of *S. aureus* and GFP fluorescence indicates which of those cells contain viable *S. aureus*. Therefore, we can group cells that have encountered the bi-fluorescent *S. aureus* into three categories: $ATTO647N^+GFP^+$ cells which have viable intracellular *S. aureus*, $ATTO647N^+GFP^-$ cells which have non-viable intracellular *S. aureus*, and $ATTO647N^-GFP^-$ cells which have not phagocytosed *S. aureus*.

10.3389/fimmu.2023.1089111

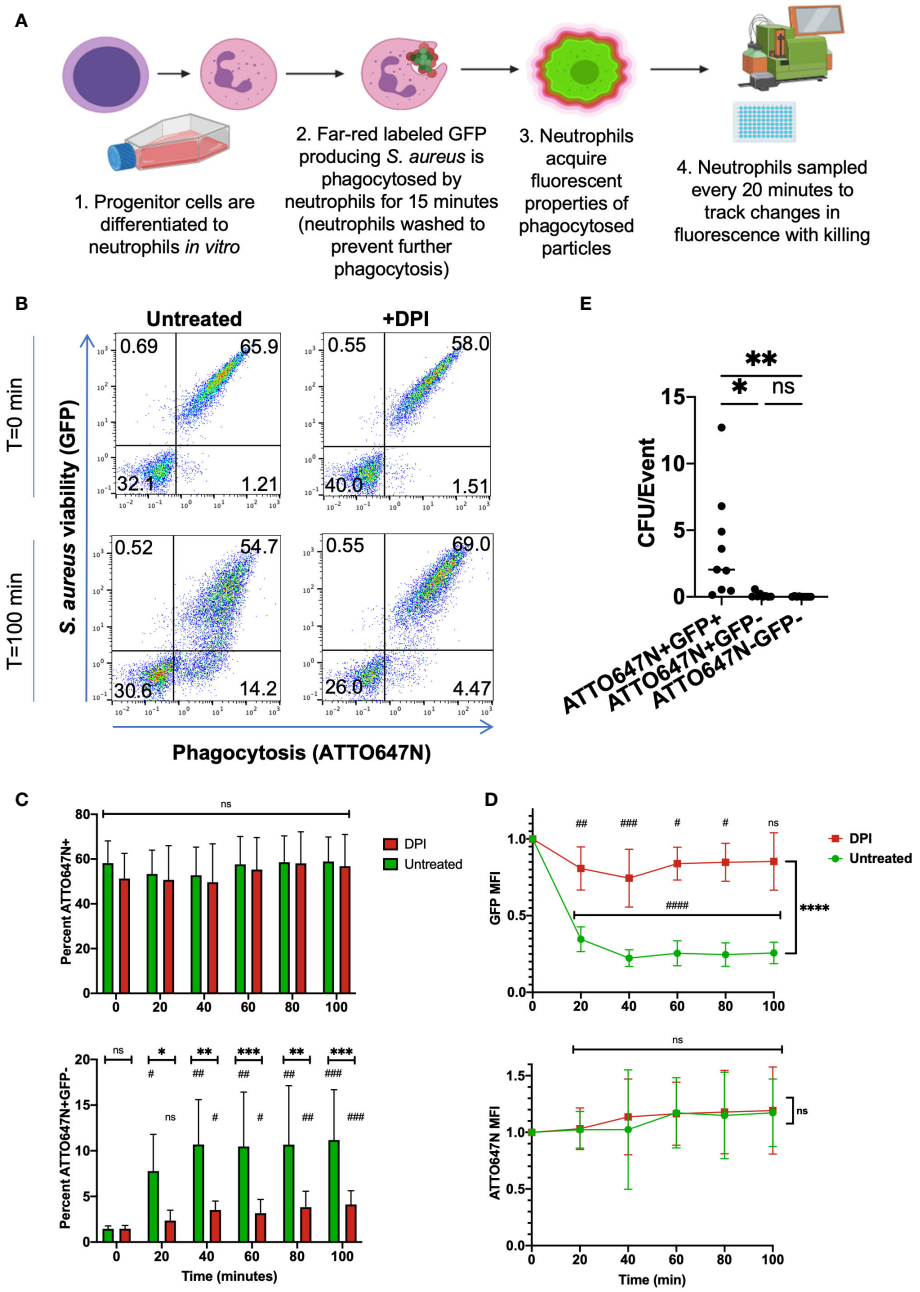

FIGURE 2
In vitro killing assay of bi-fluorescent *S. aureus*. **(A)** Schematic of *in vitro* screening process of bi-fluorescent *S. aureus*. **(B)** Immediately following phagocytosis, HB8 neutrophils are either ATTO647N$^-$GFP$^-$ or ATTO647N$^+$GFP$^+$. After 100 minutes, an ATTO647N$^+$GFP$^-$ population forms in the untreated group but not the DPI-treated group. **(C)** The percent of total ATTO647N$^+$ HB8 neutrophils remains constant over time with no significant difference between untreated and DPI groups, or between the initial time point and subsequent time points within each group. Meanwhile, the percent of ATTO$^+$GFP$^-$ cells increases over time within each group (statistical significance indicated by #) and these changes are significantly greater in the untreated cells relative to the DPI treated cells at each time point (statistical significance indicated by *) **(D)** Quantification of GFP MFI within the ATTO647N$^+$ events shows a dramatic loss of fluorescence over time in the untreated cells compared to the DPI treated cells and compared to the initial time point (the statistical significance between each time point relative to the initial time point is indicated by #; statistical significance between the untreated and DPI group is indicated by *). Meanwhile, the ATTO647N MFI remains consistent in both groups (n=9, performed across three independent experiments). **(E)** Bacterial burden from sorted cell lysates from both DPI treated and untreated cells, normalized to the total number of sorted events (n=9, performed across two independent experiments). "ns" (not significant) for p>0.05, * for p<0.05, ** for p<0.01, *** p<0.001, and **** for p<0.0001.

Fluorescent properties of neutrophils reflect intracellular *S. aureus* viability

To validate that the ATTO647N and GFP fluorescence associated with neutrophils represent the expected intracellular *S. aureus* viability, we exposed neutrophils to bi-fluorescent *S. aureus* and then sorted cells within the three quadrants described above. After allowing 120 minutes for intracellular killing of ingested *S. aureus*, both untreated and DPI-treated HB8 neutrophils were sorted, lysed, and plated on solid media to quantify the number of viable *S. aureus*. Cells were lysed using deionized water with a pH of 11 to release all viable intracellular bacteria and ensure that *S. aureus* colonies were

not under-represented due to impaired dispersal on the agar plate (23). The number of *S. aureus* colony forming units (CFUs) was normalized to the number of events (HB8 neutrophils) that were sorted from the bulk population. Both the ATTO647N^{+}GFP^{-} and ATTO647N^{-}GFP^{-} sorted cell populations yielded negligible CFU (Figure 2E). Meanwhile, the sorted ATTO647N^{+}GFP^{+} cells contained significantly more CFUs confirming the presence of viable intracellular *S. aureus* (Figure 2E). These data also validate that the quenching of GFP is a reliable marker for neutrophils that have completed intracellular killing of *S. aureus*.

Next, we investigated whether the GFP MFI was related to intracellular *S. aureus* viability. Microscopic imaging of HB8 neutrophils after 120 minutes of intracellular killing in suspension provides insight into the variability of neutrophil phagocytosis and killing (Figures 3A, B). Within the bulk population, there are HB8 neutrophils that have phagocytosed different quantities of *S. aureus* particles, as indicated by the broad range of ATTO647N fluorescent intensity by flow cytometry (Figure 2B) and visualized microscopically (Figures 3A, B). Accordingly, in the untreated HB8 neutrophil population some cells have both viable (GFP^{+}) and non-viable (GFP^{-}) particles internalized and potentially within the same phagolysosome (Figure 3B). Meanwhile, based on GFP fluorescence, nearly all *S. aureus* is near completely viable DPI-treated cells (Figure 3B). These images, in conjunction with the findings of Schwartz, et al., establish a positive relationship between GFP fluorescence and *S. aureus* cocci within neutrophils suggesting that GFP MFI may provide insight into the intracellular *S. aureus* burden of individual cells or bulk populations. We expect that cells or populations with a higher MFI have a greater bacterial burden despite some degree of variability in the fluorescent intensity of the original *S. aureus* population (Figure 1A).

To generate cell populations with various MFIs, we inoculated HB8 neutrophils with an increasing multiplicity of infection and sorted the ATTO647N^{+}GFP^{+} population of neutrophils 120 minutes after allowing the intracellular killing to occur. As expected, we found that the cell populations with higher GFP MFI had a greater intracellular bacterial burden (Figure 3C). We also wanted to determine whether the GFP MFI of DPI-treated neutrophils was

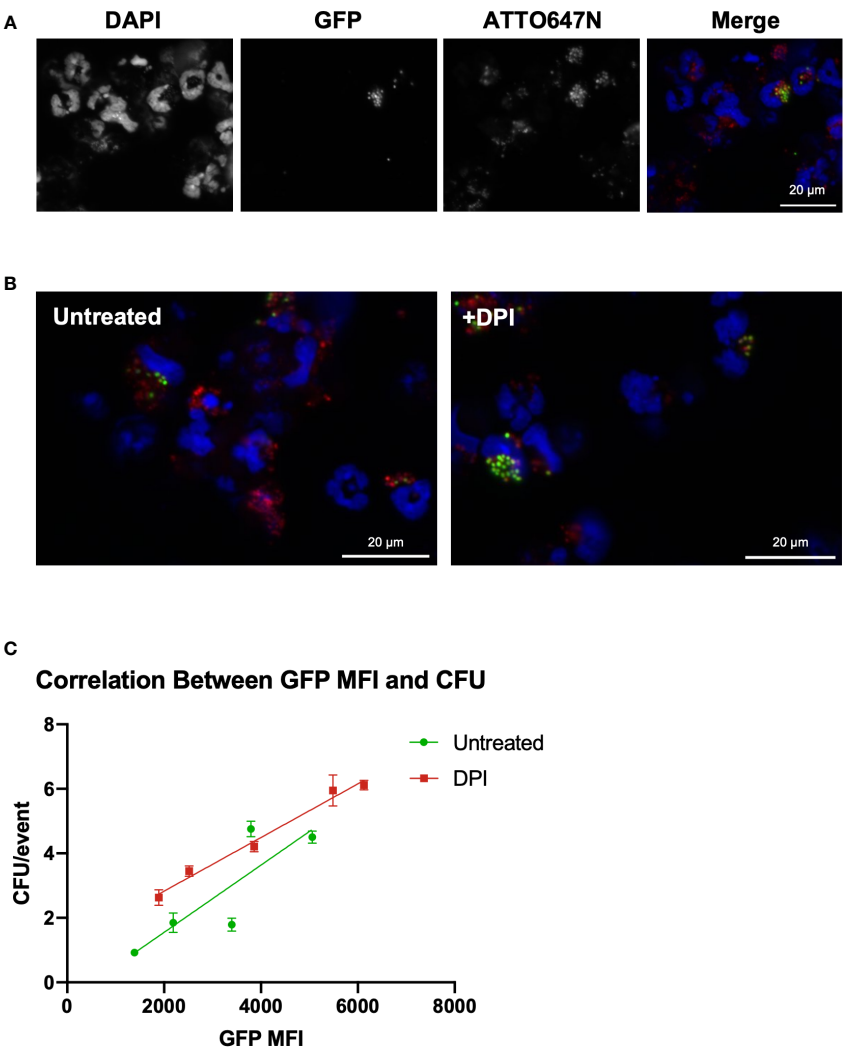

FIGURE 3
GFP fluorescent intensity correlates with the number of viable internalized *S. aureus* cocci. **(A)** Imaging of HB8 neutrophils after 2 hours of killing *in vitro* (40x). **(B)** GFP/ATTO647N merged images for untreated and DPI treated HB8 neutrophils (40x). **(C)** Correlation between GFP MFI and viable intracellular bacterial burden (CFU representative of plating lysate in triplicate).

proportionately representing viable intracellular bacterial burden, a key question given that GFP quenching is ROS-dependent (17). We found the correlation between GFP MFI and CFUs from the DPI-treated sample was comparable to that of the control, supporting the notion that GFP MFI is a robust parameter for quantifying intracellular bacterial burden (Figure 3C).

Application of bi-fluorescent *S. aureus* to demonstrate neutrophil dysfunction

Chronic granulomatous disease (CGD) is marked by neutrophil dysfunction due to a loss of function of the NADPH oxidase responsible for superoxide production in the phagolysosome. Since *S. aureus* killing is dependent on NADPH oxidase activity, hosts with CGD are disproportionately susceptible to *S. aureus* infections (7). Loss-of-function mutations in the x-linked *CYBB* gene encoding the $gp91^{phox}$ subunit are the most common cause of CGD. The widely used murine CGD model harbors knockout of the *Cybb* gene leading to loss of ROS production by neutrophils. CGD mice recapitulate the human disease well, including the impaired clearance of *S. aureus* infections (25). Therefore, we used this disease model to assess the *in vivo* use of the bi-fluorescent *S. aureus* to quantify neutrophil killing capacity.

We harvested samples from wild-type (WT) and CGD mice twelve hours after pulmonary infection with a low ($6x10^7$ CFU) or high ($8x10^7$ CFU) inoculum of bi-fluorescent *S. aureus*. Since the ATTO647N signal dilutes with significant bacterial replication, we recognize that bi-fluorescent *S. aureus* is primarily applicable to analyzing the acute response to infection. Bronchoalveolar lavages (BAL) were collected and stained with anti-Ly6G to identify the neutrophils *via* flow cytometry (Figure 4A). Very few $Ly6G^-$ events were GFP^+ or $ATTO647N^+$ indicating that neutrophils were the predominant cell type responsible for phagocytosis of *S. aureus* in the airspaces at this time point (Supplemental Figure 3).

After gating for $Ly6G^+$ events to identify neutrophils within the BAL, we were able to assess their *S. aureus* killing capacity based on the GFP and ATTO647N fluorescence associated with neutrophils (Figure 4A). Since the percent of neutrophils that engage in phagocytosis varies between experiments, we calculated a killing index defined as the percent of neutrophils that had completed killing relative to the percentage of neutrophils engaged in phagocytosis ($ATTO^+GFP^-/ATTO^+GFP^{+/-}$). Based on this metric, populations with a ratio closer to 1 represent greater success in killing *S. aureus* relative to populations closer to 0. We observed that the killing index of CGD neutrophils was significantly lower than that of the WT controls (Figure 4B).

The fraction of BAL neutrophils within each ATTO647N/GFP quadrant also behaved as expected based on genotype. The percentage of neutrophils containing viable *S. aureus* ($ATTO647N^+GFP^+$) was greater for the CGD animals than for the WT animals (Figure 4C). Since CGD leads to increased recruitment of neutrophils to the BAL (6, 25), we also compared the total number of neutrophils within each gate. Again, the CGD host trended towards a higher total neutrophil

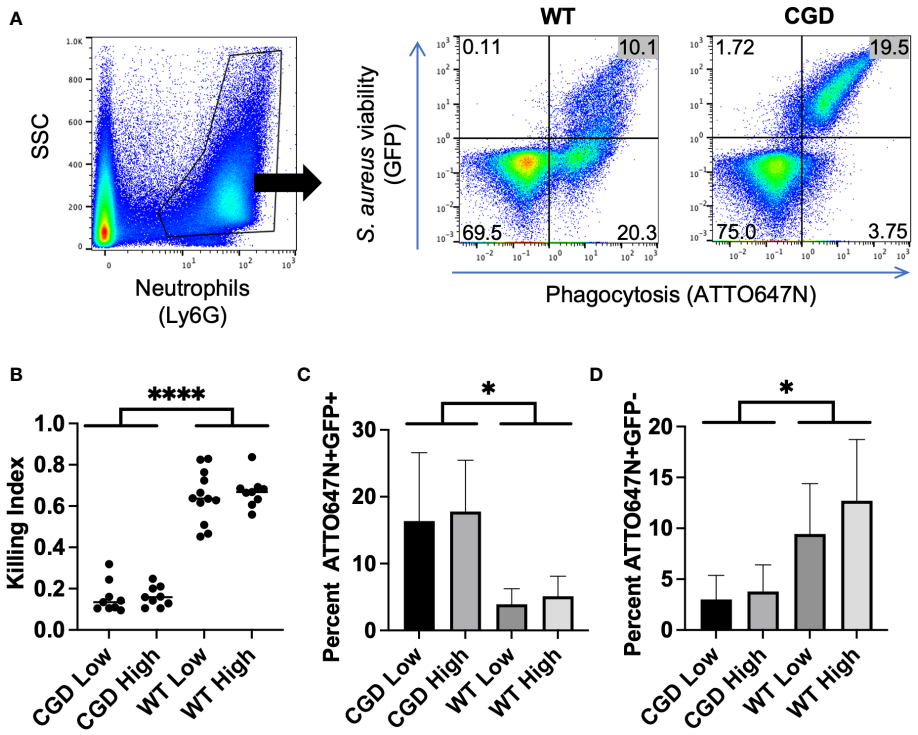

FIGURE 4
BAL from WT and CGD animals infected with bi-fluorescent *S. aureus*. **(A)** Gating on $Ly6G^+$ events within the BAL enables the separation of neutrophils based on GFP and ATTO647N fluorescence. **(B)** The ratio of $ATTO647N^+GFP^-$ cells to all $ATTO647N^+$ cells represents the neutrophils that have completely killed the *S. aureus* compared to those which have undergone phagocytosis: the killing index. **(C)** Percent of neutrophils that are $ATTO647N^+GFP^+$ indicated the intracellular burden of viable *S. aureus*. **(D)** Percent of neutrophils that are $ATTO647N^+GFP^-$ indicates the population of cells that have completed killing (n=8-11 animals per group, from 7 independent experiments). * for $p<0.05$ and **** for $p<0.0001$.

10.3389/fimmu.2023.1089111

count compared to WT mice (Supplemental Figure 4). This demonstrates a larger intracellular burden of viable *S. aureus* in CGD BAL neutrophils, accompanied by a diminished population of ATTO647N^{+}GFP^{-} neutrophils that had completed killing *S. aureus* (Figure 4D). We speculate that the small population of ATTO647N^{+}GFP^{-} cells in the CGD animals may represent the phagocytosis of dead *S. aureus* or the successful employment of non-oxidative mechanisms to kill *S. aureus*. *In vitro*, we observed that both WT and CGD neutrophils readily ingest heat-killed *S. aureus* and acquire ATTO647N fluorescence (Supplemental Figure 5). It is also possible that non-oxidative killing mechanisms are effective in cells with a low level of *S. aureus* phagocytosis, as the ATTO647N^{+}GFP^{-} neutrophil population in CGD mice has a significantly lower ATTO647N mean fluorescent intensity compared to the same population from WT mice (Figure 5A).

Having shown that the GFP MFI of neutrophils that have taken up *S. aureus* corresponds to the viable intracellular burden of *S. aureus*, we performed further analyses of BAL neutrophils from WT and CGD mice that were infected with bi-fluorescent *S. aureus*. We observed a similar relationship *in vivo* as was established *in vitro*,

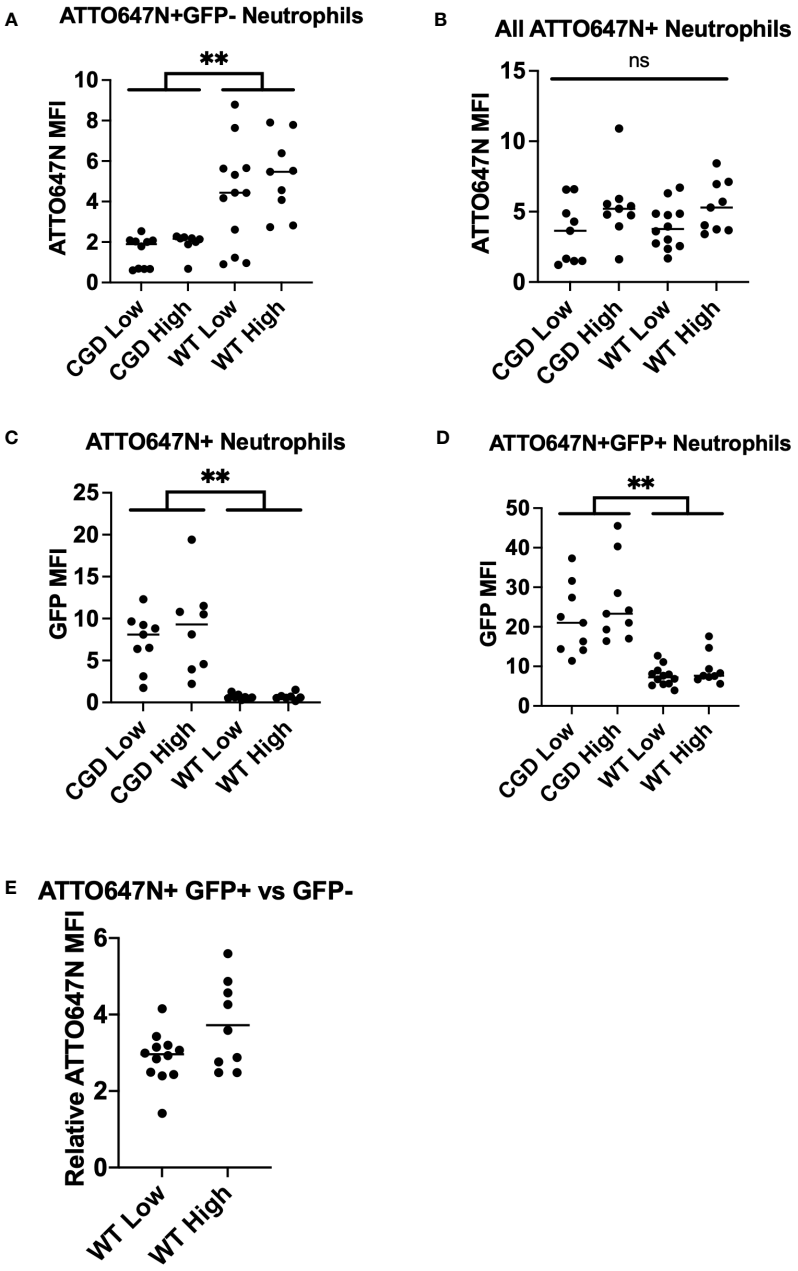

FIGURE 5
Analysis of BAL neutrophil subpopulation fluorescent intensities. **(A)** WT neutrophils have increased ATTO647N MFI for neutrophils that have completed killing, indicating clearance of larger bacterial burdens on a per-cell basis. **(B)** The neutrophil ATTO647N MFI was comparable between groups implying similar levels of phagocytosis. **(C)** The GFP MFI for all ATTO647N^{+} events demonstrate an increased bacterial burden in phagocytosing CGD neutrophils relative to WT neutrophils. **(D)** GFP MFI of the ATTO647M^{+}GFP^{+} population demonstrates the same trend of increased intensity in CGD animals. **(E)** The relative ATTO647N MFI was calculated by dividing the ATTO647N MFI of ATTO647N^{+}GFP^{+} events by ATTO647N^{+}GFP^{-} events (n=8-11 animals per group, from 7 independent experiments). "ns" (not significant) for $p>0.05$, ** for $p<0.01$.

suggesting that BAL neutrophils with a greater GFP MFI contain a greater *S. aureus* bacterial burden (Figure 3C; Supplemental Figure 6). Comparing the ATTO647N MFI for all ATTO647N$^+$ events, we observed no differences across groups (Figure 5B), implying that the degree of phagocytosis is comparable between the WT and CGD neutrophils. We first looked at the GFP MFI of all neutrophils involved in phagocytosis to understand the overall population activity. The CGD ATTO647N$^+$ neutrophils had a significantly higher GFP MFI compared to the analogous population of neutrophils in WT animals, further supporting the conclusion that the population of neutrophils with viable intracellular *S. aureus* is greater in the CGD animals (Figure 5C). Next, we analyzed the GFP MFI of only the cells with viable intracellular *S. aureus* (ATTO647N$^+$GFP$^+$) and again observed a greater GFP MFI for CGD neutrophils relative to WT (Figure 5D). We recognize that the analysis of ATTO647N$^+$GFP$^+$ may be biased if the GFP MFI of cells with a lower intracellular burden are more efficient at killing (and transitioning to the GFP$^-$ population), which may lead to a higher GFP signal in the remaining population of cells. However, MFI information from ATTO647N$^+$GFP$^+$ neutrophils is valuable to understanding the state of cells which are unable to complete ROS-dependent intracellular killing of *S. aureus*. In BAL neutrophils from WT mice, we also observe that the ATTO647N MFI is higher in the ATTO647N$^+$GFP$^+$ population than in the ATTO647N$^+$GFP$^-$ population (Figure 5E), supporting the observations of others that neutrophils with increased intracellular *S. aureus* burden have decreased intracellular killing (17).

Bi-fluorescent *S. aureus* allows localization within the airspace *in vivo*

Analyses to probe the localization of cells laden with *S. aureus* within the context of the surrounding tissue environment provide insight into the dynamics of the host response. To visualize bi-fluorescent *S. aureus in vivo*, we imaged frozen sections from WT mice twelve hours post-infection. Merging DAPI, ATTO647N, and GFP images enabled the identification and localization of viable and nonviable *S. aureus* (Figures 6A–D). We again often observed viable cocci with larger clumps or clusters compared to the non-viable ones (Figure 6D).

Visualization of infected lung tissue by microscopy emphasizes the presence of cocci throughout, as opposed to analysis of killing on a single-cell level by flow cytometry. Images were analyzed to determine the degree of colocalization of the GFP and ATTO647N fluorescent signal. Mander's coefficient was calculated to quantify spatial overlap for GFP and ATTO647N. We expected that Mander's coefficient for the GFP channel would be equivalent to one, since anywhere GFP-expressing viable *S. aureus* is detected, the ATTO647N fluorescent signal should also be present. As anticipated, the average Mander's coefficient for the GFP channel was 0.92 +/- 0.08 (Figure 6E). The Mander's coefficient in the ATTO647N channel ranged from 0.44 to 0.86 (Figure 6E). This value roughly represents the proportion of cocci that are still viable, marked by the overlapping GFP signal. This proportion is higher compared to the proportion of cells with viable internalized *S. aureus* measured by the killing index or GFP fluorescence intensity measured by flow cytometry (Figures 4, 5). However, the Mander's coefficient is representative of all cocci, both intracellular and extracellularly located, while the flow cytometry analysis only measures intracellular killing. This difference also highlights the differences in looking at *S. aureus* killing on a per-cell basis versus a per-cocci basis and further supports the notion that cells heavily loaded with cocci may have impaired killing. Finally, differences in the killing index and Mander's coefficient may represent differences in the killing capacity of cells found in the BAL as opposed to whole tissue.

Bi-fluorescent *S. aureus* is killed by human leukocytes

Animal models of infection have obvious benefits for studying disease *in vivo*. However, findings in the murine host do not always translate to human pathophysiology. To investigate whether the assay we have extensively characterized using murine neutrophils translates to human cells, we conducted a screen of the bi-fluorescent *S. aureus* in human leukocytes. Cells were obtained from freshly drawn umbilical cord blood samples that were subjected to red blood cell lysis and then inoculated with bi-fluorescent *S. aureus* to characterize changes in fluorescence over time.

The use of the ATTO647N-Ester conjugation of *S. aureus* to identify cells that have undergone *S. aureus* phagocytosis translates well to human cells, as we observed that leukocytes maintained a robust ATTO647N MFI over time (Figure 7A). Again, the GFP fluorescence intensity decreased over time, suggesting intracellular killing of *S. aureus* within the untreated group. These findings were confirmed *via* microscopic imaging of cells two hours after allowing phagocytosis and intracellular killing to occur in suspension. Many cells contain particles with ATTO647N fluorescence (red) in the absence of GFP (Figure 7B). The areas which did have viable *S. aureus*, determined by co-localized ATTO647N and GFP (yellow), were predominantly present in cells that had likely had multiple phagolysosomes based on their distribution. The DPI-treated samples largely showed viable *S. aureus* within cells (Figure 7D). Interestingly, the GFP MFI decreased more than expected—though not to the degree of the untreated cells—in the DPI-treated cells (Figures 7A, E). This apparent decrease in GFP fluorescence intensity was also accompanied by a slight decrease in percent GFP$^+$ events within the ATTO647N$^+$ population (Figure 7C). Taken together, these data indicate that bi-fluorescent S. aureus reports its internalization and eradication by human leukocytes.

Discussion

The rapid and voluminous response of neutrophils to *S. aureus* infection is critical to halt its progression from its initial site. During the acute stages of the innate immune response, there is a complex orchestration of cellular host defense as the inflammatory environment develops. Early events can quickly shift the microbial burden towards containment and eradication, or, in cases of inadequate immunity, towards the expansion and dissemination of infection. Understanding the innate immune response to *S. aureus* as it occurs at tissue sites requires innovative techniques for measuring

10.3389/fimmu.2023.1089111

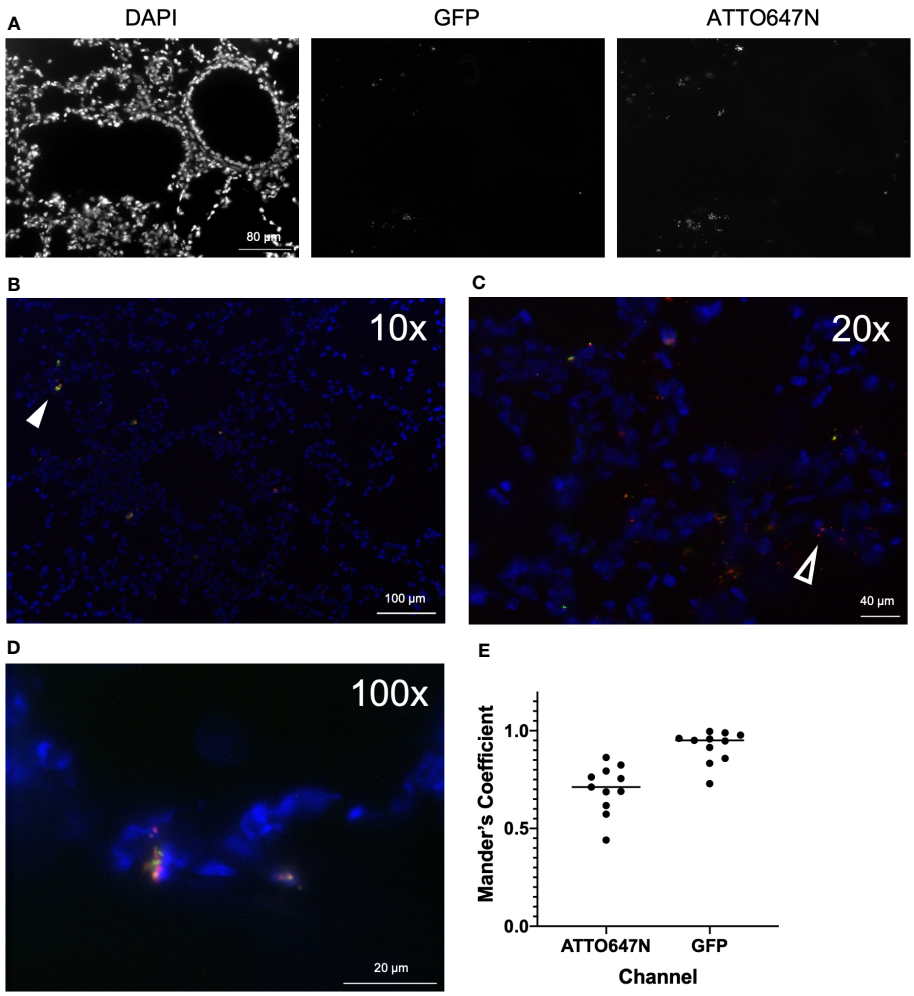

FIGURE 6
Imaging of airways post-infection with bi-fluorescent *S. aureus*. **(A)** Frozen lung sections were prepared from WT mice (n=3) 12 hours post-infection with bi-fluorescent *S. aureus* to visualize the infection in the tissue. Unmerged DAPI, GFP, and ATTO647N images show localization of airway cells, viable *S. aureus*, and total *S aureus*, respectively (20x). Merged images at **(B)** 10x **(C)** 20x and **(D)** 100x visualize both killed (red, open arrowhead) and viable (yellow, arrowhead) *S. aureus* within the tissue. **(E)** Colocalization analysis of GFP and ATTO647N images (n=11) show high overlap of the GFP signal with the ATTO647N signal (Mander's Coefficient ~1) and incomplete overlap of the ATTO647N signal with the GFP signal (Mander's Coefficient <1).

cell function against microbes. In this study, we have further developed a method to detect and quantify the intracellular eradication of *S. aureus* and demonstrate its utility *in vivo* and at the resolution of individual cells.

The use of bi-fluorescent *S. aureus* to quantify its intracellular killing *in vivo* provides convenient insight into the mechanism and dynamics of neutrophil phagocytosis and microbicidal activity of the phagosome. Single-cell analysis of killing activity provides a valuable tool for better understanding the role of cellular subpopulations in bacterial clearance *in vivo*. The relevant applications of this adapted technique include neutrophil heterogeneity studies in pathological and non-pathological states (26–31). Despite a growing understanding of the existence of different subpopulations of neutrophils, much remains unknown as to the relation between characterized differences and influence on function. Tsuda et al. previously identified three subsets of neutrophils in the context of susceptibility to *S. aureus* infection. Despite variable surface markers and cytokine production profiles, subsets were described to have similar *in vitro* MRSA killing capabilities (29). However, when subject to the *in vivo* environment these neutrophil subsets may respond differently to the cytokines they produce or their ability to crosstalk with other immune cells, modulating their bactericidal activity. Characterization of the neutrophil subpopulation which readily engulfs and kills *S. aureus*—as identified by the $ATTO^{+}GFP^{-}$ population in the assay we characterize here—may provide insight for developing therapies that support or augment innate immune function.

In the study that first characterized GFP-expressing *S. aureus* as a tool for quantifying its intracellular viability, Schwartz et al. described amplified resistance of *S. aureus* to eradication as the number of cocci within the neutrophil increased *in vitro* (17). While validating the use of this assay, we observed a similar trend *in vivo* as neutrophils with viable intracellular *S. aureus* were predominantly those that had engulfed a greater number of *S. aureus*. The relatively large population of neutrophils that have not undergone phagocytosis but are present in the BAL provokes questions as to why some cells engulf more *S. aureus* than they can efficiently kill while others do not internalize any. In studies of competitive phagocytosis, others have described phagocytosis as a

10.3389/fimmu.2023.1089111

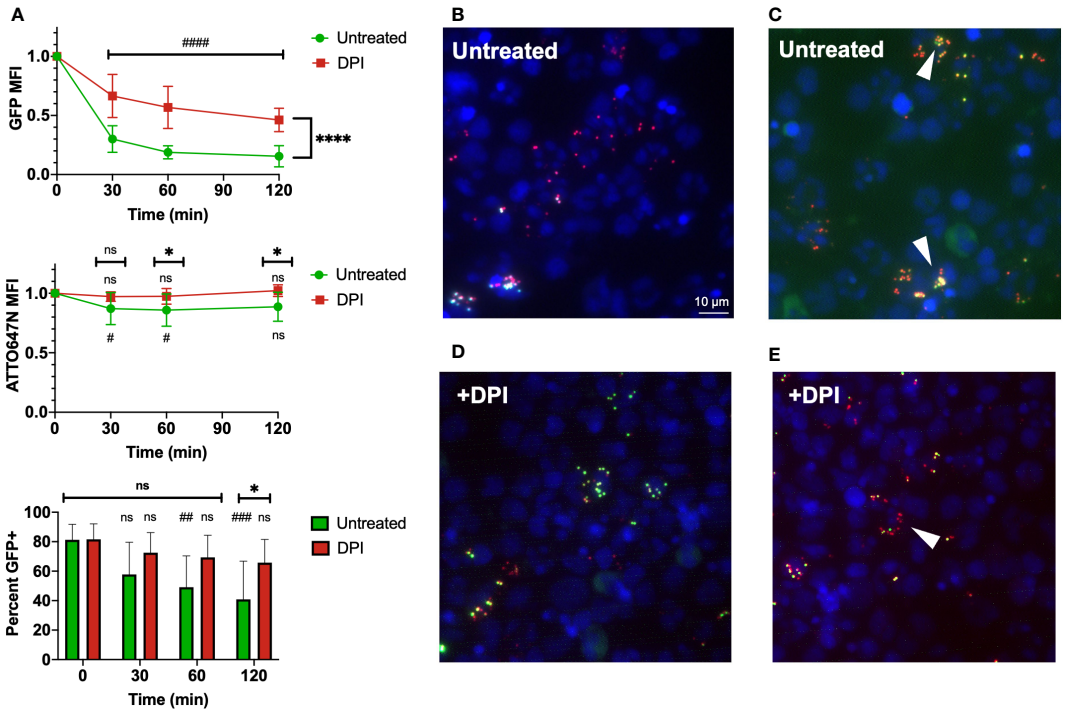

FIGURE 7
Use of bi-fluorescent *S. aureus* to model infection in human neutrophils. **(A)** Human leukocytes inoculated with bi-fluorescent *S. aureus* maintain the ATTO647N fluorescent signal while quenching the GFP fluorescent intensity over time based on intensity and percent GFP^+ cells, statistical differences between groups indicated with a * and differences within each group relative to the initial time point indicated with a # (n=8, performed across three independent experiments). **(B)** Imaging (60x) performed two hours after human cells were infected *in vitro* demonstrates cells with few cocci broadly kill the internalized *S. aureus* and fluoresce as $ATTO647N^+$ (red). **(C)** Cells that have viable *S. aureus* internalized $ATTO647N^+GFP^+$ (yellow, arrowheads) often have internalized larger clumps of *S. aureus*. **(D)** DPI treated human cells largely have viable (yellow) internalized *S. aureus* regardless of cocci internalized. **(E)** Some DPI treated cells still quench the GFP fluorescent signal (red, arrowhead). "ns" (not significant) for $p>0.05$, * for $p<0.05$ and **** for $p<0.0001$.

"nonrandom" event, with a subset of neutrophils more likely to undergo phagocytosis (32). There is even apparent variability within a single neutrophil, as the production of HOCl within the multiple phagolysosomes of the same cell can occur with widely disparate lag time after formation (26). *S. aureus* has also evolved to evade or neutralize host defenses. For example, the production of superoxide dismutase by *S. aureus* converts the free radicals in the phagolysosome to water and oxygen (15). Therefore, targeting neutrophils to improve their killing capacity through modulating their degree of phagocytosis or intracellular ROS production may improve clearance of infection.

We anticipate that in extending the capability of a *S. aureus* killing assay with single-cell resolution will also enable further pursuit of questions that remain in understanding the mechanisms by which neutrophils eradicate microbes intracellularly. There has been debate as to the precise role of the biochemical pathways and products of the NADPH oxidase in the phagosome. Specifically, there are questions about whether ROS are responsible for direct toxicity towards microbes or confer their antimicrobial capacity predominantly by buffering the phagolysosome for optimal non-oxidative killing activity (e.g., by serine proteases) (10, 12). Our results correlating intracellular CFU and GFP MFI are consistent with the idea that HOCl production, as reported by GFP bleaching, is tightly correlated with the killing of internalized *S. aureus*. However, further investigation to delineate the necessity of proteolytic enzymes is warranted and having a means to quantify both *S. aureus* burden and viability will provide additional insight to solve questions that remain.

Within this study, we included a low and high dose of *S. aureus*, distinguished as being non-lethal and lethal doses, respectively, in CGD mice. The activity of the neutrophils that are recruited to the infected airspaces of the lung was independent of dose, as there were no statistical differences in the fraction of neutrophils that had completed *S. aureus* killing or the neutrophil GFP MFI between mice of the same genotype receiving the different initial bolus of *S. aureus*. This indicates that the activity of neutrophils was dependent on genotype, but not necessarily on potential differences in the environment during the acute response to low versus the high burden of infection. As pathologic resistance to conventional antimicrobial agents steadily increases, methods such as this bi-fluorescent killing assay to study the *in vivo* dynamics of cell-mediated antimicrobial activity will be of the utmost importance to enhance the pursuit of innovative therapeutic development.

Relatedly, it is important to understand how the use of biological or pharmaceutical interventions to treat infection occurs in conjunction with the host's immune response. For example, antibiotics that interfere with the effector functions of immune cells may in turn have detrimental effects despite potent antimicrobial activity *in vitro* (33, 34). Conversely, treatments can have a synergistic effect or support the immune system's intrinsic response leading to better outcomes than expected based on *in vitro* results (35–37). Therefore, when testing and developing treatments, *in vivo* models of infection should be prioritized. This is particularly relevant for therapies targeting *in vivo* evasion tactics of *S. aureus*, which

employs numerous mechanisms to downregulate inflammation, avoid internalization, neutralize anti-microbial factors, and induce neutrophil cytolysis (15, 38). Multiple factors produced by *S. aureus* within the phagolysosome neutralize the antimicrobial components generated by the neutrophil. Anti-virulence therapies are gaining traction but also need to be understood in the context of the host response (39, 40). Consequently, methods to understand and quantify changes in immune-mediated microbial clearance are vital for developing and testing these much-needed new approaches to antimicrobial therapy.

Data availability statement

The raw data supporting the conclusions of this article will be made available by the authors, without undue reservation.

Ethics statement

The studies involving human participants were reviewed and approved by Institutional Review Board, Care New England Women & Infants Hospital. Written informed consent for participation was not required for this study in accordance with the national legislation and the institutional requirements. The animal study was reviewed and approved by Lifespan Animal Welfare Committee, Rhode Island Hospital.

Author contributions

KH: Designing research studies, conducting experiments, analyzing data, writing the manuscript. SL-N: Cord blood collection. JC: Designing research studies, conducting experiments, analyzing data. MM: Designing research studies, conducting experiments, analyzing data. JB: Supervising the project, designing research studies. AH: Developing GFP-*Staphylococcus aureus* strain. CL: Supervising the project, designing research studies, conducting experiments, analyzing data, writing the manuscript. All authors contributed to the article and approved the submitted version.

Funding

This research was supported by awards from the National Institutes of Health (GM124911 to CL; T32GM065085 supported JC).

This study also received funding from Brown Physicians, Inc. The funder was not involved in the study design, collection, analysis, interpretation of data, the writing of this article or the decision to submit it for publication.

Acknowledgments

We thank Dr. Paul Ekert and Dr. Patrice Dubreuil for kindly providing reagents/resources. We greatly appreciate the assistance of Kevin Carlson at the Brown University Flow Cytometry and Sorting Facility. Schematic diagrams were created using BioRender.

Conflict of interest

The authors declare that the research was conducted in the absence of any commercial or financial relationships that could be construed as a potential conflict of interest.

Publisher's note

Supplementary material

The Supplementary Material for this article can be found online at: https://www.frontiersin.org/articles/10.3389/fimmu.2023.1089111/full#supplementary-material

References

1. Garrood T, Lee L, Pitzalis C. Molecular mechanisms of cell recruitment to inflammatory sites: general and tissue-specific pathways. *Rheumatol (Oxford)* (2006) 45:250–60. doi: 10.1093/rheumatology/kei207

2. Margraf A, Lowell CA, Zarbock A. Neutrophils in acute inflammation: current concepts and translational implications. *Blood* (2022) 139:2130–44. doi: 10.1182/blood.2021012295

3. Kolaczkowska E, Kubes P. Neutrophil recruitment and function in health and inflammation. *Nat Rev Immunol* (2013) 13:159–75. doi: 10.1038/nri3399

4. Peiseler M, Kubes P. More friend than foe: the emerging role of neutrophils in tissue repair. *J Clin Invest* (2019) 129:2629–39. doi: 10.1172/JCI124616

5. Rigby KM, DeLeo FR. Neutrophils in innate host defense against staphylococcus aureus infections. *Semin Immunopathol* (2012) 34:237–59. doi: 10.1007/s00281-011-0295-3

6. Song Z, Huang G, Chiquetto Paracatu L, Grimes D, Gu J, Luke CJ, et al. NADPH oxidase controls pulmonary neutrophil infiltration in the response to fungal cell walls by limiting LTB4. *Blood* (2020) 135:891–903. doi: 10.1182/blood.2019003525

7. Nguyen GT, Green ER, Mecsas J. Neutrophils to the ROScue: Mechanisms of NADPH oxidase activation and bacterial resistance. *Front Cell Infect Microbiol* (2017) 7:373. doi: 10.3389/fcimb.2017.00373

8. Cheung GYC, Bae JS, Otto M. Pathogenicity and virulence of staphylococcus aureus. *Virulence* (2021) 12:547–69. doi: 10.1080/21505594.2021.1878688

9. Dinauer MC. Primary immune deficiencies with defects in neutrophil function. *Hematol Am Soc Hematol Educ Program* (2016) 2016:43–50. doi: 10.1182/asheducation-2016.1.43

10. Segal AW. How neutrophils kill microbes. *Annu Rev Immunol* (2005) 23:197–223. doi: 10.1146/annurev.immunol.23.021704.115653

11. Zeng MY, Miralda I, Armstrong CL, Uriarte SM, Bagaitkar J. The roles of NADPH oxidase in modulating neutrophil effector responses. *Mol Oral Microbiol* (2019) 34:27–38. doi: 10.1111/omi.12252

12. Reeves EP, Lu H, Jacobs HL, Messina CG, Bolsover S, Gabella G, et al. Killing activity of neutrophils is mediated through activation of proteases by k+ flux. *Nature* (2002) 416:291–7. doi: 10.1038/416291a

13. Fine N, Tasevski N, McCulloch CA, Tenenbaum HC, Glogauer M. The neutrophil: Constant defender and first responder. *Front Immunol* (2020) 11:571085. doi: 10.3389/fimmu.2020.571085

14. Bodey GP, Buckley M, Sathe YS, Freireich EJ. Quantitative relationships between circulating leukocytes and infection in patients with acute leukemia. *Ann Intern Med* (1966) 64:328–40. doi: 10.7326/0003-4819-64-2-328

15. Greenlee-Wacker M, DeLeo FR, Nauseef WM. How methicillin-resistant staphylococcus aureus evade neutrophil killing. *Curr Opin Hematol* (2015) 22:30–5. doi: 10.1097/MOH.0000000000000096

16. Zinn KR, Chaudhuri TR, Szafran AA, O'Quinn D, Weaver C, Dugger K, et al. Noninvasive bioluminescence imaging in small animals. *ILAR J* (2008) 49:103–15. doi: 10.1093/ilar.49.1.103

17. Schwartz J, Leidal KG, Femling JK, Weiss JP, Nauseef WM. Neutrophil bleaching of GFP-expressing staphylococci: probing the intraphagosomal fate of individual bacteria. *J Immunol* (2009) 183:2632–41. doi: 10.4049/jimmunol.0804110

18. Pang YY, Schwartz J, Thoendel M, Ackermann LW, Horswill AR, Nauseef WM. agr-dependent interactions of staphylococcus aureus USA300 with human polymorphonuclear neutrophils. *J Innate Immun* (2010) 2:546–59. doi: 10.1159/000319855

19. Espey MG, Xavier S, Thomas DD, Miranda KM, Wink DA. Direct real-time evaluation of nitration with green fluorescent protein in solution and within human cells reveals the impact of nitrogen dioxide vs. peroxynitrite mechanisms. *Proc Natl Acad Sci U.S.A.* (2002) 99:3481–6. doi: 10.1073/pnas.062604199

20. Cohen JT, Danise M, Hinman KD, Neumann BM, Johnson R, Wilson ZS, et al. Engraftment, fate, and function of HoxB8-conditional neutrophil progenitors in the unconditioned murine host. *Front Cell Dev Biol* (2022) 10:840894. doi: 10.3389/fcell.2022.840894

21. Cohen JT, Danise M, Machan JT, Zhao R, Lefort CT. Murine myeloid progenitors attenuate immune dysfunction induced by hemorrhagic shock. *Stem Cell Rep* (2021) 16:324–36. doi: 10.1016/j.stemcr.2020.12.014

22. Wang GG, Calvo KR, Pasillas MP, Sykes DB, Hacker H, Kamps MP. Quantitative production of macrophages or neutrophils ex vivo using conditional Hoxb8. *Nat Methods* (2006) 3:287–93. doi: 10.1038/nmeth865

23. Decleva E, Menegazzi R, Busetto S, Patriarca P, Dri P. Common methodology is inadequate for studies on the microbicidal activity of neutrophils. *J Leukoc Biol* (2006) 79:87–94. doi: 10.1189/jlb.0605338

24. Kim JH, Chaurasia AK, Batool N, Ko KS, Kim KK. Alternative enzyme protection assay to overcome the drawbacks of the gentamicin protection assay for measuring entry and intracellular survival of staphylococci. *Infect Immun* (2019) 87:e00119-19. doi: 10.1128/IAI.00119-19

25. Pollock JD, Williams DA, Gifford MA, Li LL, Du X, Fisherman J, et al. Mouse model of X-linked chronic granulomatous disease, an inherited defect in phagocyte superoxide production. *Nat Genet* (1995) 9:202–9. doi: 10.1038/ng0295-202

26. Albrett AM, Ashby LV, Dickerhof N, Kettle AJ, Winterbourn CC. Heterogeneity of hypochlorous acid production in individual neutrophil phagosomes revealed by a rhodamine-based probe. *J Biol Chem* (2018) 293:15715–24. doi: 10.1074/jbc.RA118.004789

27. Rosales C. Neutrophil: A cell with many roles in inflammation or several cell types?. *Front Physiol* (2018) 9:113. doi: 10.3389/fphys.2018.00113

28. Pillay J, Kamp VM, van Hoffen E, Visser T, Tak T, Lammers JW, et al. A subset of neutrophils in human systemic inflammation inhibits T cell responses through mac-1. *J Clin Invest* (2012) 122:327–36. doi: 10.1172/JCI57990

29. Tsuda Y, Takahashi H, Kobayashi M, Hanafusa T, Herndon DN, Suzuki F. Three different neutrophil subsets exhibited in mice with different susceptibilities to infection by methicillin-resistant staphylococcus aureus. *Immunity* (2004) 21:215–26. doi: 10.1016/j.immuni.2004.07.006

30. Silvestre-Roig C, Hidalgo A, Soehnlein O. Neutrophil heterogeneity: implications for homeostasis and pathogenesis. *Blood* (2016) 127:2173–81. doi: 10.1182/blood-2016-01-688887

31. Filep JG, Ariel A. Neutrophil heterogeneity and fate in inflamed tissues: implications for the resolution of inflammation. *Am J Physiol Cell Physiol* (2020) 319: C510–C32. doi: 10.1152/ajpcell.00181.2020

32. Hellebrekers P, Hietbrink F, Vrisekoop N, Leenen LPH, Koenderman L. Neutrophil functional heterogeneity: Identification of competitive phagocytosis. *Front Immunol* (2017) 8. doi: 10.3389/fimmu.2017.01498

33. Kristian SA, Timmer AM, Liu GY, Lauth X, Sal-Man N, Rosenfeld Y, et al. Impairment of innate immune killing mechanisms by bacteriostatic antibiotics. *FASEB J* (2007) 21:1107–16. doi: 10.1096/fj.06-6802com

34. Berti A, Rose W, Nizet V, Sakoulas G. Antibiotics and innate immunity: A cooperative effort toward the successful treatment of infections. *Open Forum Infect Dis* (2020) 7:ofaa302. doi: 10.1093/ofid/ofaa302

35. Sakoulas G, Okumura CY, Thienphrapa W, Olson J, Nonejuie P, Dam Q, et al. Nafcillin enhances innate immune-mediated killing of methicillin-resistant staphylococcus aureus. *J Mol Med (Berl)* (2014) 92:139–49. doi: 10.1007/s00109-013-1100-7

36. Lin L, Nonejuie P, Munguia J, Hollands A, Olson J, Dam Q, et al. Azithromycin synergizes with cationic antimicrobial peptides to exert bactericidal and therapeutic activity against highly multidrug-resistant gram-negative bacterial pathogens. *EBioMedicine* (2015) 2:690–8. doi: 10.1016/j.ebiom.2015.05.021

37. Ulloa ER, Uchiyama S, Gillespie R, Nizet V, Sakoulas G. Ticagrelor increases platelet-mediated staphylococcus aureus killing, resulting in clearance of bacteremia. *J Infect Dis* (2021) 224:1566–69. doi: 10.1093/infdis/jiab146

38. Spaan AN, Surewaard BG, Nijland R, van Strijp JA. Neutrophils versus staphylococcus aureus: a biological tug of war. *Annu Rev Microbiol* (2013) 67:629–50. doi: 10.1146/annurev-micro-092412-155746

39. Ford CA, Hurford IM, Cassat JE. Antivirulence strategies for the treatment of staphylococcus aureus infections: A mini review. *Front Microbiol* (2020) 11:632706. doi: 10.3389/fmicb.2020.632706

40. Fleitas Martinez O, Cardoso MH, Ribeiro SM, Franco OL. Recent advances in anti-virulence therapeutic strategies with a focus on dismantling bacterial membrane microdomains, toxin neutralization, quorum-sensing interference and biofilm inhibition. *Front Cell Infect Microbiol* (2019) 9:74. doi: 10.3389/fcimb.2019.00074

frontiers | Frontiers in Immunology

TYPE Methods
PUBLISHED 25 April 2023
DOI 10.3389/fimmu.2023.1083072

OPEN ACCESS

EDITED BY
Francesca Granucci,
University of Milano-Bicocca, Italy

REVIEWED BY
Tamás Laskay,
University of Lübeck, Germany
Vijay Kumar,
Louisiana State University, United States

*CORRESPONDENCE
Frances S. Grudzinska
f.grudzinska@bham.ac.uk

†These authors have contributed equally to this work and share first authorship

‡These authors share last authorship

SPECIALTY SECTION
This article was submitted to Molecular Innate Immunity, a section of the journal Frontiers in Immunology

RECEIVED 28 October 2022
ACCEPTED 05 April 2023
PUBLISHED 25 April 2023

CITATION
Grudzinska FS, Jasper A, Sapey E, Thickett DR, Mauro C, Scott A and Barlow J (2023) Real-time assessment of neutrophil metabolism and oxidative burst using extracellular flux analysis. *Front. Immunol.* 14:1083072. doi: 10.3389/fimmu.2023.1083072

Real-time assessment of neutrophil metabolism and oxidative burst using extracellular flux analysis

Frances S. Grudzinska[1*†], Alice Jasper[1†], Elizabeth Sapey[1,2], David R. Thickett[1], Claudio Mauro[1], Aaron Scott[1‡] and Jonathan Barlow[3‡]

[1]Birmingham Acute Care Research Group, Institute of Inflammation and Ageing, University of Birmingham, Birmingham, United Kingdom, [2]PIONEER Health Data Research- UK Hub in Acute Care, Institute of Inflammation and Ageing, University of Birmingham, Birmingham, United Kingdom, [3]Cellular Health and Metabolism Facility, School of Sport, Exercise and Rehabilitation Sciences, University of Birmingham, Birmingham, United Kingdom

Neutrophil responses are critical during inflammatory and infective events, and neutrophil dysregulation has been associated with poor patient outcomes. Immunometabolism is a rapidly growing field that has provided insights into cellular functions in health and disease. Neutrophils are highly glycolytic when activated, with inhibition of glycolysis associated with functional deficits. There is currently very limited data available assessing metabolism in neutrophils. Extracellular flux (XF) analysis assesses real time oxygen consumption and the rate of proton efflux in cells. This technology allows for the automated addition of inhibitors and stimulants to visualise the effect on metabolism. We describe optimised protocols for an XFe96 XF Analyser to (i) probe glycolysis in neutrophils under basal and stimulated conditions, (ii) probe phorbol 12-myristate 13-acetate induced oxidative burst, and (iii) highlight challenges of using XF technology to examine mitochondrial function in neutrophils. We provide an overview of how to analyze XF data and identify pitfalls of probing neutrophil metabolism with XF analysis. In summary we describe robust methods for assessing glycolysis and oxidative burst in human neutrophils and discuss the challenges around using this technique to assess mitochondrial respiration. XF technology is a powerful platform with a user-friendly interface and data analysis templates, however we suggest caution when assessing neutrophil mitochondrial respiration.

KEYWORDS

neutrophils, extracellular flux analysis, immunometabolism, glycolysis, oxidative burst

Introduction

Neutrophils are vital in the host response to infection and inflammation. Neutrophil dysfunction is described at the extremes of age, in overwhelming infection, in chronic diseases and is associated with poor outcomes for patients (1, 2). In sepsis and other disease states there is broad dysfunction with all neutrophil functions reduced (3, 4). Ineffective neutrophil responses are harmful during the acute response where dysfunction may drive increased mortality and morbidity (5, 6). Then in the resolution phase persistent neutrophilic responses potentiates tissue damage as seen in acute respiratory distress syndrome (ARDS) (7) and unopposed neutrophil action in alpha-1 anti-trypsin deficiency (8). In patients with ARDS or sepsis, studies of neutrophil extracellular traps (NETs) demonstrate that there is an optimal level of *ex-vivo* function with poor outcomes for those with the highest or lowest levels of NETosis (6, 9). While alterations to a single cell function suggests involvement of a single molecular pathway, broad cellular dysfunction implicates a central driver such as altered metabolism. Immunometabolism is defined as the role of cellular metabolism in the regulation of immune cell function (10).

Murine work by Sadiku and colleagues has demonstrated that regulation of neutrophil function is linked to metabolism (11). Neutrophils are highly glycolytic (12) and inhibition of glycolysis using 2-deoxyglucose (2-DG) significantly reduces migration, phagocytosis, NETosis and oxidative burst. Neutrophils possess a functional network of mitochondria; however, mitochondrial oxidative phosphorylation does not appear to be required for adenosine triphosphate (ATP) synthesis to meet the energetic demand of neutrophils (13–15). The bulk of ATP is synthesised by glycolysis (16, 17). Sadiku et al. demonstrated that neutrophils from patients with chronic obstructive pulmonary disease had lower baseline ATP levels and exhibited reduced glycolysis in response to a pathogen compared to age matched controls (18). Moreover, the glycolytic capacity of neutrophils can be impacted by treatment with lipopolysaccharide (LPS) (19). Developing methods to understand neutrophil metabolism may provide insights into mechanisms underpinning disease and could offer a new therapeutic paradigm, improving outcomes for patients with acute and chronic disease.

Extracellular Flux (XF) analysis assesses real-time measurement of oxygen consumption rate (OCR) and proton efflux rate (PER) of cells. XF technology allows automated addition of different stimuli or inhibitors with flexibility over timing to visualise the effect of stimulation and inhibitory factors on cellular metabolism. XF technology requires low cell numbers relative to other forms of respirometry and allows for simultaneous measurement of PER and OCR as indicators for glycolysis and mitochondrial function, respectively. The streamlined workflow combined with user-friendly interface and analysis templates have seen a worldwide boom in the use of these instruments for probing cellular metabolism. In this manuscript we describe optimised protocols for using an XFe96 XF Analyser to probe (i) glycolysis in neutrophils under basal and stimulated conditions and (ii) phorbol 12-myristate 130-acetate (PMA)-induced oxidative burst. We highlight limitations of using XF technology to examine mitochondrial function in neutrophils. Finally, we provide an overview of how to analyze XF data and identify pitfalls of probing neutrophil metabolism with XF analysis.

Materials, equipment and methods

Study subjects

11 otherwise healthy volunteers aged 22-49 years old were recruited from staff members in the Queen Elizabeth Hospital Birmingham. Written informed consent was given by all participants in accordance with the University of Birmingham Research Ethics Committee (ERN 12-1185R2).

Isolation of blood neutrophils

Neutrophils are notoriously challenging cells to work with due to their short lifespan and propensity for activation. The upmost care must be taken during cell isolation and assays should be commenced immediately following isolation to reduce risk of apoptosis.

Peripheral blood neutrophils were isolated from lithium-heparin anticoagulated (BD Bioscience, New Jersey, USA) whole venous blood as previously described (20). Briefly, whole blood was mixed 6:1 with 2% dextran (Merck Life Sciences, UK) (w/v in 0.154 M saline) for 30 minutes to allow erythrocyte sedimentation. Percoll (GE Healthcare, New York, USA) was made using 9:1 v/v Percoll to sterile saline (1.54 M) which was further diluted to 56% and 80% v/v solutions in 0.154 M saline. The buffy coat was layered on Percoll discontinuous gradients and centrifuged at 470 x *g* for 20 minutes with no brake or acceleration. Neutrophils were removed and washed in phosphate-buffered saline (Merck Life Sciences, UK) (PBS) (250 x *g*, 10 minutes, full brake and acceleration) before being resuspended at 4 x 10^6/mL in phenol red and sodium bicarbonate free, filter sterilized Roswell Park Memorial Institute-1640 (RPMI) (Merck Life Sciences, UK, R8755), supplemented with 2mM L-glutamine, 1mM sodium pyruvate, 25mM glucose and 5mM 4-(2-hydroxyethyl)-1-piperazineethanesulfonic acid (HEPES) (Merck Life Sciences, UK), pH 7.4, which will be referred to as XF media. Neutrophil purity was >99% for all assays, except where neutrophil purity is detailed in the Figure legend.

Extracellular flux assays

All assays were carried out using XFe96 V3 PS Cell Culture microplates (Agilent Technologies, California, USA) coated with 22.4 µg/mL Corning® Cell-Tak™ (Corning Inc., New York, USA) solution and stored overnight at 4°C. On the day of the assay pre-coated microplates were bought to room temperature and seeded with 2 x 10^5 cells/well (glycolysis and mitochondrial respiration) or 5 x 10^4 cells/well (oxidative burst) in 50µL XF media. Wells A1, A12, H1 and H12 contained only 50 µL/well XF media to account for background correction wells. The XFe96 microplate was centrifuged at 200 x *g* for 1 minute with maximum acceleration but no brake at room temperature before incubation in a non-CO_2, 37°C incubator

for 25-30 minutes. Wells were observed under a light microscope to ensure cell adherence before gently adding 130 µL/well pre-warmed XF media, after addition of media the plate was incubated for a further 15 minutes in a non-CO_2, 37°C incubator. 25 µL of each inhibitor/stimulant was added to injection ports A-C of the sensor cartridge (Agilent Technologies, California, USA) as follows, with stated concentrations referring to final well concentrations: *Glycolysis*- port A: 160 nM PMA (Merck Life Sciences, UK), port B: 2 µg/ml oligomycin (21) (Merck Life Sciences, UK), port C: 50 mM 2-DG (22) (Merck Life Sciences, UK). *Mitochondrial respiration* - port A: 2 µg/ml oligomycin, port B: 3 µM BAM-15 (21) (Bio-techne, Minneapolis, USA) and port C: 2 µM rotenone/antimycin A (21) (Merck Life Sciences, UK). *Oxidative burst* - port A: XF media, port B: 2 µM rotenone/antimycin A and port C: 160 nM PMA. Or port A: 2 µM rotenone/antimycin A, port B: 10ng/ml tumour necrosis factor α (TNFα) (Merck Life Sciences, UK) or XF media, port C: compound of interest. *N*-Formyl methionyl-leucyl-phenylalanine (fMLP) (Merck Life Sciences, UK). Heat killed *Streptococcus pneumoniae* (SP) and non-typeable *Haemophillus influenzae* (NTHI) were donated by Dr Kylie Belchamber (23). Mitochondrial damage associated molecular patterns (mtDAMPS) were donated by Dr Jon Hazeldine (24). All compounds were prepared in XF media.

Data analysis

OCR and extracellular acidification rate (ECAR data) were exported from WAVE to GraphPad Prism and Microsoft Excel for downstream analysis. Seahorse analytics (https://seahorseanalytics.agilent.com) was used to convert ECAR to PER using the buffer factor 2.8 as calculated by the manufacturer's protocol (https://www.agilent.com/cs/library/usermanuals/public/usermanual-xf-buffer-factor-protocol-cell-analysis-S7888-10010en-agilent.pdf) for RPMI supplemented with 25 mM glucose. Glycolytic parameters were calculated as follows: Basal glycolysis - PER value prior to the first injection, PMA-induced glycolysis - maximum PER reached over the course of the assay, and glycolytic response to PMA – PMA-induced glycolysis minus basal glycolysis. Area under the curve analysis was performed on GraphPad Prism to generate oxidative burst parameters. Mitochondrial respiration parameters were calculated by importing OCR data into pre-formatted analysis templates in Microsoft Excel to calculate basal respiration, ATP-linked respiration, proton leak respiration, maximal respiration, and non-mitochondrial respiration. Mean and standard error of the mean (SEM) are presented for data. Paired t-test was performed for data 4A-B. Linear regression analysis was performed in GraphPad Prism for mitochondrial data in 8 A-D.

Representative results

Achieving a confluent monolater of neutrophils in XFe96 microwell plates

To establish optimal cell seeding concentrations, 1 x 10^4 to 5 x 10^5 neutrophils per well were seeded into Cell-Tak™ coated XFe96 microwell cell culture plates. Cell confluence was assessed by eye using an inverted optical light microscope. The manufacturer recommends cell confluence between 50-90% while avoiding cell clusters. Figure 1 demonstrates 50-90% confluence for 5 x 10^4 and 2 x 10^5 neutrophils/well with a clear monolayer and no clustering of cells. Higher seeding densities resulted in cell clusters and disrupted the assessment of metabolism. Thus, a range of cell densities between 5 x 10^4 and 2 x 10^5 cells/well were examined for each XF assay to identify optimal cell densities.

Oxidative burst

Oxygen consumption rate (OCR) measured by XF technology can be used to quantify oxidative burst response in mononuclear cells such as neutrophils. We highlight this in the representative oxidative burst trace in Figure 2 using an acute injection of PMA to activate neutrophils seeded in XFe96 microplates. Consistent with an oxidative burst, PMA leads to a typical transient bell-shaped increase in oxygen consumption. Importantly, when rotenone plus antimycin A is added before PMA, mitochondrial complexes I and III are inhibited and the subsequent PMA-induced increase in OCR is independent of mitochondrial oxygen consumption. To quantify the oxidative burst, we assessed a) time to maximal oxygen uptake, b) maximum oxygen consumption as demonstrated by the arrow and c) total oxygen consumption after PMA injection (shaded area under the curve, Figure 2A). These metrics give a reliable quantitative comparison of oxidative burst between groups where both speed and magnitude of oxidative burst may be impacted.

Cell density and PMA titration

Given that both cell density and/or PMA concentration will affect the metrics used to quantify an oxidative burst using XF technology, we explored to what extent these factors effect neutrophil oxidative burst by assessing neutrophil cell density and PMA concentration. Initially, between 0.5 x 10^4 and 5 x 10^5 neutrophils/well were seeded onto XFe96 cell culture microplates as described in methods. Baseline OCR was measured over a period of 4 measurement cycles (2 min 30 sec mix, 30 sec wait, 3 min measure) prior to sequential injections of 2 µM rotenone plus antimycin A and 160 nM PMA to establish oxidative burst test parameters (Figure 2A). To quantify the oxidative burst time to maximum OCR (Figure 2) were calculated after injection of 160 nM PMA. Neutrophils seeded at 5 x 10^4/well showed the greatest OCR of 102.12 pmol O_2/min/well, while OCR decreased in cell densities greater than 5 x 10^4/well (Figure 2C). Combining assessment of OCR from oxidative burst activity (Figure 2) with confluence assessments (Figure 1), we show that neutrophils seeded between 0.5 x 10^4 and 5 x 10^4 per well are optimal for assessment of oxidative burst.

To establish the optimal dose of PMA required to induce an oxidative burst in 5 x 10^4/well neutrophils, a dose response of PMA was performed including 640, 320, 160, 80, 40, 20, 10, 5 and 2.5 nM. PMA concentrations below 160 nM yielded inconsistent peaks of oxygen consumption (dotted line, Figure 3A). Both maximum OCR (Figures 3B, C) over the course of the assay were consistently

10.3389/fimmu.2023.1083072

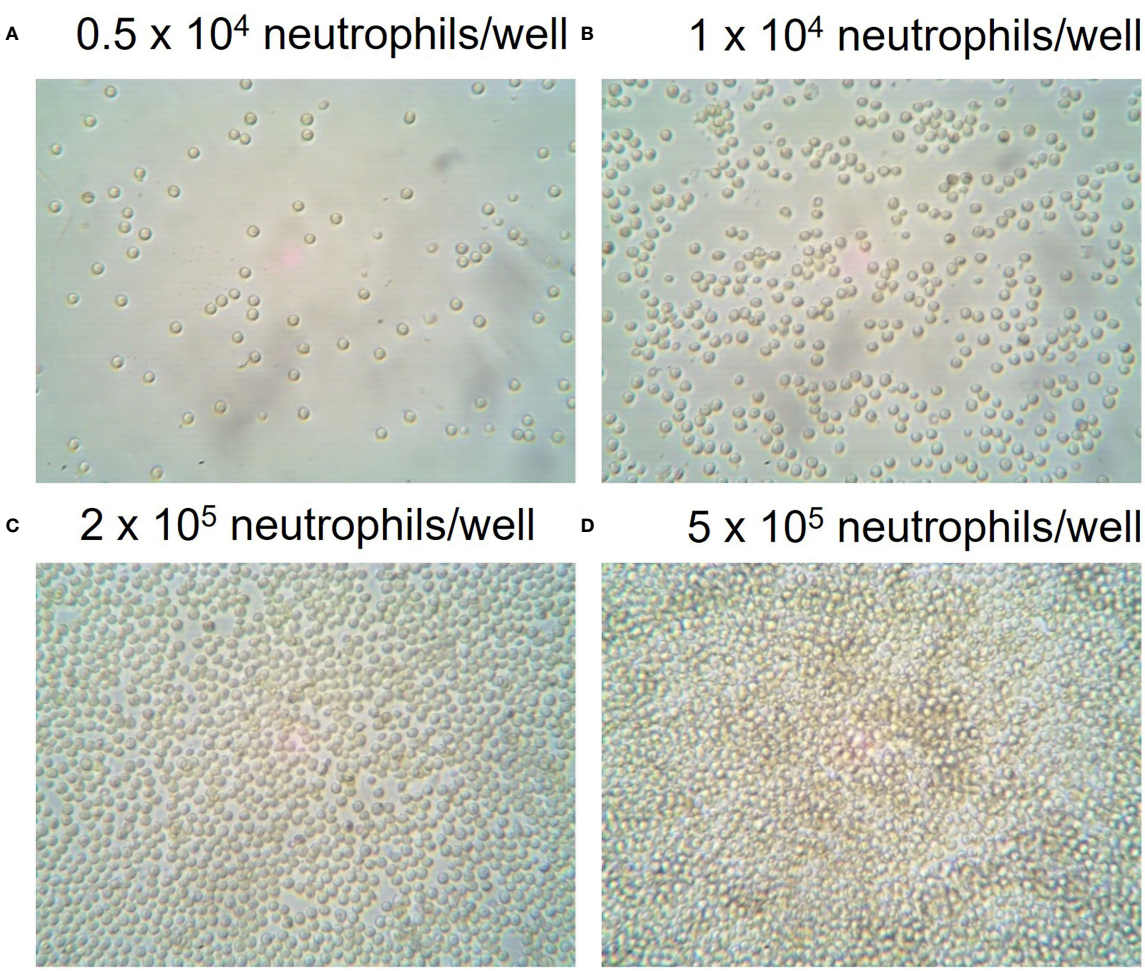

FIGURE 1
Seeding densities of neutrophils in XFe96 coated microplates. Human peripheral blood neutrophils were isolated from whole blood of donors before seeding into Cell-Tak™ coated XFe96 cell culture plates at **(A)** 1 x 10^4, **(B)** 5 x 10^4, **(C)** 2 x 10^5 or **(D)** 5 x 10^5/well. XFe96 cell culture microplates containing neutrophils were imaged under an inverted light microscope (45x magnification) and examined by eye for confluence percentage. Confluence assessments were combined with experimental data to achieve the optimal number of neutrophils per well for each test which achieved the correct confluence and consistent data outputs.

increased from baseline at PMA concentrations above 160 nM. Based on our data in Figure 3, and in agreement with published literature (25, 26) we recommend using 160 nM PMA for assessing oxidative bursts from 5 x 10^4/well neutrophils when using the XFe96 analyser. Additionally, 160 nM PMA allows for detection of both increases and decreases between groups, whereas higher concentrations result in the maximal oxidative burst response for 5 x 10^4 neutrophils/well, so increases caused by disease states or pharmacological treatments would not be detected.

Assessment of oxidative burst induced by physiological stimuli

Using neutrophils seeded at 5x10^5 cells/well we explored the effect of physiological stimuli confirmed to generate reactive oxygen species by other methods (27–30). Experimental procedure was as described in methods, except injection strategy was A:2 µM rotenone plus antimycin A, B:10ng/ml TNFα or XF media, C: fMLP, LPS, heat killed bacteria or mtDAMPS at a range of concentrations. Unprimed neutrophils did not generate a detectable increase in oxygen consumption when challenged with heat killed *SP*, *NTHI* or LPS at a range of concentrations. fMLP at 0.01µM- 10µM generated a small and rapid peak in OCR (13.35-8.11 pmol O_2/min/well) three minutes following injection (Supplementary Figure 1). mtDAMPs generated a peak oxygen consumption of 18.01 pmol O_2/min/well 130 minutes following injection without priming (Figure 4).

Priming with TNFα results in significantly greater oxygen consumption when neutrophils are challenged with fMLP ($p < 0.001$) and mtDAMPs ($p = 0.002$) compared to unprimed neutrophils. Peak oxygen consumption is rapid within three minutes of injection and overall oxygen consumption is lower than that induced by PMA. Peak oxygen consumption induced by fMLP was 38.12 pmol O_2/min/well fMLP and 29.7 pmol O_2/min/well by mtDAMPs (Figure 4A). Total oxygen consumption was greatest by mtDAMPs 4409 pmol compared to 4033pmol induced by 10µM fMLP. TNFα priming does not result in detectable oxygen consumption when neutrophils are challenged with heat killed bacteria or LPS compared to XF media alone (Figure 4).

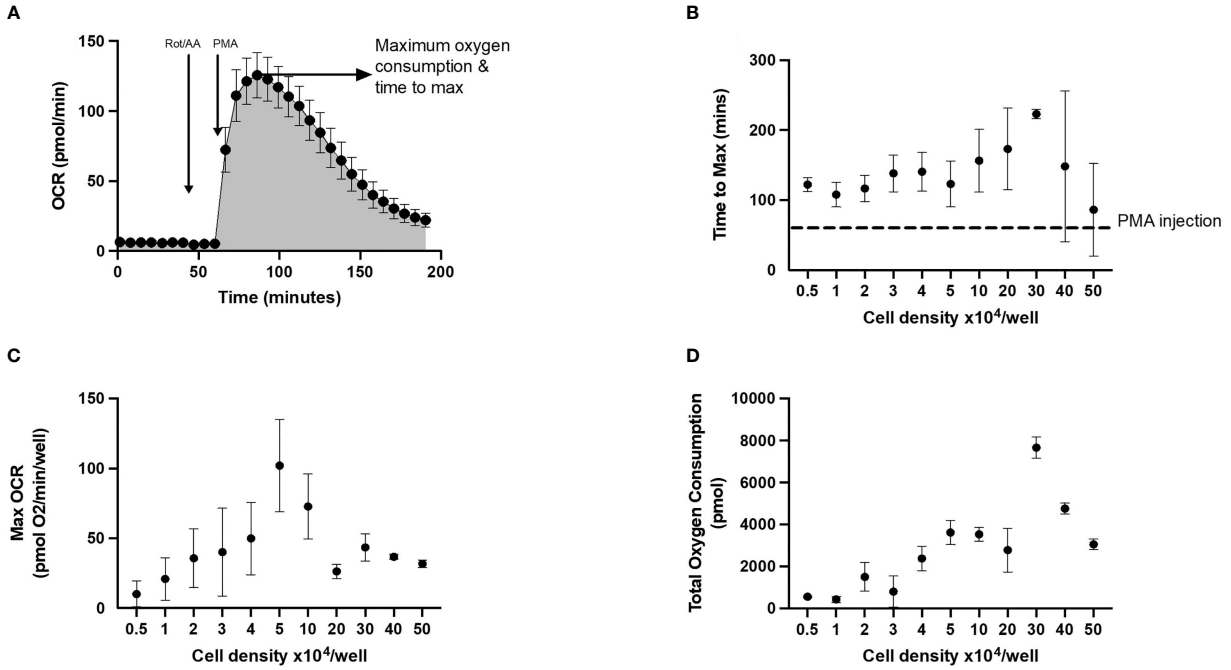

FIGURE 2
Representative trace and optimal cell seeding density to assess neutrophil oxidative burst using XF analysis. Neutrophils seeded at 0.5 – 5 x 10^4/well in XFe96 cell culture microplates were sequentially injected with 1) XF media (injection 1), 2 μM rotenone/antimycin A (injection 2) and 160 nM phorbol 12-myristate 13-acetate (PMA) (injection 3). **(A)** is a representative oxygen consumption rate (OCR) trace (n = 1). Area under the curve analysis was performed, to calculate **(B)** time to maximum OCR, **(C)** maximum OCR reached and **(D)** total oxygen consumption over the duration of the test for each cell density (as shown in figure 2). Graphs B-D represent the mean ± standard error of the mean (SEM) from 3 distinct donors.

Treatment with TNFα alone resulted in a small increase in total oxygen consumption 1533pmol compared to 443pmol in unstimulated neutrophils (Figure 4). Therefore, we recommend use of priming agents prior to testing compounds other than PMA when investigating oxidative burst by XF analyser, and titrating cell density to achieve OCR well within the limits of detection.

Glycolytic assessment

Extracellular acidification rate and proton efflux rate

XF analysis can also provide detailed information on cellular glycolytic flux. Until recently (31), ECAR was commonly used as an indicator of cellular glycolytic rate, given that at neutral pH conversion of glucose to lactate releases protons and acidifies the medium. However, the relationship between extracellular acidification and glycolytic rate can be confounded by other acidification mechanisms. Specifically, in cells that have active mitochondrial oxidative phosphorylation, CO_2 generated in the tricarboxylic acid cycle can be spontaneously or enzymatically hydrated to carbonic acid (H_2CO_3), which dissociates to HCO_3^- + H^+ in media at physiological pH. Of significance, conversion of one glucose molecule to lactate yields 2 lactate + 2 H^+, whereas complete oxidation of one glucose to CO_2 yields 6 HCO_3^- + 6 H^+, therefore when extracellular acidification of glucose is oxidized to CO_2, extracellular acidification is three times higher than conversion to lactate. Moreover, XF analysis of ECAR from changes in media pH does not consider the buffering capacity of the media, which often contain low amounts of HEPES or other buffering agents. It is therefore also important to correct for buffering capacity of the XF assay media. This correction converts ECAR into proton efflux rate (PER), which is preferable when interpreting glycolytic flux.

Stimulant/activator

Glycolytic rate assessed using XF technology is obtained in cells exposed to exogenous glucose and mitochondrial complex inhibitors such as oligomycin or rotenone plus antimycin A. Typically, treatment of cells with mitochondrial respiratory complex inhibitors such as oligomycin increases PER because of increased glycolytic flux to sustain cellular ATP supply to meet the energetic needs of the cell when mitochondrial ATP synthesis is abolished. However, in neutrophils, under basal conditions with surplus exogenous glucose, oligomycin has no effect on PER (Figure 5), suggesting a lack of mitochondrial contribution to ATP supply in blood derived neutrophils. To measure increased glycolytic rate in neutrophils a stimulation step is required to increase ATP hydrolysis rather than abolition of mitochondrial respiration. This is demonstrated in neutrophils treated ± PMA, whereby without PMA stimulation oligomycin has no impact on PER but when stimulated with PMA, PER increases more than 2-fold (Figure 5A). Oligomycin and PMA have no synergistic effect compared to PMA alone over 270 minutes (Figure 5B).

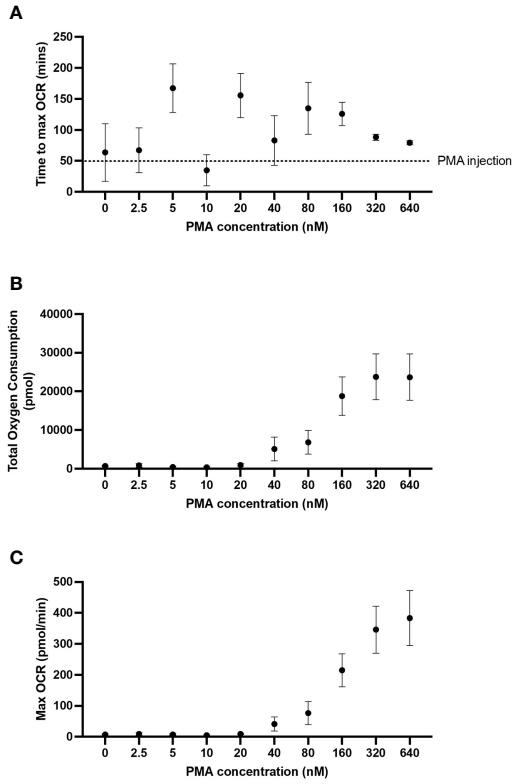

FIGURE 3
PMA-induced OCR from neutrophils. Human peripheral blood neutrophils were seeded at 5 x 10^4 cells/well onto Cell-Tak™ coated XF XFe96 microplates. Oxidative burst was probed by sequential injection of media, 2 µM rotenone plus 2 µM antimycin A and phorbol 12-myristate 13-acetate (PMA) (640, 320, 160, 80, 40, 20, 10, 5 or 2.5 nM). Oxygen consumption rate (OCR) was monitored over the duration of the test, and results were exported to GraphPad Prism for downstream analysis. Time to max OCR **(A)**, maximum OCR **(B)** and total oxygen consumption **(C)** were calculated from area under the curve analysis. Graphs represent means ± standard error of the mean (SEM) from 5 distinct donors.

Cell density

To establish what cell seeding density is required to obtain consistent and reliable glycolytic rates from neutrophils stimulated with PMA, PER was assessed in XFe96 microplates containing 0.5 – 5 x 10^5 isolated neutrophils per well. As indicated by increases in PER, basal glycolytic rate positively correlated with increased cell density (Figure 6A). However, PMA-induced fold change in PER was consistent only up to 2 x 10^5 cells/well (Figure 6B). For this reason, we suggest that 2 x 10^5 cells/well is an optimal cell density for assessing PER from neutrophils using the XFe96 analyser. This number of cells sits at the middle of the detectable baseline range and would allow for increases and decreases in glycolytic rate to be assessed under disease states. Importantly, 2 x 10^5 cells/well also coincides with our confluence assessment (Figure 1).

Mitochondrial respiration

Cell density

To establish optimal neutrophil seeding density for assessment of mitochondrial respiration using XF analysis, a range of cell seeding densities were examined from 0.5 – 5 x 10^5 cells/well. At cell concentrations less than 2 x 10^5, basal OCR was less than 20 pmol O_2/min/well (Figure 7), below the recommended threshold for OCR measured with the XFe96 analyser. Only at 2.5 and 5 x 10^5 cells/well was OCR detectable above the 20 pmol O_2/min/well threshold (Figure 7 –Light and dark purple traces). Of interest, the typical OCR curve for assessing mitochondrial function with XF technology (32) is not apparent at lower cell seeding densities (Figure 7). Notably, OCR from 2.5 and 5 x 10^5 cells/well do show sensitivity to the mitochondrial compounds oligomycin, BAM-15 and rotenone plus antimycin A, however there is considerable variability at such high cell seeding densities (Figure 7). Together with confluence images (Figure 1), at appropriate cell seeding densities (< 2 x 10^5 cells/well), OCR is below the limit of detection for the XFe96 analyser and thus OCR obtained from neutrophils at these densities should be treated with caution when inferring mitochondrial respiratory activity.

Cell purity

Given that lower cell seeding densities (<2x10^5 cells/well) make it difficult to obtain reliable OCR (Figure 7), it could be argued that increasing cell seeding would be beneficial for probing mitochondrial energy metabolism in neutrophils. That said, OCR measured during a mitochondrial stress test with higher neutrophil densities could be related to contamination from other mononuclear cells, which have higher mitochondrial activity. Typically, density gradient isolations are >97% pure, but contamination with other mononuclear cells such as monocytes or lymphocytes is a common issue when working with neutrophils.

To test this, we probed OCR in neutrophils contaminated with peripheral blood mononuclear cells (PBMCs) seeded at 2 x 10^5 cells/well. This was achieved by mixing neutrophils with defined concentrations of PBMCs to yield cell populations containing either 100%, 70% or 50% neutrophils. OCR were significantly higher in cell populations that contain PBMCs (Figures 8E, F). In 100% pure neutrophil isolations, basal OCR was 4.5 (SEM 2.0) pmol O_2/min/well compared to 26.72 (SEM 2.6) pmol O_2/min/well at 50% purity (Figures 8E, F). Basal OCR appeared to be dose-dependently higher than pure neutrophil populations with increasing proportion of PBMCs (18-fold higher for 30% contamination and 26-fold higher for 50% contamination, compared to pure neutrophils) (Figure 8E). Also, the sensitivity of OCR to mitochondrial compounds is much greater from cell suspensions containing PBMCs (Figure 8E). OCR traces from 100% pure neutrophils fall below the 20 pmol O_2/min/well threshold for the XFe96 analyser for the entirety of the mitochondrial assay, as shown in Figure 8E. We also show that basal OCR is different in neutrophil isolations between 95-100% purity (Figure 8F). When corrected for non-mitochondrial respiration (calculated as OCR after rotenone and antimycin A injection), parameters of mitochondrial respiration including basal mitochondrial respiration (Figure 8C), maximal respiration (Figure 8B) and ATP production (Figure 8A) correlate negatively with neutrophil purity ($P < 0.001$). It is also worth noting that non-mitochondrial oxygen uptake did not significantly change ($P = 0.8252$) with increasing PBMC concentration (Figure 8D).

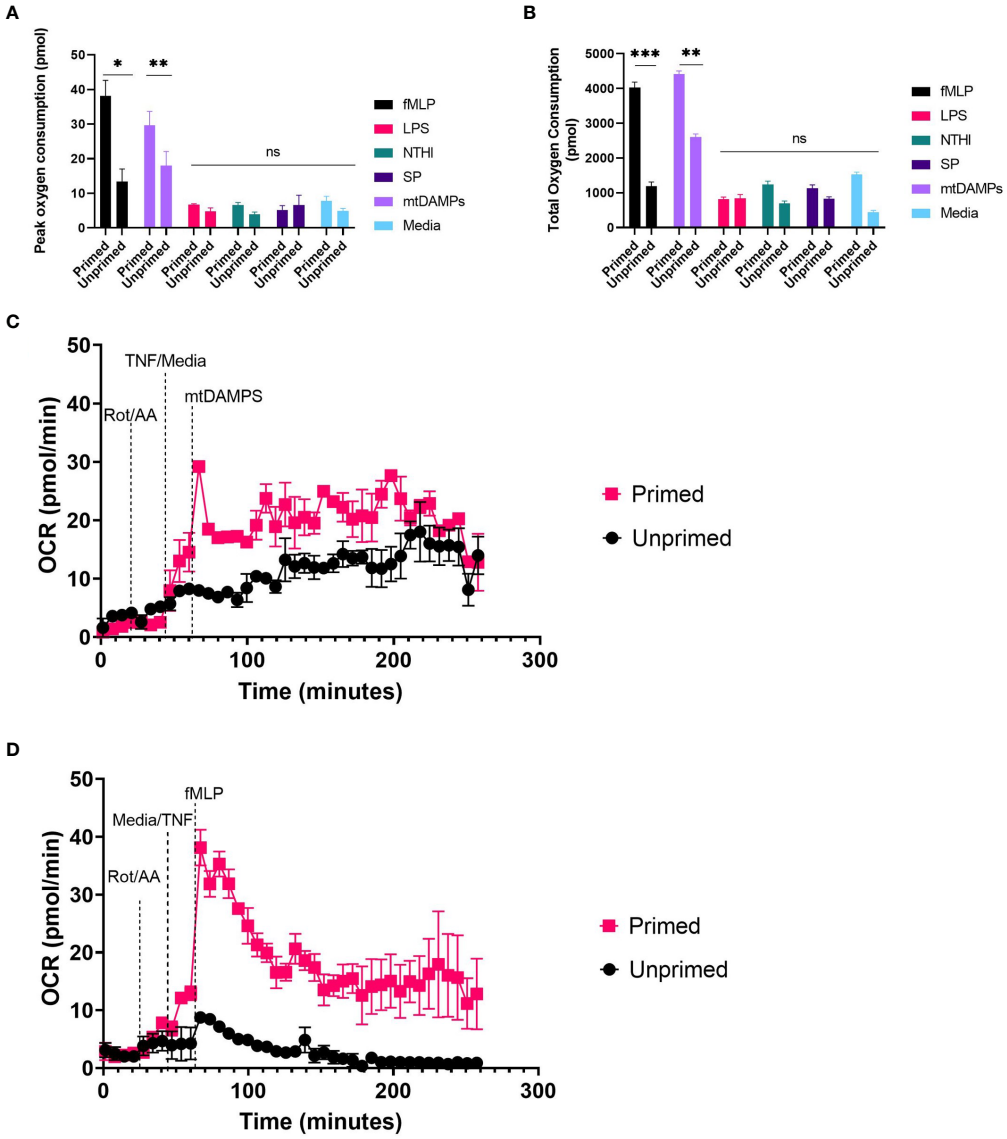

FIGURE 4
Induced OCR from activated neutrophils. Human peripheral blood neutrophils were seeded at 5 x 10^4 cells/well onto Cell-Tak™ coated XF XFe96 microplates. Oxidative burst was probed by sequential injection of 2 µM rotenone plus 2 µM antimycin A, 10ng/ml TNFα (primed), or XF media (unprimed) followed by 10µM fMLP, or 10µm LPS, NTHI at 100 bacteria:1 neutrophil, SP at 100 bacteria: neutrophil or 100µg/ml mtDAMPS. Oxygen consumption rate (OCR) was monitored over the duration of the test, and results were exported to GraphPad Prism for downstream analysis. Peak OCR **(A)** and total oxygen consumption (CB were calculated from area under the curve analysis. **(A, B)** represent means ± standard error of the mean (SEM) from 3 distinct donors. **(C, D)** are representative traces from two distinct donors. Data for 100ng/ml PMA not shown. A) fMLP primed vs. unprimed P= 0.024, mtDAMPs p=0.0037, others non-significant. B) fMLP p=0.0001, mtDAMPs p=0.0036, others non-significant. fMLP, *N*-Formyl methionyl-leucyl-phenylalanine; LPS, lipopolysaccharide; NTHI, non typeable *Haemophillus influenzae; SP, Streptococcus pneumoniae*; mtDAMPS, Mitochondrial damage associated molecular patterns; OCR, oxygen consumption rate; TNFα, tumour necrosis factor. ns, p >0.05; *, p ≤ 0.05; **, P ≤ 0.01; ***, P ≤ 0.001.

Discussion

Neutrophils are highly glycolytic cells (12); inhibition of glycolysis significantly impacts neutrophil effector functions (13). Neutrophils utilise glycogen stores to synthesise ATP in the absence of oxygen and are capable of gluconeogenesis to increase glycolytic capacity (11). The use of glycolytic inhibitors abolishes neutrophil ATP levels, while they remain unchanged after inhibition of mitochondrial respiratory complexes (33).

Activated neutrophils rapidly consume oxygen as reduced nicotinamide adenine dinucleotide phosphate (NADPH) oxidase forms superoxide anions, reactive oxygen species and hydrogen peroxide, a process commonly referred to as oxidative burst. PMA is a protein kinase C activator and a robust activator of neutrophils, albeit non-physiological (26). In cell seeding densities beyond 5 x 10^4 neutrophils/well, we saw a reduction in the size of the oxidative burst response. Typically, it would be anticipated that greater cell seeding densities would produce a larger oxidative burst response, however,

10.3389/fimmu.2023.1083072

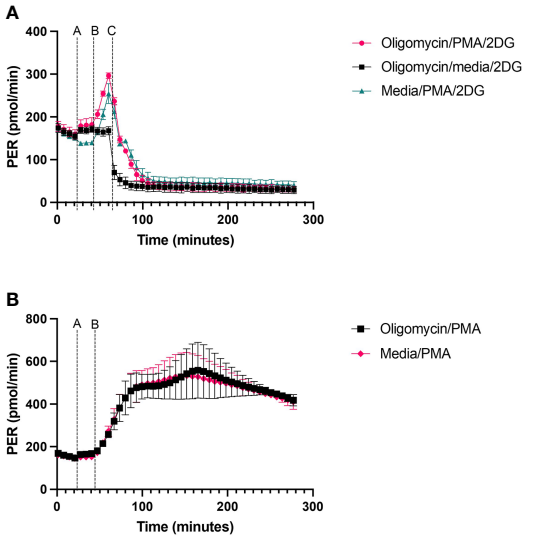

FIGURE 5
PER from neutrophils exposed to oligomycin or PMA. Human peripheral blood neutrophils were seeded at a density of 2 x 10^5 cells/well onto a Cell-Tak™ coated XFe96 microplate. **(A)** 2 µM oligomycin or XF media was injected first, followed by sequential injections of 160nM PMA or XF media and finally 50 mM 2-Deoxy-D-Glucose (2-DG) at defined time points as shown on the figure. **(B)** 2 µM oligomycin or XF media was injected first, followed by 160nM PMA. Extracellular acidification rate (ECAR) was measured across the duration of the test. Following data export, ECAR readings were converted to proton efflux rate (PER) using Seahorse analytics by accounting for the buffer capacity of the media. Data was exported to GraphPad Prism and expressed as mean ± standard error of the mean (SEM) from 3 distinct donors.

due to cell overcrowding and/or reduced PMA stimulation relative to number of cells, this was not the case. We demonstrated that 5 x 10^4 neutrophils/well combined with an injection strategy incorporating 2 µM rotenone plus 2 µM antimycin A followed by 160 nM PMA, produces a substantial and consistent oxidative burst response, without maximising the neutrophil reactive oxygen species (ROS) response. This allows for detection of both elevated and suppressed oxidative burst responses caused by disease states or exogenous treatments. We show that PMA concentrations lower than 160 nM do not produce a consistent peak following PMA injection, and therefore area under the curve analysis is unable to quantify a reliable oxidative burst response. Data in Figures 3, 4 demonstrate that when assessing oxidative burst in neutrophils a multi-parameter approach should be taken as using a single parameter may lead to false assumptions as seen in the variability of time to max oxygen consumption (2B and 3A) which is due to detection of very small peaks at extremes of cell density and or PMA concentration, and are not likely to be a true difference in time to maximum oxygen consumption. PMA is a potent and non-physiological activator of neutrophils; therefore, we explored the utility of other stimuli in the oxidative burst assay. We demonstrated that priming with TNFα enhances detection of the increased oxygen consumption induced by fMLP and mtDAMPs. In unprimed cells there was a small increase in oxygen consumption following fMLP/mtDAMPs but this was well below the recommended limits of detection for OCR. Heat killed *SP*, NT*HI*, or LPS did not induce a detectable increase in oxygen consumption with or without priming. Heat killed bacteria and LPS have been used by others to induce oxidative burst, although with different methods (27, 28).

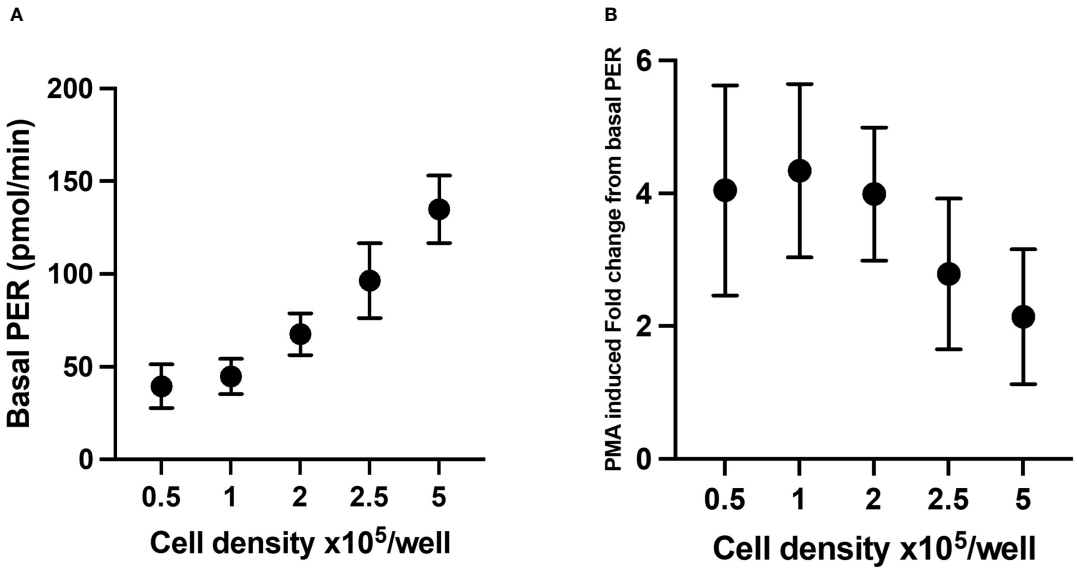

FIGURE 6
Glycolytic parameters from neutrophils seeded at different densities. Glycolytic rates of isolated neutrophils seeded at 0.5, 1.0, 2.0, 2.5 and 5 x 10^5 cells/well were established from proton efflux rate (PER) data as described previously. Basal glycolysis **(A)** represents final baseline measurement of glycolysis prior to stimulation, **(B)** phorbol 12-myristate 13-acetate (PMA)-induced fold change from basal PER. Data represent means ± standard error of the mean (SEM) from 3 distinct donors.

10.3389/fimmu.2023.1083072

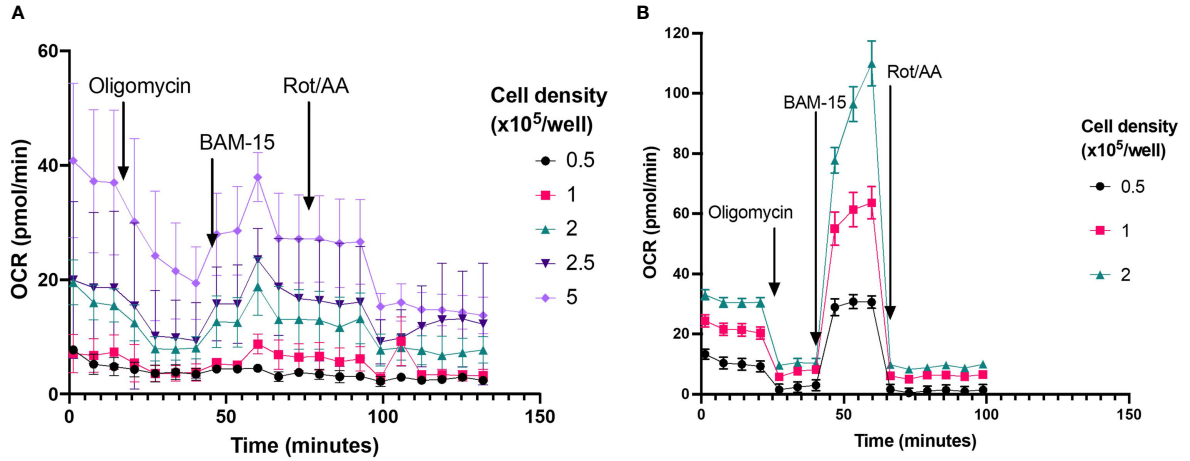

FIGURE 7
Probing OCR from neutrophils and PBMCs seeded at different cell densities. **(A)** Mitochondrial respiratory activity of isolated neutrophils seeded between 0.5-5 x 10^5 cells/well were probed by sequential injection of 2 µM oligomycin (injection 1), 3 µM BAM-15 (injection 2) and 2 µM rotenone/antimycin A (Rot/AA) (injection 3), to establish rates of adenosine triphosphate (ATP)-coupled, maximal mitochondrial respiratory activity and non-mitochondrial oxygen consumption, respectively. Cell purity was assessed using H&E staining, mean neutrophil purity was 97% the contaminating cells were 2% monocytes and 1% lymphocytes. Data are means ± standard error of the mean (SEM) from 4 distinct donors **(B)** Mitochondrial respiration of isolated PBMCs seeded between 0.5-2x10^5 cells/well were probed by sequential injection of 2 µM oligomycin (injection 1), 3 µM BAM-15 (injection 2) and 2 µM rotenone/antimycin A (Rot/AA) (injection 3), to establish rates of adenosine triphosphate (ATP)-coupled, maximal mitochondrial respiratory activity and non-mitochondrial oxygen consumption, respectively. Data are means ± standard error of the mean (SEM) 4 technical replicates.

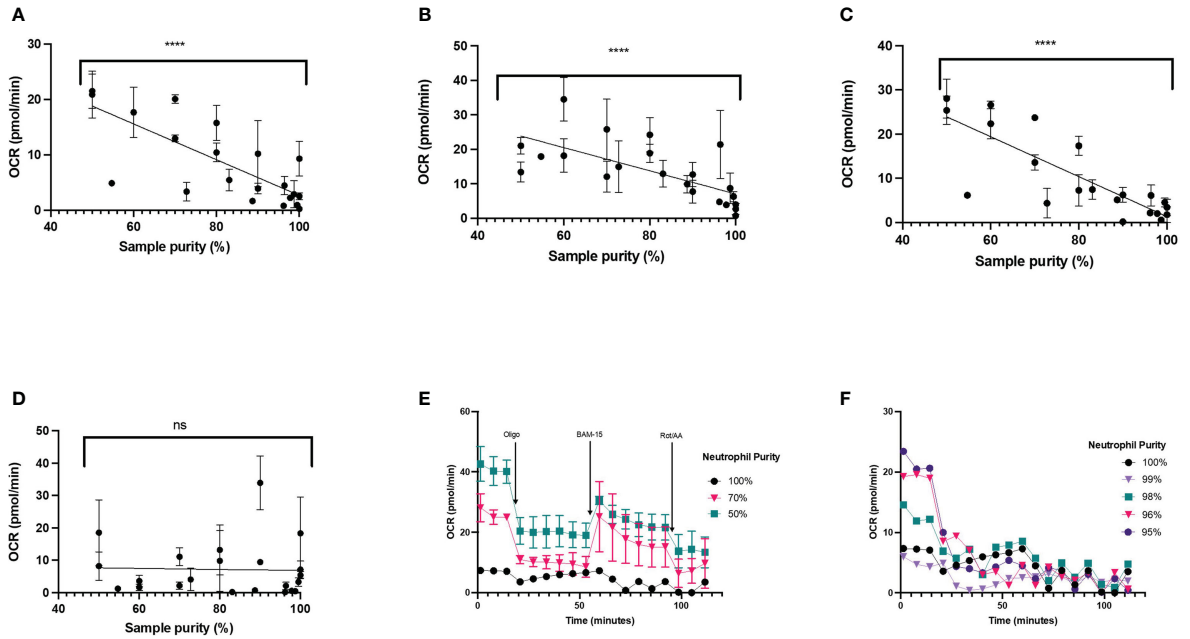

FIGURE 8
Mitochondrial respiration in varying neutrophil purities. Pure neutrophil isolations were contaminated with up to 50% peripheral blood mononuclear cells (PBMCs) harvested from the same donor and cells seeded at 2 x 10^5/well. Mitochondrial respiration was probed for in neutrophils by sequential injection of 2 µM oligomycin, 3 µM BAM-15 and 2 µM rotenone plus 2 µM antimycin A (Rot/AA). **(A)** adenosine triphosphate (ATP)-coupled mitochondrial respiration, **(B)** maximal mitochondrial respiration, **(C)** basal mitochondrial respiration, **(D)** non-mitochondrial oxygen consumption, **(E)** mean oxygen consumption rate (OCR) ± standard error of the mean (SEM) over the duration of the assay, representing 100%, 70% or 50% neutrophil purities from 2 distinct donors and **(F)** mean oxygen consumption rate (OCR) ± standard error of the mean (SEM) over the duration of the assay, representing 100%, 99%, 98%, 96% and 95% neutrophil purities from a single donor. Data in **(A-D)** consists of three unique donors, for each donor the cell preparation was intentionally contaminated to achieve 22 samples with varying neutrophil purity between 100% neutrophils and 50% neutrophils. Data points shown are mean ± SEM for four technical replicates for each donor. ns, not significant; ****, p-value <0.0001.

More commonly used methods to measure oxidative burst detect generation of ROS by a range of fluorescent, chemiluminescent probes rather than detecting environmental oxygen consumption (34). While these methods can be highly specific this can also be considered a weakness if assay conditions are not carefully controlled. Different probes have varying selectivity for different species of ROS and vary in their ability to detect intra and extracellular ROS (34), this is frequently an issue in commercially available kits where the selectivity is not always clearly documented. In addition, chemiluminescent probes such as luminol and lucigenin are prone to errors related to redox recycling as the probes can generate radicals that produce superoxide (35). Using the XF analyser to assess oxidative burst allows for measurement of the total oxygen uptake from the environment which may better represent total ROS generation, especially when mitochondrial uptake of oxygen is abolished. This assay typically uses half the cell number of chemiluminescent assays and enables simultaneous indication of glycolysis through PER data.

Neutrophils rely on glycolysis for synthesis of ATP. In the traditional glycolytic rate test (22) used in other cell types, injection of oligomycin (ATP synthase inhibitor) or rotenone and antimycin A pushes glycolysis to its capacity, as cells are unable to produce ATP *via* mitochondrial respiration and therefore upregulate glycolysis to meet the energetic demands of the cell. When testing this assay on human neutrophils, we observed no change in glycolysis after oligomycin injection. A recent publication has highlighted that by inhibiting mitochondrial respiration using mitochondrial respiratory complex inhibitors in resting state cells, cells only shift to glycolysis as a compensatory mechanism for basal ATP demand requirements, thus these agents may not actually shift cells to maximum glycolytic capacity as previously thought (36). This confirms our findings, highlighting the need for a stimulant to increase ATP demand. Here we used 160 nM PMA, to increase glycolytic activity in neutrophils and assess downstream glycolytic parameters. Seeding more than 2 x 10^5 neutrophils per well to probe glycolytic activity resulted in inconsistent and lower glycolytic responses. Similarly, to the oxidative burst test, this is likely due to overcrowding of cells in the bottom of the well, which compromises the monolayer required to run these assays.

The manufacturer states a limit of detection of 20 pmol O_2/min/well for basal OCR from cells assessed with the XFe96 and XFp analyzers. OCR below this threshold cannot be interpreted reliably and should be used with caution to infer mitochondrial function. Here, neutrophil mitochondrial metabolism is too low to detect using current XF analyzers – OCR are below the limit of detection and do not change in response to mitochondrial stressors. Moreover, this was not overcome by increasing cell seeding density. In fact, our data showed that increases in cell seeding density yields amplified the low levels of contamination by mononuclear cells which appear to skew mitochondrial respiration tests using XF analysis. These data highlight the importance of using highly pure neutrophil preparations when performing metabolic assays and suggest caution to be taken when inferring mitochondrial respiration from OCR of neutrophil preparations.

Of interest, in two recent studies, a typical mitochondrial OCR trace using XFe96 technology was reported in neutrophils seeded between 0.5-1.5 x10^5 cells/well with isolation purities >95% (19, 37). At similar cell seeding densities, in our study we were unable to achieve equivalent traces. Such responses were only apparent with much less pure (<70%) neutrophil preparations. We show that basal OCR are higher in preparations with greater PBMC contamination at levels typically deemed acceptable for neutrophil assays (7E), however these data should be interpreted with caution given the lower limit of detection for XF analyzers. Given that PBMCs have higher rates of mitochondrial respiration than neutrophils, our data demonstrated that contamination with PBMCs has significant implications when assessing mitochondrial respiratory parameters from isolated neutrophils. Notably, in both papers, basal OCR are below the optimal minimum detection threshold for the XFe96 analyser. Additionally, the results as presented are problematic. For example, Porter et al. show higher OCR in neutrophils after rotenone and antimycin A injection than basal OCR, suggesting a negative basal rate of mitochondrial respiration (38). Unless non-mitochondrial oxygen consumption is stimulated in such experiments, for example by increased ROS, such finding is not theoretically possible. Nonetheless, if increased ROS are responsible for such increases in OCR this needs to be corrected to accurately calculate parameters of mitochondrial function.

Consistent with our findings, Chacko et al. show that PER is not responsive to oligomycin in neutrophils (39). Moreover, neutrophil OCR is not sensitive to mitochondrial compounds, corroborating our findings and agreeing with the central dogma for a minimal role of mitochondrial oxidative phosphorylation in neutrophil energy generation. Our data, combined with existing evidence, suggests that mitochondrial ATP synthesis is below the limit of detection for XF analyzers, and thus play an insignificant role in supplying ATP to meet basal energetic demands in mature neutrophils. Mitochondrial ATP synthesis does appear to be required for messenger purposes (13, 40). Further, mitochondrial respiration appears to be important in supporting oxidative burst in the absence of glucose by providing NADPH oxidase (41).

XF analyzers account for the pH and oxygen content in background wells, which contain no cells. This enables background correction of the values to ensure readouts represent actual metabolism rather than changes in ambient O_2 concentration or pH fluctuations affecting media parameters. For adherent cell cultures, normalisation is required to account for well-well cell density differences across the plate. When using neutrophils, cells are plated from pre-diluted homogenous cell suspensions at defined cell seeding densities per well and therefore normalisation to cell number, protein content or DNA will have modest effects on OCR or ECAR. This is, of course, if even cell seeding across the plate is obtained by the experimenter. Reporting ECAR values (traces or extrapolated values) are no longer accepted as representative for glycolysis. Media often has a large buffering capacity, which by its nature can mask pH changes, and subsequent acidification rates. Therefore, by calculating and applying a buffering factor for each specific media to account for the buffering capacity, ECAR values can be converted to PER, a more representative readout for glycolytic tests (when corrected for any mitochondrial-linked PER).

XF analyzers allow for high throughput data and multiple metabolic tests to be performed on a single assay plate, with a minimal demand for cell numbers. The dynamics of oxygen

consumption and change in pH over the duration of the assay allows for the depiction of cellular metabolism and metabolic responses over time. XF analyzers accurately predict lactate production compared to direct lactate measurement (42). Other methods to assess glycolysis include direct measurement of glucose and or lactate in assay media, use of glucose analogs, measurement of rate limiting glycolytic enzymes, glucose tracing and metabolite quantification. Each of these has strengths and limitations, we recommend a combined approach to interrogation of metabolism for robust data. These are discussed in detail in (31). Alternative respirometers such as the Oroboros O2k analyser require 2mL of solution, with a recommended 2-4 million cells (based on HL-60 data) per chamber (43, 44), more than 40x the requirement for a well of a XFe96 cell microplate. XF technology also incorporates a pH probe to allow the determination of the glycolytic pathway alongside oxygen consumption simultaneously, without the need for additional modules. As mentioned previously, neutrophils are notoriously easy to activate by mechanical, chemical, and biological stressors. Respirometers such as Oroboros allow for inhibitor/stimulant injections but operate using continuous stirring motions, which may activate neutrophils, skewing metabolic readouts. Adherent cells lend themselves naturally to XF assays, as they can be cultured in a monolayer directly in the cell plate. By incorporating a molecular adhesion step, cells in suspension can be manipulated into a monolayer to perform metabolic assays without exposing them to rigorous mixing. It has been demonstrated previously that plate adhesion using Cell-Tak™ does not affect neutrophil ROS production (37).

XF analyzers are highly sensitive; however, care must be taken in ensuring an evenly distributed monolayer of cells is formed. If cells are not distributed directly under the probe, or if they begin to detach from the base of the well due to disruptions, probes can lack fine discrimination. Further, introduction of pharmaceutical treatments or other stimulants/inhibitors requires further assay validation to ensure they do not interact with the probes themselves, which are sensitive to pH. Despite these limitations, we have demonstrated how XF technology can be harnessed for neutrophil bioenergetic analysis. XF analyzers are costly to run compared to other respirometers, however the high throughput and automated nature of the system allows for efficient data collection.

In conclusion, we have presented optimised protocols for the assessment of neutrophil glycolysis and oxidative burst using XF technology. The metabolic tests outlined here can be applied to any project context by incorporating pharmacological treatments, disease state neutrophils or neutrophils from different developmental stages. We demonstrate robust methodology to achieve neutrophil monolayers to perform metabolic assays for assessing glycolytic rate and oxidative burst. We highlight the challenges of these assays and mitigating strategies when assessing mitochondrial respiration. Overall, XF technology represents a powerful platform with a user-friendly interface and data analysis templates which has the potential to revolutionise our understanding of neutrophil metabolism. The protocols described in our manuscript provide a template to enhance discovery and ensure a standardised approach to neutrophil measurements using XF analysis.

Data availability statement

The raw data supporting the conclusions of this article will be made available by the authors, without undue reservation.

Ethics statement

The studies involving human participants were reviewed and approved by University of Birmingham Research Ethics Committee (ERN 12-1185R2). The patients/participants provided their written informed consent to participate in this study.

Author contributions

AJ and FG performed all experiments. JB, AS, AJ and FG designed the study with critical review by DT, ES and CM. Data analysis was undertaken by AJ, FG, and JB. All authors contributed to the article and approved the submitted version.

Funding

CM, Medical Research Council (MR/T016736/1), University of Birmingham Professorial fellowship. ES, Alpha One Foundation (617303), Health Data Research-UK. DT/AS/ES/FSG; Dunhill trust (RTF1906\86). AS/DT/ES, Efficacy and Mechanism Evaluation (NIHR131600) Health Technology Assessment (NIHR129593), Medical Research Council (MR/L002736/1).

Conflict of interest

CM is a Scientific Advisory Board member of Lmito Therapeutics.

The remaining authors declare that the research was conducted in the absence of any commercial or financial relationships that could be constructed as a potential conflict of interest.

Publisher's note

Supplementary material

The Supplementary Material for this article can be found online at: https://www.frontiersin.org/articles/10.3389/fimmu.2023.1083072/full#supplementary-material

References

1. Giam YH, Shoemark A, Chalmers JD. Neutrophil dysfunction in bronchiectasis: an emerging role for immunometabolism. *Eur Respir J* (2021) 58, 2003157. doi: 10.1183/13993003.03157-2020

2. Grudzinska FS, Brodlie M, Scholefield BR, Jackson T, Scott A, Thickett DR, et al. Neutrophils in community-acquired pneumonia: parallels in dysfunction at the extremes of age. *Thorax* (2020) 75(2):164. doi: 10.1136/thoraxjnl-2018-212826

3. Alves-Filho JC, Spiller F, Cunha FQ. Neutrophil paralysis in sepsis. *Shock* (2010) 34 Suppl 1:15–21. doi: 10.1097/SHK.0b013e3181e7e61b

4. Sapey E, Patel JM, Greenwood HL, Walton GM, Hazeldine J, Sadhra C, et al. Pulmonary infections in the elderly lead to impaired neutrophil targeting, which is improved by simvastatin. *Am J Respir Crit Care Med* (2017) 196(10):1325–36. doi: 10.1164/rccm.201704-0814OC

5. Winkelstein JA, Marino MC, Johnston RBJr., Boyle J, Curnutte J, Gallin JI, et al. Chronic granulomatous disease. report on a national registry of 368 patients. *Medicine* (2000) 79(3):155–69. doi: 10.1097/00005792-200005000-00003

6. Patel JM, Sapey E, Parekh D, Scott A, Dosanjh D, Gao F, et al. Sepsis induces a dysregulated neutrophil phenotype that is associated with increased mortality. *Mediators Inflamm* (2018) 2018:4065362. doi: 10.1155/2018/4065362

7. Matthay MA, Ware LB, Zimmerman GA. The acute respiratory distress syndrome. *J Clin Invest* (2012) 122(8):2731–40. doi: 10.1172/JCI60331

8. McCarthy C, Reeves EP, McElvaney NG. The role of neutrophils in alpha-1 antitrypsin deficiency. *Ann Am Thorac Soc* (2016) 13 Suppl 4:S297–304. doi: 10.1513/AnnalsATS.201509-634KV

9. Lefrancais E, Mallavia B, Zhuo H, Calfee CS, Looney MR. Maladaptive role of neutrophil extracellular traps in pathogen-induced lung injury. *JCI Insight* (2018) 3(3). doi: 10.1172/jci.insight.98178

10. Bird L. Getting enough energy for immunity. *Nat Rev Immunol* (2019) 19 (5):269–. doi: 10.1038/s41577-019-0159-y

11. Sadiku P, Willson JA, Dickinson RS, Murphy F, Harris AJ, Lewis A, et al. Prolyl hydroxylase 2 inactivation enhances glycogen storage and promotes excessive neutrophilic responses. *J Clin Invest* (2017) 127(9):3407–20. doi: 10.1172/JCI90848

12. Borregaard N, Herlin T. Energy metabolism of human neutrophils during phagocytosis. *J Clin Invest* (1982) 70(3):550–7. doi: 10.1172/JCI110647

13. Fossati G, Moulding DA, Spiller DG, Moots RJ, White MR, Edwards SW. The mitochondrial network of human neutrophils: role in chemotaxis, phagocytosis, respiratory burst activation, and commitment to apoptosis. *J Immunol* (2003) 170 (4):1964–72. doi: 10.4049/jimmunol.170.4.1964

14. van Raam BJ, Sluiter W, de Wit E, Roos D, Verhoeven AJ, Kuijpers TW. Mitochondrial membrane potential in human neutrophils is maintained by complex III activity in the absence of supercomplex organisation. *PloS One* (2008) 3(4):e2013. doi: 10.1371/journal.pone.0002013

15. Maianski NA, Geissler J, Srinivasula SM, Alnemri ES, Roos D, Kuijpers TW. Functional characterization of mitochondria in neutrophils: a role restricted to apoptosis. *Cell Death Differ* (2004) 11(2):143–53. doi: 10.1038/sj.cdd.4401320

16. Bao Y, Ledderose C, Seier T, Graf AF, Brix B, Chong E, et al. Mitochondria regulate neutrophil activation by generating ATP for autocrine purinergic signaling. *J Biol Chem* (2014) 289(39):26794–803. doi: 10.1074/jbc.M114.572495

17. Sadiku P, Willson JA, Ryan EM, Sammut D, Coelho P, Watts ER, et al. Neutrophils fuel effective immune responses through gluconeogenesis and glycogenesis. *Cell Metab* (2021) 33(2):411–23.e4. doi: 10.1016/j.cmet.2020.11.016

18. Sadiku P, Walmsley SR. Hypoxia and the regulation of myeloid cell metabolic imprinting: consequences for the inflammatory response. *EMBO Rep* (2019) 20(5). doi: 10.15252/embr.201847388

19. Pan T, Sun S, Chen Y, Tian R, Chen E, Tan R, et al. Immune effects of PI3K/Akt/HIF-1α-regulated glycolysis in polymorphonuclear neutrophils during sepsis. *Crit Care (London England)* (2022) 26(1):29.

20. Hughes MJ, McGettrick HM, Sapey E. Importance of validating antibody panels: anti-PD-L1 clone binds AF700 fluorophore. *J Immunol Methods* (2020) 483:112795. doi: 10.1016/j.jim.2020.112795

21. Barlow J, Solomon TPJ, Affourtit C. Pro-inflammatory cytokines attenuate glucose-stimulated insulin secretion from INS-1E insulinoma cells by restricting mitochondrial pyruvate oxidation capacity - novel mechanistic insight from real-time analysis of oxidative phosphorylation. *PloS One* (2018) 13(6):e0199505. doi: 10.1371/journal.pone.0199505

22. Technologies A. *Agilent seahorse XF glycolysis stress test kit*. Agilent Technologies: United States (2019).

23. Belchamber KBR, Singh R, Batista CM, Whyte MK, Dockrell DH, Kilty I, et al. Defective bacterial phagocytosis is associated with dysfunctional mitochondria in COPD macrophages. *Eur Respir J* (2019) 54(4). doi: 10.1183/13993003.02244-2018

24. Hazeldine J, Hampson P, Opoku FA, Foster M, Lord JM. N-formyl peptides drive mitochondrial damage associated molecular pattern induced neutrophil activation through ERK1/2 and P38 MAP kinase signalling pathways. *Injury* (2015) 46(6):975–84. doi: 10.1016/j.injury.2015.03.028

25. Hickman E, Herrera CA, Jaspers I. Common e-cigarette flavoring chemicals impair neutrophil phagocytosis and oxidative burst. *Chem Res Toxicol* (2019) 32 (6):982–5. doi: 10.1021/acs.chemrestox.9b00171

26. Swain P, Romero N, Dranka BP. Modulation of oxidative burst with exposure to cytokines in neutrophil cell activation. *J Immunol* (2018) 200(1 Supplement):49.26. doi: 10.4049/jimmunol.200.Supp.49.26

27. Hazeldine J, Dinsdale RJ, Harrison P, Lord JM. Traumatic injury and exposure to mitochondrial-derived damage associated molecular patterns suppresses neutrophil extracellular trap formation. *Front Immunol* (2019) 10. doi: 10.3389/fimmu.2019.00685

28. Britt EC, Lika J, Giese MA, Schoen TJ, Seim GL, Huang Z, et al. Switching to the cyclic pentose phosphate pathway powers the oxidative burst in activated neutrophils. *Nat Metab* (2022) 4(3):389–403. doi: 10.1038/s42255-022-00550-8

29. McGovern NN, Cowburn AS, Porter L, Walmsley SR, Summers C, Thompson AAR, et al. Hypoxia selectively inhibits respiratory burst activity and killing of staphylococcus aureus in human neutrophils. *J Immunol* (2011) 186(1):453–63. doi: 10.4049/jimmunol.1002213

30. Swain P, Natalia R, Dranka B. Modulation of oxidative burst with exposure to cytokines in neutrophil cell activation. *J Immunol* (2018) 2000(1):49.26. doi: 10.4049/jimmunol.200.Supp.49.26

31. TeSlaa T, Teitell MA. Techniques to monitor glycolysis. *Methods Enzymol* (2014) 542:91–114. doi: 10.1016/B978-0-12-416618-9.00005-4

32. Brand MD, Nicholls DG. Assessing mitochondrial dysfunction in cells. *Biochem J* (2011) 435(2):297–312. doi: 10.1042/BJ20110162

33. Kumar S, Dikshit M. Metabolic insight of neutrophils in health and disease. *Front Immunol* (2019) 10(2099):2099. doi: 10.3389/fimmu.2019.02099

34. Murphy MP, Bayir H, Belousov V, Chang CJ, Davies KJA, Davies MJ, et al. Guidelines for measuring reactive oxygen species and oxidative damage in cells and in vivo. *Nat Metab* (2022) 4(6):651–62. doi: 10.1038/s42255-022-00591-z

35. Zielonka J, Lambeth JD, Kalyanaraman B. On the use of l-012, a luminol-based chemiluminescent probe, for detecting superoxide and identifying inhibitors of NADPH oxidase: a reevaluation. *Free Radic Biol Med* (2013) 65:1310–4. doi: 10.1016/j.freeradbiomed.2013.09.017

36. Mookerjee SA, Nicholls DG, Brand MD. Determining maximum glycolytic capacity using extracellular flux measurements. *PloS One* (2016) 11(3):e0152016. doi: 10.1371/journal.pone.0152016

37. Porter L, Toepfner N, Bashant KR, Guck J, Ashcroft M, Farahi N, et al. Metabolic profiling of human eosinophils. *Front Immunol* (2018) 9:1404. doi: 10.3389/fimmu.2018.01404

38. Aguilera L, Campos E, Gimenez R, Badia J, Aguilar J, Baldoma L. Dual role of LldR in regulation of the lldPRD operon, involved in l-lactate metabolism in escherichia coli. *J Bacteriol* (2008) 190(8):2997–3005. doi: 10.1128/JB.02013-07

39. Chacko BK, Kramer PA, Ravi S, Johnson MS, Hardy RW, Ballinger SW, et al. Methods for defining distinct bioenergetic profiles in platelets, lymphocytes, monocytes, and neutrophils, and the oxidative burst from human blood. *Lab investigation J Tech Methods pathol* (2013) 93(6):690–700. doi: 10.1038/labinvest.2013.53

40. Bao Y, Ledderose C, Graf AF, Brix B, Birsak T, Lee A, et al. mTOR and differential activation of mitochondria orchestrate neutrophil chemotaxis. *J Cell Biol* (2015) 210(7):1153–64. doi: 10.1083/jcb.201503066

41. Rice CM, Davies LC, Subleski JJ, Maio N, Gonzalez-Cotto M, Andrews C, et al. Tumour-elicited neutrophils engage mitochondrial metabolism to circumvent nutrient limitations and maintain immune suppression. *Nat Commun* (2018) 9(1):5099. doi: 10.1038/s41467-018-07505-2

42. Mookerjee SA, Goncalves RLS, Gerencser AA, Nicholls DG, Brand MD. The contributions of respiration and glycolysis to extracellular acid production. *Biochim Biophys Acta* (2015) 1847(2):171–81. doi: 10.1016/j.bbabio.2014.10.005

43. Silva RP, Carvalho LAC, Patricio ES, Bonifacio JPP, Chaves-Filho AB, Miyamoto S, et al. Identification of urate hydroperoxide in neutrophils: a novel pro-oxidant generated in inflammatory conditions. *Free Radical Biol Med* (2018) 126:177–86. doi: 10.1016/j.freeradbiomed.2018.08.011

44. Sumbalova Z, Garcia-Souza LF, Calabria E, Volani C, Gnaiger E. O2k-protocols: isolation of peripheral blood mononuclear cells and platelets from human blood for HRR. *Mitochondrial Physiol Network* (2020).

frontiers | Frontiers in Immunology

TYPE Original Research
PUBLISHED 30 August 2023
DOI 10.3389/fimmu.2023.1204126

OPEN ACCESS

EDITED BY
Jorg Hermann Fritz,
McGill University, Canada

REVIEWED BY
Aranzazu Cruz Adalia,
Complutense University of Madrid, Spain
Ayaka Ito,
Nagoya University, Japan

*CORRESPONDENCE
Sylvie Legrand-Poels
s.legrand@uliege.be

RECEIVED 11 April 2023
ACCEPTED 01 August 2023
PUBLISHED 30 August 2023

CITATION
Iovino M, Colonval M, Wilkin C, L'homme L, Lassence C, Campas M, Peulen O, de Tullio P, Piette J and Legrand-Poels S (2023) Novel XBP1s-independent function of IRE1 RNase in HIF-1α-mediated glycolysis upregulation in human macrophages upon stimulation with LPS or saturated fatty acid.
Front. Immunol. 14:1204126.
doi: 10.3389/fimmu.2023.1204126

Novel XBP1s-independent function of IRE1 RNase in HIF-1α-mediated glycolysis upregulation in human macrophages upon stimulation with LPS or saturated fatty acid

Margaud Iovino[1], Megan Colonval[1], Chloé Wilkin[1], Laurent L'homme[2], Cédric Lassence[3], Manon Campas[4], Olivier Peulen[5], Pascal de Tullio[4], Jacques Piette[3] and Sylvie Legrand-Poels[1]*

[1]Laboratory of Immunometabolism and Nutrition, GIGA, ULiège, Liège, Belgium, [2]Univ. Lille, Inserm, CHU Lille, Institut Pasteur de Lille, U1011-EGID, Lille, France, [3]Laboratory of Virology and Immunology, GIGA, ULiège, Liège, Belgium, [4]Clinical Metabolomics Group, CIRM, ULiège, Liege, Belgium, [5]Metastasis Research Laboratory, GIGA, ULiège, Liège, Belgium

In obesity, adipose tissue infiltrating macrophages acquire a unique pro-inflammatory polarization, thereby playing a key role in the development of chronic inflammation and Type 2 diabetes. Increased saturated fatty acids (SFAs) levels have been proposed to drive this specific polarization. Accordingly, we investigated the immunometabolic reprogramming in SFA-treated human macrophages. As expected, RNA sequencing highlighted a pro-inflammatory profile but also metabolic signatures including glycolysis and hypoxia as well as a strong unfolded protein response. Glycolysis upregulation was confirmed in SFA-treated macrophages by measuring glycolytic gene expression, glucose uptake, lactate production and extracellular acidification rate. Like in LPS-stimulated macrophages, glycolysis activation in SFA-treated macrophages was dependent on HIF-1α activation and fueled the production of pro-inflammatory cytokines. SFAs and LPS both induced IRE1α endoribonuclease activity, as demonstrated by *XBP1* mRNA splicing, but with different kinetics matching HIF-1α activation and the glycolytic gene expression. Interestingly, the knockdown of IRE1α and/or the pharmacological inhibition of its RNase activity prevented HIF-1α activation and significantly decreased glycolysis upregulation. Surprisingly, XBP1s appeared to be dispensable, as demonstrated by the lack of inhibiting effect of XBP1s knockdown on glycolytic genes expression, glucose uptake, lactate production and HIF-1α activation. These experiments demonstrate for the first time a key role of IRE1α in HIF-1α-mediated glycolysis upregulation in macrophages stimulated with pro-inflammatory triggers like LPS or SFAs through XBP1s-independent mechanism. IRE1 could mediate this novel function by targeting

10.3389/fimmu.2023.1204126

other transcripts (mRNA or pre-miRNA) through a mechanism called regulated IRE1-dependent decay or RIDD. Deciphering the underlying mechanisms of this novel IRE1 function might lead to novel therapeutic targets to curtail sterile obesity- or infection-linked inflammation.

KEYWORDS

saturated fatty acid, macrophages, glycolysis, HIF-1α, IRE1α, inflammation

Introduction

The prevalence of overweight and obesity is increasing worldwide, and this is forecast to continue in the coming years. One in two adults in the USA are projected to have obesity by 2030, and about one in four to have severe obesity (1). Obesity promotes not only type 2 diabetes (T2D) and cardiovascular diseases, but also some cancers (2, 3). Metaflammation, an atypical metabolically-induced and chronic low-grade inflammation, is associated with obesity and plays an important role in the development of these comorbidities (4, 5). This one is initiated in visceral adipose tissue and is characterized by recruitment and activation of monocytes that differentiate into pro-inflammatory macrophages (4). However, these adipose tissue macrophages (ATMs), although they secrete pro-inflammatory cytokines (TNFα, IL-6, IL-1β), do not express the classical activation markers (M1) but present at their membrane alternative activation markers (M2) known to be involved in lipid metabolism (6). Interestingly, this phenotype of "Metabolically activated macrophages" (MMe) can be recapitulated by treating naive macrophages with long-chain saturated fatty acids (SFAs) like palmitate (C16:0) or stearate (C18:0) (6).

SFAs, unlike unsaturated fatty acids (UFAs), have long been recognized as pro-inflammatory mediators through Toll like receptor 4 (TLR4) activation (7–9). However, Lancaster et al. demonstrated very convincingly that palmitate does not bind to TLR4 (10). Instead, they showed that the palmitate-mediated c-jun N-terminal kinase (JNK) activation and pro-inflammatory cytokines expression require both palmitate uptake by macrophages and TLR4-dependent priming by endogenous TLR4 agonists present within serum (10). It is becoming increasingly clear that long chain SFAs mediate their impact after they are taken up by the cell and converted in acyl-coenzyme A, allowing them to be used in metabolic pathways such as lipid synthesis. Such events have been described upstream of the activation of the NLRP3 inflammasome by SFAs (11, 12). This intracellular protein complex assembles in response to homeostasis-altering molecular processes (HAMPs) and catalyzes the cleavage and maturation of the cytokines IL-1β and IL-18 (13). We and others have demonstrated that this complex is activated in ATMs of obese patients and diet induced obese (DIO) mice (14, 15) and that treatment of human and murine macrophages with SFAs recapitulates this activation (12, 16, 17). The incorporation of SFAs into membrane phospholipids followed by membrane stiffening has been proposed to trigger the loss of membrane homeostasis and the activation of the NLRP3 inflammasome (11, 12).

Such lipid bilayer stress can be at the origin of endoplasmic reticulum (ER) stress followed by unfolded protein response (UPR) (18, 19). Classical ER stress inducers like thapsigargin (Tg) and tunicamycin (Tm) induce an ER overload of unfolded/misfolded proteins that is sensed by the luminal domain of three ER-resident transmembrane proteins, PKR-like endoplasmic reticulum kinase (PERK), activating transcription factor 6 (ATF6), and inositol-requiring enzyme 1 (IRE1) (20, 21). Coordinated activation of these UPR sensors serves as the quality control mechanism to govern ER proteostasis and cope with ER stress (20, 21). Long-chain SFAs have been described to induce ER membrane disruption that is sensed by IRE1 and PERK transmembrane domain, leading to their oligomerization and activation (18, 19). By contrast, ATF6 is an ER stress sensor that has not been implicated in lipid sensing (11).

IRE1 regulates the most evolutionarily conserved arm of UPR (20, 21). In response to ER stress, IRE1 is activated through autophosphorylation, oligomerization and allosteric activation of its cytosolic RNase domain (20, 21). Once activated, IRE1 can induce three kinds of signaling pathways. IRE1 RNase activity promotes non canonical splicing of *XBP1* mRNA that produces the adaptive transcription factor XBP1s (20, 21). Sustained IRE1 RNase activity can also lead to the degradation of some mRNAs as well as certain pre-miRNAs through a process called regulated IRE1-dependent decay (RIDD) (22, 23). When chronically activated, phosphorylated IRE1 recruits TRAF2 to initiate JNK-mediated pro-apoptotic pathway and NF-κB-regulated pro-inflammatory signaling (24). IRE1 is involved in many biological processes in mammals, including cell survival/death determination, immunity and metabolism (25–28).

Although LPS does not elicit typical ER stress response, it specifically induces IRE1 activation by promoting its auto-phosphorylation through tumor necrosis factor (TNF) receptor-associated factor 6 (TRAF6)-dependent mechanism (29). This IRE1 activation was shown to regulate the TLR4/2-mediated pro-inflammatory activation of macrophages through the transcription factor XBP1s recruitment to the *IL6* and *TNF* gene promoters (30).

In this work, we highlight a new mechanism by which IRE1 RNase, independently of XBP1s, contributes to the pro-inflammatory polarization of macrophages upon stimulation with SFAs or LPS. This involves the activation of hypoxia-inducible factor 1-alpha (HIF-1α)-mediated aerobic glycolysis required to fuel the production of proinflammatory cytokines.

10.3389/fimmu.2023.1204126

Materials and methods

Preparation of FFA solutions

The palmitic acid (C16:0, #P0500), stearic acid (C18:0, #S4751) and oleic acid (C18:1 #O1008) were purchased from Sigma (St Louis, USA). A 100 mM stock solution of sodium salt was prepared by dissolving fatty acids in 0.1 M NaOH. A 5% fatty acid free, low endotoxin BSA (#A8806, Sigma, St Louis, USA) solution was prepared in RPMI 1640. The FFA stock solution and the 5% BSA solution were mixed together to obtain a 2.5 mM working solution with FFA : BSA molar ratio at 3.4:1. After pH adjustment, the working solution was filtered through a 0.2 µm pore size membrane filter, aliquoted, and stored at -20°C for less than two months.

Cell culture and treatments

Peripheral blood mononuclear cells (PBMCs) were purified by single step density gradient centrifugation with Ficoll-Paque PLUS (GE Healthcare, Chicago, USA) from buffy coat obtained from healthy donors after informed consent (Croix Rouge de Belgique). Monocytes were isolated from PBMCs using EasySep human CD14 positive selection kit II (StemCell) according to the manufacturer's instructions. Monocyte-derived macrophages (MDMs) were generated by culturing freshly isolated monocytes (0.5, 1, 2 or $4x10^6$ monocytes/well for 24-, 12-, 6-well plate or 60 mm dish, respectively) in RPMI 1640 (Lonza, Basel, Switzerland) with 20% heat-inactivated FBS (Life Technologies Europe, 10270-106), 100 IU/mL penicillin (Lonza, Basel, Switzerland), 100 IU/mL streptomycin (Lonza, Basel, Switzerland) and 100 ng/mL of human M-CSF premium grade (Miltenyi Biotec, Bergisch Gladbach, Germany) for 7 days at 37°C under 5% CO2 atmosphere.

On the day prior to MDMs treatment, M-CSF-containing medium was replaced with new medium containing 10% FBS and 0.2% or 0.4% BSA (wt/vol) in experiments in which MDMs were to be treated with fatty acids 100µM or 200µM, respectively. On the day of MDMs treatments, this medium was replaced by RPMI + 10% FBS alone or supplemented with either BSA (0.2% or 0.4%) or FFA (100 µM or 200 µM) or LPS (Sigma Aldrich, SL2654, *Escherichia coli* 026: B6, 10 or 20 ng/ml) for various times according the experiment.

Appropriate vehicle or inhibitors, including STF-083010 (Sigma Aldrich, #SML0409), 4µ8C (Sigma Aldrich, #SML0949), trans-ISRIB (Cayman Chemicals, #16258), TAK242 (Sanbio) and 2-Deoxy-D-glucose (2-DG) (Sigma Aldrich) were added 1h before FFAs or LPS stimulation and maintained through the experiment.

RNAseq

MDMs were treated by BSA, C18:0 and C18:1 (100 µM) for 3 and 16 hours. Total RNA was extracted using High pure RNA isolation kit (Roche) according to manufacturer's instruction. RNA quantity was assessed using a spectrophotometer (NanoDrop Technologies). Total RNA integrity was evaluated by an Agilent 2100 Bioanalyser with a RNA 6000 Nano chip (Agilent Technologies) and all the samples had a RNA Integrity Number (RIN) ≥ 7.3. RNA libraries were prepared for each group of MDMs with the Truseq stranded mRNA sample prep kit from Illumina, based on polyA selection of mRNAs. cDNAs fragments were sequenced using the Illumina NextSeq500. Biological triplicates of the RNA Sequencing were performed for all the conditions.

Raw sequences were subjected to quality control analysis using FastQC (http://www.bioinformatics.babraham.ac.uk/projects/fastqc/). The reads for each condition were mapped the human reference genome hg19 from UCSC using TopHat2 version 2.0.7 and stored as BAM files. Differential expression values were evaluated using Cufflinks 2.1.1 package (31). The three MDM replicates treated with C18:0 belonging to the different timepoints (3 hours and 16 hours) were tested for differential expression versus the control condition (BSA 3 hours and 16 hours respectively). Genes with a q value below 0.05 were considered as significant for differential expression.

RT-qPCR analysis

Total RNAs were extracted with RNeasy Mini Kit (Qiagen) according to the manufacturer's recommendations. Purified RNAs were reverse-transcribed to complementary DNA (cDNA) by using the RevertAid H Minus First Strand cDNA Synthesis Kit (Thermo Scientific). qPCR was performed by using FastStart Universal SYBR Green Master Mix (Roche) and ran on a LightCycler 480 (Roche Applied Science, Penzberg, Germany). Gene expressions were calculated using the 2^-ΔΔCT method. TBPH (TAR Binding-Protein) was chosen as housekeeping gene. Primers were designed with Primer-BLAST (National Center for Biotechnology Information (NCBI)) to amplify all the isoforms of the target gene, except for XBP1-s primers that were designed to only amplify the spliced isoform (isoform 2, NM_001079539). Primer sequences are provided in Supplementary Table S1.

Glucose and lactate measurements

The NMR spectra were recorded at 298 K on a Bruker Neo spectrometer (Bruker) operating at 500.13 MHz for proton and equipped with a TCI cryoprobe (Bruker). Deuterium oxide (99.96% D) and trimethylsilyl-3-propionic acid-d4 (TMSP) were purchased from Eurisotop (St-Aubin, France), phosphate buffer powder 0.1 M and calcium formate were purchased from Sigma-Aldrich. Deuterated solvents were used as the internal lock. The data have been processed with Bruker TOSPIN 4.1 (Bruker) software with standard parameter set. Phase and baseline correction were performed manually over the entire range of the spectra and the δ scale was calibrated to 0 ppm using the internal standard TMSP. For extracellular lactate and glucose dosage, 400 µl of collected culture media supernatants were supplemented with 47 µl of deuterated phosphate buffer (pH 7.4), 24 µl of a 10 mM deuterated solution of calcium formate and 70 µl of a 5mM deuterated solution of TMSP. The solution was distributed into 5-mm tubes for NMR measurement. 1H NMR spectra were acquired

using a 1D NOESY sequence with presaturation and 64 transients and 4 dummy scans. Based on the formate peak (8.46 ppm), lactate and glucose concentration were then obtained by using the Chenomx NMR Suite software (version 9.02, Edmonton, CA).

2-NBDG uptake

The fluorescent glucose analogue 2-(N-(7-nitrobenz-2-oxa-1,3-diazol-4-yl)amino)-2-deoxyglucose (2-NBDG, Invitrogen) was used to measure glucose uptake by MDMs. After treatment of the macrophages for various times, the medium was replaced by RPMI 1640 without glucose supplemented with 2-NBDG (30μM). The MDMs were maintained in culture for 30 min before being gently scrapped with EDTA (10mM, pH 6.14). Following two PBS washes, labeling with 7-aminoactinomycin D (7-AAD, Thermo Scientific) was carried out according to the company's instructions in order to assess cell viability. Results are acquired on a FACS Verse flow cytometer (Becton Dickinson) and analyzed using FlowJo 9.3.2 software (Tree Star Inc., 645 Ashland, OR).

Extracellular flux analysis

Real time bioenergetic profiles of MDMs were obtained by measuring oxygen consumption rate (OCR – pmol/min) and extracellular acidification rate (ECAR – mpH/min) using a Seahorse XFp extracellular flux analyzer (Agilent, Santa Clara, CA, USA). Monocytes were differentiated in MDMs for 7 days in XFp mini-plates (Agilent). MDMs were left untreated or treated with LPS (20 ng/ml) for 16 h, or with BSA and C18:0 (200μM) for 24h. After treatments, cells were kept in unbuffered serum-free DMEM (Basal DMEM) supplemented with glutamine (2mM), pH 7.4 at 37°C, and ambient CO2 for 1 h before the assay. During the assay, cells were successively treated with glucose (10mM), oligomycin (1μM), FCCP (2μM) and rotenone/antimycin A mix (0.5μM each). OCR and ECAR were normalized according to cell number evaluated by Hoechst incorporation (arbitrary unit – A.U.).

ELISA

IL-1 beta, IL-6 and IL-8 human uncoated ELISA Kits (ThermoFisher) were used to measure secreted cytokines in supernatants according to the manufacturer's recommendations.

Western blot analysis

Cells were lysed in total lysis buffer (50 mM Tris-HCl at pH 8, 150mM NaCl, 5mM EDTA, 1% NP-40, 0.5% Na-deoxycholate, SDS 0.1%, 1mM PMSF and complete protease inhibitor cocktail (Roche)) and subjected to SDS-PAGE. For the preparation of nuclear extracts, approximately $4x10^6$ cells (dish 60 mm) were scrapped in the hypotonic buffer 1 [10 mM HEPES-KOH pH 7.9, 10 mM KCl, 0.5% Igepal, 0.1 mM EDTA, 1 mM DTT, 1 mM PMSF and complete protease inhibitor cocktail (Roche)] and incubated for 10 min at 4°C. Samples were centrifuged and nuclei pellets were incubated for 30 min in the hypertonic buffer 2 (50 mM HEPES-KOH pH 7.9, 50 mM KCl, 400 mM NaCl, 10% glycerol, 0.1 mM EDTA, 1 mM PMSF, complete protease inhibitor cocktail). After centrifugation for 30 min, the supernatants containing nuclear proteins were harvested.

The following primary antibodies were used: anti-HIF-1α (Cell Signaling Technology, #36169), anti-XBP1s (Cell Signaling Technology, #12782), anti-GLUT1 (Cell Signaling Technology, #12939), anti-IRE1α (Cell Signaling Technology, #3294), anti-RNA polymerase II (Santa Cruz, sc-899), anti-HSP90 (Cell Signaling Technology, #4877s) and anti-GAPDH (Thermo Ambion, #AM4300). The secondary antibodies used for the revelation were HRP-linked anti-rabbit or anti-mouse IgG (Cell Signaling Technology, #7074 or #7076). For chemiluminescent western blot, revelation was performed with ECL (Pierce, Waltham, USA) by using the digital imaging system ImageQuant LAS 4000 (GE Healthcare, Chicago, USA) and quantification achieved with the ImageQuant TL software (version 7.0, GE Healthcare, Chicago, USA) or the ImageJ 2.0.0 software.

siRNA transfection

MDMs were transfected by using lipofectamine RNAiMax (13778, Invitrogen) according to manufacturer's instructions. Predesigned siRNA targeting human HIF-1α, XBP-1s and IRE1α mRNA or control (CT) siRNA targeting any sequence were purchased from Integrated DNA Technologies (IDT, Coralville, USA) (TriFECTa DsiRNA Kit) (Table S2). MDMs were transfected with siRNA XBP1s and siRNA HIF-1α for 24h and siRNA IRE1α for 48h before SFAs or LPS stimulation.

Statistical analyses

All statistical analyses were carried out using GraphPad Prism 7 for Windows (GraphPad Software, Inc., San Diego, USA) and presented as the means ± standard deviation (SD). When one independent variable was involved, two-tailed Student's t-test was performed to compare two groups and one-way ANOVA with Dunnett's multiple comparisons test to compare more than two groups. When two independent variables were involved, two-way ANOVA was used with Sidak's or Tukey's multiple comparisons test. The statistical test used and the number of biological replicates (n) are described in each figure legend.

Results

Transcriptome of C18:0-treated human macrophages highlights both glycolysis and hypoxia signatures

To assess the phenotype of macrophages maintained in FFA-rich environment, we sequenced the whole transcriptome of

10.3389/fimmu.2023.1204126

monocytes-derived macrophages (MDMs) treated with saturated or unsaturated fatty acid or with vehicle (BSA) for a short (3h) or extended period (16h). Stearate (C18:0) was chosen because it is the second most abundant SFA in tissues and blood after palmitate (C16:0) and has been shown to be more effective than palmitate in inducing cytokine production at low concentrations in our previous studies (12, 17). The low cytotoxic concentration of 100 µM was chosen for both C18:0 and the corresponding UFA, C18:1 or oleate.

The principal component analysis (Figure 1A) shows that C18:0, unlike C18:1, induces a strong MDMs transcriptome modulation after 16 hours; 1482 and 1861 genes are down- and up-regulated, respectively, compared to control MDMs (BSA) (Figure 1B). No significant change in the transcriptome has been observed after 3 h of treatment with C18:0 compared to BSA (data not shown). Gene set enrichment analysis (GSEA) was performed on differentially upregulated genes in C18:0 (16h)-treated MDMs. There were 20 hallmark gene sets upregulated with a q-value ≤ 0.05 (Figure 1C). As expected, GSEA highlighted the pro-inflammatory profile of SFA-treated macrophages as well as a strong unfolded protein response (UPR). This analysis also allowed to reveal metabolic signatures like glycolysis and hypoxia (Figure 1D).

The pro-inflammatory activation and return to homeostasis of macrophages are intimately linked and dependent on dynamic changes in cellular metabolism; an increased aerobic glycolysis is notably required to fuel the LPS-mediated pro-inflammatory polarization of macrophages (32). Accordingly, we wanted to investigate whether C18:0-treated MDMs are also subject to glycolysis activation and whether this is involved in their pro-inflammatory polarization.

Like in LPS-challenged MDMs, glycolysis is preferentially adopted by human macrophages upon activation with C18:0

Almost all studies using exogenous fatty acids solutions take BSA to conjugate fatty acids. However, it is now well accepted that BSA-associated contaminants may activate some TLR4-mediated signaling pathways (10, 32–35). To minimize such potentially confounding effects, differentiated MDMs were cultured overnight in medium containing FBS (10%) and BSA (*i.e.*, the medium used for treating MDMs, but without fatty acids) prior to treatment with either SFA or vehicle (BSA). This pre-treatment induces TLR4 tolerance that can be described as a transient state of altered responsiveness of cells to the repeated or chronic activation of TLRs (36). In this way, MDMs are tolerant when we apply the second treatment with SFAs, which allows us to dissociate the impact of SFAs from this of BSA and to investigate the response to SFAs per se.

First, we wanted to confirm the upregulation of genes involved in glycolysis by qRT-PCR experiments in C18:0-treated MDMs in comparison with LPS-stimulated MDMs. The heatmap of the Figure 2A shows the fold change (log2 FC) induced by C18:0 or LPS for each gene relative to the respective control, BSA or RPMI. C18:0 treatment induces a significant upregulation of both genes (*SLC2A1* and *SLC2A3*) encoding for glucose transporters, GLUT1 and GLUT3, respectively, as well as those encoding for the two first rate-limiting enzymes involved in the glycolytic pathway, Hexokinase II (HK2) and phosphofructokinase (PFKP). The C18:0-mediated activation kinetics are slow with no visible induction before 16h of treatment while the LPS upregulating effect is already observed after 3h, shows a peak between 6 and 12 hours and then gradually decreases. Another difference between C18:0 and LPS is the lack of stimulatory effect of C18:0 on the expression of genes encoding downstream enzymes such as the aldolase A (ALDOA), the two isoforms of pyruvate kinase (PKM1 and PKM2) and the lactate dehydrogenase A (LDHA). Interestingly, C18:0 induces the expression of the pyruvate dehydrogenase kinase 1 (PDK1) that phosphorylates and inhibits the pyruvate dehydrogenase and, thereby, prevents the pyruvate from entering the mitochondria and favors the glycolytic switch.

The glucose consumption and lactate production were assessed by comparing extracellular concentrations of glucose and lactate between C18:0- and BSA-treated MDMs or between MDMs stimulated with LPS and those maintained in medium alone for 24h. Both glucose and lactate concentrations were measured by NMR. The Figure 2B shows that C18:0 and LPS treatments induce both a significant decrease of glucose levels and significant increase of lactate concentrations compared to their respective control, suggesting an increased aerobic glycolysis. As expected, MDMs treatment with palmitate (C16:0) also stimulates both glucose uptake and lactate secretion at similar extent than C18:0 (Figure S1A). Increased glucose consumption was also validated by measuring the uptake of 2NBDG, a fluorescent glucose analog (Figure S1B).

To further investigate the impact of SFAs on macrophage bioenergetic metabolism, we performed extracellular flux analysis with the Seahorse XFp-analyzer. As expected, MDMs challenging with LPS results in greater extracellular acidification rate (ECAR), an index of glycolysis (Figure 2C). However, as already reported (37), resting and LPS-stimulated human MDMs, unlike murine bone marrow-derived macrophages (BMDMs), do not show any glycolytic reserve (spare-ECAR) when treated with oligomycin that blocks oxidative phosphorylation (OxPhos) and allows maximal glycolysis. C18:0 treatment also significantly upregulates ECAR in MDMs but induces a significant decrease of the glycolytic reserve compared to BSA (Figure 2C). As previously reported (38), neither basal oxygen consumption rate (OCR) nor maximal OCR induced upon uncoupling the respiratory chain with FCCP are affected by LPS treatment in human MDMs (Figure 2D) while LPS challenge is known to downregulate both basal and maximal OCR in BMDMs. The OCR profile of C18:0-stimulated MDMs shows no effect on basal OCR but demonstrates a significant decrease in maximal OCR compared to BSA-treated MDMs. The spare OCR capacity is greatly reduced, the oxygen consumption associated with proton leak is significantly increased while OCR-linked ATP production remains unchanged compared to MDMs treated with BSA (Figure 2D).

Altogether, these data suggest that, like in LPS-stimulated human MDMs, glycolysis is preferentially adopted by human macrophages upon activation with C18:0.

10.3389/fimmu.2023.1204126

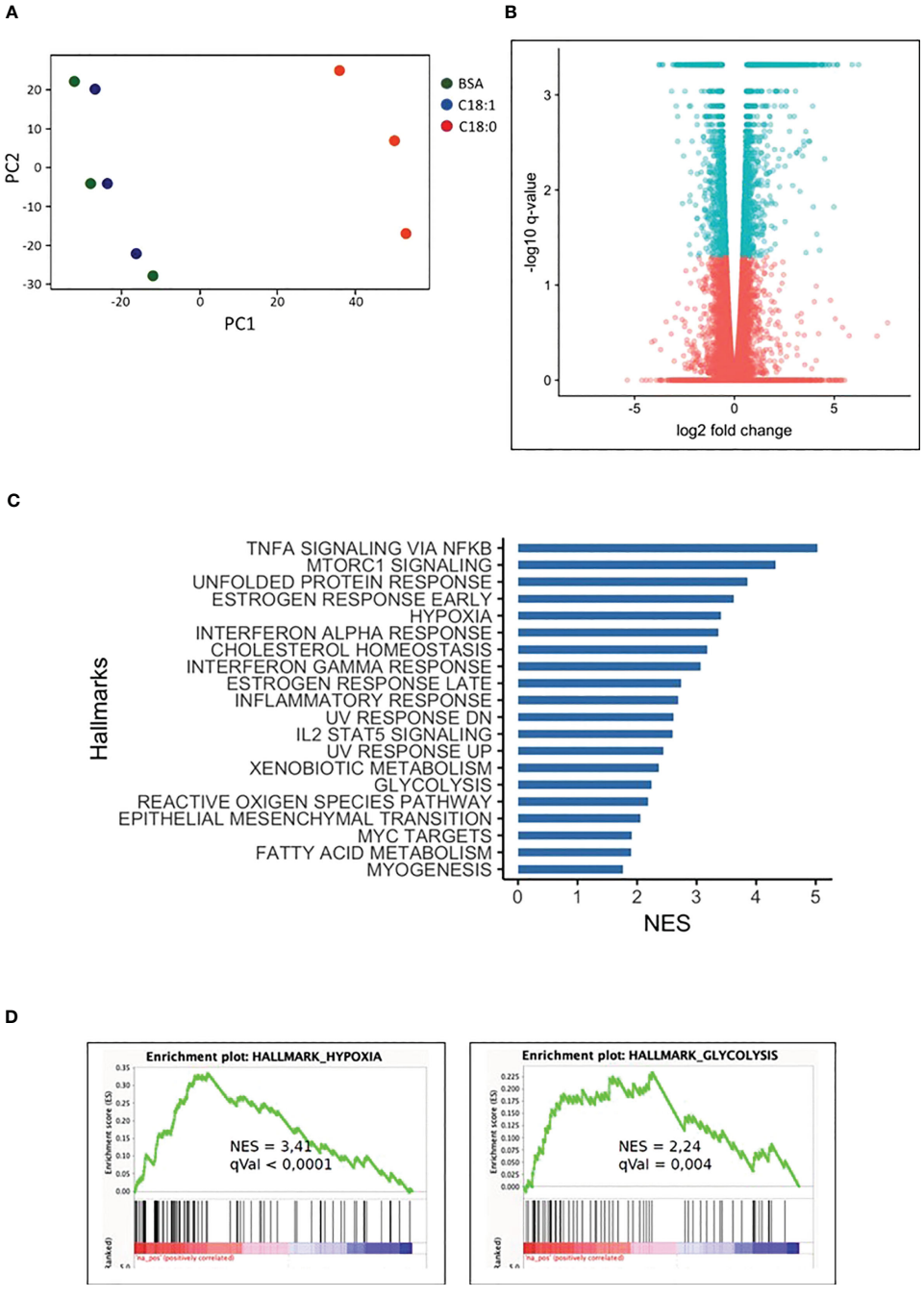

FIGURE 1
C18:0-treated human macrophages transcriptome. MDMs were treated for 16 hours with BSA, C18:0 and C18:1 at 100μM. **(A)** Principal component analysis (PCA) was performed using normalized RNA-Seq data of all the genes obtained with the three different treatments of MDMs coming from 3 independent buffy coats. **(B)** Volcano plot representation of differential expression analysis of genes in C18:0-treated MDMs. Blue points mark the genes with significantly increased or decreased (q value < 0,05) expression and pink points correspond to genes with no significantly different expression in C18:0-treated MDMs compared to BSA-treated MDMs. **(C)** Top 20 of upregulated "Hallmark pathways" in C18:0-treated MDMs vs BSA-treated MDMs. Gene set enrichment analysis (GSEA) was made with genes differentially expressed by MDMs treated for 16 hours with C18:0 100μM compared to BSA 100μM and having a q value smaller than 0.05 (NES = normalized enrichment score). **(D)** GSEA plots showing enrichment of hypoxia and glycolysis hallmark pathways in C18:0-treated MDMs with their NES and q values.

Glycolysis fuels the production of pro-inflammatory cytokines by human macrophages upon activation with C18:0

To investigate whether this C18:0-induced metabolic reprogramming promotes pro-inflammatory cytokines release, we tested the effect of 2-deoxy glucose (2-DG), a competitive glycolysis inhibitor, on IL-6, IL-1β and IL-8 secretion (Figure 3). As expected, LPS challenging of MDMs induces an important IL-6 secretion that is partially, but significantly, decreased by 2-DG pretreatment (Figure 3A). MDMs cultured with BSA produce significant IL-6 levels that are not affected by 2-DG addition. Treatment with C18:0

10.3389/fimmu.2023.1204126

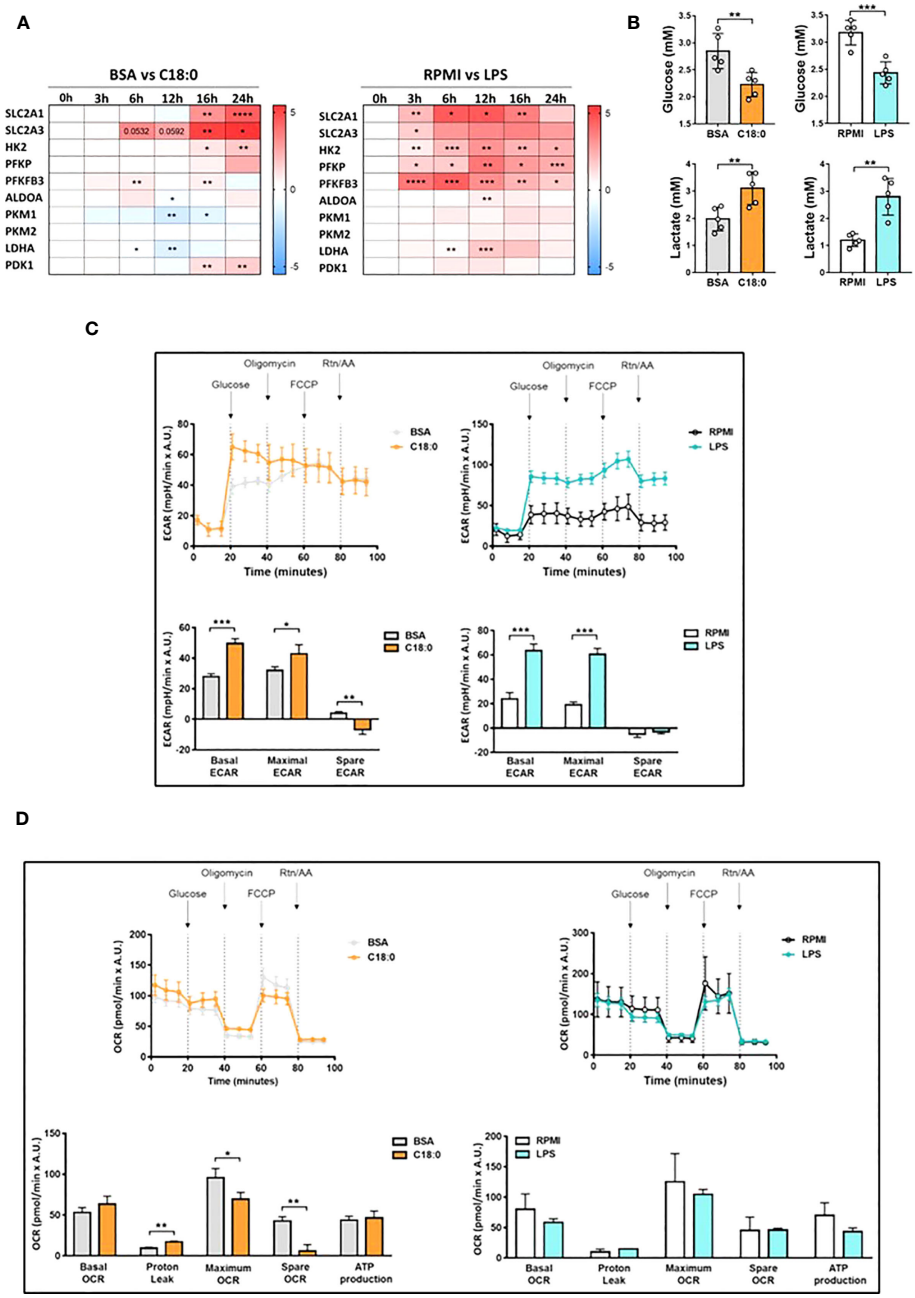

FIGURE 2
Upregulation of aerobic glycolysis in C18:0- and LPS-treated human macrophages. **(A)** Heatmap depicting Log2 fold change of glycolytic genes determined by qRT-PCR experiments in MDMs cultured with C18:0 (100μM) or LPS (10 ng/ml) for indicated times compared to MDMs cultured with BSA or medium alone (RPMI), respectively (n=4). Data are mean ± SD. Unpaired t-test. *p<0.05, **p<0.01, ***p<0.001, ****p<0.0001. **(B)** Glucose and lactate concentrations in supernatants of MDMs treated with BSA, C18:0 (100 μM), LPS (10 ng/ml) or maintained in medium alone (RPMI) for 24h. Extracellular glucose and lactate concentrations were measured by NMR (n=5). Data are mean ± SD. Unpaired t-test. **p<0.01, ***p<0.001. **(C, D)** Seahorse analysis of extracellular acidification rate (ECAR) **(C)** and oxygen-consumption rate (OCR) **(D)** on MDMs treated with BSA and C18:0 (200 μM) for 24h or maintained in medium alone (RPMI) and treated with LPS (20 ng/ml) for 16h. ECAR and OCR were normalized according to Hoechst incorporation (A.U.). Data are mean ± SD from three technical replicates for each condition. Statistical analysis of basal and maximal ECAR, maximum and spare OCR and OCR-related proton leak was performed by Student's t-test. *p < 0.05, **p < 0.01, ***p < 0.001.

further stimulates IL-6 secretion that is significantly reduced in the presence of 2-DG suggesting that glycolysis controls IL-6 release in response to C18:0.

As shown in Figure 3B, LPS treatment leads to a moderate IL-1β release compared to C18:0. This result can be explained by the fact that IL-1β release requires two signals; (1) a first priming signal leading to *IL1B* gene transcription and IL-1β precursor (pro-IL1β) synthesis mediated by TLR agonists like LPS and (2) a second signal triggered by homeostasis-altering molecular processes (HAMPs) or Danger-Associated Molecular Patterns (DAMPs) to activate NLRP3

10.3389/fimmu.2023.1204126

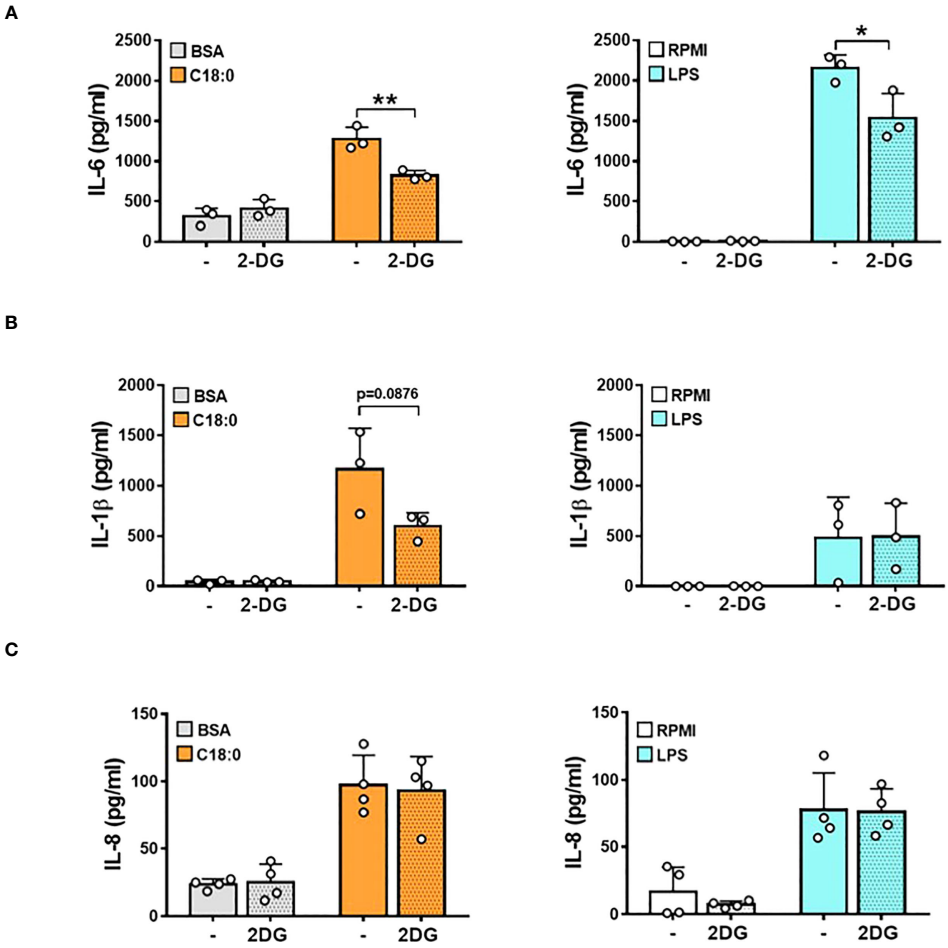

FIGURE 3
Glycolysis fuels the production of pro-inflammatory cytokines in C18:0- and LPS-stimulated human macrophages. MDMs were pre-treated or not with 2-DG (10 mM) for 1h before being stimulated with BSA, C18:0 (100 µM), LPS (10 ng/ml) or maintained in RPMI alone for 24h. The concentrations of IL-6 **(A)**, IL-1β **(B)** and IL-8 **(C)** were measured in the supernatants by ELISA. Data are mean ± SD. Unpaired t-test (n=3). *p < 0.05, **p < 0.01.

inflammasome-mediated pro-IL-1β processing and mature IL-1β release (13). In LPS-treated MDMs, a small fraction of *de novo* synthesized pro-IL-1β is probably cleaved by a weak constitutive activity of caspase 1 (39), leading to the secretion of low IL-1β levels as observed in Figure 3B. We previously demonstrated that SFAs are able to induce NLRP3 inflammasome activation in human monocytes and macrophages (12, 17). In this study, the BSA priming of MDMs probably induces the moderate synthesis of the pro-IL-1β that is efficiently cleaved by C18:0-stimulated NLRP3 inflammasome, as demonstrated by significant levels of secreted IL-1β (Figure 3B). While inhibiting glycolysis by 2-DG has no effect on LPS-induced IL-1β levels, this treatment tends to decrease IL-1β secretion in response to C18:0 probably by impacting NLRP3 inflammasome activation as already reported (40). The treatment with 2-DG has no effect on LPS- and C18:0-induced IL-8 production (Figure 3C), excluding the hypothesis that the inhibiting effect of 2-DG on IL-6 and IL-1β release could be due to a cytotoxic effect.

HIF-1α is involved in the upregulation of the glycolysis in C18:0- and LPS-treated human macrophages

In a resting cell, HIF-1α is hydroxylated at conserved proline residues by the prolyl hydroxylases (PHDs) (41). This hydroxylation targets HIF-1α for ubiquitination and rapid proteasomal degradation. The PHDs are oxygen dependent; thus, under normoxic conditions, HIF-1α is continuously turned over, resulting in low basal HIF-1α levels. In hypoxic conditions, PHDs are inhibited and HIF-1α can accumulate and form a heterodimeric complex with HIF-1β that translocates to the nucleus and increases transcription of hypoxia response elements (HRE)-containing genes (41). HIF target genes are involved in cellular adaptation to hypoxia, metabolism, and cell function (41). In addition to be implicated in adaptation to environmental changes, HIF pathway has been linked to the key metabolic changes in innate immune cells in response to pattern recognition receptor (PRR) ligation (41). In LPS-treated

macrophages, HIF-1α drives the glycolytic switch by inducing the expression of several genes including *SLC2A1*, *HK2*, *PFKP* and *PDK1*.

To investigate whether C18:0 treatment also leads to HIF-1α activation, we proceeded to the detection of HIF-1α in the nuclear extracts of BSA- and C18:0 -treated MDMs. We used LPS-stimulated MDMs as positive controls. As expected, LPS induces a strong, rapid and transient HIF-1α accumulation in the nucleus, with a peak at 5 hours (Figure 4A). C18:0 is also able to drive HIF-1α activation that is much slower (peak at 10h) and extended until 24h (Figure 4A). In addition to post-transcriptional activation of HIF-1α, LPS also induces upregulation of *HIF1A* mRNA as previously described (42) unlike C18:0 which has very little impact on *HIF1A* mRNA levels relative to BSA control (Figure 4B).

To confirm the role of HIF-1α in the glycolytic switch, we performed the knockdown of HIF-1α with two different siRNA and study the impact on GLUT1 protein levels in total cellular extracts. The depletion of HIF-1α in nuclear extracts of MDMs after siRNA transfection and treatments is shown in the Figure 4C (right panel). The knockdown of HIF-1α by both siRNA prevents GLUT1 upregulation in response to both C18:0 and LPS (Figure 4C, left panel). The glucose uptake and lactate secretion by C18:0- and LPS-treated MDMs are also affected by the knockdown of HIF-1α (Figure 4D, left panel). However, the effect is not significant for C18:0, maybe because the silencing of HIF-1α is less pronounced (Figure 4D, right panel).

Involvement of IRE1's RNase activity in both C18:0- and LPS-induced glycolytic switch

The transcriptome of human macrophages treated with stearate reveals a strong UPR signature (Figure 1C). We have previously shown a significant activation of both UPR branches involving IRE1 and PERK sensors in MDMs treated with C18:0 (12, 17). To test the potential role of both these pathways in C18:0-mediated glycolytic switch, we first used two pharmacological inhibitors, STF and ISRIB (integrated stress response inhibitor), previously reported to efficiently target the IRE1's RNase activity and the eIF2α phosphorylation by PERK, respectively, in C18:0-treated MDMs (12, 17). A specific inhibitor of both TLR4-induced MyD88 and TRIF-dependent pathways [TAK-242 (43)] was also used. The impact of all inhibitors was first tested on 2NBDG uptake induced by C18:0 and LPS. As expected, TAK242 prevents LPS but not C18:0 to upregulate the glucose uptake (Figure 5A). Interestingly, while the inhibition of the PERK-eIF2α pathway by ISRIB has no effect, the inhibition of IRE1's RNase activity by STF completely prevents the stimulation of the glucose uptake in response to both C18:0 and LPS (Figure 5A).

Since the IRE1 RNase activity seems to be required for both C18:0- and LPS-stimulated glucose uptake, we investigated whether the IRE1 activation kinetics in response to C18:0 and LPS fit with both HIF-1α and glycolysis activation. IRE1 activation was assessed by measuring both spliced *XBP1S* mRNA and nuclear XBP1s protein levels. Again, the accumulation of the *XBP1S* mRNA is rapid and transient in response to LPS with a peak at 3h while the splicing is much slower and sustained until 24h in the case of C18:0 (Figure 5B, top panel). A slight upregulation of unspliced mRNA (*XBP1U*) levels is also observed but this alone cannot explain the large increase in spliced mRNA levels (Figure 5B, top panel). Once translated, the XBP1s protein translocates into the nucleus. As expected, its appearance in nuclei is rapid and very transient in the case of LPS. In the C18:0-treated MDMs, the translocation of XBP1s is slower, reaches its peak between 5h and 10h then decreases but XBP1s is still detectable in the nuclei after 24h (Figure 5B, middle and bottom panels). Interestingly, the fate of IRE1α protein in macrophages during LPS challenge is completely different than after activation with C18:0. In resting macrophages, the levels of IRE1α protein are low (Figure S2A). Upon activation with C18:0, these levels begin to gradually increase from time 5h and are maintained until at least 24h, while two induction waves are observed for LPS, the first at a short time (3h) and the second later (16 to 24h) (Figure S2A).

Altogether, these data demonstrate that each inducer, C18:0 or LPS, activates the three pathways, IRE1-XBP1s, HIF-1α and glycolysis, with matching kinetics. Both transcription factors, HIF-1α and XBP1s, are therefore found simultaneously in the nucleus. Knowing that XBP1s has already been reported as a co-activator of HIF-1α in the transcription of the gene encoding GLUT1 (*SLC2A1*) in breast cancer cells (44), it was tempting to speculate such a role in our model of proinflammatory macrophages.

To investigate whether the IRE1-XBP1s pathway is involved in the upregulation of glycolysis genes, we studied the impact of both inhibitors of IRE1's RNase activity (STF and 4μ8C) on their expression in MDMs stimulated with LPS or C18:0. Figure 5C confirms that both drugs are able to inhibit the splicing of *XBP1* mRNA as demonstrated by the significant decrease of the *XBP1S* mRNA levels in both LPS- and C18:0-treated MDMs. The levels of *SLC2A1* and *PFKP* mRNA are also significantly downregulated by both inhibitors suggesting a role of IRE1's RNase activity in the expression of these genes in response to LPS and C18:0 (Figure 5C). The effect of STF and 4μ8C was also investigated on the expression of *SLC2A3*, *HK2* and *PDK1* genes known to be involved in glycolytic shift and previously reported to be also upregulated in C18:0- and LPS-treated MDMs (Figure 2A). Both drugs exert an inhibiting effect on *PDK1* but not *SLC2A3* expression (Figure S2B). Surprisingly, LPS-mediated *HK2* gene upregulation is significantly impacted by both inhibitors while no effect is observed in the case of C18:0 (Figure S2B). The role of IRE1's RNase activity in glycolysis upregulation was also confirmed by showing that 4μ8C reverses the increase of both GLUT1 protein expression (Figure 5D, top and middle panels) and glucose uptake in response to both LPS and C18:0 (Figure 5D, bottom panel).

XBP1s is dispensable in both C18:0- and LPS-induced glycolytic switch

The next step was to study the involvement of the transcription factor XBP1s in the activation of glycolysis in macrophages in

10.3389/fimmu.2023.1204126

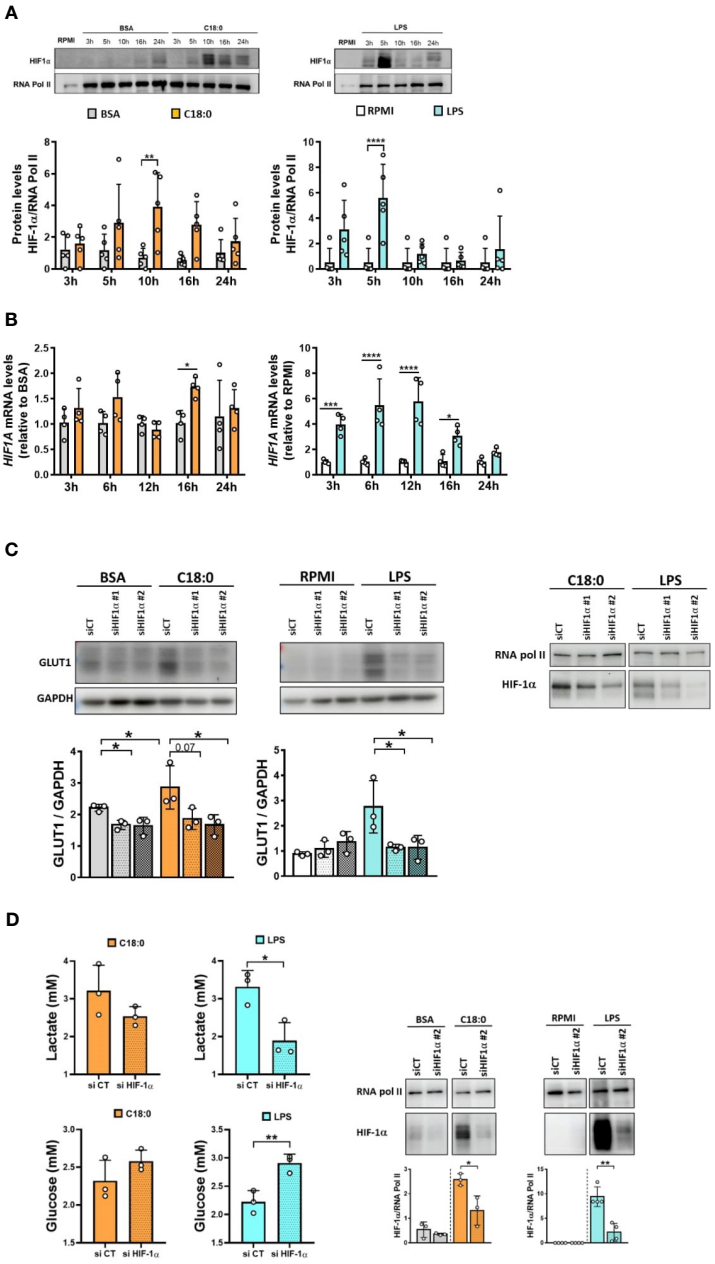

FIGURE 4
HIF-1α is involved in C18:0- and LPS-mediated glycolysis activation. **(A, B)** MDMs were treated with BSA, C18:0 (100 µM), LPS (10 ng/ml) or maintained in RPMI alone for indicated times. **(A)** Western Blot analysis of HIF-1α and RNA polymerase II protein levels in nuclear extracts (n=5). **(B)** qRT-PCR analysis of *HIF1A* mRNA levels (n=4). Data are mean ± SD. Two-Way ANOVA, Sidak's multiple comparisons test, *p < 0.05, **p < 0.01, ***p < 0.001, ****p<0.0001. **(C)** MDMs were transfected with siRNA control (CT) or siRNA targeting HIF-1α (siRNA#1 or siRNA#2) 24h before treating them or not (RPMI) with BSA, C18:0 (100 µM) or LPS (10 ng/ml). On the left: Western Blot analysis of GLUT1 and GAPDH protein levels in total extracts after 24h treatment (n=3). One-way ANOVA with Dunnett's multiple comparisons test. On the right: Western Blot analysis of HIF-1α and RNA polymerase II protein levels in nuclear extracts after treatment for 10h (C18:0) or 5h (LPS) (one representative experiment). **(D)** MDMs were transfected with siRNA control (CT) or siRNA targeting HIF-1α (siRNA#2) 24h before treating them or not (RPMI) with BSA, C18:0 (100 µM) or LPS (10 ng/ml). On the left: Lactate and glucose concentrations were measured by NMR in the supernatants of MDMs treated for 24h (n=3). On the right: Western Blot analysis of HIF-1α and RNA polymerase II protein levels in nuclear extracts after treatment for 10h (BSA, C18:0) or 5h (RPMI, LPS) (n=3). Unpaired t-test *p < 0.05, **p < 0.01.

response to both inducers. First, we studied the impact of XBP-1 silencing using two different siRNAs on glycolytic genes expression (Figure 6A). The XBP1s knockdown was checked by monitoring XBP1S mRNA levels through qRT-PCR assay. For C18:0 treatment, we can see a partial but significant depletion of XBP1S mRNA with siRNA #2 but not with siRNA #1 (Figure 6A). To ensure that this level of *XBP1S* mRNA depletion is sufficient to affect the expression of a XBP1s target gene, we measured the expression of the *DNAJB9*

10.3389/fimmu.2023.1204126

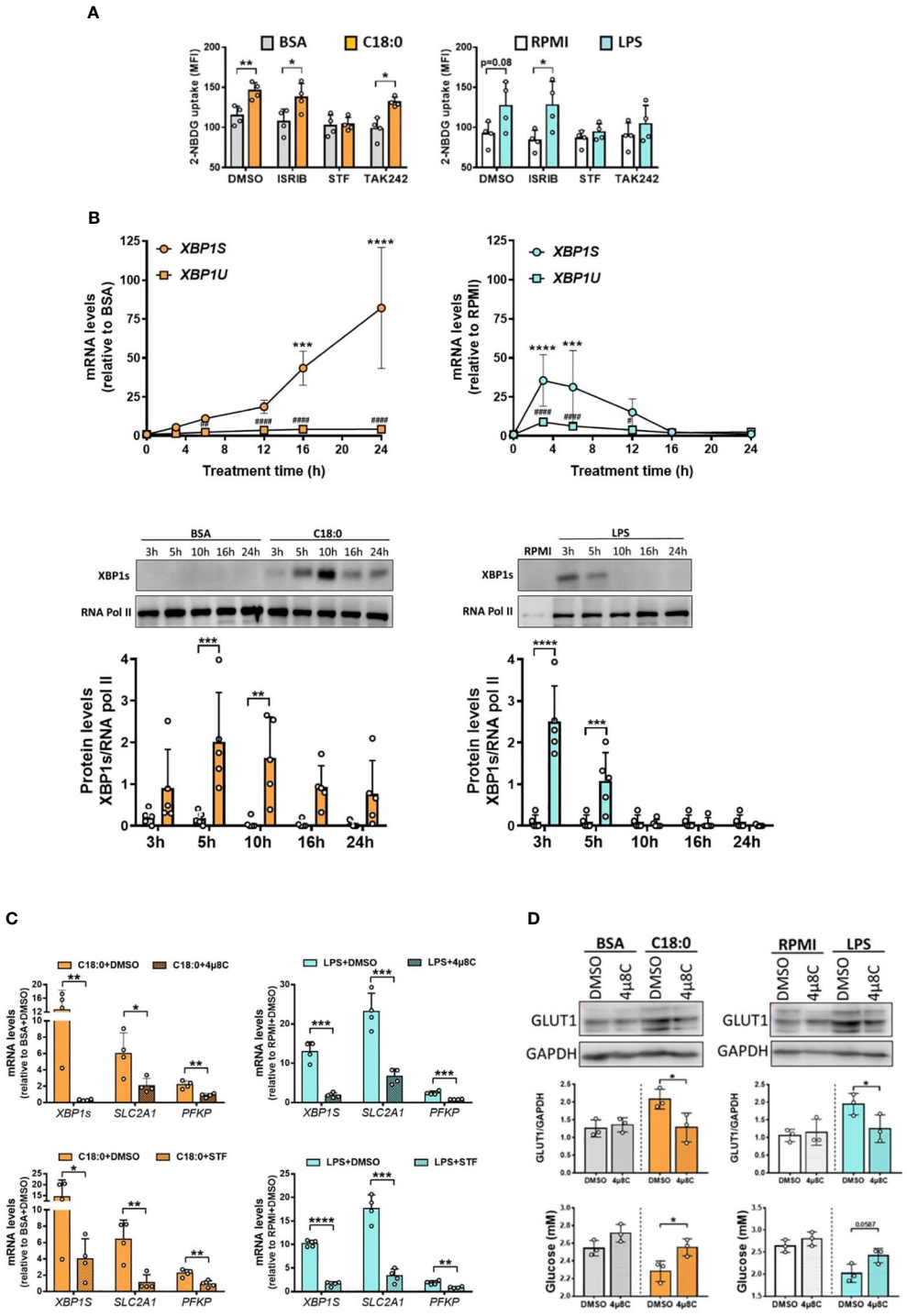

FIGURE 5
IRE1's RNase activity is involved in C18:0- and LPS-mediated glycolysis activation. **(A)** MDMs were pre-treated for 1h with ISRIB (10nM), STF (100μM), TAK 242 (1μM) or vehicle (DMSO) before the addition or not (RPMI) of BSA, C18:0 (100 μM) or LPS (10 ng/ml). After 24h, glucose uptake was determined by the fluorescence of 2-NBDG (n=4). Data are mean ± SD. Unpaired t-test *p < 0.05, **p < 0.01. **(B)** MDMs were treated with BSA, C18:0 (100 μM), LPS (10 ng/ml) or maintained in medium (RPMI) alone for indicated times. qRT-PCR analysis of unspliced (*XBP1U*) and spliced (*XBP1S*) *XBP1* mRNA levels (top panel) and western blot analysis of XBP1s and RNA polymerase II protein levels in nuclear extracts (middle and bottom panels). Two-Way ANOVA, Sidak's multiple comparisons test; *XBP1S* mRNA or XBP1s protein (C18:0 or LPS vs BSA or RPMI, respectively), ****p< 0.0001, ***p< 0.001, **p<0.01, *p<0.05 and *XBP1U* mRNA (C18:0 or LPS vs BSA or RPMI, respectively), $^{###}$p<0.001, $^{##}$p<0.01, $^{#}$p<0.05. **(C)** MDMs were pre-treated for 1h with STF (100 μM), 4μ8C (50 μM) or vehicule (DMSO) before the addition or not (RPMI) of BSA and C18:0 (100 μM) for 24h or LPS (10 ng/ml) for 6h. qRT-PCR analysis of *XBP1S, SLC2A1* and *PFKP* mRNA levels. Unpaired t-test, ****p< 0.0001, ***p< 0.001, **p<0.01, *p<0.05. **(D)** MDMs were pre-treated for 1h with 4μ8C (50 μM) or vehicule (DMSO) before the addition or not (RPMI) of BSA, C18:0 (100 μM) or LPS (10 ng/ml) for 24h. Western blot analysis of GLUT1 and GAPDH protein levels in total extracts (Top and middle panels) and determination of extracellular glucose concentrations by NMR (bottom panel). Unpaired t-test, *p<0.05.

10.3389/fimmu.2023.1204126

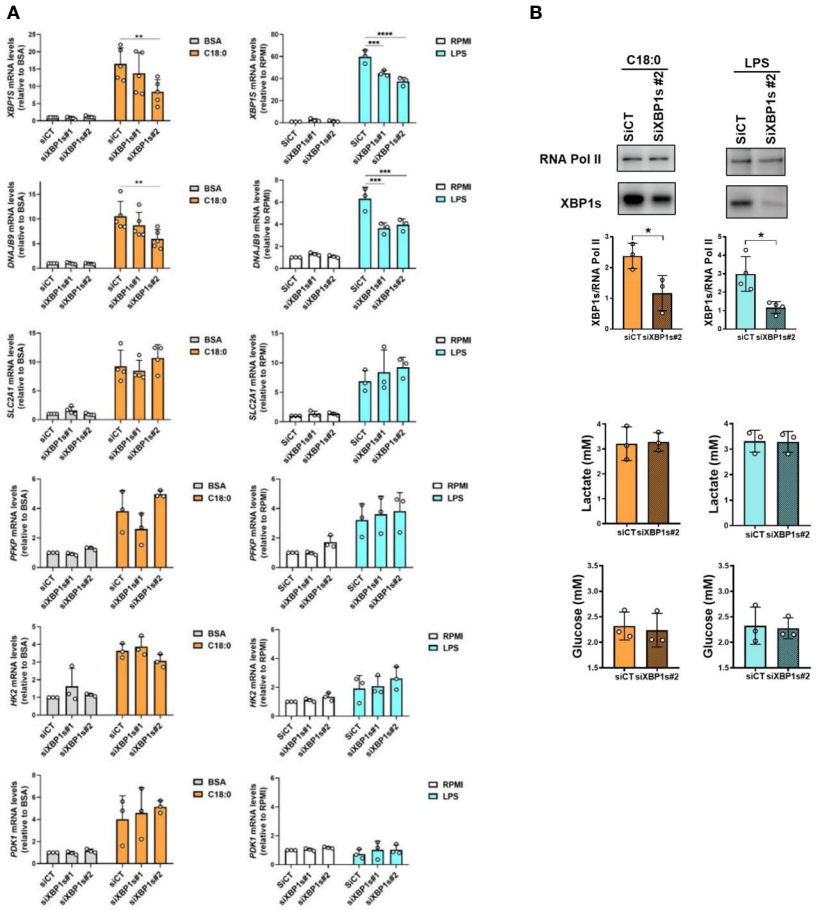

FIGURE 6
XBP1s is dispensable in C18:0- and LPS-mediated glycolysis activation. MDMs were transfected with siRNA control (siCT) or siRNA targeting XBP1s (siXBP1s#1 or siXBP1s#2) 24h before treating them or not (RPMI) with BSA, C18:0 (100 µM) or LPS (10 ng/ml). **(A)** After treatment for 24 hours with BSA or C18:0 and 3 hours with LPS, *XBP1S, DNAJB9, SLC2A1, PFKP, HK2* and *PDK1* mRNA levels were analysed by qRT-PCR. Two-Way ANOVA, Tukey's multiple comparisons test, ****p< 0.0001, ***p< 0.001, **p<0.01. **(B)** Top panel: After 10h or 5h of treatment with C18:0 or LPS, respectively, XBP1s and RNA polymerase II protein levels were analysed by Western blotting on nuclear extracts. Unpaired t-test, *p<0.05. Bottom panel: After 24h of treatment with C18:0 or LPS, glucose and lactate extracellular concentrations were measured by NMR. Unpaired t-test.

gene encoding the chaperone ERdj4 (45). As expected, the decrease in *XBP1S* mRNA levels is accompanied by a significant decrease in the expression of the *DNAJB9* gene but not of the glycolytic genes *SLC2A1, PFKP, HK2* and *PDK1* (Figure 6A). We observed a very significant increase in *XBP1S* mRNA levels after 3 hours of treatment with LPS (Figure 6A). These levels were partially but significantly downregulated with both siRNAs #1 and #2 (Figure 6A). Again, as expected, silencing of XBP1s induced a significant decrease in the induction of the *DNAJB9* gene but not of the glycolytic genes (Figure 6A). It should be noted that 3 hours of treatment with LPS was not enough to observe an upregulation of both *HK2* and *PDK1* genes; indeed, their induction requires a slightly longer treatment time (Figure 2A). XBP1s silencing, also confirmed by the decrease in XBP1s protein levels in nuclear extracts (Figure 6B, top panels), has no impact on lactate production and glucose consumption either (Figure 6B, bottom panels). Altogether, these experiments suggest that XBP1s is dispensable in both C18:0- and LPS-induced glycolytic switch.

IRE1's RNase activity is involved in both C18:0- and LPS-mediated HIF-1α activation through XBP1s-independent way

Since XBP1s is dispensable, we dropped the idea of an interaction between both transcription factors HIF-1α and XBP1s. Therefore, the impact of IRE1's RNase inhibition was studied directly on HIF-1α activation. IRE1 inhibition by 4µ8C, as confirmed by the lack of XBP1s in the nuclei of C18:0- and LPS-treated macrophages, significantly impairs the accumulation of HIF-1α in the nuclei (Figure 7A). On the other hand, no effect of either 4µ8C or STF is observed on *HIF1A* mRNA levels (Figure S3). Interestingly, while both IRE1α and XBP1s knockdown induce a decrease in nuclear XBP1s levels, yet they have opposite effects on HIF-1α activation; knockdown of IRE1α inhibits while that of XBP1s promotes HIF-1α activation (Figures 7B, C). These results demonstrate that XBP1s is absolutely not required for the activation

10.3389/fimmu.2023.1204126

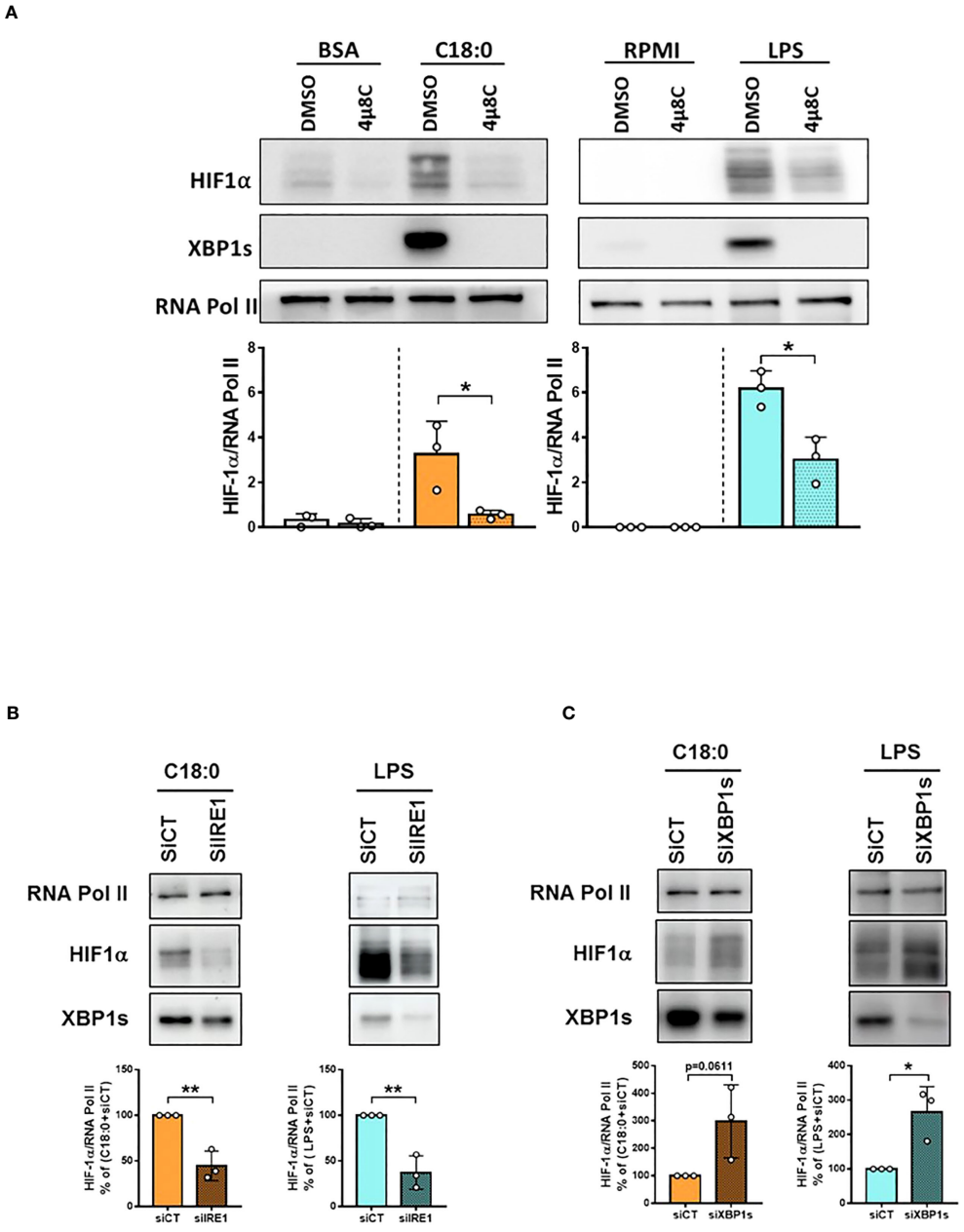

FIGURE 7
IRE1's RNase activity is involved in C18:0- and LPS-induced HIF-1α activation through XBP1s-independent way. MDMs were pre-treated with DMSO or 4μ8C (50μM) for 1h **(A)** or transfected with siRNA control (CT) or siRNA targeting IRE1α for 48h **(B)** or siRNA targeting XBP1s for 24h **(C)** before treating them or not (RPMI) with BSA (10h), C18:0 (100 μM, 10h) or LPS (10 ng/ml, 5h). HIF-1α, XBP1s and RNA polymerase II protein levels were analysed by Western blotting on nuclear extracts. Unpaired t-test, *p<0.05, **p<0.01.

of HIF-1α. Another piece of information derives from these experiences; since XBP1s deficiency was shown to lead to a feedback hyperactivation of IRE1α and RIDD (46, 47), these results suggest that the activation of HIF-1α would involve RIDD activity.

Discussion

A chronic low-grade inflammation, also called metaflammation, contributes to the pathological development of obesity (4, 5). This inflammation originates in the visceral adipose tissue undergoing significant remodeling characterized by both adipocyte hyperplasia and hypertrophy and a significant recruitment of immune cells. In this complex microenvironment enriched with nutrients (glucose, FFA), hormones (insulin), adipokines, the macrophages acquire a 'metabolically activated' phenotype with pro-inflammatory properties (6). SFAs released in excess from adipocyte lipolysis and cell death in obese adipose tissue have been proposed as triggers in shaping this ATM phenotype (6).

In order to better understand the mechanisms underlying this specific polarization, we sequenced the whole transcriptome of

human macrophages treated with SFA. As expected, GSEA highlighted the pro-inflammatory profile at the top of the list. This analysis also revealed metabolic signatures like glycolysis and hypoxia. We confirmed the activation of both HIF-1α and aerobic glycolysis in SFAs-treated MDMs and demonstrated that this glycolytic switch supports the proinflammatory polarization. Since UPR is a prominent signature in this macrophage model and mediates most of SFAs effects, we tested its involvement in HIF-1α-dependent glycolytic switch. In this work, we demonstrate a role of IRE1's RNase activity in HIF-1α activation driving the glycolytic switch in SFAs-activated macrophages. Interestingly, IRE1 fulfills this novel function independently on XBP1s.

LPS was used in each experiment as a M1 polarization inducer. Although this TLR4 agonist does not drive classical ER stress and UPR, it does induce specific activation of IRE1 by promoting its auto-phosphorylation through TRAF6-dependent mechanism (29). Interestingly, we also observed in these macrophages challenged with LPS a role of IRE1's RNase activity in the activation of both HIF-1α and glycolysis supporting pro-inflammatory polarization. Again, XBP1s was dispensable. This novel function of IRE1 RNase in immunometabolic activation of macrophages may contribute to the development of metabolic inflammation in response to higher SFAs concentrations and/or to abnormal levels of circulating LPS resulting from increased intestinal permeability in obesity (48). This work also suggests such a role for IRE1 RNase in the pro-inflammatory response following infection by exogenous pathogens activating TLR4 or other pathogen recognition receptors (PRRs).

To our knowledge, these results are the first to demonstrate a role of IRE1, independent of XBP1s, in the activation of HIF-1α and glycolysis within pro-inflammatory macrophages. In patients with Cystic Fibrosis (CF), a recessive genetic disorder caused by mutations in the cystic fibrosis transmembrane conductance regulator (CFTR), accumulation of the misfolded CFTR induces a perpetual ER stress (49). An overactive IRE1α-XBP1 pathway reprograms CF M1 macrophages toward an increased metabolic state with increased glycolytic rates and mitochondrial function, associated with exaggerated production of TNFα and IL-6. This hyper-metabolic and -inflammatory state, seen in CF macrophages, is reversed by inhibiting the RNase domain of IRE1α (49). However, a possible role of HIF-1α is not mentioned. More recently, a role of IRE1's RNase activity was demonstrated in upregulation of both *HIF1A* mRNA and glycolysis in macrophages following *B. abortus* infection but this pathway relies on XBP1s (50). Only one report demonstrated a link between IRE1's RNase activity and HIF-1α activation through XBP1s-independent mechanism in endothelial cells under hypoxia (51).

Although IRE1's RNase activity is required for HIF-1α activation by both LPS and SFAs, underlying mechanisms and kinetics are quite different. LPS-mediated IRE1 activation is rapid, as demonstrated by both *XBP1S* mRNA and XBP1s protein peaking at 3 h. Furthermore, the XBP1s protein is no longer visible beyond 5 hours of activation by LPS, demonstrating a more transient activation of IRE1 than with the classic inducers, Tm and Tg (52). This particular kinetics may be related to a two-wave modulation of IRE1 protein levels in macrophages after LPS challenge; indeed, IRE1 levels seem to increase very transiently at short times (3h), then decrease before increasing again at long times (16-24h). The activation of IRE1 in response to C18:0 results from phospholipid saturation and lipid bilayer stress (18, 19). Accordingly, the kinetics are slower and sustained over time since the *XBP1S* mRNA accumulates for up to 24 h. Similarly, the XBP1s protein shows a peak at 10h but is still visible at 24h. This kinetics is consistent with the progressive accumulation of IRE1 protein in macrophages upon activation with C18:0. Such increase in IRE1 levels has been also observed in response to classical ER stress inducers in several cell lines and has been shown to result, at least partially, from JNK-dependent transcriptional activation (52). However, accumulation of IRE1 protein during ER stress was also reported to be caused by attenuation of BiP-dependent degradation of IRE1 (53). Further investigation will be required to resolve the origin of these IRE1 protein modulations in macrophages upon LPS or SFA stimulation.

Anyway, the kinetics of IRE1 activation, although different for each inducer, match perfectly with those of HIF-1α activation and glycolytic genes expression. We also observed a very significant upregulation of IRE1 protein levels in C18:0- and LPS-treated macrophages when HIF-1α was knocked down (data not shown), which looks like to a feedback during which the cell compensates for the loss of HIF-1α by upregulating IRE1 levels. Taken together, these observations further strengthen our results demonstrating a crosstalk between both pathways, IRE1 and HIF-1α.

Since XBP1s is dispensable, IRE1 RNase should fulfill this novel function through RIDD. Such mechanism suggests the involvement of a mRNA or pre-miRNA target which would be cleaved by IRE1 endonuclease in the consensus sequence 5′-CUG↓CAG located within a stem-loop secondary structure similar to the one observed in *XBP1S* mRNA and would be subsequently rapidly degraded by cellular exoribonucleases (20–23). RIDD regulates several additional cellular functions besides reducing ER load, including triglyceride and cholesterol metabolism (54), apoptosis signaling (55), protective autophagy (56) and DNA repair (57). Several dozen RIDD mRNA targets have been highlighted so far but these may depend on the nature of the stress stimuli and tissue and cell context (58). Many RIDD targets are yet to be identified.

Interestingly, we noted that the XBP1s knockdown, that is known to induce hyperactivation of IRE1 and increased RIDD activity (46, 47), further increases HIF-1α activation in C18:0- and LPS-treated macrophages. These observations support the hypothesis involving RIDD as the missing link between IRE1 and HIF-1α. What could be the mRNA or pre-miRNA targeted by RIDD whose degradation favors the accumulation of HIF-1α? Given the complexity of the multilayer HIF-1α regulation, the possibilities are multiple. The nonhypoxic stabilization of HIF-1α in LPS-activated macrophages is mediated by tricarboxylic acid (TCA) cycle intermediates like succinate and citrate that accumulate following LPS treatment in macrophages and lead to

PHD inhibition through various mechanisms, notably through the production of reactive oxygen species (ROS) (41). Since the transcriptomic analysis revealed a ROS signature (Figure 1C) and the modulation of some TCA cycle enzymes (data not shown) in C18 :0-treated MDMs, we can suggest the involvement of such mechanism in C18 :0-mediated HIF-1α activation.

IRE1α activation has been frequently observed in multiple tissues and cell types from dietary and genetic obesity mouse models (26, 28). Hyperactivation of the IRE1α–XBP1 pathway has been also documented in adipose tissue of obese humans (59, 60). This state of so-called metabolic ER stress is provoked by a multitude of stimuli, mainly nutrients like glucose, lipids,… arising from both systemic and tissue microenvironmental changes in the face of energy surplus (28). Chronic IRE1 activation under such metabolic ER stress contributes to the pathological progression of obesity by disrupting some metabolic and inflammatory pathways in tissues like liver and pancreatic islets (28). While XBP1s can be viewed as an adaptive effector in the homeostatic control of metabolism, it has been increasingly recognized that hyperactivation of IRE1's RIDD activity can mediate its maladaptive, pathological effects during obesity-induced metabolic stress (28).

Interestingly, IRE1α was shown to be also activated in ATMs of DIO mice (61). Myeloid-specific IRE1α abrogation in mice blocked high fat diet (HFD)-induced obesity and insulin resistance and reversed HFD-induced M1–M2 imbalance in white adipose tissue (WAT) (61). To define the role of IRE1α in shaping the inflammatory properties of macrophages, Shan et al. (61) stimulated BMDMs with LPS or IL4 to mimic M1 or M2 polarization *in vitro*. They demonstrated a role of IRE1α both in upregulation of M1 markers such as iNOS and IL-6 and in downregulation of some M2 markers and proposed XBP1s- and RIDD-dependent mechanisms, respectively. Our results fit with those of Shan et al. since they also demonstrate a role of IRE1 RNAse in the M1-like polarization of human macrophages. The mechanism highlighted in our work is different but complementary since it involves IRE1's RNase activity, but not XBP1s, in the HIF-1α-mediated glycolytic switch required for the M1-like polarization of macrophages. This mechanism probably relies on RIDD.

Although activation of glycolysis controlling cytokine release has been validated in ATMs of DIO mice (62), a limitation of this work is that it does not allow to confirm the causal link between IRE1α activation and glycolysis stimulation *in vivo*. Comparing the transcriptome of ATMs from WT mice with myeloid-specific IRE1α deficient mice after a normal chow or high-fat diet would allow us to confirm or not the involvement of IRE1α in the activation of glycolysis *in vivo*. This analysis could also highlight genes that are downregulated by HFD in an IRE1α-dependent manner and that constitute potential RIDD targets. These relevant RIDD substrates would be selected for a functional study in the model of BMDMs (or MDMs) + SFA (or LPS). The best RIDD candidates could be the target of new therapeutic strategies that would have the advantage of not impacting the production of XBP1s that functions rather to protect metabolic tissues in obesity (28).

Data availability statement

The original contributions presented in the study are publicly available. This data can be found here: [https://www.ncbi.nlm.nih.gov/geo/query/acc.cgi?acc=GSE233446].

Author contributions

MI performed most of the experiments, collected and analyzed the research data. MCo performed MDMs differentiation and treatments for RNAseq as well as data analyses. CW, MCa, CL, OP, and PT contributed to technical assistance. MI, MCo, LL, JP, and SL-P conceived and designed the experiments. SL-P wrote the manuscript. All authors revised and approved the manuscript.

Acknowledgments

This work was supported by the Belgian F.R.S.-FNRS and the Leon Fredericq funds for Biomedical Research from the University of Liege, Belgium. SL-P, JP, and PT are Research Associate, Honorary Research Director, and Research Director of the Belgian F.R.S.-FNRS, respectively. MI received a PhD fellowship from Télévie (Belgian F.R.S.-FNRS). The authors thank the GIGA transcriptomic Platform and the CIRM NMR-Santé platform. We are grateful to Marco Gianfrancesco (Laboratory of Immunometabolism and Nutrition, GIGA, ULiège, Belgium), Matthieu Schoumacher (Clinical Metabolomics group, CIRM, ULiège, Belgium) and Ferman Agirman (Metastasis Research Laboratory, GIGA, ULiège, Belgium) for technical assistance.

Conflict of interest

The authors declare that the research was conducted in the absence of any commercial or financial relationships that could be construed as a potential conflict of interest.

Publisher's note

Supplementary material

The Supplementary Material for this article can be found online at: https://www.frontiersin.org/articles/10.3389/fimmu.2023.1204126/full#supplementary-material

References

1. Ward ZJ, Bleich SN, Cradock AL, Barrett JL, Giles CM, Flax C, et al. Projected U.S. state-level prevalence of adult obesity and severe obesity. *N Engl J Med* (2019) 381:2440–50. doi: 10.1056/nejmc1917339

2. Larsson SC, Burgess S. Causal role of high body mass index in multiple chronic diseases: a systematic review and meta-analysis of Mendelian randomization studies. *BMC Med* (2021) 19:320. doi: 10.1186/s12916-021-02188-x

3. Font-Burgada J, Sun B and Karin M. Obesity and cancer: the oil that feeds the flame. *Cell Metab* (2016) 23:48–62. doi: 10.1016/j.cmet.2015.12.015

4. Esser N, Legrand-Poels S, Piette J, Scheen AJ and Paquot N. Inflammation as a link between obesity, metabolic syndrome and type 2 diabetes. *Diabetes Res Clin Pract* (2014) 105:141–50. doi: 10.1016/j.diabres.2014.04.006

5. So JS. Roles of endoplasmic reticulum stress in immune responses. *Mol Cells* (2018) 41:705–16. doi: 10.14348/molcells.2018.0241

6. Kratz M, Coats BR, Hisert KB, Hagman D, Mutskov V, Peris P, et al. Metabolic dysfunction drives a mechanistically distinct proinflammatory phenotype in adipose tissue macrophages. *Cell Metab* (2014) 20:614–25. doi: 10.1016/j.cmet.2014.08.010

7. Huang S, Rutkowsky JM, Snodgrass RG, Ono-Moore KD, Schneider DA, Newman JW, et al. Saturated fatty acids activate TLR-mediated proinflammatory signaling pathways. *J Lipid Res* (2012) 53:2002–13. doi: 10.1194/jlr.d029546

8. Nguyen MT, Favelyukis S, Nguyen AK, Reichart D, Scott PA, Jenn A, et al. A subpopulation of macrophages infiltrates hypertrophic adipose tissue and is activated by free fatty acids via Toll-like receptors 2 and 4 and JNK-dependent pathways. *J Biol Chem* (2007) 282:35279–92. doi: 10.1074/jbc.m706762200

9. Shi H, Kokoeva MV, Inouye K, Tzameli I, Yin H, Flier JS. TLR4 links innate immunity and fatty acid-induced insulin resistance. *J Clin Invest* (2006) 116:3015–25. doi: 10.1172/jci28898

10. Lancaster GI, Langley KG, Berglund NA, Kammoun HL, Reibe S, Estevez E, et al. Evidence that TLR4 is not a receptor for saturated fatty acids but mediates lipid-induced inflammation by reprogramming macrophage metabolism. *Cell Metab* (2018) 27:1096–110. doi: 10.1016/j.cmet.2018.03.014

11. Robblee MM, Kim CC, Abate JP, Valdearcos M, Sandlund KLM, Shenoy MK, et al. Saturated fatty acids engage an IRE1a-dependent pathway to activate the NLRP3 inflammasome in myeloid cells. *Cell Rep* (2016) 14:2611–23. doi: 10.1016/j.celrep.2016.02.053

12. GianFrancesco MA, Dehairs J, L'homme L, Herinckx G, Esser N, Jansen O, et al. Saturated fatty acids induce NLRP3 activation in human macrophages through K+ efflux resulting from phospholipid saturation and Na, K-ATPase disruption. *Biochim Biophys Acta Mol Cell Biol Lipids* (2019) 1864:1017–30. doi: 10.1016/j.bbalip.2019.04.001

13. Lamkanfi M, Dixit VM. Mechanisms and functions of inflammasomes. *Cell* (2014) 157:1013–22. doi: 10.1016/j.cell.2014.04.007

14. Vandanmagsar B, Youm YH, Ravussin A, Galgani JE, Stadler K, Mynatt RL, et al. The NLRP3 inflammasome instigates obesity-induced inflammation and insulin resistance. *Nat Med* (2011) 17:179–88. doi: 10.1038/nm.2279

15. Esser N, L'homme L, De Roover A, Kohnen L, Scheen AJ, Moutschen M, et al. Obesity phenotype is related to NLRP3 inflammasome activity and immunological profile of visceral adipose tissue. *Diabetologia* (2013) 56:2487–97. doi: 10.1007/s00125-013-3023-9

16. Wen H, Gris D, Lei Y, Jha S, Zhang L, Huang MT, et al. Fatty acid-induced NLRP3-ASC inflammasome activation interferes with insulin signaling. *Nat Immunol* (2011) 12:408–15. doi: 10.1038/ni.2022

17. L'homme L, Esser N, Riva L, Scheen A, Paquot N, Piette J, et al. Unsaturated fatty acids prevent activation of NLRP3 inflammasome in human monocytes/macrophages. *J Lipid Res* (2013) 54:2998–3008. doi: 10.1194/jlr.m037861

18. Volmer R, van der Ploeg K and Ron D. Membrane lipid saturation activates endoplasmic reticulum unfolded protein response transducers through their transmembrane domains. *Proc Natl Acad Sci USA* (2013) 110:4628–33. doi: 10.1073/pnas.1217611110

19. Volmer R, Ron D. Lipid-dependent regulation of the unfolded protein response. *Curr Opin Cell Biol* (2015) 33:67–73. doi: 10.1016/j.ceb.2014.12.002

20. Ron D, Walter P. Signal integration in the endoplasmic reticulum unfolded protein response. *Nat Rev Mol Cell Biol* (2007) 8:519–29. doi: 10.1038/nrm2199

21. Hetz C, Zhang K, Kaufman RJ. Mechanisms, regulation and functions of the unfolded protein response. *Nat Rev Mol Cell Biol* (2020) 21:421–38. doi: 10.1038/s41580-020-0250-z

22. Hollien J, Weissman JS. Decay of endoplasmic reticulum-localized mRNAs during the unfolded protein response. *Science* (2006) 313:104. doi: 10.1126/science.1129631

23. Maurel M, Chevet E, Tavernier J, Gerlo S. Getting RIDD of RNA: IRE1 in cell fate regulation. *Trends Biochem Sci* (2014) 39:245–54. doi: 10.1016/j.tibs.2014.02.008

24. Urano F, Wang X, Bertolotti, Zhang Y, Chung P, Harding HP, et al. Coupling of stress in the ER to activation of JNK protein kinases by transmembrane protein kina IRE1. *Science* (2000) 287:664. doi: 10.1126/science.287.5453.664

25. Hetz C, Papa FR. The unfolded protein response and cell fate control. *Mol Cell* (2018) 69:169–81. doi: 10.1016/j.molcel.2017.06.017

26. Hotamisligil GS. Endoplasmic reticulum stress and the inflammatory basis of metabolic disease. *Cell* (2010) 140:900–17. doi: 10.1016/j.cell.2010.02.034

27. Grootjans J, Kaser A, Kaufman RJ, Blumberg RS. The unfolded protein response in immunity and inflammation. *Nat Rev Immunol* (2016) 16:469–84. doi: 10.1038/nri.2016.62

28. Huang S, Xing Y, Liu Y. Emerging roles for the ER stress sensor IRE1α in metabolic regulation and disease. *J Biol Chem* (2019) 294:18726–41. doi: 10.1074/jbc.rev119.007036

29. Qiu Q, Zheng Z, Chang L, Zhao Y, Tan C, Dandekar A, et al. Toll-like receptor-mediated IRE1α activation as a therapeutic target for inflammatory arthritis. *EMBO J* (2013) 32:2477–90. doi: 10.1038/emboj.2013.183

30. Martinon F, Chen X, Lee A-H, Glimcher LH. TLR activation of the transcription factor XBP1 regulates innate immune responses in macrophages. *Nat Immunol* (2010) 11(5):411–8. doi: 10.1038/ni.1857

31. Trapnell C, Roberts A, Goff L, Pertea G, Kim D, Kelley DR, et al. Differential gene and transcript expression analysis of RNA-seq experiments with TopHat and Cufflinks. *Nat Protoc* (2012) 7:562–78. doi: 10.1038/nprot.2012.016

32. O'Neill LAJ, Kishton RJ, Rathmell J. A guide to immunometabolism for immunologists. *Nat Rev Immunol* (2016) 16(9):553–65. doi: 10.1038/nri.2016.70

33. Erridge C. Endogenous ligands of TLR2 and TLR4: agonists or assistants? *J Leukoc Biol* (2010) 87:989–99. doi: 10.1189/jlb.1209775

34. Erridge C, Samani NJ. Saturated fatty acids do not directly stimulate Toll-like receptor signaling. *Arterioscler Thromb Vasc Biol* (2009) 29:1944–9. doi: 10.1161/ATVBAHA.109.194050

35. Pal D, Dasgupta S, Kundu R, Maitra S, Das G, Mukhopadhyay S, et al. Fetuin-A acts as an endogenous ligand of TLR4 to promote lipid-induced insulin resistance. *Nat Med* (2012) 18:1279–85. doi: 10.1038/nm.2851

36. Butcher SK, O'Carroll CE, Wells CA and Carmody RJ. Toll-like receptors Drive specific Patterns of Tolerance and Training on restimulation of Macrophages. *Front Immunol* (2018) 9:933. doi: 10.3389/fimmu.2018.00933

37. Vrieling F, Kostidi S, Spaink HP, Haks MC, Mayboroda OA, Ottenhoff THM, et al. Analyzing the impact of Mycobacterium tuberculosis infection on primary human macrophages by combined exploratory and targeted metabolomics. *Sci Rep* (2020) 10(1):7085. doi: 10.1038/s41598-020-62911-1

38. Vijayana V, Pradhana P, Braudb L, Fuchsc HR, Guelerd F, Motterlinib R, et al. Human and murine macrophages exhibit differential metabolic responses to lipopolysaccharide-A divergent role for glycolysis. *Redox Biol* (2019) 22:101147. doi: 10.1016/j.redox.2019.101147

39. Kahlenberg JM, Dubyak GR. Differing caspase-1 activation states in monocyte versus macrophage models of IL-1beta processing and release. *J Leukoc Biol* (2004) 76:676–684. doi: 10.1189/jlb.0404221

40. Yu Q, Guo M, Zeng W, Zeng M, Zhang X and Zhang Y. Interactions between NLRP3 inflammasome and glycolysis in macrophages: New insights into chronic inflammation pathogenesis. *Immun Inflamm Dis* (2022) 10:e581. doi: 10.1002/iid3.581

41. Corcoran SE, O'Neill LAJ. HIF1α and metabolic reprogramming in inflammation. *J Clin Invest* (2016) 126(10):3699–707. doi: 10.1172/JCI84431

42. Rius J, Guma M, Schachtrup C, Akassoglou K, Zinkernagel AS, Nizet V, et al. NF-kappaB links innate immunity to the hypoxic response through transcriptional regulation of HIF-1alpha. *Nature* (2008) 453(7196):807–11. doi: 10.1038/nature06905

43. Matsunaga N, Tsuchimori N, Matsumoto T and Ii M. TAK-242 (resatorvid), a small-molecule inhibitor of Toll-like receptor (TLR) 4 signaling, binds selectively to TLR4 and interferes with interactions between TLR4 and its adaptor molecules. *Mol Pharmacol* (2011) 79(1):34–41. doi: 10.1124/mol.110.068064

44. Chen X, Iliopoulos D, Zhang Q, Tang Q, Greenblatt MB, Hatziapostolou M, et al. XBP1 promotes triple-negative breast cancer by controlling the HIF1a pathway. *Nature* (2014) 508:103–7. doi: 10.1038/nature13119

45. Lee AH, Iwakoshi NN, Glimcher LH. XBP-1 regulates a subset of endoplasmic reticulum resident chaperone genes in the unfolded protein response. *Mol Cell Biol* (2003) 23:7448–59. doi: 10.1128/MCB.23.21.7448-7459.2003

46. Lee AH, Heidtman K, Hotamisligil GS, Glimcher LH. Dual and opposing roles of the unfolded protein response regulated by IRE1alpha and XBP1 in proinsulin processing and insulin secretion. *Proc Natl Acad Sci USA* (2011) 108:8885–90. doi: 10.1073/pnas.1105564108

47. Akiyama M, Liew CW, Lu S, Hu J, Martinez R, Hambro B, et al. X-box binding protein 1 is essential for insulin regulation of pancreatic α-cell function. *Diabetes* (2013) 62:2439–49. doi: 10.2337/db12-1747

48. Cani PD, Amar J, Iglesias MA, Poggi M, Knauf C, Bastelica D, et al. Metabolic endotoxemia initiates obesity and insulin resistance. *Diabetes* (2007) 56:1761–72. doi: 10.2337/db06-1491

49. Lara-Reyna S, Scambler T, J Holbrook J, Wong C, Jarosz-Griffiths HH, Martinon F, et al. Metabolic reprograming of cystic fibrosis macrophages via the IRE1a arm of the

unfolded protein response results in exacerbated inflammation. *Front Immunol* (2019) 10:1789. doi: 10.3389/fimmu.2019.01789

50. Guimarães ES, Gomes MTR, Sanches RCO, Matteucci KC, Marinho FV and Oliveira SC. The endoplasmic reticulum stress sensor IRE1a modulates macrophage metabolic function during Brucella abortus infection. *Front Immunol* (2023) 13:1063221. doi: 10.3389/fimmu.2022.1063221

51. Moszynska A, Collawn JF, Bartoszewski R. IRE1 endoribonuclease activity modulates hypoxic HIF-1 signaling in human endothelial cells. *Biomol* (2020) 10:895. doi: 10.3390/biom10060895

52. Walter F, O'Brien A, Concannon CG, Düssmann H, Prehn JHM. ER stress signaling has an activating transcription factor 6 (ATF6)-dependent "off-switch". *J Biol Chem* (2018) 293(47):18270–84. doi: 10.1074/jbc.ra118.002121

53. Sun S, Shi G, Sha H, Ji Y, Han X, Shu X, et al. IRE1 is an endogenous substrate of endoplasmic-reticulum-associated degradation. *Nat Cell Biol* (2015) 17:1546–55. doi: 10.1038/ncb3266

54. So JS, Hur KY, Tarrio M, Ruda V, Frank-Kamenetsky M, Fitzgerald K, et al. Silencing of lipid metabolism genes through IRE1alpha mediated mRNA decay lowers plasma lipids in mice. *Cell Metab* (2012) 16:487–99. doi: 10.1016/j.cmet.2012.09.004

55. Lam M, Marsters SA, Ashkenazi A, Walter P. Misfolded proteins bind and activate death receptor 5 to trigger apoptosis during unresolved endoplasmic reticulum stress. *eLife* (2020) 9:e52291. doi: 10.7554/elife.52291

56. Bae D, Moore KA, Mella JM, Hayashi SY, Hollien J. Degradation of Blos1 mRNA by IRE1 repositions lysosomes and protects cells from stress. *J Cell Biol* (2019) 218:1118–27. doi: 10.1083/jcb.201809027

57. Dufey E, Bravo-San Pedro JM, Eggers C, González-Quiroz M, Urra H, Sagredo AI, et al. Genotoxic stress triggers the activation of IRE1alpha dependent RNA decay to modulate the DNA damage response. *Nat Commun* (2020) 11:2401. doi: 10.1038/s41467-020-15694-y

58. Lhomond S, Avril T, Dejeans N, Voutetakis K, Doultsinos D, McMahon M, et al. Dual IRE1 RNase functions dictate glioblastoma development. *EMBO Mol Med* (2018) 10:e7929. doi: 10.15252/emmm.201707929

59. Boden G, Duan X, Homko C, Molina EJ, Song W, Perez O, et al. Increase in endoplasmic reticulum stress-related proteins and genes in adipose tissue of obese, insulin-resistant individuals. *Diabetes* (2008) 57:2438–44. doi: 10.2337/db08-0604

60. Gregor MF, Yang L, Fabbrini E, Mohammed BS, Eagon JC, Hotamisligil GS, et al. Endoplasmic reticulum stress is reduced in tissues of obese subjects after weight loss. *Diabetes* (2009) 58:693–700. doi: 10.2337/db08-1220

61. Shan B, Wang X, Wu Y, Xu C, Xia Z, Dai J, et al. The metabolic ER stress sensor IRE1alpha suppresses alternative activation of macrophages and impairs energy expenditure in obesity. *Nat Immunol* (2017) 18:519–29. doi: 10.1038/ni.3709

62. Boutens L, Hooiveld GJ, Dhingra S, Cramer RA, Netea MG, Stienstra R. Unique metabolic activation of adipose tissue macrophages in obesity promotes inflammatory responses. *Diabetologia* (2018) 61:942–53. doi: 10.1007/s00125-017-4526-6

frontiers | Frontiers in Immunology

TYPE Original Research
PUBLISHED 22 September 2023
DOI 10.3389/fimmu.2023.1198310

OPEN ACCESS

EDITED BY
Jorg Hermann Fritz,
McGill University, Canada

REVIEWED BY
Nicolas Jacquelot,
University of Calgary, Canada
Sarah Q. Crome,
University of Toronto, Canada

*CORRESPONDENCE
Fumio Takei
ftakei@bccrc.ca

†These authors have contributed equally to this work

RECEIVED 01 April 2023
ACCEPTED 30 August 2023
PUBLISHED 22 September 2023

CITATION
Sadeghalvad M, Khijakadze D, Orangi M and Takei F (2023) Flow cytometric analysis of innate lymphoid cells: challenges and solutions.
Front. Immunol. 14:1198310.
doi: 10.3389/fimmu.2023.1198310

Flow cytometric analysis of innate lymphoid cells: challenges and solutions

Mona Sadeghalvad[1†], Davit Khijakadze[1,2†], Mona Orangi[1,2†] and Fumio Takei[1,3*]

[1]Terry Fox Laboratory, British Columbia Cancer, Vancouver, BC, Canada, [2]Interdisciplinary Oncology Program, University of British Columbia (UBC), Vancouver, BC, Canada, [3]Department of Pathology and Laboratory Medicine, University of British Columbia (UBC), Vancouver, BC, Canada

Introduction: The three groups of helper innate lymphoid cells (ILCs), namely ILC1, ILC2 and ILC3, have been identified by flow cytometry by combinations of cell surface markers. Here, we review various ways ILCs are currently identified, focusing on potential problems and their solutions. The first step to identify all ILCs is to exclude other lymphocytes and myeloid cells by their lineage-specific markers (Lin). However, the Lin cocktail varies in various studies, and the definition of Lin- population containing ILCs is often ambiguous, resulting in contamination of Lin^+ cells, particularly T cells.

Method: We have designed combinations of cell surface markers to identify ILC populations in various tissues of B6 mice by flow cytometry. To minimize T cell contamination, TCR/CD3ϵ antibodies were used separately from the Lin cocktail. ILCs identified by surface markers are confirmed by the expression of the transcription factors GATA3, RORγt, T-bet and Eomes.

Result: ILC1s in the B6 mouse liver are identified by Lin-$NKp46^+NK1.1^+$TCR/$CD3\epsilon^-CD49a^+CD49b^-$. However, defining ILC1s in other tissues remains a challenge. ILC2s in the lung are identified by Lin^-TCR/$CD3\epsilon^-$ $Thy1^+CD127^+ST2^+$ whereas ILC2s in the small intestine and liver are identified by Lin^-TCR/$CD3\epsilon^-Thy1^+GATA3^+ROR\gamma t^-$. ILC3s in B6 mouse spleen, liver, lung and small intestine are identified by Lin^-TCR/$CD3\epsilon^-$ $Thy1^+CD127^+ROR\gamma t^+$.

Discussion: The ILC population is heterogeneous and the strategies to identify ILCs have to be designed for each ILC population and tissue. Excluding T cells in all cases is crucial, and a combination of transcription factors GATA3, RORγt, T-bet, and Eomes should be used to identify ILCs. Using CD3ϵ/TCRs in a different fluorochrome not in Lin cocktail minimizes contamination of T cells specifically identify individual ILC populations in various tissues.

KEYWORDS

innate lymphoid cells, ILC1, ILC2, ILC3, flow cytometry, analysis

1 Introduction

The family of cytokine-producing helper innate lymphoid cells (ILCs) consists of three groups, namely, ILC1, ILC2, and ILC3 (1). ILCs do not express unique markers, and they can only be distinguished from each other and other lymphocytes by combinations of markers. All ILCs are negative for mature hematopoietic cell lineage surface markers (Lin^-). For mouse ILCs, the Lin cocktail typically includes Ter119 for erythroid cells, Gr-1 for granulocytes, CD11c for dendritic cells, CD11b for monocytes/macrophages, CD19 for B cells, and CD3ϵ/TCR for T cells (2). With this Lin cocktail, Lin^- cells include all ILCs and also a subset of NK cells that is CD11b negative. To avoid NK cell contamination, NK1.1 is used in the lineage cocktail or in separate fluorochrome to exclude NK cells (3). However, the separation between Lin^+ and Lin^- cells is often not clear due to the presence of cells expressing an intermediate level of Lin markers. Because the Lin^- gate is often arbitrarily set, some Lin^+ cells, particularly T cells, can be included in the Lin^- population. ILCs within the Lin^- population can be further identified by CD127 and/or Thy1 expression. However, some ILC1s do not express Thy1 and CD127, while some NK cells express Thy1 and CD127. Currently, there is no simple gating strategy to identify all ILCs by combinations of cell surface markers, and the Lin cocktail and subsequent gating for ILCs have to be designed for each ILC population.

Each ILC population is heterogeneous, and cell surface marker expression varies among ILCs in different tissues (4–6), making it difficult to identify ILCs in various tissues by cell surface markers alone. ILCs can also be identified by the expression of the transcription factors T-bet, Eomes, GATA3, and RORγt. ILC2s are $T\text{-bet}^-Eomes^-GATA3^{hi}ROR\gamma t^-$, ILC3s are $Eomes^-GATA3^{lo}ROR\gamma t^+$, and ILC1s and NK cells are $T\text{-bet}^+ROR\gamma t^-$ (7, 8). The distinction between NK cells and ILC1s is complicated by the heterogeneity of ILC1s. ILC1s in the liver are $Eomes^-GATA3^-$, while salivary gland ILC1s express Eomes and T-bet. Intestinal and thymic ILC1s are $Eomes^-T\text{-bet}^+GATA3^+$ (9). As T cells also express these transcription factors, it is critical to exclude T cells from this analysis. Recent reports have also shown that ILC progenitors expressing those transcription factors are found in various tissues (10), further complicating ILC analyses.

While the transcription factor staining can confirm the identity of individual ILC populations, it requires fixing and permeabilization of cells and cannot be applied to isolate live ILCs. There are fluorescent reporter mice that can be used to identify ILCs without fixing/permeabilization of cells, including reporters for GATA3 (11), IL-5 and IL-13 (12), RORγt (13), and NKp46 (14). Because those genes are not specific to ILCs but are also expressed in some other lymphocytes, combinations of other cell surface markers are required to identify individual ILC populations.

Here, we discuss problems with the ways ILCs are currently identified by flow cytometry and how individual ILC populations in the lung, liver, and small intestine (SI) can be identified by combinations of cell surface markers and transcription factors without contamination of other lymphocytes.

2 Materials and methods

2.1 Mice

C57BL/6J (B6) mice were bred in-house and purchased from breeders of Jackson Laboratory (Bar Harbor, ME, USA). *Rorc(γt)*-eGFP reporter mice (JAX stock #007572) and $Rag1^{-/-}$ mice (JAX stock #002216) on a B6 background were originally purchased from Jackson Laboratory. Homozygous *Rorc(γt)*-eGFP mice were crossed with B6 mice to generate heterozygous *Rorc(γt)*-eGFP mice. All mice were maintained in the British Columbia Cancer Research Centre animal facility under specific pathogen-free conditions. The use of these mice was approved by the animal committee of the University of British Columbia and in accordance with the guidelines of the Canadian Council on Animal Care.

2.2 Tissue processing and leukocyte preparation

All tissues including the liver, lung, spleen, and SI were processed as described previously in detail (15). Mice were anesthetized with isoflurane (5%) and then euthanized with CO_2 until respiratory arrest. Tissues were collected in a tube containing 5 ml of Dulbecco's modified Eagle medium (DMEM) with 2% fetal bovine serum (FBS).

2.2.1 Liver

Livers were mashed and passed through 40-μm cell strainers (BD Falcon or Sarstedt) with 10 ml of DMEM (Thermo Fisher Scientific, Waltham, MA, USA; #11995073) + 10% (v/v) FBS, and the strainers were washed with 15 ml of the same media. After centrifugation (4°C, 3 min, 30 × *g*) for hepatocyte sedimentation, the supernatant was collected and centrifuged (4°C, 5 min, 300 × *g*). The pellet was resuspended in 16 ml of 40% Percoll. After centrifugation (room temperature (RT), 20 min, 1,400 × *g*), the pellet resuspended in 3 ml of red blood cell (RBC) lysis buffer (ammonium chloride, NH_4Cl; MilliporeSigma, St. Louis, MO, USA; cat. no. A9434-500G; sodium bicarbonate, $NaHCO_3$; Thermo Fisher Scientific, cat. no. BP328-500; EDTA disodium salt, Thermo Fisher Scientific, cat. no. BP120-1, pH 7.2–7.4).

2.2.2 Spleen

Spleens were mashed through 70-μm strainers in 5 ml phosphate-buffered saline (PBS) + 2% FBS. Strainers were washed with 5 ml of the same buffer. After centrifugation (4°C, 5 min, 400 × *g*), the supernatant was discarded, and RBCs were lysed using RBC lysis buffer.

2.2.3 Lung

Lungs were minced in a 10-cm petri dish by using a razor and then placed in a tube containing 5 ml of digestion buffer (DMEM + 10% FBS + 142.5 U/ml Collagenase IV, Thermo Fisher Scientific, cat. no. 17104019; 118.05 KU/ml of DNase I from bovine pancreas, MilliporeSigma, cat. no. 11284932001). Tubes were incubated for

25 min at 37°C in a shaker at 200 rpm. Digested tissues were mashed and passed through 70-µm cell strainers by adding 5 ml DMEM + 10% FBS. After centrifugation (4°C, 5 min, 400 × *g*), the supernatant was discarded, and the pellet was resuspended in 5 ml of 36% Percoll and centrifuged at RT, 20 min, 650 × *g*. RBCs were lysed using RBC lysis buffer.

2.2.4 Small intestine

The SIs were extensively washed with intestine wash buffer (Ca^{2+}/Mg^{2+}-free (CMF) HBSS + 15 mM HEPES/pH = 7.2) and were cut into ~1-cm pieces after discarding the fat and Peyer's patches. With the use of surgical scissors, each fragment was cut open longitudinally. Then, the luminal contents were rinsed three times using an intestine wash buffer. The intestinal epithelial cells were removed by incubation in CMF/EDTA/FBS buffer (HBSS + 15 mM HEPES + 10% FBS + 2.5 mM EDTA + 1 mM DTT/pH = 7.2) for 20 min at 37°C in a shaker at 250 rpm. The tubes were shaken manually 10 times, and then the contents were passed through sieves and rinsed with wash buffer. This step could be repeated for two more times. Tissues were digested using 100 U/ml of Collagenase VIII (Sigma-Aldrich, cat. no. C2139-500MG) and 9.41 U/ml of DNase I from bovine pancreas (Millipore Sigma, cat. no. 11284932001). Digestion buffer was prepared in DMEM containing 10% FBS. Tissue digestion was performed in a shaker for 25 min at 37°C and 5% CO_2. The contents were filtered through a 100-µm cell strainer, and 10 ml of intestine washing buffer was added. After centrifugation (4°C, 5 min, 400 × *g*), the pellet was resuspended in 5 ml of PBS containing 2% FBS and filtered through 70-µm and then 40-µm cell strainers. Cells were centrifuged (4°C, 5 min, 400 × *g*), and then RBCs were lysed using RBC lysis buffer.

After adding RBC lysis buffer, cells were incubated for 5 min at RT. DMEM at a volume of 5 ml with 2% FBS was added and centrifuged (4°C, 5 min, 400 × *g*). The supernatant was discarded, and the pellet was resuspended in 1 ml PBS + 2% FBS and then transferred to a 5-ml flow tube through a 35-µm strainer cap. Cells were then stained with antibodies in PBS containing 2% FBS.

2.3 Intracellular cytokine staining

Leukocytes were incubated at 37°C for 3 hours in 500 µl of Roswell Park Memorial Institute (RPMI) 1640 media containing 10% FBS, 100 U/ml of P/S, 50 mM of 2-ME, Brefeldin A (Golgi Plug, BD Biosciences, San Jose, CA, USA), 30 ng/ml of phorbol 12-myristate 13-acetate (PMA; Sigma, P1585), and 500 ng/ml of ionomycin (Sigma, 10634). Intracellular cytokine staining was performed after the incubation and surface staining using Cytofix/Cytoperm Fixation/Permeabilization Solution kit (BD Biosciences) according to the manufacturer's protocol. Intracellular GATA3, RORγt, T-bet, and Eomes staining were carried out similarly without preincubation using Foxp3/Transcription Factor Staining Buffer Set (Thermo Fisher Scientific) according to the manufacturer's protocol. Simultaneous intracellular RORγt and cytokine staining were performed using Foxp3/Transcription Factor Staining Buffer Set according to the manufacturer's protocol.

TABLE 1 Antibody list for flow cytometry.

Antigen	Clone	Fluorochrome	Brand	Dilution
Viability dye	—	eFIuor780	Thermo Fisher	500
CD45	30-F11	BV510	BD Biosciences	100
CD127	A7R34	PE	Thermo Fisher	250
CD127	A7R34	AF700	Thermo Fisher	80
NKP46	29A1.4	eFluor450	Thermo Fisher	250
NKP46	29A1.4	PerCPeF710	Thermo Fisher	200
NKP46	29A1.4	AF700	Invitrogen	
CD19	ID3	eFluor450	Thermo Fisher	750
LY6G and LY6C (GR-1)	R86-8C5	eFluor450	Thermo Fisher	1000
TCRβ	H57-597	PE	BioLegend	250
TCRβ	H57-597	FITC	BD Biosciences	250
TCRγδ	eBioGL3	PE	BD Biosciences	750
TCRγδ	GL3	FITC	BD Biosciences	750
CD3	145-2C11	PE	BD Biosciences	125
CD3	145-2C11	FITC	Thermo Fisher	250

(Continued)

TABLE 1 Continued

Antigen	Clone	Fluorochrome	Brand	Dilution
GATA3	TWAJ	APC	Thermo Fisher	50
Rorγt	B2D	PE	Thermo Fisher	50
Eomes	Dna11mag	PerCPeF710	Thermo Fisher	50
T-bet	eBio4B10	PECY7	Thermo Fisher	50
Ter119	TER119	eFluor450	Thermo Fisher	250
Thy1.2	33-2.1	BV605	BD Biosciences	250
B220	RA3-6B2	eFluor450	Thermo Fisher	750
NK1.1	PK136	eFluor450	Thermo Fisher	250
NK1.1	PK136	APC	BD Biosciences	150
CD11c	N418	eFluor450	Thermo Fisher	750
CD11b	M1/70	eFluor450	Thermo Fisher	750
ST2	RMST2-2	PECY7	Thermo Fisher	80
CD49a	Ha31/8	BV711	BD Biosciences	250
CD49b	DX5	AF647	BioLegend	250
CCR6	140706	BV711	BD Biosciences	250
IFNγ	XMG1.2	PECY7	Thermo Fisher	50
IL-5	TRFK5	APC	BD Biosciences	100
IL-13	eBio13A	PECY7	Thermo Fisher	50
Rorγt	B2D	PE	Thermo Fisher	50
IL-17	TC11-18H10	PE	BD Biosciences	50
IL-22	1H8PWSR	PerCPeF710	Thermo Fisher	50

2.4 Antibodies and flow cytometry

Single-cell suspensions were incubated with anti-mouse CD16/32 antibody (clone 2.4G2) to block non-specific binding to Fc receptors before surface staining. Antibodies used in this study are listed in Table 1. Flow cytometry analysis was performed on a BD Fortessa flow cytometer and FACSDiva software (BD Biosciences). Flow cytometry data were analyzed using FlowJo 8.7. GraphPad Prism 7 was used for data analysis. Data shown in the figures are mean ± SEM.

3 Results

3.1 Analysis of ILC1

To accurately identify ILC1s in the liver under steady-state conditions, we performed 12-color flow cytometry (Table 2) and sequential gating analysis (Figure 1). Our lineage cocktail contained Ter119, Gr-1, CD220, and CD19 to exclude erythrocytes, granulocytes, and B cells. We used a T-cell antibody cocktail including TCRβ, TCRγδ, and CD3ϵ in a separate color to avoid NKT cell contamination. We used NK1.1 and NKp46 (NCR1) as shared markers for identifying NK cells and ILC1s. It is important to note that NK1.1 is expressed in B6 and SJL strains but not in other strains (16).

For our analysis of ILC1 in B6 mice, we used CD49b as an NK cell marker and CD49a as an ILC1 marker. However, we found that CD49a is not a specific marker of liver ILC1s, as other liver cells including some T cells and NKT cells also express CD49a (Figures 2A, B). Therefore, using a combination of markers is critical to define ILC1s. $Lin^-NK1.1^+NKp46^+CD3\epsilon/TCRs^-$ cells can be divided into $CD49b^+CD49a^-$ NK cells and $CD49b^-CD49a^+$ILC1s. The former express Eomes and T-bet, whereas the latter express $Eomes^-T\text{-}bet^+$ (Figure 2C). Furthermore, both populations are $ROR\gamma t^-$, indicating the absence of $NKp46^+$ILC3 contamination (Figure 2D). Thy1 and CD127 are not reliable markers to distinguish ILC1s from NK cells, as some NK cells express Thy1 and CD127, while not all ILC1s are Thy1 and CD127 positive (Figure 2E). Approximately 80% (mean ± SEM) of ILC1s are positive for intracellular IFNγ (Figure 2F). This strategy is designed for B6 mouse liver ILC1s. However, defining ILC1s in other tissues remains a challenge. We found a small population of $CD49a^+$ cells expressing Eomes in the lung and spleen (Figure 3). Therefore, it is critical to analyze the expression of transcription factors including Eomes and RORγt in addition to surface marker staining to define the ILC1 population in various tissues.

10.3389/fimmu.2023.1198310

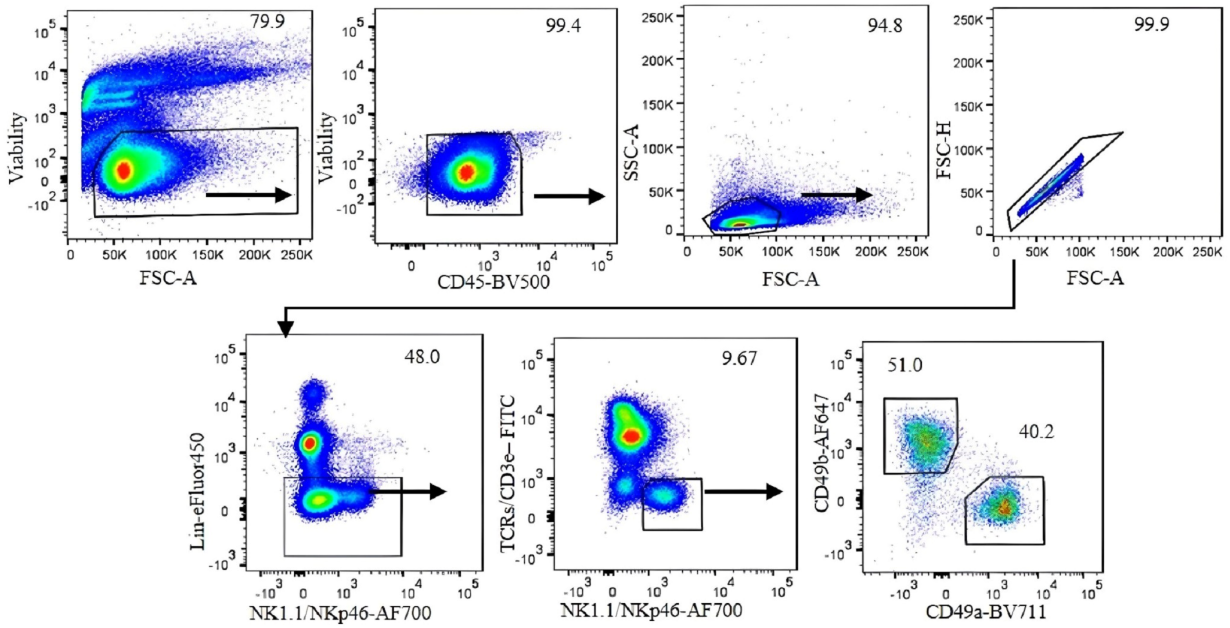

FIGURE 1
Gating strategy for analysis of liver ILC1 in C57BL/6 mice. Gating was applied on live CD45$^+$ leukocytes. Lymphocytes were gated with the forward scatter/side scatter (FSC/SSC) method, followed by gating on single cells using FSC-A/FSC-H. Negative lineage cells were gated to exclude erythrocytes, myeloid cells, and B cells. NK1.1- and NKp46-positive, T-cell marker-negative cells were gated. CD49b and CD49a markers were used to define NK cells and ILC1, respectively. Numbers indicate percentages of cells in each gate.

TABLE 2 Antibody panel for ILC1, ILC2, and ILC3 identification.

ILC1 panel											
FITC	PerCPeF710	AF647	AF-700	R780	eFlour450	BV510	BV605	BV650	BV711	PE	PECy7
CD3ϵ, TCRβ, TCRγδ	Eomes	CD49b	NK1.1, NKp46	Viab	Ter119, Gr-1 CD19, B220	CD45	Thy1.2	CD160	CD49a	CD127	T-bet
ILC2 panel											
FITC	PerCPeF710	R670	AF-700	R780	eFlour450	BV510	BV605	BV650	BV711	PE	PECy7
CD3ϵ, TCRβ, TCRγδ	ST2	GATA3	–	Viab	Ter119, Gr-1 CD19, B220, NK1.1, NKp46	CD45	Thy1.2	–	–	Rorγt	CD127
ILC3 panel											
FITC	PerCPeF710	R670	AF-700	R780	eFlour450	BV510	BV605	BV650	BV711	PE	PECy7
CD3ϵ, TCRβ, TCRγδ	ST2	GATA3	CD127	Viab	Ter119, Gr-1 CD19, B220	CD45	Thy1.2	–	–	Rorγt	NK1.1 (or in Lin cocktail)

3.2 Analysis of ILC2s

Currently, ILC2s are defined by combinations of markers that vary among different studies. For example, lung ILC2s are defined by Lin$^-$ST2$^+$Thy1$^+$CD25$^+$ (17), Lin$^-$CD45$^+$, CD127$^+$, ST2$^+$ (18), CD45$^+$CD3ϵ$^-$CD19$^-$CD127$^+$CD25$^+$ST2$^+$ (19), and Lin$^-$GATA3$^+$ (20). Liver ILC2s are also defined by Lin$^-$Sca-1$^+$ST2$^+$ (21), Lin$^-$CD127$^+$ST2$^+$ (22), and Lin$^-$CD45$^+$GATA3$^+$Thy1$^+$ST2$^+$ (23). In the literature, lung ILC2 numbers in naïve mice vary from approximately 2,000–3,000 cells (24, 25) to 8,000–15,000 (26)

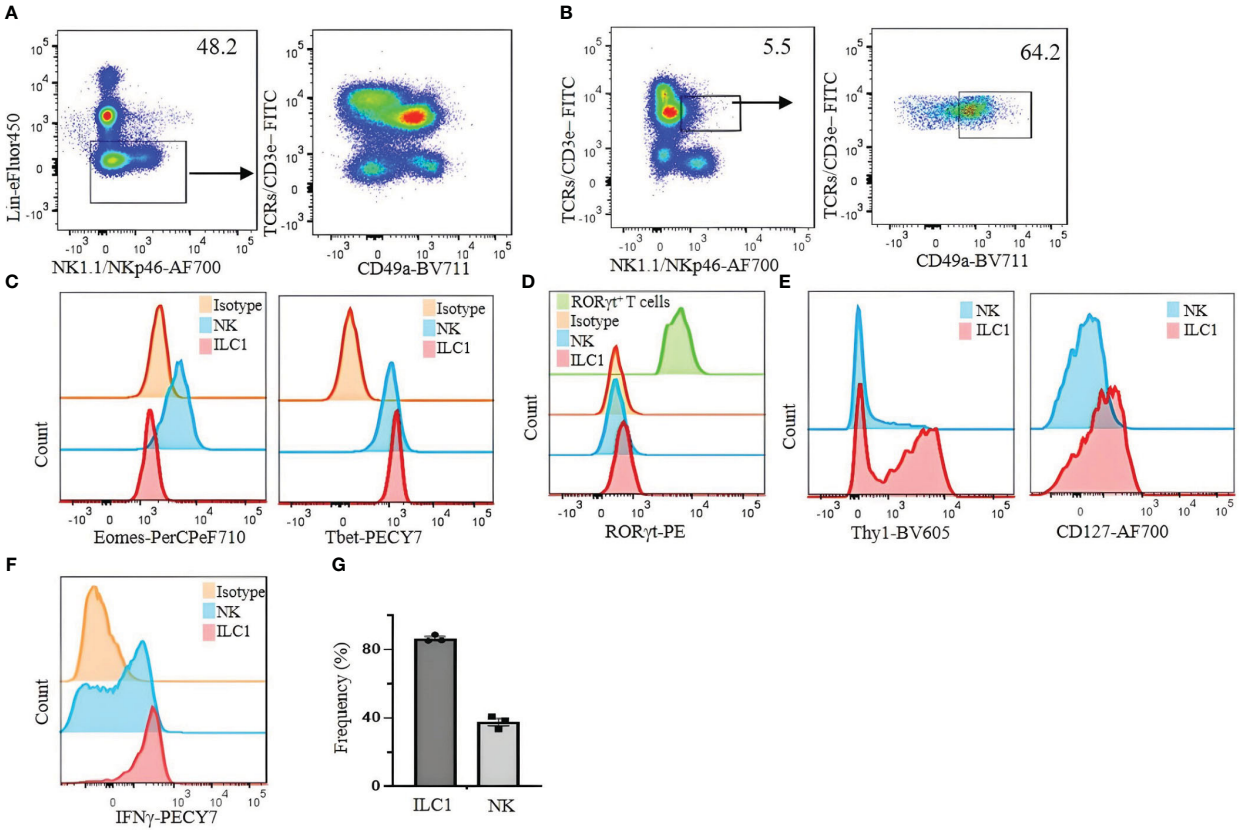

FIGURE 2
Limitations of CD49a as a selective marker for identifying liver ILC1s in C57BL/6 mice. **(A)** Lin$^-$ cells were analyzed for the expression of CD49a on T cells. **(B)** NKT cells (TCRs/CD3ε$^+$/NK1.1/NKp46$^+$) were analyzed for CD49a expression. **(C)** Eomes and T-bet were analyzed on liver NK cells and ILC1s. **(D)** RORγt expression on liver NK cells and ILC1s; Lin$^-$TCR/CD3ε$^+$RORγt$^+$ cells were used as positive control (green histogram). **(E)** Thy1 and CD127 expression on liver ILC1s and NK cells were analyzed. **(F)** Liver lymphocytes were incubated with phorbol 12-myristate 13-acetate (PMA)/ionomycin plus Brefeldin A for 4 hours and stained for intracellular IFNγ. CD49a$^-$CD49b$^+$ NK cells and CD49a$^+$CD49b$^-$ ILC1s were gated and analyzed for intracellular expression of IFNγ. Numbers indicate percentages of cells in indicated gates. **(G)** Frequency of IFNγ expressing ILC1 and NK cells. Data are shown as mean ± SEM.

likely due to different strategies to identify ILC2s. One problem is the lack of consensus on which markers to include in the lineage cocktail among studies (Table 3). This can lead to the contamination of T cells, which have a similar phenotype as ILC2s (Figure 4), resulting in differences in the identification and enumeration of ILC2s. To avoid T-cell contamination, we propose to use T-cell markers in a separate channel from the lineage cocktail. This approach ensures that T cells are excluded from the ILC2 population.

To identify ILC2s in the lung, we used a Lin cocktail of CD19, Ter119, B220, NK1.1, NKp46, GR-1, CD11b, and CD11c labeled with eFluor450 combined with CD3ε/TCRs labeled with fluorescein isothiocyanate (FITC) or allophycocyanin (APC). ILC2s are then gated by Lin$^-$Thy1$^+$CD3ε/TCRs$^-$CD127$^+$ST2$^+$. The number of ILC2s in the naïve B6 mouse lungs identified by this strategy is approximately 3,000 cells per mouse. It should be noted that not all ILC2s in the lung are Lin negative, but some of them seem to weakly express Lin markers (Figure 5A, contour plots). ILC2s thus identified can be confirmed by transcription factor staining (GATA3$^+$RORγt$^-$) (Figure 5A, histograms). Most (approximately 80%) lung ILC2s (Lin$^-$Thy1$^+$CD3ε/TCRs$^-$ST2$^+$GATA3$^+$) also express CD25 (Figure 5B). Intercellular cytokines in ILC2s are analyzed by the expression of IL-5 and IL-13 in the same gate following a short-term (3 hours) incubation with PMA/ionomycin in the presence of Brefeldin A. Approximately 7% (mean ± SEM) of ILC2s express intracellular IL-5 and IL-13 (Figure 5C).

SI ILC2s (Lin$^-$hy1$^+$CD3ε/TCRs$^-$GATA3$^+$RORγt$^-$) are ST2$^-$, but approximately 90% express KLRG1, and over 90% are IL-17RB positive (Figure 6A). Liver ILC2s (Lin$^-$Thy1$^+$CD3ε/TCRs$^-$GATA3$^+$RORγt$^-$) can be divided into ST2$^+$ (approximately 70%) and ST2$^-$ populations. Approximately 50% of them are KLRG1$^+$, and over 90% are IL-17RB$^+$ (Figure 6B). The frequency and number of ILC2s in the liver, SI, and lung are shown in Figure 6C.

3.3 Analysis of ILC3s

We investigated strategies to identify ILC3s in the lung, spleen, liver, and SI. ILC3s are similar to other ILCs in terms of surface markers and are Lin$^-$Thy1$^+$CD127$^+$. Because some ILC3s express NKp46, the Lin cocktail for ILC3s excludes this marker. There is no

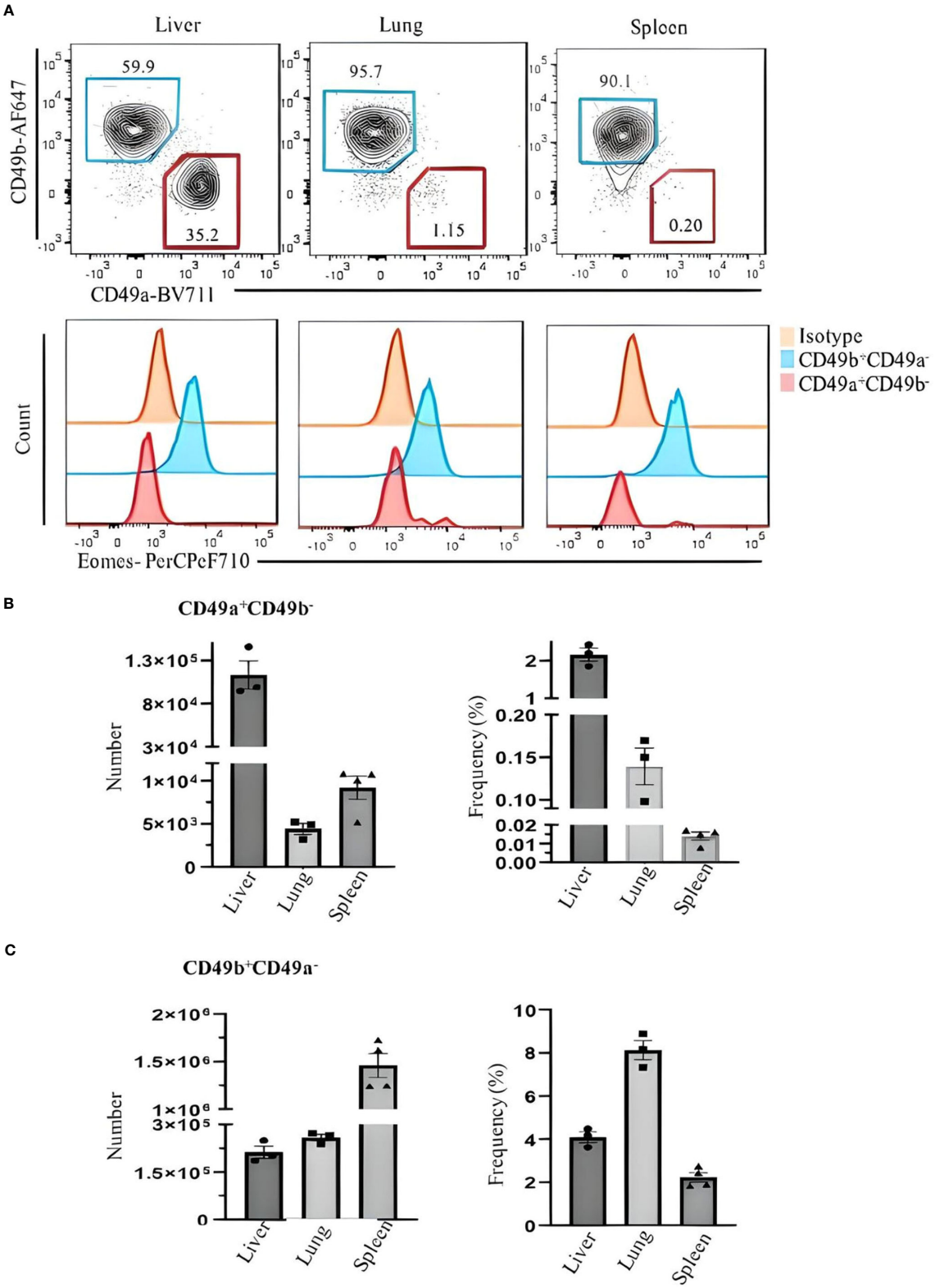

FIGURE 3
Comparing Eomes expression in ILC1s and NK cells in the liver, lung, and spleen of C57BL/6 mice. **(A)** Live CD45$^+$Lin$^-$NK1.1$^+$NKp46$^+$CD3ε/TCRs$^-$ were gated and analyzed for CD49a and CD49b expression. Blue and red gates show CD49b$^+$CD49a$^-$ NK cells and CD49a$^+$CD49b$^-$ ILC1s, respectively. Numbers indicate percentages of cells in each gate. **(B)** Frequency and number of CD49a$^+$CD49b$^-$ and **(C)** CD49b$^+$CD49a$^-$ cells of CD45$^+$ leukocytes in liver, lung, and spleen. Data are shown as mean ± SEM.

TABLE 3 Lineage cocktails used in different studies.

#	Paper Title	Lineage cocktail	Ref
1	IL-17-producing ST2$^+$ group 2 innate lymphoid cells play a pathogenic role in lung inflammation	CD3ϵ, B220, CD11b, CD11c, Gr-1, NK1.1, and FcεRI	(27)
2	IL-33 promotes the egress of group 2 innate lymphoid cells from the bone marrow	CD3, CD5, CD45R (B220), CD11b, Gr-1 (Ly-6G/C), 7-4, and Ter-119	(28)
3	IL-25-responsive, lineage-negative KLRG1^{hi} cells are multipotential "inflammatory" type 2 innate lymphoid cells	CD3ϵ, CD5, CD19, B220, TCRγδ, NK1.1, CD11b, CD11c, Gr-1, FcεR1, and TER119	(29)
4	A tissue checkpoint regulates type 2 immunity	B220, CD11b, CD19, TCRgd, CD11c, CD3, CD5, Ter 119, NK 1.1, and CD8	(30)

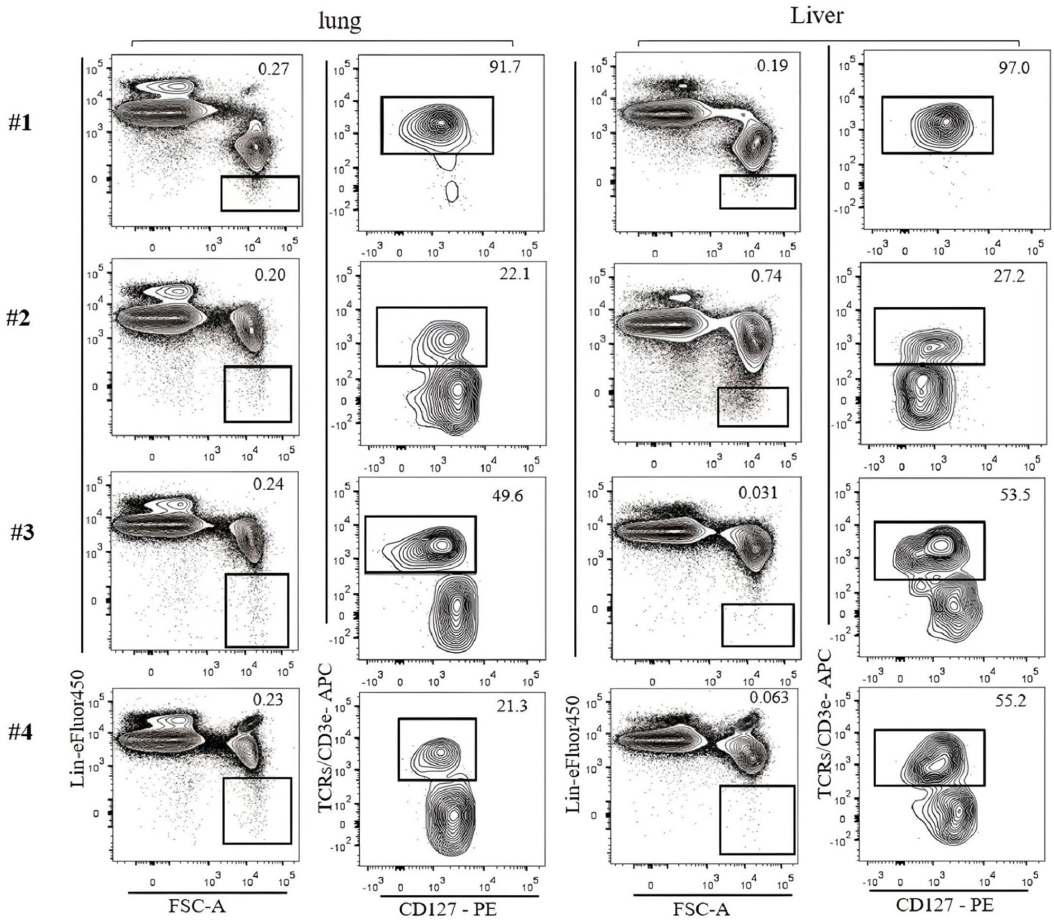

FIGURE 4
Lin-negative populations defined by different lineage cocktails were analyzed for T-cell contamination. ILC2s in the lung and the liver of C57BL/6 mice were analyzed. Gating was applied on live, single-cell, CD45$^+$ leukocytes. The numbers on the left indicate Lin cocktails listed in Table 3. Numbers indicate percentages of cells in each gate.

ILC3-specific surface marker, and it is difficult to discriminate them from other ILCs by cell surface markers alone. Therefore, staining for RORγt, which is expressed in ILC3s but not in other ILCs, is required to specifically identify ILC3s. When CD3ϵ/TCR are included in the Lin cocktail for analysis of ILC3s in the naïve B6 mouse lungs, there is no clear separation between Lin$^+$ and Lin$^-$ populations, and both populations include RORγt$^+$ cells (Figure 7A). When TCR/CD3ϵ is in separate fluorochrome, it became clear that some T cells express RORγt (Figure 7B). ILC3s in naïve C57BL/6 lung are a very rare population, but they could be identified by Lin$^-$Thy1$^+$CD127$^+$CD3ϵ/TCR$^-$RORγt$^+$ (Figure 7C). Rag1-ko mice have more ILC3s in the lung than wild-type B6 and

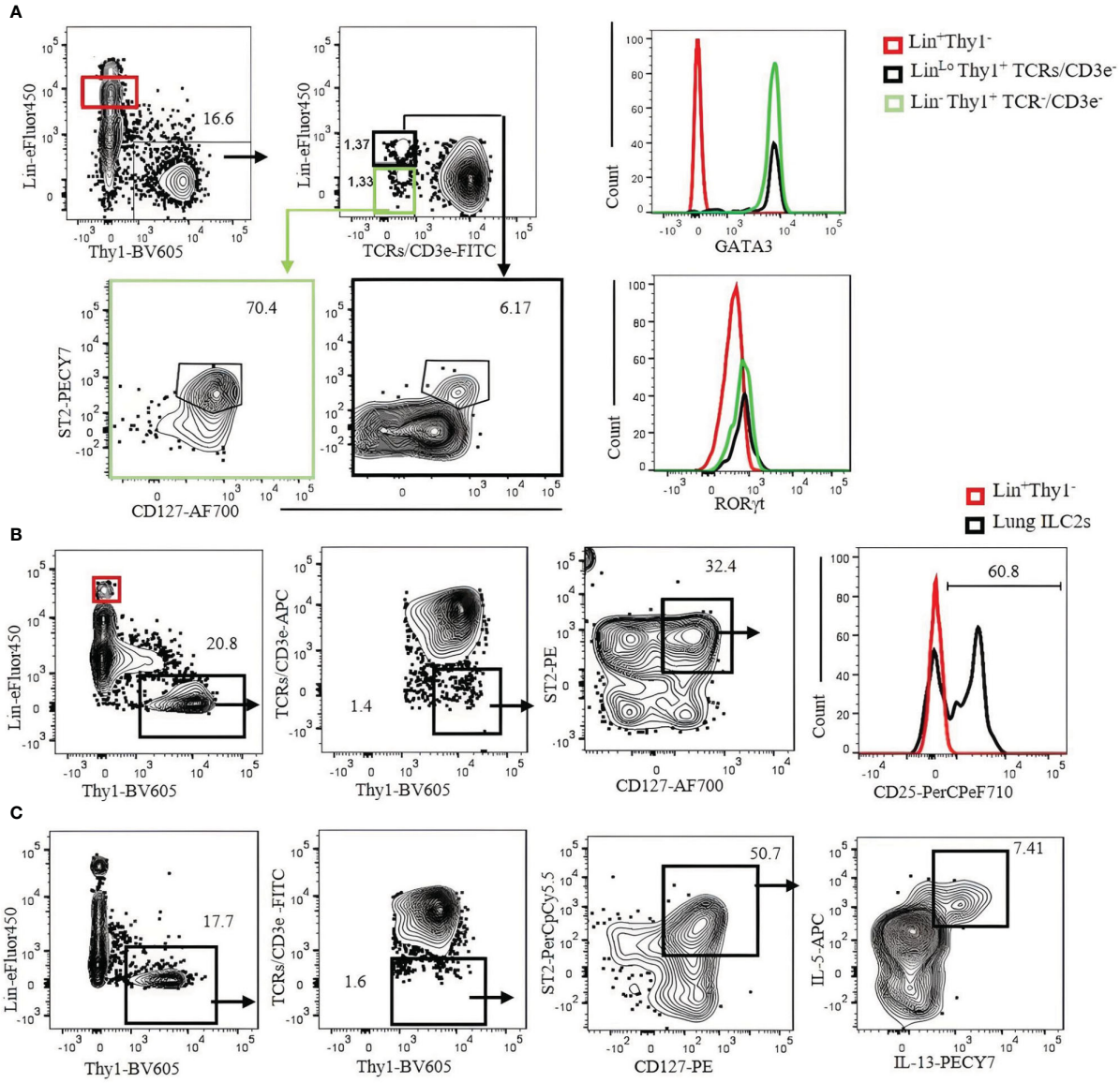

FIGURE 5
Characterization of C57BL/6 mouse lung ILC2s with CD3ε/TCR separated from the Lin cocktail. **(A)** Lin-negative/low Thy1$^+$ cells were gated, and TCR/CD3ε$^-$ cells were further divided into Lin$^-$ (green gate) and Lin^{lo} (bold black gate). ILC2s in each gate were identified by CD127$^+$ST2$^+$ and confirmed by GATA3$^+$RORγt$^-$ (right histograms). Lin$^+$ population (red gate) was used as negative control. **(B)** Lung ILC2s were gated by Lin$^-$/low Thy1$^+$TCR/CD3ε$^-$ST2$^+$CD127$^+$ and analyzed for CD25 expression. Lin$^+$ population (red gate and red histogram) was used as negative control. **(C)** Lung lymphocytes were incubated with phorbol 12-myristate 13-acetate (PMA)/ionomycin and Brefeldin A for 3 hours. ILC2s (Thy1$^+$Lin$^-$TCR/CD3ε$^-$ST2$^+$CD127$^+$) were analyzed for intracellular IL-5 and IL-13. Gating was applied on live, single-cell, CD45$^+$ leukocytes. Numbers indicate percentages of cells in each gate.

can be divided into CD4$^+$, NKp46$^+$, and CCR6$^+$ subsets (Figure 7D). ILC3s in the spleen, liver, and SI were also detected by Lin$^-$Thy1$^+$CD127$^+$CD3ε/TCR$^-$RORγt$^+$ (Figures 8A-D). Approximately 4% and 0.4% (mean ± SEM) of ILC3s are IL-17 and IL-22 positive, respectively (Figures 8E, F).

Transcription factor staining requires fixation and permeabilization steps. To analyze live ILC3s, we used heterozygous *Rorc(γt)*-eGFP reporter mice. ILC3s in these mice can be detected by Lin$^-$Thy1$^+$NK1.1$^-$CD3ε/TCR$^-$CD127$^+$GFP$^+$. ILC3s are mostly IL-18R$^+$ and CD49a$^+$ (Figure 9).

4 Discussion

The ILC population is heterogeneous, and currently, there is no single way to identify all ILCs in various tissues. This study has focused on flow cytometric analyses of ILC1s in the liver, ILC2s in the lung and liver, and ILC3s in the lung, spleen, and SI. The common first step to identify ILCs is to exclude myeloid cells, erythroid cells, dendritic cells, T cells, and B cells based on Lin marker expression. The Lin cocktail commonly includes T-cell markers (CD3ε/TCRs), and the Lin$^-$ population is expected to be T cell-free. However, in our

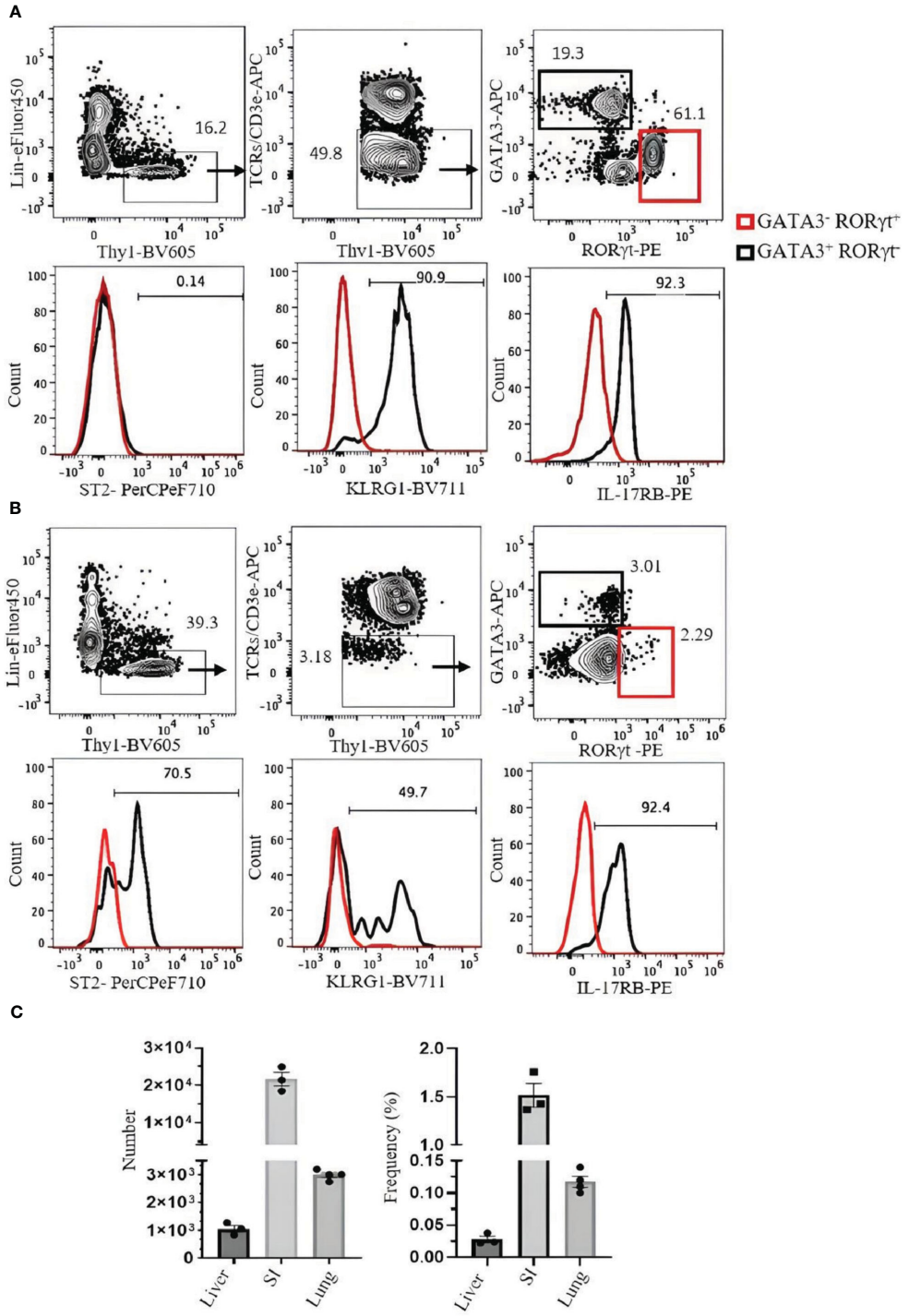

FIGURE 6
Analysis of ILC2s in the small intestine (SI) and liver of C57BL/6 mouse. **(A)** ILC2s in the SI were gated as Thy1$^+$Lin$^-$TCRs/CD3ε$^-$ST2$^+$GATA3$^+$RORγt$^-$, and RORγt$^+$ILC3s (red square) were used as negative control. Histograms show the expression of ST2, KLRG1, and IL-17RB on ILC2s. **(B)** ILC2s in the liver were gated as Thy1$^+$Lin$^-$TCRs/CD3ε$^-$GATA3$^+$RORγt$^-$. RORγt$^+$ILC3s (red square) were used as negative control. Histograms show the expression of ST2, KLRG1, and IL-17RB. Gating was applied on live, single-cell, CD45$^+$ leukocytes. Numbers indicate percentages of cells in each gate. **(C)** Frequency and number of ILC2s (of CD45$^+$ leukocytes). Data are shown as mean ± SEM.

analyses, T-cell contamination is still the biggest potential problem in identifying ILCs (7, 31). Lin$^-$ cells are not clearly separated from Lin$^+$ cells, and some ILCs seem to weakly express some Lin markers. Therefore, Lin$^-$ gate is ambiguous and subjective, and it is difficult to exclude all T cells from the Lin$^-$ population. We have found that the best way to avoid T-cell contamination is not to include CD3ε/TCRs in the Lin cocktail but to have them in a different fluorochrome instead. In this way, T cells can be more clearly excluded. Because apparent ILC functions can be attributed to contaminating T cells, it is critical to specifically exclude all T cells. In conventional flow

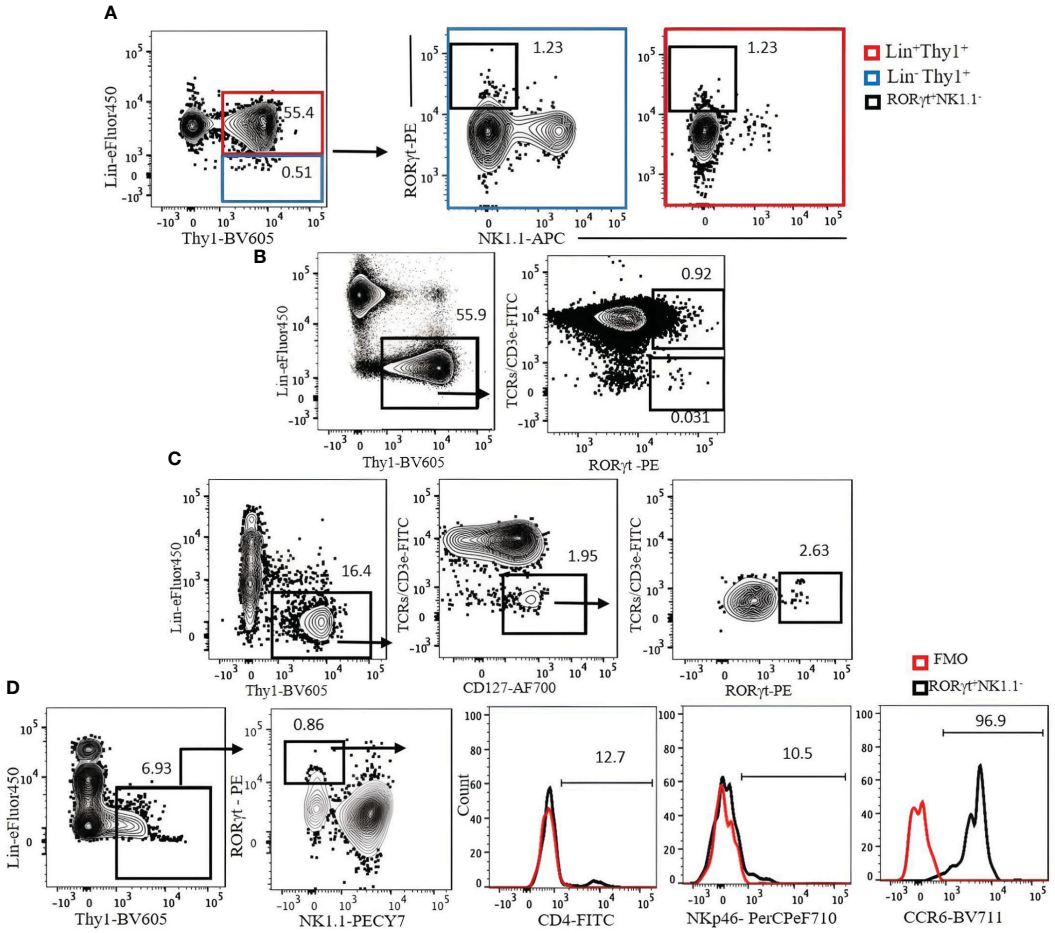

FIGURE 7
(A) The expression of Lin markers on RORγt$^+$NK1.1$^-$ cells (bold black square) in C57BL/6 mouse lung. Lin cocktail included TCR/CD3ε, CD11b, CD11c, GR-1, B220, and Ter119. Lin$^+$ cells (red square) were used as positive control. Gating was applied on live, single-cell, CD45$^+$ leukocytes. **(B)** The expression of RORγt on T cells. **(C)** ILC3s in C57BL/6 mouse lung were identified by serial gating as shown. **(D)** Expression of CD4, NKp46, and CCR6 on Rag1$^{-/-}$ mouse lung ILC3s. Fluorescence minus one (FMO) was used as control negative. Gating applied on live, single, CD45$^+$Lin$^-$Thy1$^+$NK1.1$^-$ cells. Lin cocktail included Ter119, B220, CD11c, CD11b, and Gr-1. Numbers indicate percentages of cells in each gate.

cytometry, having CD3ε/TCRs in separate fluorochrome from the Lin cocktail reduces the capability of other marker analyses due to the limited number of fluorescence combinations. This can be resolved by the use of a spectral flow cytometer (32).

For ILC1 analysis, distinguishing them from NK cells and other ILCs especially ILC3s is necessary. In our current study, liver ILC1s are identified by Lin$^-$NKp46$^+$NK1.1$^+$CD49a$^+$CD49b$^-$. The combination of CD49a and CD49b clearly separates ILC1s from NK cells, whereas NK1.1 expression excludes ILC3s. This can be confirmed by the expression of the NK-associated transcription factor Eomes in CD49a$^-$CD49b$^+$, while the CD49a$^+$CD49b$^-$ population lacks Eomes and the ILC3-associated transcription factor RORγt. It should be noted that CD49a is expressed not only on ILC1s but also on other lymphocytes, including ILC3s and NKT cells, and it is important to have CD3ε/TCR in separate fluorochrome to avoid contamination of T cells as discussed above. This strategy cannot be universally applied to ILC1s in all tissues and other strains of mice lacking NK1.1. It has been reported that salivary gland ILC1s express CD49b and Eomes, and intestinal ILC1s also express Eomes (9).

ILC2s in the lung are identified by Lin$^-$CD127$^+$Thy1$^+$ST2$^+$. We have shown that unless those cells are separately stained for CD3ε/TCRs, it is very difficult to avoid T-cell contamination. While ILC2s in the lung are efficiently identified by this strategy, a minor population of lung ILC2s termed inflammatory ILC2s is known to be ST2$^-$ (33). CD25 can be used to identify lung ILC2s, but not all lung ILC2s express CD25. The majority of ILC2s in the SI do not express ST2 (24), and KLRG1 may be used to identify them instead. However, approximately 10% of SI ILC2s are KLRG1 negative.

Approximately 30% of Liver ILC2s do not express ST2. For those, IL-17RB (IL-25R) can be used in place of ST2 to identify ILC2s. However, recently reported IL-18R$^+$ ILC progenitors also express IL-17RB (34), and IL-18R$^+$ cells have to be excluded from the analysis of ST2$^-$ ILC2s.

Activated lung ILC2s may downregulate CD127 and ST2. Cavagnero K et al. reported ST2$^+$CD127$^-$ and ST2$^-$CD127$^-$ cells in the lung of *Alternaria*-treated mice (35). Staining for GATA3, RORγt, T-bet, and Eomes should determine their identity.

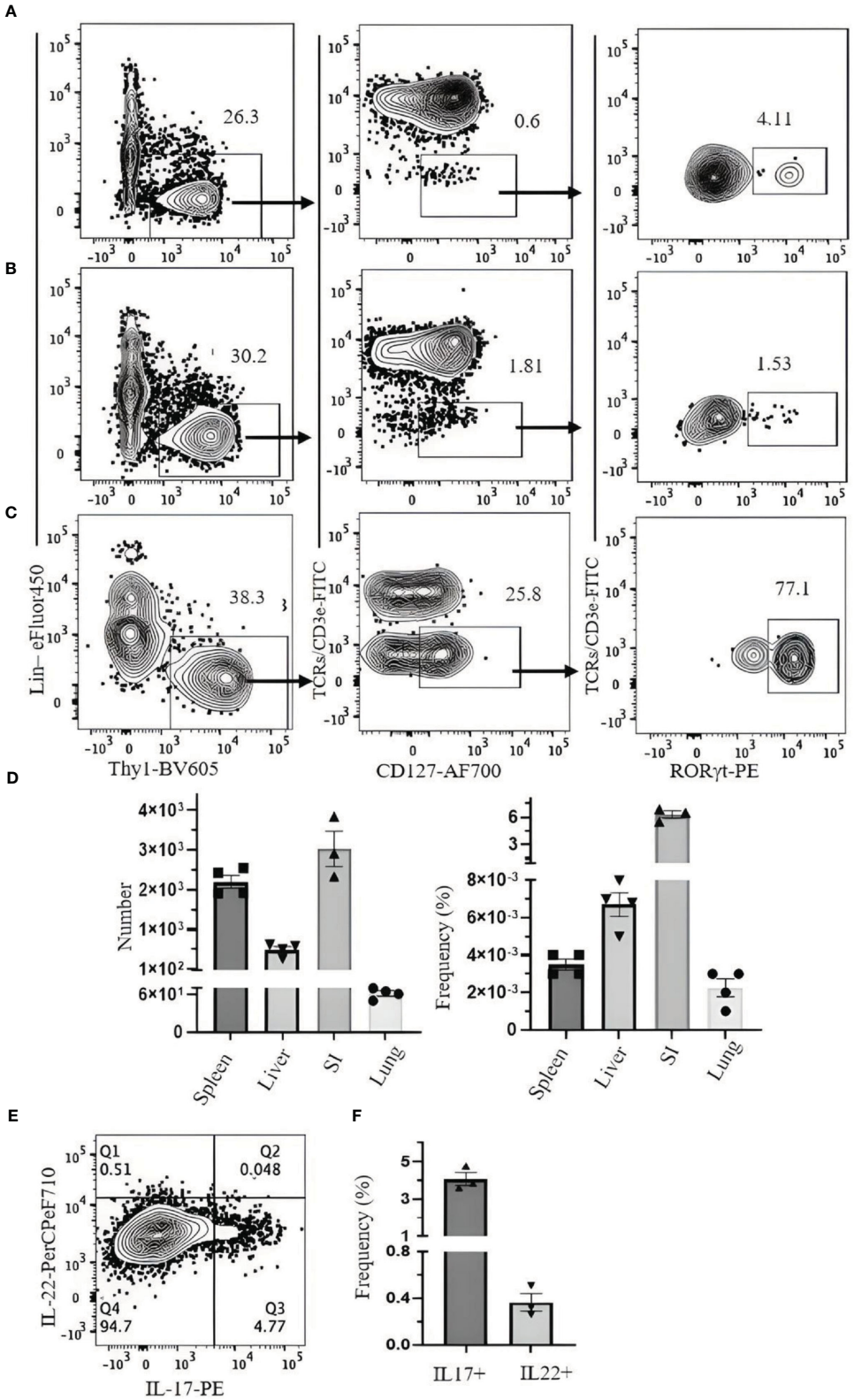

FIGURE 8
Gating strategy for ILC3 characterization in C57BL/6 mouse. Lymphocytes were isolated from **(A)** spleen, **(B)** liver, and **(C)** small intestine. **(D)** Frequency and number of ILC3s (of CD45$^+$ leukocytes) in spleen, liver, small intestine (SI), and lung. **(E)** SI lymphocytes were incubated with phorbol 12-myristate 13-acetate (PMA)/ionomycin and Brefeldin A for 3 hours. ILC3s (Thy1$^+$Lin$^-$TCR/CD3ϵ$^-$CD127$^+$Rorgt$^+$) were analyzed for intracellular IL-17 and IL-22. **(F)** The frequency of IL-17- and IL-22-producing ILC3s. Data plotted are means ± SEM. Gating applied on live CD45$^+$lin$^-$Thy1$^+$TCRs/CD3ϵ$^-$CD127$^+$RORγt$^+$ cells. Lin cocktail included Ter119, CD19, B220, CD11c, CD11b, GR-1, and NK1.1. Numbers indicate percentages of cells in each gate.

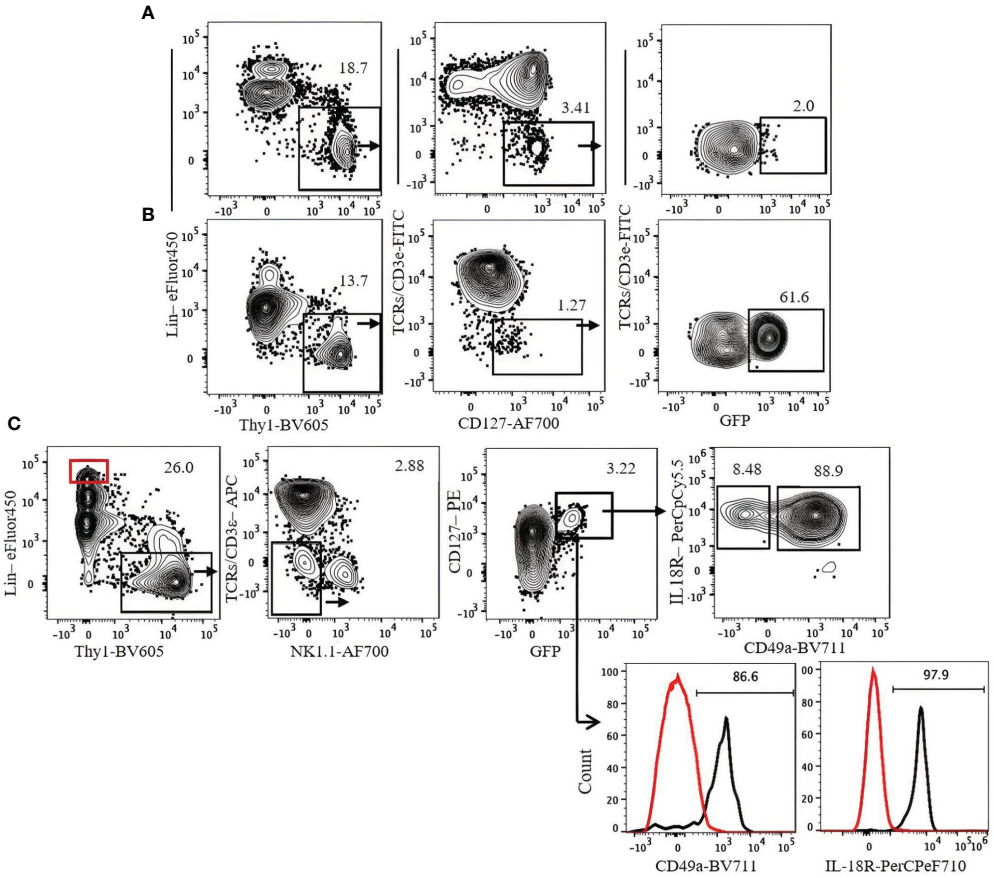

FIGURE 9
Gating strategy for ILC3 characterization in *Rorc(γt)*-eGFP mice. **(A)** Lung. **(B)** Spleen. **(C)** Expression of CD49a and IL-18R on lung ILC3s. Lin$^+$Thy1$^-$ cells (red gate and red histogram) were used as control. Gating applied on live CD45$^+$lin$^-$Thy1$^+$TCRs/CD3ε$^-$NK1.1$^-$CD127$^+$GFP$^+$ cells. Lin cocktail included Ter119, CD19, B220, CD11c, CD11b, and GR-1. Numbers indicate percentages of cells in each gate.

ILC3s share many surface markers with other ILCs; to identify and distinguish ILC3s from other ILCs, analysis for RORγt expression is critical. RORγt expression also distinguishes ILC3s from the IL-18R$^+$ ILC progenitors discussed above. While both are IL-18R$^+$, ILC3s but not ILC progenitors are RORγt$^+$. RORγt expression can be analyzed by nuclear staining of fixed and permeabilized cells or by the *Rorc(γt)*-eGFP reporter mice (13). The latter allows the identification of live ILC3s. Because homozygous *Rorc(γt)*-eGFP mice are RORγt-deficient, only heterozygous mice can be analyzed for ILC3s. Due to a half-dose of RORγt in the heterozygous mice, ILC3 numbers in the heterozygous mice are lower than wild type. Because RORγt is also expressed in some T cells, T cells have to be excluded from ILC3 analyses by the strategy described above for ILC1s and ILC2s. A subpopulation of ILC3s also expresses NKp46 but not NK1.1, while NK cells and ILC1s express both. In our study, NK1.1 was used to discriminate ILC3s from ILC1s and NK cells.

In summary, the strategies to identify ILCs have to be designed for each ILC population and tissue due to the heterogeneity of ILCs. In all cases, it is critical to exclude T cells, and the identity of ILCs should be confirmed by a combination of transcription factors GATA3, RORγt, T-bet, and Eomes.

Data availability statement

The original contributions presented in the study are included in the article/supplementary material. Further inquiries can be directed to the corresponding author.

Ethics statement

The use of these mice was approved by the animal committee of the University of British Columbia and in accordance with the guidelines of the Canadian Council on Animal Care. The study was conducted in accordance with the local legislation and institutional requirements.

Author contributions

MS, DK, and MO wrote and edited the manuscript. MS, DK, and MO performed the experiments and generated figures and tables. FT reviewed the drafts, provided critical input, and edited the

manuscript and figures. All authors contributed to the article and approved the submitted version.

Funding

This work was supported by a grant from the Canadian Institute for Health Research.

Acknowledgments

We thank Dr. Monica Romera-Hernandez for technical advice on ILC3 analyses and the Terry Fox Laboratory Flow Core staff for their expert assistance in flow cytometry.

Conflict of interest

The authors declare that the research was conducted in the absence of any commercial or financial relationships that could be construed as a potential conflict of interest.

Publisher's note

References

1. Mathä L, Martinez-Gonzalez I, Steer CA, Takei F. The fate of activated group 2 innate lymphoid cells. *Front Immunol* (2021) 12:671966. doi: 10.3389/fimmu.2021.671966

2. Tait Wojno ED, Beamer CA. Isolation and identification of innate lymphoid cells (ILCs) for immunotoxicity testing. *Immunotoxicity Testing: Methods and Protocols* (2018) 1803:353–70. doi: 10.1007/978-1-4939-8549-4_21

3. Chiossone L, Chaix J, Fuseri N, Roth C, Vivier E, Walzer T. Maturation of mouse NK cells is a 4-stage developmental program. *Blood* (2009) 113(22):5488–96. doi: 10.1182/blood-2008-10-187179

4. Spits H, Mjösberg J. Heterogeneity of type 2 innate lymphoid cells. *Nat Rev Immunol* (2022) 22(11):701–12. doi: 10.1038/s41577-022-00704-5

5. Lopes N, Galluso J, Escaliere B, Carpentier S, Kerdiles YM, Vivier E. Tissue-specific transcriptional profiles and heterogeneity of natural killer cells and group 1 innate lymphoid cells. *Cell Rep Med* (2022) 3(11):100812. doi: 10.1016/j.xcrm.2022.100812

6. Ghaedi M, Shen ZY, Orangi M, Martinez-Gonzalez I, Wei L, Lu X, et al. Single-cell analysis of RORα tracer mouse lung reveals ILC progenitors and effector ILC2 subsets. *J Exp Med* (2020) 217(3):jem.20182293. doi: 10.1084/jem.20182293

7. Zhong C, Zheng M, Cui K, Martins AJ, Hu G, Li D, et al. Differential expression of the transcription factor GATA3 specifies lineage and functions of innate lymphoid cells. *Immunity* (2020) 52(1):83–95.e4. doi: 10.1016/j.immuni.2019.12.001

8. Valle-Noguera A, Gómez-Sánchez MJ, Girard-Madoux MJ, Cruz-Adalia A. Optimized protocol for characterization of mouse gut innate lymphoid cells. *Front Immunol* (2020) 11:563414. doi: 10.3389/fimmu.2020.563414

9. Seillet C, Brossay L, Vivier E. Natural killers or ILC1s? That is the question. *Curr Opin Immunol* (2021) 68:48–53. doi: 10.1016/j.coi.2020.08.009

10. Mincham KT, Snelgrove RJ. OMIP-086: Full spectrum flow cytometry for high-dimensional immunophenotyping of mouse innate lymphoid cells. *Cytometry A* (2023) 103(2):110–6. doi: 10.1002/cyto.a.24702

11. Gurram RK, Wei D, Yu Q, Kamenyeva O, Chung H, Zheng M, et al. Gata3 ZsG and Gata3 ZsG-fl: Novel murine Gata3 reporter alleles for identifying and studying Th2 cells and ILC2s in vivo. *Front Immunol* (2022) 13:97595. doi: 10.3389/fimmu.2022.975958

12. Loering S, Cameron GJ, Bhatt NP, Belz GT, Foster PS, Hansbro PM, et al. Differences in pulmonary group 2 innate lymphoid cells are dependent on mouse age, sex and strain. *Immunol Cell Biol* (2021) 99(5):542–51. doi: 10.1111/imcb.12430

13. Eberl G, Marmon S, Sunshine M-J, Rennert PD, Choi Y, Littman DR. An essential function for the nuclear receptor RORγt in the generation of fetal lymphoid tissue inducer cells. *Nat Immunol* (2004) 5(1):64–73. doi: 10.1038/ni1022

14. Wang Y, Dong W, Zhang Y, Caligiuri MA, Yu J. Dependence of innate lymphoid cell 1 development on NKp46. *PloS Biol* (2018) 16(4):e2004867. doi: 10.1371/journal.pbio.2004867

15. Romera-Hernández M, Mathä L, Steer CA, Ghaedi M, Takei F. Identification of group 2 innate lymphoid cells in mouse lung, liver, small intestine, bone marrow, and mediastinal and mesenteric lymph nodes. *Curr Protoc Immunol* (2019) 125(1):e73. doi: 10.1002/cpim.73

16. Carlyle JR, Mesci A, Ljutic B, Belanger S, Tai L-H, Rousselle E, et al. Molecular and genetic basis for strain-dependent NK1. 1 alloreactivity of mouse NK cells. *J Immunol* (2006) 176(12):7511–24. doi: 10.4049/jimmunol.176.12.7511

17. Naito M, Nakanishi Y, Motomura Y, Takamatsu H, Koyama S, Nishide M, et al. Semaphorin 6D–expressing mesenchymal cells regulate IL-10 production by ILC2s in the lung. *Life Sci Alliance* (2022) 5(11):e202201486. doi: 10.26508/lsa.202201486

18. Hurrell BP, Galle-Treger L, Jahani PS, Howard E, Helou DG, Banie H, et al. TNFR2 signaling enhances ILC2 survival, function, and induction of airway hyperreactivity. *Cell Rep* (2019) 29(13):4509–24.e5. doi: 10.1016/j.celrep.2019.11.102

19. Miyamoto C, Kojo S, Yamashita M, Moro K, Lacaud G, Shiroguchi K, et al. Runx/Cbfβ complexes protect group 2 innate lymphoid cells from exhausted-like hyporesponsiveness during allergic airway inflammation. *Nat Commun* (2019) 10(1):447. doi: 10.1038/s41467-019-08365-0

20. Feng B, Lin L, Li L, Long X, Liu C, Zhao Z, et al. Glucocorticoid induced group 2 innate lymphoid cell overactivation exacerbates experimental colitis. *Front Immunol* (2022) 13. doi: 10.3389/fimmu.2022.863034

21. Steinmann S, Schoedsack M, Heinrich F, Breda PC, Ochel A, Tiegs G, et al. Hepatic ILC2 activity is regulated by liver inflammation-induced cytokines and effector CD4+ T cells. *Sci Rep* (2020) 10(1):1071. doi: 10.1038/s41598-020-57985-w

22. Mchedlidze T, Waldner M, Zopf S, Walker J, Rankin AL, Schuchmann M, et al. Interleukin-33-dependent innate lymphoid cells mediate hepatic fibrosis. *Immunity* (2013) 39(2):357–71. doi: 10.1016/j.immuni.2013.07.018

23. Nakamura R, Yoshizawa A, Moriyasu T, Deloer S, Senba M, Kikuchi M, et al. Group 2 innate lymphoid cells exacerbate amebic liver abscess in mice. *Iscience* (2020) 23(9):101544. doi: 10.1016/j.isci.2020.101544

24. Halim TY, Steer CA, Mathä L, Gold MJ, Martinez-Gonzalez I, McNagny KM, et al. Group 2 innate lymphoid cells are critical for the initiation of adaptive T helper 2 cell-mediated allergic lung inflammation. *Immunity* (2014) 40(3):425–35. doi: 10.1016/j.immuni.2014.01.011

25. Walford HH, Lund SJ, Baum RE, White AA, Bergeron CM, Husseman J, et al. Increased ILC2s in the eosinophilic nasal polyp endotype are associated with corticosteroid responsiveness. *Clin Immunol* (2014) 155(1):126–35. doi: 10.1016/j.clim.2014.09.007

26. Howard E, Lewis G, Galle-Treger L, Hurrell BP, Helou DG, Shafiei-Jahani P, et al. IL-10 production by ILC2s requires Blimp-1 and cMaf, modulates cellular metabolism, and ameliorates airway hyperreactivity. *J Allergy Clin Immunol* (2021) 147(4):1281–95.e5. doi: 10.1016/j.jaci.2020.08.024

27. Cai T, Qiu J, Ji Y, Li W, Ding Z, Suo C, et al. IL-17–producing ST2+ group 2 innate lymphoid cells play a pathogenic role in lung inflammation. *J Allergy Clin Immunol* (2019) 143(1):229–44.e9. doi: 10.1016/j.jaci.2018.03.007

28. Stier MT, Zhang J, Goleniewska K, Cephus JY, Rusznak M, Wu L, et al. IL-33 promotes the egress of group 2 innate lymphoid cells from the bone marrow. *J Exp Med* (2018) 215(1):263–81. doi: 10.1084/jem.20170449

29. Huang Y, Guo L, Qiu J, Chen X, Hu-Li J, Siebenlist U, et al. IL-25-responsive, lineage-negative KLRG1hi cells are multipotential 'inflammatory'type 2 innate lymphoid cells. *Nat Immunol* (2015) 16(2):161–9. doi: 10.1038/ni.3078

30. Van Dyken SJ, Nussbaum JC, Lee J, Molofsky AB, Liang H-E, Pollack JL, et al. A tissue checkpoint regulates type 2 immunity. A tissue checkpoint regulates type 2 immunity. *Nat Immunol* (2016) 17(12):1381–7. doi: 10.1038/ni.3582

31. Satoh-Takayama N, Ohno H. Unraveling the heterogeneity and specialization of ILCs. *Immunity* (2020) 53(4):699–701. doi: 10.1016/j.immuni.2020.09.017

32. Mincham KT, Snelgrove RJ. Full spectrum flow cytometry for high-dimensional immunophenotyping of mouse innate lymphoid cells. *Cytometry A.* (2023) 103(2):110–6. doi: 10.1002/cyto.a.24702

33. Stier MT, Zhang J, Goleniewska K, Cephus JY, Rusznak M, Wu L, et al. IL-33 promotes the egress of group 2 innate lymphoid cells from the bone marrow. *J Exp Med* (2018) 215(1):263-81. doi: 10.1084/jem.20170449

34. Zeis P, Lian M, Fan X, Herman JS, Hernandez DC, Gentek R, et al. *In situ* maturation and tissue adaptation of type 2 innate lymphoid cell progenitors. *Immunity* (2020) 53(4):775–92.e9. doi: 10.1016/j.immuni.2020.09.002

35. Cavagnero KJ, Badrani JH, Naji LH, Amadeo MB, Shah VS, Gasparian S, et al. Unconventional ST2-and CD127-negative lung ILC2 populations are induced by the fungal allergen Alternaria alternata. *J Allergy Clin Immunol* (2019) 144(5):1432–5.e9. doi: 10.1016/j.jaci.2019.07.018

frontiers | Frontiers in Immunology

TYPE Original Research
PUBLISHED 05 October 2023
DOI 10.3389/fimmu.2023.1275413

OPEN ACCESS

EDITED BY
Jorg Hermann Fritz,
McGill University, Canada

REVIEWED BY
Christoph Siegfried Niki Klose,
Charité University Medicine Berlin, Germany
Gokhan Cildir,
University of South Australia, Australia

*CORRESPONDENCE
Sarah Q. Crome
sarah.crome@utoronto.ca

RECEIVED 09 August 2023
ACCEPTED 05 September 2023
PUBLISHED 05 October 2023

CITATION
Audouze-Chaud J, Mathews JA and Crome SQ (2023) Efficient and stable CRISPR/Cas9-mediated genome-editing of human type 2 innate lymphoid cells. *Front. Immunol.* 14:1275413. doi: 10.3389/fimmu.2023.1275413

Efficient and stable CRISPR/Cas9-mediated genome-editing of human type 2 innate lymphoid cells

Johanne Audouze-Chaud[1,2], Jessica A. Mathews[2] and Sarah Q. Crome[1,2]*

[1]Department of Immunology, Temerty Faculty of Medicine, University of Toronto, Toronto, ON, Canada, [2]Toronto General Hospital Research Institute, Ajmera Transplant Centre, University Health Network, Toronto, ON, Canada

Innate lymphoid cells (ILCs) are a family of innate lymphocytes with important roles in immune response coordination and maintenance of tissue homeostasis. The ILC family includes group 1 (ILC1s), group 2 (ILC2s) and group 3 (ILC3s) 'helper' ILCs, as well as cytotoxic Natural Killer (NK) cells. Study of helper ILCs in humans presents several challenges, including their low proportions in peripheral blood or needing access to rare samples to study tissue resident ILC populations. In addition, the lack of established protocols harnessing genetic manipulation platforms has limited the ability to explore molecular mechanism regulating human helper ILC biology. CRISPR/Cas9 is an efficient genome editing tool that enables the knockout of genes of interest, and is commonly used to study molecular regulation of many immune cell types. Here, we developed methods to efficiently knockout genes of interest in human ILC2s. We discuss challenges and lessons learned from our CRISPR/Cas9 gene editing optimizations using a nucleofection transfection approach and test a range of conditions and nucleofection settings to obtain a protocol that achieves effective and stable gene knockout while maintaining optimal cell viability. Using IL-4 as a representative target, we compare different ribonucleoprotein configurations, as well as assess effects of length of time in culture and other parameters that impact CRISPR/Cas9 transfection efficiency. Collectively, we detail a CRISPR/Cas9 protocol for efficient genetic knockout to aid in studying molecular mechanism regulating human ILC2s.

KEYWORDS

innate lymphoid cells, ILC2s, natural killer cells, CRISPR/Cas9, nucleofection, IL-4, knockout, genome editing

Abbreviations: CRISPR/Cas9, Clustered Regularly Interspaced Short Palindromic Repeats/CRISPR-associated nuclease 9; DSB, Double-Stranded Break; EOMES, Eomesodermin; GATA3, GATA-associated protein 3; GM-CSF, Granulocyte Monocyte – Colony Stimulating Factor; gRNA, guide Ribonucleic Acid; IFN, Interferon; IL, Interleukin; ILCs, Innate Lymphoid Cells; ILC1, Group 1 innate lymphoid cells; ILC2, Group 2 innate lymphoid cells; ILC3, Group 3 innate lymphoid cells; KIR, Killer Cell Immunoglobulin-like Receptors; NHEJ, Non-Homologous End Joining; NK Cells, Natural Killer cells; PMA, Phorbol 12-myristate 13-acetate; RORC2, RAR-related Orphan Receptor 2; RT, Room Temperature; Th1, T helper 1 cell; Th2, T helper 2 cell; Th17, T helper 17 cell; TBET, T-Box Transcription Factor; TNF, Tumor Necrosis Factor.

Introduction

Innate Lymphoid Cells (ILCs) are a family of innate lymphocytes with important roles in host defense, as well as immune and tissue homeostasis (1–5). Cytotoxic Natural Killer (NK) cells produce Interferon-γ (IFN-γ) and Tumor Necrosis Factor-α (TNF-α) and are defined by co-expression of T-Box Transcription Factor (TBET) and Eomesodermin (EOMES) (1, 3). In humans they are further classified as $CD56^{dim}$ which express antibody dependent cellular cytotoxicity (ADCC)-mediating receptor CD16, or as $CD56^{bright}$ NK cells that exhibit low or no cytotoxicity, but instead are potent cytokine producers. NK cells have established roles in host defense against intracellular parasites as well as in antitumor immunity (3, 6). So called "helper" ILCs, including group 1 (ILC1s), group 2 (ILC2s) and group 3 (ILC3s) ILCs are not cytotoxic, and are classified based on their transcription factor and cytokine expression profiles (1, 7). ILC1s express TBET but not EOMES, secrete TNF-α and IFN-γ and participate in host defense against viruses and intracellular bacteria (1, 8, 9). ILC2s express the GATA binding protein 3 (GATA3) and produce IL-4 (in humans), IL-5, IL-9 and IL-13 (1, 3, 7). ILC2s are involved in immunity to extracellular parasites, and have important functions in tissue repair and regeneration (10, 11). ILC3s are characterized by expression of the RAR-related Orphan Receptor 2 (RORC2) and the production of IL-22, either alone or in combination with IL-17A and Granulocyte-Macrophage-Colony Stimulating Factor (GM-CSF) (1, 3, 7). They promote the defense against extracellular bacteria and fungi, and similar to ILC2s, can also participate in tissue repair processes (1, 12, 13). The majority of our current understanding of helper ILCs has come from murine studies. This is due in part to challenges in studying human ILCs that include; (i) non-NK cell ILCs are present in very low abundance in human blood (14), (ii) study of tissue-resident requires access to rare human samples, and (iii) a lack of tools to genetically manipulate human ILCs to explore molecular mechanism that control their development, function, and interactions with other immune and parenchymal cells.

CRISPR/Cas9 is an effective genome-editing tool that has emerged as a platform of choice for genetic manipulation (15). With CRISPR/Cas9 approaches, the endonuclease Cas9 induces a double-stranded break (DSB) in a specific target DNA sequence recognized by a guide RNA (gRNA) (15). The gRNA and Cas9 can be delivered into the cells via different approaches, including viral vector delivery and electroporation (16, 17). Those approaches can support gRNA and Cas9 being associated prior to delivery to form a ribonucleoprotein (RNP), or instead delivered in DNA form in a plasmid.

Previous studies have shown RNP approaches are associated with fewer off-target effects, reduced cytotoxicity (18) and increased genome editing efficiency (19). Lentiviral delivery requires CRISPR/Cas9 to be in a plasmid (DNA) format, and while very efficient, results in increased insertional mutagenesis and random integrations (16). Adenoviral (and adeno-associated) delivery also requires a DNA format, and although is non-integrating, is less efficient than lentiviral delivery. Adenoviral delivery also presents other disadvantages, such as limited cloning capacity and the potential for initiation of immune responses (16, 17). Electroporation-based delivery involves applying a high voltage pulse to cells that creates membrane pores, or nuclear pores in the case of nucleofection. It is generally reported to be as efficient as lentiviral delivery, and enables the use of both RNP and DNA formats, with reduced risks of mutagenesis (16). A caveat of this approach, however, is that it is often associated with poor cell viability (16). Thus when optimizing a CRISPR/Cas9 approach, it is important to consider cell viability, transfection efficiency and potential for off-target effects, and select an approach that balances these factors.

CRISPR/Cas9 has been used in multiple NK cells studies, providing protocols for NK cell lines (20), as well as primary human NK cells (21–27). Most human NK cells studies used electroporation delivery of an RNP (21–27), however, protocols differ in parameters such as electroporation settings and quantities of CRISPR/Cas9 components being delivered. Thus, even though this technique has been extensively used in NK cells, several factors could be optimized to enhance effectiveness of harnessing CRISPR/Cas9. Beyond NK cells, studies employing CRISPR/Cas9 in ILC2s or other ILCs are extremely limited, with to our knowledge only one protocol to date using plasmid delivery in mouse ILC2s (28, 29), and only one human study using lenti-CRISPR in human ILC2s to knockout PD-1 and HS3ST1 in stage IV colorectal patients ILC2s (30). Thus, development of CRISPR/Cas9 protocols are greatly needed to aid in translating mouse findings to human ILC2s, as well as to understand novel aspects of human ILC2s biology.

In this study, we developed an efficient protocol to mediate CRISPR/Cas9 knockout in human ILC2s. The protocol employed utilizes a nucleofection approach to deliver an RNP to knockout the cytokine IL-4, which was selected as a representative gene due to being a signature human ILC2 cytokine and an important mediator of ILC2s function (1). We report a method that achieves efficient and stable knockout of IL-4, while being optimized to minimize nucleofection-based impacts on cell viability. Having tested a wide range of parameters, the findings herein can aid development of protocols to target any gene of interest in human ILC2s.

Materials and methods

Human PBMC isolation

Healthy peripheral blood was obtained from donors through the Canadian Blood Services Blood4Research program, with each donor providing written, informed consent (UHN REB 17-6229, CBS Approved Study 2020-047). PBMCs were isolated using Lymphoprep (STEMCELL Technologies) per manufacturer instructions.

ILC sorting and culture

Peripheral blood mononuclear cells (PBMCs) were stained with human TruStain FcX (BioLegend) and incubated with a cocktail of lineage antibodies conjugated to the FITC listed in Supplemental Table 2. Cells were washed in FACS buffer, resuspended in EasySep

Buffer (STEMCELL Technologies), and enriched using the EasySep FITC Positive Selection Kit II (STEMCELL Technologies) per manufacturer instructions. Enriched cells were stained with antibody cocktail (Supplemental Table 2) and sorted using a FACSAria Fusion (BD Biosciences) or Symphony S6 sorter (BD Biosciences).

PBMCs were sorted by flow cytometry as live, lineage negative populations. Specifically, $CD56^{dim}$ NK cells were defined as live $lineage^{-}CD45^{+}CD56^{dim}CD16^{+}$, $CD56^{bright}$ NK cells as live $lineage^{-}CD45^{+}CD56^{bright}CD16^{-}$ and ILC2s as live $lineage^{-}CD45^{+}CD94^{-}CD16^{-}NKG2D^{-}CD56^{-}CD127^{+}CRTh2^{+}CCR6^{-}$. NK cells were cultured in MACS (Miltenyi) media supplemented with IL-2, IL-15, and IL-18 to maintain an activated state. Similarly, ILC2s were cultured in X-VIVO15 (Lonza) supplemented with 5% human AB serum (Sigma), 100U/mL Penicillin-Streptomycin (Gibco) and 1X GlutaMAX (Gibco) with recombinant human IL-2, IL-7, and IL-33 as described in Reid et al. (31). Cytokine analysis was performed pre and post IL-4 knockout by flow cytometry and cytometric bead array (Figure 1).

Staining and flow cytometry

ILCs were counted and 100,000-200,000 cells were stained per condition. Cells were first washed with FACS buffer (PBS + 2% FCS) and blocked with human TruStain FcX (BioLegend) (diluted 1:10 in FACS buffer) for 15 min at 4°C. Next, they were stained for surface markers (Supplemental Table 2) (diluted in FACS buffer) for 30 min at 4°C, washed with FACS buffer, and fixed with FOXP3/Transcription Factor Staining set (eBioscience) buffer if performing phenotyping, or with 2% Paraformaldehyde (PFA) if assessing GFP expression. In the case of an intracellular staining, cells were washed with FACS buffer, and human TruStain FcX (BioLegend) (diluted 1:10 in permeabilization buffer from FOXP3/Transcription Factor Staining set (eBioscience)) was added one more time, 15 min at RT following surface staining and fixation. Cells were then stained for intracellular markers (Supplemental Table 2) in FOXP3/Transcription Factor Staining set permeabilization buffer (eBioscience) for 30 min at RT, then assessed by flow cytometry. Data was collected using a LSR Fortessa flow cytometer (BD Biosciences) and Diva software and analyzed with FlowJo v10.8.1 software.

Cytokine stimulation

100,000-200,000 ILCs were plated in IL-2 overnight (O/N) the day before the stimulation. Supernatants were collected for Cytometric Bead Array (CBA). Cells were stimulated with PMA/Ionomycin (Invitrogen) for 6h. Golgi plug (BD Biosciences) and Golgi stop (BD Biosciences) were added after 4h. Following stimulation, cells were washed with FACS, and surface and intracellular flow cytometry staining was performed.

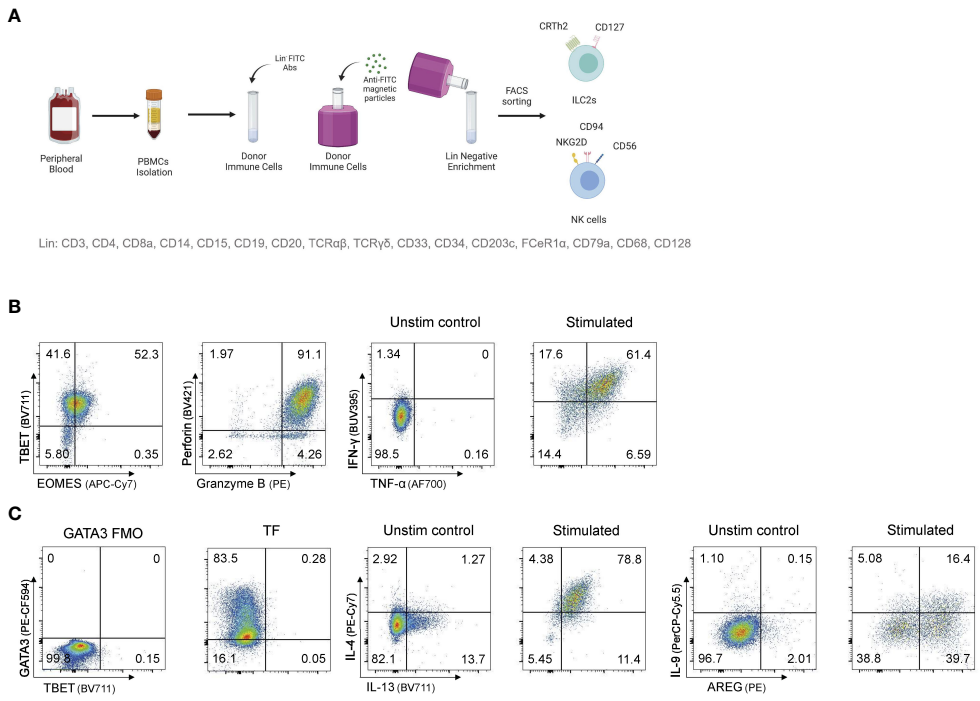

FIGURE 1
Sorting and expanding ILC2s and NK cells for CRISPR/Cas9 gene editing **(A)** Sorting strategy to isolate ILC2s and NK cells from human peripheral blood. PBMCs are stained for lineage with FITC antibodies and ILC2s and NK cells are FACS sorted after $FITC^{-}$ PBMCs enrichment. **(B)** Representative TF expression and cytotoxic granules expression, and cytokine profile of NK cells after intracellular staining. **(C)** Representative TF expression and cytokine profile of ILC2s after intracellular staining. Figure in **(A)** created with Biorender.com.

Cytometric bead array

Cytometric bead array analysis was performed using the Legendplex Human Cytokine Panel kit (BioLegend) instructions. Briefly, 25 µL of supernatants collected after O/N incubation in IL-2 were transferred into a V-bottom plate. 25 µL of assay buffer and 25 µL of beads were also added. The plate was incubated for 2h while being shaken at 500 rpm. Wells were then washed twice and 25 µL of detection antibodies were added. The plate was incubated for 1h while being shaken at 500 rpm. Finally, 25 µL of Streptavidin-PE were added and the plate was incubated for 30 more minutes while being shaken at 500 rpm. Wells were then washed and read immediately by flow cytometry using a LSR Fortessa flow cytometer (BD Biosciences).

Results

Optimization of an electroporation-based CRISPR/Cas9 protocol for human ILC2s

As ILC2s are rare in blood, and access to tissue samples is limited, we elected to develop a protocol that could be used on activated and expanded human ILC2s, that for the purpose of this study were isolated from peripheral blood. Here, human ILC2s, as well as NK cells for a comparator, were isolated by flow cytometry sorting (Figure 1A), and then expanded in activating cytokines for 2 to 12 weeks. After expansion, NK cells and ILC2s maintained expression of signature cytokines and transcription factors (Figures 1B, C) allowing for testing gene knockout strategies on conventional ILC2-associated genes.

In order to maximize genome targeting efficiency while reducing cytotoxicity and off-target editing (16, 18, 19), we elected to develop a CRISPR/Cas9 approach combining an RNP delivery format in combination with nucleofection (Lonza, Supplemental Table 1). This combination has been successfully employed in a wide range of studies in human T lymphocytes and NK cells (21–27, 32, 33), yet the major limitation is that it is often associated with poor viability (16). We therefore tested a wide range of nucleofector settings to identify nucleofector pulse codes that achieved the best efficiency possible while preserving cell viability (Figure S1; Figure 2). We conducted those experiments using a GFP vector (Lonza) as a marker for successful delivery of genetic material into the cells. Flow cytometry at 18-24h post-electroporation was used to assess efficiency, as this corresponded to peak GFP fluorescence expression (Figure 2A). Here, live $CD45^+GFP^+$ NK cells and ILC2s were assessed for a range of pulse codes (Figure 2B), and cell viability and electroporation efficiency (% $CD45^+GFP^+$ cells, gated on live) determined.

We noted that experiment-to-experiment, differences in the electroporation efficiency was observed in ILC2s from different donors. We hypothesized that, in addition to donor-to-donor variability, the time ILC2s were in culture prior to electroporation might influence the effectiveness of nucleofection. To assess this, we examined how both viability and efficiency of transfection across multiple pulse codes differed in experiments performed on NK cells and ILC2s expanded for different lengths of time *ex vivo* prior to transfection, and further assessed individually one of our lead pulse codes (DN100) (Figures 2C-F; Figure S1). For both ILC2s and NK cells, cell viability post-electroporation was not impacted by the time in culture (Figures 2C; S1D, E, B), a finding that was observed across multiple pulse codes, including DN100 (Figures 2C, D; S1D, E; S2B-E). However, a negative correlation was clearly observed between electroporation efficiency and the time in culture for both ILC2s and NK cells, with an even stronger correlation in NK cells (Figures 2E, F; S1F, G; S2F-I). This trend was further confirmed when looking at individual pulse codes, including DN100 (Figures 2F; S1F, G; S2G-I). Therefore optimal nucleofection of both ILC2s and NK cells occurs with minimal *ex vivo* culturing time, with <6 weeks being acceptable for ILC2s and <5 weeks for NK cells.

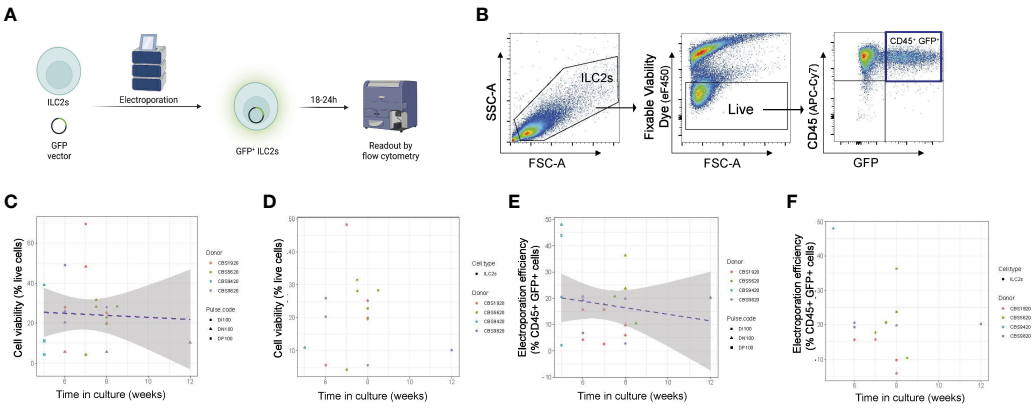

FIGURE 2
Optimization of time of ILC2 transfection across multiple electroporation settings. **(A)** ILC2s were transfected with a GFP vector by electroporation and GFP fluorescence was examined 18-24h post electroporation. **(B)** Representative gating of electroporated cells. The %live cells is referred to as viability and the %$CD45^+GFP^+$ cells is referred to as efficiency. **(C)** ILC2s viability in function of the time in culture across multiple pulse codes. **(D)** ILC2s viability in function of the time in culture for pulse code DN100. **(E)** Efficiency of ILC2s electroporation across multiple pulse codes. **(F)** Efficiency of ILC2s electroporation for pulse code DN100. (n=14-18). Figure in **(A)** created with Biorender.com.

We next focused on defining the ideal nucleofector settings for human ILC2s. We first identified nucleofection codes previously used on primary human T cells (32, 33) or NK cells (21, 22, 24, 25), or recommended by the manufacturer. We then assessed cell viability and efficiency over a wide range of nucleofector settings (CA-137, CM-137, DH100, DI100, DN100, DP100, EH100, EN-138, EO-115, FI-115) (Figures S1A-C). Based on a preliminary screening, we identified the three lead pulse codes and performed multiple independent experiments using these codes to identify the nucleofector pulse code that would yield the greatest number of successfully transfected and viable ILC2s (Figures 3A–C). We examined nucleofection efficiency as well as cell viability and established an overall score that combined these parameters (multiplied cell viability by nucleofection efficiency). Throughout, NK cells were used as comparator (Figures S2J-L).

For these experiments $1x10^6$ ILC2s per condition were centrifuged at 100xg for 10 min at RT in 15 mL Falcon tubes. The supernatant was discarded, and cells were washed with 10 mL of serum free media to prevent any interference of the serum with CRISPR/Cas9 components. The cell pellet was mixed with electroporation solutions from the P3 primary cell kit (Lonza) as well as the GFP vector and transferred into a nucleocuvette. Next, ILC2s were electroporated using various pulses codes, immediately toped up with 80 µL warm complete media, and transferred into a 96-well plate pre-filled with their culture media.

Of nucleofector pulse codes tested, DI100 consistently maintained the highest ILC2 viability (38.70% ± 10.51), while DN100 had the highest efficiency (22.81% ± 10.09 $CD45^+GFP^+$ ILC2s). As a comparison, DN100 obtained the highest viability among pulse codes screened in NK cells (29.09% ± 14.78) and a similar efficiency to ILC2s (19.66% ± 14.54 $CD45^+GFP^+$ NK cells). When the combination of parameters was assessed, DI100 and DN100 obtained a similar score when used for ILC2s (0.04 ± 0.037 and 0.04 ± 0.020 respectively). However, DI100 efficiency was particularly low (10.0% ± 9.32 $CD45^+GFP^+$ cells), while DN100 maintained an acceptable viability (19.05% ± 8.65). Therefore, we moved forward to test additional parameters using DN100. An overview of the optimized RNP delivery protocol for CRISPR/Cas9 is detailed in Figure 3D. The next step was to determine an optimal RNP composition.

Optimization of RNP composition for efficient IL-4 knockout

To determine optimal RNP composition, we elected to induce a CRISPR/Cas9 knockout of the cytokine IL-4, as it is stably expressed in high amounts by human ILC2s, making it an ideal proof-of-concept target. We tested three different RNP compositions (Supplemental Table 3) that differed in terms of sgRNA : Cas9 ratio, sgRNA and Cas9 quantities being delivered, and reconstitution buffer. For each RNP composition, we tested three different sgRNAs targeting *IL4* sequence (Supplemental Table 4). To determine our knockout efficiency, we assessed the IL-4 expression both by intracellular cytokine staining and measuring IL-4 secretion by cytometric bead array (CBA) of untreated ILC2s, control treated ILC2s or ILC2s receiving sgRNA targeting *IL4*. For IL-4 analysis by CBA, at day 2 and day 6 of ILC cultures, ILC2s were counted and replated in IL-2 overnight. Supernatants were then collected for subsequent secreted IL-4 analysis, as well as analysis of effects on other ILC-associated cytokines (Figure 4A; Figure S3A). Intracellular cytokine staining was performed on day 3 and day 7 post-transfection; the later time point being the most important, as our aim was to generate a protocol that results in stable genome edited cells to enable downstream *in vitro* or *in vivo* experiments. For intracellular cytokine staining, ILC2s were stimulated with PMA/Ionomycin and assessed for effective CRISPR/Cas9 knockout of IL-4, as well as other cytokines expressed by ILC2s or other ILC family members. A representative gating of IL-4 and IL-13 cytokines can be found in Figure 4B.

At day 3, ILC2s maintained good viability across all conditions, however RNP2 exhibited the highest viability across three independent donors (35.83% ± 14.35 – 39.83% ± 14.42 depending on the sgRNA used) (Figure S3C). When IL-4 expression was

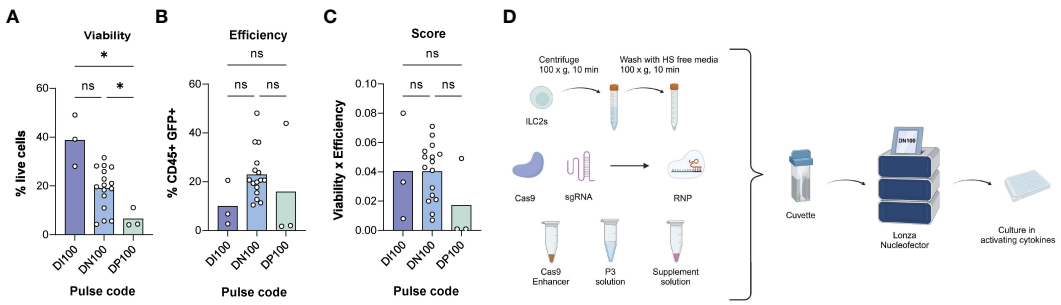

FIGURE 3
Determining the optimal electroporation pulse code for human ILC2s. **(A)** % live cells across pulse codes DI100, DN100 and DP100. **(B)** Efficiency of transfection across pulse codes DI100, DN100 and DP100. Efficiency was determined as the $\%CD45^+GFP^+$ cells. **(C)** Score of pulse codes DI100, DN100 and DP100. Scores were calculated by multiplying %live cells x % $CD45^+GFP^+$ cells. **(D)** Optimized delivery protocol for CRISPR/Cas9 in ILC2s. 1M ILC2s are centrifuged at 100xg for 10 min and then washed with human serum (HS) free media. The pellet is then mixed with electroporation solutions and CRISPR/Cas9 in form of a RNP, and electroporated with the pulse code DN100. Following electroporation, cells are gently resuspended in their media overnight, and assessed for GFP expression at 24hrs (n=3-16). *= $P \leq 0.05$, ns = non significant. Figure in **(D)** created with Biorender.com.

10.3389/fimmu.2023.1275413

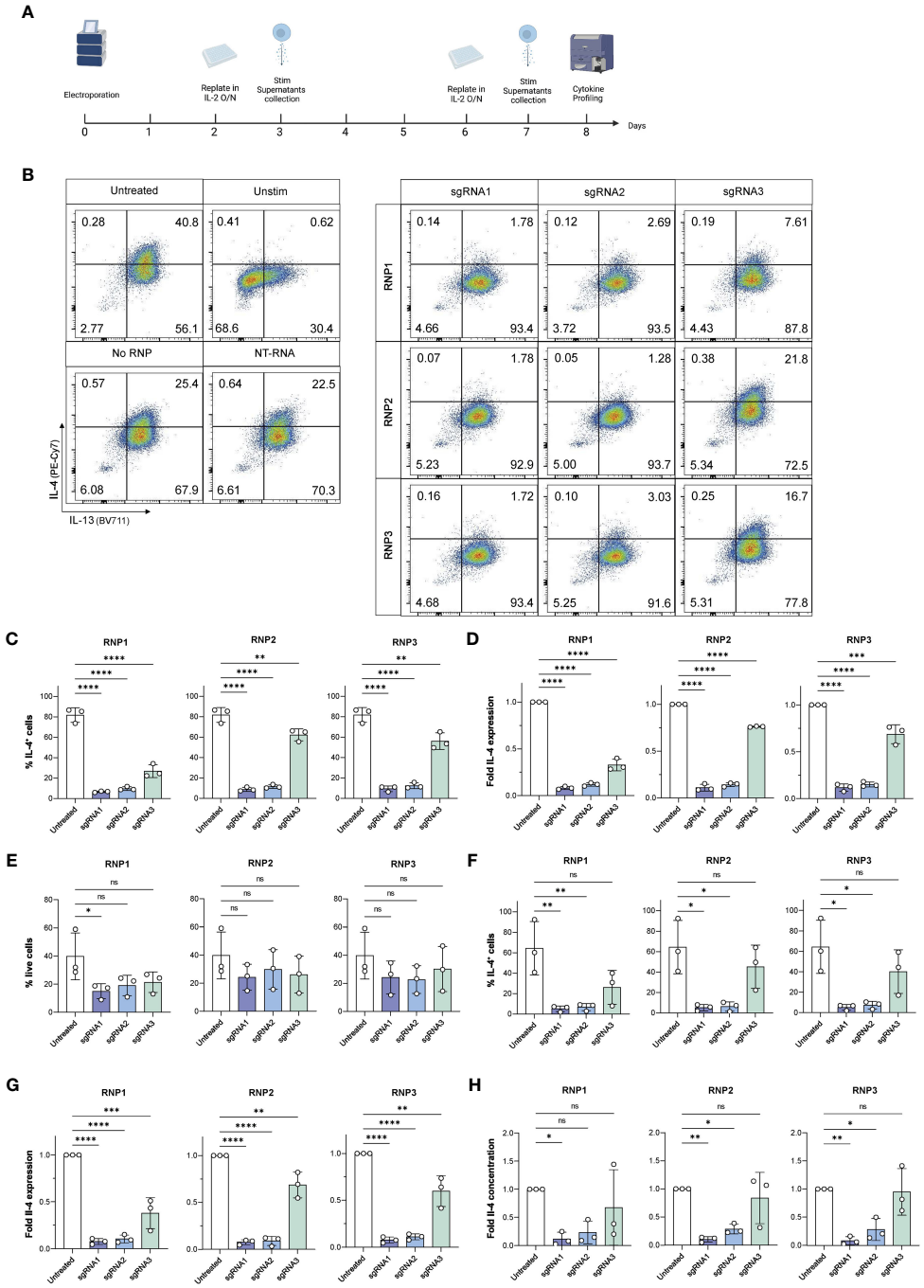

FIGURE 4
Viable, efficient and stable knockout of IL-4 in human ILC2s. **(A)** ILC2s were replated in IL-2 O/N at day 2 and day 6 following electroporation. At day 3 and day 7, supernatants were collected for Cytometric Bead Array analysis, and ILC2s were stimulated phorbol 12-myristate 13-acetate (PMA)/Ionomycin and stained intracellularly to examine their cytokine profile by flow cytometry. **(B)** Representative gating of IL-4 and IL-13 expression in untreated and knockout ILC2s at day 7. **(C)** Day 3 %IL-4$^+$ cells in IL-4 knockout ILC2s electroporated with RNP Protocol 1, 2 or 3 (RNP1, RNP2, RNP3) compared to untreated ILC2sby flow cytometry after stimulation. **(D)** Day 3 fold change in IL-4 expression of IL-4 knockout ILC2s electroporated with RNP Protocol 1, 2 or 3 (RNP1, RNP2, RNP3) compared to untreated ILC2s by flow cytometry after stimulation. **(E)** Day 7 viability of IL-4 knockout ILC2s electroporated with RNP Protocol 1, 2 or 3 (RNP1, RNP2, RNP3) compared to untreated ILC2s by flow cytometry after stimulation. **(F)** Day 7 %IL-4$^+$ cells in IL-4 knockout ILC2s electroporated with RNP Protocol 1, 2 or 3 (RNP1, RNP2, RNP3) compared to untreated ILC2s by flow cytometry after stimulation. **(G)** Day 7 fold change in IL-4 expression of IL-4 knockout ILC2s electroporated with RNP Protocol 1, 2 or 3 (RNP1, RNP2, RNP3) compared to untreated ILC2s by flow cytometry after stimulation. **(H)** Day 7 fold change in IL-4 concentration in supernatants of IL-4 knockout ILC2s electroporated with RNP Protocol 1, 2 or 3 (RNP1, RNP2, RNP3) compared to untreated ILC2s. (n=3). * = P ≤ 0.05; ** = P ≤ 0.01; *** = P ≤ 0.001; **** = P ≤ 0.0001, ns = non significant.

assessed in ILC2s, ILC2s receiving sgRNA1 and sgRNA2 displayed almost no IL-4 staining, with a fold IL-4 expression comprised between 0.08 and 0.12 for sgRNA1 and between 0.12 and 0.14 for sgRNA2, respectively, depending on the RNP (Figures 4C, D). We calculated the knockout score (% IL-4$^+$ cells/% live cells), where a lower score meant a high knockout efficiency and a high viability. We observed sgRNA1 combined with RNP2 obtained the lowest score at day 3 (0.26 ± 0.04) (Figure S3D).

At day 7, no significant differences were observed in the viability of untreated and IL-4 ko ILC2s electroporated with the RNP2 and RNP3 protocol, regardless of the sgRNA used (Figure 4E). Both RNP2 and RNP3 did not have significant effects on cell viability. However, the RNP1 protocol had an overall lower viability, with a significant decrease when combining sgRNA1 and RNP1 ($p = 0.042$).

Both sgRNA1 and sgRNA2 effectively inhibited IL-4 expression in each RNP compositions tested (Figure 4F). The lowest IL-4 expression was achieved with sgRNA1 combined with RNP3 (5.12% ± 2.81 IL-4$^+$ cells) followed by sgRNA1 combined with RNP2 (5.13% ± 10.09 3.07 IL-4$^+$ cells) (Figure 4F). Accordingly, the fold decrease compared to untreated cells was most significant with sgRNA1 across all RNP protocols ($p < 0.0001$) (Figure 4G). The fold decrease compared to NT-RNA was also most significant with sgRNA1 across all RNP protocols ($p < 0.0001$) (Figure S6I). While sgRNA2 performed well, the combination of sgRNA1 with RNP2 obtained the best score (0.27 ± 0.25) (Figure S4A).

CBA analysis confirmed effective knockout of IL-4. We noted very low IL-4 secreted in ILC2s receiving with sgRNA1 across all donors compared to untreated ILC2s (5.74 ± 4.33 - 8.29 ± 7.33 pg/ml/100,000 cells for sgRNA1 transfected cells vs 97.05 ± 73.03 pg/ml/100,000 cells for untreated control) (Figure S4B). It is important to note that some of the individual repetitions were below the threshold of detection of the assay (2.83 pg/ml), meaning IL-4 was no longer detectable in those samples, and if above detection, was exceptionally low in the other independent experiments. The fold decrease in secreted IL-4 was significant with sgRNA1 across all RNPs, however the highest significance was observed with the combination of sgRNA1 and RNP2 ($p = 0.004$) (Figure 4H), in line with intracellular staining data for IL-4. While it is sometimes an effective strategy to combine two different sgRNAs, combining sgRNA1 and sgRNA2 did not result in better IL-4 knockout efficiency (Figure S5).

To assess if CRISPR/Cas9 IL-4 knockout or nucleofection might have inadvertent effects on ILC2 functions, we examined if ILC2s receiving sgRNAs targeting the *IL4* sequence maintained expression of IL-13 and IL-9, two other ILC2-associated cytokines, or upregulated expression of cytokines associated with other ILCs such as IFN-γ or IL-17A (Figure 5). IL-13 expression was unchanged compared to untreated ILC2s (Figures 5A, B). Additionally, NK cell and ILC1 associated IFN-γ was not upregulated with IL-4 knockout (Figures 5A, C). When secreted cytokines were examined, expression of IL-9, TNF-α (associated with NK cells) and IL-17A (associated with ILC3s) were not altered in IL-4 knockout ILC2s (Figures 5D–F). Furthermore, cytokine expression (including IL-4) was not affected in non-targeting (NT) RNA and No RNP negative controls (Figure S6), further supporting the specificity of the IL-4 knockout.

To confirm our protocol would be effective at targeting other genes in ILC2s, we performed a pilot experiment with sgRNAs targeting *IL10*, which we and others have linked to ILC2s immunoregulatory effects in the context of allergy (11), cell therapy approaches for transplantation (28) and Graft-versus-Host Disease (GvHD) (31). We observed IL-10 expression was efficiently downregulated at day 3 post-transfection using our protocol (Figure S7), indicating the approach is effective at knocking out genes in different genomic positions.

Taken together, we report a protocol for efficient knockout of IL-4 in ILC2s that maintains good cell viability with sgRNA1 combined with RNP2, using the pulse code DN100. Day 7 post-knockout timepoint supports this result in stable IL-4 knockout. Furthermore, analysis of ILC2 and non-ILC2-associated cytokines supports CRISPR/Cas9 genome editing of IL-4 did not alter cytokine expression profiles of ILC2s. The overall protocol is summarized in Figure 6, with a complete detailed protocol included as Supplemental Document 1.

Discussion

We report an effective CRISPR/Cas9 protocol to knockout genes of interest in human ILC2s. While IL-4 was used as a proof-of-concept target, optimization experiments included here can inform CRISPR/Cas9 gene editing strategies for targeting other genes of interest in human ILC2s. The nucleofection pulse code DN100 in combination with the RNP2 resulted in stable IL-4 knockout, and can be adapted to any target by screening for the best specific sgRNA for a gene of interest.

Here, CRISPR/Cas9 was delivered by electroporation, as this method has been proven successful in studies of human NK cells and T lymphocytes (21–27, 32–34). In addition, using an electroporation approach is associated with higher efficiency and less off-target effects in comparison to other techniques such as lentiviral delivery (16), and allowed us to deliver CRISPR/Cas9 in the form of an RNP. As expected, the main challenge associated with the electroporation was the poor viability. During the initial screening of pulse codes for ILC2s, we tested pulse codes previously used in human NK cells and T cells, as well as manufacturer's pulse code recommendations for primary lymphocytes. Most of these settings led to efficient transfection in human NK cells, but resulted in either low viability or poor vector delivery to human ILC2s. While some pulse codes were associated with high viability, those generally displayed lower efficiency. On the other hand, pulse codes with a high percentage of CD45$^+$GFP$^+$ ILC2s had an extremely low percentage of live cells. For this reason, we established a score considering both parameters to assess the best pulse code. DN100, which had been successfully implemented in a study by Huang et al. in NK cells (27), appeared as an ideal middle ground for ILC2s, providing a relatively high efficiency while maintaining a reasonably high cell viability. We tried improving cell viability by letting ILC2s recover for 15 min the nucleocuvette in the incubator before transferring them into the 96-well plate, and by changing media 5 hours post-transfection, as previously documented (34), but this did not

10.3389/fimmu.2023.1275413

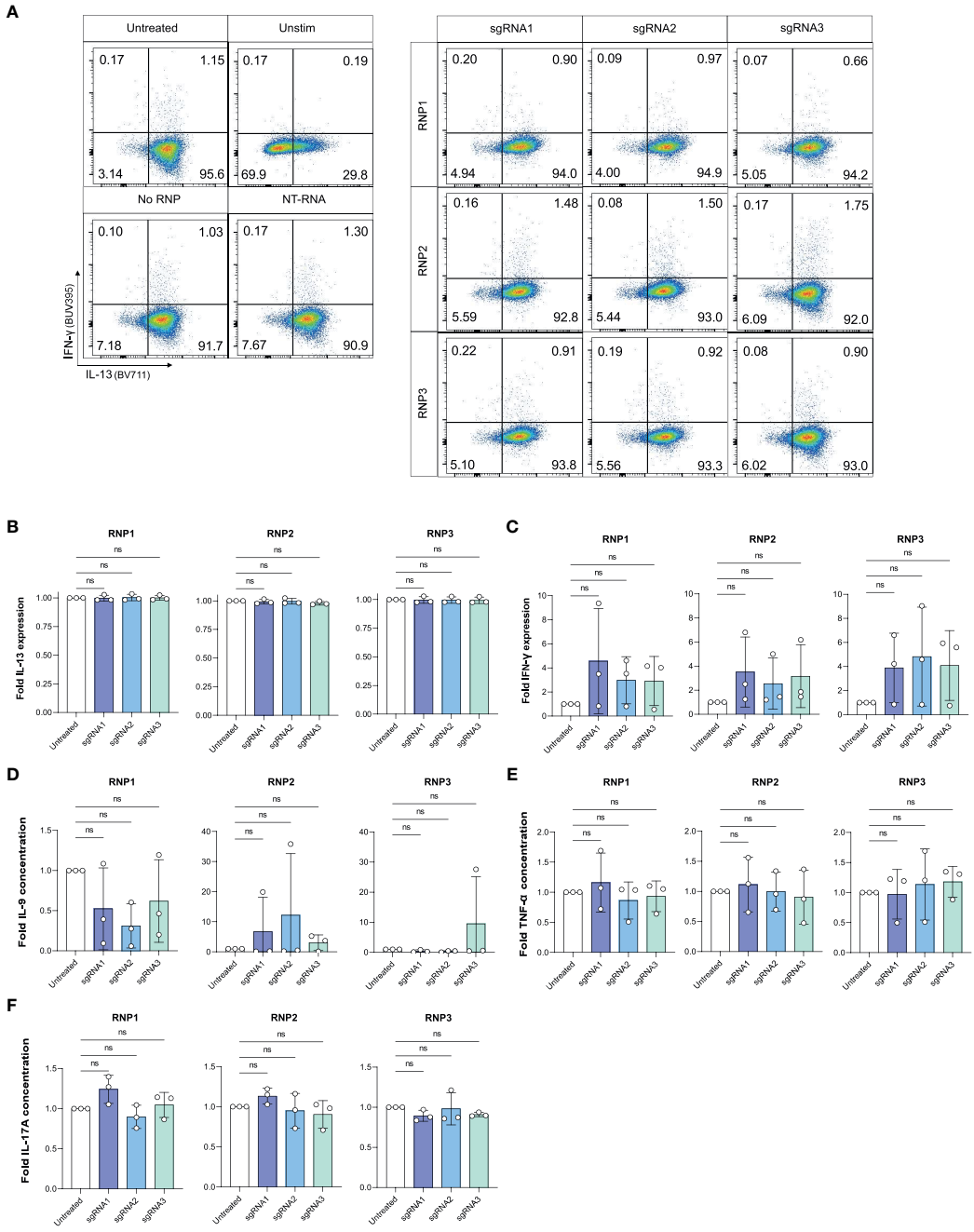

FIGURE 5
IL-4 knockout does not impact expression of other cytokines by ILC2s. **(A)** Representative gating of IFN-γ and IL-13 expression in untreated and knockout cells at Day 7. **(B)** Fold change in IL-13 expression of phorbol 12-myristate 13-acetate (PMA)/Ionomycin stimulated IL-4 knockout ILC2s electroporated with RNP Protocol 1, 2 or 3 (RNP1, RNP2, RNP3) or untreated ILC2s. **(C)** Fold change in IFN-γ expression of stimulated IL-4 knockout ILC2s electroporated with RNP Protocol 1, 2 or 3 (RNP1, RNP2, RNP3) or untreated ILC2s. **(D)** Fold change in IL-9 concentration in supernatants of IL-4 knockout ILC2s electroporated with RNP Protocol 1, 2 or 3 (RNP1, RNP2, RNP3) compared to untreated ILC2s. **(E)** Fold change in TNF-α concentration in supernatants of IL-4 knockout ILC2s electroporated with RNP Protocol 1, 2 or 3 (RNP1, RNP2, RNP3) compared to untreated ILC2s. **(F)** Fold change in IL-17A concentration in supernatants of IL-4 knockout ILC2s electroporated with RNP Protocol 1, 2 or 3 (RNP1, RNP2, RNP3) compared to untreated ILC2s. (n=3). ns = non significant.

improve viability in ILC2s. Interestingly, electroporation seemed to be better tolerated by NK cells than helper ILCs. This is illustrated by consistent better viability and efficiency in NK cells with the same pulse codes. We also observed donor-to-donor variability in efficiency of GFP transfection in ILC2s, that is at least partially influenced by the length of time ILC2s were cultured, but also could be related to heterogeneity of ILC2s between donors. Of note, however, is that gene editing of *IL4* was less heterogeneous in terms of efficiency than transfection of the GFP vector.

We observed a very low percentage of IL-4$^+$ cells when using sgRNA1 and sgRNA2. The efficiency of the knockout was better than anticipated, based on prediction with the GFP vector, with IL-

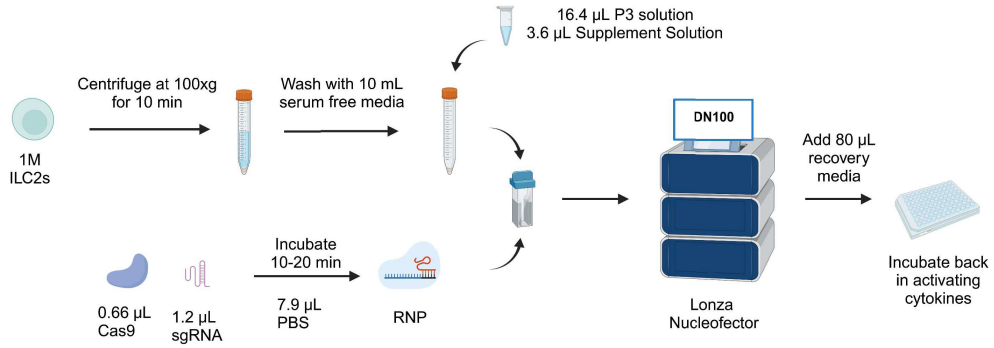

FIGURE 6
Workflow of CRISPR/Cas9-mediated knockout protocol in human ILC2s. ILC2s are centrifuged at 100xg for 10 min and washed with 10 mL serum free media. During that time, the RNP is reconstituted by mixing 1.2 µL sgRNA and 0.66 µL Cas9. The RNP is mixed with the pellet along with nucleofection solutions. Next, the mix is transferred into a nucleocuvette and electroporated with the pulse code DN100. Following electroporation, 80µL of recovery media is added and cells are incubated back in their activating cytokines. Figure created with Biorender.com.

4 expression in the knockout ILC2s reduced by approximately 10-fold, despite only achieved 25% transfection efficiency based on analysis of GFP expression. A possible explanation is the bigger size of the vector, which might prevent it to enter the pores as efficiently as the RNP. Indeed, it has been shown that a smaller sized-plasmid resulted better transfection efficiencies than a bigger sized-plasmid, suggesting the size of the format used to deliver CRISPR/Cas9 is an important parameter to consider (35). Furthermore, ILC2s viability post electroporation with the RNP was significantly higher than with the GFP vector. This could be explained by the fact that the GFP vector is delivered in a DNA form and thus needs to be transcribed and translated, exhausting the cell machinery, leading to higher cell death (17). In contrast, the RNP can directly reach the nucleus and induce the DSB without utilizing the cell machinery.

RNP composition 2 (RNP2), derived from Riggan et al. achieved the best viability (23). This is likely due to the difference in buffer used for the RNP reconstitution. RNP2 was reconstituted in PBS, whereas RNP1 and RNP3 were reconstituted in P3 nucleofection solution to reduce the volume being electroporated, which was another constraint in the protocol optimization. Reconstituting the RNP in PBS rather than nucleofection solution led to a higher cell viability, supporting that electroporation solution might be harmful to ILC2s when used for RNP reconstitution.

The choice of RNP did not impact IL-4 expression in controls, supporting that efficiency of knockout was sgRNA-dependent and not RNP-dependent. sgRNA1 and sgRNA2 outperformed sgRNA3, with sgRNA1 leading the highest editing efficiency. This was expected and concordant with the predicted scores. We tried to further optimize efficiency of the knockout by combing sgRNA1 and sgRNA2, however this did not improve the gene editing efficiency. CBA analysis of secreted cytokines confirmed the findings from intracellular cytokine staining. We noted that IL-4 expression tended as higher in NT-RNA and No RNP controls than in untreated cells by CBA (Supplemental Figure 6). The reason behind this is not completely clear, and may be due to the remaining cells after electroporation-induced cell death were the most viable and active. Another explanation is that the electroporation itself may activate ILC2s to a certain degree. While we analyzed our knockout compared to untreated controls as this is standard practice, knockout efficiency scores would have been even higher if compared to NT-RNA or No RNP controls (Figure S6I; Supplemental Figure 6).

We also assessed potential inadvertent impacts on ILC2s phenotype and cytokine expression with CRISPR/Cas9 IL-4 knockout. All parameters examined remained unchanged, beyond loss of IL-4 expression in IL-4 knockout ILC2s. However, a limitation of our study is that we did not perform extensive analysis of other potential off-target effects at the DNA level. For studies of ILC2 biology, this would be an important consideration, however analysis would differ between target genes of interest. For a given target gene, confirming that expression of nearby genes on the chromosome or that genes with similar sequences are not impacted is good practice.

While this protocol provides an efficient platform for knockout in human ILC2s, additional optimizations might improve CRISPR/Cas9 approaches. We observed a low percentage of IL-4$^+$ cells even with sgRNA1 and RNP2. This low percentage is not the result of inefficient knock-down, as CRISPR/Cas9 acts directly on the cell DNA, but could rather be explained by transfection not being 100% efficient, and as a result not all the ILC2s being successfully transfected. In that regard, the purity of the sample could be increased by using a Cas9 coupled with GFP and sorting Cas9/GFP$^+$ cells. In addition, CRISPR/Cas9 can sometimes induce silent mutations, as Non-Homologous End Joining (NHEJ) is a random process. As a result, some ILC2s could have been transfected but still express IL-4. In addition to increasing purity of knockout ILC2s, adapting this protocol (currently optimized for 1x10^6 cells) to be able to transfect larger ILC2s numbers would be helpful for experiments requiring a higher yield. While it remains challenging to study human ILCs *ex vivo* due to the scarcity of human ILC2s in peripheral blood and limited tissue availability, more and more groups are developing efficient ways to expand human ILC2s to enable complex analysis of their biology, including assessment of effects on ILC2 metabolism, regulation, and *in vivo* function in humanized mice. Therefore, adapting this protocol to allow transfection of larger cell volumes or comparison with other

approaches that preserve cell viability and do not present the disadvantages of viral vectors, such as peptide-mediated delivery (36), and viral-like particles (37) could be explored in future studies. The protocol we report herein, however, provides a base protocol for stable and efficient CRISPR/Cas9-mediated knockout of human ILC2s that maintains good cell viability, and can be employed to target any gene of interest in human ILC2s.

Data availability statement

The original contributions presented in the study are included in the article/Supplementary Material. Further inquiries can be directed to the corresponding author.

Ethics statement

The studies involving humans were approved by University Health Network Research Ethics Board. Healthy peripheral blood was obtained from donors through the Canadian Blood Services Blood4Research program, with each donor providing written, informed consent (UHN REB 17-6229, CBS Approved Study 2020-047).

Author contributions

JA-C: Conceptualization, Data curation, Investigation, Methodology, Writing – original draft, Writing – review & editing, Formal Analysis, Validation, Visualization. JM: Investigation, Methodology, Writing – review & editing. SC: Investigation, Methodology, Writing – review & editing, Conceptualization, Data curation, Funding acquisition, Project administration, Resources, Software, Supervision, Writing – original draft.

Funding

The author(s) declare financial support was received for the research, authorship, and/or publication of this article. This research was supported by funding from the Natural Sciences and Engineering Research Council of Canada (RGPIN-2021-03672), the Canadian Institutes for Health Research (169084), and the Canadian Innovation fund (38308).

Acknowledgments

JA-C was supported by a Canadian Graduate Scholarship - Masters award. SC is a Tier 2 Canada Research Chair in Tissue-Specific Immune Tolerance. We are grateful to Canadian Blood Services and donors for providing research samples that enabled this study. Schematic Figure created with Biorender.com.

Conflict of interest

The authors declare that the research was conducted in the absence of any commercial or financial relationships that could be construed as a potential conflict of interest.

Publisher's note

Author disclaimer

The reporting and interpretation of research findings are the responsibility of the authors, the views expressed herein do not necessarily represent the view of Canadian Blood Services.

Supplementary material

The Supplementary Material for this article can be found online at: https://www.frontiersin.org/articles/10.3389/fimmu.2023.1275413/full#supplementary-material

References

1. Vivier E, Artis D, Colonna M, Diefenbach A, Di Santo JP, Eberl G, et al. Innate lymphoid cells: 10 years on. *Cell* (2018) 174(5):1054–66. doi: 10.1016/j.cell.2018.07.017

2. Spits H, Di Santo JP. The expanding family of innate lymphoid cells: regulators and effectors of immunity and tissue remodeling. *Nat Immunol* (2011) 12(1):21–7. doi: 10.1038/ni.1962

3. Murphy JM, Ngai L, Mortha A, Crome SQ. Tissue-dependent adaptations and functions of innate lymphoid cells. *Front Immunol 10 mars* (2022) 13:836999. doi: 10.3389/fimmu.2022.836999

4. Klose CSN, Artis D. Innate lymphoid cells control signaling circuits to regulate tissue-specific immunity. *Cell Res* (2020) 30(6):475–91. doi: 10.1038/s41422-020-0323-8

5. Halim TYF, Rana BMJ, Walker JA, Kerscher B, Knolle MD, Jolin HE, et al. Tissue-restricted adaptive type 2 immunity is orchestrated by expression of the costimulatory molecule OX40L on group 2 innate lymphoid cells. *Immunity* (2018) 48(6):1195–1207.e6. doi: 10.1016/j.immuni.2018.05.003

6. Liu S, Galat V, Galat Y, Lee YKA, Wainwright D, Wu J. NK cell-based cancer immunotherapy: from basic biology to clinical development. *J Hematol Oncol* (2021) 14 (1):7. doi: 10.1186/s13045-020-01014-w

7. Spits H, Artis D, Colonna M, Diefenbach A, Di Santo JP, Eberl G, et al. Innate lymphoid cells — a proposal for uniform nomenclature. *Nat Rev Immunol* (2013) 13 (2):145–9. doi: 10.1038/nri3365

8. Klose CSN, Flach M, Möhle L, Rogell L, Hoyler T, Ebert K, et al. Differentiation of type 1 ILCs from a common progenitor to all helper-like innate lymphoid cell lineages. *Cell* (2014) 157(2):340–56. doi: 10.1016/j.cell.2014.03.030

9. Abt MC, Lewis BB, Caballero S, Xiong H, Carter RA, Sušac B, et al. Innate Immune Defenses Mediated by Two ILC Subsets Are Critical for Protection against Acute Clostridium difficile Infection. *Cell Host Microbe* (2015) 18(1):27–37. doi: 10.1016/j.chom.2015.06.011

10. Mjösberg J, Bernink J, Golebski K, Karrich JJ, Peters CP, Blom B, et al. The transcription factor GATA3 is essential for the function of human type 2 innate lymphoid cells. *Immunity* (2012) 37(4):649–59. doi: 1016/j.immuni.2012.08.015

11. Golebski K, Layhadi JA, Sahiner U, Steveling-Klein EH, Lenormand MM, Li RCY, et al. Induction of IL-10-producing type 2 innate lymphoid cells by allergen immunotherapy is associated with clinical response. *Immunity* (2021) 54(2):291–307.e7. doi: 10.1016/j.immuni.2020.12.013

12. Sonnenberg GF, Monticelli LA, Alenghat T, Fung TC, Hutnick NA, Kunisawa J, et al. Innate lymphoid cells promote anatomical containment of lymphoid-resident commensal bacteria. *Science* (2012) 336(6086):1321–5. doi: 10.1126/science.1222551

13. Cupedo T, Crellin NK, Papazian N, Rombouts EJ, Weijer K, Grogan JL, et al. Human fetal lymphoid tissue–inducer cells are interleukin 17–producing precursors to RORC+ CD127+ natural killer–like cells. *Nat Immunol* (2009) 10(1):66–74. doi: 10.1038/ni.1668

14. Falquet M, Ercolano G, Jandus P, Jandus C, Trabanelli S. Healthy and patient type 2 innate lymphoid cells are differently affected by in *vitro* culture conditions. *J Asthma Allergy* (2021) 14:773–83. doi: 10.2147/JAA.S304126

15. Ma Y, Zhang L, Huang X. Genome modification by CRISPR/cas9. *FEBS J* (2014) 281(23):5186–93. doi: 10.1111/febs.13110

16. Yip BH. Recent advances in CRISPR/cas9 delivery strategies. *Biomolecules* (2020) 10(6):839. doi: 10.3390/biom10060839

17. Chong ZX, Yeap SK, Ho WY. Transfection types, methods and strategies: a technical review. *PeerJ* (2021) 9:e11165. doi: 10.7717/peerj.11165

18. Kim S, Kim D, Cho SW, Kim J, Kim JS. Highly efficient RNA-guided genome editing in human cells via delivery of purified Cas9 ribonucleoproteins. *Genome Res* (2014) 24(6):1012–9. doi: 10.1101/gr.171322.113

19. Liang X, Potter J, Kumar S, Zou Y, Quintanilla R, Sridharan M, et al. Rapid and highly efficient mammalian cell engineering via Cas9 protein transfection. *J Biotechnol* (2015) 208:44–53. doi: 10.1016/j.jbiotec.2015.04.024

20. Grote S, Ureña-Bailén G, Chan KCH, Baden C, Mezger M, Handgretinger R, et al. *In vitro* evaluation of CD276-CAR NK-92 functionality, migration and invasion potential in the presence of immune inhibitory factors of the tumor microenvironment. *Cells* (2021) 10(5):1020. doi: 10.3390/cells10051020

21. Rautela J, Surgenor E, Huntington ND. *Efficient genome editing of human natural killer cells by CRISPR RNP* (bioRxiv: preprint). (2018). p. 406934. doi: 10.1101/406934v1.

22. Kararoudi MN, Dolatshad H, Trikha P, Hussain SRA, Elmas E, Foltz JA, et al. Generation of knockout primary and expanded human NK cells using cas9 ribonucleoproteins. *JoVE (Journal Visualized Experiments).* (2018) 136):e58237. doi: 10.3791/58237

23. Riggan L, Hildreth AD, Rolot M, Wong YY, Satyadi W, Sun R, et al. CRISPR-cas9 ribonucleoprotein-mediated genomic editing in mature primary innate immune cells. *Cell Rep* (2020) 31(7):107651. doi: 10.1016/j.celrep.2020.107651

24. Lambert M, Leijonhufvud C, Segerberg F, Melenhorst JJ, Carlsten M. CRISPR/cas9-based gene engineering of human natural killer cells: protocols for knockout and readouts to evaluate their efficacy. In: Amarnath S, editor. *Innate Lymphoid Cells : Methods and Protocols*. New York, NY: Springer US (2020). p. 213–39. doi: 10.1007/978-1-0716-0338-3_18

25. Pomeroy EJ, Hunzeker JT, Kluesner MG, Lahr WS, Smeester BA, Crosby MR, et al. A genetically engineered primary human natural killer cell platform for cancer immunotherapy. *Mol Ther* (2020) 28(1):52–63. doi: 10.1016/j.ymthe.2019.10.009

26. Morimoto T, Nakazawa T, Matsuda R, Nishimura F, Nakamura M, Yamada S, et al. CRISPR-cas9-mediated TIM3 knockout in human natural killer cells enhances growth inhibitory effects on human glioma cells. *Int J Mol Sci 28 mars* (2021) 22 (7):3489. doi: 10.3390/ijms22073489

27. Huang RS, Lai MC, Shih HA, Lin S. A robust platform for expansion and genome editing of primary human natural killer cells. *J Exp Med* (2021) 218(3). doi: 10.1084/jem.20201529

28. Huang Q, Ma X, Wang Y, Niu Z, Wang R, Yang F, et al. IL-10 producing type 2 innate lymphoid cells prolong islet allograft survival. *EMBO Mol Med* (2020) 12(11): e12305. doi: 10.15252/emmm.202012305

29. Cao Q, Wang R, Niu Z, Chen T, Azmi F, Read SA, et al. Type 2 innate lymphoid cells are protective against hepatic ischemia reperfusion injury. *JHEP Rep 3 juill* (2023) 100837. doi: 10.1016/j.jhepr.2023.100837

30. Wang S, Qu Y, Xia P, Chen Y, Zhu X, Zhang J, et al. Transdifferentiation of tumor infiltrating innate lymphoid cells during progression of colorectal cancer. *Cell Res* (2020) 30(7):610–22. doi: 10.1038/s41422-020-0312-y

31. Reid KT, Colpitts SJ, Mathews JA, Carreira AS, Murphy JM, Borovsky DT, et al. Cell therapy with IL-10-producing group 2 innate lymphoid cells suppresses Graft-versus-Host disease. *bioRxiv* (2023) 08:21.554158. doi: 10.1101/2023.08.21.554158

32. Puig-Saus C, Sennino B, Peng S, Wang CL, Pan Z, Yuen B, et al. Neoantigen-targeted CD8+ T cell responses with PD-1 blockade therapy. *Nature* (2023) 615 (7953):697–704. doi: 10.1038/s41586-023-05787-1

33. Mueller KP, Piscopo NJ, Forsberg MH, Saraspe LA, Das A, Russell B, et al. Production and characterization of virus-free, CRISPR-CAR T cells capable of inducing solid tumor regression. *J Immunother Cancer.* (2022) 10(9):e004446. doi: 10.1136/jitc-2021-004446

34. Ng MSF, Roth TL, Mendoza VF, Marson A, Burt TD. Helios enhances the preferential differentiation of human fetal CD4+ naïve T cells into regulatory T cells. *Sci Immunol* (2019) 4 (41). doi: 10.1126/sciimmunol.aav5947

35. Søndergaard JN, Geng K, Sommerauer C, Atanasoai I, Yin X, Kutter C. Successful delivery of large-size CRISPR/Cas9 vectors in hard-to-transfect human cells using small plasmids. *Commun Biol* (2020) 3(1):1–6. doi: 10.1038/s42003-020-1045-7

36. Foss DV, Muldoon JJ, Nguyen DN, Carr D, Sahu SU, Hunsinger JM, et al. Peptide-mediated delivery of CRISPR enzymes for the efficient editing of primary human lymphocytes. *Nat BioMed Eng.* (2023) 7(5):647–60. doi: 10.1038/s41551-023-01032-2

37. Jo DH, Kaczmarek S, Shin O, Wang L, Cowan J, McComb S, et al. Simultaneous engineering of natural killer cells for CAR transgenesis and CRISPR-Cas9 knockout using retroviral particles. *Mol Ther - Methods Clin Dev* (2023) 29:173–84. doi: 10.1016/j.omtm.2023.03.006

frontiers | Frontiers in Immunology

TYPE Original Research
PUBLISHED 23 November 2023
DOI 10.3389/fimmu.2023.1270391

OPEN ACCESS

EDITED BY
Thomas A. Kufer,
University of Hohenheim, Germany

REVIEWED BY
Liwu Li,
Virginia Tech, United States
Tammy Ozment,
East Tennessee State University,
United States

*CORRESPONDENCE
Mario Romeo
mario.romeo@unicampania.it

†These authors have contributed equally to this work and share first authorship

RECEIVED 31 July 2023
ACCEPTED 06 November 2023
PUBLISHED 23 November 2023

CITATION
Dallio M, Ventriglia L, Romeo M, Scognamiglio F, Diano N, Moggio M, Cipullo M, Coppola A, Ziogas A, Netea MG and Federico A (2023) Environmental bisphenol A exposure triggers trained immunity-related pathways in monocytes. *Front. Immunol.* 14:1270391. doi: 10.3389/fimmu.2023.1270391

Environmental bisphenol A exposure triggers trained immunity-related pathways in monocytes

Marcello Dallio[1†], Lorenzo Ventriglia[1†], Mario Romeo[1*], Flavia Scognamiglio[1], Nadia Diano[2], Martina Moggio[2], Marina Cipullo[1], Annachiara Coppola[1], Athanasios Ziogas[3], Mihai G. Netea[3,4] and Alessandro Federico[1]

[1]Hepatogastroenterology Division, Department of Precision Medicine, University of Campania "Luigi Vanvitelli", Naples, Italy, [2]Department of Experimental Medicine, University of Campania "Luigi Vanvitelli", Naples, Italy, [3]Department of Internal Medicine and Radboud Center for Infectious Diseases (RCI), Radboud University Nijmegen Medical Centre, Nijmegen, Netherlands, [4]Department of Immunology and Metabolism, Life and Medical Sciences Institute (LIMES), University of Bonn, Bonn, Germany

Introduction: Trained Immunity represents a novel revolutionary concept of the immunological response involving innate immune cells. Bisphenol A is a well-known endocrine disrupter, widely disseminated worldwide and accumulated in the human body. Due to the increased interest regarding the effects of plastic-derived compounds on the immune system, our purpose was to explore whether BPA was able to induce trained immunity in human primary monocytes *in vitro* using low environmental concentrations.

Materials and methods: We extracted BPA from the serum of 10 healthy individuals through a liquid-liquid extraction followed by a solid phase extraction and measured the concentration using an HPLC system coupled to a triple quadrupole mass spectrometer. In parallel, monocytes were isolated from whole blood and acutely stimulated or trained with BPA at three different concentrations (1 nM, 10 nM, 20 nM). Pro- and anti-inflammatory cytokines (IL-1β, TNF-α, IL-6, and IL-10) production were assessed after 24 hours of acute stimulation and after Lipopolysaccharide (LPS) rechallenge. A comprehensive overview of the metabolic changes after BPA acute stimulation and trained immunity induction was assessed through extracellular lactate measurements, Seahorse XFb metabolic flux analysis and ROS production.

Results: Monocytes primed with BPA showed increased pro- and anti-inflammatory cytokine responses upon restimulation, sustained by the modulation of the immunometabolic circuits. Moreover, we proved the non-toxic effect of BPA at each experimental concentration by performing an MTT assay. Additionally, correlation analysis were performed between pro- and anti-inflammatory cytokines production after LPS acute stimulation or BPA-mediated trained immunity and BPA serum concentrations showing a significant association between TNF-α and BPA circulating levels.

Discussion: Overall, this study pointed out for the first time the immunological effects of an environmental chemical and plastic-derived compound in the induction of trained immunity in a healthy cohort.

KEYWORDS

trained immunity, bisphenol A, endocrine-disrupting compounds, innate response, inflammation

1 Introduction

In the last decades, an increasing number of studies assessing adaptive mechanisms within the innate immune system have described long-term functional changes in innate immune cells after an insult, a de-facto innate immune memory that was termed *trained immunity* (TI) (1–3). After exposure to certain infections or vaccines, innate immune cells appear able to react more strongly to a second stimulation in an antigen-agnostic manner: this is functionally equivalent to a memory response, not described previously by the scientific community (2–4). At a molecular level, TI is induced by the activation of different signaling pathways that lead to epigenetic remodeling and consequently, the rewiring of intracellular metabolic pathways, determining the acquisition of a long-lasting and self-regulating phenotype associated with an increase of pro-inflammatory cytokine production (5). The immunological phenotype of TI has been proven to last up to 1 year, although heterologous protection against infections induced by live vaccines has been documented for longer periods (6). While induction of TI constitutes a natural defense response in infections, an inappropriate TI induction may contribute to the onset and worsening of several chronic inflammatory diseases (5).

Endocrine-disrupting compounds (EDCs) are a heterogeneous class of molecules mimicking, blocking, or interfering with hormone signaling, implicated in the pathogenesis of various human diseases (7). Bisphenol A (BPA) is a synthetic organic EDC with a molecular weight of 228 Da and chemical formula $(CH_3)_2C(C_6H_4OH)_2$ included in the group of diphenylmethane and bisphenol derivatives (8). It is mainly used for the production of polycarbonate plastic, whose wide diffusion is responsible for its ubiquitous human exposure (9). Alarmingly, BPA chronic ingestion and dermal absorption have been associated with different immunological and metabolic human disorders, representing thus a global health concern (8–10). From a pathogenetic point of view, BPA exposure may determine pleiotropic effects. First, it promotes systemic oxidative stress by increasing the production of reactive oxygen species (ROS), mainly through the blockade of the cytochrome P450 enzyme complex, as well as by inhibiting antioxidant genes expression such as superoxide dismutase (SOD), catalase (CAT), and reduced glutathione (GSH), playing a pivotal role in the maintenance of redox and immunological balance (11, 12). Second, BPA can directly influence gene transcription through epigenetic regulation by DNA methylation, histone modifications, and microRNA (miRNA) profile alterations (10). Finally, BPA can alter metabolic homeostasis, influencing glucose and lipid metabolism, through the activation of various inflammatory pathways (9, 13).

Considering the strong immunological impact and the widespread dissemination of environmental BPA, in this study we aimed to explore the role of BPA as a novel triggering stimulus of TI in primary cultured monocytes.

2 Materials and methods

2.1 Individuals' enrollment and sample preparations

Ten healthy individuals of normal weight (6 males and 4 females; ranging-age: 24-52 years old) were recruited in compliance with the ethical guidelines of the Helsinki Declaration (1975) and after the approval of the ethical committee of the University of Campania "Luigi Vanvitelli" in Naples (protocol N17234/2022). All the subjects were recruited in the geographic area of Naples (Campania Region).

From each participant, written informed consent was obtained, and subsequently, 25 mL of peripheral blood sample was collected. Ten mL of blood were harvested in sodium-citrate BPA-free tubes (BD biosciences, USA) to obtain serum for BPA extraction and quantification, while 15 mL were placed in ethylene-diamine-tetra-acetic acid (EDTA) tubes (BD biosciences, USA) for peripheral blood mononuclear cells (PBMCs) and monocytes isolation.

The entire amount of blood was immediately used after the collection for the specific investigations. The entire experimental setup is summarized in Figure 1.

2.2 Bisphenol A extraction and LC-MS/MS analysis

The blood collected in sodium-citrate BPA-free tubes was immediately centrifuged for 15 minutes at 2000 rpm. After centrifugation, the serum was separated from the corpuscular part and placed in 15 mL glass tubes. Detailed BPA analysis methods have been published by Nicolucci et al., (14) including the quality control system used to monitor method performance and to prevent analysis contamination. Briefly, serum samples were undergone to liquid-liquid

10.3389/fimmu.2023.1270391

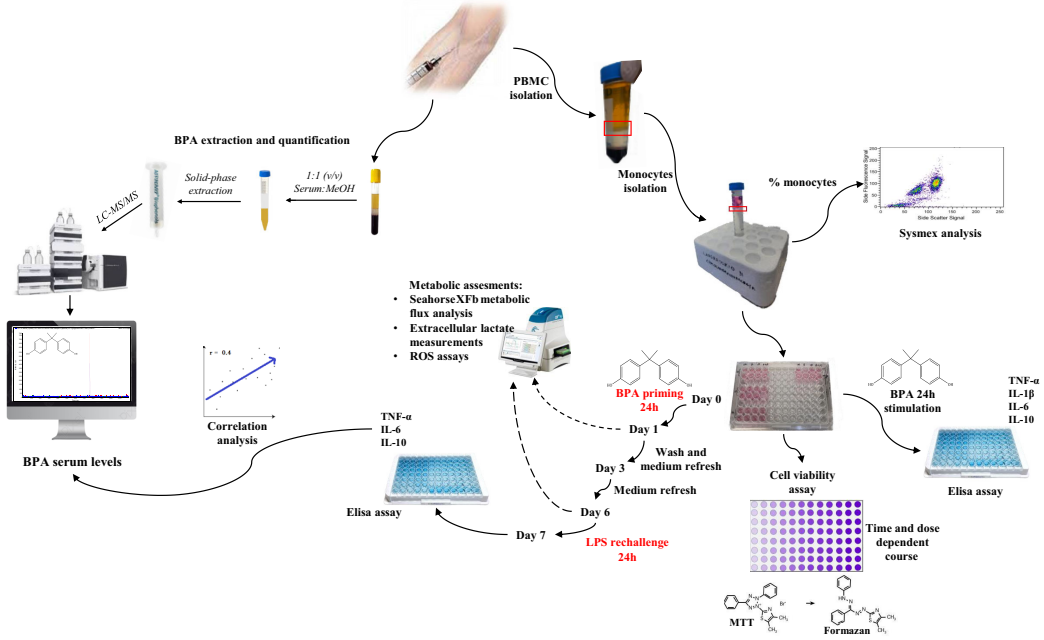

FIGURE 1
Summarized experimental setup.

extraction of BPA with methanol (1:1, v/v) and to solid-phase extraction cartridge (AFFINIMIP Bisphenols, Polyntell SA, Paris, France) for the clean-up and concentration. The analysis of sample extracts was carried out by a DionexUltiMate 3000 High-Performance Liquid Chromatography (HPLC) system coupled to a triple quadrupole mass spectrometer (API 2000; AB Sciex, Germany).

A Kinetex F5 (100 x 4.6 mm, 2.6 µm) stainless-steel column (Phenomenex, Italy) was used for reversed-phase separation.

Chromatography was run at room temperature by linear gradient elution in water and methanol. The analytes were quantified in a multiple-reaction monitoring mode, according to Nicolucci et al., 2017.

All samples were analyzed in triplicate with their relative standard deviations (RSDs), less than 13% (14).

2.3 PBMCs and monocytes isolation

The isolation of PBMCs was performed starting with the dilution of whole blood samples (15 mL) of each subject in Phosphate-buffered saline (PBS) and density centrifugation over Lymphoprep™ (STEM CELL™ TECHNOLOGIES, Germany).

Cells were washed three times in cold PBS and afterward resuspended in a warm RPMI 1640 (with L-glutamine) culture medium (Life Technologies, Italy). Percoll isolation of monocytes was performed according to Domìnguez-Andrès et al., protocol (15). Briefly, previously isolated PBMCs were layered on top of a hyperosmotic Percoll solution (48.5% Percoll [Cytiva, Sweden], 41.5% sterile H_2O, and 10% of 0.22 µM filter-sterilized 1.6 M NaCl) and centrifuged for 15 minutes at 580 x g, 20°C, acceleration 1, no break. The interphase layer was isolated, and the cells were washed with cold PBS. Cells were resuspended in warm RPMI 1640 (with L-glutamine) culture medium supplemented with 10% Foetal Bovine Serum (FBS, Life Technologies, Italy), 50 µg/mL gentamycin (Sigma-Aldrich, USA) and 1 mM sodium pyruvate (Sigma-Aldrich, USA) [RPMI+] and counted.

To guarantee adequate purity, the Percoll-obtained monocytes were plated and incubated for 1 h at 37°C to let them appropriately adhere to the well of a 96-polystyrene flat-bottom plate (Thermofisher, Italy). The monocytes were then washed with warm PBS with calcium and magnesium (Life technologies, Italy) to obtain maximal purity avoiding T-cell contamination and kept in culture in RPMI+.

The efficiency of monocyte isolation according to this protocol was established at 95% as described by Domìnguez-Andrès et al. (15).

2.4 Sysmex analyses

To further confirm the identity of isolated monocytes, 25 µL of the enriched suspensions were analyzed with an XN Sysmex hematology analyzer (Sysmex, Kobe) to count and obtain monocyte percentages. The density plots are based on the side scatter signal and side fluorescence signal, while histograms are on the side scatter signal and event count.

2.5 BPA acute stimulation

Monocytes of each individual were seeded in duplicate (100,000 cells/well) in a flat-bottom 96-well plate. Cells were washed with warm PBS with calcium and magnesium after 1h of incubation at 37°C, 5%

CO_2, and incubated with three different concentrations of BPA- 1 nM, 10 nM, 20 nM – (Sigma Aldrich, Italy), Lipopolysaccharide (LPS) 10 ng/mL (O111:B4, Sigma Aldrich, Italy) as a positive control and RPMI + as negative control (in 200 µL/well). After 24 hours, supernatants were collected and centrifuged for 5 minutes at 500 x g avoiding the presence of residual debris and stored at -20°C until cytokine measurements.

2.6 Trained immunity protocol induction using BPA as a training stimulus

Monocytes of each individual were seeded in duplicate (100,000 cells/well) in a flat-bottom 96-well plate. Cells were washed with warm PBS with calcium and magnesium after 1h of incubation at 37°C, 5% CO_2, and incubated with three different concentrations of BPA- 1 nM, 10 nM, 20 nM – (Sigma Aldrich, Italy) and RPMI+ as negative control (in 200 µL/well). After 24 hours, the stimulation was removed by washing each well with warm PBS with calcium and magnesium, and fresh culture medium RPMI+ was added to the monocytes and incubated for 48 h at 37°C, 5% CO_2. At day 3, the medium has been refreshed and monocytes were incubated for another 48 hours to let them rest for 6 days after the first stimulation. Cells were restimulated at day 6 with 10 ng/mL LPS (O111:B4, Sigma Aldrich, Italy) for 24 hours or left unstimulated. On the last day of protocol (day 7), supernatants were collected and centrifuged for 5 minutes at 500 x g avoiding the presence of residual debris and stored at -20°C until cytokine measurements.

2.7 Cytokine measurements

Cytokine measurement in supernatants was assessed using commercial enzyme-linked immunosorbent assay kits for Tumor necrosis factor alpha (TNF-α; BD biosciences), Interleukin 1β (IL-1β, Life technologies), Interleukin 6 (IL-6, BD biosciences), and Interleukin-10 (IL-10, BD biosciences) following the instruction of manufacturers.

2.8 Extracellular lactate measurements

Lactate concentrations in cell culture supernatants collected after 24h and 6 days were quantified using Amplex® Red reagent (10-acetyl-3,7-dihydroxyphenoxazine, 0.2 mM, Thermo Fisher Scientific). First, lactate oxidase (2 U/mL, derived from Aerococcus viridans, Sigma Aldrich) was used to break down lactate, yielding hydrogen peroxide (H2O2). In the presence of horseradish peroxidase (0.2 U/mL HRP, Thermo Fisher Scientific), hydrogen peroxide reacts with Amplex® Red to generate the fluorescent product resorufin. Because the oxidase- and peroxidase-mediated reactions are coupled, the amount of fluorescence directly correlates to the amount of lactate. Cell-free medium samples, incubated for the same amount of time, were included to allow for background correction. Fluorescence was measured (Ex: 570 nM, Em: 585 nM) and concentrations were derived from a standard curve of sodium-L-lactate (Sigma Aldrich).

2.9 Seahorse XFb metabolic flux analysis

Percoll-isolated monocytes (1×10^6) were seeded into Seahorse XF cell culture plate and acutely stimulated for 24h with BPA for the first time point analysis. 10^7 monocytes were cultured in 10 cm tissue culture plates (VWR) and BPA training protocol was applied as described before. At day 6, macrophages were detached with PBS+EDTA 2 mM and counted. 105 cells were seeded into Seahorse XF cell culture plate and incubated for 1 h at 37 °C, 5% CO2. After adhering for 1 h, the medium was changed to Seahorse XF assay medium pH 7.4 (Agilent) supplemented with 1 mM L-glutamine for Seahorse XF Glycolysis Stress Test or 2 mM L-glutamine, 11 mM D-glucose, and 1 mM pyruvate for Seahorse XF Cell Mito Stress Test. Cells were incubated in a non-CO2-corrected incubator at 37°C for 1 h. Oxygen consumption rate (OCR) was measured using Seahorse XF Cell Mito Stress Test, with final concentrations of 1 µM oligomycin (Sigma-Aldrich), 10 µM FCCP (1 carbonyl cyanide-4-(trifluoromethoxy) phenylhydrazone, Sigma-Aldrich), and 0.5 µM Antimycine A/Rotenone (Sigma-Aldrich). Extracellular acidification rate (ECAR) was measured using Seahorse XF Glycolysis Stress Test, with final concentrations of 11 mM D-glucose (Sigma-Aldrich), 1 µM oligomycin (Sigma-Aldrich), and 22 mM 2-DG (2-Deoxy-D-glucose, Sigma-Aldrich). All the measurements were carried out in quadruplicate or quintuplicate using an XFp Analyzer (Seahorse Bioscience).

2.10 ROS assay

Superoxide anion levels were detected using luminol-enhanced chemiluminescence and determined in a luminometer (Biotek Synergy HT). 10^5 monocytes were incubated with BPA 1 nM or RPMI alone in a tissue culture white plate (Corning) for 24 h. ROS levels were measured after 24h or 6 days following opsonized zymosan (10 mg/mL) restimulation. Luminol (5-Amino-2,3-dihydro-1,4-phthalazinedione, Sigma Aldrich) was added to each well in order to start the chemiluminescence reaction. Each measurement was carried out in quadruplicates. Chemiluminescence was determined every 145 s at 37°C for 1h. Luminescence was expressed as relative light units (RLU) per second and as area under the curve (AUC).

2.11 Cell viability assay

Cell viability was determined on human primary monocytes using thiazolyl blue tetrazolium bromide [3-(4,5-dimethylthiazol-2-yl)-2,5-di-phenyltetrazolium bromide] (MTT; Sigma-Aldrich, Schnellendorf, Germany) assay, following the manufacturer's instructions. A total of 1×10^4 cells/well were plated in a 96-well plate and then treated with BPA; experiments were performed in triplicates and repeated for three different healthy individuals (S01, S02, S03). Absorbance was read at a wavelength of 570 nm with a TECAN INFINITE M PLEX reader (Tecan, Austria).

2.12 Statistical analysis and data availability

Continuous data were described as mean and standard deviations, while categorical variables were summarized as n (%). The Kolmogorov-Smirnov test for normality was performed to evaluate if parametric or non-parametric analysis should be applied. Wilcoxon signed ranks test, t-test for dependent groups, the Kruskal-Wallis test or ANOVA test with posthoc Tukey analysis, in the case of non-normal or normal distribution respectively, were performed to compare the continuous variables. Statistical significance was defined as $p < 0.05$ in a two-tailed test with a 95% confidence interval.

Pearson correlations were used to test the strength of the association between cytokines production of LPS acute stimulated monocytes or BPA-trained macrophages and BPA serum levels.

The analysis was performed using the R statistical software (version 4.3.0) with the *cor. test* function of the *stats* package. A *p-value* < 0.05 was considered to indicate statistical significance.

Cytokine production and viability data were analyzed and plotted with GraphPad Prism software version 8.4.3. Pearson correlations were analyzed and plotted with R.

All data and materials used in the analysis are available upon reasonable request for collaborative studies regulated by materials/data transfer agreements (MTA/DTAs) to the corresponding author.

3 Results

3.1 LC-MS/MS and BPA acute stimulation

The LC-MS/MS analysis on the serum of healthy donors demonstrated a low mean (16) BPA concentration of 0.148 ng/mL ± 0.084 (0,65 nM ± 0,37) for the analyzed population (Figure 2 and Table 1).

After the isolation of the enriched monocyte suspensions, their identity was further confirmed (Supplementary Figure 1) with a mean purity percentage of 70.35%. However, the purity increases after the 1-hour washing step as previously demonstrated by Bekkering et al., (17). Acute stimulation with LPS and BPA showed an increase in pro- and anti-inflammatory cytokines production compared to the baseline levels (Figure 3). Particularly, LPS stimulation (positive control) strongly induced the production of pro-inflammatory cytokines such as IL-1β (2931.70 pg/mL ± 2020.71) (Figure 3A), TNF-α (477.46 pg/mL ± 345.94) (Figure 3B), and IL-6 (8380.21 pg/mL ± 2950.11) (Figure 3C), along with the anti-inflammatory cytokine IL-10 (1691.38 pg/mL ± 1313.31) (Figure 3D) showing statistically significant differences with baseline cytokine levels ($p<0.005$).

BPA acute stimulation at the three different concentrations slightly induced the production of IL-1β (BPA 1 nM: 1696.29 pg/mL ± 754.54; BPA 10 nM: 1479.04 pg/mL ± 635.55, BPA 20 nM: 1402.97 pg/mL ± 707.20) (Figure 3A) and TNF-α (BPA 1 nM: 231.59 pg/mL ± 90.40; BPA 10 nM: 204.07 pg/mL ± 69.56, BPA 20 nM: 156.04 pg/mL ± 46.73) (Figure 3B) resulting in not statistically significant differences with baseline cytokine levels.

Conversely, IL-6 production appeared highly expressed in all BPA concentrations (BPA 1 nM: 3862.15 pg/mL ± 1341.71; BPA 10 nM: 3704.13 pg/mL ± 2087.22, BPA 20 nM: 3118.94 pg/mL ± 945.17) (Figure 3C) with a statistically significant difference compared to baseline levels. BPA acute stimulation induced a raise of anti-inflammatory IL-10 as well, but only BPA 1 nM (600.95 pg/mL ± 419.35) and BPA 10 nM (486.87 pg/mL ± 365.51) reached the statistically significant difference compared to the baseline levels, while the difference with BPA 20 nM (469.69 pg/mL ± 361.60) resulted not statistically significant (Figure 3D).

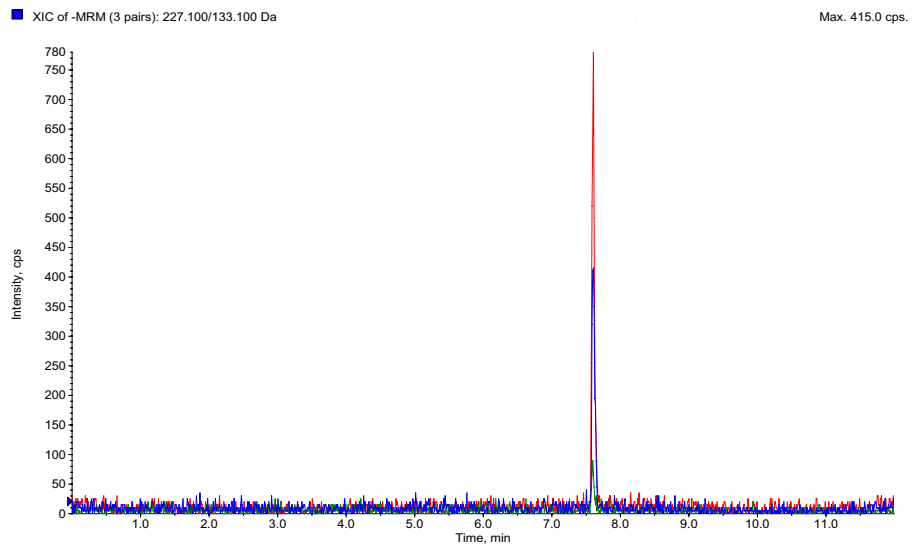

FIGURE 2
LC-MS/MS data showed BPA accumulation in the serum of 10 healthy donors. *BPA, Bisphenol A; LC-MS/MS, Liquid chromatography-mass spectrometry.*

10.3389/fimmu.2023.1270391

TABLE 1 LC-MS/MS data showed BPA accumulation in the serum of 10 healthy donors.

Donors	Serum BPA concentration (ng/mL)	Serum BPA concentration (nM)
DONOR_A	0.1	0.44
DONOR_B	0.157	0.68
DONOR_C	0.172	0.75
DONOR_D	0.148	0.65
DONOR_E	0.204	0.89
DONOR_F	0	0
DONOR_G	0.238	1.04
DONOR_H	0.229	1.00
DONOR_I	0.019	0.083
DONOR_L	0.213	0.93

BPA, Bisphenol A; LC-MS/MS, Liquid chromatography-mass spectrometry.

3.2 Induction of pro-inflammatory cytokine production consequent to BPA-trained stimulation

Monocytes were exposed only for the first 24 hours to three different concentrations of BPA (1 nM, 10 nM, 20 nM) and subsequently treated with LPS, as a second unrelated stimulus on day 6. This treatment induced a trained immune phenotype characterized by increased production of pro-inflammatory cytokines (TNF-α, IL-6) as shown in Figure 4 (4A and 4B). Our data highlighted the establishment of a trained phenotype response to each BPA concentration chosen in combination with the LPS heterologous stimulus. Notably, our data showed that the pre-treatment with BPA 1 nM induced the highest output of TNF-α (BPA 1nM: 300.06 pg/mL ± 158.79) followed by BPA 10 nM and 20 nM (BPA 10 nM: 242.71 pg/mL ± 159.58; BPA 20 nM: 278.62 pg/mL ± 128.85), after secondary stimulation with LPS. All the concentrations determined statistically significant differences ($p<0.005$) between BPA-trained cells and LPS-stimulated cells in TNF-α production (Figure 4A).

Similar results were found analyzing the production of IL-6. The most triggering BPA concentration was 20 nM with an output of 918.65 pg/mL ± 648.24 compared to an amount of 626.42 pg/mL ± 494.45 and 726.25 pg/mL ± 422.89 in BPA 1nM and 10 nM respectively. All the IL-6 concentrations showed statistically significant differences (BPA 1 nM $p<0.05$; BPA 10 nM and 20 nM $p<0.005$) between BPA-trained cells and non-trained cells after secondary stimulation with LPS (Figure 4B). The same trend was still detectable at half of the median serum concentration (Supplementary Figure 2). The significant rise of pro-inflammatory cytokines argues that BPA could be considered a TI-inducing agent.

3.3 BPA-induced trained immunity determines an increased production of anti-inflammatory cytokine IL-10

A build-up in the production of the anti-inflammatory cytokine IL-10, upon the second stimulation with LPS at day 6 was also observed (Figure 4C). The powerful anti-inflammatory response was induced after secondary stimulation with LPS after pre-exposure to 1 nM of BPA exposure (568.05 pg/mL ± 361.93),

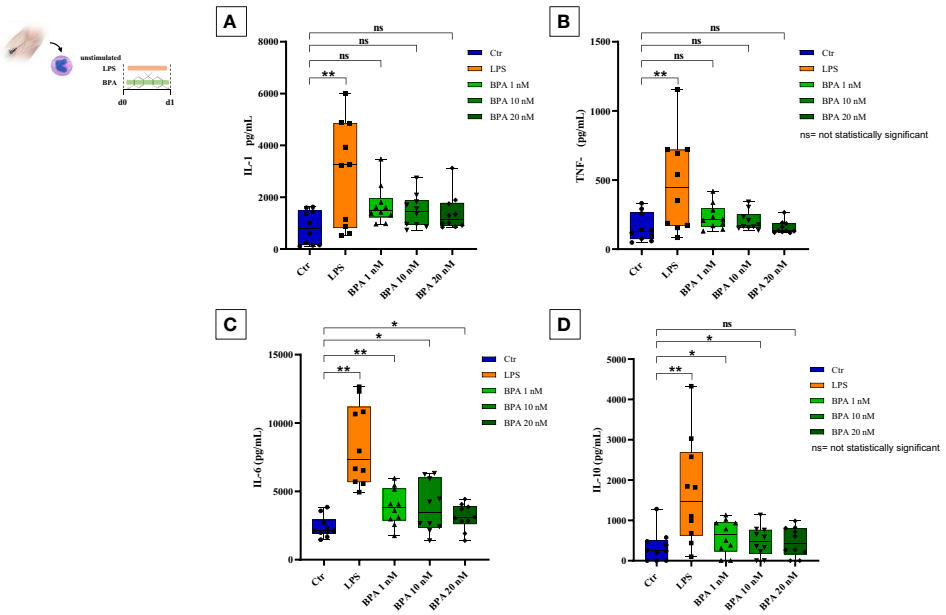

FIGURE 3
BPA acute stimulation. Pro-inflammatory **(A–C)** and anti-inflammatory **(D)** cytokines production after BPA 1 nM, 10 nM, and 20 nM acute stimulation (*Wilcoxon signed ranks test *p<0.05; **p<0.005*). *BPA, Bisphenol A*. ns, not statistically significant.

10.3389/fimmu.2023.1270391

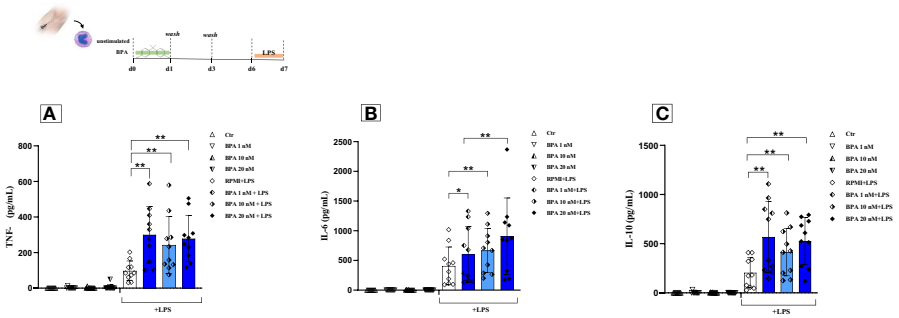

FIGURE 4
BPA-induced trained immunity and compensation mechanisms in healthy individuals. Pro-inflammatory and anti-inflammatory cytokines [Tumour necrosis factor alpha **(A)**; Interleukin-6 **(B)** and *Interleukin-10***(C)**] production after BPA 1 nM, 10 nM, and 20 nM training (*Wilcoxon signed ranks test *p<0.05; **p<0.005*). *BPA, Bisphenol A; TNF-a, Tumour necrosis factor alpha; IL-6, Interleukin-6; IL-10, Interleukin-10; Ctr, controls; LPS, Lipopolysaccharide*.

although a trained phenotype was displayed also with the other BPA concentrations (BPA 10 nM: 412.89 pg/mL ± 239.74; BPA 20 nM: 525.94 pg/mL ± 239.72; all p<0.005).

3.4 BPA triggers changes in the immune metabolism

To further confirm the BPA-induced reprogramming of monocytes we extensively investigated the metabolic features following acute stimulation and trained immunity induction (Figure 5). To this aim, we measured extracellular lactate after 24h and from day 3 to day 6 in the training protocol. Our data showed a significant increase in lactate secretion both after 24h monocytes stimulation (Figure 5C) and at day 6 in BPA-trained macrophages (Figure 5G) in all the concentrations tested compared to the controls, suggesting a metabolic switch towards a glycolytic metabolism. However, no significant differences in lactate secretion were highlighted between the different BPA concentrations, therefore 1 nM was chosen for further experiments. In order to delve deeper into this indication, we carried out Seahorse metabolic flux analyses to probe glycolytic and oxidative metabolism of BPA acutely stimulated cells after 24 h, BPA-trained cells at day 6 and each unstimulated controls. BPA acute stimulation induced significantly higher basal glycolysis and glycolytic capacity (Figure 5B, left), while no differences were highlighted in the oxidative metabolism compared to the control (Figure 5B, right). Accordingly, no differences in ROS production were detected in BPA-treated cells compared to the control (Figure 5D).

More interestingly, BPA training had a marked effect on metabolic parameters measured on day 6, with a significant higher basal glycolysis and a significant increase of oligomycin-triggered maximum glycolytic capacity (Figure 5F, left). Additionally, both baseline- and carbonyl cyanide-p-trifluoromethoxyphenylhydrazone-triggered maximum respiration rates were significantly augmented by BPA training (Figure 5F; right) along with an increase in ROS production (Figure 5H).

3.5 BPA did not affect cell viability

We assessed cell viability with an MTT assay to show the effect of BPA at each concentration used for this purpose. We performed a time-course and dose-response experiment measuring the cell viability at 4-time points (24h, 72h, 6 days, and 7 days) after the BPA stimulation. The stimulation with BPA 1 nM had no strong effects after 24 hours, resulting in a cell viability rate of 78.59% and a mortality rate of 21.41%, similar to the results obtained after 72 hours (79.3% viability, 20.7% mortality rate), compared to unstimulated cells. Interestingly, after 6 days of rest from BPA 1 nM treatment, we found an increase in the cell viability of 2.88%, compared to controls. This percentage of viability was maintained also at day 7, after the restimulation with LPS (Figure 6A). Despite the stimulation with a higher concentration of BPA (10 nM), the cell viability, after 24h and 72h, remained similar (84.7% viability, 15.3% mortality rate) and even higher than the viability with BPA 1nM. Furthermore, after 6 days of rest from BPA 10 nM treatment cell viability was slightly augmented by 1%, compared to control cells. We obtained the same results also after the restimulation with LPS, on day 7 (Figure 6B).

At the final concentration of BPA 20 nM, the cell viability rate after 24 hours and 72 hours of treatment was 80.1% and 87.7% with a mortality rate of 19.9% and 12.3%, respectively, compared to untreated cells. After 6 days of rest, the cell viability rate was equal to the controls. On day 7, after the restimulation with LPS, two subjects showed an increase in cell viability of 17.5% and 19.3%, whilst only one subject exhibited a reduction in the cell viability of 15.3%, in contrast to the previous two, compared to the controls (Figure 6C). Additionally, to strengthen the information acquired about the cell proliferation rate, we analyzed the cell number detaching the cells at day 6 before restimulation. Subsequently, cells were reseeded and counted also at day 7 after restimulation with LPS, and we observed an overall rise in cell number of about 5%, compared to the controls.

10.3389/fimmu.2023.1270391

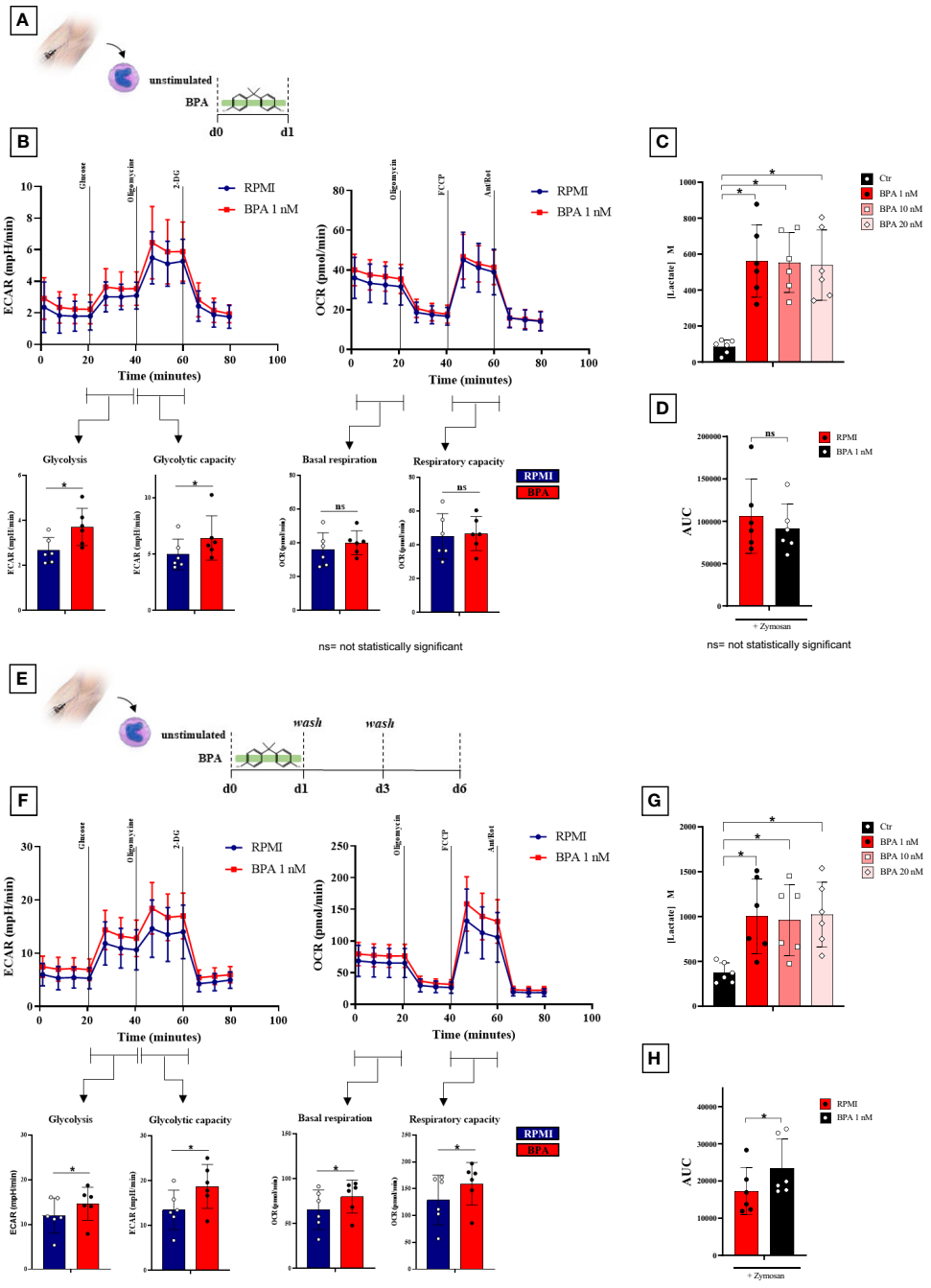

FIGURE 5
BPA induces a rewiring of the immune metabolism after acute stimulation and trained immunity induction. **(A)** Schematic of *in vitro* BPA acute experiments. **(B)**, Seahorse metabolic flux analyses of glycolytic (left) and mitochondrial (right) metabolism after BPA acute stimulation. **(C)** Extracellular lactate production after 24 h BPA stimulation. **(D)**, ROS levels in monocytes pre-treated for 24h with BPA and then stimulated with 10 mg/mL zymosan. **(E)** Schematic of *in vitro* trained immunity experiments. **(F)** Seahorse metabolic flux analyses of glycolytic (left) and mitochondrial (right) metabolism in BPA-trained cells. **(G)** Extracellular lactate production from day 3 to day 6 in BPA-trained cells. **(H)** ROS levels in macrophages trained with BPA and then stimulated with 10 mg/mL zymosan. (*Wilcoxon signed ranks test *p<0.05*). *BPA, Bisphenol A; ECAR, extracellular acidification rate; OCR, oxygen consumption rate; ROS, Reactive Oxygen Species; AUC, Area Under the Curve*. ns, not statistically significant.

3.6 Correlation analysis

TNF-α production in ex vivo BPA-treated monocytes at each concentration was significantly associated with circulating concentrations of BPA (BPA 1 nM + LPS cor. index 0.703, p-value 0.023; BPA 10 nM + LPS cor. index 0.655, p-value 0.040; BPA 20 nM cor. index 0.744, p-value 0.014). Conversely, IL-6 and IL-10 did not significantly associate with serum concentrations of BPA (Figures 7). Additionally, we tested the possibility of a BPA-mediated training phenotype *in vivo* performing correlation analysis between cytokine response after LPS acute stimulation and BPA serum levels. TNF-α production again resulted

10.3389/fimmu.2023.1270391

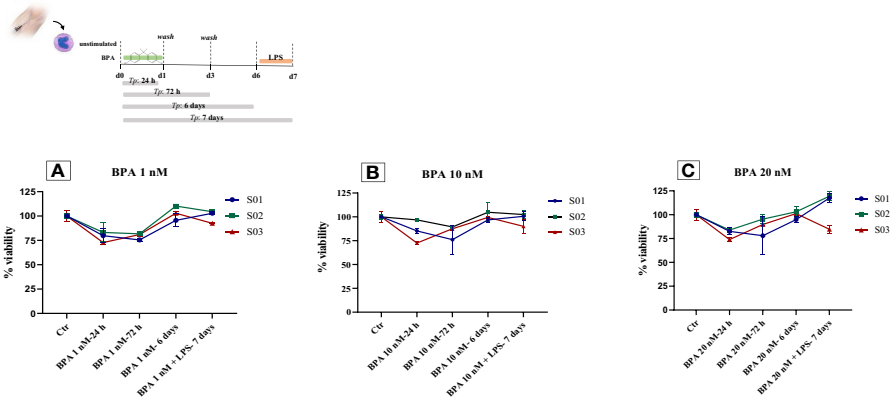

FIGURE 6
Monocytes viability after BPA 1 nM **(A)**, 10 nM **(B)** and 20 nM **(C)** stimulations: Time-course dose-dependent MTT assays. *BPA, Bisphenol A; Ctr, controls; LPS, Lipopolysaccharide.*

significantly associated with circulating concentrations of BPA (cor. index 0.835, p-value 0.003), while IL-6, IL-1β and IL-10 did not significantly associate (Figure 8).

4 Discussion

The increased environmental pollution can lead to the accumulation of pollutants in several tissues in the human body and can induce inflammation or even cause disease (18–22). The continuous accumulation and long-term effects of these molecules in immune responses are largely unknown. Recently, several studies reported the association between environmental BPA exposure and immunologic-related diseases (18–20). BPA is a well-known EDC that can interfere with endocrine balance (23). Particularly, the exposure to low doses may be related to different biologic effects in comparison to high doses, determining a variable dose-response relationship. The most relevant BPA metabolic and immunological

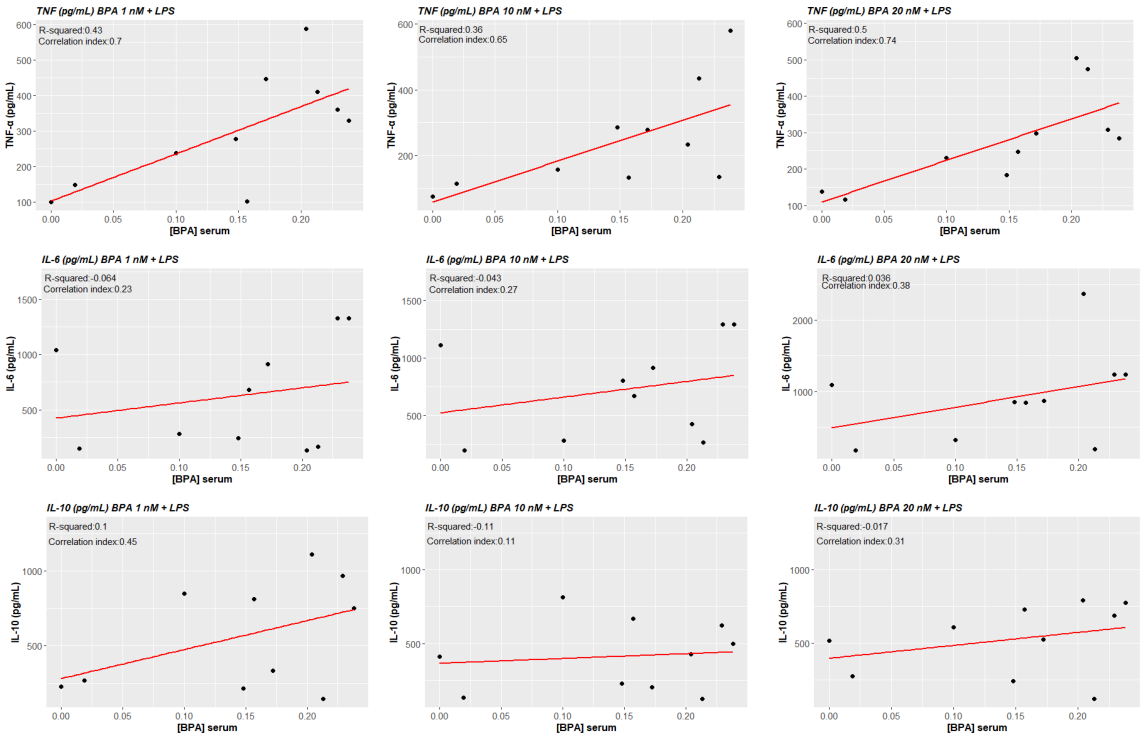

FIGURE 7
Correlations between cytokines levels BPA-trained cells' production and circulating serum levels of BPA. Pearson correlations show a statistically significant association between ex vivo TNF-α production of BPA-trained cells and circulating serum levels of BPA ($p<0.05$), while no statistical significance was reached for IL-6 and IL-10. *BPA, Bisphenol A; TNF-a, Tumour necrosis factor alpha; IL-6, Interleukin-6; IL-10, Interleukin-10.*

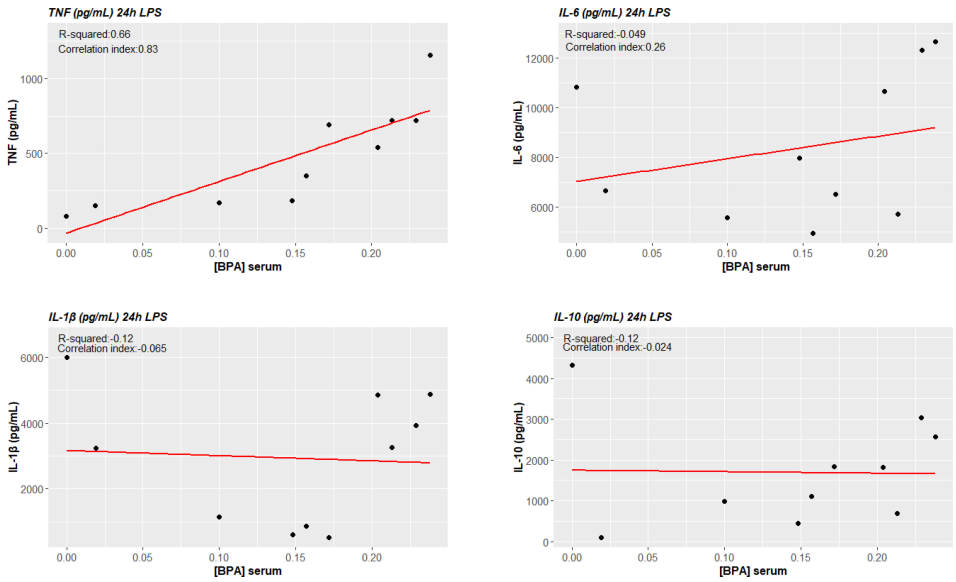

FIGURE 8
BPA-mediated trained immunity *in vivo*: TNF-α production after LPS acute stimulation correlates with circulating serum levels of BPA. Pearson correlations show a statistically significant association between ex vivo TNF-α production of LPS acute stimulated cells and circulating serum levels of BPA ($p<0.05$), while no statistical significance was reached for IL-6 and IL-10. *BPA, Bisphenol A; TNF-a, Tumour necrosis factor alpha; IL-6, Interleukin-6; IL-10, Interleukin-10.*

effects occur in the case of low-dose exposure, while they are not observed by using higher concentrations (24).

In our study, we shed light on the role of BPA as a novel TI-inducing factor in human primary monocytes. Considering the BPA accumulation in several human tissue reservoirs such as adipose tissue, we demonstrated its serum detectability in nanomolar levels from a healthy cohort of individuals. In recent research carried out by Meslin et al., the authors highlighted the risk of toxicity related to low-dose exposure in a European cohort of individuals, although the tangled network of mechanisms underlying its effect still remains largely unclear (25). Based on these findings, we tested if different concentrations (1 nM, 10 nM, and 20 nM) of BPA widely considered as low concentrations and in line with circulating serum concentrations could induce TI *in vitro* (16, 26, 27). Moreover, we assessed the BPA direct effect in terms of cytokines production after 24 hours of acute stimulation including LPS as positive control. Data showed a slightly increased in pro-inflammatory cytokines TNF-α and IL-1β, while IL-6 resulted in higher expression together with the anti-inflammatory cytokine IL-10. Nevertheless, comparing the quantity of cytokines produced by BPA and LPS stimulations, it is possible to figure out that BPA is not a strong stimulator in the acute phase. Taken together, these data further confirm the widely described role of BPA at low concentrations in the establishment of low-grade inflammation (13, 28–30). However, chronic exposure to low concentrations of BPA could lead to functional changes in different cell types.

In our setting, following the optimal protocol for the detection of the trained response, we trained the primary monocytes isolated from venous blood samples with BPA for 24 hours (training period) with a consequent resting period of 6 days, before the re-stimulation with LPS. BPA demonstrated a key role as a priming stimulus in the establishment of a trained phenotype. The induction of TI by BPA exposure could open the way for the study of the role of environmental pollutants in the long-term modulation of innate immune cells. Herein, we describe a new protocol of TI in which BPA demonstrated a key role as a priming stimulus in the establishment of a trained phenotype.

In all experimental conditions, our data show the increase of both pro-inflammatory (TNF-α and IL-6) cytokines highlighting TI features. Moreover, it is important to point out that the effects of TNF-α are more striking even for low concentration. Additionally, we found an increase in the anti-inflammatory IL-10 production possibly due to a compensative phenomenon, characterizing healthy subjects, that prevents overshooting inflammation and tissue damage by limiting the inflammatory response in time. These results further support the hypothesis of a strong immunological impact of BPA at low doses commonly found in the circulation of healthy volunteers.

Importantly, correlation analysis between TNF-α production after BPA-mediated TI and BPA serum concentrations showed that these parameters are significantly associated, linking *in vitro* and *in vivo* data. In addition, we explored the possibility if the cells were already to some extent trained *in vivo* by BPA. Interestingly, we found the same correlation between TNF-α production after LPS acute stimulation and BPA circulating levels.

Cellular metabolism is a critical mediator of the trained immunity-dependent reprogramming of innate immune cells (31–33). Indeed, the rewiring of the immunometabolic circuits is

reflected in the profound changes in cellular metabolic pathways such as glycolysis and oxidative phosphorylation, increasing the capacity of the innate immune cells to respond to a secondary stimulation (33, 34).

To this aim, we broadly investigated the possibility of BPA-induced changes in the immune metabolism. Particularly, we observed a metabolic switch towards an aerobic glycolytic metabolism after acute stimulation, which can be explained with the acute need of rapid energy production in the low-grade inflammatory context BPA-mediated (35). More noteworthy, here we showed that BPA-induced trained immunity enhances not only glycolysis with a higher lactate production, but also oxygen consumption and increased ROS levels pointing that trained cells use different metabolic pathways to adapt their function to produce energy faster and more efficiently.

Several lines of evidence in the trained immunity field highlighted the key role of the aerobic glycolytic metabolism as a hallmark of β-glucan and BCG-trained cells (36, 37). However, several studies investigated the role of TCA cycle and OXPHOS in trained immunity revealing that the TCA cycle remains function for ATP production by OXPHOS as demonstrated by the augmented basal and maximum oxygen consumption rate on day 6 before restimulation of the cells (38, 39).

Additionally, to give further relevance to the effects induced by BPA, we proved that these concentrations of BPA do not have toxic effects on cell viability. Altogether, the treatment with each concentration employed showed only a slight reduction in cell viability (~ 20%) after 24 hours, as already shown in a macrophage mouse cell line by Huang et al., 2018 (40). In addition, when BPA stimulus was removed by one washing step, cell viability was also ~ 80% 72 hours later. Interestingly, the resting period and the re-stimulation influence positively the cell growth, determining an increase in the cell proliferation rate, as demonstrated also by Camarca et al. (26) These results provide us a reason to state that BPA does not affect cell viability and further support the functional changes induced by BPA observed in this study.

Recently, Wang et al. (41) demonstrated the role of BPA in inducing RNA and protein overexpression of TLR-4/NF-κB pathway and downregulating IκBα both *in vivo* and *in vitro* experiments. Interestingly, the same molecular mechanisms (TLR/MyD88 activation) have been found at the basis of trained immunity induction in macrophages in an *in vivo* experiment on mice, in which knock-out mice MyD88-/- did not show trained immunity phenotype (42).

In conclusion, our study demonstrates that the environmental chemical compound BPA has important immunological effects. In particular, we describe the role of BPA as a stimulus that can induce Trained Immunity, demonstrating that even low doses of this endocrine disrupter can affect immune cells of healthy individuals. Inappropriately activated trained immunity responses can contribute to pathogenesis of inflammatory diseases, resulting in either a chronic hyper-inflammatory state or a persistent state of immunological tolerance. Considering this double role of trained immunity, it is reasonable to consider BPA as a potential driver of trained immunity dysregulation, especially in combination with other insults over lifetime, leading to different pathologies.

Data availability statement

The original contributions presented in the study are included in the article/Supplementary Material. Further inquiries can be directed to the corresponding author.

Ethics statement

The studies involving humans were approved by The University of Campania "L. Vanvitelli" in Naples (protocol N17234/2022). The studies were conducted in accordance with the local legislation and institutional requirements. The participants provided their written informed consent to participate in this study.

Author contributions

MD: Conceptualization, Formal Analysis, Investigation, Methodology, Writing – original draft. LV: Conceptualization, Formal Analysis, Investigation, Methodology, Writing – original draft, Writing – review & editing. MR: Conceptualization, Formal Analysis, Investigation, Methodology, Writing – original draft, Writing – review & editing. FS: Data curation, Investigation, Resources, Visualization, Writing – review & editing. ND: Conceptualization, Data curation, Project administration, Supervision, Writing – review & editing. MM: Data curation, Investigation, Resources, Visualization, Writing – review & editing. MC: Data curation, Investigation, Resources, Visualization, Writing – review & editing. AC: Data curation, Investigation, Resources, Visualization, Writing – review & editing. AZ: Data curation, Investigation, Resources, Visualization, Writing – review & editing. MN: Conceptualization, Data curation, Project administration, Supervision, Writing – review & editing. AF: Conceptualization, Data curation, Project administration, Supervision, Writing – review & editing.

Funding

The author(s) declare that no financial support was received for the research, authorship, and/or publication of this article.

Conflict of interest

The authors declare that the research was conducted in the absence of any commercial or financial relationships that could be construed as a potential conflict of interest.

The author(s) declared that they were an editorial board member of Frontiers, at the time of submission. This had no impact on the peer review process and the final decision

Publisher's note

All claims expressed in this article are solely those of the authors and do not necessarily represent those of their affiliated organizations, or those of the publisher, the editors and the reviewers. Any product that may be evaluated in this article, or claim that may be made by its manufacturer, is not guaranteed or endorsed by the publisher.

Supplementary material

The Supplementary Material for this article can be found online at: https://www.frontiersin.org/articles/10.3389/fimmu.2023.1270391/full#supplementary-material

References

1. Groh L, Netea MG, Riksen NP, Keating ST. Getting to the marrow of trained immunity. *Epigenomics* (2018) 10:1151–4. doi: 10.2217/epi-2018-0098

2. Netea MG, Joosten LAB, Latz E, Mills KHG, Natoli G, Stunnenberg HG, et al. Trained immunity: A program of innate immune memory in health and disease. *Sci (1979)* (2016) 352. doi: 10.1126/science.aaf1098

3. Yi Z, Deng M, Scott MJ, Fu G, Loughran PA, Lei Z, et al. Immune-responsive gene 1/itaconate activates nuclear factor erythroid 2–related factor 2 in hepatocytes to protect against liver ischemia–reperfusion injury. *Hepatology* (2020) 72:1394–411. doi: 10.1002/hep.31147

4. Dominguez-Andres J, Netea MG. Long-term reprogramming of the innate immune system. *J Leukoc Biol* (2019) 105:329–38. doi: 10.1002/JLB.MR0318-104R

5. Domínguez-Andrés J, dos Santos JC, Bekkering S, Mulder WJM, van der Meer JWM, Riksen NP, et al. Trained immunity: adaptation within innate immune mechanisms. *Physiol Rev* (2023) 103:313–46. doi: 10.1152/physrev.00031.2021

6. Nankabirwa V, Tumwine JK, Mugaba PM, Tylleskär T, Sommerfelt H. Child survival and BCG vaccination: a community based prospective cohort study in Uganda. *BMC Public Health* (2015) 15:175. doi: 10.1186/s12889-015-1497-8

7. Yilmaz B, Terekeci H, Sandal S, Kelestimur F. Endocrine disrupting chemicals: exposure, effects on human health, mechanism of action, models for testing and strategies for prevention. *Rev Endocr Metab Disord* (2020) 21:127–47. doi: 10.1007/s11154-019-09521-z

8. Maniradhan M, Calivarathan L. Bisphenol A-induced endocrine dysfunction and its associated metabolic disorders. *Endocr Metab Immune Disord Drug Targets* (2023) 23:515–29. doi: 10.2174/1871530322666220928144043

9. Dallio M, Diano N, Masarone M, Gravina AG, Patanè V, Romeo M, et al. Chemical effect of bisphenol A on non-alcoholic fatty liver disease. *Int J Environ Res Public Health* (2019) 16:3134. doi: 10.3390/ijerph16173134

10. Kharrazian D. The potential roles of bisphenol A (BPA) pathogenesis in autoimmunity. *Autoimmune Dis* (2014) 2014:1–12. doi: 10.1155/2014/743616

11. Ferreira AV, Koeken VACM, Matzaraki V, Kostidis S, Alarcon-Barrera JC, de Bree LCJ, et al. Glutathione metabolism contributes to the induction of trained immunity. *Cells* (2021) 10:971. doi: 10.3390/cells10050971

12. Meli R, Monnolo A, Annunziata C, Pirozzi C, Ferrante MC. Oxidative stress and BPA toxicity: an antioxidant approach for male and female reproductive dysfunction. *Antioxidants* (2020) 9:405. doi: 10.3390/antiox9050405

13. Savastano S, Tarantino G, D'Esposito V, Passaretti F, Cabaro S, Liotti A, et al. Bisphenol-A plasma levels are related to inflammatory markers, visceral obesity and insulin-resistance: a cross-sectional study on adult male population. *J Transl Med* (2015) 13:169. doi: 10.1186/s12967-015-0532-y

14. Nicolucci C, Errico S, Federico A, Dallio M, Loguercio C, Diano N. Human exposure to Bisphenol A and liver health status: Quantification of urinary and circulating levels by LC–MS/MS. *J Pharm BioMed Anal* (2017) 140:105–12. doi: 10.1016/j.jpba.2017.02.058

15. Domínguez-Andrés J, Arts RJW, Bekkering S, Bahrar H, Blok BA, de Bree LCJ, et al. *In vitro* induction of trained immunity in adherent human monocytes. *STAR Protoc* (2021) 2:100365. doi: 10.1016/j.xpro.2021.100365

16. Colorado-Yohar SM, Castillo-González AC, Sánchez-Meca J, Rubio-Aparicio M, Sánchez-Rodríguez D, Salamanca-Fernández E, et al. Concentrations of bisphenol-A in adults from the general population: A systematic review and meta-analysis. *Sci Total Environ* (2021) 775:145755. doi: 10.1016/j.scitotenv.2021.145755

17. Bekkering S, Blok BA, Joosten LAB, Riksen NP, van Crevel R, Netea MG. *In vitro* experimental model of trained innate immunity in human primary monocytes. *Clin Vaccine Immunol* (2016) 23:926–33. doi: 10.1128/CVI.00349-16

18. Huang R-G, Li X-B, Wang Y-Y, Wu H, Li K-D, Jin X, et al. Endocrine-disrupting chemicals and autoimmune diseases. *Environ Res* (2023) 231:116222. doi: 10.1016/j.envres.2023.116222

19. Aljadeff G, Longhi E, Shoenfeld Y. Bisphenol A: A notorious player in the mosaic of autoimmunity. *Autoimmunity* (2018) 51:370–7. doi: 10.1080/08916934.2018.1551374

20. Xu J, Huang G, Guo T. Developmental bisphenol A exposure modulates immune-related diseases. *Toxics* (2016) 4:23. doi: 10.3390/toxics4040023

21. Suzuki T, Hidaka T, Kumagai Y, Yamamoto M. Environmental pollutants and the immune response. *Nat Immunol* (2020) 21:1486–95. doi: 10.1038/s41590-020-0802-6

22. Kannan K, Vimalkumar K. A review of human exposure to microplastics and insights into microplastics as obesogens. *Front Endocrinol (Lausanne)* (2021) 12:724989. doi: 10.3389/fendo.2021.724989

23. Kodila A, Franko N, Sollner Dolenc M. A review on immunomodulatory effects of BPA analogues. *Arch Toxicol* (2023) 97:1831–46. doi: 10.1007/s00204-023-03519-y

24. Gioiosa L, Palanza P, Parmigiani S, vom Saal FS. Risk evaluation of endocrine-disrupting chemicals. *Dose-Response* (2015) 13:155932581561076. doi: 10.1177/1559325815610760

25. Meslin M, Beausoleil C, Zeman FA, Antignac J-P, Kolossa-Gehring M, Rousselle C, et al. Human biomonitoring guidance values (HBM-GVs) for bisphenol S and assessment of the risk due to the exposure to bisphenols A and S, in europe. *Toxics* (2022) 10:228. doi: 10.3390/toxics10050228

26. Camarca A, Gianfrani C, Ariemma F, Cimmino I, Bruzzese D, Scerbo R, et al. Human peripheral blood mononuclear cell function and dendritic cell differentiation are affected by bisphenol-A exposure. *PloS One* (2016) 11:e0161122. doi: 10.1371/journal.pone.0161122

27. Ratajczak-Wrona W, Rusak M, Nowak K, Dabrowska M, Radziwon P, Jablonska E. Effect of bisphenol A on human neutrophils immunophenotype. *Sci Rep* (2020) 10:3083. doi: 10.1038/s41598-020-59753-2

28. González-Casanova JE, Bermúdez V, Caro Fuentes NJ, Angarita LC, Caicedo NH, Rivas Muñoz J, et al. New evidence on BPA's role in adipose tissue development of proinflammatory processes and its relationship with obesity. *Int J Mol Sci* (2023) 24:8231. doi: 10.3390/ijms24098231

29. Valentino R, D'Esposito V, Ariemma F, Cimmino I, Beguinot F, Formisano P. Bisphenol A environmental exposure and the detrimental effects on human metabolic health: is it necessary to revise the risk assessment in vulnerable population? *J Endocrinol Invest* (2016) 39:259–63. doi: 10.1007/s40618-015-0336-1

30. Liu Z, Lu Y, Zhong K, Wang C, Xu X. The associations between endocrine disrupting chemicals and markers of inflammation and immune responses: A systematic review and meta-analysis. *Ecotoxicol Environ Saf* (2022) 234:113382. doi: 10.1016/j.ecoenv.2022.113382

31. Penkov S, Mitroulis I, Hajishengallis G, Chavakis T. Immunometabolic crosstalk: an ancestral principle of trained immunity? *Trends Immunol* (2019) 40:1–11. doi: 10.1016/j.it.2018.11.002

32. Norata GD, Caligiuri G, Chavakis T, Matarese G, Netea MG, Nicoletti A, et al. The cellular and molecular basis of translational immunometabolism. *Immunity* (2015) 43:421–34. doi: 10.1016/j.immuni.2015.08.023

33. Domínguez-Andrés J, Joosten LA, Netea MG. Induction of innate immune memory: the role of cellular metabolism. *Curr Opin Immunol* (2019) 56:10–6. doi: 10.1016/j.coi.2018.09.001

34. Netea MG, Domínguez-Andrés J, Barreiro LB, Chavakis T, Divangahi M, Fuchs E, et al. Defining trained immunity and its role in health and disease. *Nat Rev Immunol* (2020) 20:375–88. doi: 10.1038/s41577-020-0285-6

35. O'Neill LAJ, Kishton RJ, Rathmell J. A guide to immunometabolism for immunologists. *Nat Rev Immunol* (2016) 16:553–65. doi: 10.1038/nri.2016.70

36. Arts RJW, Carvalho A, La Rocca C, Palma C, Rodrigues F, Silvestre R, et al. Immunometabolic pathways in BCG-induced trained immunity. *Cell Rep* (2016) 17:2562–71. doi: 10.1016/j.celrep.2016.11.011

37. Cheng S-C, Quintin J, Cramer RA, Shepardson KM, Saeed S, Kumar V, et al. mTOR- and HIF-1α–mediated aerobic glycolysis as metabolic basis for trained immunity. *Sci (1979)* (2014) 345. doi: 10.1126/science.1250684

38. van der Heijden CDCC, Groh L, Keating ST, Kaffa C, Noz MP, Kersten S, et al. Catecholamines induce trained immunity in monocytes *in vitro* and in vivo. *Circ Res* (2020) 127:269–83. doi: 10.1161/CIRCRESAHA.119.315800

39. Keating ST, Groh L, van der Heijden CDCC, Rodriguez H, dos Santos JC, Fanucchi S, et al. The set7 lysine methyltransferase regulates plasticity in oxidative phosphorylation necessary for trained immunity induced by β-glucan. *Cell Rep* (2020) 31:107548. doi: 10.1016/j.celrep.2020.107548

40. Huang F-M, Chang Y-C, Lee S-S, Ho Y-C, Yang M-L, Lin H-W, et al. Bisphenol A exhibits cytotoxic or genotoxic potential via oxidative stress-associated mitochondrial apoptotic pathway in murine macrophages. *Food Chem Toxicol* (2018) 122:215–24. doi: 10.1016/j.fct.2018.09.078

41. Wang S, Yang Y, Luo D, Zhai L, Bai Y, Wei W, et al. Bisphenol A increases TLR4-mediated inflammatory response by up-regulation of autophagy-related protein in lung of adolescent mice. *Chemosphere* (2021) 268:128837. doi: 10.1016/j.chemosphere.2020.128837

42. Owen AM, Luan L, Burelbach KR, McBride MA, Stothers CL, Boykin OA, et al. MyD88-dependent signaling drives toll-like receptor-induced trained immunity in macrophages. *Front Immunol* (2022) 13:1044662. doi: 10.3389/fimmu.2022.1044662

frontiers | Frontiers in Immunology

TYPE Methods
PUBLISHED 29 November 2023
DOI 10.3389/fimmu.2023.1227175

OPEN ACCESS

EDITED BY
Thomas A. Kufer,
University of Hohenheim, Germany

REVIEWED BY
Kelly M. Mcnagny,
University of British Columbia, Canada
Simon Jochems,
Leiden University Medical Center (LUMC), Netherlands

*CORRESPONDENCE
Barbara C. Mindt
Barbara.Mindt@gmail.com

RECEIVED 22 May 2023
ACCEPTED 06 November 2023
PUBLISHED 29 November 2023

CITATION
Mindt BC, Kim J, Warren T, Song Y and DiGiandomenico A (2023) Differential *in vivo* labeling with barcoded antibodies allows for simultaneous transcriptomic profiling of airway, lung tissue and intravascular immune cells. *Front. Immunol.* 14:1227175. doi: 10.3389/fimmu.2023.1227175

Differential *in vivo* labeling with barcoded antibodies allows for simultaneous transcriptomic profiling of airway, lung tissue and intravascular immune cells

Barbara C. Mindt[1]*, John Kim[1], Troy Warren[1], Yang Song[2] and Antonio DiGiandomenico[1]

[1]Vaccines & Immune Therapies, Biopharmaceuticals R&D, AstraZeneca, Gaithersburg, MD, United States, [2]Biologics Engineering, Oncology R&D, AstraZeneca, Gaithersburg, MD, United States

Single-cell RNA sequencing (scRNA-seq) is the state-of-the-art approach to study transcriptomic signatures in individual cells in respiratory health and disease. However, classical scRNA-seq approaches provide no spatial information and are performed using either bronchoalveolar lavage fluid (BAL) or lung single cell suspensions to assess transcript levels in airway and tissue immune cells, respectively. Herein we describe a simple method to simultaneously characterize transcriptomic features of airway, lung parenchymal and intravascular immune cells based on differential *in vivo* labeling with barcoded antibodies. In addition to gaining basic spatial information, this approach allows for direct comparison of cells within different anatomical compartments. Furthermore, this method provides a time- and cost-effective alternative to classical scRNA-seq where lung and BAL samples are processed individually, reducing animal and reagent use. We demonstrate the feasibility of this approach in a preclinical mouse model of bacterial lung infection comparing airway, parenchymal and vasculature neutrophils early after infection.

KEYWORDS

respiratory disease, *in vivo* antibody labeling, spatial transcriptomics, scRNA-seq, bacterial lung infection, neutrophils

1 Introduction

Acute and chronic lung diseases are a leading cause of death and disability worldwide. Chronic obstructive pulmonary disease (COPD) alone accounted for more than 3.23 million deaths in 2019 representing the 3rd leading cause on a global scale (1). On the other hand, lower respiratory infections (LRIs) including pneumonia and bronchiolitis are still a substantial cause of mortality in the elderly population and young children, respectively (2, 3).

To counteract this trend and identify new therapeutic targets to tailor novel more effective intervention strategies, it is crucial to understand disease-associated changes in lung immune cells. Constant advances in single-cell RNA sequencing (scRNA-seq) technologies such as cellular indexing of transcriptomes and epitopes by sequencing (CITE-seq) which uses oligonucleotide-labeled antibodies now enable simultaneous analysis of gene as well as surface protein expression on a single cell level (4). However, scRNA-seq data provide no spatial information, which is especially problematic when analyzing immune responses in functionally highly compartmentalized organs such as the lung where expression profiles vary substantially based on whether cells are localized in the airways, the parenchyma or the vasculature.

Here, we developed a simple method to differentially label airway and blood immune cells by intravenous and intratracheal administration of distinct barcoded pan-leukocyte anti-CD45 antibodies. Single cell suspensions of lung and airway cells are further labeled with additional CITE-seq antibodies and transcript and cell surface protein expression levels are obtained following a generic CITE-seq workflow. Airway and intravascular leukocytes can be further stratified based on their respective anti-CD45 barcode, whereas parenchymal immune cells remain unlabeled. We demonstrate that antibody staining is highly specific for the respective compartment with minimal inter-anatomical cross-contamination. Using this basic spatial separation, we further show how neutrophil gene expressions profiles differ in the airways, tissue and vasculature following infection with non-typeable *Haemophilus influenzae* (NTHi), a bacterium often associated with exacerbations of chronic airway disease.

This method has a wide scope of applications and can be employed to analyze homeostatic differences in transgenic animal models as well immune responses in pre-clinical mouse models of lung disease including allergic airway inflammation, bacterial and viral lung infection as well as sterile injury models. The protocol is simple, adaptable and allows for simultaneous analysis of parenchymal, airway and blood immune cells from the same animal, thereby saving time and reagents.

2 Materials and equipment

2.1 Reagents

- NTHi glycerol stock
- Chocolate agar (Hardy Diagnostics; cat# E14)
- Phosphate buffered saline (PBS) pH 7.2 (Gibco, cat# 20012-043)
- KetaVed® Ketamine Hydrochloride injection (100 mg/mL, VedCo Inc.)
- AnaSed® Xylazine injection (20 mg/mL, Akorn Animal Health)
- Sterile saline (0.9%; Covetrus, cat# 069169)
- Dulbecco's phosphate buffered saline (DPBS) (Gibco, cat# 14190-144)
- heat-inactivated fetal bovine serum (HI-FBS) (Gibco, cat# 10082-147)
- RPMI-1640 + L-Glutamine (Gibco, cat# 11875-085)
- recombinant murine CD45 (rmCD45) (100 µg/ml in DPBS; R&D, cat# 114-CD-050)
- Liberase™ TM (4 mg/mL in DPBS; Roche, cat# 5401127001)
- dsDNAse (ThermoFisher, cat# EN0771)
- ACK Lysing buffer (Gibco, cat# A10492-01)
- 0.4% Trypan Blue Stain (Gibco, cat# 15250-061)
- 0.5 M EDTA (Invitrogen, cat# 15575-038)
- 10% Bovine Serum Albumin (BSA) solution (Sigma-Aldrich, cat# A1595-50ML)
- Mouse anti-Ly-6G microbeads (Miltenyi Biotec, cat# 130-120-337)
- TruStain FcX™ (anti-mouse CD16/32) Antibody (BioLegend, cat# 101320)
- LIVE/DEAD™ Fixable Blue Dead Cell Stain Kit (Invitrogen, cat# L23105)
- eBioscience™ FoxP3/Transcription Factor Staining Buffer Set (Invitrogen, cat# 00-5523-00)

2.2 Equipment and consumables

- Sterile cotton tipped applicators (Dukal Corporation, cat# 9016)
- CO_2 incubator
- PIPETBOY acu 2 pipet aid (Integra Biosciences)
- Serological pipettes (25 mL, 10 mL, 5 mL)
- Single-channel Micropipettes (P1000, P200, P10, P1; Gilson) + tips
- UV-Vis Scanning Spectrophotometer (GENESYS 10; Thermo Scientific)
- Disposable polystyrene cuvettes (ThermoFisher Scientific, cat# 221S)
- Heat Lamp and mouse restraint for i.v. injections
- 1 ml TB syringe 27G x 1/2 (BD, cat# 309623) for i.v. injections
- 1 ml TB syringe 25G x 5/8" (BD, cat#309626) for i.p. injections
- Dissection tools (tweezers, scissors)
- Gauze sponges (Dukal Corporation, cat# 4162)
- i.v. catheters (20G x 1"; Terumo, cat# SR*FF2025)
- 1 mL syringes (BD, cat# 309659)
- 500 mL Vacuum Filter/Storage Bottle Systems, 0.22 µm pore size (Corning, cat# 431097)
- 250 mL Vacuum Filter/Storage Bottle System, 0.22 µm pore size (Corning, cat# 431096)
- GentleMACS™ C tubes (Miltenyi Biotec, cat# 130-093-237)
- GentleMACS™ Octo Dissociator (Miltenyi Biotec, cat# 130-096-427)
- 50 mL Centrifuge tubes (VWR, cat# 89039-662)

- 70 µM cell strainers (Corning, cat# 431751)
- 40 µM cell strainers (Corning, cat# 431750)
- 3 mL syringes (BD, cat# 309657)
- 15 mL Centrifuge tubes (VWR, cat# 89039-670)
- Vi-CELL™ XR Cell Viability Analyzer (Beckman Coulter)
- Hemacytometer (Hausser Scientific, cat# 3100)
- QuadroMACS™ Separator (Miltenyi Biotec, cat# 130-090-976)
- MACS MultiStand (Miltenyi Biotec, cat# 130-042-303)
- LS columns (Miltenyi Biotec, cat# 130-042-401)
- Microcentrifuge (5427 R; Eppendorf)
- 96-well v-bottom microplates (Corning, cat# 3897)
- Chromium Next GEM Single Cell 3' Kit v3.1 (10x Genomics, cat# 1000269)
- Dual Index Kit TT Set A (10x Genomics, cat# 1000215)
- Dual Index kit NT Set A (10x Genomics, cat# 1000242)
- NovaSeq 6000 SP Reagent Kit v1.5 (cat# 20028319)
- BD FACSymphony™ A5 cell analyzer (BD Biosciences)
- Chromium Controller (10x Genomics)
- NovaSeq 6000 Sequencing System (Illumina)

2.3 Solutions

- Ketamine (67 mg/kg) + xylazine (13 mg/kg) for anesthesia
  - o 1.68 mL ketamine (100 mg/mL)
  - o 1.63 mL xylazine (20 mg/mL)
  - o 21.7 mL isotonic saline
  - o Prepare fresh before use.
- Ketamine (500 mg/kg) + xylazine (50 mg/kg) for euthanasia
  - o 1.6 mL ketamine (100 mg/mL)
  - o 0.8 mL xylazine (20 mg/mL)
  - o 0.8 mL isotonic saline
  - o Prepare fresh before use.
- FACS buffer (DPBS + 2% FBS)
  - o 10 mL HI-FBS
  - o 490 mL DPBS
  - o Sterile filter and store at 4°C
- PBE buffer (PBS + 0.5% BSA + 2 mM EDTA)
  - o 25 mL 10% BSA solution
  - o 2 mL 0.5 M EDTA
  - o 473 mL PBS (pH7.2)
  - o Sterile filter and store at 4°C
- Staining buffer (PBS + 1% BSA)
  - o 20 mL 10% BSA solution
  - o 180 mL DPBS
  - o Sterile filter and store at 4°C

3 Methods

All procedures described in this study were performed in accordance with federal, state and institutional guidelines and were approved by the AstraZeneca Institutional Animal Care and Use Committee. Procedures were carried out using adult female Balb/cJ mice purchased from Taconic Biosciences (Germantown, NY). Animals were maintained under specific pathogen-free conditions with *ad libitum* access to food and water.

3.1 Preparation of bacterial inoculum and intranasal infection

- The day before infection, streak bacteria from frozen glycerol stock as a lawn on a nutrient agar plate using a sterile cotton swab. Incubate overnight at the requisite growth temperature. In our case NTHi was plated on chocolate agar and grown at 37°C in the presence of 5% CO_2.
- Collect bacteria from the plate using a sterile cotton swab and suspend in sterile PBS (pH 7.2) to an optical density at 600 nm (OD_{600}) of 1.0 which corresponds to a known amount of colony forming units (CFU)/mL.
- If necessary, dilute bacterial suspension further with PBS (pH 7.2) to the desired CFU/mL. Keep inoculum at room temperature and use within 15 min of preparation.
- Anesthetize mice by intraperitoneal injection of 200 µL ketamine/xylazine solution until a proper plane of anesthesia is attained as assessed by absence of pedal withdrawal reflex.
- Hold fully anesthetized mouse vertically and administer a total of 50 µL bacterial suspension dropwise in the middle of the nostrils using a P200 pipettor. Wait for mice to completely inhale the liquid before administering the next drop.

3.2 *In vivo* antibody labeling and lung isolation

- To label intravascular leukocytes, administer 150 µL (2 µg/mouse diluted in sterile DPBS) of anti-CD45 (clone 30-F11) intravenously via tail vein injection and let antibody circulate for 5 min.
- Euthanize animals by intraperitoneal injection of 200 µL concentrated ketamine/xylazine. Alternatively, a lethal dose of sodium pentobarbital can be used.

- Note: It is vital that lung barrier remains intact during euthanasia to avoid entry of blood in the alveoli and thereby mislabeling of blood leukocytes by the intratracheally administered pan-leukocyte antibody and *vice versa*. Consequently, euthanasia by carbon dioxide asphyxiation should be avoided since it may lead to alveolar extravasation, pulmonary oedema, and hemorrhage (5, 6). Also, refrain from cervical dislocation as a method of euthanasia to preserve the integrity of the trachea and adjacent neck structures.
- Pin mouse on its back on an angled (approximately 45°) dissecting tray and disinfect the neck area with 70% ethanol.
- Lift skin using forceps and make an incision at the mid-line of the neck with anatomical scissors.
- Use two fine-tipped forceps to carefully pull the salivary glands covering the trachea to the side. If blood vessels are damaged, use gauze pads to absorb blood before proceeding.
- Pull the muscle surrounding the trachea apart using tweezers and insert an i.v. catheter between the cartilage rings below the larynx. To avoid lung damage do not insert the catheter too far into the trachea.
- To label airway immune cells, carefully remove the puncture needle and slowly instill 800 µL cold anti-CD45.2 (clone 104; 2 µg/mouse diluted in sterile RPMI-1640) via the catheter using a 1 mL syringe.
- Leave the syringe attached to the catheter for 5 min before retrieving BAL.
- Transfer BAL to a GentleMACS C tube on ice containing 600 µL RPMI-1640 medium, 125 µL HI-FBS and 50 µL rmCD45 (100 µg/mL in PBS). Swirl to mix.
- Instill lungs once more with 800 µL cold RPMI-1640 + 50 µL rmCD45. Wait for 5 min, retrieve liquid and pool with the first lavage in the GentleMACS tube.
- Optional: Add appropriate volumes of TruStain FcX™ (anti-mouse CD16/32) antibody to the instillation mix and additionally to the pooled cells in the GentleMACS tube to prevent potential binding of rmCD45-anti-CD45 complexes to Fcγ receptors on respective cells. TruStain FcX™ should be used at 1 µg per 10^6 cells. Adjust volume based on expected cell numbers in BAL and whole lung accordingly.
- Adjust volume in the GentleMACS to 2.35 mL with cold RPMI-1640.
- For lung isolation lift skin and peritoneal wall using forceps and make an incision beneath the ribcage. Cut the skin and peritoneal wall along the ribcage towards both sides of the abdomen without damaging underlying organs.
- Pierce and cut the diaphragm along the ribcage on both sides avoiding the lung.
- Cut the ribcage on both sides and remove the sternum and isolate lung from pleural cavity.
- Transfer to the GentleMACS tube containing the pooled BAL fractions.

3.3 Preparation of single cell suspensions from lung tissue

- Attach tubes on the GentleMACS dissociator and mince lung tissue using program "m_lung_01_02" (36 sec, 165 rpr).
- Add 125 µL Liberase™ (4 mg/mL in DPBS) and 3 µL dsDNAse, mix and digest for 30 min at 37°C (5% CO_2).
- Further homogenize digested tissue on the GentleMACS dissociator using program "m_lung_02_01" (37 sec, 2079 rpr).
- Strain homogenate over a 70 µM cell strainer into a 50 mL Falcon tube
- Rinse cell strainer with 10 mL cold FACS buffer and centrifuge (5 min, 450 x g, 4°C).
- Remove supernatant, suspend pellet in 10 mL cold FACS buffer and centrifuge (5 min, 450 x g, 4°C).
- Remove supernatant, suspend pellet in 2 mL ACK lysing buffer and incubate for 4 min at room temperature to lyse red blood cells.
- Bring volume to 15 mL with FACS buffer, centrifuge (5 min, 450 x g, 4°C) and remove supernatant.
- Suspend pellet in 10 mL FACS buffer, centrifuge (5 min, 450 x g, 4°C), pipet off supernatant completely and resuspend cells in 1 mL staining buffer (PBS + 1% BSA)
- Dilute cells 1:10 in PBS (100 µL cells + 900 µL PBS) and determine viable cell counts using an automated cell counter. Alternatively, dilute cells in Trypan Blue solution and count manually with a hemacytometer according to the manufacturer's instructions.
- Transfer 3 x 10^6 cells/sample to each well of a 96-well v-bottom plate for FACS staining.

3.4 Neutrophil magnetic bead enrichment

Neutrophils are isolated using anti-Ly-6G microbeads according to the manufacturer's instructions.

- Strain cells over a 70 µM cell strainer and wash strainer with 5 ml cold PBE buffer.
- Centrifuge cells at 300 x g for 10 min and completely remove supernatant.
- Suspend cell pellet in 90 µL cold PBE buffer per 1 x 10^7 cells and add 10 µL anti-Ly-6G microbeads per 1 x 10^7 cells. Adjust buffer and bead volumes accordingly.
- Mix and incubate at 4°C (no for 10 min.
- Add 2 mL cold PBE buffer/10^7 cells and centrifuge for 10 min at 300 x g.
- During the spin, load an LS column in the QuadroMACS™ Separator attached to the MACS MultiStand and equilibrate with 3 mL cold PBE buffer.

- Discard supernatant and suspend up to 10^8 cells in 500 µL cold PBE buffer.
- Load cell suspension on LS column and wait for column reservoir to empty by gravity flow.
- Wash column 3x with 3 ml cold PBE buffer, remove column from magnet and transfer to a 15 mL centrifugation tube.
- Add 5 ml cold PBE buffer and immediately force liquid through column using the provided plunger.
- Spin cells at 300 x g for 10 min, suspend in 1 mL cold FACS buffer and determine viable cell counts using an automated cell counter or count manually with a hemacytometer and Trypan Blue solution according to the manufacturer's instructions.

3.5 Cell surface protein labeling with TotalSeq-B antibodies for CITE-seq analysis

- Spin cells and suspend in 50 µl staining buffer per 10^6 cells.
- Transfer 150 µl sample to the wells of a 96-well v-bottom plate for FACS staining and keep on ice (see 3.6).
- Transfer 50 µl cell suspension to a 1.5 mL Eppendorf tube and add 5 µl TruStain FcX blocking reagent.
- Mix and incubate for 10 min at 4°C to block FcγRII/III receptors.
- Add 45 µl TotalSeq-B antibody mix prepared in staining buffer (0.5 µg antibody/sample). All antibodies used in the mix are listed in Supplementary Table 1.
- Incubate for 30 min at 4°C and centrifuge (5 min, 350 x g, 4°C).
- Discard supernatant and wash cell pellets 3x with 1 mL staining buffer.
- Resuspend in 300 µl PBS and determine cell counts with a hemacytometer.
- Dilute to 700 - 1200 cells/µL (= 0.7 – 1.2 x 10^6 cells/mL).

3.6 Cell surface protein labeling for flow cytometry

- Transfer 1-5 x 10^6 cells/sample to the wells of a 96-well v-bottom plate, centrifuge (5 min, 450 x g, 4°C) and discard supernatant.
- Resuspend cells in 50 µL cold CD16/CD32 dilution (1:100 in FACS buffer) and incubate for 15 min on ice to block FcγRII/III receptors.
- While cells are blocking prepare antibody cocktail in cold FACS buffer (antibodies used and dilutions are provided in Supplementary Table 1.
- Centrifuge (5 min, 450 x g, 4°C), discard supernatant, resuspend cell pellet in 50 µL antibody dilution and incubate for 30 min on ice in the dark.
- Add 120 µl cold DPBS and spin (5 min, 450 x g, 4°C).
- Remove supernatant, resuspend cells in 150 µl cold DPBS and spin again (5 min, 450 x g, 4°C).
- While cells are spinning, resuspend Fixable Blue viability dye in anhydrous DMSO according to the manufacturer's instructions, further prepare a 1:1000 dilution in cold DPBS and store in the dark on ice until use.
- Remove supernatant, resuspend cell pellet in 50 µl viability dye dilution and incubate on ice in the dark for 30 min.
- Add 120 µl cold FACS buffer, spin (5 min, 450 x g, 4°C) and remove supernatant.
- Resuspend cells in 150 µl cold FACS buffer, spin again (5 min, 450 x g, 4°C).
- During spin, prepare Fix/Perm solution of FoxP3/Transcription Factor Staining Buffer Set according to the manufacturer's protocol (1 part concentrate + 3 parts diluent).
- Discard supernatant, resuspend cells in 50 µl Fix/Perm solution and incubate in the dark on ice for 30 min.
- Spin (5 min, 450 x g, 4°C), remove supernatant and resuspend pellet in 150 µl cold FACS buffer.
- Centrifuge again (5 min, 450 x g, 4°C) and add 150 µl cold FACS buffer.
- Cover plate with a sealing film, wrap in tin foil and store in the fridge for up to three days until acquisition on a flow cytometer.

3.7 CITE-seq

Labeled cell suspensions were partitioned into single-cell droplets with a Chromium Controller (10x Genomics) and gene expression and cell surface protein libraries were further generated using Chromium Single Cell 3' Reagent Kits with Feature Barcoding Technology (10x Genomics) following the manufacturer's recommendations. Samples were sequenced on a NovaSeq 6000 Sequencing System (Illumina) and the resulting FASTQ files were processed with CellRanger (version 6.0.1, 10X Genomics). Unless noted, all the analysis for the single-cell RNA-sequencing was done using the Python Scanpy framework (Scanpy version 1.9.1) (7). Cells were further filtered to include cells with log1p values of isotype control antibody reads (< 6), number of antibodies detected per cell (< 30), mitochondrial reads (< 30%), total RNA reads (< 40000), number of genes (< 6000 and > 200). To normalize antibody reads in the dataset, denoised and scaled by background (DSB) program (8) using the default parameters implemented in MUON package (version 0.1.2) was used (9). Filtered raw RNA reads were further normalized and log-transformed using *normalize_total* and *log1p* functions, respectively and data were further scaled using *scale* function. Before data scaling, log-normalized data were stored

separately for further downstream analysis such as differential expression test. DSB-normalized protein reads were clustered using Leiden algorithm after generating a neighborhood graph with default parameters and for three different resolution settings (0.25, 0.5, 0.75). For each resolution, a heatmap was plotted for the average expression of proteins per cluster to determine at which resolution biologically relevant clusters can be visualized. To assign the respective anatomical location to each cell, we first used histograms of DSB-normalized CD45 and CD45.2 antibody reads to determine the cut-offs. Respective cut-offs were applied to each separate anatomical location (0.3 for $CD45.2^{+}CD45^{-}$ airway cells; > 0.28 for $CD45.2^{-}CD45^{+}$ intravascular leukocytes; < 0.3 and < 0.28 for $CD45.2^{-}CD45^{-}$ parenchymal cells). For differential expression (DE) test per cluster, *tl.rank_genes_groups* function with Wilcoxon rank-sum test was used.

3.8 Statistical analyses

All data were analyzed with GraphPad Prism software (GraphPad Software). P values below 0.05 were regarded as statistically significant (*p<0.05, **p<0.01, ***p<0.001). Unless otherwise indicated, figures display means ± standard deviation (SD). Experiment sample sizes (n), experiment replicate numbers and statistical tests used are included in the respective figure legends.

4 Results

4.1 Administration of i.v. and i.t. anti-CD45 antibodies results in efficient and stable labeling of intravascular and airway immune cells

For *in vivo* labeling of immune cells in the vasculature and the airways, two different clones of pan-leukocyte anti-CD45 antibodies, clone 30-F11 and clone 104, are administered intravascularly or intratracheally, respectively. To ensure the amount of antibody used is sufficient to label all cells present in the respective anatomical compartment, we administered fluorescently labeled antibody versions via the designated route. In addition, we stained the labeled BAL or blood cells with the other anti-CD45 clone to gate on all $CD45^{+}$ cells. Potential steric competition between antibodies was assessed beforehand by preincubation of mouse splenocytes with either fluorescent clone 104 or 30-F11 followed by staining with the respective other clone and comparison to single-stained cells (Supplementary Figure 1). 30-F11 staining intensity, depicted as geometric mean fluorescence intensity (gMFI), was not affected by prior labeling of cells with clone 104 (Supplementary Figure 1A). When cells were prelabeled with 30-F11, staining intensity of 104 was significantly lower compared to the single-labeled cells indicating some binding interference (Supplementary Figure 1B). However, frequencies of double-positive cells remained comparable to the 104-only stained control indicating both clones can be used for simultaneous labeling of leukocytes (Supplementary Figures 1C, D). Importantly, flow cytometric analysis following *in vivo* antibody instillation showed that all immune cells in the airway and vasculature were labeled with clone 104 or 30-F11 respectively, indicating that the used concentrations and experimental conditions were suitable to efficiently tag leukocytes *in vivo* (Figures 1A, B). Studies were performed on infected as well as uninfected animals to ensure consistent labeling under both conditions and antibody concentrations should be tested beforehand when a different model is used. To determine whether CD45 labeling remains stable during downstream processing steps, we labeled airway and blood leukocytes with fluorescently labeled antibodies *in vivo*. Isolated BAL and blood cells further underwent enzymatic digestion with Liberase and dsDNase and CD45 gMFI was compared to that of undigested cells (Figures 1C, D). Double strand-specific DNase was used to preserve the integrity of the TotalSeq B-barcodes since regular DNase I also utilizes single-stranded DNA as a substrate. gMFIs did not change with digestion indicating that anti-CD45 antibodies remain stably bound to their epitopes during processing and can be confidently used under the tested conditions for scRNA-seq analysis.

4.2 Excess anti-CD45 antibodies can be effectively neutralized with recombinant CD45

During downstream lung processing, the airway and intravascular boundaries are disintegrated, and excess antibodies need to be neutralized to avoid cross-labeling of blood cells with unbound airway anti-CD45 or *vice versa*. We therefore instilled recombinant murine CD45 (rmCD45) intratracheally after antibody labeling and added additional recombinant protein to the lung digestion medium. The amount of rmCD45 needed to neutralize potentially unbound antibody was assessed by titration experiments where we incubated the respective fluorescent antibodies with increasing concentrations of rmCD45. This was followed by addition of mouse splenocytes and analysis of CD45 labeling by flow cytometry. As expected, all splenocytes were stained with either antibody in the absence of rmCD45 (Figures 2A, B). Clone 104 staining was completely abolished with 2.5 µg rmCD45 indicating that all antibody in solution had been effectively neutralized (Figure 2A). Similar observations were made with clone 30-F11, albeit 10 µg of rmCD45 were needed to achieve a similar degree of neutralization (Figure 2B). We next assessed whether 10 µg rmCD45 was a suitable concentration to neutralize unbound antibodies *in vivo*. We first analyzed neutralization efficiency in the airways by consecutive intratracheal administration of fluorescent anti-CD45 (clone 104) and rmCD45. To assess neutralization of anti-CD45 (30-F11), we administered a fluorescent version via tail vein injection, allowed the antibody to circulate and injected rmCD45 via the same route. Neutralization efficiency was assessed by the ability of BAL supernatant or plasma to label naïve mouse splenocytes and was analyzed by flow cytometry (Figure 2C). As expected, when only anti-CD45 was administered, all splenocytes were labeled, whereas the presence of rmCD45 in either airway or blood completely neutralized unbound antibody, evident by the lack of splenocyte labeling. We therefore chose 10 µg rmCD45 to proceed with our

10.3389/fimmu.2023.1227175

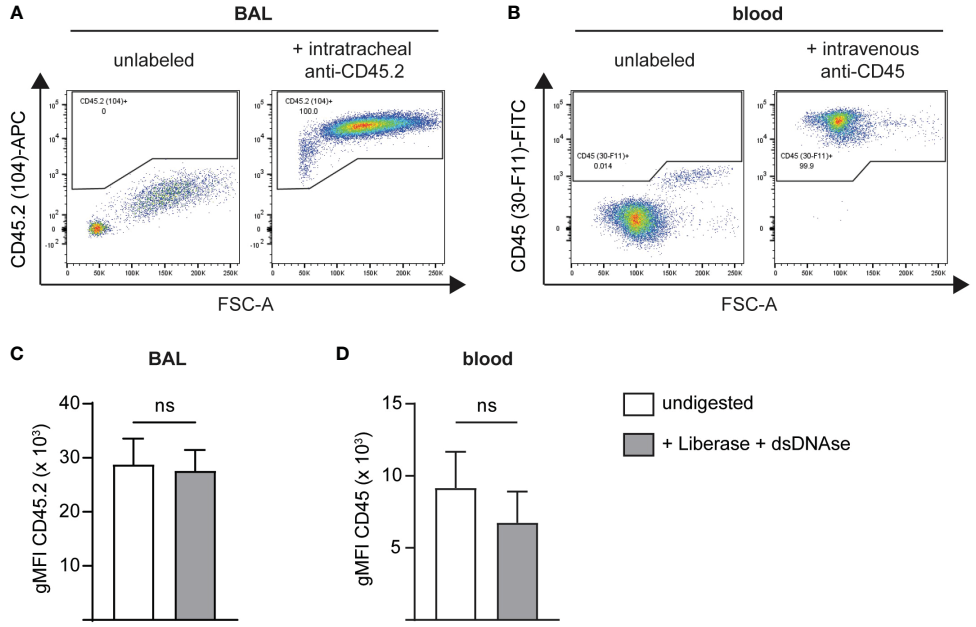

FIGURE 1
Administration of i.v. and i.t. anti-CD45 antibodies results in efficient and stable labeling of intravascular and airway immune cells. BAL or blood cells were *in vivo* labeled, isolated and co-stained with an anti-CD45 antibody binding to a different CD45 epitope followed by flow cytometric analysis. Representative flow cytometry plots of single live CD45$^+$ **(A)** airway cells after intratracheal administration of 2 µg anti-CD45.2 (clone 104)-APC followed by BAL cell staining with anti-CD45 (clone 30-F11)-FITC or **(B)** blood leukocytes following intravascular administration with 2 µg anti-CD45 (clone 30-F11)-FITC via tail vein injection and staining of blood cells with anti-CD45.2 (clone 104)-APC. **(C)** gMFI of CD45.2 (clone 104) on BAL cells before (white bar) and after digestion (grey bar) with Liberase and dsDNAse. **(D)** gMFI of CD45 (clone 30-F11) on blood cells before (white bar) and after digestion (grey bar) with Liberase and dsDNAse. Data are representative of three independent experiments with n = 3–5 mice per group. Data are shown as mean ± SD and significance between groups was determined using a Mann-Whitney test. i.v., intravenous; i.t., intratracheal; FITC, fluorescein isothiocyanate; APC, allophycocyanin; BAL, bronchoalveolar lavage; gMFI, geometric mean fluorescence intensity. ns, non-significant.

evaluation. It should be noted that this is a reference value for our model system. Component concentrations for other *in vivo* models should be tested and confirmed empirically before RNA-seq analysis.

4.3 Intravascular and airway immune cells can be distinguished by compartmental CD45 labeling

To test the validity of our method we used an acute bacterial pneumonia model where we intranasally infected mice with a high dose of NTHi or administered PBS as a control. We additionally employed an acute LPS-induced lung inflammation model to further validate the specificity of our *in vivo* staining procedure. Blood and airway leukocytes were labeled with either fluorescent or TotalSeq-B anti-CD45 antibodies at 48 hours post-infection or 24 h after LPS challenge. Depending on the cell population of interest, enrichment is usually performed preceding scRNA-seq to increase sequencing resolution. This often entails positive selection for CD45$^+$ leukocytes using magnetic bead enrichment. We therefore tested whether *in vivo* CD45 labeling would interfere with positive selection via bead-bound anti-CD45 antibodies using lung cells labeled with anti-CD45-FITC (clone 30-F11), anti-CD45.2-APC (clone 104) or a combination thereof. While the purity of the CD45$^+$ fraction was comparable in all conditions (>97%) after enrichment, the flowthrough (CD45$^-$ fraction) of cells previously labelled with anti-CD45 (clone 30-F11) contained significantly higher frequencies of CD45$^+$ cells than the unstained control or cells pre-labeled with anti-CD45.2 (clone 104) (Supplementary Figure 2A). In accordance, numbers of CD45$^+$ cells (Supplementary Figure 2B) were markedly lower in CD45$^+$ fractions from 30-F11-stained cells as opposed to unstained or 104-stained cells. On the other hand, there was a >25-fold increase of CD45$^+$ cells recovered in the flowthrough, indicating insufficient retention of 30-F11-stained cells in the column. CD45$^+$ enrichment should therefore be avoided, and enrichment should be performed by negative selection or with magnetic beads of a different specificity. We therefore directly enriched for neutrophils with Ly6G microbeads and using fluorescently labeled antibodies showed they are almost exclusively found in the lung vasculature of uninfected animals (Figures 3A, B). As expected, inoculation with NTHi or LPS challenge resulted in neutrophil recruitment from the blood to the site of infection indicated by distinct populations of CD45.2(104)$^+$CD45.2(30-F11)$^-$ airway, and smaller populations of CD45.2(104)$^-$CD45.2(30-F11)$^+$ intravascular and CD45.2(104)$^-$CD45.2(30-F11)$^-$ parenchymal neutrophils (Figures 3A, C; Supplementary Figure 5A). Importantly, almost no double-positive cells were observed indicating the absence of cross-labeling. This can be attributed to efficient neutralization of excess antibodies since all cells were labeled with intratracheal anti-CD45 antibody in the absence of rmCD45 after NTHi infection (Supplementary Figure 3). No staining with intravascular antibody could be detected on Siglec-F$^+$CD11c$^+$ airway-resident alveolar macrophages after NTHi infection, confirming the absence of

10.3389/fimmu.2023.1227175

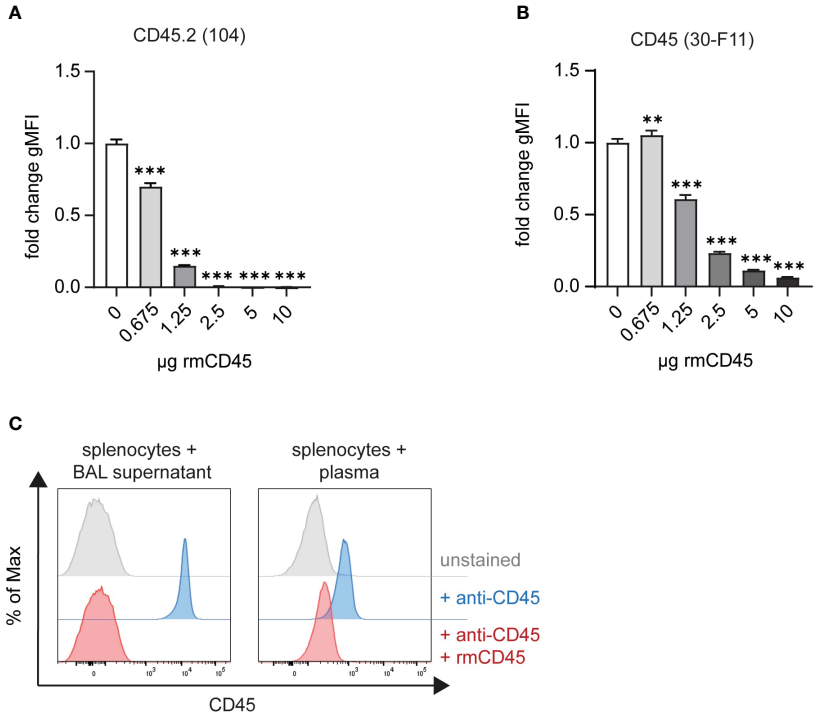

FIGURE 2
Excess anti-CD45 antibodies can be effectively neutralized with recombinant CD45. *In vitro* neutralization of 2 µg **(A)** anti-CD45.2 (clone 104)-APC or **(B)** anti-CD45 (clone 30-F11)-FITC with 0.675 – 10 ug rmCD45. Fluorochrome-labeled antibodies were incubated for 30 min with indicated amounts of rmCD45 in lung digestion medium and neutralization efficiency was assessed based on the antibody's ability to stain naïve mouse splenocytes thereafter. Labeling efficiency is depicted as gMFI on single live cells. **(C)** Representative histograms plots of anti-CD45 *in vivo* neutralization in BAL (left panel) following consecutive i.t. administration of anti-CD45.2 (2 µg; clone 104)-APC and rmCD45 (10 µg) or in blood (right panel) after consecutive i.v. injection of anti-CD45 (2 µg; clone 30-F11)-FITC rmCD45 (10 µg). Neutralization efficiency was assessed by the ability of BAL supernatant or plasma to label naïve mouse splenocytes and was analyzed by flow cytometry. Unlabeled splenocytes or blood cells (grey histograms) were used as negative controls and mice that received antibody only (red histograms) served as maximum staining controls. Data are representative of three independent experiments with n = 3–5 mice per group. Data are shown as mean ± SD with **p < 0.01, ***p < 0.001 as determined by one-way ANOVA followed by Dunnett's multiple comparisons test. rmCD45, recombinant murine CD45; i.v., intravenous; i.t., intratracheal; FITC, fluorescein isothiocyanate; APC, allophycocyanin; BAL, bronchoalveolar lavage; gMFI, geometric mean fluorescence intensity.

antibody cross-contamination under the indicated conditions (Supplementary Figure 3C). Distinct neutrophil populations could also be distinguished following infection based on distribution of CD45 barcodes after labeling with TotalSeq-B antibodies (Figure 3B) validating the compartmentalized *in vivo* labeling approach. Double positive signals exclusively stemmed from non-single cells and were filtered based on total antibody and RNA reads per cell. Specifically, cells that have detectable reads of 30 or more surface proteins used for labelling were deemed to be cell clumps or doublets and removed from the downstream analysis. In addition, cells with high RNA reads per cell (> 40,000) were also filtered out to remove low-quality or doublets from the analysis.

4.4 Neutrophils exhibit location-specific gene expression signatures after NTHi infection

To analyze location-specific gene expression profiles, filtered scRNA-seq data were projected into two dimensions using Uniform Manifold Approximation and Projection (UMAP) based on their CD45 surface label. Unbiased clustering identified three distinct neutrophil subpopulations, cluster 0 (airway), cluster 2 (blood) and cluster 1 (parenchyma) (Figure 4A). Higher transcript levels of inflammatory and antibacterial neutrophil response genes such as *Sod2, Cd274*, *Ncf1*, *Lcn2*, *FceR1g* and the cytokines/chemokines *Il1a*, *Ccl3*, *Ccl4* and *Cxcl2* suggest increased activation of airway over tissue and blood subpopulations (Figures 4B, C). Downregulated genes in airway neutrophils including *Sell*, *Zyx*, *Selplg*, *Coro1a, S100a8, S100a9* and *Cxcr2* were mainly associated with neutrophil locomotion and adhesion (Figure 4C). In general, tissue and blood neutrophils were more similar in their expression profiles. In accordance, subclustering based on transcriptomic data alone and subsequent analysis of CD45 surface labeling in the resulting clusters showed that airway neutrophils are transcriptionally distinct while gene expression of blood and parenchyma neutrophils was partially overlapping (Supplementary Figures 4A, B). Like airway neutrophils, upregulated genes in blood and tissue neutrophils were involved in inflammatory and antibacterial responses (*Cd14, Acod1, Ccrl2, Cxcl2, Il1rn, Ncf1, Ptafr, Clec4d, B2m*) while downregulated genes were associated with cytoplasmic translation (*Rpl7, Rpl30, Rps9, Rps27a, Rplp0*) (Figure 4C). We further assessed PD-L1 surface expression in neutrophil populations by flow cytometry after *in vivo* labeling with

10.3389/fimmu.2023.1227175

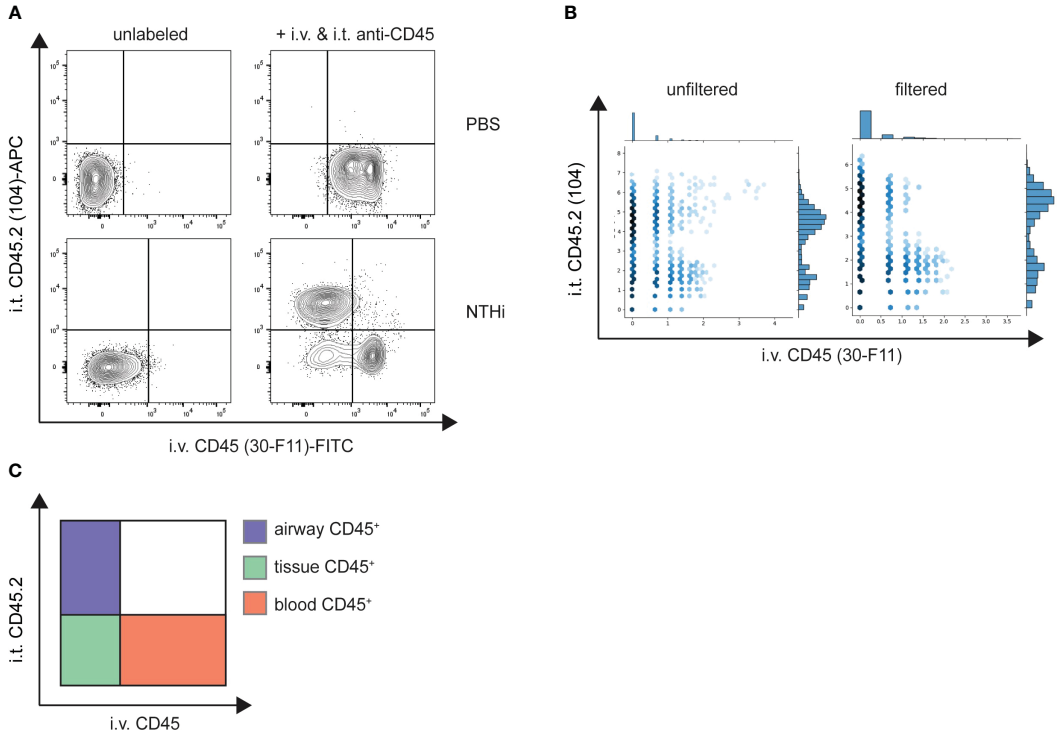

FIGURE 3
Intravascular and airway immune cells can be distinguished by compartmental CD45 labeling. Mice were intranasally infected with NTHi (5 x 10^7 CFU/mouse) or PBS as a control. 48 h post infection mice were administered with 2 µg fluorescent **(A)** or 2 µg TotalSeq-B **(B)** anti-CD45 (clone 30-F11) and anti-CD45.2 (clone 104) intravenously or intratracheally, respectively. Excess antibodies were neutralized with 10 µg of rmCD45 and BAL and lungs were isolated. CD45 labeling on isolated neutrophils was analyzed by flow cytometry or scRNA-seq and designated as airway, blood or tissue cells based on their respective label **(C)**. **(A)** Representative flow cytometry plots of $Ly6G^+$ neutrophils isolated from lungs of control PBS (top panel) or NTHi-infected mice (bottom panel). Unlabeled control mice were used to define positive populations (left). **(B)** Unfiltered (left) and filtered (right) hexagon plots showing the distribution of CD45 antibody barcodes on $Ly6G^+$ neutrophils from infected mice. Non-single cells were filtered out based on antibody and RNA reads. Flow cytometry data are representative of two experiments with n = 3 – 5 mice per group. scRNA-seq was performed once. NTHi, non-typeable *Haemophilus influenzae*; i.v., intravenous; i.t., intratracheal; FITC, fluorescein isothiocyanate; APC, allophycocyanin.

fluorescent anti-CD45 antibodies. Surface PD-L1 was highly expressed on airway neutrophils, with intermediate and low levels found in lung parenchyma and blood neutrophils, respectively (Figure 4D). This finding was validated in an LPS-induced acute lung inflammation model showing high expression of PD-L1 on lung and parenchymal neutrophils while their blood counterparts only exhibited low PD-L1 levels (Supplementary Figure 5B). These findings correlated strongly with transcript levels after NTHi infection further validating our *in vivo* labeling approach for scRNA-seq.

5 Discussion

Herein we describe a simple, time- and cost-efficient protocol that allows for simultaneous transcriptomic analysis of mouse airway, lung tissue and blood leukocytes. This is especially important during lower respiratory tract infection and inflammation models where immune cells are rapidly recruited to the airways and adapt their gene expression profile to perform their respective effector functions. Spatial clustering based on compartmental antibody labeling allows not only for differential gene expression analysis within the same population, which may not be obvious on the whole-population level, but also to deduct trajectories across pseudotime. This method can be employed at steady state or in a wide array of pre-clinical respiratory disease models including pulmonary infection as well as sterile injury and allergic airway inflammation models. However, in models with extensive vascular leakage which may compromise the integrity of the staining it would be advised to perform appropriate controls such as intravenous Evans blue injection followed by lung histology.

Our method is highly adaptable and has only minor drawbacks that can be easily counteracted. Importantly, we demonstrate that *in vivo* labelling interferes with commercial magnetic bead CD45 positive selection kits, therefore other enrichment kits should be considered. It may also affect the binding of CD45 hashtag antibodies and hashing and demultiplexing should therefore be performed using antibodies against other ubiquitously expressed surface markers, such as H-2 MHC Class I. If only specific cell populations are of interest, *in vivo* labelling can also be performed with population-specific antibodies given the availability of more than one clone and non-overlapping epitope binding. This would again allow for leukocyte positive selection and the use of anti-CD45 hashtag antibodies.

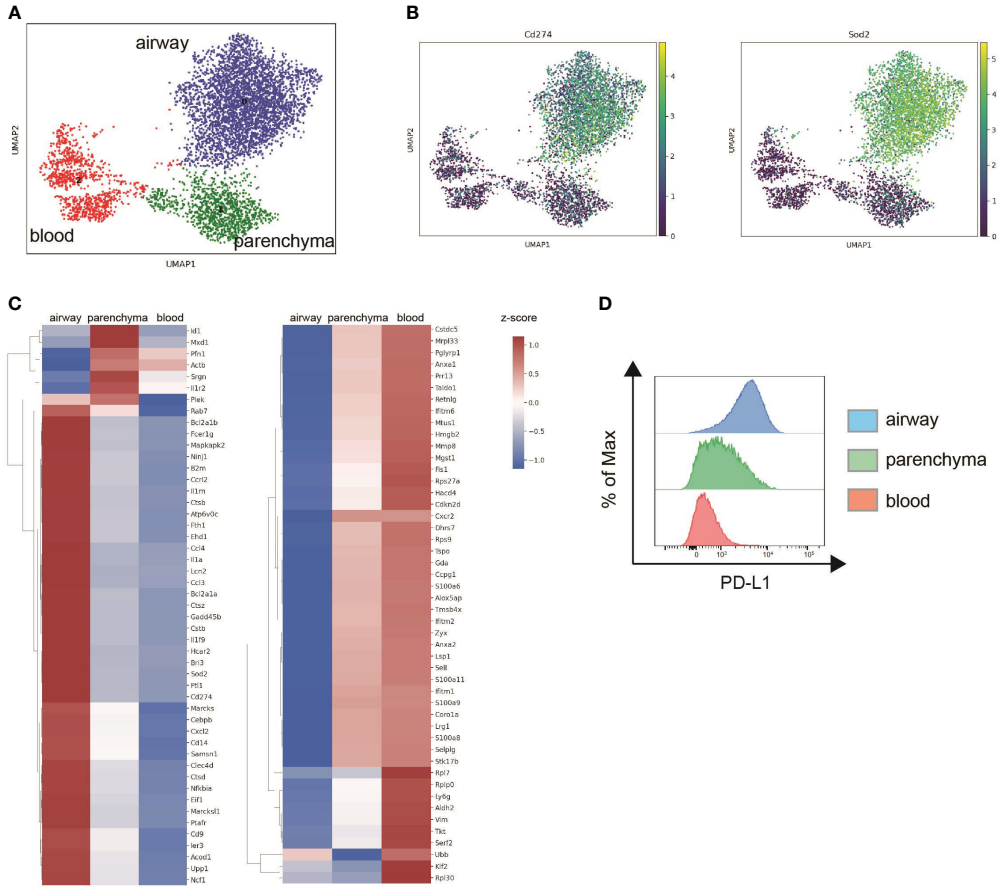

FIGURE 4
Neutrophils exhibit location-specific gene expression signatures after NTHi infection. Mice were intranasally infected with NTHi (5 x 10^7 CFU/mouse) and administered with i.v. or i.t. anti-CD45 antibodies at 48 h post infection followed by scRNA-seq or flow cytometry analysis. **(A)** UMAP of 5,543 lung neutrophils subclustered based on CD45 surface labeling in airway (blue), parenchymal (green), and blood neutrophils (red). **(B)** UMAP of relative expression of Cd274 (PD-L1) (left) and Sod2 (right) in neutrophil subclusters. **(C)** Clustered heat maps depicting relative expression of top 30 upregulated (left) and downregulated genes (right) in airway and parenchymal neutrophils compared to blood neutrophils. Differentially expressed genes over blood neutrophils were determined using Wilcoxon test and genes differentially expressed in both airway and parenchyma are only displayed once. The log-normalized expression values were standardized (z-score) for visualization. **(D)** Representative flow cytometry histogram plot of PD-L1 cell surface expression on airway (blue), parenchymal (green), and blood neutrophils (red). Data are representative of one sequencing experiment **(A, B)** and two independent flow cytometry experiments **(C)** with n = 3–5 mice per group.

Altogether, our approach builds upon existing scRNA-seq protocols by describing a simple method to simultaneously characterize transcriptomic features of airway, lung parenchymal and intravascular immune cells. We believe this approach is applicable to multiple disease models and will further aid in elucidating mechanisms of disease development and progression. In addition, this approach could help identify novel therapeutic targets or delineate disease-specific biomarkers.

Data availability statement

The original contributions presented in the study are publicly available. This data can be found here: GEO, GSE246845.

Ethics statement

The animal study was approved by AstraZeneca Institutional Animal Care and Use Committee. The study was conducted in accordance with the local legislation and institutional requirements.

Author contributions

BM designed the study, performed experiments and wrote the manuscript. JK analyzed scRNA-seq data and edited the manuscript. YS prepared libraries and performed sequencing. TW assisted with *in vivo* experiments. AD contributed to writing and editing. All authors contributed to the article and approved the submitted version.

Funding

The funding required for the preparation of this manuscript was provided by AstraZeneca.

Acknowledgments

The authors want to thank the AstraZeneca Gaithersburg Flow Cytometry Core for technical support.

Conflict of interest

Authors BM, JK, YS, TW, and AD were employed by the company AstraZeneca.

The authors declare that this study received funding from AstraZeneca. The funder had the following involvement in the study: all authors are employed by the funder.

Publisher's note

All claims expressed in this article are solely those of the authors and do not necessarily represent those of their affiliated organizations, or those of the publisher, the editors and the reviewers. Any product that may be evaluated in this article, or claim that may be made by its manufacturer, is not guaranteed or endorsed by the publisher.

Supplementary material

The Supplementary Material for this article can be found online at: https://www.frontiersin.org/articles/10.3389/fimmu.2023.1227175/full#supplementary-material

References

1. Chronic obstructive pulmonary disease (COPD) and World Health Organization. (2023). Available at: https://www.who.int/news-room/fact-sheets/detail/chronic-obstructive-pulmonary-disease-(copd).

2. Diseases GBD, Injuries C. Global burden of 369 diseases and injuries in 204 countries and territories, 1990-2019: a systematic analysis for the Global Burden of Disease Study 2019. *Lancet* (2020) 396(10258):1204–22. doi: 10.1016/S0140-6736(20)30925-9

3. Li Y, Nair H. Trends in the global burden of lower respiratory infections: the knowns and the unknowns. *Lancet Infect Dis* (2022) 22(11):1523–5. doi: 10.1016/S1473-3099(22)00445-5

4. Stoeckius M, Hafemeister C, Stephenson W, Houck-Loomis B, Chattopadhyay PK, Swerdlow H, et al. Simultaneous epitope and transcriptome measurement in single cells. *Nat Methods* (2017) 14(9):865–8. doi: 10.1038/nmeth.4380

5. Conlee KM, Stephens ML, Rowan AN, King LA. Carbon dioxide for euthanasia: concerns regarding pain and distress, with special reference to mice and rats. *Lab Anim* (2005) 39(2):137–61. doi: 10.1258/0023677053739747

6. Fisher S, Burgess WL, Hines KD, Mason GL, Owiny JR. Interstrain differences in CO2-induced pulmonary hemorrhage in mice. *J Am Assoc Lab Anim Sci* (2016) 55(6):811–5.

7. Wolf FA, Angerer P, Theis FJ. SCANPY: large-scale single-cell gene expression data analysis. *Genome Biol* (2018) 19(1):15. doi: 10.1186/s13059-017-1382-0

8. Mule MP, Martins AJ, Tsang JS. Normalizing and denoising protein expression data from droplet-based single cell profiling. *Nat Commun* (2022) 13(1):2099. doi: 10.1038/s41467-022-29356-8

9. Bredikhin D, Kats I, Stegle O. MUON: multimodal omics analysis framework. *Genome Biol* (2022) 23(1):42. doi: 10.1186/s13059-021-02577-8

frontiers | Frontiers in Immunology

TYPE Methods
PUBLISHED 21 October 2024
DOI 10.3389/fimmu.2024.1493848

OPEN ACCESS

EDITED BY
Paige Lacy,
University of Alberta, Canada

REVIEWED BY
Stefan Floess,
Helmholtz Association of German Research Centers (HZ), Germany
Yanek Jimenez Andrade,
Massachusetts General Hospital, Harvard Medical School, United States

*CORRESPONDENCE
Jörg H. Fritz
jorg.fritz@mcgill.ca

†These authors have contributed equally to this work

RECEIVED 09 September 2024
ACCEPTED 24 September 2024
PUBLISHED 21 October 2024

CITATION
Roy-Dorval A, Deagle RC, Roth F, Raybaud M, Ismailova N, Krisna SS, Aboud DGK, Stegen C, Leconte J, Berberi G, Esomojumi A and Fritz JH (2024) Analysis of lipid uptake, storage, and fatty acid oxidation by group 2 innate lymphoid cells.
Front. Immunol. 15:1493848.
doi: 10.3389/fimmu.2024.1493848

Analysis of lipid uptake, storage, and fatty acid oxidation by group 2 innate lymphoid cells

Audrey Roy-Dorval[1,2,3†], Rebecca C. Deagle[1,2,3†], Frederik Roth[1,2,3], Mathilde Raybaud[1,2,3], Nailya Ismailova[1,2,3], Sai Sakktee Krisna[2,3,4], Damon G. K. Aboud[5], Camille Stegen[1,2,3], Julien Leconte[1,2,3], Gabriel Berberi[1,2,3], Ademola Esomojumi[1,2,3] and Jörg H. Fritz[1,2,3,4*]

[1]Department of Microbiology and Immunology, McGill University, Montréal, QC, Canada, [2]McGill University Research Center on Complex Traits (MRCCT), McGill University, Montréal, QC, Canada, [3]Dahdaleh Institute of Genomic Medicine (DIgM), McGill University, Montréal, QC, Canada, [4]Department of Physiology, McGill University, Montréal, QC, Canada, [5]Department of Chemical Engineering, McGill University, Montréal, QC, Canada

Group 2 Innate Lymphoid Cells (ILC2) are critical drivers of both innate and adaptive type 2 immune responses, known to orchestrate processes involved in tissue restoration and wound healing. In addition, ILC2 have been implicated in chronic inflammatory barrier disorders in type 2 immunopathologies such as allergic rhinitis and asthma. ILC2 in the context of allergen-driven airway inflammation have recently been shown to influence local and systemic metabolism, as well as being rich in lipid-storing organelles called lipid droplets. However, mechanisms of ILC2 lipid anabolism and catabolism remain largely unknown and the impact of these metabolic processes in regulating ILC2 phenotypes and effector functions has not been extensively characterized. ILC2 phenotypes and effector functions are shaped by their metabolic status, and determining the metabolic requirements of ILC2 is critical in understanding their role in type 2 immune responses and their associated pathophysiology. We detail here a novel experimental method of implementing flow cytometry for large scale analysis of fatty acid uptake, storage of neutral lipids, and fatty acid oxidation in primary murine ILC2 with complementary morphological analysis of lipid storage using confocal microscopy. By combining flow cytometry and confocal microscopy, we can identify the metabolic lipid requirements for ILC2 functions as well as characterize the phenotype of lipid storage in ILC2. Linking lipid metabolism pathways to ILC2 phenotypes and effector functions is critical for the assessment of novel pharmaceutical strategies to regulate ILC2 functions in type 2 immunopathologies.

KEYWORDS

group 2 innate lymphoid cells (ILC2), type 2 immunity, immunometabolism, fatty acid uptake, lipid droplets, fatty acid oxidation (FAO), microscopy, flow cytometry

1 Introduction

Group 2 innate lymphoid cells (ILC2) instruct innate type 2 immune responses, exerting critical roles in the initiation and orchestration of anti-helminth immunity as well as allergic inflammation (1–3). ILC2 share functional overlap with antigen-specific $CD4^+$ type 2 T helper (Th2) cells, including the requirement of the transcriptional regulator GATA3 as well as the release of type 2 signature cytokines such as interleukin (IL)-4, IL-5 and IL-13, facilitating eosinophil recruitment, goblet cell hyperplasia and mucus production (4, 5). ILC2 are located at internal and external barrier surfaces including the lung (6). However, in contrast to Th2 cells, ILC2 lack the expression of specific antigen receptors and are primarily activated in an antigen-independent fashion in response to alarmins such as IL-33, IL-25 and/or thymic stromal lymphopoietin (TSLP) that are released upon tissue perturbation or immune challenge (4, 5). IL-33 has been described as the most potent activator of lung ILC2 (7), signaling through the heterodimeric IL-33 receptor (IL-33R) composed of the ligand-binding chain ST2 and IL-1 receptor accessory protein (IL-1RacP) (8, 9). Furthermore, it was recently demonstrated that ILC2 require cell-intrinsic ST2 signals to promote type 2 responses, including allergic airway inflammation (10).

Due to the potency to rapidly release type 2 signature cytokines such as IL-4, IL-5 and IL-13 upon activation, ILC2 have been suggested to constitute a critical therapeutic target to treat human type 2 immunopathologies (11). Indeed, elevated frequencies and numbers of ILC2 have been found in patients with asthma, allergic rhinitis and chronic rhinosinusitis, correlating with disease severity and resistance to corticosteroid therapy (12, 13). Biologics, including mepolizumab, benralizumab, and dupilumab, targeting cytokines IL-5, and IL-4/IL-13, respectively, have shown promising effects, leading to the reduction in annualized asthma exacerbation rates (AER), oral corticosteroid-sparing effects and improved Asthma Control Questionnaire scores (14, 15). However, despite these clinical advances, approximately 30% of patients with severe asthma receiving biologics do not experience meaningful improvements in their AER (14, 16). Hence, instead of blocking downstream type 2 signature cytokines, the targeting of upstream alarmins, including IL-33 and TSLP has been proposed as an alternative treatment strategy for asthma and type 2 immunopathologies (14, 15). Indeed, initial clinical trials targeting IL-33 using Itepekimab (17, 18) or TSLP through the application of Tezepelumab (19) show promising clinical results by reducing asthma symptoms. However, the cost of biologics is high and can place financial pressures on patients and health care systems, estimating the annual net price for each of the drugs at approximately $30,000 annually (20). In addition, asthma phenotypes are multi-layered and a better understanding of their diversity is needed to allow individualized treatment strategies for patients (14, 21).

Fueled by a wealth of mechanistic insights from studies in oncology and on metabolic disorders it has become increasingly clear that targeting the metabolism of immune responses can improve clinical treatment outcomes (22, 23). As such, a better understanding of the metabolic wiring of the diseased tissue and its cellular components is critical to understand strengths and limitations of current treatment strategies of type 2 immunpathologies. Indeed, metabolomic studies have revealed associations between altered lipid metabolism, amino acid metabolism and disease pathogenesis in asthmatic patients (24–26). Moreover, obesity was shown to be the most common comorbidity of asthma (27), revealing that energy metabolism is altered in obese asthmatics (28). As ILC2 have been shown to exert critical roles in the regulation of tissue as well as systemic metabolism (29) they constitute a critical target for metabolic intervention to treat type 2 immunopathologies.

While glucose and amino acid metabolism were shown to be important to sustain ILC2 proliferation and effector functions (29–31) it has recently become increasingly clear that uptake and metabolism of lipids also exerts critical metabolic functions in ILC2. During helminth infection and allergen-induced airway inflammation intestinal as well as lung ILC2 were found to increase their exogenous fatty acid (FA) intake, respectively (32–35). Moreover, it was observed that in addition to increasing exogenous lipid acquisition, lung ILC2 store more lipids in lipid droplets, facilitating ILC2 functions during allergen-induced airway inflammation (33, 35). In correlation with increased lipid droplets in ILC2, *in vivo* treatment with papain or with IL-33 increased DGAT1 gene expression (33), an enzyme involved in triacylglyceride (TAG) formation and LD biogenesis (36, 37). ILC2-specific deletion was found to reduce ILC2 effector function and allergic airway inflammation (33), demonstrating a critical role for LD biogenesis and DGAT1 in the regulation of ILC2 effector functions. FAs can be catabolized in mitochondria by fatty acid β-oxidation (FAO) (38). As a result, acetyl-CoA is produced and can help fuel numerous metabolic pathways including the tricarboxylic acid (TCA) cycle (38). In addition, FAO results in the reduction of flavin adenine dinucleotide (FAD) to FADH2 and nicotinamide adenine dinucleotide (NAD) to NADH, important electron donors to the respiratory chain (38). It has previously been reported that IL-33-stimulated ILC2 employ oxidative phosphorylation to a greater extent than steady state ILC2 (31). In fact, during helminth infection, it has been reported that ILC2 metabolize exogenous FA via FAO to fuel oxidative phosphorylation, which was necessary for ILC2 proliferation and cytokine production (32, 33). IL-33 treated lung-derived ILC2 also required FAO to produce cytokines and proliferate (39). Therefore, lipid uptake and lipid metabolism play an important role in ILC2 metabolism for proliferation and the regulation of effector functions. We thus aimed to develop a methodological workflow to enable rapid analysis of lipid uptake, lipid storage and fatty acid oxidation by primary ILC2.

2 Materials and methods

2.1 Mice

C57BL/6J wildtype (WT) mice were originally purchased from the Jackson Laboratory (Bar Harbor, ME) and bred in house at McGill University. All animals were maintained on a C57BL/6J background, bred, and housed under specific pathogen-free conditions with ad libitum access to food and water. All experiments were performed on female mice (aged 6-12 weeks) in accordance with the guidelines and policies of the Canadian Council on Animal Care and those of McGill University.

2.2 *In vivo* intranasal treatment for *ex vivo* experiments

As previously reported (40), mice were anaesthetized with 5% Isoflurane USP (Fresenius Kabi, Catalog No. CP0406V2) and intranasally challenged with 250 ng of carrier-free recombinant murine IL-33 (R&D Systems, Catalog No. 3626-ML-010/CF) in 40 µL of Dulbecco's Phosphate Buffered Saline (DPBS; Fisher Scientific, Catalog No. SH30028.02) or DPBS alone for three consecutive days. The 40 µL volume was divided, whereby 20 µL was administrated per nostril. On the fifth day, lungs were collected and isolated as outlined in Section 2.4 (Figure 1).

2.3 Isolation of bone marrow-derived ILC2

Mice were anaesthetized with 5% isoflurane and euthanized via CO_2 asphyxiation, followed by cervical dislocation as confirmation of death. The femurs and tibias were collected, cleaned with sterilized gauze (Fisher Scientific, Catalog No. 22-037-907), and washed in 75% ethanol prior to bone marrow (BM) extraction. Sterile BM extraction tubes were prepared by using an 18-gauge needle (Becton Dickinson, Catalog No. 305196) to puncture a single hole in the bottom of a 0.5 mL tube (Sarstedt, Catalog No. 72.737.002). These tubes were then autoclaved and set inside a sterile 1.5 mL collection tube (Progene, Catalog No. 87-B150-C) containing 100 µL of DPBS. Both ends of the cleaned bones were cut at the epiphysis to expose the BM and a single bone was placed vertically inside each 0.5 mL tube. The 1.5 mL tubes were then sealed and centrifuged (1900*g, 5 min, 4°C), which allowed the BM to be extracted from the bone, through the punctured hole, and into the 1.5 mL tube containing DPBS. The 0.5 mL tubes containing the empty bones were discarded, and the DPBS was resuspended with the pellet of BM and then consolidated into a 50 mL tube (Fisher Scientific, Catalog No. 14-432-22) with a maximum of 20 bones (5 mice) per tube. Each tube was filled to 50 mL with DPBS, centrifuged (450*g, 5 min, 4°C), and the supernatant was discarded. The cell pellet was resuspended in 1.5 mL of

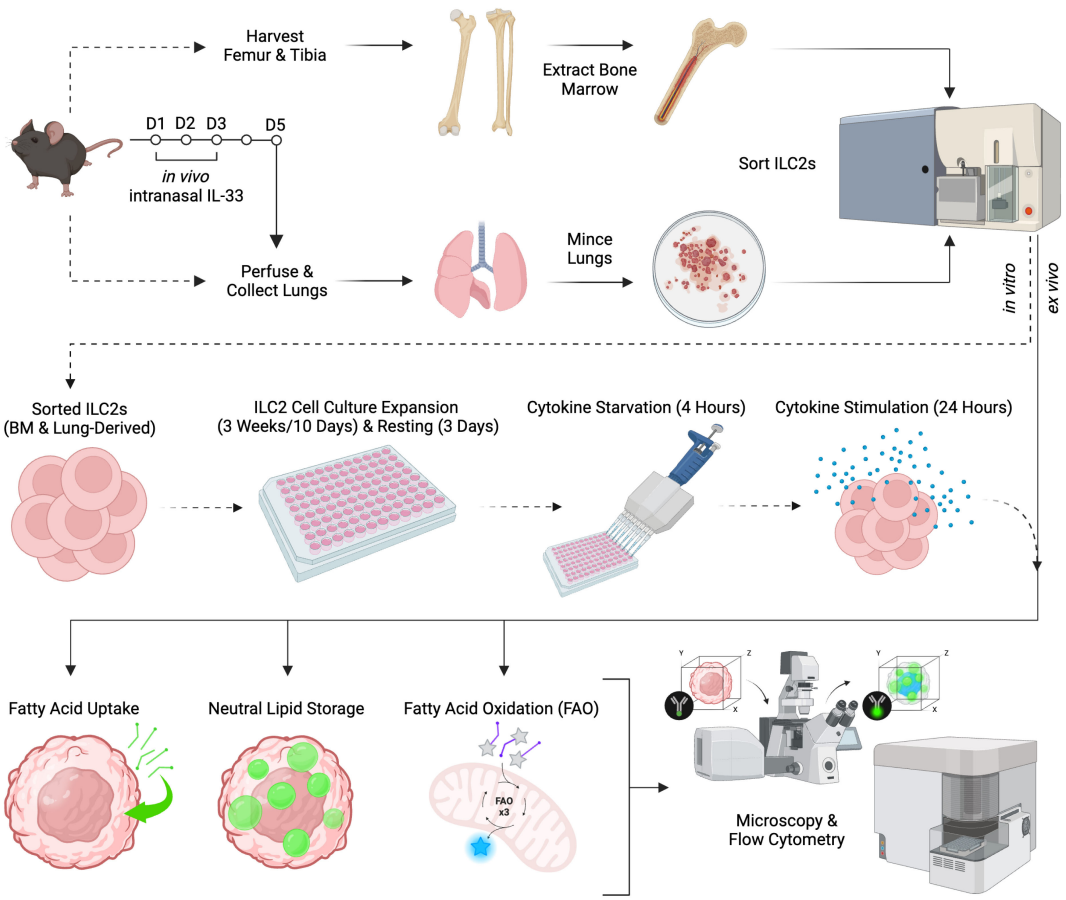

FIGURE 1
Schematic of experimental workflow. Female C57BL/6J wild-type mice aged 6-12 weeks were selected for either bone marrow or lung group 2 innate lymphoid cell (ILC2) isolation. Femurs and tibias were harvested to obtain bone marrow-derived ILC2 by flow cytometric cell sorting and were then cultured *in vitro* (dashed line) for expansion, followed by cytokine starvation and subsequent cytokine re-stimulation. Lung-derived ILC2 were obtained by flow cytometric cell sorting from naïve mice followed by *in vitro* cell culture expansion (dashed line). Alternatively, lung-derived ILC2 were obtained by flow cytometric cell sorting from animals that were challenged intranasally with PBS as control or IL-33 for three consecutive days (solid line). Bone marrow- and lung-derived ILC2 were used for the quantification of fatty acid uptake, neutral lipid storage, and fatty acid oxidation (FAO) by flow cytometry or microscopy. Created in BioRender.com. Deagle, R. (2024) BioRender.com/v17y111.

Ammonium-Chloride-Potassium (ACK) lysing buffer (Thermo Scientific, Catalog No. A1049201) for approximately 20-30 seconds to lyse red blood cells within the sample. This reaction was neutralized immediately by filling the tube with fluorescence-activated cell sorting (FACS) buffer to 50 mL followed by centrifugation (450*g, 5 min, 4°C) and a second wash with FACS buffer (450*g, 5 min, 4°C). FACS buffer was made in-house using DPBS and 2% fetal bovine serum (FBS; Wisent Bioproducts, Catalog No. 080150). To prevent non-specific binding of antibodies to the fragment crystallization receptors (FcRs), the cells were blocked for 15 minutes on ice using a 1:10 dilution of in-house formulated "Fc-block" (supernatant of the 2.4G2 hybridoma producing the purified anti-mouse CD16/CD32 monoclonal antibody (mAb)) in FACS buffer. The BM cells were then stained for 30 minutes on ice in the dark with an antibody cocktail (Table 1). The BM cells were then washed twice in FACS buffer as described above and filtered through a 70 µm cell strainer (Fisher Scientific, Catalog No. 22-363-548) prior to cell sorting. ILC2 were sorted using a FACS Aria III and FACSAria Fusion (BD Biosciences) equipped with 405 nm, 488 nm, 561 nm (Fusion only) and 640 nm lasers using FACSDiva version 6.0 (Aria III) or version 8.0 (Fusion) based on the absence of lineage markers and the expression of ILC2 specific markers (Table 1; Supplementary Figure 1 reference to isolation of BM and lung ILC2).

2.4 Isolation of lung-derived ILC2

Mice were anaesthetized with 5% isoflurane and euthanized via CO_2 asphyxiation, followed by cervical dislocation as confirmation of death. The mice were then bisected at the sternum to facilitate the puncturing of the thoracic diaphragm and removal of the ribcage to expose the lungs. A 23-gauge needle (Becton Dickinson, Catalog No. 305145) attached to a 10 mL syringe (Becton Dickinson, Catalog No. 302995) filled with DPBS was used to perfuse the lungs via the heart by piercing the apex of the left ventricle. After perfusion, the thymus and heart were discarded, and the lungs were removed as a whole unit to be kept in cell culture media (Table 2) on ice until all the mice were processed. The lungs were cleaned using sterile gauze, and each lobe was separated from its connective tissue before being placed into a dry, sterile 6-well plate (VWR, Catalog No. 62406-161) with a maximum of 5 lungs per well. The lungs were mechanically minced to a fine paste using scissors, and 5 mL of cell culture media (Table 2) containing DNase (Roche, Catalog No. 10104159001) and Liberase (Milipore Sigma, Catalog No. 5401127001) with a final concentration of 100 µg/mL and 200 µg/mL, respectively, were added to each well for enzymatic digestion. The lung tissues were incubated with the enzymes at 37°C in 5% CO_2 for a total of 30 minutes, stirring the plate at 10 minute intervals. To further homogenize the tissue, an 18-gauge needle attached to a 5 mL syringe (Becton Dickinson, Catalog No. 309646) was used to aspirate and dispense the tissue suspension a maximum of 3 times to prevent excessive shear-stress. The tissue suspension was then transferred to a 70 µm cell-strainer set inside a 50 mL tube for cell collection. The plunger of the 5 mL syringe was removed and the blunt, rubber end was used to mechanically dissolve the remaining pieces of lung tissue in the cell-strainer. The blunt end of the plunger and the 6-well plate were washed frequently with DPBS and added to the cell-strainer to maximize the cell yield. The 50 mL tubes were filled with DPBS to 50 mL and centrifuged (450*g, 5 min, 4°C) followed by a second wash of DPBS (450*g, 5 min, 4°C). The procedure for lysing red blood cells, blocking, antibody staining, and filtration followed the exact same guidelines as the BM-derived ILC2 isolation outlined in Section 2.3. Lung-derived ILC2 were then sorted purified using a BD FACS Aria III and BD FACSAria Fusion based on the absence of lineage markers and the expression of lung ILC2 specific markers (Table 1; Supplementary Figure 1 for isolation of BM and lung ILC2).

2.5 *In vitro* expansion and resting of bone marrow and lung-derived ILC2

Sorted ILC2 were cultured in 96-well round-bottom plates (VWR, Catalog No. CA62406-121) at 37°C in 5% CO_2 with a seeding density of $2.5x10^4$ cells per well in 200 µL of complete ILC2 cell culture media (Table 2) (40, 41). For BM-derived ILC2, 50 ng/mL of IL-2 (R&D Systems, Catalog No. 402-ML-100/CF), IL-7 (R&D Systems, Catalog No. 407-ML-200/CF), and IL-33 (R&D Systems, Catalog No. 3626-ML-010/CF) as well as 20 ng/mL of TSLP (R&D Systems, Catalog No. 555-TS-010/CF) were added to the cell culture media to promote the survival and expansion of the ILC2 *in vitro* cell culture. For lung-derived ILC2, 50 ng/mL each of IL-2 and IL-7 were added to the complete cell culture media for *in vitro* expansion. Phenol-red free complete media (Table 2) was specifically used to culture cells for fatty acid oxidation (FAO) experiments (Section 2.11) to avoid auto-fluorescent interference. Every 2 days the cell culture was split; whereby each well of ILC2 were resuspended and 100µL of cell suspension was transferred to an empty well and 100 µL of complete media with expansion cytokines were added to all wells containing ILC2 for a total volume of 200 µL. BM-derived ILC2 expanded *in vitro* for up to 3 weeks whereas lung-derived ILC2 were expanded *in vitro* for up to 10 days. BM- and lung-derived ILC2 intended for *ex vivo* experiments were used immediately after the sorting process and did not undergo *in vitro* expansion. After expansion was complete, the ILC2 were pooled, the expansion media was removed, and the cells were washed in RPMI 1640 (450*g, 5 min, 4°C) to remove any trace of expansion cytokines. The ILC2 were then re-seeded at $2.5x10^4$ cells per well for 3 days at 37°C in 5% CO_2 in complete media containing 10 ng/mL of IL-2 and IL-7 to "rest" the cells. This period of reduced activity, or rest, was necessary to bring the ILC2 down to a homeostatic baseline level of activity (proliferation & cytokine production) after the demands of expansion.

2.6 ILC2 seeding and stimulation for flow cytometric assays and microscopy

After 3 days of resting, *in vitro* ILC2 were pooled together in a 50 mL tube and washed twice with RPMI 1640 media (450*g, 5 min, 4°C) to remove any trace of resting cytokines. *In vitro* ILC2 were

10.3389/fimmu.2024.1493848

TABLE 1 Antibody staining panels for bone marrow- and lung-derived ILC2.

Target	Vendor	Catalog Number	Concentration (µg/mL)	RRID
Lineage Cocktail (LC)				
TCRβ	ThermoFisher Scientific	12-5961-83	0.50	AB_466067
TCRγδ	ThermoFisher Scientific	12-5711-82	0.25	AB_465934
CD3ε	ThermoFisher Scientific	12-0031-83	0.25	AB_465497
Gr-1	ThermoFisher Scientific	12-5931-83	0.20	AB_466046
CD11b	ThermoFisher Scientific	12-0112-83	0.20	AB_2734870
Ter-119	ThermoFisher Scientific	12-5921-83	0.25	AB_466043
B220	ThermoFisher Scientific	12-0452-83	0.50	AB_465672
CD19	ThermoFisher Scientific	12-0193-83	0.50	AB_657660
NK1.1	ThermoFisher Scientific	12-5941-83	2.00	AB_466051
CD5	ThermoFisher Scientific	12-0051-83	0.50	AB_465524
CD11c	ThermoFisher Scientific	12-0114-83	1.00	AB_465553
FcεR1α	ThermoFisher Scientific	12-5898-83	1.00	AB_466029
Bone marrow-derived ILC2				
LC				
Sca-1	BioLegend	122516	1.25	AB_756201
CD25	ThermoFisher Scientific	48-0251-82	2.00	AB_10671550
c-kit	ThermoFisher Scientific	17-1171-83	4.00	AB_469431
BODIPY staining of lung-derived ILC2				
LC				
CD25	ThermoFisher Scientific	48-0251-82	1.00	AB_10671550
ST2	ThermoFisher Scientific	47-9335-82	2.00	AB_2848379
CD90.2	BioLegend	140319	0.17	AB_2561395
CD45	BioLegend	103149	0.50	AB_2564590
7-AAD (viability dye)	ThermoFisher Scientific	00-6993-50	0.84	NA
FAO-Blue staining of lung-derived ILC2				
LC				
CD25	ThermoFisher Scientific	53-0251-82	2.50	AB_763472
ST2	ThermoFisher Scientific	47-9335-82	2.00	AB_2848379
CD90.2	BD Biosciences	567736	0.33	NA
CD45 (*ex vivo*)	BioLegend	103114	0.50	NA
CD45 (*in vitro*)	BioLegend	103149	0.50	NA
7-AAD (viability dye)	ThermoFisher Scientific	00-6993-50	0.84	NA

resuspended in complete cell culture media (Table 2), counted, and the cell concentration was adjusted to 500,000 cells/mL. For flow cytometric assays, 100 µl of *in vitro* ILC2 ($5x10^4$ cells) were seeded per well in a sterile 96-well round-bottom culture plate, whereas for microscopy, 1 mL of *in vitro* ILC2 ($5x10^5$ cells) were seeded per well in a sterile 6-well plate. Seeded *in vitro* ILC2 incubated for 4 hours at 37°C in 5% CO_2 to cytokine starve the cells, bringing the cells to a quiescent state prior to cytokine stimulation. The cytokine

TABLE 2 Complete RPMI media recipes for bone marrow- and lung-derived ILC2.

Component	Complete Cell Culture Media	FAO-Blue Staining Solution
RPMI 1640 Media without L-Glutamine	45 mL *With Phenol Red: Cytiva, Catalog No. SH30096.02; Phenol Red-Free: Cytiva, Catalog No. SH30605.01*	5 mL *(Phenol Red-Free)*
Fetal Bovine Serum (FBS), Heat inactivated *Wisent Bioproducts, Catalog No. 080150*	5 mL (10%)	100 µL (2%)
L-Glutamine (200mM) *Cytiva, Catalog. No. SH30034.01*	0.5 mL (2000 µM)	50 µL (2000 µM)
Penicillin/Streptomycin (10,000 U/mL/10,000 ug/mL) *Cytiva, Catalog No. SV30010*	0.5 mL (100 U/mL/100 µg/mL)	0 µL
Gentamycin (10 mg/mL) *Sigma Aldrich, Catalog No. G1272-100ML*	120 µL (24 µg/mL)	0 µL
β-mercaptoethanol (55mM) *Gibco, Catalog No.* 21-985-023	50 µL (55 µM) *Omitted for resting and experiments*	0 µL

stimulations used for all *in vitro* experiments were the following: IL-7, IL-2, IL-33, IL-7+IL-33, and IL-2+IL-33. Each cytokine stimulation was made at a 2X concentration (20 ng/mL) in complete cell culture media and was added to the appropriate wells (100 µL for flow cytometry or 1 mL for microscopy) for a final 1X concentration (10 ng/mL). Cells were then incubated for 24 hours at 37°C in 5% CO_2 prior to further analyses. *Ex vivo* ILC2 were seeded at the same density as described above after being retrieved from the cell sorter but did not undergo cytokine starvation or stimulation prior to further analyses.

2.7 Enzyme-linked immunosorbent assay

Production of IL-5 was quantified from supernatant of cultured murine bone marrow- and lung-derived ILC2 using the IL-5 mouse DuoSet ELISA kits (R&D Systems, Catalog No. DY405) according to the manufacturer's instructions. Absorbance at 450 nm was measured using an Enspire™ 2300 Multilabel Reader (PerkinElmer).

2.8 Proliferation assay

Bone marrow ILC2 were stained with CellTrace Yellow Cell Proliferation Kit (Invitrogen, Catalog No. C34573) according to manufacturer's instructions. Cells were plated at 20,000 cells/well with respective cytokines. After 3 days, ILC2 were stained with eFluor 780 Fixable Viability Dye (Invitrogen, Catalog No. 65-0865-18), fixed and permeabilized with FoxP3 Transcription Factor Staining Buffer Set (Invitrogen, Catalog No. 00-5523-00). Data were acquired using an Aurora Spectral Flow Cytometer (Cytek).

2.9 Flow cytometric staining of fatty acid uptake

The fatty acid (FA) uptake dye, BODIPY™ FL C16 (Invitrogen, Catalog No. D3821), was stored at -20°C at a stock concentration of 1 mM (1 mg stock powder in 2.11 mL DMSO) and diluted to an intermediate concentration of 5 µM. At the 23-hour mark of cytokine stimulation (*in vitro*) or after cell sorting (*ex vivo*), 50 µL of prepared 5 µM BODIPY™ FL C16 was added to each well to obtain a final working concentration of 1 µM and the cells were then incubated with the dye for 1 hour at 37°C in 5% CO_2. After incubation, stimulated ILC2 were resuspended and transferred to a sterile 96-well conical-bottom culture plate (Sarstedt, Catalog No. 82.1583.001). The plate was then centrifuged (450*g, 5 min, 4 °C), the supernatant was removed, and cells were washed twice with 200 µL of FACS buffer. The supernatant was removed and the ILC2 were resuspended in 150 µL of FACS buffer, followed by an additional 5 µL of 7-AAD viability staining solution. All samples were immediately acquired by flow cytometry (Section 2.12).

2.10 Flow cytometric staining of neutral lipid content

The neutral lipid dye, BODIPY™ 493/503 (Invitrogen, Catalog No. D3922), was stored at -20°C at a stock concentration of 1.9 mM (10 mg stock powder in 1mL DMSO) and diluted to a working concentration of 2 µM in DPBS. After 24 hours of cytokine stimulation, ILC2 cultured *in vitro* were resuspended and transferred to a sterile 96-well conical-bottom culture plate. *Ex vivo* ILC2 were plated directly after sort purification into the sterile 96-well conical-bottom culture plate. The plate was then centrifuged (450*g, 5 min, 4 °C), the supernatant was removed, and the ILC2 were washed twice with 200 µL of cold DPBS (450*g, 5 min, 4 °C). After the supernatant was removed, the ILC2 were resuspended in 50 µL of prepared 2 µM BODIPY™ 493/503 and incubated for 20 minutes at 37°C in 5% CO_2. After incubation, ILC2 were washed twice with 150 µL of FACS buffer (450*g, 5 min, 4 °C). The supernatant was removed and ILC2 were resuspended in 150 µL of FACS buffer in addition to 5 µL of 7-AAD viability staining solution. All samples were immediately acquired by flow cytometry (Section 2.12).

2.11 Flow cytometric staining of fatty acid oxidation

The fatty acid oxidation (FAO) detection dye, FAOBlue (DiagnoCine, Catalog No. FNK-FDV-0033) was stored at -20°C at a stock concentration of 1 mM (0.2 mg stock powder in 418.84 µL

DMSO) and diluted to a working concentration of 20 µM in FAOBlue Staining Solution (Table 2). Throughout the staining procedure the FAOBlue dye as well as all the stained cells were kept on ice in the dark. After 24 hours of cytokine stimulation, ILC2 cultured *in vitro* were resuspended and transferred to a sterile 96-well conical-bottom culture plate. *Ex vivo* ILC2 were plated directly after sort purification into the sterile 96-well conical-bottom culture plate. The plate was centrifuged (450*g, 5 min, 4 °C), the supernatant was removed, and the ILC2 were washed twice with 200µL Phenol Red-Free RPMI 1640 (450*g, 5 min, 4 °C). The supernatant was removed and the cells were resuspended in 200 µL of the prepared 20 µM FAOBlue staining solution (Table 2). ILC2 were then incubated with the dye for 1 hour at 37°C in 5% CO_2. The plate was centrifuged (450*g, 5 min, 4 °C), the supernatant was removed, and cells were washed twice with 200µL DPBS (450*g, 5min, 4°C). The supernatant was removed, and the cells were resuspended in 150 µL Phenol Red-Free RPMI 1640 and 5 µL of 7-AAD viability staining was added to each well immediately before acquiring data by flow cytometry (Section 2.12).

2.12 Flow cytometry analysis

Samples were acquired on a BD FACSCanto II (BD Biosciences) equipped with a 488 nm and a 633 nm laser and FACSDiva 8.0 (BODIPY) or on an Aurora Spectral Flow Cytometer (Cytek) (FAO Blue) equipped with 405 nm, 488 nm, 561 nm and 641 nm lasers and Spectroflo 2.0. Each sample was run until 20,000 events were recorded. All samples were gated on lymphocytes excluding debris, singlets, and dead ILC2 using 7-AAD viability staining following the manufacturer's instructions. Then, FA uptake, neutral lipid content, or FAO were quantified by gating on BODIPY™ FL C16, BODIPY™ 493/503, and FAO Blue, respectively (Figure 2). Flow cytometry analysis was performed using FlowJo software (BD, Version 10.10.0).

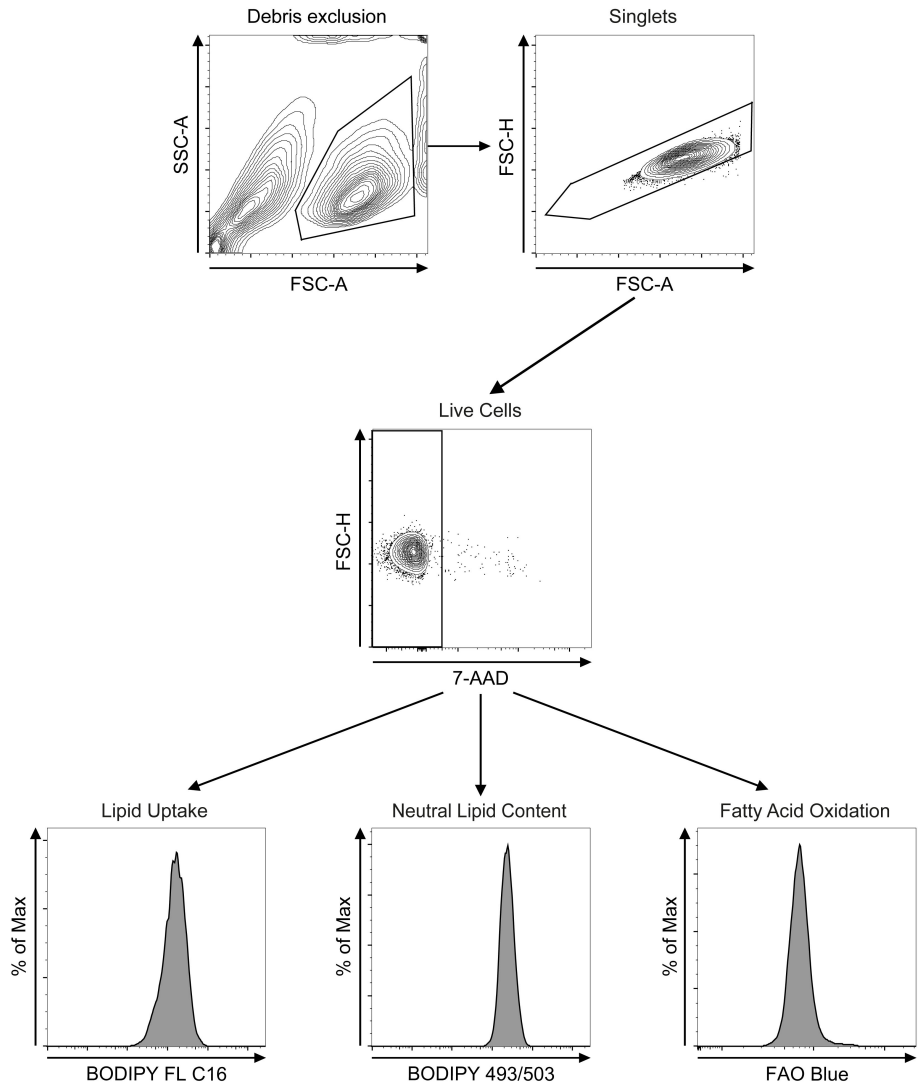

FIGURE 2
Flow cytometry gating strategies. After debris exclusion (FSC-A vs SSC-A) bone marrow- or lung-derived group 2 innate lymphoid cells (ILC2) were gated on singlets (FSC-A vs FSC-H) and on 7-AAD-negative live cells (7-AAD vs FSC-H). ILC2 were subsequently analyzed for lipid uptake (BODIPY FL C16), neutral lipid content (BODIPY 493/503) or fatty acid oxidation (FAO Blue).

Geometric mean fluorescence intensity (MFI) of the signals was calculated, duplicates were averaged per stimulatory condition and presented in bar graphs with all flow cytometry data represented as mean ± standard deviation. Histograms and bar graphs were created using FlowJo and Prism softwares (Graphpad, Version 9) respectively. Statistical analysis was performed as ordinary one-way ANOVA and *post-hoc* Tukey's multiple comparison tests to obtain statistical significance (P-values) between experimental conditions.

2.13 Staining of ILC2 for microscopy analyses

ILC2 were stained with the nuclear dye Hoechst 33342 (ThermoFisher Scientific, Catalog No. 62249), and with BODIPY™ 493/503 to visualize neutral lipid storage. Prior to staining, an intermediate concentration of Hoechst 33342 (stored at 4°C, stock concentration of 20 mM) was made by diluting 81.3 µl in 1 mL of DPBS for a concentration of 1 mg/mL. After 24 hours of cytokine stimulation (*in vitro*) or after cell sorting (*ex vivo*), 1 mL of cell culture media from each well was transferred to a 15 mL tube (Fisher Scientific, Catalog No. 14-959-49B). This media was used to make a 2X concentrated staining solution of Hoechst 33342 (3.25 µM) and BODIPY™ 493/503 (4 µM). The staining solution was thoroughly mixed and then added to each well, whereby the solution was pipetted slowly against the edge of the well to minimize cellular disturbance. The plate was gently tipped to ensure a homogenous distribution of the dye for a final working concentration of 1.6 µM of nuclear dye and 2 µM of neutral lipid dye. The cells were then incubated for 30 minutes at 37°C in 5% CO_2.

After incubation, *in vitro* BM-derived ILC2 were resuspended and transferred to a 15 mL tube and centrifuged (450*g, 5min, 4°C). The supernatant was removed, and the cell pellet was resuspended in 1 mL of Hank's Balanced Salt Solution (HBSS; ThermoFisher Scientific, Catalog No. 14175095) then transferred to a 1.5 mL tube and washed a second time with HBSS (450*g, 5 min, 4 °C). The supernatant was removed, and the cell pellet was resuspended in 500 µL of 4% formaldehyde fixative solution (Sigma-Aldrich, Catalog No. 252549) and incubated at room temperature for 10 minutes. After incubation, 1 mL of DPBS was added to each tube and centrifuged (450*g, 5 min, 4 °C) followed by a wash of DPBS with the same settings. After the supernatant was removed, the cell pellet was resuspended in 20 µL of de-ionized water and transferred to a 18x18 mm square #1.5 glass coverslip (Fisher Scientific, Catalog No. 12541A, 0.15-0.19 mm thickness). The cell suspension was spread over the coverslip surface area as much as possible and left to dry in the dark at room temperature for approximately 30 minutes. *Ex vivo* lung-derived ILC2 were extremely adherent and therefore plated directly onto the glass coverslips in the 6-well plate after the cell sorting process. The washing buffer, fixative solution, and DPBS washes described above were executed at the same concentrations in the 6-well plate by gently aspirating and dispensing the solutions against the edge of the well to minimize detachment of the cells. After the last DPBS wash, these coverslips were left to dry at room temperature in the dark for 30 minutes as well.

Once the coverslips were dry, 70 µL of ProLong™ Gold Antifade Mountant (ThermoFisher Scientific, Catalog No. P36930) was added to the center of each coverslip using low-retention wide-bore pipette tips (Fisher Scientific, Catalog No. 14-222-726). Glass microscopy slides (Fisher Scientific, Catalog No. 12-552-3) were lowered onto the mounting medium until the surface tension pulled the coverslip up and onto the microscope slide to minimize the production of air bubbles. The slides were kept inverted and placed inside a microscope slide box, taking care to not disturb the coverslip. The slides were left in the dark for 24 hours at room temperature to allow the mounting media to cure. Nail polish was traced around the edges of the coverslip to seal and preserve the samples; once the nail polish was dry the samples were stored at 4°C in a closed slide box. All samples were produced in triplicate and imaged within 3 days of the sample preparation.

2.14 Image acquisition

Images of ILC2 were acquired as three-dimensional z-stacks on a Zeiss LSM800 AxioObserver Z.1 fully motorized inverted confocal microscope equipped with a 40x/1.30NA Plan Neofluar oil immersion lens. A 405 nm diode laser at 1.0% laser power and 700 gain was tuned to visualize the nucleus (Hoechst 33342) using a multialkali (MA) PMT. A 488 nm diode laser at 0.2% laser power and 700 gain was tuned to visualize lipid droplets (BODIPY 493/503) using a gallium arsenide phosphide (GaAsP) PMT. The following acquisition parameters were used: sequential scanning, 1 Airy unit, 1 digital gain, 1.03 µs pixel dwell time, 4-line averaging, at scan zoom 10. Images were acquired as 1024x1024 pixel frames, with a pixel size of 0.016 x 0.016 µm, and a z-step of 0.5 µm. An average of 10 to 20 frames (5-10 µm depth) were acquired per cell and all image files were saved as 16-bit CZI images (format.czi). An average of 30 cells were acquired per experimental condition, and the same acquisition parameters were used for all conditions.

2.15 Image processing

Image files in.czi format were converted to.ims files using the software ImarisFileConverter (Bitplane, Version 10.0.0, Oxford Instruments). The converted files in.ims format were opened in Imaris 3D/4D Visualization and Analysis Software (Bitplane, Version 10.1.0, Oxford Instruments) for analysis of neutral lipid droplets. The *Section* icon was selected to visualize the xy, yz, and xz planes of the image file and an image plane was selected in the center of the cell. A fluorescence intensity line profile was drawn to determine the value of non-specific cytosolic signal in the green channel (BODIPY 493/503 signal). The *Image Proc* icon was then selected for image processing, and the *Baseline Subtraction* function in the green channel (BODIPY 493/503 signal) was selected. The *Baseline Subtraction* threshold was set to the fluorescence intensity previously determined in the *Section* icon and removed from the image to improve the signal-to-background ratio and facilitate

neutral LD detection. The same threshold was used for all images within the same parameters.

2.16 Neutral lipid droplet detection

Neutral lipid droplet (LD) detection began in the *3D View* and *Surpass* windows of Imaris, where the image file could be viewed as a fully rendered 3D image. Neutral LDs were detected using the *Surface* function, whereby a 3D object was constructed to represent the fluorescent signal in the image file based on a K-means clustering threshold algorithm. The *Surface* function was selected to open the *Creation Wizard* and the option *Start creation with slicer view* was checked before continuing to the next step. Next, the green channel (BODIPY 493/503 signal) was selected under *Source Channel* and the thresholding was set to *Absolute Intensity* before continuing to the next step. In the *Thresholding* step, the thresholding for detecting the fluorescent signal from the neutral LDs was determined. The image file was viewed alternately between the *3D Volume View* and the *Slicer View* while the threshold was being selected to determine the most accurate thresholding value to represent the neutral LD fluorescent signal. When the threshold value was determined to be an accurate representation, the analysis continued to the next step. In the *Filter Surface* step, the *+Add* button was selected under *Filters* to add a *Volume* filter; this filter allowed for the removal of any anomalies based on volume from the overall selection before finalizing the surface construction. The parameters were saved under *Favorite Creation Parameters* so that the same parameters could be used for all image files. Due to the fluorescence intensity variations between large and small neutral LDs, 2-3 different thresholds settings were necessary in most files to detect all the neutral LD and avoid the over- and under-selecting data issue that occurs with using a single threshold. A minimum of 30 cells were analyzed per experimental condition.

2.17 Cell volume analysis

Cell volume detection began in the *3D View* and *Surpass* windows of Imaris on.ims formatted files without conducting any image processing. The *Surface* function was selected to open the *Creation Wizard*, and the option *Start creation with slicer view* was checked before continuing to the next step. Next, the green channel (BODIPY 493/503 signal) was selected under *Source Channel* so that cytosolic and auto-fluorescent signals could be used to detect the cell volume. The *Surfaces Detail* was modified to be double the calculated default value (4X the pixel size in total) to improve detection and surface granularity, and the thresholding was set to *Absolute Intensity* before continuing to the next step. In the *Thresholding* step, the thresholding for detecting the cytosolic fluorescent signal was determined. The image file was viewed alternately between the *3D Volume View* and the *Slicer View* while the threshold was being selected to determine the most accurate thresholding value to represent the volume of the cell. When the threshold value was determined to be an accurate representation, the analysis continued to the next step. In the *Filter Surface* step, the *+Add* button was selected under *Filters* to add a *Volume* filter; this filter allowed for the removal of any anomalies based on volume from the overall selection before finalizing the surface construction. The parameters were saved under *Favorite Creation Parameters* so that the same parameters could be used for all image files. A minimum of 30 cells were analyzed per experimental condition.

2.18 Data export and quality control

For LD analysis, the *Data Settings* icon was selected in Imaris where the metrics *Intensity Sum, Voxels*, and *Sphericity* were selected under the *Surfaces* category. The *Intensity Sum* is the cumulative fluorescence value of every voxel within the neutral LD surface, *Voxel* is the total number of volumetric pixels in the neutral LD surface, and the *Sphericity* measures how close to a perfect sphere (value of 1.0) the neutral LD surface is. These metrics were exported for every image file in Excel and the data from the green channel (BODIPY 493/503 signal) was consolidated into a master Excel file. Each data point was representative of a single neutral LD, and these datapoints were used to calculate the total neutral lipid fluorescence intensity (*Intensity Sum*) and the total neutral lipid volume (*Voxels*) for each individual cell. Datapoints were removed from the dataset if the sphericity values were above or equal to 1.0 and any voxel values below 10 were considered insignificant. Any datapoints that were abnormally large compared to the distribution of the dataset were reviewed in Imaris for validity before they were removed from the dataset. After the dataset was quality controlled in the manner described above, a MATLAB (Version R2023b, MathWorks, Natick, MA) script was implemented to recalculate the number of neutral LD per cell and to bin the LD into volume (small, intermediate, large) and sphericity (irregular, intermediate, spherical) categories. For cell volume analysis, the *Data Settings* icon was selected in Imaris where the *Voxels* metric selected under the *Surfaces* category. This metric was exported for every image file in Excel and the data from the green channel (BODIPY 493/503 signal) was consolidated into a master Excel file. Each data point was representative of a single cell.

2.19 Microscopy graphs and statistical analysis

All data was acquired from three independent experiments for a total of three replicates for each condition. A sample size of 30 cells was chosen to represent each experimental condition to account for normal distribution. All statistical analysis and bar graphs were conducted in the Prism software (Graphpad, Version 9). Statistical analysis for *in vitro* experiments were performed as ordinary one-way ANOVA and *post-hoc* Tukey's multiple comparison tests to obtain statistical significance (P-values) between experimental conditions. Unpaired two-tailed Student's t-tests were performed for *ex vivo* experiments to obtain statistical significance (P-values) between populations. All data representing individual cells is presented as mean ± standard deviation (SD), and all data

representing individual neutral LD is presented as mean ± standard error of the mean (SEM). Correlation analysis was conducted using JMP 16.1.0 (Statistical Discovery, SAS Institute, NC) to obtain the correlation coefficients between each combination of metrics.

3 Results

3.1 Activation of group 2 innate lymphoid cells induces fatty acid uptake

As lipid metabolism has been shown to be a significant driver of pathogenic ILC2 function in allergic airway inflammation (33, 39) we aimed at establishing an integrated analytical framework to determine levels of cellular fatty acid (FA) uptake, neutral lipid storage, and fatty acid oxidation (FAO) in primary ILC2 (Figure 1). To this end, we obtained primary murine sort purified bone marrow-derived (Supplementary Figure 1A) or lung-derived ILC2 (Supplementary Figure 1B) that were further expanded *in vitro* as previously described (40, 41). Alternatively, lung-derived ILC2 were obtained by flow cytometric cell sorting (Supplementary Figure 1B) from animals that were challenged intranasally with PBS as a control or IL-33 for three consecutive days, which were then further used for *ex vivo* experiments. These three distinct primary murine ILC2 populations were used for the quantification of FA uptake, neutral lipid storage, and FAO by flow cytometry *in vitro* as well as *ex vivo* (Figure 2).

ILC2 activation by IL-33 has been established as a hallmark of allergic airway inflammation (7). IL-7 and IL-2 secreted by other resident non-hematopoietic stromal cells as well as innate and adaptive immune cells, respectively, have been shown to act in synergy with IL-33 for enhanced ILC2 proliferation and elevated cytokine production (41–43). To first demonstrate the functionality of our ILC2 *in vitro* culture systems, we stimulated bone marrow- (Figures 3A, B, E, F) or lung-derived ILC2 (Figures 3C, D) with IL-7 (Figures 3A, C, E) or IL-2 (Figures 3B, D, F) alone or in combination with IL-33 and analyzed the production of IL-5 in cell culture supernatants as well as the proliferative capacity. As

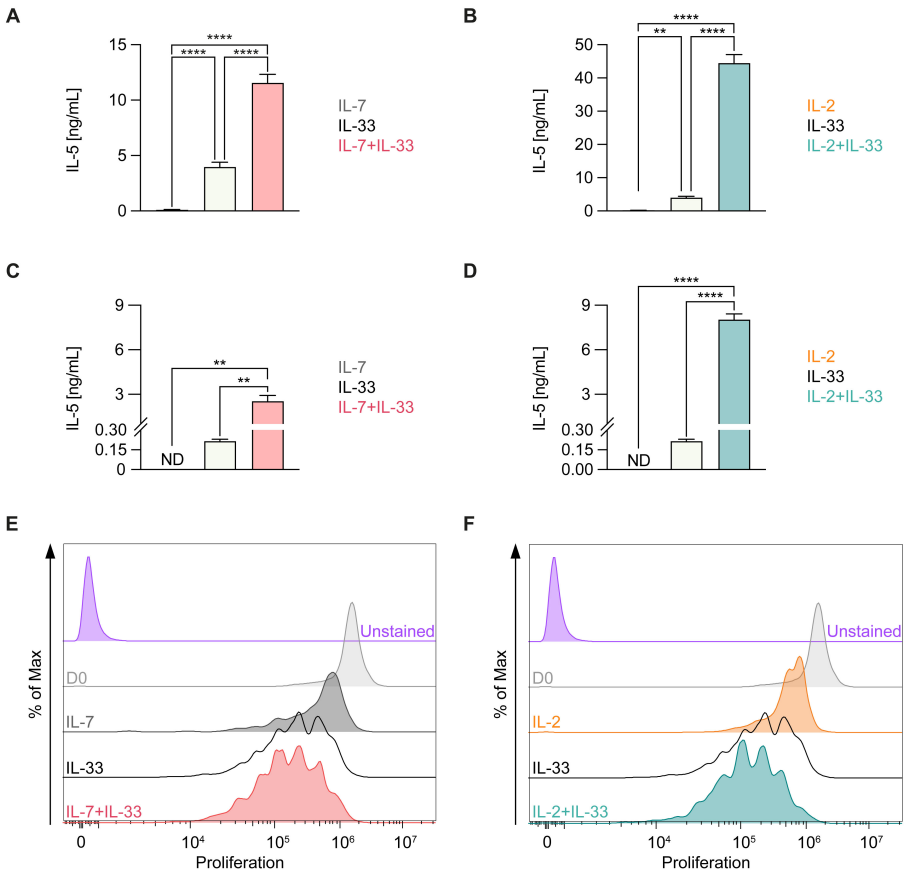

FIGURE 3
Cytokine production and proliferation of murine ILC2 upon treatment with distinct cytokine combinations. Bone marrow-derived **(A, B, E, F)** or lung-derived **(C, D)** group 2 innate lymphoid cells (ILC2) were stimulated with either IL-7 only, IL-33 only, or a combination of IL-7 and IL-33 **(A, C, E)** or IL-2 only, IL-33 only, or a combination of IL-2 and IL-33 **(B, D, F)**. All cytokines were applied at 10 ng/mL. **(A–D)** After 24 hours of stimulation, supernatants were harvested and analyzed for IL-5 content by ELISA. **(E, F)** Proliferation of ILC2 was assessed using CellTrace Yellow Cell Proliferation Kit after 3 days of incubation with respective cytokines. The data representing the IL-33 stimulation is the same for **(A–F)**. Data are representative of three independent experiments with stimulations performed in duplicates. Data are shown as average ± standard deviation (SD). Statistical analysis was performed using one-way ANOVA followed by Tukey's multiple comparisons test ($p < 0.01$ = ** and $p < 0.0001$ = ****); ND, not detectable.

previously reported (41), IL-7 and IL-2 act in synergy with IL-33 to induce cell proliferation as well as secretion of type 2 cytokines in both bone marrow- as well as lung-derived ILC2 (Figures 3A–F).

However, the functions and effects of these cytokines (IL-2, IL-7, IL-33) alone or in synergy (IL-7+IL-33 or IL-2+IL-33) as they pertain to lipid metabolism in ILC2 remains incompletely understood. Therefore, to investigate the ability of ILC2 to acquire exogenous FAs during defined activation states, we optimized a flow cytometric assay, by incubating ILC2 *ex vivo* or *in vitro* with BODIPY FL C16, a fluorescent FA analog (Figure 4). We first analyzed sort-purified ILC2 from mice that were treated intranasally with PBS or IL-33 *ex vivo* (Figures 4A, B). Although ILC2 from PBS-treated mice acquired exogenous FAs, ILC2 from IL-33 treated animals had a significantly higher FA intake (Figures 4A, B). To further analyze how distinct activating cytokines impact FA uptake by ILC2, bone marrow-derived (Figures 4C–F) and lung-derived ILC2 (Figures 4G–J) were treated *in vitro* with IL-7, IL-2, IL-33 alone or with combinations of IL-7+IL-33 or IL-2+IL-33 for 24 hours. BODIPY FL C16 was then added 23 hours after cytokine stimulation, incubated for one hour and subsequently analyzed by flow cytometry (Figures 4C–J). Similarly to ILC2 analyzed *ex vivo* (Figures 4A, B), bone-marrow and lung-derived ILC2 treated with IL-7 or IL-2 alone display moderate exogenous FA intake, whereas IL-33 treated ILC2 exert a significant increase in FA acquisition (Figures 4C–J). Furthermore, bone marrow-derived ILC2 treated with the combination of IL-7 +IL-33 or IL-2+IL-33 significantly increased FA uptake when compared to IL-7, IL-2 or IL-33 alone (Figures 4C–F). Lung-derived ILC2 were also found to acquire more exogenous FAs when stimulated by IL-7+IL-33 compared to IL-7, or IL-33 alone, but no significant increase was observed comparing stimulations with IL-33 alone vs IL-2+IL-33 (Figures 4G–J). Collectively, these observations demonstrate that ILC2 are actively taking up FA from the environment at steady state, which is further reinforced by stimulation with IL-33 only as well as by synergistic activation with IL-7+IL-33 or IL-2+IL-33.

3.2 Activation of group 2 innate lymphoid cells induces increased storage of neutral lipids

To further analyze to which extent FA uptake correlates with storage of neutral lipids we optimized a flow-cytometry-based protocol, enabling the rapid quantification of neutral lipid storage by ILC2. First, lung ILC2 were sort-purified from mice challenged intranasally with PBS as control or IL-33 for three consecutive days and were then stained *ex vivo* with BODIPY 493/503 for 20 minutes at 37 degrees Celsius. At steady state (PBS control treatment), ILC2 were found to store moderate levels of neutral lipids, while upon IL-33 treatment ILC2 considerably increased their neutral lipid storage (Figures 5A, B). To understand how cytokines known to drive ILC2 effector functions regulate neutral lipid storage, bone marrow- or lung-derived ILC2 were incubated with IL-7, IL-2 and IL-33 alone, or with combinations of IL-7+IL-33 or IL-2+IL-33 for 24 hours and subsequently stained with BODIPY493/503 (Figures 5C–J). Neutral lipid storage of bone marrow-derived ILC2 (Figures 5C–F) or lung-derived ILC2 (Figures 5G–J) treated with IL-7 or IL-2 alone was low but considerably increased in the presence of IL-33 (Figures 5C–J). Furthermore, combined cytokine treatment with IL-2+IL-33 significantly increased the accumulation of neutral lipids compared to stimulations with IL-2 or IL-33 alone in bone marrow-derived ILC2 (Figures 5E, F) as well as lung-derived ILC2 (Figures 5I, J). In contrast, no significant elevation of neutral lipid storage was observed in bone marrow-derived ILC2 (Figures 5C, D) as well as lung-derived ILC2 (Figures 5G, H) when comparing treatments of IL-33 alone vs IL-7+IL-33. However, the combined cytokine treatment of IL-7+IL-33 showed significantly higher levels of neutral lipid storage when compared to IL-7 alone (Figure 5C, D, G, H). These findings show that ILC2 at steady state harbor moderate levels of neutral lipids, actively increase their neutral lipid content upon treatment with IL-33, but especially when synergistically activated by IL-2+IL-33.

3.3 Activation of group 2 innate lymphoid cells induces mitochondrial β-oxidation of fatty acids

Studies investigating the impact of ILC2-specific deletion of DGAT1 (33) and PPARγ (33–35, 44), genes involved in lipid droplet formation (45) and lipid metabolism (46), respectively, as well as insights gained by pharmacological inhibition of Cpt1a through Etomoxir in *in vitro* and *in vivo* assays (32, 39) led to the conclusion that lipid metabolism constitutes a significant driver of pathogenic ILC2 function in allergic airway inflammation. These insights were further substantiated by the observations that PPARγ deletion impacts mitochondrial activities of ILC2 (35) and that FA supplementation of ILC2 cultures increases oxygen consumption rates (OCR) (33). However, it remains poorly defined to which extent FAs taken up from the extracellular environment or catabolized from stored triglyceride (TG) pools serve as a critical energy source and mechanistic driver for ILC2 proliferation and type 2 cytokine production. We therefore developed a rapid and easily applicable flow cytometry-based assay that enables direct analysis of mitochondrial β-oxidation levels of FAs in living ILC2 *ex vivo* and *in vitro* utilizing a recently developed reagent referred to as FAOBlue (47). FAOBlue is a coumarin dye coupled to a nonanoic acid (C9), which is protected by an acetoxymethyl ester, showing no fluorescence at 405 nm. FAOBlue can simply enter cells as it is permeable to the cell membrane. Upon cytosolic localization the acetoxymethyl ester is hydrolyzed by intracellular esterases, providing the free FA type of FAOBlue, which is further converted to an acyl-CoA form and thereby incorporated into the FAO pathway. Subsequently, acyl-CoA-type FAOBlue is then degraded by three FAO cycles to non-fluorescent coumarin possessing a propionic acid (C3). Then after the 4th FAO cycle degradation, the coumarin dye is released from the propionic acid. The released coumarin dye derived from FAO cycles exerts strong blue fluorescence excited by 405 nm, allowing sensitive detection of FAO activity in living cells.

We first applied FAOBlue to assess the extent by which ILC2 use mitochondrial FAO at steady state compared to IL-33-induced

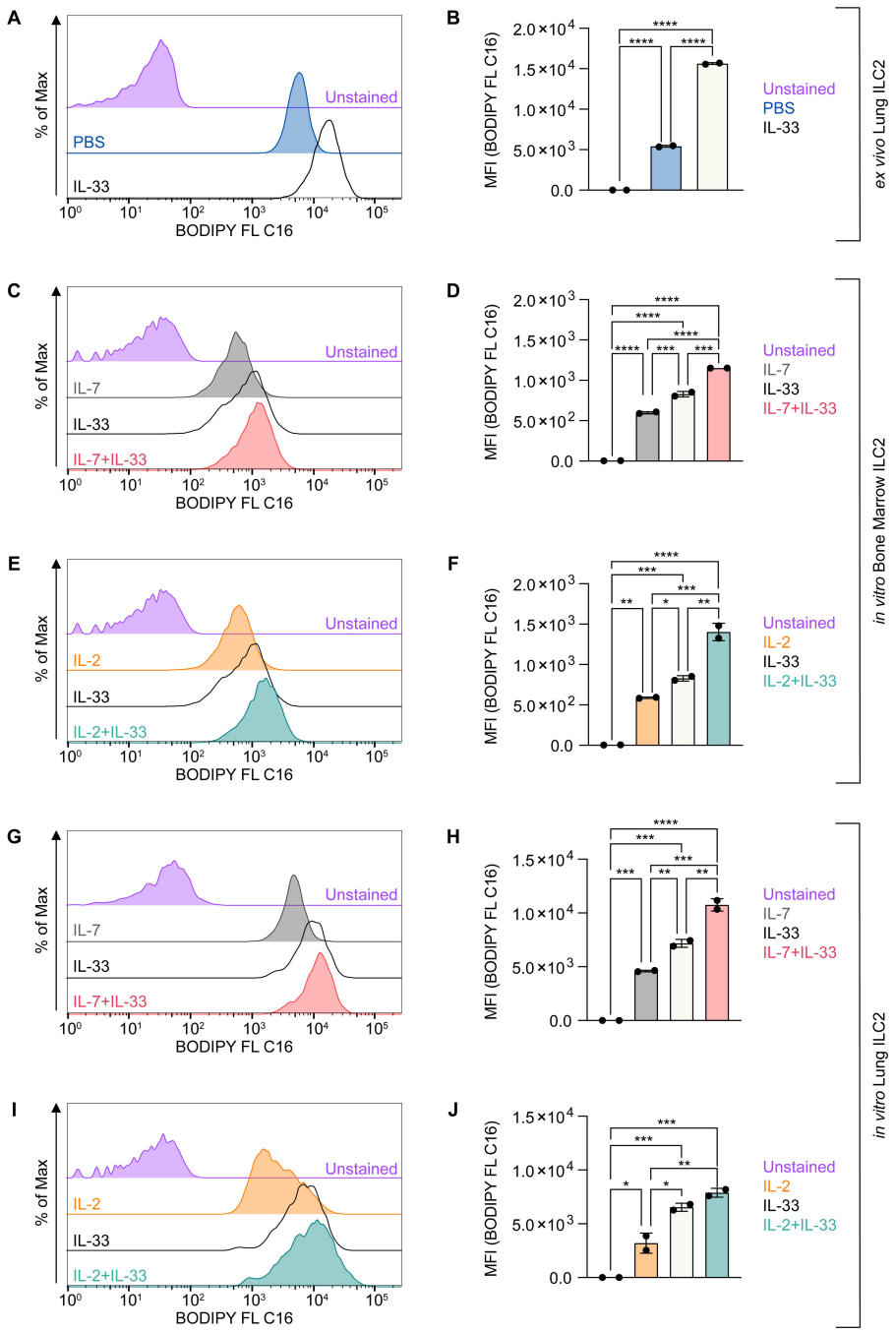

FIGURE 4
ILC2 increase fatty acid uptake upon stimulation with activating cytokines. **(A, B)** Mice were treated intranasally with either PBS as control or with 250 ng of IL-33 for three consecutive days. Two days after the last treatment, lungs were collected and group 2 innate lymphoid cells (ILC2) were sort-purified and subsequently incubated with BODIPY FL C16 for one hour to assess capacity of lipid uptake by flow cytometric analysis (MFI, geometric mean fluorescence intensity). Bone marrow-derived **(C–F)** or lung-derived **(G–J)** ILC2 were stimulated with either IL-7 only, IL-33 only, or a combination of IL-7 and IL-33 **(C, D, G, H)** or IL-2 only, IL-33 only, or a combination of IL-2 and IL-33 **(E, F, I, J)**. The data representing the IL-33 stimulation is the same for **(C–J)**. All cytokines were applied at 10 ng/mL. BODIPY FL C16 was added after 23 hours of cytokine stimulation and incubated for one hour to assess capacity of lipid uptake by flow cytometric analysis. ILC2 that were not incubated with BODIPY FL C16 served as negative control (Unstained). Data are shown as average ± standard deviation (SD). Statistical analysis was performed using one-way ANOVA followed by Tukey's multiple comparisons test ($p < 0.05$ = *, $p < 0.01$ = **, $p < 0.001$ = ***, $p < 0.0001$ = ****).

airway inflammation *in vivo* (Figures 6A, B). To this end mice were challenged intranasally with PBS or IL-33 for three consecutive days. Pulmonary ILC2 were sort-purified 48 hours after the last treatment and stained *ex vivo* with FAOBlue dye for 1 hour at 37 degrees Celsius (Figures 6A, B). At steady state, pulmonary ILC2 displayed moderate levels of FAO while intranasal IL-33 treatment led to a significant increase of FAO by ILC2 (Figures 6A, B). To investigate how cytokines known to drive ILC2 effector functions regulate FAO,

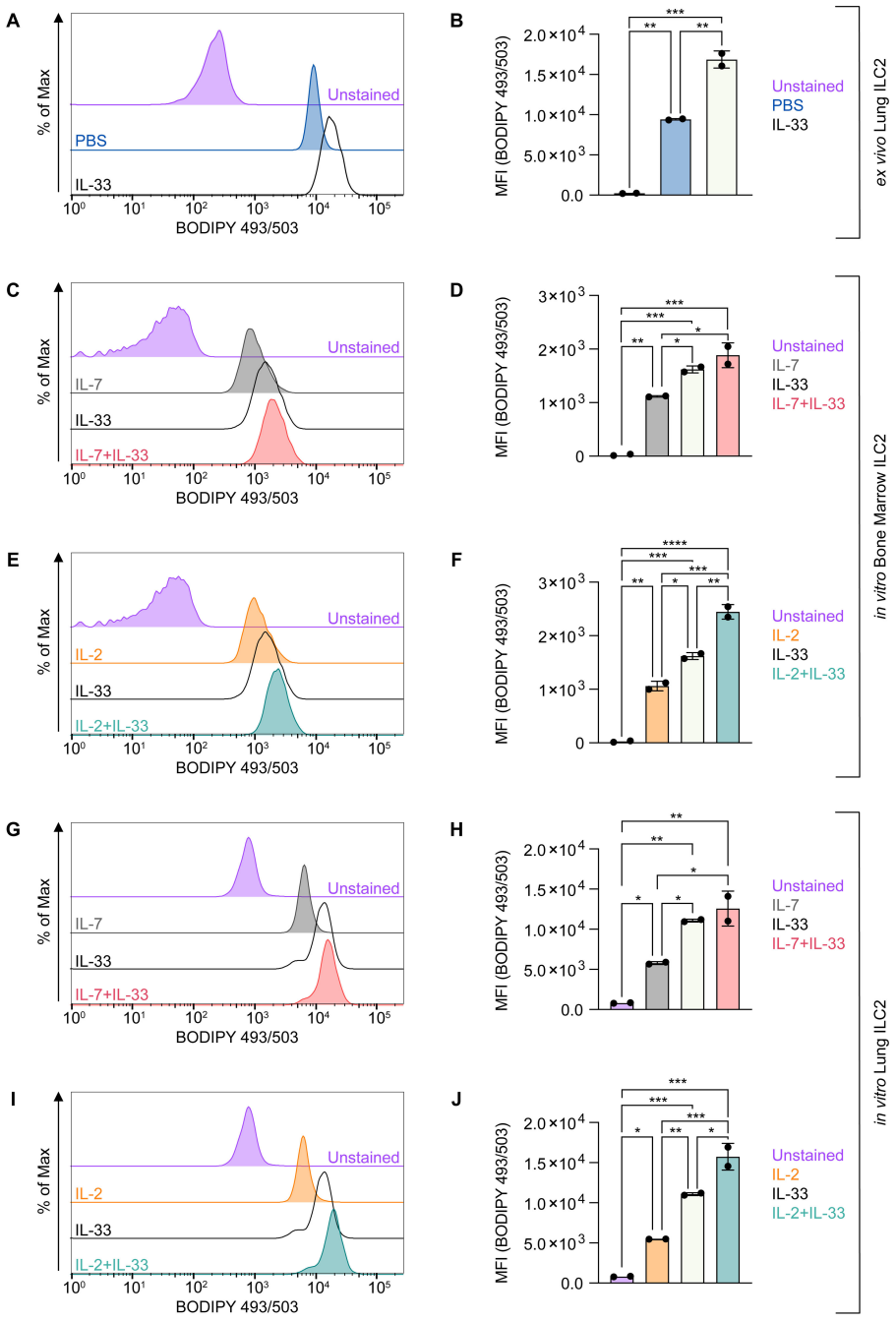

FIGURE 5
ILC2 increase neutral lipid storage upon stimulation with activating cytokines. **(A, B)** Mice were treated intranasally with either PBS as control or with 250 ng of IL-33 for three consecutive days. Two days after the last treatment, lungs were collected and group 2 innate lymphoid cells (ILC2) were sorted and subsequently incubated with BODIPY 493/503 for 20 minutes to assess capacity of neutral lipid storage by flow cytometric analysis (MFI, geometric mean fluorescence intensity). Bone marrow-derived **(C–F)** or lung-derived **(G–J)** ILC2 were stimulated with either IL-7 only, IL-33 only, or a combination of IL-7 and IL-33 **(C, D, G, H)** or IL-2 only, IL-33 only, or a combination of IL-2 and IL-33 **(E, F, I, J)**. The data representing the IL-33 stimulation is the same for **(C–J)**. All cytokines were applied at 10 ng/mL. BODIPY 493/503 was added after 24 hours of cytokine stimulation and incubated for 20 minutes to assess capacity of neutral lipid storage by flow cytometric analysis. ILC2 that were not incubated with BODIPY 493/503 served as negative control (Unstained). Data are shown as average ± standard deviation (SD). Statistical analysis was performed using one-way ANOVA followed by Tukey's multiple comparisons test ($p < 0.05$ = *, $p < 0.01$ = **, $p < 0.001$ = ***, $p < 0.0001$ = ****).

bone marrow- or lung-derived ILC2 were incubated with IL-7, IL-2 and IL-33 alone or with combinations of IL-7+IL-33 or IL-2+IL-33 for 24 hours and were subsequently stained with FAOBlue (Figures 6C–J). FAO by bone marrow-derived ILC2 (Figures 6C–F) or lung-derived ILC2 (Figures 6G–J) treated with IL-7 or IL-2 alone was moderate but considerably increased in the presence of IL-33 (Figures 6C–J). Furthermore, combined cytokine treatment with IL-2 +IL-33 significantly increased FAO compared to stimulations with

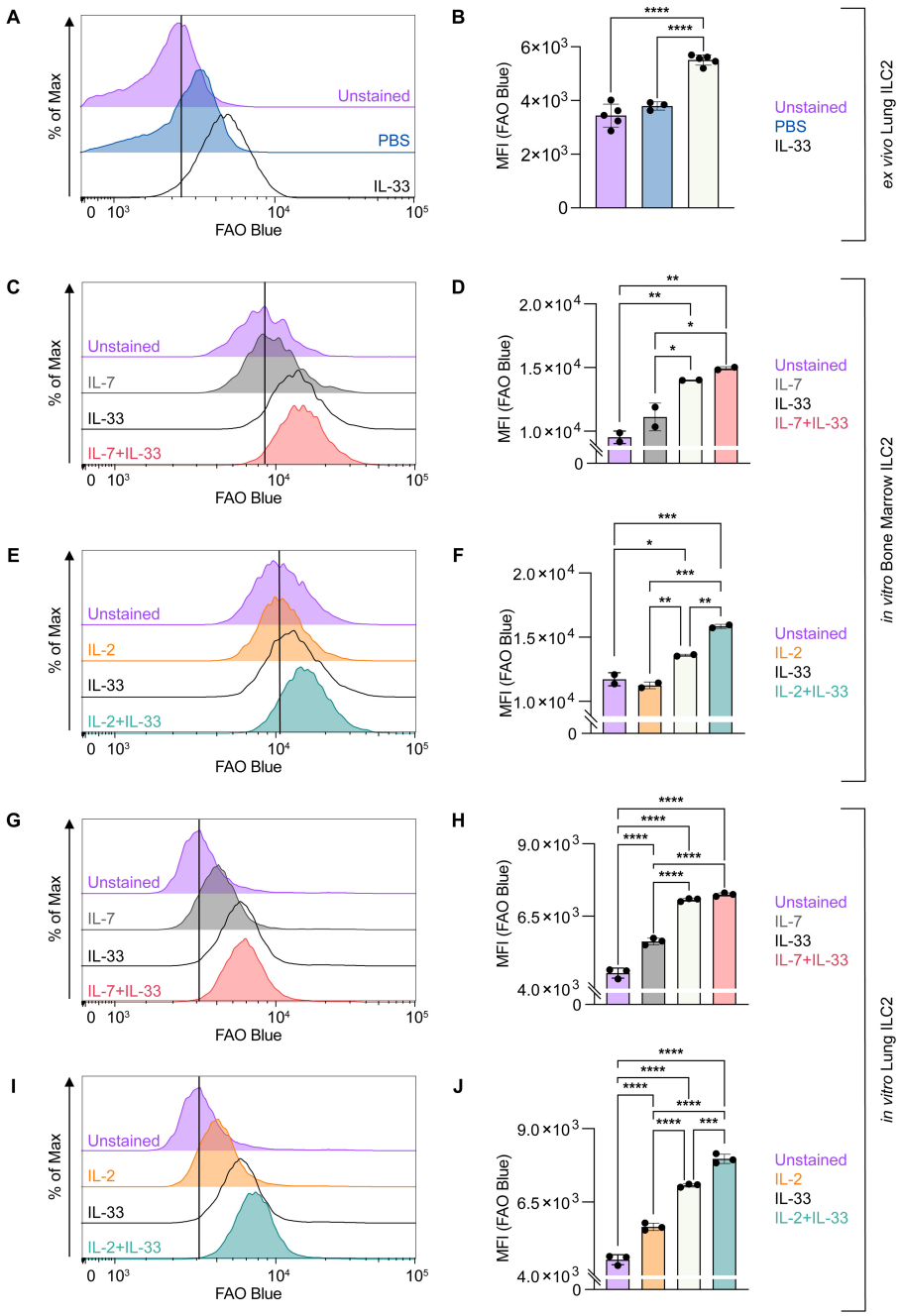

FIGURE 6
ILC2 increase fatty acid oxidation upon stimulation with activating cytokines. **(A, B)** Mice were treated intranasally with either PBS as control or with 250 ng of IL-33 for three consecutive days. Two days after the last treatment, lungs were collected, and group 2 innate lymphoid cells (ILC2) were sorted and subsequently stained with FAO Blue for one hour to assess capacity of fatty acid oxidation by flow cytometric analysis (MFI, geometric mean fluorescence intensity). Bone marrow-derived **(C–F)** or lung-derived **(G–J)** ILC2 were stimulated with either IL-7 only, IL-33 only, or a combination of IL-7 and IL-33 **(C, D, G, H)** or IL-2 only, IL-33 only, or a combination of IL-2 and IL-33 **(E, F, I, J)**. The data representing the IL-33 stimulation is the same for **(C–J)**. All cytokines were applied at 10 ng/mL. After 24 hours of cytokine stimulation cells were incubated for one hour with FAO Blue and analyzed using flow cytometry. ILC2 that were not incubated with FAO Blue served as negative control (Unstained). Data are shown as average ± standard deviation (SD). Statistical analysis was performed using one-way ANOVA followed by Tukey's multiple comparisons test ($p < 0.05$ = *, $p < 0.01$ = **, $p < 0.001$ = ***, $p < 0.0001$ = ****).

IL-2 or IL-33 alone in bone marrow-derived ILC2 (Figures 6E, F) as well as lung-derived ILC2 (Figures 6I, J). In contrast, no significant elevation of FAO was observed in bone marrow-derived ILC2 (Figures 6C, D) as well as lung-derived ILC2 (Figures 6G, H) when comparing treatments of IL-33 alone vs IL-7+IL-33. However, the combined cytokine treatment of IL-7+IL-33 showed significantly higher levels of FAO when compared to IL-7 alone (Figure 6C, D, G, H). These findings demonstrate that FAO by ILC2 is low, significantly increases by stimulation with IL-33, but were found to be highest when ILC2 were synergistically activated by IL-2+IL-33.

3.4 Cytokine stimulation of group 2 innate lymphoid cells induces specific morphologies of neutral lipid droplets

ILC2 are a rare, non-adherent type of innate immune cell, making them an excellent candidate for flow cytometric assays and analysis. However, these two factors make ILC2 samples difficult to prepare for microscopy and therefore visualization of intracellular morphologies of ILC2 has been largely unexplored. The majority of ILC2 images that exist are from the ImageStream platform where a fluorescent 2D projection of a 3-dimensional cell is used primarily for qualitative purposes (33, 40). Furthermore, microscopy sample preparation of non-adherent cells traditionally implements either the use of a cytospin which risks bursting the cell membrane or disrupting intracellular architecture (48), or extracellular matrix coverslip coatings that influence protein expression at the cell membrane to promote cell adhesion (49). In Section 3.2, using flow cytometry, we demonstrated that activation of ILC2 induces increased storage of neutral lipids, but these assays did not provide detailed insights of these intracellular lipid pools. To elucidate the morphologies and distribution of neutral lipids in ILC2, we developed a novel sample preparation protocol for acquiring high-resolution 3D images for lipid droplet quantification that conserves ILC2 morphology across equipment platforms.

First, lung ILC2 were sort-purified from mice challenged intranasally with PBS as control or IL-33 for three consecutive days and were then stained *ex vivo* with BODIPY 493/503 for 30 minutes at 37˚C prior to fixation, mounting, and imaging (Figure 7A). These microscopy images were analyzed in software that allowed for 3D reconstruction of the neutral lipid fluorescent

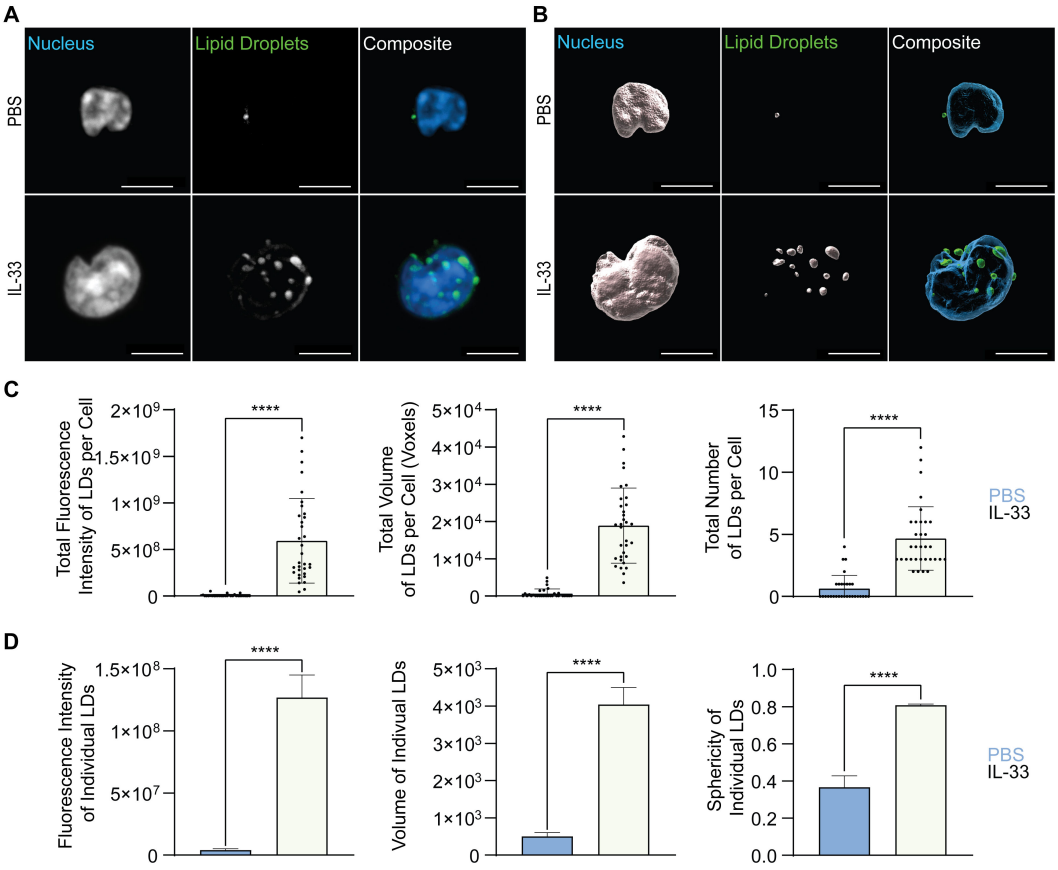

FIGURE 7
Allergic airway inflammation increases the lipid droplet number and size in pulmonary ILC2. Mice were treated intranasally with either PBS as control or with 250 ng of IL-33 for three consecutive days. Two days after the last treatment, lungs were collected, and group 2 innate lymphoid cells (ILC2) were sorted by flow cytometry and labelled with Hoechst 33342 to visualize the nucleus (blue) and BODIPY 493/503 to visualize neutral lipid storage **(A, B)**. Confocal images **(A)** and 3D fluorescence reconstructions from Imaris **(B)** are shown (PBS - top row; IL-33 treatments - bottom row). Confocal images are displayed as a maximum intensity projection of approximately 10-20 frames (5-10 µm depth) produced in ImageJ. Images are representative from 3 independent experiments, scale bars represent 5 µm. **(C)** Quantification of the total fluorescence intensity (left), total volume (middle), and total number (right) of neutral lipid droplets cumulatively per cell. Fluorescence and morphology metrics were taken from individual neutral lipid droplets and were added together based on cell of origin and then by intranasal challenge. ILC2 that underwent PBS intranasal challenge are shown in blue (n = 30) and those treated with IL-33 are shown in off-white (n = 33). **(D)** Quantification of the total fluorescence intensity (left), total volume (middle), and sphericity (right) of individual neutral lipid droplets. Fluorescence and morphology metrics were taken from the same individual neutral lipid droplets shown in **(C)** and compiled based on intranasal challenge alone; PBS (n = 39) and IL-33 (n = 154). The data representing the IL-33 stimulation is the same for A-D. Data are represented as average ± standard deviation (SD) where n = number of cells **(C)** or average ± standard error of measurement (SEM) where n = number of neutral lipid droplets **(D)**. Statistical significance (*p*-values) was calculated using unpaired two-tailed Student's t-test ($p < 0.0001$ = ****).

signal from which fluorescence intensity and morphology metrics could be extracted (Figure 7B). At steady state (PBS control treatment), ILC2 were shown to store low total fluorescence intensity of neutral lipids concurrent with the flow cytometry data (Figure 5B), explained by a low total volume and number of lipid droplets (LDs) per cell (Figure 7C). When treated with IL-33, the total neutral lipid fluorescence intensity, total volume, and number of LDs per cell dramatically increased (Figure 7C).

To further understand how cytokines known to drive ILC2 effector functions regulate neutral lipid storage, *in vitro* bone marrow-derived ILC2 were incubated with IL-7, IL-2, or IL-33 alone, or with combinations of IL-7+IL-33 or IL-2+IL-33 for 24 hours. These cells were subsequently stained with BODIPY493/503, fixed, mounted, and imaged (Figures 8A, 9A) followed by 3D image analysis (Figures 8B, 9B). Similarly to the *ex vivo* lung-derived ILC2, the total fluorescence intensity, total volume, and number of all neutral LDs per cell presented by *in vitro* bone marrow-derived ILC2 treated with IL-7 alone were significantly lower in comparison to all other cytokine treatments (Figures 8A–C). Marked elevation in the total fluorescence intensity, total volume, and number of all LDs in the presence of IL-33 alone, as well as with the combined treatment of IL-7+IL-33 was observed (Figures 8A–C). In contrast,

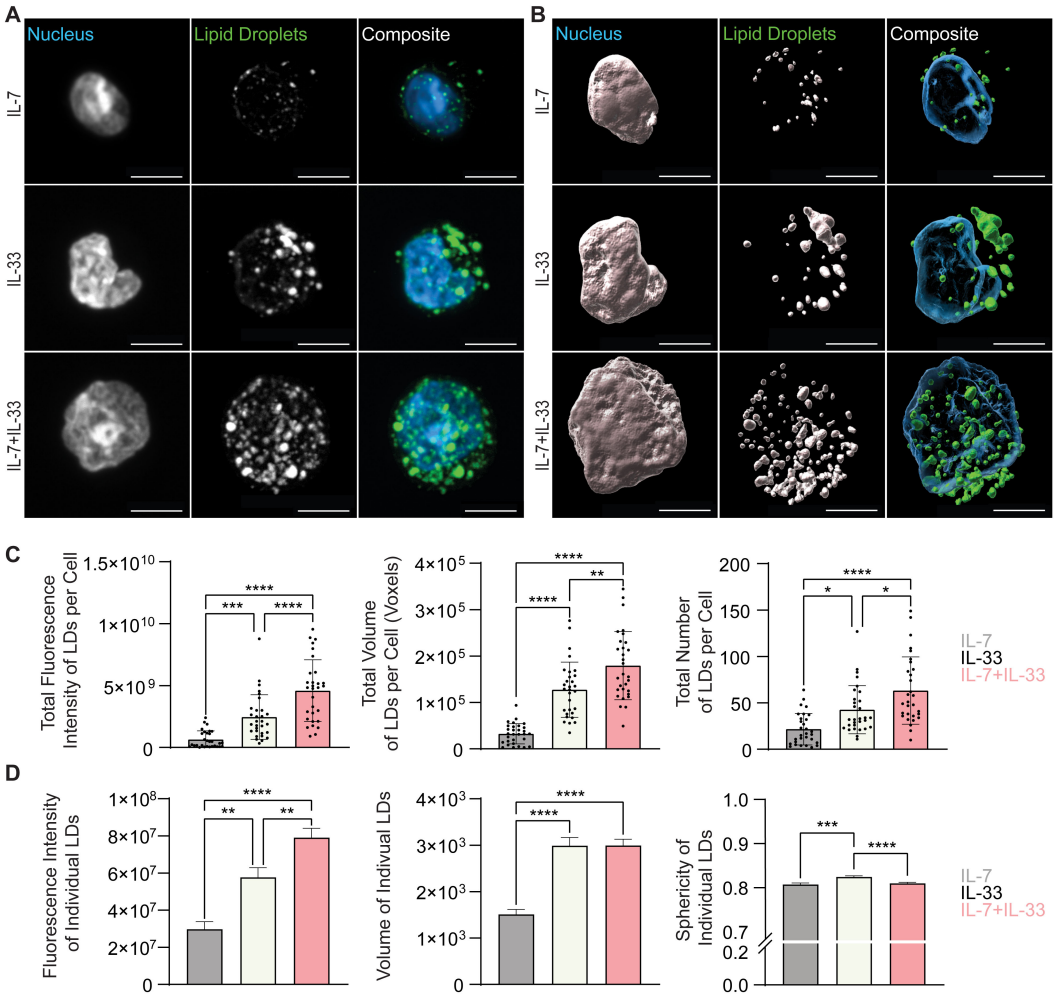

FIGURE 8
In vitro stimulation of ILC2 with combinations of IL-7 and IL-33 changes the neutral lipid droplet size and number. Bone marrow-derived group 2 innate lymphoid cells (ILC2) were stimulated for 24 hours with either IL-7 only, IL-33 only, or a combination of IL-7 and IL-33 (all cytokines were applied at 10 ng/mL) and labelled with Hoechst 33342 to visualize the nucleus (blue) and BODIPY 493/503 to visualize neutral lipid storage **(A, B)**. Confocal images **(A)** and 3D fluorescence reconstructions from Imaris **(B)** are shown. Confocal images are displayed as a maximum intensity projection of approximately 10-20 frames (5-10 µm depth) produced in ImageJ. Images are representative from 3 independent experiments, scale bars represent 5 µm. **(C)** Quantification of the total fluorescence intensity (left), total volume (middle), and total number (right) of neutral lipid droplets cumulatively per cell. Fluorescence and morphology metrics were taken from individual neutral lipid droplets and were added together based on cell of origin and then by cytokine treatment. ILC2 were treated with either IL-7 (grey, n = 30), IL-33 (off-white, n = 30), or IL-7+IL-33 (pink, n =30) for 24 hours prior to imaging. **(D)** Quantification of the total fluorescence intensity (left), total volume (middle), and sphericity (right) of individual neutral lipid droplets. Fluorescence and morphology metrics were taken from the same individual neutral lipid droplets shown in **(C)** and were compiled based on cytokine treatment alone; IL-7 (n = 637), IL-33 (n = 1,267), or IL-7+IL-33 (n = 1,569). The data representing the IL-33 stimulation is the same for **(A–D)**. Data are represented as average ± standard deviation (SD) where n = the number of cells **(C)** or average ± standard error of measurement (SEM) where n = number of neutral lipid droplets **(D)**. Statistical significance (*p*-values) was calculated using ordinary one-way ANOVA and *post-hoc* Tukey's multiple comparison tests ($p < 0.05$ = *, $p < 0.01$ = **, $p < 0.001$ = ***, $p < 0.0001$ = ****).

treatment of ILC2 with IL-2 only already led to high levels of total fluorescence intensity, total volume, and number of all LDs (Figures 9A–C). In addition, when compared to stimulations by IL-2 alone, no significant changes in total fluorescence intensity, total volume, or number of all LDs per cell compared to treatments with IL-33, or a combination of IL-2+IL-33 (Figures 9A–C) were observed.

Microscopy is a very time-consuming process, easily susceptible to sample heterogeneity, where the target sample number is approximately 30 cells per condition. To overcome these obstacles, we further investigated the morphological neutral LD diversity as an entire population outside the confines of individual cell analysis. Individual neutral LDs in pulmonary ILC2 isolated from naïve mice (PBS control treatments), exhibited a small volume, were irregularly shaped, and low in fluorescence intensity (Figure 7D). In contrast, in lung ILC2 isolated from IL-33 treated animals, the individual neutral LDs significantly increased in volume, became more spherical, and subsequently increased in fluorescence intensity (Figure 7D).

When analyzing bone marrow-derived ILC2 treated with distinct cytokines *in vitro*, we revealed that the fluorescence intensity and volume of the individual neutral LDs is low in cells

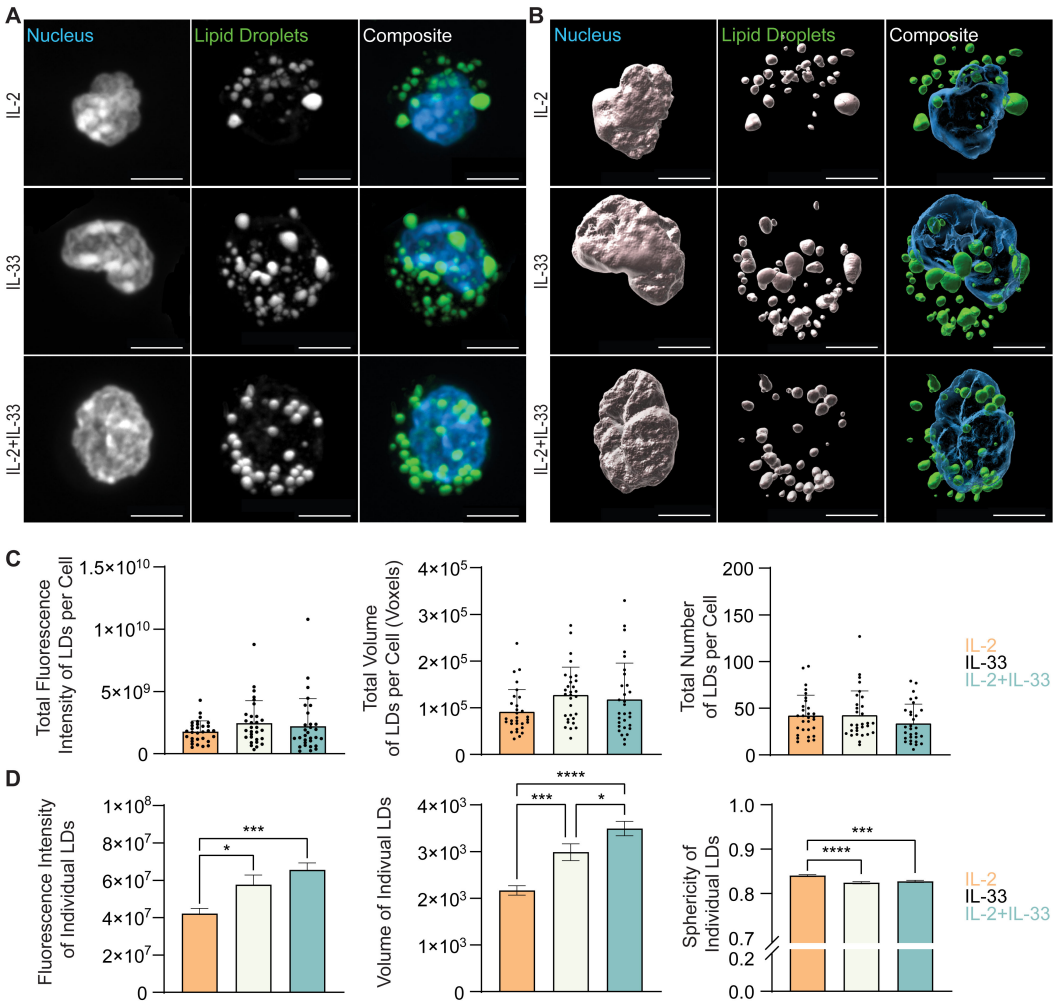

FIGURE 9
In vitro stimulation of ILC2 with combinations of IL-2 and IL-33 changes the neutral lipid droplet volume. Bone marrow-derived group 2 innate lymphoid cells (ILC2) were stimulated for 24 hours with either IL-2 only, IL-33 only, or a combination of IL-2 and IL-33 (all cytokines were applied at 10 ng/mL) and labelled with Hoechst 33342 to visualize the nucleus (blue) and BODIPY 493/503 to visualize neutral lipid storage **(A, B)**. Confocal images **(A)** and 3D fluorescence reconstructions from Imaris **(B)** are shown. Confocal images are displayed as a maximum intensity projection of approximately 10-20 frames (5-10 µm depth) produced in ImageJ. Images are representative from 3 independent experiments, scale bars represent 5 µm. **(C)** Quantification of the total fluorescence intensity (left), total volume (middle), and total number (right) of neutral lipid droplets cumulatively per cell. Fluorescence and morphology metrics were taken from individual neutral lipid droplets and were added together based on cell of origin and then by cytokine treatment. ILC2 were treated with either IL-2 (orange, n = 30), IL-33 (off-white, n = 30), or IL-2+IL-33 (teal, n = 30) for 24 hours prior to imaging. **(D)** Quantification of the total fluorescence intensity (left), total volume (middle), and sphericity (right) of individual neutral lipid droplets. Fluorescence and morphology metrics were taken from the same individual neutral lipid droplets in **(C)** and compiled based on cytokine treatment alone; IL-2 (n = 1,266), IL-33 (n = 1,267), or IL-2+IL-33 (n = 1,015). The data representing the IL-33 stimulation is the same for **(A–D)**. Data are represented as average ± standard deviation (SD) where n = the number of cells **(C)** or average ± standard error of measurement (SEM) where n = number of neutral lipid droplets **(D)**. Statistical significance (*p*-values) was calculated using ordinary one-way ANOVA and *post-hoc* Tukey's multiple comparison tests ($p < 0.05$ = *, $p < 0.001$ = ***, $p < 0.0001$ = ****).

10.3389/fimmu.2024.1493848

treated with IL-7 (Figure 8D) or IL-2 alone (Figure 9D) but considerably increased when treated with IL-33. Furthermore, ILC2 treated with cytokine combinations IL-7+IL-33 or IL-2+IL-33 markedly increased the fluorescence intensity as well as the volume of individual LDs compared to stimulations with either IL-7 (Figure 8D) or IL-2 (Figure 9D) alone. While a significant elevation in neutral LD fluorescence intensity was observed in ILC2 treated with IL-7+IL-33 compared to IL-33 only stimulations, no changes with regards to LD volume were found (Figure 8D). Moreover, while no significant differences in neutral LD fluorescence intensity were observed in ILC2 stimulated with IL-33 alone versus IL-2+IL-33, a significant elevation in LD volume was observed between the two treatment groups (Figure 9D). In addition, the neutral LDs of ILC2 stimulated with IL-33 alone were closer to a perfect sphere compared to treatments with IL-7 alone or IL-7+IL-33 (Figure 8D). In contrast, the LDs in ILC2 activated with IL-2 only were the closest to a perfect sphere compared to stimulations with IL-33 alone or IL-2+IL-33 (Figure 9D). These findings demonstrate that the cytokines known to drive ILC2 effector functions play a significant role in determining morphology of neutral LDs.

3.5 Cytokine stimulation of group 2 innate lymphoid cells induces a shift in the distribution of neutral lipid droplet morphology

When the individual neutral LD datapoints are compiled into a single value to represent an entire cell, potential information is lost. However, additional valuable insight can be uncovered by investigating the distribution of the datapoints within each cell, as opposed to only taking an average of analyzed values. To address this query, we binned the volume and sphericity (Table 3) of individual LDs for each cell into categories and took the average of each category's frequency. The LD volumes were separated into large, intermediate, and small sized droplets, and the sphericity of each lipid droplet was described as either spherical, intermediate, or irregularly shaped.

When comparing the frequencies of each morphology metric between cytokine stimulations *in vitro*, there is a shift in the morphology of neutral LDs between the different cytokines (Table 3). IL-7 holds the lowest average proportion of large neutral LDs compared to other cytokine stimulations at 10% of the population, whereas IL-2+IL-33 has the highest average proportion at 24%. This correlates with the inverse as well, where IL-7 holds the highest average proportion of small neutral LDs at 57% of the population, and IL-2+IL-33 has the smallest average proportion at 27%. There is a marked shift in the distribution of the LD volume between either IL-7 or IL-2 alone and the respective combination treatment with IL-7+IL-33 or IL-2+IL-33 (Table 3). The average proportion of large neutral LDs in IL-2 and IL-7 nearly doubles when combined with IL-33, and the average proportion of small neutral LDs specifically in IL-2 nearly halves (Table 3). This distribution data sheds light on a trend that the specific combination of IL-7+IL-33 produces both large and small LDs, whereas the IL-2+IL-33 treated LDs shift towards larger and intermediate-sized LDs, and away from smaller LDs as observed in the representative microscopy images (Figures 8A, B, 9A, B). Furthermore, the neutral LDs in IL-7 have the most intermediate and irregularly shaped LDs, whereas the LDs in IL-2 have the most spherical (Table 3). Interestingly, the LDs in IL-7 are mostly irregularly or intermediately shaped and shift towards being more spherical upon activation with IL-7+IL-33, whereas LDs in IL-2 alone exhibit a shift to become less spherical with IL-33 activation (Table 3). In both LD volume and sphericity, IL-33 is shown to be a true median between the solitary treatments of IL-7 and IL-2 and the activation of ILC2 with the combinations of IL-7+IL-33 and IL-2+IL-33 (Table 3). The data acquired from the *ex vivo* dataset was not included in the distribution analysis due to the infrequent presence of neutral LDs in the PBS-treated ILC2. Taken together, these data demonstrate that each cytokine induces specific phenotypes in neutral LD storage that may be related to the catabolism and anabolism of LDs in ILC2.

TABLE 3 Distribution of neutral lipid droplet morphology.

Lipid Droplet Volume					
Bin Size	IL-7	IL-2	IL-33	IL-7+IL-33	IL-2+IL-33
Large (Above 5,000)	10	13	16	19	24
Intermediate (1,000 to 4,999)	33	36	46	48	49
Small (Below 1,000)	57	51	38	33	27
Lipid Droplet Sphericity					
Bin Size	IL-7	IL-2	IL-33	IL-7+IL-33	IL-2+IL-33
Spherical (Above 0.85)	42	59	51	49	56
Intermediate (0.7 to 0.84)	48	36	40	41	37
Irregular (Below 0.7)	10	5	9	10	7

The average distribution (in %) of lipid droplet volumes (top) and sphericity (bottom) per cell between each cytokine stimulation population. Lipid droplet volumes are categorized as large, intermediate, or small. Lipid droplet sphericity is categorized as spherical, intermediate, or irregular-shaped. Each row is color-coded to distinguish shifts in distribution where red indicates the lowest value in the row, yellow is median, and green is the highest value.

3.6 Activation of group 2 innate lymphoid cells increases the cell volume

Cell volume can be estimated using flow cytometry by investigating forward scatter (FSC) and side scatter (SSC) values, however these metrics are merely comparative without the application of beads with a known size. Fluorescence microscopy offers an advantage where cytosolic fluorescence or autofluorescence can be utilized to calculate the volume of a cell. Previous studies have qualitatively observed that

ILC2 increase in cell volume following activation, but this has not been extensively quantified (50). Increases in cell volume require the synthesis of phospholipids for cell membrane production, which have been traced from exogenous FAs transiently stored in neutral LDs in ILC2 (33).

The cells from which the neutral LD analysis was performed in Sections 3.4 and 3.5 were also utilized for cell volume analysis. At steady state (PBS control treatment), *ex vivo* lung-derived ILC2 were shown to exhibit a very small cell volume which significantly increased when treated with IL-33 (Figure 10A). To further understand how cytokines known to drive ILC2 effector functions regulate cell volume, we analyzed *in vitro* bone marrow-derived ILC2 in the same conditions outlined in previous sections (Sections 3.1–3.5). Similarly to the *ex vivo* lung-derived ILC2, the cell volume presented by *in vitro* bone marrow-derived ILC2 treated with IL-7 alone were significantly smaller in comparison to all other cytokine treatments (Figure 10B). A dramatic increase in cell volume was observed in the presence of IL-33 alone, as well as with the combined treatment of IL-7+IL-33 (Figure 10B). This trend held true for ILC2 treated with IL-2 alone, which were significantly smaller in volume compared to all other cytokine treatments (Figure 10C). Concurrently, a significant increase in cell volume was observed in the presence of IL-33 alone, and with the combined treatment of IL-2+IL-33 (Figure 10C). In both cases the cell volume of either IL-7 alone or IL-2 alone doubled or nearly doubled when combined with IL-33. These data clearly demonstrate that cell volume is inextricably linked to ILC2 activation.

3.7 Neutral lipid droplet volume, number, and cell volume are correlated in group 2 innate lymphoid cells

There are many metrics that can be used to describe the diversity of LDs such as: volume, number, shape, and the size of the cell in which they reside. Large volumes of LDs have been correlated with large cell sizes in adipocytes (51) and the volume of LDs has been shown to correlate with the number of LDs in fibroblasts (52). We established in Section 3.5 that the distribution of neutral LD morphology is specific to different cytokine stimulations, but the intricacies of the relationships between these metrics have been unexplored in ILC2.

To investigate the potential relationships between cell volume, total lipid volume, and number of LDs, we performed correlation analysis between each of these metrics for each cytokine stimulation (Table 4). The data from Sections 3.4 – 3.6 were collated such that each cell volume corresponded with a total neutral lipid volume and neutral LD number. The strongest correlation among all the tested conditions was between the total volume of neutral lipids and the number of neutral LDs. Both IL-2 alone and IL-2+IL-33 exhibited a strong correlation between total volume and the number of neutral LDs, whereas IL-7 alone and IL-7+IL-33 exhibited a moderate correlation (Table 4). These data suggest that the synergy between IL-2 and IL-33 have the greatest impact on how neutral lipids are stored, as suggested in Section 3.5 (Table 3).

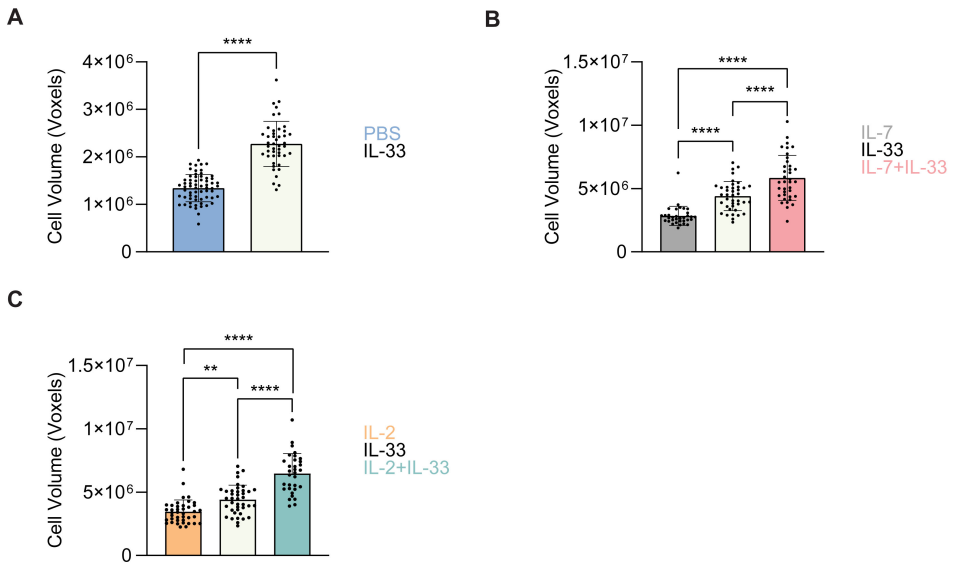

FIGURE 10
ILC2 increase in cell volume upon stimulation with activating cytokines. Quantification of the total cell volume using cytosolic BODIPY (493/503) fluorescence from confocal images. **(A)** group 2 innate lymphoid cells (ILC2) that underwent PBS intranasal challenge for three consecutive days are shown in blue (n = 30) and those treated with 250 ng/mL of IL-33 are shown in off-white (n = 33). **(B)** ILC2 were treated with either IL-7 (grey, n = 30), IL-33 (off-white, n = 30), or IL-7+IL-33 (pink, n = 30) for 24 hours prior to imaging. **(C)** ILC2 were treated with either IL-2 (orange, n = 30), IL-33 (off-white, n = 30), or IL-2+IL-33 (teal, n = 30) for 24 hours prior to imaging. All cytokines were administered at 10 ng/mL. Data are represented as average ± standard deviation (SD) where n = number of cells. The data representing the IL-33 stimulation is the same for **(B, C)**. **(A)** Statistical significance (*p*-values) was calculated using unpaired two-tailed Student's t-test. **(B, C)** Statistical significance (*p*-values) was determined by applying ordinary one-way ANOVA and *post-hoc* Tukey's multiple comparison tests ($p < 0.01$ = ** and $p < 0.0001$ = ****).

10.3389/fimmu.2024.1493848

TABLE 4 Correlation analysis between morphology metrics.

Cytokine Treatment	LD Volume by LD Number	LD Volume by Cell Volume	LD Number by Cell Volume
ex vivo PBS	0.959*	0.479	0.461
ex vivo IL-33	0.081	0.348	0.063
IL-7	0.569	0.033	0.353
IL-2	0.773	0.606	0.532
IL-33	0.275	0.193	0.352
IL-7+IL-33	0.511	0.714	0.412
IL-2+IL-33	0.766	-0.11	-0.075

The values for total neutral lipid droplet (LD) volume per cell, total number of neutral lipid droplets per cell, and the volume of each cell were used to calculate correlating factors. Each cell is color-coded to distinguish significant correlation coefficients where grey shows no correlation (below 0.3), red indicates a low correlation (0.3-0.5), yellow is moderately correlated (0.5-0.7), and green is highly correlated (0.7-0.9). Values above 0.9 are very highly correlated and indicated with an asterisk.

The *ex vivo* lung-derived ILC2 at steady state (PBS) exhibited the strongest correlation between the total volume and the number of neutral LDs, where the low volume of neutral lipids and low number of droplets was very consistent (Figure 7). IL-7+IL-33 presented with the strongest correlation between total volume of neutral lipids and the cell volume, where there were consistently high volumes of neutral lipids and large cell volumes (Figures 8, 10). A moderate correlation between total neutral lipid volume and cell volume was observed in IL-2 alone, whereas the *ex vivo* lung-derived ILC2 at both steady state (PBS) and with IL-33 activation exhibited a low correlation. Nearly every cytokine stimulation including the *ex vivo* naïve lung-derived ILC2 at steady state showed a low correlation between the number of neutral LDs and the cell volume (Table 4). These findings show that depending on how much neutral lipid content is present, ILC2 will selectively distribute their neutral lipid storage regardless of cytokine stimulation.

4 Discussion

ILC2 are vital to tissue barrier integrity, providing immunological protection by orchestrating innate and adaptive immune process as well as wound healing and tissue restoration. Recent data has implicated metabolic factors, such as lipid metabolism, that influence the role of ILC2 in airway inflammation and lung homeostasis (32, 33). The interplay of the immune system and lipid metabolism is highly complex, and the rarity of ILC2 *in situ* demands improved methodologies to study the intricacies of these relationships during type 2 immune responses and its associated pathologies. Here, we investigated the exogenous uptake of fatty acids (FAs), the transient storage of those FAs in neutral lipid droplets (LDs), and the utilization of FAs by mitochondrial fatty acid β-oxidation (FAO) for energy production to elucidate the phenotypes and effector functions associated with ILC2 lipid metabolism.

Our novel methods described here demonstrate that the utilization of lipid metabolism is markedly elevated upon ILC2 activation, revealing consistent findings comparing lung- and bone marrow-derived ILC2, as well as *ex vivo* and *in vitro* cultures. Our study reveals that ILC2 take up minimal levels of FAs, harbor low quantities of neutral LDs, and utilize FAO at a minimum rate during steady state (PBS controls, or stimulations with IL-7, or IL-2 only), but gradually increase lipid metabolism upon activation with IL-33 regardless of ILC2 origin. Concurrently, ILC2 from various tissues have been observed to take up FA at steady state (32) and were shown to considerably increase FA uptake upon activation (33, 34). Although the acquisition of *ex vivo* samples is necessary to capture the parameters of lipid metabolism during ILC2-mediated airway inflammation, the cost of acquiring these samples is high and detailed implications of single cytokine stimulations cannot be deciphered. We therefore made use of our efficient *in vitro* cell culture models of primary ILC2 (41), and our findings align well with previously reported observations demonstrating that FA uptake and lipid storage increases in ILC2 stimulated by IL-7+IL-33 (33). However, our study extends these findings, demonstrating increased FA uptake and storage upon stimulation with IL-2 alone as well as with the combination of IL-2+IL-33. Biologically, FAs are important for ILC2 proliferation and effector functions (33, 35, 53). Cell proliferation has a high energy demand; with increased proliferation following ILC2 activation we observe an increase in FA uptake, cell volume, and FAO.

A previous study demonstrated that cells prioritize phospholipid synthesis in the presence of glucose (54). In parallel, another study traced phospholipids in the membrane of activated ILC2 from exogenously acquired FAs (33). It is likely that in the early stages of ILC2 activation when glucose availability is high, FAs are utilized first for phospholipid synthesis resulting in a larger cell volume. As glucose levels decline, ILC2 may begin to breakdown stored or exogenous FA via β-oxidation as an energy source. In fact, during helminth infection, it has been reported that ILC2 metabolize exogenous FAs via FAO to fuel oxidative phosphorylation, which is necessary for ILC2 proliferation and cytokine production (32). Our study corroborates this data, supporting the notion that cell proliferation, cytokine production, FA uptake and storage, and FAO activity are all inextricably linked with ILC2 activation. The combination of IL-7 or IL-2 with IL-33 displayed the strongest increase in FA uptake and FAO. It is likely that this increase in FAO among strongly activated ILC2 provides a source of acetyl-CoA to help fuel the tricarboxylic acid (TCA) cycle and a source of NADH and $FADH_2$ to in turn fuel the respiratory chain, subsequently promoting pro-inflammatory ILC2 activity (53). Although there are other methods to measure FAO, such as the tracing of radiolabeled FAs, the Agilent Seahorse XF Palmitate Oxidation Stress Test, targeted gene knockouts, or the pharmacological inhibition of carnitine palmitoyl transferases (CPTs), our implementation of FAO-Blue provides a more feasible and rapidly accessible flow cytometry-based method for measuring FAO levels in ILC2. This innovative assay allows analysis of FAO levels in small and heterogenous *ex vivo*-isolated cell populations or limiting *in vitro* cell culture systems and opens the

door for future studies where the effect of FAO inhibitors or nutrient availability could be directly measured using FAO-Blue.

Neutral lipids are packaged in LDs, which is driven by lipid neogenesis, exogenous acquisition of FAs, or internal recycling of FAs and are transiently stored in the form of triglycerides (TGs) (45). It has been recently shown that LDs help drive pathogenic airway inflammation mediated by ILC2 (33). Although the effect of IL-33 or allergen intranasal challenge on lipid storage in ILC2 has been thoroughly investigated using flow cytometry, the representation of intracellular lipid storage has been shown almost exclusively using qualitative assessments (33, 34). Hence, we employed here microscopy to quantify how neutral lipids are stored in droplets, demonstrating that each cytokine treatment induced a unique LD distribution phenotype that could only be discovered through visual intracellular investigation. While in flow cytometry, ILC2 treated with IL-7 or IL-2 alone both harbor low levels of stored lipids, IL-7 uniquely has the fewest number of LDs overall with the largest proportion of small-sized LDs (57%). ILC2 stimulated with IL-7 or IL-2 in combination with IL-33 also share similarity in their high levels of stored lipids measured through flow cytometry, however, the latter has the smallest proportion of small-sized LDs at only 27%. This is a significant shift from its steady state condition in IL-2 alone where 51% of the LD population were small-sized. The most common and strongest correlation found was between the total volume of stored lipids and the number of LDs. This suggests that ILC2 distribute their lipid storage between many droplets as opposed to several extremely large droplets either due to cytoplasmic restrictions or to accommodate distinct metabolic requirements.

Indeed, a previous study demonstrated that during nutrient deprivation, LDs undergo dispersion along microtubules to efficiently supply FAs for β-oxidation in mitochondria (54). As LDs are formed as an energy reserve, it is possible that variations in nutrient accessibility during the period of ILC2 stimulation directly impacts the distribution of LD size, which remains to be explored in future studies.

Taken together this data suggests that as ILC2 are being strongly activated they acquire large levels of exogenous FAs that are used for FAO, and any excess FAs are stored in LDs to avoid lipotoxicity resulting in large-sized LDs. Furthermore, small-sized LDs are likely degraded before large-sized LDs through lipolysis or lipophagy to create an easily accessible pool of free FA to fuel FAO when energy demands are high. Interestingly, we observed that the sphericity of LDs in ILC2 shifts from being spherical when stimulated IL-2 alone to being more irregularly-shaped following activation with IL-33. This phenomenon corresponds with observation of a study demonstrating that marked changes in LD morphology are due to an increased number of contact sites with mitochondria (54). The consistently large proportion of intermediate-sized LDs among highly activated ILC2 could have several explanations as the transition states of small to large-sized LDs is likely a highly dynamic process. Potentially, small LDs may be catabolized by lipolysis into FAs that are immediately stored again into pre-existing small LDs alongside exogenously acquired FAs to form intermediate-sized LDs. Conversely, these intermediate LDs could be formed through the degradation of large-sized LDs into smaller volumes. The dynamic nature of this process could be further investigated through the implementation of live imaging, where LD size transition could be recorded in real time to explain these morphological and distribution differences. Moreover, kinetic experiments involving earlier time points or live imaging of LDs in tandem with other organelles, such as lysosomes or mitochondria, could explain these morphological and distribution differences, and could provide further in-depth insights of the lipid metabolism in ILC2.

Data availability statement

The raw data supporting the conclusions of this article will be made available by the authors, without undue reservation.

Ethics statement

The animal study was approved by Canadian Council on Animal Care of McGill University. The study was conducted in accordance with the local legislation and institutional requirements.

Author contributions

AR-D: Conceptualization, Data curation, Formal analysis, Investigation, Methodology, Validation, Visualization, Writing – original draft, Writing – review & editing. RD: Conceptualization, Data curation, Formal analysis, Investigation, Methodology, Validation, Visualization, Writing – original draft, Writing – review & editing. FR: Data curation, Formal analysis, Writing – original draft. MR: Data curation, Formal analysis, Writing – original draft. NI: Visualization, Writing – review & editing. SK: Investigation, Writing – original draft, Data curation. DA: Writing – original draft, Formal analysis. CS: Writing – original draft, Methodology. JL: Writing – original draft, Methodology. GB: Investigation, Writing – original draft. AE: Investigation, Writing – original draft. JHF: Funding acquisition, Investigation, Project administration, Supervision, Visualization, Writing – original draft, Writing – review & editing.

Funding

The author(s) declare financial support was received for the research, authorship, and/or publication of this article. Work in the laboratory of JHF is supported by a project grant (PJT -175173) from the Canadian Institutes of Health Research (CIHR), a Leaders Opportunity Fund infrastructure grant from the Canadian Foundation of Innovation (CFI; 38958) and a Miravo Healthcare Research Grant in Allergic Rhinitis or Urticaria by the Canadian Allergy, Asthma and Immunology Foundation (CAAIF; # 3656894). NI and SK both acknowledge support of a Doctoral Training Scholarship by the Fonds de recherche du Québec -Santé (FRQS) (325991 for NI, 284343 for SK).

Acknowledgments

Flow cytometric sorting and analysis was performed in the Flow Cytometry Core Facility (FCCF) at the Life Science Complex downtown campus at McGill University. The FCCF acknowledges support by the Canadian Foundation for Innovation (CFI) and by the Faculty of Medicine and Health Sciences at McGill University. Microscopy images for this manuscript were acquired, processed, and analyzed in the McGill University Advanced BioImaging Facility (ABIF), acknowledging funding by the Canadian Foundation for Innovation (CFI) and by the Faculty of Medicine and Sciences at McGill University.

Conflict of interest

The authors declare that the research was conducted in the absence of any commercial or financial relationships that could be construed as a potential conflict of interest.

JHF declares that he was an editorial board member of Frontiers, at the time of submission. This had no impact on the peer review process and the final decision.

Publisher's note

Supplementary material

The Supplementary Material for this article can be found online at: https://www.frontiersin.org/articles/10.3389/fimmu.2024.1493848/full#supplementary-material

SUPPLEMENTARY FIGURE 1
Gating strategies for the sorting of murine bone marrow-derived ILC2 progenitors and lung ILC2. **(A)** After the exclusion of debris and doublets, murine bone marrow-derived group 2 innate lymphoid cells (ILC2) precursors were defined and isolated by flow cytometric sorting as lineage-negative, c-kit^{-}Sca-1^{+}CD25^{+} cells. **(B)** After excluding dead cells, debris and doublets, murine lung ILC2s were isolated by flow cytometric sorting as lineage-negative, CD45^{+}Thy-1.2^{+}ST2^{+}CD25^{+} cells.

References

1. Helfrich S, Mindt BC, Fritz JH, Duerr CU. Group 2 innate lymphoid cells in respiratory allergic inflammation. *Front Immunol*. (2019) 10:930. doi: 10.3389/fimmu.2019.00930

2. Kobayashi T, Motomura Y, Moro K. The discovery of group 2 innate lymphoid cells has changed the concept of type 2 immune diseases. *Int Immunol*. (2021) 33:705–9. doi: 10.1093/intimm/dxab063

3. Zaiss DMW, Pearce EJ, Artis D, McKenzie ANJ, Klose CSN. Cooperation of ilc2s and T(H)2 cells in the expulsion of intestinal helminth parasites. *Nat Rev Immunol*. (2024) 24:294–302. doi: 10.1038/s41577-023-00942-1

4. Starkey MR, McKenzie AN, Belz GT, Hansbro PM. Pulmonary group 2 innate lymphoid cells: surprises and challenges. *Mucosal Immunol*. (2019) 12:299–311. doi: 10.1038/s41385-018-0130-4

5. Ricardo-Gonzalez RR, Molofsky AB, Locksley RM. Ilc2s - development, divergence, dispersal. *Curr Opin Immunol*. (2022) 75:102168. doi: 10.1016/j.coi.2022.102168

6. Akdis CA, Arkwright PD, Bruggen MC, Busse W, Gadina M, Guttman-Yassky E, et al. Type 2 immunity in the skin and lungs. *Allergy*. (2020) 75:1582–605. doi: 10.1111/all.14318

7. Barlow JL, Peel S, Fox J, Panova V, Hardman CS, Camelo A, et al. Il-33 is more potent than il-25 in provoking il-13-producing nuocytes (Type 2 innate lymphoid cells) and airway contraction. *J Allergy Clin Immunol*. (2013) 132:933–41. doi: 10.1016/j.jaci.2013.05.012

8. Cayrol C, Girard JP. Interleukin-33 (Il-33): A critical review of its biology and the mechanisms involved in its release as a potent extracellular cytokine. *Cytokine*. (2022) 156:155891. doi: 10.1016/j.cyto.2022.155891

9. Dwyer GK, D'Cruz LM, Turnquist HR. Emerging functions of il-33 in homeostasis and immunity. *Annu Rev Immunol*. (2022) 40:15–43. doi: 10.1146/annurev-immunol-101320-124243

10. Topczewska PM, Rompe ZA, Jakob MO, Stamm A, Leclere PS, Preusser A, et al. Ilc2 require cell-intrinsic st2 signals to promote type 2 immune responses. *Front Immunol*. (2023) 14:1130933. doi: 10.3389/fimmu.2023.1130933

11. Yashiro T, Moro K. Crossing the valley of death: toward translational research regarding ilc2. *Allergol Int*. (2023) 72:187–93. doi: 10.1016/j.alit.2022.12.006

12. Fan D, Wang X, Wang M, Wang Y, Zhang L, Li Y, et al. Allergen-dependent differences in ilc2s frequencies in patients with allergic rhinitis. *Allergy Asthma Immunol Res*. (2016) 8:216–22. doi: 10.4168/aair.2016.8.3.216

13. van der Ploeg EK, Golebski K, van Nimwegen M, Fergusson JR, Heesters BA, Martinez-Gonzalez I, et al. Steroid-resistant human inflammatory ilc2s are marked by cd45ro and elevated in type 2 respiratory diseases. *Sci Immunol*. (2021) 6(55). doi: 10.1126/sciimmunol.abd3489

14. Chan R, Stewart K, Misirovs R, Lipworth BJ. Targeting downstream type 2 cytokines or upstream epithelial alarmins for severe asthma. *J Allergy Clin Immunol Pract*. (2022) 10:1497–505. doi: 10.1016/j.jaip.2022.01.040

15. Gauvreau GM, Bergeron C, Boulet LP, Cockcroft DW, Cote A, Davis BE, et al. Sounding the alarmins-the role of alarmin cytokines in asthma. *Allergy*. (2023) 78:402–17. doi: 10.1111/all.15609

16. Struss N, Hohlfeld JM. Biologics in asthma management - are we out of breath yet? *Allergol Select*. (2021) 5:96–102. doi: 10.5414/ALX02192E

17. Wechsler ME, Ruddy MK, Pavord ID, Israel E, Rabe KF, Ford LB, et al. Efficacy and safety of itepekimab in patients with moderate-to-severe asthma. *N Engl J Med*. (2021) 385:1656–68. doi: 10.1056/NEJMoa2024257

18. Kosloski MP, Kalliolias GD, Xu CR, Harel S, Lai CH, Zheng W, et al. Pharmacokinetics and pharmacodynamics of itepekimab in healthy adults and patients with asthma: phase I first-in-human and first-in-patient trials. *Clin Transl Sci*. (2022) 15:384–95. doi: 10.1111/cts.13157

19. Panettieri R Jr., Lugogo N, Corren J, Ambrose CS. Tezepelumab for severe asthma: one drug targeting multiple disease pathways and patient types. *J Asthma Allergy*. (2024) 17:219–36. doi: 10.2147/JAA.S342391

20. Tice JA, Campbell JD, Synnott PG, Walsh JME, Kumar VM, Whittington M, et al. The effectiveness and value of biologic therapies for the treatment of uncontrolled asthma. *J Manag Care Spec Pharm*. (2019) 25:510–4. doi: 10.18553/jmcp.2019.25.5.510

21. Miller RL, Grayson MH, Strothman K. Advances in asthma: new understandings of asthma's natural history, risk factors, underlying mechanisms, and clinical management. *J Allergy Clin Immunol*. (2021) 148:1430–41. doi: 10.1016/j.jaci.2021.10.001

22. Stine ZE, Schug ZT, Salvino JM, Dang CV. Targeting cancer metabolism in the era of precision oncology. *Nat Rev Drug Discovery*. (2022) 21:141–62. doi: 10.1038/s41573-021-00339-6

23. Pillai UJ, Ray A, Maan M, Dutta M. Repurposing drugs targeting metabolic diseases for cancer therapeutics. *Drug Discovery Today*. (2023) 28:103684. doi: 10.1016/j.drudis.2023.103684

24. Li WJ, Zhao Y, Gao Y, Dong LL, Wu YF, Chen ZH, et al. Lipid metabolism in asthma: immune regulation and potential therapeutic target. *Cell Immunol*. (2021) 364:104341. doi: 10.1016/j.cellimm.2021.104341

25. Dasgupta S, Ghosh N, Bhattacharyya P, Roy Chowdhury S, Chaudhury K. Metabolomics of asthma, copd, and asthma-copd overlap: an overview. *Crit Rev Clin Lab Sci*. (2023) 60:153–70. doi: 10.1080/10408363.2022.2140329

26. Yoshida K, Morishima Y, Ishii Y, Mastuzaka T, Shimano H, Hizawa N. Abnormal saturated fatty acids and sphingolipids metabolism in asthma. *Respir Investig*. (2024) 62:526–30. doi: 10.1016/j.resinv.2024.04.006

27. Miethe S, Karsonova A, Karaulov A, Renz H. Obesity and asthma. *J Allergy Clin Immunol*. (2020) 146:685–93. doi: 10.1016/j.jaci.2020.08.011

28. Liu Y, Zheng J, Zhang HP, Zhang X, Wang L, Wood L, et al. Obesity-associated metabolic signatures correlate to clinical and inflammatory profiles of asthma: A pilot study. *Allergy Asthma Immunol Res*. (2018) 10:628–47. doi: 10.4168/aair.2018.10.6.628

29. Li JH, Hepworth MR, O'Sullivan TE. Regulation of systemic metabolism by tissue-resident immune cell circuits. *Immunity*. (2023) 56:1168–86. doi: 10.1016/j.immuni.2023.05.001

30. Salmond RJ, Mirchandani AS, Besnard AG, Bain CC, Thomson NC, Liew FY. Il-33 induces innate lymphoid cell-mediated airway inflammation by activating mammalian target of rapamycin. *J Allergy Clin Immunol*. (2012) 130:1159–66 e6. doi: 10.1016/j.jaci.2012.05.018

31. Surace L, Doisne JM, Croft CA, Thaller A, Escoll P, Marie S, et al. Dichotomous metabolic networks govern human ilc2 proliferation and function. *Nat Immunol*. (2021) 22:1367–74. doi: 10.1038/s41590-021-01043-8

32. Wilhelm C, Harrison OJ, Schmitt V, Pelletier M, Spencer SP, Urban JF Jr., et al. Critical role of fatty acid metabolism in ilc2-mediated barrier protection during malnutrition and helminth infection. *J Exp Med*. (2016) 213:1409–18. doi: 10.1084/jem.20151448

33. Karagiannis F, Masouleh SK, Wunderling K, Surendar J, Schmitt V, Kazakov A, et al. Lipid-droplet formation drives pathogenic group 2 innate lymphoid cells in airway inflammation. *Immunity*. (2020) 52:620–34.e6. doi: 10.1016/j.immuni.2020.03.003

34. Fali T, Aychek T, Ferhat M, Jouzeau JY, Busslinger M, Moulin D, et al. Metabolic regulation by pparγ Is required for il-33-mediated activation of ilc2s in lung and adipose tissue. *Mucosal Immunol*. (2021) 14:585–93. doi: 10.1038/s41385-020-00351-w

35. Ercolano G, Gomez-Cadena A, Dumauthioz N, Vanoni G, Kreutzfeldt M, Wyss T, et al. Pparγ Drives il-33-dependent ilc2 pro-tumoral functions. *Nat Commun*. (2021) 12:2538. doi: 10.1038/s41467-021-22764-2

36. Wilfling F, Haas JT, Walther TC, Farese RV Jr. Lipid droplet biogenesis. *Curr Opin Cell Biol*. (2014) 29:39–45. doi: 10.1016/j.ceb.2014.03.008

37. Nguyen TB, Louie SM, Daniele JR, Tran Q, Dillin A, Zoncu R, et al. Dgat1-dependent lipid droplet biogenesis protects mitochondrial function during starvation-induced autophagy. *Dev Cell*. (2017) 42:9–21.e5. doi: 10.1016/j.devcel.2017.06.003

38. Houten SM, Violante S, Ventura FV, Wanders RJ. The biochemistry and physiology of mitochondrial fatty acid β-oxidation and its genetic disorders. *Annu Rev Physiol*. (2016) 78:23–44. doi: 10.1146/annurev-physiol-021115-105045

39. Galle-Treger L, Hurrell BP, Lewis G, Howard E, Jahani PS, Banie H, et al. Autophagy is critical for group 2 innate lymphoid cell metabolic homeostasis and effector function. *J Allergy Clin Immunol*. (2020) 145:502–17.e5. doi: 10.1016/j.jaci.2019.10.035

40. Mindt BC, Krisna SS, Duerr CU, Mancini M, Richer L, Vidal SM, et al. The nf-kappab transcription factor C-rel modulates group 2 innate lymphoid cell effector functions and drives allergic airway inflammation. *Front Immunol*. (2021) 12:664218. doi: 10.3389/fimmu.2021.664218

41. Duerr CU, McCarthy CD, Mindt BC, Rubio M, Meli AP, Pothlichet J, et al. Type I interferon restricts type 2 immunopathology through the regulation of group 2 innate lymphoid cells. *Nat Immunol*. (2016) 17:65–75. doi: 10.1038/ni.3308

42. Sheikh A, Abraham N. Interleukin-7 receptor alpha in innate lymphoid cells: more than a marker. *Front Immunol*. (2019) 10:2897. doi: 10.3389/fimmu.2019.02897

43. Roediger B, Kyle R, Tay SS, Mitchell AJ, Bolton HA, Guy TV, et al. Il-2 is a critical regulator of group 2 innate lymphoid cell function during pulmonary inflammation. *J Allergy Clin Immunol*. (2015) 136:1653–63.e7. doi: 10.1016/j.jaci.2015.03.043

44. Xiao Q, He J, Lei A, Xu H, Zhang L, Zhou P, et al. Ppargamma enhances ilc2 function during allergic airway inflammation via transcription regulation of st2. *Mucosal Immunol*. (2021) 14:468–78. doi: 10.1038/s41385-020-00339-6

45. Walther TC, Chung J, Farese RV Jr. Lipid droplet biogenesis. *Annu Rev Cell Dev Biol*. (2017) 33:491–510. doi: 10.1146/annurev-cellbio-100616-060608

46. Christofides A, Konstantinidou E, Jani C, Boussiotis VA. The role of peroxisome proliferator-activated receptors (Ppar) in immune responses. *Metabolism*. (2021) 114:154338. doi: 10.1016/j.metabol.2020.154338

47. Uchinomiya S, Matsunaga N, Kamoda K, Kawagoe R, Tsuruta A, Ohdo S, et al. Fluorescence detection of metabolic activity of the fatty acid beta oxidation pathway in living cells. *Chem Commun (Camb)*. (2020) 56:3023–6. doi: 10.1039/c9cc09993j

48. Weiss T, Semmler L, Millesi F, Mann A, Haertinger M, Salzmann M, et al. Automated image analysis of stained cytospins to quantify schwann cell purity and proliferation. *PloS One*. (2020) 15:e0233647. doi: 10.1371/journal.pone.0233647

49. Zhang Y, He Y, Bharadwaj S, Hammam N, Carnagey K, Myers R, et al. Tissue-specific extracellular matrix coatings for the promotion of cell proliferation and maintenance of cell phenotype. *Biomaterials*. (2009) 30:4021–8. doi: 10.1016/j.biomaterials.2009.04.005

50. Chen R, Smith SG, Salter B, El-Gammal A, Oliveria JP, Obminski C, et al. Allergen-induced increases in sputum levels of group 2 innate lymphoid cells in subjects with asthma. *Am J Respir Crit Care Med*. (2017) 196:700–12. doi: 10.1164/rccm.201612-2427OC

51. Moren B, Fryklund C, Stenkula K. Surface-associated lipid droplets: an intermediate site for lipid transport in human adipocytes? *Adipocyte*. (2020) 9:636–48. doi: 10.1080/21623945.2020.1838684

52. Rambold AS, Cohen S, Lippincott-Schwartz J. Fatty acid trafficking in starved cells: regulation by lipid droplet lipolysis, autophagy, and mitochondrial fusion dynamics. *Dev Cell*. (2015) 32:678–92. doi: 10.1016/j.devcel.2015.01.029

53. Yu H, Jacquelot N, Belz GT. Metabolic features of innate lymphoid cells. *J Exp Med*. (2022) 219(11): e20221140. doi: 10.1084/jem.20221140

54. Herms A, Bosch M, Reddy BJ, Schieber NL, Fajardo A, Ruperez C, et al. Ampk activation promotes lipid droplet dispersion on detyrosinated microtubules to increase mitochondrial fatty acid oxidation. *Nat Commun*. (2015) 6:7176. doi: 10.1038/ncomms8176

frontiers | Frontiers in Immunology

TYPE Review
PUBLISHED 16 December 2024
DOI 10.3389/fimmu.2024.1510628

OPEN ACCESS

EDITED BY
Thomas A. Kufer,
University of Hohenheim, Germany

REVIEWED BY
Junji Xing,
Houston Methodist Research Institute, United States
Robert B. Levy,
University of Miami, United States

*CORRESPONDENCE
Yujiao Sun
sunyujiao@tjutcm.edu.cn
Yingpeng Li
liyingpeng@tjutcm.edu.cn

†These authors have contributed equally to this work

RECEIVED 13 October 2024
ACCEPTED 29 November 2024
PUBLISHED 16 December 2024

CITATION
Zhi H, Fu H, Zhang Y, Fan N, Zhao C, Li Y, Sun Y and Li Y (2024) Progress of cGAS-STING signaling pathway-based modulation of immune response by traditional Chinese medicine in clinical diseases.
Front. Immunol. 15:1510628.
doi: 10.3389/fimmu.2024.1510628

Progress of cGAS-STING signaling pathway-based modulation of immune response by traditional Chinese medicine in clinical diseases

Hui Zhi[1†], Hui Fu[2†], Yunxin Zhang[1], Ni Fan[1], Chengcheng Zhao[3], Yunfei Li[1], Yujiao Sun[1*] and Yingpeng Li[1*]

[1]College of Chinese Materia Medica, Tianjin University of Traditional Chinese Medicine, Tianjin, China, [2]College of Integrated Chinese and Western Medicine, Tianjin University of Traditional Chinese Medicine, Tianjin, China, [3]Experimental Teaching and Practical Training Center, Heilongjiang University of Chinese Medicine, Harbin, China

The cGAS-STING signaling pathway is a critical component of the innate immune response, playing a significant role in various diseases. As a central element of this pathway, STING responds to both endogenous and exogenous DNA stimuli, triggering the production of interferons and pro-inflammatory cytokines to enhance immune defenses against tumors and pathogens. However, dysregulated activation of the STING pathway is implicated in the pathogenesis of multiple diseases, including autoinflammation, viral infections, and cancer. Traditional Chinese Medicines (TCMs), which have a long history of use, have been associated with positive effects in disease prevention and treatment. TCM formulations (e.g., Lingguizhugan Decoction, Yi-Shen-Xie-Zhuo formula) and active compounds (e.g., Glabridin, Ginsenoside Rd) can modulate the cGAS-STING signaling pathway, thereby influencing the progression of inflammatory, infectious, or oncological diseases. This review explores the mechanisms by which TCMs interact with the cGAS-STING pathway to regulate immunity, focusing on their roles in infectious diseases, malignancies, and autoimmune disorders.

KEYWORDS

cGAS-STING pathway, traditional Chinese medicine, immunity, disease, cancer, infection6 cGAS-STING pathway, infection

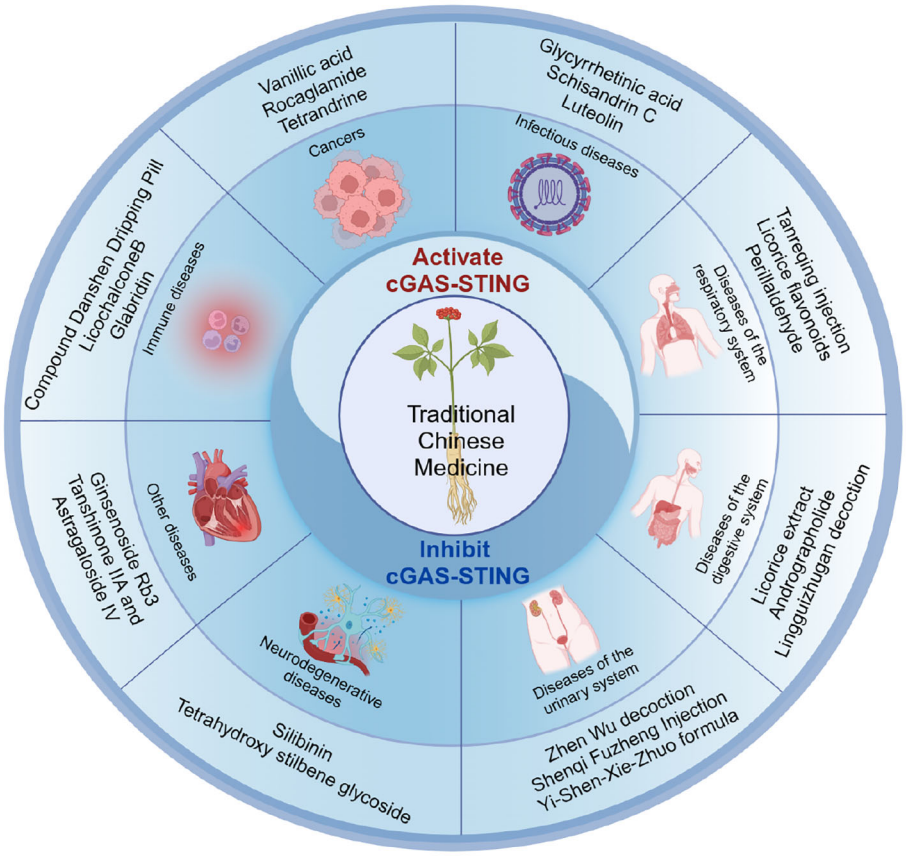

GRAPHICAL ABSTRACT

Highlights

- Traditional Chinese Medicine (TCM) has a rich history of preventing and treating many diseases. This review explores how TCM modulates the cGAS-STING signaling pathway and its therapeutic potential.
- To elucidate the intricate relationship between the STING pathway and different diseases, and to analyze TCM as a potential agonist or inhibitor of the STING pathway.
- By conducting an extensive literature review, we explore the key proteins within the cGAS-STING pathway and their significance as biomarkers in TCM-based immunomodulation and the treatment of various diseases.

1 Introduction

Immune system homeostasis is vital to overall health, as proper immune regulation ensures normal physiological functions, while dysregulation can lead to various diseases (1, 2). The innate immune system play a crucial role in recognizing pathogen-associated molecular patterns and danger-associated molecular patterns through pathogen recognition receptors. These receptors form as the first line of defense against bacterial and viral infections, as well as aseptic inflammatory, by triggering the production of pro-inflammatory and anti-viral cytokines (3).

The cGAS-STING signaling pathway, as an important element of innate immunity, has garnered significant attention in recent years for its role in maintaining immune system homeostasis (4). This pathway plays a crucial role in antitumor immunity, and inflammatory and infectious diseases, as it recognizes various sources of cytoplasmic DNA, including bacterial, viral, and mitochondrial DNA (5). Upon detection of cytoplasmic DNA, cGAS generates cyclic GMP-AMP (2′3′-cGAMP), which activates STING. This process leads to TANK-binding kinase 1 (TBK1) phosphorylation (pTBK1) and induces type I interferon (IFN-I) transcription (6–8). In antiviral infections, STING acts through an IFN-I-driven immune response (7, 9). Activation of cGAS-STING enhances the ability of immune cells to target antigens through multiple pathways, thereby defending against pathogen invasion (10, 11). However, structural or functional abnormalities in this pathway may also contribute to the development of autoimmune and inflammatory diseases, such as systemic lupus erythematosus (SLE) and non-alcoholic fatty liver disease (NAFLD). Although

cGAS is able to sense double-stranded DNA (dsDNA), it is unable to distinguish between its own DNA and exogenous DNA (12). Prolonged stimulation of aberrant DNA can lead to the overactivation activation of the STING pathway, resulting in excessive synthesis and release of IFN-I and inflammatory cytokines, which drive the progression of inflammatory or autoimmune diseases (13). In addition, tumor-derived dsDNA activates the STING pathway in antigen-presenting cells, promoting interferon production. This process facilitates dendritic cell maturation, T cell recruitment, and enhances anti-tumor responses (14).

Traditional Chinese Medicine (TCM) has a long history, traditionally employed for the prevention and treatment of a wide spectrum of diseases. Studies have shown that TCM has a bidirectional regulatory effect in immunomodulation, both activating the immune system and suppressing excessive immune responses (15). For example, ginseng contains a variety of active ingredients (e.g., ginsenosides, ginseng polysaccharides) that have immunomodulatory effects. A randomized controlled trial showed that ginseng polysaccharide for 8-14 weeks enhanced the cytotoxic activity of NK cells and up-regulated serum TNF-α levels (16). TCM has been associated with potential benefits in adjunct cancer therapy, particularly in alleviating clinical symptoms, extending patient survival, and modulating immune functions (17–19). TCM principles identify 'yang deficiency' as the underlying cause of breast cancer. The classic anti-neoplastic formula, Yanghe Decoction (YHD), has been shown in contemporary research to decrease myeloid-derived suppressor cells (MDSCs) and suppress the tumor microenvironment's iNOS and ARG-1 expression. At the same time, it enhances the immune response by increasing the number of natural killer T cells (NKTs) and CD4 T cells (20). Unlike chemotherapy, traditional Chinese medicine (TCM) not only directly targets tumor cells but also effectively boosts the immune response. For instance, the TCM formula Shugan Jianpi Decoction has been shown to suppress the proliferation of MDSCs and enhance the inflammatory regulatory functions of NKT cells (21). In addition, certain herbal components, such as astragaloside derived from Huangqi (*Radix Astragali*), can significantly promote IFN-γ secretion from T cells and enhance T cell immunoreactivity (22).

Increasing attention has been given to the immunomodulatory potential of TCM, particularly the ability of TCM active compounds or formulations to address diseases such as inflammation, infection, and cancer, by modulating the cGAS-STING signaling pathway (Figure 1). By regulating this pathway, Chinese medicines may enhance the body's immune response to pathogens and tumors, as well as inhibit excessive immune responses. However, these effects are primarily observed in preclinical studies investigating underlying mechanisms of disease treatment. Further well-designed clinical trials are necessary to confirm these findings.

Despite the growing recognition of the cGAS-STING signaling pathway's significance in immunomodulation, comprehensive reviews on how TCMs target this pathway remain scarce. This paper aims to address this gap by summarizing recent advancements in understanding the cGAS-STING pathway's role in immune regulation and the potential mechanisms underlying herbal interventions. The findings are expected to serve as a valuable reference for future in-depth mechanistic research.

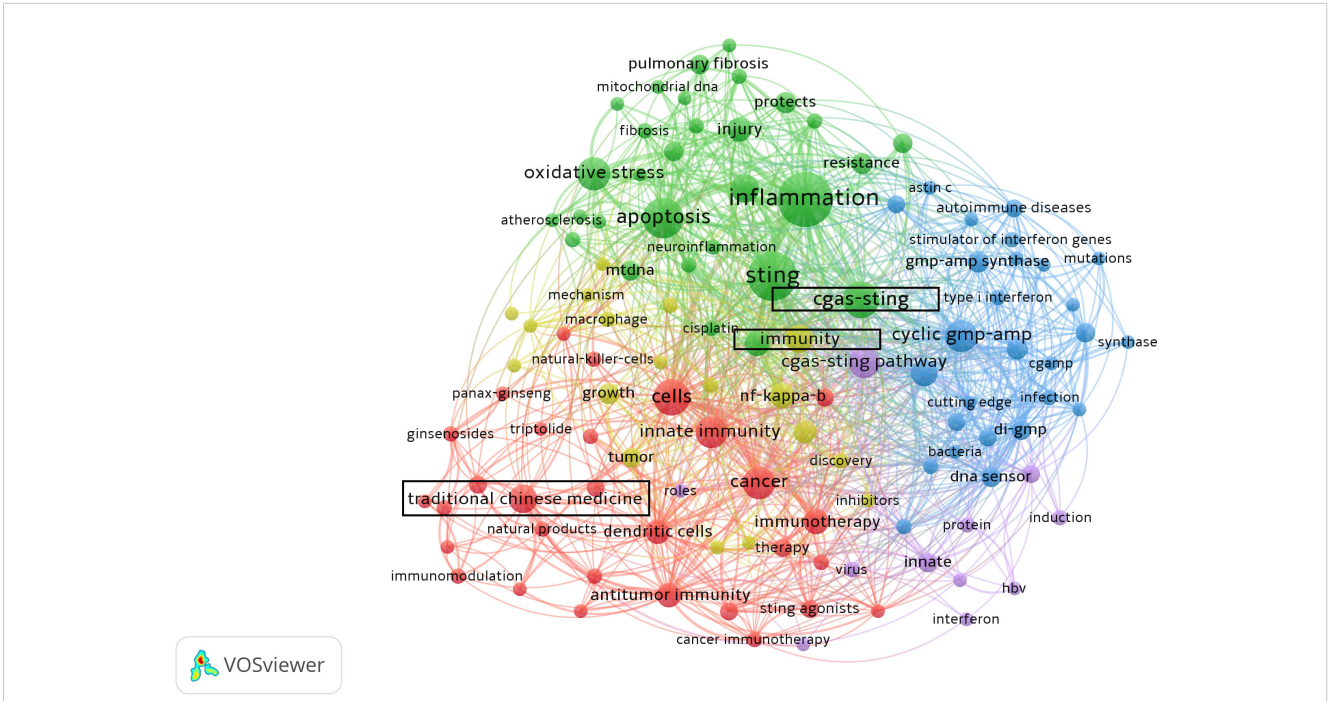

FIGURE 1
A VOSviewer analysis of key terms related to TCM and the cGAS-STING signaling pathway underscores their significance as prominent and actively explored research areas. Created with VOSviewer.

2 Structural characterization of STING and its application in clinical therapy

Innate immunity serves as the body's first line of defense against invading pathogens (23). The stimulator of interferon genes (STING) is a critical protein that mediates various DNA receptors in this system. STING, also referred to as ERIS, MYPS, and MITA, is a conserved transmembrane protein encoded by the TMEM173 gene. Predominantly localized in the endoplasmic reticulum, it is also found on Golgi and mitochondrial membranes (24). STING consists of 379 amino acids and contains an N-terminal transmembrane region and a C-terminal cytoplasmic globular structural domain, which interacts with another STING molecule to form an intact dimer (25).

STING detects cytoplasmic dsDNA and serves as a direct sensor for endogenous cyclic dinucleotides (CDNs) (26). Activation of cGAS, a nucleotidyltransferase that senses cytoplasmic non-self DNA, catalyzes the production of 2′3′-cGAMP, a CDN composed of adenosine and guanosine (Figure 2) (27, 28). In addition to cGAMP, STING can be triggered by bacterial-derived CDNs, such as cyclic di-AMP and cyclic di-GMP (29). CDNs and 2′3′-cGAMP bind to STING in the endoplasmic reticulum, facilitating the dimerization and translocation of STING to the perinuclear region (29, 30). STING recruits TBK1 and IκB kinase (IKK) during translocation, which then relocates to the perinuclear region. These kinases phosphorylate interferon regulatory factor 3 (IRF3) and nuclear factor-κB (NF-κB), which activates the expression of IFN-I and pro-inflammatory cytokines (31–33). IFN-I enhances immune responses by promoting the activation and function of immune cells such as dendritic cells, T cells, and natural killer cells (34).

The cGAS-STING pathway is a conserved innate immune mechanism that responds to pathogenic infections, DNA damage, and aberrant cell activities like uncontrolled replication or senescence (35). In cancer therapy, activation of STING enhances tumor antigen presentation and promotes antitumor immunity, making it an attractive immunotherapeutic target (36). Studies have shown that cGAS-STING agonists not only induce tumor cell senescence but also boost adaptive anticancer immunity and combine efforts with immunotherapy (37, 38). Clinical trials have explored two main types of STING agonists: cyclic dinucleotides (CDNs, e.g., ADU-S100) and non-CDN (e.g., DMXAA) (39, 40). For instance, ADU-S100, the first CDN derivative in clinical trials, has demonstrated the ability to stimulate IFN-β production by human immune cells, showcasing its therapeutic potential (41). Additionally, cGAS activity is critical for the success of immune checkpoint blockade therapies, with STING agonists showing promise in enhancing vaccine efficacy for tumors resistant to PD-1 inhibitors (42).

In addition to cancer therapy, the cGAS/STING pathway plays a vital role in viral infections. Many DNA viruses, such as herpes simplex virus (HSV) and hepatitis B virus (HBV), are able to inhibit viral replication by initiating IFN-I production through activation of this pathway (43, 44). This suggests that STING agonists may have broad-spectrum antiviral potential (45). For example, DMXAA is a potent antiviral agent in mice; α-Mangostin, a

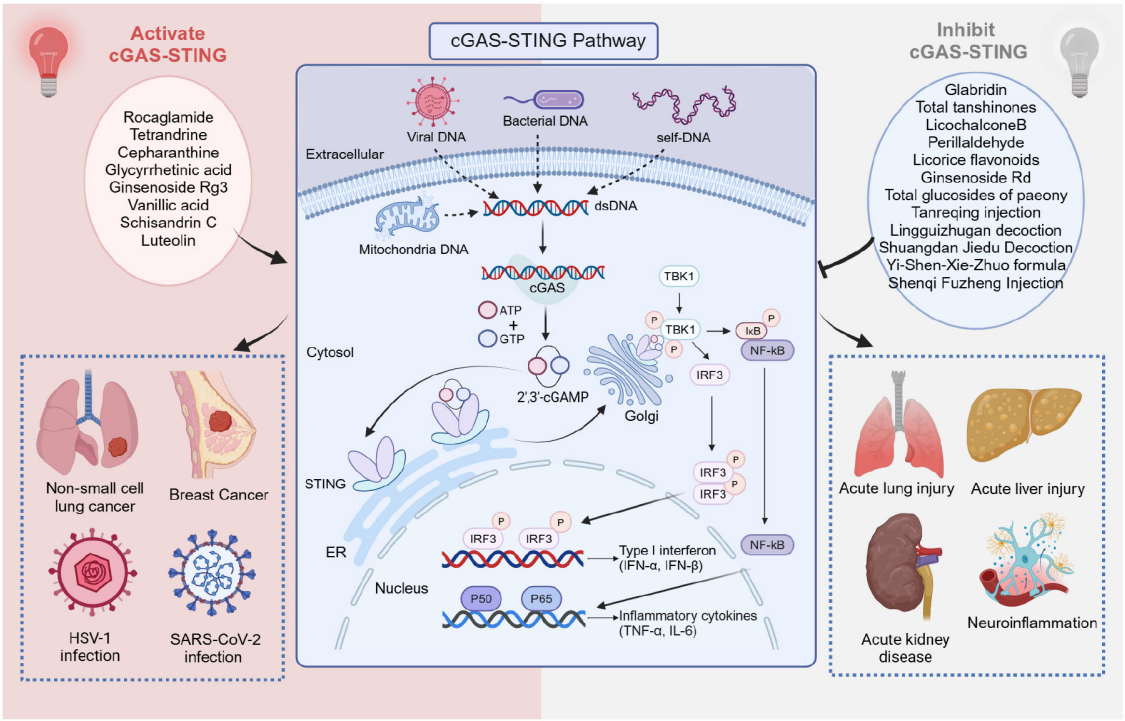

FIGURE 2
Mechanisms of cGAS-STING pathway activation, Chinese medicine inhibits or activates cGAS-STING signaling pathway to treat various diseases. Created with BioRender.com.

flavonoid with antimicrobial properties, has been shown to possess antiviral properties and anti-DENV and HBV replicative activity in cellular experiments (46–48). However, numerous viruses such as HSV, Human CMV (HCMV), etc. have evolved mechanisms to circumvent this pathway (49–51). For instance, Epstein-Barr virus (EBV) suppresses localized innate immunity by targeting STING for degradation through the E3 ubiquitin ligase TRIM29 (52).

However, despite its protective roles, excessive activation of STING can lead to autoimmune conditions like Aicardi-Goutières syndrome (AGS) and SLE (53–55). In these diseases, both autologous DNA and mitochondrial DNA may be misrecognized by cGAS, leading to the activation of STING and an excessive IFN-I response (56). To address this, inhibitors targeting STING or cGAS have emerged as therapeutic candidates. Compounds like Acrinamin and Oxychloroquine show potential in blocking cGAS activation, offering new avenues for treating autoimmune disorders (57).

Although several STING agonists and inhibitors have been developed, they have had limited effect in clinical translation. TCM offers a valuable resource for the development of STING modulators, including inhibitors and activators. This underscores TCM's potential to address various diseases through immunomodulatory mechanisms, providing a robust foundation for future research and drug development (Figure 2).

3 Role of Chinese medicines in immunomodulation

Chinese medicines play a vital bidirectional role in immunomodulation, both activating the immune system and suppressing excessive immune responses. This regulation is achieved by influencing various aspects such as immune cells, cytokines, and immune organs. Studies have shown that certain Chinese medicines can effectively regulate the production of immune cells and cytokines (58, 59). Certain herbal medicines boost innate immune system activity, while others act on cellular subpopulations of adaptive immunity (60).

Chinese medicines act by enhancing the function of various immune cells, including macrophages, dendritic cells, NK cells, T cells, and B cells. For example, Ganoderma lucidum polysaccharide (PS-G), the primary active compound in Ganoderma lucidum, has been shown to promote activation and maturation of dendritic cells derived from human monocytes (61). Herbal medicines also regulate T lymphocyte activity by stimulating their proliferation and differentiation, promoting cytotoxic T lymphocyte production, and modulating the TH1/TH2 balance as well as the function of T helper (TH) cell subsets (59). For example, polysaccharides from *Cordyceps sinensis* enhance the expression of transcription factors such as T-bet, GATA-3, and RoR-γt in TH cells, thereby increasing the number of TH1, TH2, and TH17 cells (62). B lymphocytes, the main cells of humoral immunity, depend on antigen stimulation to release antibodies (63). Research indicates that polysaccharides from *Dendrobium huoshanense* and *Atractylodes macrocephala* Koidz significantly increase B lymphocyte populations, thereby strengthening humoral immunity (64, 65).

In addition, herbal medicines can regulate the production of specific cytokines, including interferons (IFN-α, IFN-β, IFN-γ), tumor necrosis factor (TNF-α), and interleukins (e.g., IL-1, IL-2, IL-4), which are pivotal in immune and inflammatory processes. For example, polysaccharides from *Atractylodes macrocephala* and *Astragalus membranaceus* markedly upregulated IFN-γ expression *in vitro* experiments (66, 67).

The diversity of immunomodulatory components in TCM provides a wide range of therapeutic potential for clinical applications. These components are mainly divided into two categories: anti-inflammatory and immune-enhancing. The anti-inflammatory category includes phenolic acids (e.g., vanillic acid, salvianolic acid B), flavonoids (e.g., luteolin, glabridin), volatile oils (e.g., perillaldehyde, zingiber officinale), lignans (e.g., schisandrin C, asarinin), and alkaloids (e.g., rocaglamide, tetrandrine), while the immune-enhancing category mainly consists of polysaccharides (e.g., lycium barbarum polysaccharides, astragalus membranaceus polysaccharides) and glycosides (e.g., ginsenoside Rg3, ginsenoside Rd) (68–72). These components regulate the body's immune response through different pathways, enabling TCM to demonstrate unique advantages in the treatment of immune-related diseases.

Additionally, TCM is closely related to the concept of "medicine and food," i.e., certain species offer both nutritional benefits and therapeutic effects (73). With the growing emphasis on preventive care and holistic health in recent years, many TCM ingredients have been incorporated into daily diets as functional foods or dietary supplements and have become an important part of alternative therapies (74, 75).

4 The role of TCM in modulating the cGAS/STING pathway in clinical diseases

In recent years, activators and inhibitors of the cGAS-STING pathway have attracted widespread attention, but clinical translation still faces challenges. TCM, as a valuable cultural heritage of the Chinese nation, has shown promising potential in modulating immune-related diseases. Several active compounds have been found to effectively modulate the cGAS/STING signaling pathway and improve diseases. These include ginsenoside Rg3 and ginsenoside Rd, which are derived from *Panax ginseng*; glabridin and licochalcone B, obtained from *Glycyrrhiza uralensis*; perillaldehyde, isolated from *Perilla frutescens*; and schisandrin C, extracted from *Schisandra chinensis* (Figure 2). Natural products have been valued as indispensable resources for discovering novel therapeutic molecules and are instrumental in managing diseases (76–78). The mechanisms and clinical applications of TCM in modulating this pathway will be summarized below, categorized by different types of diseases.

4.1 Immune diseases

Normal activation of the cGAS-STING pathway can trigger immune responses and enhance the ability of immune cells to

eliminate antigens and defend against pathogens. Nevertheless, excessive or abnormal activation of this pathway may trigger immune dysregulation, which in turn leads to the development of autoimmune diseases such as SLE and NAFLD. Research has demonstrated that TREX1 deficiency has a close association with various autoimmune diseases (e.g., AGS, SLE) and that in TREX1-deficient mouse models, deletion of cGAS or STING can ameliorate these disease phenotypes (79–81).

TCM has demonstrated promise in modulating the cGAS-STING pathway. For instance, total tanshinones, the main active ingredient of Salvia miltiorrhiza, can block STING-IRF3 binding, thereby suppressing aberrant pathway activation and alleviating autoimmune conditions associated with TREX1 deficiency TREX1 deficiency (82). Perillaldehyde (PAH), another TCM ingredient, is a natural monoterpenoid extracted from Perilla frutescens, has demonstrated the ability to inhibit STING pathway activation significantly (83). By targeting cGAS proteins, PAH reduces the interferon response, offering a potential therapeutic approach for cGAS-mediated autoimmune diseases (84).

Glabridin, an active ingredient in licorice, specifically inhibits the cGAS-STING pathway by decreasing the levels of IFN-I, IL-6, and TNF-α, thereby alleviating immune disorders triggered by TREX1 deficiency (85). In addition, Licochalcone B and Licochalcone D also showed significant anti-inflammatory effects by inhibiting STING downstream signaling and improved symptoms of inflammatory diseases, such as colitis, in experimental models (86, 87).

In addition, Compound Danshen Dropping Pills, widely utilized for managing cardiovascular conditions such as angina pectoris and acute myocardial infarction, have successfully completed Phase III clinical trials with the U.S. Food and Drug Administration (88–90). This TCM formulation has shown efficacy in reducing multi-organ inflammatory responses in TREX1-deficient mice by disrupting STING-TBK1 interactions and blocking cGAS-STING pathway activation, highlighting its therapeutic potential for inflammatory conditions, including obesity-induced insulin resistance (91).

4.2 Cancers

Tumorigenesis is a complex, multistep process, and conventional cancer research usually focuses on a single target (92). However, due to their diversity and complexity, the therapeutic effects are often limited. TCM has unique advantages in tumor therapy through holistic regulation and multi-target intervention (93, 94).

Ginsenoside Re, derived from ginseng, can regulate the host immune system and exert anticancer effects through multiple pathways (95). In non-small cell lung cancer (NSCLC), ginsenoside Re exerts antitumor effects by inhibiting the epithelial-mesenchymal transition (EMT) process. It does so through the inhibition of the AMPKα1/STING positive feedback loop and the reduction of M2-like macrophage formation (96). In addition, Rocaglamide (RocA), a compound extracted from Aglaia odorata, promotes the leakage of mitochondrial DNA (mtDNA) into the cytoplasm and activates the cGAS-STING pathway. This process increases tumor infiltration of NK cells and significantly enhances anti-tumor immunity in NSCLC (97).

Tetrandrine, derived from *Stephania tetrandra* S. Moore, is a bisbenzylisoquinoline alkaloid with the ability to inhibit tumor proliferation and angiogenesis (98). Tetrandrine activates the STING/TBK1/IRF3 pathway, promoting CCL5 and CXCL10 production. This enhances the infiltration of macrophages, dendritic cells, and CD8 T cells in the tumor microenvironment, significantly inhibiting the growth of NSCLC (99).

Vanillic acid is a phenolic compound present in TCMs such as Angelica sinensis and ginseng, with antioxidant and antimicrobial properties (100). It promotes macrophage polarization to the M1 type through activation of the STING pathway and enhances tumor cell apoptosis and anti-tumor immune response (101).

Breast cancer is a common tumor in women with high morbidity and mortality rates (102). Formononetin, an active ingredient in red clover and astragalus, inhibits the proliferation of BC cells by interfering with PD-L1 and inhibiting the activation of the STING-NF-κB pathway (103). Ginsenoside Rg3 inhibits tumor growth by inhibiting angiogenesis, inducing apoptosis, and other mechanisms. When combined with STING agonists, Rg3 can induce tumor-associated macrophages to polarize from M2 to M1 and improve the tumor microenvironment, effectively inhibiting the growth and invasion of triple-negative breast cancer (104).

4.3 Infectious diseases

The cGAS-STING pathway has played a crucial antiviral role during evolution, and its activation is closely linked to antiviral cellular responses (105). cGAMP synthesis is the critical first step in initiating cGAS-mediated antiviral effects. The downstream effects mainly include the synthesis of antiviral type I interferon and related genes (106, 107). TCM provides a rich source of natural compounds, and many herbs show antiviral, anti-inflammatory, and immunomodulatory effects, making them potential candidates for the development of antiviral drugs.

Schisandra chinensis (Turcz.) Baill., a long-established TCM, has been shown to modulate host immunity and exhibit anticancer, antiviral, and hepatoprotective effects (108, 109). Its active ingredient, Schisandrin C, was found to inhibit HBV replication by promoting the interaction between TBK1 and STING, enhancing the activation of the cGAS-STING pathway and promoting the expression of IFN-β and interferon-stimulated genes (110). Another active ingredient is luteolin, a natural flavonoid found in various plants (111). Research indicates that luteolin combats HSV-1 by activating the cGAS-STING pathway, thereby enhancing antiviral interferon production (112). Liuwei Wuling Tablet consists of various ingredients, including Schisandra chinensis and chasteberry, which have been shown to nourish the kidneys and liver while also exhibiting antiviral activity (113). The combination of Schisandrin C and Luteolin has been found to inhibit HBV replication and attenuate HBV infection by activating the cGAS-STING pathway (114).

Glycyrrhetinic acid (GA), a major constituent of licorice, exhibited anti-inflammatory, antioxidant, and antiviral effects

during the COVID-19 pandemic (115, 116). GA was found to inhibit SARS-CoV-2 infection by activating cGAS-STING pathway (117). Cepharanthine (CEP) has demonstrated inhibitory effects against viruses such as HIV, SARS, and HSV-1 (118). CEP promotes cellular autophagy, thereby inhibiting HSV-1 infection (119). Euphorbia fischeriana Steud is a perennial herb whose root has traditionally been utilized in TCM to treat diseases such as cancer, edema, and ascites. Dpo, a compound isolated from the root of E. fischeriana, has been found to activate antiviral innate immune responses by targeting STING and utilizing the IRFs/ELF4 pathway (120). Similarly, Ginsenoside Rg3 has been shown to stimulate a type I interferon response via the cGAS-STING signaling axis. This response is supported by gut-derived short-chain fatty acids like acetate and propionate, offering protection against enteroviral infections (104).

In the context of sepsis—a severe systemic inflammatory condition triggered by bacterial or fungal infections and often leading to multiple organ dysfunction—Glycyrrhiza uralensis polysaccharides have demonstrated protective effects. These are achieved by disrupting the interactions between STING, TBK1, and IRF3, thereby reducing cGAS-STING pathway activation and mitigating sepsis-related damage (121).

4.4 Diseases of the respiratory system

Acute lung injury (ALI) is a serious lung disease recognized globally, manifesting as a persistent acute inflammatory response that is associated with high morbidity and mortality (122). Despite significant advances in therapy, treating ALI remains a major clinical challenge. The cGAS-STING pathway plays a vital role in the pathogenesis of ALI, affecting immune response, apoptosis, vascular permeability, and oxidative stress, which exacerbate inflammation and tissue damage (123). Various herbal medicines can improve ALI or pulmonary fibrosis by modulating this pathway (Table 1).

For example, licorice flavonoids possess anti-inflammatory activity and inhibit cGAMP synthesis, thereby preventing overactivation of the cGAS-STING pathway and ameliorating lipopolysaccharide (LPS)-induced ALI (124). Perillaldehyde alleviated acute lung injury by inhibiting the cGAS-STING-mediated IRF3/NF-κB pathway (125). Additionally, apigenin and ursodeoxycholic acid (UDCA) have demonstrated efficacy in alleviating ALI by inhibiting STING-related signaling pathways. Apigenin attenuates the LPS-induced inflammatory response by inhibiting the STING/IRF3 pathway, whereas UDCA mitigates sepsis-induced lung injury by blocking cell death via the STING pathway (126, 127). Traditional Chinese medicine compound preparations, such as Shuangdan Jiedu Decoction and Tanreqing injection (TRQ), have also significantly ameliorated LPS-induced ALI and other respiratory-related diseases by regulating the STING pathway through multiple mechanisms (128, 129). TRQ is a proprietary Chinese medicine that is commonly used for lung diseases such as pneumonia and idiopathic pulmonary fibrosis (IPF) (132–134). Clinical evidence suggests that TRQ can alleviate the development of pulmonary fibrosis and improve lung function in patients (130). Recent studies have shown that 20(S)-Protopanaxadiol, isolated from ginseng, and TRQ can improve pulmonary fibrosis by modulating the cGAS-STING pathway (130, 131).

4.5 Diseases of the digestive system

Liver fibrosis is a chronic liver disease triggered by various factors, including excessive alcohol consumption, viral infections (HBV and HCV), and non-alcoholic steatohepatitis (NASH) (135–137). Recent studies have shown that the cGAS-STING pathway plays an important role in the pathological process of liver fibrosis, and various traditional Chinese medicines can exert anti-fibrotic effects by regulating this pathway.

Naringenin, an anti-inflammatory flavonoid extracted from citrus plants, has been shown to directly bind to cGAS (138). It reduces inflammatory factors secreted by hepatic stellate cells by inhibiting the cGAS-STING pathway, thereby alleviating liver fibrosis (139). Licorice extract improved hepatic inflammation and fibrosis in a mouse model of NASH, with its mechanism of action including inhibition of the cGAS-STING pathway (140). Oroxylin A, a baicalin derivative, activated the cGAS-STING pathway, promoted the secretion of cytokine IFN-β, induced hepatic stellate cell senescence, and acted as an antifibrotic agent (141).

Modulation of the cGAS-STING pathway by TCM can also alleviate acute liver injury. For example, total glucosides of paeon, on the other hand, reduced hepatic inflammation in an acute liver injury (ALI) model by inhibiting the STING-IRF3 interaction (142). Ginsenoside Rd protects mice from CCl_4-induced ALI by inhibiting the cGAS-STING pathway and reducing iron death (143).

Lingguizhugan Decoction (LGZG) is a traditional Chinese herbal decoction that has been used for many years in the treatment of metabolic disorders and has been effective in alleviating obesity and dyslipidemia (144, 145). LGZG significantly reduced high-fat diet (HFD)-induced hepatic lipid deposition by inhibiting the STING-TBK1-NF-κB pathway in hepatic macrophages (146).

Additionally, drug-induced liver injury is a leading cause of acute liver injury and liver transplantation (147). Studies have shown that jujuboside B ameliorated acetaminophen-induced liver injury by upregulating Nrf2 protein expression and inhibiting the cGAS-STING pathway (148). Similarly, rhodopsin protected hepatocytes from APAP-induced toxicity by regulating Nrf2 and NLRP3 inflammatory vesicles, while inhibiting the cGAS-STING pathway (149).

Andrographolide, derived from Andrographis paniculata, has been shown to ameliorate chemotherapeutic drug-induced gastrointestinal mucosal inflammation by down-regulating the cGAS-STING pathway (150). Naringin can also attenuate intestinal ischemia-reperfusion injury by inhibiting the cGAS-STING pathway (151).

4.6 Diseases of the urinary system

Acute kidney injury (AKI) is a global health problem. Although cisplatin is an effective chemotherapeutic agent, its nephrotoxicity

TABLE 1 Traditional Chinese medicine can treat or alleviate respiratory diseases by regulating the cGAS-STING signaling pathway.

Compounds/ single TCM	Origins	Molecular formula	Cells/ Animals	Mode of administration	Doses	Course of treatment	Functions	Mechanisms	References
Licorice flavonoids	*Glycyrrhiza glabra L.*	–	BMDMs, THP-1 cells, HEK-293 Cells, C57BL/ 6J mice	Gavage	20 mg/kg, 40 mg/kg	10hours	Inhibition of the expression of type I interferons and related downstream genes, as well as inflammatory cytokines and TNF-α	Blocking of cGAMP synthesis	(124)
Perillaldehyde	*Perilla frutescens* (L.) Britt.	$C_{10}H_{14}O$	RAW264.7 cells, C57BL/ 6 mice	Intraperitoneal injection	50 mg/kg, 10 0 mg/kg, 2 0 0 mg/kg	24hours	Inhibiting LPS-induced lung histological changes, inflammatory cell infiltration and oxidative stress	Inhibiting cGAS/STING-mediated IRF3/NF-κB signaling	(125)
Apigenin	*Matricaria chamomilla* L., Perilla frutescens (L.) Britt.	$C_{15}H_{10}O_5$	THP-1 cells, HEK293T cells, C57BL/ 6 mice	Intraperitoneal injection	50 mg/kg	24hours	Alleviating innate immune responses and mitigating inflammation in LPS-induced ALI	Inhibits STING expression, reduces dimerization, phosphorylates nuclear translocation of IRF3, and disrupts the association between STING and IRF3, IFNβ1↓	(126)
Ursodeoxycholic acid	*Selenaretos thibetanus* Cuvier	$C_{24}H_{40}O_4$	C57BL/6 mice	Oral pre-treatment	30 mg/kg, 60 mg/kg	24hours	Inhibiting pulmonary edema, inflammatory cell infiltration, pro-inflammatory cytokines production, and oxidative stress	Blocking PANoptosis-like cell death via STING pathway	(127)
Shuangdan Jiedu Decoction	*Lonicera japonica* Thunb, *Forsythia suspensa* (Thunb.) Vahl,*Paeonia lactiflora* Pall,*Salvia miltiorrhiza* Bunge,*Paeonia suffruticosa* Andr,*Glycyrrhiza uralensis* Fisch	–	BMDMs, THP-1 cells, C57BL/6 mice	Gavage	3.7 g/kg,7.4 g/ kg,0.98 g/kg	12hours	Alleviating LPS-induced ALI by suppressing the levels of proinflammatory cytokines, and the number of neutrophils, decreasing the inflammatory factor-associated gene expression	Inhibit multiple stimulus-driven activation of cGAS-STING and inflammasome	(128)
Tanreqing injection	*Scutellaria baicalensis* Georgi, *Selenaretos thibetanus* Cuvier, *Capra hircus* Linnaeus,*Lonicera japonica* Thunb.,*Forsythia suspensa* (Thunb.) Vahl	–	RAW 264.7 cell,Mouse bone marrow neutrophils, C57BL/6 mice	Intraperitoneal injection	2.6 ml/kg,5.2 ml/kg	6hours	Inhibiting inflammatory responses and oxidative stress	Downregulating STING signaling pathway	(129)
			C57BL/6 mice	Intraperitoneal injection	2.6 ml/kg,5.2 ml/kg	21 days	Inhibiting inflammatory responses and reducing the occurrence of fibrosis	Inhibiting STING-mediated endoplasmic reticulum stress signaling pathway	(130)
20(S)-Protopanaxadiol	*Panax ginseng* C. A. Mey.	$C_{30}H_{52}O_3$	MLE-12 cell, C57BL/6 mice	Gavage	10 or 40 mg/kg	2 weeks	Inhibiting inflammatory responses and reducing the occurrence of fibrosis	Inhibiting STING expression by activating AMPK	(131)

10.3389/fimmu.2024.1510628

limits clinical use (152). Therefore, there is a need for nephroprotective drugs that are safe and do not compromise the antitumor effect. TCMs are widely used for preventing and treating renal diseases. From the Western medicine perspective, cisplatin triggers AKI primarily due to drug toxicity or edema, while from the TCM perspective, its pathogenesis involves spleen and kidney qi deficiency, damp-heat underflow, and blood stasis (153). Various traditional Chinese medicines and compound formulas can effectively alleviate cisplatin-induced AKI by regulating the cGAS/STING pathway.

Yi-Shen-Xie-Zhuo formula (YSXZF) is a Chinese herbal formula composed of four herbs: *Astragali Radix* (Huangqi), *Alismatis Rhizoma* (Zexie), *Paeoniae Radix Rubra* (Chishao), *Sargassum* (Haizao). Studies have shown that YSXZF can inhibit the cGAS/STING pathway, reduce the expression of inflammatory factors such as TNF-α, IL-3, and IL-1β, and decrease IRF1 activity, which in turn reduces the inflammatory response and prevents acute kidney injury (154). Shenqi Fuzheng Injection (SQFZ) consists of extracts from Codonopsis Radix and Astragali Radix, both of which possess anti-tumor and anti-inflammatory effects. It has been found that SQFZ can effectively inhibit the cGAS/STING pathway, attenuate cisplatin-induced nephrotoxicity, and improve the effectiveness of chemotherapeutic agents (155).

To improve the bioavailability of active ingredients in traditional Chinese medicine, recent studies have explored the use of nanotechnology. For example, baicalein (5,6,7-trihydroxyflavone, BA) possesses antioxidant and antitumor effects, but its poor water solubility and low bioavailability limit its clinical application. Self-assembly of silk fibroin peptide (SFP) into nanofibers encapsulating baicalein (SFP/BA NFs) enhances its *in vivo* efficacy, inhibits cisplatin-induced DNA damage and cGAS/STING pathway activation, and exerts a nephroprotective effect to prevent AKI (156).

Similarly, naringenin (NGN) has poor water solubility, limiting its application. To address this, researchers have developed NGN-loaded silk fibroin peptide nanofibers (SFP/NGN NFs). Cisplatin-induced mitochondrial damage leads to the release of mtDNA and activation of the cGAS-STING pathway, which in turn triggers the expression of inflammatory factors, such as IL-6 and TNF-α. SFP/NGN NFs effectively attenuated cisplatin-induced acute kidney injury by facilitating mitochondrial autophagy, decreasing the release of mtDNA and inhibiting the cGAS-STING pathway (157).

In addition, Zhen Wu decoction (a prescription composed of five herbs: Radix *Aconiti lateralis Preparata*, Poria, Radix *Paoniae alba*, ginger, and Rhizoma *Atractylodis macrocephalae*, which are decocted together for extraction) inhibited renal fibrosis by activating NRF2 and TFAM in renal tubules and promoting mitochondrial bioenergy production (158).

4.7 Neurodegenerative diseases

Neurodegenerative diseases are a group of chronic neurological disorders characterized by a progressive loss of neurons and an abnormal accumulation of specific proteins in the brain, accompanied by a decline in cognitive and motor function (159). This group includes Alzheimer's disease (AD), Parkinson's disease (PD), multiple sclerosis (MS), and amyotrophic lateral sclerosis (ALS) (160). Among these, Alzheimer's disease (AD) is the most common neurodegenerative disorder worldwide, manifesting as severe cognitive decline (161).

As an anti-aging traditional Chinese medicine, Polygonum multiflorum has received widespread attention for its role in diseases such as AD, PD, and MS (162). Studies have shown that tetrahydroxy stilbene glucoside (TSG), the main active ingredient of Polygonum multiflorum, possesses significant anti-inflammatory, anti-aging, and memory-improving effects (163). TSG prevents neuroinflammation by modulating the cGAS-STING pathway, leading to significant improvement in cognitive decline in AD patients. In addition, TSG can reduce the formation of NLRP3 inflammatory vesicles by inhibiting the activation of the cGAS-STING pathway, thereby reducing the neuroinflammatory response and demonstrating its potential therapeutic value in Alzheimer's disease (164).

Silibinin, an active ingredient extracted from the TCM silymarin, has attracted attention for its neuroprotective effects in AD models. Research has found that silibinin administration, downregulated the levels of IL-1β, TNF-α and IFN-β, as well as STING and IRF3, ameliorating depression/anxiety-like behaviors of Parkinson's disease mouse model (165). While these findings suggest that silibinin may modulate the cGAS-STING pathway, it is important to note that the inhibition of pro-inflammatory cytokines such as IL-1β and TNF-α could also involve other signaling pathways, including NLRP3 inflammasome activation, NF-κB signaling, and the MAPK pathway (166, 167). And silibinin exerts significant neuroprotective effects by downregulating iron death injury and STING-mediated neuroinflammation, particularly in the STZ-induced sporadic AD model. This provides an important basis for silymarin as a potential drug for the treatment of AD (168). Given the multi-target nature of TCM, further studies are needed to clarify the mechanisms underlying silibinin's effects on neuroinflammation and behavioral outcomes.

4.8 Other diseases

In addition to autoimmune diseases, tumors, and viral infections, a variety of Chinese herbal medicines can ameliorate other diseases by impacting the cGAS-STING pathway, potentially in conjunction with other molecular targets. For example, atherosclerosis is a chronic inflammatory disease of the arterial lining (169). Tetrandrine was found to inhibit the STING/TBK1/NF-κB pathway, reducing inflammation in macrophages attacked by oxidized low-density lipoprotein, and attenuating atherosclerosis in HFD-fed ApoE mice (170).

Myocardial ischemia-reperfusion injury (MIRI) is a major challenge in the treatment of acute myocardial infarction, primarily caused by oxidative stress and inflammatory responses induced by blood reperfusion (171, 172). *Astragalus membranaceus* (Fisch.) Bunge and *Salvia miltiorrhiza* Bunge are representative herbs used for replenishing Qi and activating blood circulation in traditional Chinese medicine, respectively. According to the

compatibility theory of traditional Chinese medicine (173, 174), they are often used in combination (175). Astragaloside IV (As-IV) and Tanshinone IIA (Ta-IIA) are the primary active components of Astragalus membranaceus and Salvia miltiorrhiza, respectively. Research has indicated that the combined use of As-IV and Ta-IIA significantly reduces oxidative stress and apoptosis in cardiomyocytes by enhancing the inhibition of cGAS/STING signaling, thereby improving the therapeutic effect on MIRI (176).

In skin flap transplantation, ischemia/reperfusion (I/R) injury is the main cause of flap necrosis (177, 178). Ginsenoside Rb3, an active component of ginseng, has been shown to reduce leukocyte-endothelial cell adhesion and improve local microcirculation by inhibiting the phosphorylation of IRF3 in the STING pathway, effectively alleviating I/R injury in transregional flaps (179).

In addition, overactivation of the cGAS-STING pathway is closely related to cellular senescence. Liuwei Dihuang (LWDH), a classic Chinese herbal formula, shows potential for anti-endothelial cellular senescence. Studies have shown that LWDH reverses LPS-induced endothelial cell senescence by inhibiting the activation of the cGAS-STING pathway and blocking the interaction between JPX and STING. This provides a new approach for preventing and treating vascular endothelial cell aging (180).

In conclusion, TCM has demonstrated significant therapeutic potential in diseases such as atherosclerosis, myocardial ischemia-reperfusion injury, skin flap transplantation injury, and cellular senescence by modulating the cGAS/STING pathway. These studies provide a new scientific basis for the application of TCM in the treatment of modern diseases, as well as insights for the clinical development of more targeted TCM.

5 cGAS-STING pathway key proteins as biomarkers for TCM in immunomodulation and treatment of various diseases

Due to their multi-component and multi-target characteristics, traditional quality control methods have difficulty comprehensively assessing the safety and efficacy of Chinese medicines (181–183). To cope with these challenges, biomarkers have shown significant potential as tools for quality evaluation of TCM in recent years. Using technologies such as metabolomics, biomarkers can more comprehensively assess the systemic effects and compatibility of TCM. The components of schisandrol A, schisandrin A, gomisin N, and schisandrin B can be used as biomarkers for evaluating the quality standard of *Schisandra chinensis* (Turcz.) Baill (184). In addition, biomarkers can evaluate the clinical efficacy of TCM, such as NF2 and PPP1CA in CDDP, which are thought to be associated with its vasodilatory effects (185).

Biomarkers are equally important in disease treatment. In viral infections, IFN, a central factor in the antiviral response, has emerged as a potential therapeutic target for infections such as HCV and HBV (186). IL-6 plays an important role in the acute inflammatory response, and changes in its level correlate with the severity of infection. Especially in COVID-19, elevated IL-6 levels are closely associated with disease progression, suggesting its potential as a marker for monitoring treatment efficacy (187).

The cGAS-STING pathway is an important part of the innate immune system and has emerged as a potential therapeutic target for a variety of diseases in recent years (188–190). cGAS recognizes intracellular DNA and activates STING proteins, which in turn initiates downstream signaling pathways and induces antiviral and pro-inflammatory factors (191). cGAS-activated signaling molecules, such as TBK1 and IRF3, play a key role in immunoregulation (10). These proteins are not only key regulators of disease progression, but they may also be important biomarkers for evaluating therapeutic effects.

Traditional Chinese medicine plays an immunomodulatory role in the treatment of many diseases by modulating the cGAS-STING pathway. For example, total glucosides of paeony can alleviate liver inflammation caused by acute liver injury by inhibiting the STING-IRF3 interaction (142). Tetrahydroxy stilbene glucoside from Polygonum multiflorum was found to reduce neuroinflammation by inhibiting the cGAS-STING pathway, thereby improving cognitive function in patients with Alzheimer's disease (164). In addition, ginsenoside Rb3 was effective in ameliorating ischemia-reperfusion injury in skin flap transplantation by inhibiting the STING-mediated inflammatory response (179). These studies demonstrated the modulatory effects of TCM on key proteins in the cGAS-STING pathway, suggesting that these proteins can be used as biomarkers of TCM therapy for assessing efficacy and potential for individualized treatment.

In summary, key proteins such as cGAS, STING, TBK1, and IRF3 play important roles in the occurrence and development of diseases. By regulating the expression and activity of these proteins, TCM can effectively regulate immune responses and treat a variety of diseases. Therefore, the key proteins in the cGAS-STING pathway can not only be used as targets for TCM to regulate immune and inflammatory responses, but they also have the potential to serve as biomarkers for clinical therapeutic effects. This provides a new direction for the future application of TCM in precision medicine.

6 Summary and prospect

TCM holds an important position in the field of medicine due to its unique bidirectional immunomodulatory ability, which can activate the immune system to enhance the body's defense, while also moderately inhibiting excessive immune responses and reducing inflammation and autoimmune diseases. The cGAS-STING pathway, an important component of the innate immune system, plays a key role in defending against viral and bacterial infections, modulating cellular damage, inflammatory responses, autophagy, and tumor immunity (56, 192). Therefore, the cGAS-STING pathway has become a potential drug target for treating inflammatory diseases, tumors, and immune dysregulation. TCM has shown unique potential in modulating this pathway, providing new strategies for the treatment of a variety of diseases.

Currently, the development of activators and inhibitors of the cGAS-STING pathway is a research priority. Although STING agonists have shown promising results in preclinical antitumor

studies, their clinical translation faces many challenges. For example, modified CDN compounds are rapidly degraded *in vivo* due to poor metabolic stability, which affects the durability of their efficacy (193). In addition, the low cellular uptake rate of CDN makes it difficult for the drug to efficiently enter target cells, which in turn limits its antitumor effects (194). While most studies rely on intra-tumor drug delivery, there is a lack of delivery technologies that can be applied on a large scale, further limiting the potential application of STING agonists in clinical therapy. In addition, the limited targeting of STING agonists may lead to off-target effects, triggering unnecessary immune activation and increasing autoimmune risks (195). Thus, improving the targeting and safety of STING agonists remains a critical issue for realizing their clinical applications. Regarding STING inhibitors, although compounds such as H-151, C-176, BB-Cl-amidine, and sulforaphane have been reported to inhibit the activation of the cGAS-STING pathway, their therapeutic potential remains limited (196–200). H-151, as the most promising STING inhibitor, inhibits palmitoylation by binding to the Cys91 site of the STING protein (196). However, studies on it are still at the animal experiment stage. Therefore, the development of clinically applicable STING inhibitors in inflammatory and autoimmune diseases remains an urgent topic.

Chinese medicines show remarkable potential in modulating the cGAS-STING pathway, especially in the treatment of inflammatory diseases. For example, compounds such as perilla aldehyde, ursodeoxycholic acid, total glucosides of paeony, and andrographolide affect the activity of this pathway through different mechanisms. Perillaldehyde has been shown to inhibit the innate immune response induced by cytosolic DNA by inhibiting cGAS activity and to attenuate the inflammatory response by reducing the release of inflammatory factors through inhibition of downstream signaling after STING activation. Ursodeoxycholic acid, on the other hand, inhibits the production of pro-inflammatory cytokines by blocking PANoptosis-like cell death through inhibition of the STING pathway. Various active components in licorice, such as glabridin, licorice flavonoids, and licorice chalcone B, can inhibit cGAS-STING-mediated inflammatory responses by modulating the cGAS-STING pathway, thereby exerting therapeutic effects on inflammatory diseases. TRIM29 has been reported to contribute to the pathogenesis of viral myocarditis by enhancing ROS-mediated oxidation of TBK1, thereby inhibiting its function (201). Both TRIM29 and TRIM18 play pivotal roles in the progression of various virus infections, including viral enteritis, viral myocarditis, and various organ inflammations (52, 202, 203). Studies suggest that TCM, with its rich repertoire of antiviral herbal compounds (such as quercetin and ginsenosides), may offer therapeutic potential in treating these infectious diseases. TCM may modulate immune responses by downregulating the expression of TRIM29 and TRIM18, thereby mitigating the inflammatory damage caused by these viral infections. These findings provide important clues for the development of novel herbal therapies based on the cGAS-STING pathway and open up new directions for immunomodulation in a variety of diseases.

Studying the targeting of the cGAS-STING pathway by TCM reflects the unique advantages of TCM in immunomodulation, providing both a scientific basis for modernizing traditional medicine and a new strategy for immunotherapy. However, while studies have demonstrated the potential of TCM in modulating the cGAS-STING pathway, more high-quality research is needed to validate these effects for true clinical applications. Meanwhile, an in-depth understanding of the mechanism of action of TCM can help promote the modernization of TCM and enhance its value for clinical application (204). In the future, with in-depth studies on the mechanisms of the cGAS-STING pathway, TCM may become an effective tool for modulating immune and inflammatory responses, bringing new hope for the treatment of a variety of diseases.

Author contributions

HZ: Conceptualization, Formal analysis, Methodology, Visualization, Writing – original draft. HF: Conceptualization, Formal analysis, Methodology, Visualization, Writing – original draft. YZ: Data curation, Investigation, Writing – original draft. NF: Data curation, Investigation, Writing – original draft. CZ: Software, Validation, Writing – original draft. YFL: Software, Validation, Writing – review & editing. YS: Funding acquisition, Project administration, Resources, Supervision, Writing – review & editing. YPL: Funding acquisition, Project administration, Resources, Supervision, Writing – review & editing.

Funding

The author(s) declare financial support was received for the research, authorship, and/or publication of this article. This research was funded by the National Natural Science Foundation of China, grant numbers 82104568, 82074030, and 82374050.

Conflict of interest

The authors declare that the research was conducted in the absence of any commercial or financial relationships that could be construed as a potential conflict of interest.

Generative AI statement

The author(s) declare that no Generative AI was used in the creation of this manuscript.

Publisher's note

References

1. Takeuchi O, Akira S. Pattern recognition receptors and inflammation. *Cell*. (2010) 140:805–20. doi: 10.1016/j.cell.2010.01.022

2. Ma H-D, Deng Y-R, Tian Z, Lian Z-X. Traditional Chinese medicine and immune regulation. *Clin Rev Allergy Immunol*. (2013) 44:229–41. doi: 10.1007/s12016-012-8332-0

3. Brubaker SW, Bonham KS, Zanoni I, Kagan JC. Innate immune pattern recognition: A cell biological perspective. *Annu Rev Immunol*. (2015) 33:257–90. doi: 10.1146/annurev-immunol-032414-112240

4. Kwon J, Bakhoum SF. The cytosolic DNA-sensing cgas-sting pathway in cancer. *Cancer Discovery*. (2020) 10:26–39. doi: 10.1158/2159-8290.CD-19-0761

5. Zhang X, Wu J, Liu Q, Li X, Li S, Chen J, et al. Mtdna-sting pathway promotes necroptosis-dependent enterocyte injury in intestinal ischemia reperfusion. *Cell Death Dis*. (2020) 11:1050. doi: 10.1038/s41419-020-03239-6

6. Woo SR, Fuertes MB, Corrales L, Spranger S, Furdyna MJ, Leung MY, et al. Sting-dependent cytosolic DNA sensing mediates innate immune recognition of immunogenic tumors. *Immunity*. (2014) 41:830–42. doi: 10.1016/j.immuni.2014.10.017

7. Ishikawa H, Barber GN. Sting is an endoplasmic reticulum adaptor that facilitates innate immune signalling. *Nature*. (2008) 455:674–8. doi: 10.1038/nature07317

8. Burdette DL, Monroe KM, Sotelo-Troha K, Iwig JS, Eckert B, Hyodo M, et al. Sting is a direct innate immune sensor of cyclic Di-Gmp. *Nature*. (2011) 478:515–8. doi: 10.1038/nature10429

9. Guo F, Han Y, Zhao X, Wang J, Liu F, Xu C, et al. Sting agonists induce an innate antiviral immune response against hepatitis B virus. *Antimicrob Agents Chemother*. (2015) 59:1273–81. doi: 10.1128/AAC.04321-14

10. Hopfner KP, Hornung V. Molecular mechanisms and cellular functions of cgas-sting signalling. *Nat Rev Mol Cell Biol*. (2020) 21:501–21. doi: 10.1038/s41580-020-0244-x

11. Luo W, Zou X, Wang Y, Dong Z, Weng X, Pei Z, et al. Critical role of the cgas-sting pathway in doxorubicin-induced cardiotoxicity. *Circ Res*. (2023) 132:e223–e42. doi: 10.1161/CIRCRESAHA.122.321587

12. Gao D, Li T, Li X-D, Chen X, Li Q-Z, Wight-Carter M, et al. Activation of cyclic Gmp-Amp synthase by self-DNA causes autoimmune diseases. *Proc Natl Acad Sci*. (2015) 112:E5699–E705. doi: 10.1073/pnas.1516465112

13. Chauvin SD, Stinson WA, Platt DJ, Poddar S, Miner JJ. Regulation of Cgas and sting signaling during inflammation and infection. *J Biol Chem*. (2023) 299:104866. doi: 10.1016/j.jbc.2023.104866

14. Liu Z, Wang D, Zhang J, Xiang P, Zeng Z, Xiong W, et al. Cgas-sting signaling in the tumor microenvironment. *Cancer Lett*. (2023) 577:216409. doi: 10.1016/j.canlet.2023.216409

15. Levander OA, Whanger PD. Deliberations and evaluations of the approaches, endpoints and paradigms for selenium and iodine dietary recommendations. *J Nutr*. (1996) 126:2427S–34S. doi: 10.1093/jn/126.suppl_9.2427S

16. Cho YJ, Son HJ, Kim KS. A 14-week randomized, placebo-controlled, double-blind clinical trial to evaluate the efficacy and safety of ginseng polysaccharide (Y-75). *J Transl Med*. (2014) 12:283. doi: 10.1186/s12967-014-0283-1

17. Guo Q, Li J, Lin H. Effect and molecular mechanisms of traditional Chinese medicine on regulating tumor immunosuppressive microenvironment. *BioMed Res Int*. (2015) 2015:261620. doi: 10.1155/2015/261620

18. Liu J, Wang S, Zhang Y, Fan HT, Lin HS. Traditional Chinese medicine and cancer: history, present situation, and development. *Thorac Cancer*. (2015) 6:561–9. doi: 10.1111/1759-7714.12270

19. Ye L, Jia Y, Ji KE, Sanders AJ, Xue K, Ji J, et al. Traditional Chinese medicine in the prevention and treatment of cancer and cancer metastasis. *Oncol Lett*. (2015) 10:1240–50. doi: 10.3892/ol.2015.3459

20. Mao D, Feng L, Gong H. The antitumor and immunomodulatory effect of Yanghe decoction in breast cancer is related to the modulation of the Jak/Stat signaling pathway. *Evid Based Complement Alternat Med*. (2018) 2018:8460526. doi: 10.1155/2018/8460526

21. Taniguchi M, Seino K, Nakayama T. The Nkt cell system: bridging innate and acquired immunity. *Nat Immunol*. (2003) 4:1164–5. doi: 10.1038/ni1203-1164

22. Wan CP, Gao LX, Hou LF, Yang XQ, He PL, Yang YF, et al. Astragaloside Ii triggers T cell activation through regulation of Cd45 protein tyrosine phosphatase activity. *Acta Pharmacol Sin*. (2013) 34:522–30. doi: 10.1038/aps.2012.208

23. Aoshi T, Koyama S, Kobiyama K, Akira S, Ishii KJ. Innate and adaptive immune responses to viral infection and vaccination. *Curr Opin Virol*. (2011) 1:226–32. doi: 10.1016/j.coviro.2011.07.002

24. Pryde DC, Middya S, Banerjee M, Shrivastava R, Basu S, Ghosh R, et al. The discovery of potent small molecule activators of human sting. *Eur J Med Chem*. (2021) 209:112869. doi: 10.1016/j.ejmech.2020.112869

25. Shang G, Zhang C, Chen ZJ, Bai XC, Zhang X. Cryo-Em structures of sting reveal its mechanism of activation by cyclic Gmp-Amp. *Nature*. (2019) 567:389–93. doi: 10.1038/s41586-019-0998-5

26. Ding CY, Song ZL, Shen AC, Chen TT, Zhang A. Small molecules targeting the innate immune Cgas-Sting-Tbk1 signaling pathway. *Acta Pharm Sin B*. (2020) 10:2272–98. doi: 10.1016/j.apsb.2020.03.001

27. Sun LJ, Wu JX, Du FH, Chen X, Chen ZJJ. Cyclic Gmp-Amp synthase is a cytosolic DNA sensor that activates the type I interferon pathway. *Science*. (2013) 339:786–91. doi: 10.1126/science.1232458

28. Ablasser A, Goldeck M, Cavlar T, Deimling T, Witte G, Röhl I, et al. Cgas produces a 2′-5′-linked cyclic dinucleotide second messenger that activates sting. *Nature*. (2013) 498:380–+. doi: 10.1038/nature12306

29. Marinho FV, Benmerzoug S, Oliveira SC, Ryffel B, Quesniaux VFJ. The emerging roles of sting in bacterial infections. *Trends Microbiol*. (2017) 25:906–18. doi: 10.1016/j.tim.2017.05.008

30. Dobbs N, Burnaevskiy N, Chen DD, Gonugunta VK, Alto NM, Yan N. Sting activation by translocation from the Er is associated with infection and autoinflammatory disease. *Cell Host Microbe*. (2015) 18:157–68. doi: 10.1016/j.chom.2015.07.001

31. Li AP, Yi M, Qin S, Song YP, Chu Q, Wu KM. Activating cgas-sting pathway for the optimal effect of cancer immunotherapy. *J Hematol Oncol*. (2019) 12:1–12. doi: 10.1186/s13045-019-0721-x

32. Corrales L, McWhirter SM, Dubensky TW, Gajewski TF. The host sting pathway at the interface of cancer and immunity. *J Clin Invest*. (2016) 126:2404–11. doi: 10.1172/Jci86892

33. Burdette DL, Vance RE. Sting and the innate immune response to nucleic acids in the cytosol. *Nat Immunol*. (2013) 14:19–26. doi: 10.1038/ni.2491

34. Fuertes MB, Woo SR, Burnett B, Fu YX, Gajewski TF. Type I interferon response and innate immune sensing of cancer. *Trends Immunol*. (2013) 34:67–73. doi: 10.1016/j.it.2012.10.004

35. Decout A, Katz JD, Venkatraman S, Ablasser A. The Cgas–sting pathway as a therapeutic target in inflammatory diseases. *Nat Rev Immunol*. (2021) 21:548–69. doi: 10.1038/s41577-021-00524-z

36. Corrales L, Glickman LH, McWhirter SM, Kanne DB, Sivick KE, Katibah GE, et al. Direct activation of sting in the tumor microenvironment leads to potent and systemic tumor regression and immunity. *Cell Rep*. (2015) 11:1018–30. doi: 10.1016/j.celrep.2015.04.031

37. Vasiyani H, Wadhwa B, Singh R. Regulation of cgas-sting signalling in cancer: approach for combination therapy. *Biochim Biophys Acta (BBA) Reviews Cancer*. (2023) 1878:188896. doi: 10.1016/j.bbcan.2023.188896

38. Pan X, Zhang W, Guo H, Wang L, Wu H, Ding L, et al. Strategies involving sting pathway activation for cancer immunotherapy: mechanism and agonists. *Biochem Pharmacol*. (2023) 213:115596. doi: 10.1016/j.bcp.2023.115596

39. Woon ST, Reddy CB, Drummond CJ, Schooltink MA, Baguley BC, Kieda C, et al. A comparison of the ability of Dmxaa and xanthenone analogues to activate Nf-Kappab in murine and human cell lines. *Oncol Res*. (2005) 15:351–64. doi: 10.3727/096504005776449743

40. Eckstein F. Phosphorothioates, essential components of therapeutic oligonucleotides. *Nucleic Acid Ther*. (2014) 24:374–87. doi: 10.1089/nat.2014.0506

41. Meric-Bernstam F, Sweis RF, Hodi FS, Messersmith WA, Andtbacka RH, Ingham M, et al. Phase I dose-escalation trial of Miw815 (Adu-S100), an intratumoral sting agonist, in patients with advanced/metastatic solid tumors or lymphomas. *Clin Cancer Res*. (2022) 28:677–88. doi: 10.1158/1078-0432.CCR-21-1963

42. Wang H, Hu S, Chen X, Shi H, Chen C, Sun L, et al. Cgas is essential for the antitumor effect of immune checkpoint blockade. *Proc Natl Acad Sci*. (2017) 114:1637–42. doi: 10.1073/pnas.1621363114

43. Lucas-Hourani M, Dauzonne D, Jorda P, Cousin G, Lupan A, Helynck O, et al. Inhibition of pyrimidine biosynthesis pathway suppresses viral growth through innate immunity. *PloS Pathog*. (2013) 9:e1003678. doi: 10.1371/journal.ppat.1003678

44. Shin HJ, Kim C, Cho S. Gemcitabine and nucleos(T)Ide synthesis inhibitors are broad-spectrum antiviral drugs that activate innate immunity. *Viruses*. (2018) 10(4):211. doi: 10.3390/v10040211

45. Paulis A, Tramontano E. Unlocking sting as a therapeutic antiviral strategy. *Int J Mol Sci*. (2023) 24:7448. doi: 10.3390/ijms24087448

46. Kim S, Li L, Maliga Z, Yin Q, Wu H, Mitchison TJ. Anticancer flavonoids are mouse-selective sting agonists. *ACS Chem Biol*. (2013) 8:1396–401. doi: 10.1021/cb400264n

47. Yongpitakwattana P, Morchang A, Panya A, Sawasdee N, Yenchitsomanus PT. Alpha-mangostin inhibits dengue virus production and pro-inflammatory cytokine/chemokine expression in dendritic cells. *Arch Virol*. (2021) 166:1623–32. doi: 10.1007/s00705-021-05017-x

48. Tarasuk M, Songprakhon P, Chieochansin T, Choomee K, Na-Bangchang K, Yenchitsomanus PT. Alpha-mangostin inhibits viral replication and suppresses nuclear factor kappa B (Nf-Kappab)-mediated inflammation in dengue virus infection. *Sci Rep*. (2022) 12:16088. doi: 10.1038/s41598-022-20284-7

49. Christensen MH, Jensen SB, Miettinen JJ, Luecke S, Prabakaran T, Reinert LS, et al. Hsv-1 icp27 targets the Tbk1-activated sting signalsome to inhibit virus-induced type I Ifn expression. *EMBO J*. (2016) 35:1385–99. doi: 10.15252/embj.201593458

50. Fu YZ, Su S, Gao YQ, Wang PP, Huang ZF, Hu MM, et al. Human cytomegalovirus tegument protein Ul82 inhibits sting-mediated signaling to evade antiviral immunity. *Cell Host Microbe*. (2017) 21:231–43. doi: 10.1016/j.chom.2017.01.001

51. Zhang K, Huang Q, Li X, Zhao Z, Hong C, Sun Z, et al. The cgas-sting pathway in viral infections: A promising link between inflammation, oxidative stress and autophagy. *Front Immunol*. (2024) 15:1352479. doi: 10.3389/fimmu.2024.1352479

52. Xing J, Zhang A, Zhang H, Wang J, Li XC, Zeng M-S, et al. Trim29 promotes DNA virus infections by inhibiting innate immune response. *Nat Commun*. (2017) 8:945. doi: 10.1038/s41467-017-00101-w

53. Kato Y, Park J, Takamatsu H, Konaka H, Aoki W, Aburaya S, et al. Apoptosis-derived membrane vesicles drive the cgas-sting pathway and enhance type I Ifn production in systemic lupus erythematosus. *Ann Rheum Dis*. (2018) 77:1507–15. doi: 10.1136/annrheumdis-2018-212988

54. Gray EE, Treuting PM, Woodward JJ, Stetson DB. Cutting edge: Cgas is required for lethal autoimmune disease in the Trex1-deficient mouse model of Aicardi-Goutières syndrome. *J Immunol*. (2015) 195:1939–43. doi: 10.4049/jimmunol.1500969

55. Ding C, Song Z, Shen A, Chen T, Zhang A. Small molecules targeting the innate immune Cgas-Sting-Tbk1 signaling pathway. *Acta Pharm Sin B*. (2020) 10:2272–98. doi: 10.1016/j.apsb.2020.03.001

56. Wang MM, Zhao Y, Liu J, Fan RR, Tang YQ, Guo ZY, et al. The role of the cgas-sting signaling pathway in viral infections, inflammatory and autoimmune diseases. *Acta Pharmacol Sin*. (2024) 45:1997–2010. doi: 10.1038/s41401-023-01185-5

57. An J, Woodward JJ, Sasaki T, Minie M, Elkon KB. Cutting edge: antimalarial drugs inhibit Ifn-B Production through blockade of cyclic Gmp-Amp synthase-DNA interaction. *J Immunol*. (2015) 194:4089–93. doi: 10.4049/jimmunol.1402793

58. Huang CF, Lin SS, Liao PH, Young SC, Yang CC. The immunopharmaceutical effects and mechanisms of herb medicine. *Cell Mol Immunol*. (2008) 5:23–31. doi: 10.1038/cmi.2008.3

59. Jiang MH, Zhu LA, Jiang JG. Immunoregulatory actions of polysaccharides from Chinese herbal medicine. *Expert Opin Ther Tar*. (2010) 14:1367–402. doi: 10.1517/14728222.2010.531010

60. Borchers AT, Sakai S, Henderson GL, Harkey MR, Keen CL, Stern JS, et al. Shosaiko-to and other Kampo (Japanese herbal) medicines: A review of their immunomodulatory activities. *J Ethnopharmacol*. (2000) 73:1–13. doi: 10.1016/s0378-8741(00)00334-2

61. Lin YL, Liang YC, Lee SS, Chiang BL. Polysaccharide purified from ganoderma lucidum induced activation and maturation of human monocyte-derived dendritic cells by the Nf-Kappab and P38 mitogen-activated protein kinase pathways. *J Leukoc Biol*. (2005) 78:533–43. doi: 10.1189/jlb.0804481

62. Ying M, Yu Q, Zheng B, Wang H, Wang J, Chen S, et al. Cultured Cordyceps sinensis polysaccharides modulate intestinal mucosal immunity and gut microbiota in cyclophosphamide-treated mice. *Carbohydr Polymers*. (2020) 235:115957. doi: 10.1016/j.carbpol.2020.115957

63. LeBien TW, Tedder TF. B lymphocytes: how they develop and function. *Blood*. (2008) 112:1570–80. doi: 10.1182/blood-2008-02-078071

64. Xie S-Z, Liu B, Ye H-Y, Li Q-M, Pan L-H, Zha X-Q, et al. Dendrobium huoshanense polysaccharide regionally regulates intestinal mucosal barrier function and intestinal microbiota in mice. *Carbohydr Polymers*. (2019) 206:149–62. doi: 10.1016/j.carbpol.2018.11.002

65. Li W, Guo S, Xu D, Li B, Cao N, Tian Y, et al. Polysaccharide of Atractylodes macrocephala koidz (Pamk) relieves immunosuppression in cyclophosphamide-treated geese by maintaining a humoral and cellular immune balance. *Molecules*. (2018) 23 (4):932. doi: 10.3390/molecules23040932

66. Xu W, Fang S, Cui X, Guan R, Wang Y, Shi F, et al. Signaling pathway underlying splenocytes activation by polysaccharides from Atractylodis macrocephalae koidz. *Mol Immunol*. (2019) 111:19–26. doi: 10.1016/j.molimm.2019.03.004

67. Hwang J, Zhang W, Dhananjay Y, An E-K, Kwak M, You S, et al. Astragalus membranaceus polysaccharides potentiate the growth-inhibitory activity of immune checkpoint inhibitors against pulmonary metastatic melanoma in mice. *Int J Biol Macromol*. (2021) 182:1292–300. doi: 10.1016/j.ijbiomac.2021.05.073

68. Zhong H, Han L, Lu RY, Wang Y. Antifungal and immunomodulatory ingredients from traditional Chinese medicine. *Antibiotics-Basel*. (2023) 12(1):48. doi: 10.3390/antibiotics12010048

69. Fu Y, Zhou X, Wang L, Fan W, Gao S, Zhang D, et al. Salvianolic acid B attenuates liver fibrosis by targeting Ecm1 and inhibiting hepatocyte ferroptosis. *Redox Biol*. (2024) 69:103029. doi: 10.1016/j.redox.2024.103029

70. Zhou H-l, Deng Y-m, Xie Q-m. The modulatory effects of the volatile oil of ginger on the cellular immune response *in vitro* and *in vivo* in mice. *J Ethnopharmacol*. (2006) 105:301–5. doi: 10.1016/j.jep.2005.10.022

71. Zeng Q, Zhou T-t, Huang W-j, Huang X-t, Huang L, Zhang X-h, et al. Asarinin attenuates bleomycin-induced pulmonary fibrosis by activating Pparγ. *Sci Rep*. (2023) 13:14706. doi: 10.1038/s41598-023-41933-5

72. Gao LL, Ma JM, Fan YN, Zhang YN, Ge R, Tao XJ, et al. Lycium barbarum polysaccharide combined with aerobic exercise ameliorated nonalcoholic fatty liver disease through restoring gut microbiota, intestinal barrier and inhibiting hepatic inflammation. *Int J Biol Macromol*. (2021) 183:1379–92. doi: 10.1016/j.ijbiomac.2021.05.066

73. Hou Y, Jiang JG. Origin and concept of medicine food homology and its application in modern functional foods. *Food Funct*. (2013) 4:1727–41. doi: 10.1039/c3fo60295h

74. Ma A, Zou F, Zhang R, Zhao X. The effects and underlying mechanisms of medicine and food homologous flowers on the prevention and treatment of related diseases. *J Food Biochem*. (2022) 46:e14430. doi: 10.1111/jfbc.14430

75. Song DX, Jiang JG. Hypolipidemic components from medicine food homology species used in China: pharmacological and health effects. *Arch Med Res*. (2017) 48:569–81. doi: 10.1016/j.arcmed.2018.01.004

76. Newman DJ, Cragg GM. Natural products as sources of new drugs over the nearly four decades from 01/1981 to 09/2019. *J Nat Prod*. (2020) 83:770–803. doi: 10.1021/acs.jnatprod.9b01285

77. Xu L, Zhang X, Yang W, Li H, Wang J, Wang L, et al. Advanced technology based on poly(Deep eutectic solvent) core–shell nanomaterials enriched with Fructus choerospondias phenols for efficient defense against Uvb-induced ferroptosis. *Chem Eng J*. (2024) 498:155224. doi: 10.1016/j.cej.2024.155224

78. Wang L, Li M, Wang Y, Xu L, He X, Li H, et al. Harnessing two-dimensional magnetic poly(Deep eutectic solvents) for matrix solid-phase dispersion extraction of polyphenols from roselle: promoting antiphotoaging strategy. *Chem Eng J*. (2024) 496:154019. doi: 10.1016/j.cej.2024.154019

79. Stetson DB, Ko JS, Heidmann T, Medzhitov R. Trex1 prevents cell-intrinsic initiation of autoimmunity. *Cell*. (2008) 134:587–98. doi: 10.1016/j.cell.2008.06.032

80. Grieves JL, Fye JM, Harvey S, Grayson JM, Hollis T, Perrino FW. Exonuclease Trex1 degrades double-stranded DNA to prevent spontaneous lupus-like inflammatory disease. *Proc Natl Acad Sci U.S.A*. (2015) 112:5117–22. doi: 10.1073/pnas.1423804112

81. Wu J, Dobbs N, Yang K, Yan N. Interferon-independent activities of mammalian sting mediate antiviral response and tumor immune evasion. *Immunity*. (2020) 53:115–26 e5. doi: 10.1016/j.immuni.2020.06.009

82. Li C, Wen J, Zhan X, Shi W, Ye X, Yao Q, et al. Total tanshinones ameliorates cgas-sting-mediated inflammatory and autoimmune diseases by affecting sting-Irf3 binding. *Chin Med*. (2024) 19:107. doi: 10.1186/s13020-024-00980-4

83. Bumblauskiene L, Jakstas V, Janulis V, Mazdzieriene R , Ragazinskiene O. Preliminary analysis on essential oil composition of Perilla L. cultivated in Lithuania. *Acta Pol Pharm*. (2009) 66:409–13. Available at: https://hdl.handle.net/20.500.12512/85784

84. Chu L, Li CH, Li YX, Yu QY, Yu HS, Li CH, et al. Perillaldehyde inhibition of Cgas reduces Dsdna-induced interferon response. *Front Immunol*. (2021) 12:655637. doi: 10.3389/fimmu.2021.655637

85. Wen J, Mu W, Li H, Yan Y, Zhan X, Luo W, et al. Glabridin improves autoimmune disease in Trex1-deficient mice by reducing type I interferon production. *Mol Med*. (2023) 29:167. doi: 10.1186/s10020-023-00754-y

86. Luo W, Song Z, Xu G, Wang H, Mu W, Wen J, et al. Licochalconeb inhibits cgas-sting signaling pathway and prevents autoimmunity diseases. *Int Immunopharmacol*. (2024) 128:111550. doi: 10.1016/j.intimp.2024.111550

87. Zhang Y, Liu Y, Jiang B, Chen L, Hu J, Niu B, et al. Targeting sting oligomerization with licochalcone D ameliorates sting-driven inflammatory diseases. *Sci China Life Sci*. (2024), 1–4. doi: 10.1007/s11427-024-2703-6

88. Yang Y, Feng K, Yuan L, Liu Y, Zhang M, Guo K, et al. Compound Danshen dripping pill inhibits hypercholesterolemia/atherosclerosis-induced heart failure in Apoe and Ldlr dual deficient mice *via* multiple mechanisms. *Acta Pharm Sin B*. (2023) 13:1036–52. doi: 10.1016/j.apsb.2022.11.012

89. Lei W, Li X, Li L, Huang M, Cao Y, Sun X, et al. Compound Danshen dripping pill ameliorates post ischemic myocardial inflammation through synergistically regulating Mapk, Pi3k/Akt and Ppar signaling pathways. *J Ethnopharmacol*. (2021) 281:114438. doi: 10.1016/j.jep.2021.114438

90. Liao W, Ma X, Li J, Li X, Guo Z, Zhou S, et al. A review of the mechanism of action of dantonic® for the treatment of chronic stable angina. *Biomed Pharmacother*. (2019) 109:690–700. doi: 10.1016/j.biopha.2018.10.013

91. Shi W, Xu G, Gao Y, Yang H, Liu T, Zhao J, et al. Compound Danshen dripping pill effectively alleviates cgas-sting-triggered diseases by disrupting sting-Tbk1 interaction. *Phytomedicine*. (2024) 128:155404. doi: 10.1016/j.phymed.2024.155404

92. Wang X, Wang N, Cheung F, Lao L, Li C, Feng Y. Chinese medicines for prevention and treatment of human hepatocellular carcinoma: current progress on pharmacological actions and mechanisms. *J Integr Med*. (2015) 13:142–64. doi: 10.1016/S2095-4964(15)60171-6

93. Ling CQ, Yue XQ, Ling C. Three advantages of using traditional Chinese medicine to prevent and treat tumor. *J Integr Med*. (2014) 12:331–5. doi: 10.1016/S2095-4964(14)60038-8

94. Wang J, Luo ZJ, Lin LZ, Sui XB, Yu LL, Xu C, et al. Anoikis-associated lung cancer metastasis: mechanisms and therapies. *Cancers*. (2022) 14(19):4791. doi: 10.3390/cancers14194791

95. Gao XY, Liu GC, Zhang JX, Wang LH, Xu C, Yan ZA, et al. Pharmacological properties of ginsenoside re. *Front Pharmacol*. (2022) 13:754191. doi: 10.3389/fphar.2022.754191

96. Tang X, Zhu M, Zhu Z, Tang W, Zhang H, Chen Y, et al. Ginsenoside re inhibits non-small cell lung cancer progression by suppressing macrophage M2 polarization

induced by Ampkalpha1/sting positive feedback loop. *Phytother Res*. (2024) 1-19. doi: 10.1002/ptr.8309

97. Yan X, Yao C, Fang C, Han M, Gong C, Hu D, et al. Rocaglamide promotes the infiltration and antitumor immunity of Nk cells by activating cgas-sting signaling in non-small cell lung cancer. *Int J Biol Sci*. (2022) 18:585–98. doi: 10.7150/ijbs.65019

98. Bhagya N, Chandrashekar KR. Autophagy and cancer: can tetrandrine be a potent anticancer drug in the near future? *Biomed Pharmacother*. (2022) 148:112727. doi: 10.1016/j.biopha.2022.112727

99. Tan Y, Zhu QC, Yang ML, Yang F, Zeng Q, Jiang ZB, et al. Tetrandrine activates sting/Tbk1/Irf3 pathway to potentiate anti-Pd-1 immunotherapy efficacy in non-small cell lung cancer. *Pharmacol Res*. (2024) 207:107314. doi: 10.1016/j.phrs.2024.107314

100. Punvittayagul C, Chariyakornkul A, Jarukamjorn K, Wongpoomchai R. Protective role of vanillic acid against diethylnitrosamine- and 1,2-dimethylhydrazine-induced hepatocarcinogenesis in rats. *Molecules*. (2021) 26:2718. doi: 10.3390/molecules26092718

101. Zhu M, Tang XY, Zhu ZR, Gong ZY, Tang WJ, Hu Y, et al. Sting activation in macrophages by vanillic acid exhibits antineoplastic potential. *Biochem Pharmacol*. (2023) 213:115618. doi: 10.1016/j.bcp.2023.115618

102. Siegel RL, Miller KD, Jemal A. Cancer statistics, 2019. *CA: Cancer J Clin*. (2019) 69:7–34. doi: 10.3322/caac.21551

103. Liu H, Wang Z, Liu Z. Formononetin restrains tumorigenesis of breast tumor by restraining sting-Nf-Kappab and interfering with the activation of Pd-L1. *Discovery Med*. (2024) 36:613–20. doi: 10.24976/Discov.Med.202436182.58

104. Fu Q, Lu Z, Chang Y, Jin T, Zhang M. Ginseng extract (Ginsenoside Rg3) combined with sting agonist reverses Tam/M2 polarization to inhibit Tnbc evolution. *Ind Crops Prod*. (2024) 222:119589. doi: 10.1016/j.indcrop.2024.119589

105. Schoggins JW, Wilson SJ, Panis M, Murphy MY, Jones CT, Bieniasz P, et al. A diverse range of gene products are effectors of the type I interferon antiviral response. *Nature*. (2011) 472:481–5. doi: 10.1038/nature09907

106. Diner Elie J, Burdette Dara L, Wilson Stephen C, Monroe Kathryn M, Kellenberger Colleen A, Hyodo M, et al. The innate immune DNA sensor Cgas produces a noncanonical cyclic dinucleotide that activates human sting. *Cell Rep*. (2013) 3:1355–61. doi: 10.1016/j.celrep.2013.05.009

107. Wu J, Sun L, Chen X, Du F, Shi H, Chen C, et al. Cyclic Gmp-Amp is an endogenous second messenger in innate immune signaling by cytosolic DNA. *Science*. (2012) 339(6121):826–30. doi: 10.1126/science.1229963

108. Kopustinskiene DM, Bernatoniene J. Antioxidant effects of Schisandra chinensis fruits and their active constituents. *Antioxidants-Basel*. (2021) 10:620. doi: 10.3390/antiox10040620

109. Nowak A, Zakłos-Szyda M, Błasiak J, Nowak A, Zhang Z, Zhang B. Potential of Schisandra chinensis (Turcz.) baill. In human health and nutrition: A review of current knowledge and therapeutic perspectives. *Nutrients*. (2019) 11:333. doi: 10.3390/nu11020333

110. Zhao J, Xu G, Hou XR, Mu WQ, Yang HJ, Shi W, et al. Schisandrin C enhances cgas-sting pathway activation and inhibits Hbv replication. *J Ethnopharmacol*. (2023) 311:116427. doi: 10.1016/j.jep.2023.116427

111. Lin Y, Shi R, Wang X, Shen HM. Luteolin, a flavonoid with potential for cancer prevention and therapy. *Curr Cancer Drug Targets*. (2008) 8:634–46. doi: 10.2174/156800908786241050

112. Wang Y, Li F, Wang Z, Song X, Ren Z, Wang X, et al. Luteolin inhibits herpes simplex virus 1 infection by activating cyclic guanosine monophosphate-adenosine monophosphate synthase-mediated antiviral innate immunity. *Phytomedicine*. (2023) 120:155020. doi: 10.1016/j.phymed.2023.155020

113. Lei YC, Li W, Luo P. Liuweiwuling tablets attenuate acetaminophen-induced acute liver injury and promote liver regeneration in mice. *World J Gastroenterol*. (2015) 21:8089–95. doi: 10.3748/wjg.v21.i26.8089

114. Wu ZX, Zhao XM, Li RS, Wen XR, Xiu Y, Long MJ, et al. The combination of schisandrin C and luteolin synergistically attenuates hepatitis B virus infection *via* repressing Hbv replication and promoting cgas-sting pathway activation in macrophages. *Chin Med Uk*. (2024) 19:48. doi: 10.1186/s13020-024-00888-z

115. Yi Y, Li JH, Lai XY, Zhang M, Kuang Y, Bao YO, et al. Natural triterpenoids from licorice potently inhibit Sars-Cov-2 infection. *J Adv Res*. (2022) 36:201–10. doi: 10.1016/j.jare.2021.11.012

116. Zheng WJ, Huang XF, Lai YN, Liu XH, Jiang Y, Zhan SF. Glycyrrhizic acid for Covid-19: findings of targeting pivotal inflammatory pathways triggered by Sars-Cov-2. *Front Pharmacol*. (2021) 12:631206. doi: 10.3389/fphar.2021.631206

117. Qi H, Ma QH, Feng W, Chen SM, Wu CS, Wang YN, et al. Glycyrrhetinic acid blocks Sars-Cov-2 infection by activating the cgas-sting signalling pathway. *Brit J Pharmacol*. (2024) 181(20):3976–92. doi: 10.1111/bph.16473

118. Bailly C. Cepharanthine: an update of its mode of action, pharmacological properties and medical applications. *Phytomedicine*. (2019) 62:152956. doi: 10.1016/j.phymed.2019.152956

119. Liu Y, Tang Q, Rao ZL, Fang Y, Jiang XN, Liu WJ, et al. Inhibition of Herpes Simplex Virus 1 by Cepharanthine *Via* Promoting Cellular Autophagy through up-Regulation of Sting/Tbk1/P62 Pathway. *Antivir Res*. (2021) 193:105143. doi: 10.1016/j.antiviral.2021.105143

120. Chen JX, Du HQ, Cui S, Liu T, Yang G, Sun HP, et al. *E. Fischeriana* root compound Dpo activates antiviral innate immunity. *Front Cell Infect Mi*. (2017) 7:456. doi: 10.3389/fcimb.2017.00456

121. Hui S, Kan W, Qin S, He P, Zhao J, Li H, et al. Frontiers | Glycyrrhiza uralensis polysaccharides ameliorates cecal ligation and puncture-induced sepsis by inhibiting the cgas-sting signaling pathway. *Front Pharmacol*. (2024) 15. doi: 10.3389/fphar.2024.1374179

122. Song L, Li G, Guan W, Zeng Z, Ou Y, Zhao T, et al. Design, synthesis and anti-inflammatory activity study of lansiumamide analogues for treatment of acute lung injury. *BioMed Pharmacother*. (2023) 166:115412. doi: 10.1016/j.biopha.2023.115412

123. Comish PB, Liu MM, Huebinger R, Carlson D, Kang R, Tang D. The cgas-sting pathway connects mitochondrial damage to inflammation in burn-induced acute lung injury in rat. *Burns*. (2022) 48:168–75. doi: 10.1016/j.burns.2021.04.007

124. Wen J, Qin S, Li Y, Zhang P, Zhan X, Fang M, et al. Flavonoids derived from licorice suppress Lps-induced acute lung injury in mice by inhibiting the cgas-sting signaling pathway. *Food Chem Toxicol*. (2023) 175:113732. doi: 10.1016/j.fct.2023.113732

125. Wei JH, Liu ZJ, Sun HB, Xu L. Perillaldehyde ameliorates lipopolysaccharide-induced acute lung injury *via* suppressing the Cgas/sting signaling pathway. *Int Immunopharmacol*. (2024) 130:111641. doi: 10.1016/j.intimp.2024.111641

126. Zhou XW, Wang J, Tan WF. Apigenin suppresses innate immune responses and ameliorates lipopolysaccharide-induced inflammation *via* inhibition of sting/Irf3 pathway. *Am J Chin Med*. (2024) 52:471–92. doi: 10.1142/S0192415x24500204

127. He YQ, Deng JL, Zhou CC, Jiang SG, Zhang F, Tao X, et al. Ursodeoxycholic acid alleviates sepsis-induced lung injury by blocking panoptosis *via* sting pathway. *Int Immunopharmacol*. (2023) 125:111161. doi: 10.1016/j.intimp.2023.111161

128. Yao Q, Wen J, Chen S, Wang Y, Wen X, Wang X, et al. Shuangdan Jiedu decoction improved Lps-induced acute lung injury by regulating both cgas-sting pathway and inflammasome. *J Ethnopharmacol*. (2024) 336:118661. doi: 10.1016/j.jep.2024.118661

129. He Y-Q, Zhou C-C, Deng J-L, Wang L, Chen W-S. Tanreqing inhibits Lps-induced acute lung injury *in vivo* and *in vitro* through downregulating sting signaling pathway. *Front Pharmacol*. (2021) 12. doi: 10.3389/fphar.2021.746964

130. Deng J, He Y, Sun G, Yang H, Wang L, Tao X, et al. Tanreqing injection protects against bleomycin-induced pulmonary fibrosis *via* inhibiting sting-mediated endoplasmic reticulum stress signaling pathway. *J Ethnopharmacol*. (2023) 305:116071. doi: 10.1016/j.jep.2022.116071

131. Ren G, Lv W, Ding Y, Wang L, Cui Z, Li R, et al. Ginseng saponin metabolite 20 (S)-protopanaxadiol relieves pulmonary fibrosis by multiple-targets signaling pathways. *J Ginseng Res*. (2023) 47(4):543–51. doi: 10.1016/j.jgr.2023.01.002

132. Chen X, Kang F, Lai J, Deng X, Guo X, Liu S. Comparative effectiveness of phlegm-heat clearing Chinese medicine injections for aecopd: A systematic review and network meta-analysis. *J Ethnopharmacol*. (2022)292:115043. doi: 10.1016/j.jep.2022.115043

133. Zhong Y, Mao B, Wang G, Fan T, Liu X, Diao X, et al. Tanreqing injection combined with conventional western medicine for acute exacerbations of chronic obstructive pulmonary disease: A systematic review. *J Integr Complement Med*. (2010) 16(12):1309–19. doi: 10.1089/acm.2009.0686

134. Tong Y, Wen J, Yang T, Li H, Wei S, Jing M, et al. Clinical efficacy and safety of tanreqing injection combined with antibiotics versus antibiotics alone in the treatment of pulmonary infection patients after chemotherapy with lung cancer: A systematic review and meta-analysis. *Phytother Res*. (2021) 35:122–37. doi: 10.1002/ptr.6790

135. Parola M, Pinzani M. Liver fibrosis: pathophysiology, pathogenetic targets and clinical issues. *Mol Aspects Med*. (2019) 65:37–55. doi: 10.1016/j.mam.2018.09.002

136. Affo S, Yu LX, Schwabe RF. The role of cancer-associated fibroblasts and fibrosis in liver cancer. *Annu Rev Pathol*. (2017) 12:153–86. doi: 10.1146/annurev-pathol-052016-100322

137. Kakino S, Ohki T, Nakayama H, Yuan X, Otabe S, Hashinaga T, et al. Pivotal role of Tnf-A in the development and progression of nonalcoholic fatty liver disease in a murine model. *Horm Metab Res*. (2018) 50:80–7. doi: 10.1055/s-0043-118666

138. Hernández-Aquino E, Muriel P. Beneficial effects of naringenin in liver diseases: molecular mechanisms. *World J Gastroenterol*. (2018) 24:1679–707. doi: 10.3748/wjg.v24.i16.1679

139. Chen L, Xia S, Wang S, Zhou Y, Wang F, Li Z, et al. Naringenin is a potential immunomodulator for inhibiting liver fibrosis by inhibiting the cgas-sting pathway. *J Clin Trans Hepatol*. (2022) 11(1):26–37. doi: 10.14218/jcth.2022.00120

140. Luo W, Xu G, Song Z, Mu W, Wen J, Hui S, et al. Licorice extract inhibits the cgas-sting pathway and protects against non-alcoholic steatohepatitis. *Front Pharmacol*. (2023) 14. doi: 10.3389/fphar.2023.1160445

141. Sun Y, Weng J, Chen X, Ma S, Zhang Y, Zhang F, et al. Oroxylin a activates ferritinophagy to induce hepatic stellate cell senescence against hepatic fibrosis by regulating cgas-sting pathway. *Biomed Pharmacother*. (2023) 162:114653. doi: 10.1016/j.biopha.2023.114653

142. Xiu Y, Wang S, Zhang P, Li C, Wu Z, Wen J, et al. Total glucosides of paeony alleviates cgas-sting-mediated diseases by blocking the sting-Irf3 interaction. *Chin J Natural Medicines*. (2024) 22(5):402–15. doi: 10.1016/s1875-5364(24)60572-8

143. Li Y, Yu P, Fu W, Wang S, Zhao W, Ma Y, et al. Ginsenoside Rd inhibited ferroptosis to alleviate Ccl4-induced acute liver injury in mice *via* Cgas/sting pathway. *Am J Chin Med*. (2022) 51(01):91-105. doi: 10.1142/s0192415x23500064

144. Ding G, Yu G, Zhang J, Liang S, Liu L, Huang P, et al. The therapeutic effects of Ling Gui Zhu Gan Tang Mixture in 50 psychotic patients with obesity induced by the psychoactive drugs. *J Tradit Chin Med*. (2005) 25:25–8.

145. Dai L, Xu J, Liu B, Dang Y, Wang R, Zhuang L, et al. Lingguizhugan decoction, a Chinese herbal formula, improves insulin resistance in overweight/obese subjects with non-alcoholic fatty liver disease: A translational approach. *Front Med*. (2022) 16:745–59. doi: 10.1007/s11684-021-0880-3

146. Cao L, Xu E, Zheng RD, Zhangchen ZL, Zhong RL, Huang F, et al. Traditional Chinese medicine Lingguizhugan decoction ameliorate Hfd-induced hepatic-lipid deposition in mice by inhibiting sting-mediated inflammation in macrophages. *Chin Med Uk*. (2022) 17(7):1-16. doi: 10.1186/s13020-021-00559-3

147. Andrade RJ, Chalasani N, Bjornsson ES, Suzuki A, Kullak-Ublick GA, Watkins PB, et al. Drug-induced liver injury. *Nat Rev Dis Primers*. (2019) 5:58. doi: 10.1038/s41572-019-0105-0

148. Wang HF, Xu JS, Zong K, Liang ZW, Li RF, Xue JF, et al. Jujuboside B alleviates acetaminophen-induced hepatotoxicity in mice by regulating Nrf2-sting signaling pathway. *Ecotoxicol Environ Saf*. (2024) 269:115810. doi: 10.1016/j.ecoenv.2023.115810

149. Shen P, Han L, Chen G, Cheng Z, Liu Q. Emodin attenuates acetaminophen-induced hepatotoxicity *via* the cgas-sting pathway. *Inflammation*. (2021) 45:74–87. doi: 10.1007/s10753-021-01529-5

150. Wang Y, Wei B, Wang D, Wu J, Gao J, Zhong H, et al. DNA damage repair promotion in colonic epithelial cells by andrographolide downregulated Cgas-Sting pathway activation and contributed to the relief of Cpt-11-induced intestinal mucositis. *Acta Pharm Sin B*. (2021) 12(1):262–73. doi: 10.1016/j.apsb.2021.03.043

151. Gu L, Wang F, Wang Y, Sun D, Sun Y, Tian T, et al. Naringin Protects against Inflammation and Apoptosis Induced by Intestinal Ischemia–Reperfusion Injury through Deactivation of Cgas-Sting Signaling Pathway. *Phytother Res*. (2023) 37 (8):3495–507. doi: 10.1002/ptr.7824

152. Pabla N, Dong Z. Cisplatin nephrotoxicity: mechanisms and renoprotective strategies. *Kidney Int*. (2008) 73:994–1007. doi: 10.1038/sj.ki.5002786

153. Miller RP, Tadagavadi RK, Ramesh G, Reeves WB. Mechanisms of cisplatin nephrotoxicity. *Toxins*. (2010) 2(11):2490–518. doi: 10.3390/toxins2112490

154. Qi JY, Luo Q, Zhang QY, Wu MN, Zhang LL, Qin LS, et al. Yi-Shen-Xie-Zhuo formula alleviates cisplatin-induced Aki by regulating inflammation and apoptosis *via* the Cgas/sting pathway. *J Ethnopharmacol*. (2023) 309:116327. doi: 10.1016/j.jep.2023.116327

155. Ma Y, Bai B, Liu D, Shi R, Zhou Q. Shenqi fuzheng injection reduces cisplatin-induced kidney injury *via* Cgas/sting signaling pathway in breast cancer mice model. *Breast Cancer: Targets Ther*. (2024) 16:451–69. doi: 10.2147/bctt.s475860

156. Liu S, Gao X, Wang Y, Wang J, Qi X, Dong K, et al. Baicalein-loaded silk fibroin peptide nanofibers protect against cisplatin-induced acute kidney injury: fabrication, characterization and mechanism. *Int J Pharm*. (2022) 626:122161. doi: 10.1016/j.ijpharm.2022.122161

157. Liu S, Gao X, Yin Y, Wang J, Dong K, Shi D, et al. Silk fibroin peptide self-assembled nanofibers delivered naringenin to alleviate cisplatin-induced acute kidney injury by inhibiting Mtdna-cgas-sting pathway. *Food Chem Toxicol*. (2023) 177:113844. doi: 10.1016/j.fct.2023.113844

158. Zheng M, Hu Z, Wang Y, Wang C, Zhong C, Cui W, et al. Zhen Wu decoction represses renal fibrosis by invigorating tubular Nrf2 and Tfam to fuel mitochondrial bioenergetics. *Phytomedicine*. (2022) 108:154495. doi: 10.1016/j.phymed.2022.154495

159. Appel SH, Smith RG, Le WD. Immune-mediated cell death in neurodegenerative disease. *Adv Neurol*. (1996) 69:153–9.

160. Calsolaro V, Edison P. Neuroinflammation in Alzheimer's disease: current evidence and future directions. *Alzheimers Dement*. (2016) 12:719–32. doi: 10.1016/j.jalz.2016.02.010

161. Monteiro AR, Barbosa DJ, Remião F, Silva R. Alzheimer's disease: insights and new prospects in disease pathophysiology, biomarkers and disease-modifying drugs. *Biochem Pharmacol*. (2023) 211:115522. doi: 10.1016/j.bcp.2023.115522

162. Lin L, Ni B, Lin H, Zhang M, Li X, Yin X, et al. Traditional usages, botany, phytochemistry, pharmacology and toxicology of polygonum multiflorum thunb.: A review. *J Ethnopharmacol*. (2015) 159:158–83. doi: 10.1016/j.jep.2014.11.009

163. Gao D, Chen C, Huang R, Yang CC, Miao BB, Li L, et al. Tetrahydroxy stilbene glucoside ameliorates cognitive impairments and pathology in App/Ps1 transgenic mice. *Curr Med Sci*. (2021) 41:279–86. doi: 10.1007/s11596-021-2344-z

164. Gao D, Hao J-P, Li B-Y, Zheng C-C, Miao B-B, Zhang L, et al. Tetrahydroxy stilbene glycoside ameliorates neuroinflammation for Alzheimer's disease *via* cgas-sting. *Eur J Pharmacol*. (2023) 953:175809. doi: 10.1016/j.ejphar.2023.175809

165. Liu X, Chen W, Wang C, Liu W, Hayashi T, Mizuno K, et al. Silibinin ameliorates depression/anxiety-like behaviors of Parkinson's disease mouse model and is associated with attenuated sting-Irf3-Ifn-B Pathway activation and neuroinflammation. *Physiol Behav*. (2021) 241:113593. doi: 10.1016/j.physbeh.2021.113593

166. Tian L, Li W, Wang T. Therapeutic effects of silibinin on Lps-induced acute lung injury by inhibiting Nlrp3 and Nf-Kb signaling pathways. *Microb Pathogen*. (2017) 108:104–8. doi: 10.1016/j.micpath.2017.05.011

167. Chen J, Li D-L, Xie L-N, Ma Y-r, Wu P-P, Li C, et al. Synergistic anti-inflammatory effects of silibinin and thymol combination on Lps-induced Raw264.7 cells by inhibition of Nf-Kb and Mapk activation. *Phytomedicine*. (2020) 78:153309. doi: 10.1016/j.phymed.2020.153309

168. Liu P, Chen W, Kang Y, Wang C, Wang X, Liu W, et al. Silibinin ameliorates sting-mediated neuroinflammation *via* downregulation of ferroptotic damage in a sporadic Alzheimer's disease model. *Arch Biochem Biophys*. (2023). doi: 10.1016/j.abb.2023.109691

169. Lan TH, Huang XQ, Tan HM. Vascular fibrosis in atherosclerosis. *Cardiovasc Pathol*. (2013) 22:401–7. doi: 10.1016/j.carpath.2013.01.003

170. Li W, Huang Z, Luo Y, Cui Y, Xu M, Luo W, et al. Tetrandrine alleviates atherosclerosis *via* inhibition of sting-Tbk1 pathway and inflammation in macrophages. *Int Immunopharmacol*. (2023) 119:110139. doi: 10.1016/j.intimp.2023.110139

171. Oseran AS, Yeh RW. Time to treatment in St-segment elevation myocardial infarction: identifying dangerous delays or diminishing returns? *Jama*. (2022) 328:2016–7. doi: 10.1001/jama.2022.19441

172. Chen J, Huang Q, Li J, Yao Y, Sun W, Zhang Z, et al. Panax ginseng against myocardial ischemia/reperfusion injury: A review of preclinical evidence and potential mechanisms. *J Ethnopharmacol*. (2023) 300:115715. doi: 10.1016/j.jep.2022.115715

173. Liu Y, Xue Q, Li A, Li K, Qin X. Mechanisms exploration of herbal pair of Huangqi-Danshen on cerebral ischemia based on metabonomics and network pharmacology. *J Ethnopharmacol*. (2020) 253:112688. doi: 10.1016/j.jep.2020.112688

174. Liu X, Lu J, Liu S, Huang D, Chen M, Xiong G, et al. Huangqi-danshen decoction alleviates diabetic nephropathy in Db/Db mice by inhibiting Pink1/Parkin-mediated mitophagy. *Am J Transl Res*. (2020) 12:989–98.

175. Rao S, Lin Y, Lin R, Liu J, Wang H, Hu W, et al. Traditional Chinese medicine active ingredients-based selenium nanoparticles regulate antioxidant selenoproteins for spinal cord injury treatment. *J Nanobiotechnol*. (2022) 20:278. doi: 10.1186/s12951-022-01490-x

176. Zhai P, Chen Q, Wang X, Ouyang X, Yang M, Dong Y, et al. The combination of tanshinone Iia and astragaloside Iv attenuates myocardial ischemia–reperfusion injury by inhibiting the sting pathway. *Chin Med Uk*. (2024) 19:34. doi: 10.1186/s13020-024-00908-y

177. Mohan AT, Sur YJ, Zhu L, Morsy M, Wu PS, Moran SL, et al. The concepts of propeller, perforator, keystone, and other local flaps and their role in the evolution of reconstruction. *Plast Reconstr Surg*. (2016) 138:710e–29e. doi: 10.1097/prs.0000000000002610

178. Siemionow M, Arslan E. Ischemia/reperfusion injury: A review in relation to free tissue transfers. *Microsurgery*. (2004) 24:468–75. doi: 10.1002/micr.20060

179. Li YB, Liu HF, Zeng ZH, Lin H, Chen X, Yuan XL, et al. Ginsenoside Rb3 attenuates skin flap ischemia-reperfusion damage by inhibiting sting-Irf3 signaling. *J Mol Histol*. (2022) 53:763–72. doi: 10.1007/s10735-022-10081-x

180. Xu C, Cai T, Du X. Liuwei Dihuang prevents human umbilical vein endothelial cells senescence *via* the Jpx-Sting-Irf3 pathway. *Combinatorial Chem High Throughput Screening*. (2023). doi: 10.2174/1386207326666230901163717

181. Guo S, Wang J, Wang Y, Zhang Y, Bi K, Zhang Z, et al. Study on the multitarget synergistic effects of Kai-Xin-San against Alzheimer's disease based on systems biology. *Oxid Med Cell Longev*. (2019) 2019:1707218. doi: 10.1155/2019/1707218

182. Pan JJ, He SY, Shao JY, Li N, Gong YQ, Gong XC. Critical pharmaceutical process identification considering chemical composition, biological activity, and batch-to-batch consistency: A case study of notoginseng total saponins. *Chin Herb Med*. (2020) 12:29–35. doi: 10.1016/j.chmed.2019.11.002

183. Wang D, Ding J, Feng X, Chai X, Yang J, Liu C, et al. Identification of Q-markers from Hedan tablet by employing "Spider-web" Mode and taking compounds' Hepatotoxicity into account. *Chin Herbal Medicines*. (2022) 14(4):612–21. doi: 10.1016/j.chmed.2021.08.007

184. Zhang Y, Lv X, Liu R, Zhang M, Liu H, Gao H, et al. An integrated strategy for ascertaining quality marker of Schisandra chinensis (Turcz.) baill based on correlation analysis between depression-related monoaminergic metabolites and chemical components profiling. *J Chromatogr A*. (2019) 1598:122–31. doi: 10.1016/j.chroma.2019.03.056

185. Shen Q, Wu Y, Li Z, Wu X, Wang Y, Chen Y, et al. Quality assessment of traditional Chinese medicine using quality biomarkers: compound Danshen dripping pills as an example. *Phytochem Anal*. (2023) 34(5):580–93. doi: 10.1002/pca.3238

186. Koyama S, Ishii KJ, Coban C, Akira S. Innate immune response to viral infection. *Cytokine*. (2008) 43:336–41. doi: 10.1016/j.cyto.2008.07.009

187. Rong L, Perelson AS. Treatment of hepatitis C virus infection with interferon and small molecule direct antivirals: viral kinetics and modeling. *Crit Rev Immunol*. (2010) 30:131–48. doi: 10.1615/critrevimmunol.v30.i2.30

188. Liu Y, Pu F. Updated roles of cgas-sting signaling in autoimmune diseases. *Front Immunol*. (2023) 14. doi: 10.3389/fimmu.2023.1254915

189. Ablasser A, Goldeck M, Cavlar T, Deimling T, Witte G, Röhl I, et al. Cgas produces a 2'-5'-linked cyclic dinucleotide second messenger that activates sting. *Nature*. (2013) 498:380–4. doi: 10.1038/nature12306

190. Liu N, Pang X, Zhang H, Ji P. The cgas-sting pathway in bacterial infection and bacterial immunity. *Front Immunol*. (2022) 12:814709. doi: 10.3389/fimmu.2021.814709

191. Zhang X, Bai X-C, Chen ZJ. Structures and mechanisms in the cgas-sting innate immunity pathway. *Immunity*. (2020) 34(5):580–93. doi: 10.1016/j.immuni.2020.05.013

192. Fan N, Zhao F, Meng Y, Chen L, Miao L, Wang P, et al. Metal complex lipid-based nanoparticles deliver metabolism-regulating lomitapide to overcome Ctc immune evasion *via* activating sting pathway. *Eur J Pharm Biopharm*. (2024) 203:114467. doi: 10.1016/j.ejpb.2024.114467

193. Irvine DJ, Aung A, Silva M. Controlling timing and location in vaccines. *Adv Drug Delivery Rev*. (2020) 158:91–115. doi: 10.1016/j.addr.2020.06.019

194. Meric-Bernstam F, Sandhu SK, Hamid O, Spreafico A, Kasper S, Dummer R, et al. Phase Ib study of Miw815 (Adu-S100) in combination with spartalizumab (Pdr001) in patients (Pts) with advanced/metastatic solid tumors or lymphomas. *J Clin Oncol*. (2019) 37:2507. doi: 10.1200/JCO.2019.37.15_suppl.2507

195. Shae D, Becker KW, Christov P, Yun DS, Lytton-Jean AKR, Sevimli S, et al. Endosomolytic polymersomes increase the activity of cyclic dinucleotide sting agonists to enhance cancer immunotherapy. *Nat Nanotechnol*. (2019) 14:269–78. doi: 10.1038/s41565-018-0342-5

196. Haag SM, Gulen MF, Reymond L, Gibelin A, Abrami L, Decout A, et al. Targeting sting with covalent small-molecule inhibitors. *Nature*. (2018) 559:269–73. doi: 10.1038/s41586-018-0287-8

197. Feng X, Ge J, Fu H, Miao L, Zhao F, Wang J, et al. Discovery of small molecule B-catenin suppressors that enhance immunotherapy. *Bioorg Chem*. (2023) 139:106754. doi: 10.1016/j.bioorg.2023.106754

198. Li S, Hong Z, Wang Z, Li F, Mei J, Huang L, et al. The cyclopeptide astin C specifically inhibits the innate immune Cdn sensor sting. *Cell Rep*. (2018) 25:3405–21 e7. doi: 10.1016/j.celrep.2018.11.097

199. Humphries F, Shmuel-Galia L, Jiang Z, Zhou JY, Barasa L, Mondal S, et al. Targeting sting oligomerization with small-molecule inhibitors. *Proc Natl Acad Sci*. (2023) 120:e2305420120. doi: 10.1073/pnas.2305420120

200. Wang M, Sooreshjani MA, Mikek C, Opoku-Temeng C, Sintim HO. Suramin potently inhibits Cgamp synthase, Cgas, in Thp1 cells to modulate Ifn-beta levels. *Future Med Chem*. (2018) 10:1301–17. doi: 10.4155/fmc-2017-0322

201. Wang J, Lu W, Zhang J, Du Y, Fang M, Zhang A, et al. Loss of Trim29 mitigates viral myocarditis by attenuating perk-driven Er stress response in male mice. *Nat Commun*. (2024) 15:3481. doi: 10.1038/s41467-024-44745-x

202. Wang J, Wang L, Lu W, Farhataziz N, Gonzalez A, Xing J, et al. Trim29 controls enteric Rna virus-induced intestinal inflammation by targeting Nlrp6 and Nlrp9b signaling pathways. *Mucosal Immunol*. (2024). doi: 10.1016/j.mucimm.2024.10.004

203. Fang M, Zhang A, Du Y, Lu W, Wang J, Minze LJ, et al. Trim18 is a critical regulator of viral myocarditis and organ inflammation. *J Biomed Sci*. (2022) 29:55. doi: 10.1186/s12929-022-00840-z

204. Li H, Li J, Zhang Y, Zhao C, Ge J, Sun Y, et al. The therapeutic effect of traditional Chinese medicine on breast cancer through modulation of the Wnt/B-catenin signaling pathway. *Front Pharmacol*. (2024) 15:1401979. doi: 10.3389/fphar.2024.1401979

frontiers | Frontiers in Immunology

TYPE Methods
PUBLISHED 13 March 2025
DOI 10.3389/fimmu.2025.1545790

OPEN ACCESS

EDITED BY
Paige Lacy,
University of Alberta, Canada

REVIEWED BY
Mattia Laffranchi,
Sapienza University of Rome, Italy
Cyril Seillet,
The University of Melbourne, Australia

*CORRESPONDENCE
Jörg H. Fritz
jorg.fritz@mcgill.ca

†These authors have contributed equally to this work

RECEIVED 15 December 2024
ACCEPTED 05 February 2025
PUBLISHED 13 March 2025

CITATION
Krisna SS, Deagle RC, Ismailova N, Esomojumi A, Roy-Dorval A, Roth F, Berberi G, del Rincon SV and Fritz JH (2025) Immunometabolic analysis of primary murine group 2 innate lymphoid cells: a robust step-by-step approach.
Front. Immunol. 16:1545790.
doi: 10.3389/fimmu.2025.1545790

Immunometabolic analysis of primary murine group 2 innate lymphoid cells: a robust step-by-step approach

Sai Sakktee Krisna[1,2,3,4†], Rebecca C. Deagle[3,4,5†], Nailya Ismailova[3,4,5], Ademola Esomojumi[3,4,5], Audrey Roy-Dorval[3,4,5], Frederik Roth[3,4,5], Gabriel Berberi[3,4,5], Sonia V. del Rincon[2,6,7] and Jörg H. Fritz[1,3,4,5*]

[1]Department of Physiology, Faculty of Medicine and Health Sciences, McGill University, Montréal, QC, Canada, [2]Segal Cancer Centre, Lady Davis Institute for Medical Research, Jewish General Hospital, Montréal, QC, Canada, [3]McGill University Research Centre on Complex Traits (MRCCT), Faculty of Medicine and Health Sciences, McGill University, Montréal, QC, Canada, [4]Dahdaleh Institute of Genomic Medicine (DIgM), McGill University, Montréal, QC, Canada, [5]Department of Microbiology and Immunology, Faculty of Medicine and Health Sciences, McGill University, Montréal, QC, Canada, [6]Division of Experimental Medicine, Faculty of Medicine and Health Sciences, McGill University, Montréal, QC, Canada, [7]Department of Oncology, Faculty of Medicine and Health Sciences, McGill University, Montréal, QC, Canada

Group 2 Innate Lymphoid Cells (ILC2s) have recently been shown to exert key regulatory functions in both innate and adaptive immune response networks that drive the establishment and progression of type 2 immunity. Although mainly tissue resident, ILC2s and their crosstalk within tissue microenvironments influence metabolism at both the local and systemic levels. In turn, the energetic demand and metabolic status within these systems shape the diverse phenotypes and effector functions of ILC2s. Deciphering these metabolic networks in ILC2s is therefore essential in understanding their various roles in health as well as their associated pathophysiologies. Here we detail a framework of experimental approaches to study key immunometabolic states of primary murine ILC2s and link them to unique phenotypes and their corresponding functionality. Utilizing flow cytometry, Single Cell ENergetic metabolism by profilIng Translation inHibition (SCENITH), and the Seahorse platform we provide a framework that allows in-depth analysis of cellular bioenergetic states to determine the immunometabolic wiring of ILC2s. Connecting immunometabolic states and networks to ILC2 phenotypes and effector functions with this method will allow future in-depth studies to assess the potential of novel pharmaceutics in altering ILC2 functionality in clinical settings.

KEYWORDS

group 2 innate lymphoid cells (ILC2), immunometabolism, mitochondria, seahorse analysis, SCENITH (Single Cell ENergetic metabolism by profilIng Translation inhibition)

1 Introduction

Large extracellular helminths have been suggested to constitute a major evolutionary driving force of the effector mechanisms of type 2 immune responses, conferring protection from parasites invading barrier tissues (1, 2). However, the precise factors that shape the magnitude and quality of type 2 immune cell responses remain incompletely understood. Interestingly, chronic helminth infections have been shown to be associated with significant morbidity, including malnutrition, suggesting competition between parasites and host for metabolic resources, potentially leading to immunomodulatory consequences and alterations in protective type 2 immunity (3). An emerging body of evidence suggests that the immune system senses and utilizes nutrients and metabolites derived directly from the diet or produced by commensal or pathogenic microbes (4, 5). During the early phases of helminth infection, alarmin signals such as interleukin (IL)-25, IL-33, and thymic stromal lymphopoietin (TSLP) are released by non-hematopoietic cells in response to tissue damage and act to induce rapid proliferation and expansion of group 2 innate lymphoid cells (ILC2). Primarily found at mucosal barrier sites, ILC2 are transcriptionally and functionally poised innate type 2 effector immune cells that, once activated, can rapidly release large quantities of IL-5 and IL-13 to elicit eosinophilia, goblet cell hyperplasia, epithelial cell extrusion, and smooth muscle hypercontractility (6). Furthermore, it is gradually appreciated that ILC2 respond to changes in the richness and accessibility of microbially- as well as dietary-derived metabolites, such as vitamin A–derived retinoic acid (7), aryl-hydrocarbon receptor ligands (8), short chain fatty acids (9), succinate (10, 11), and iron (12). These findings suggest that ILC2, in addition to danger signals, are poised to respond to the broader metabolic milieu of barrier tissues (13). Moreover, nutrients are essential components, providing fundamental metabolic substrates for the production of energy to fuel protein translation, cellular proliferation and immune cell effector functions (4, 5). Indeed, the ability of ILC2 to induce rapid effector functions depend on the ability to engage cell-intrinsic metabolic pathways to catabolize glucose, fatty acids and amino acids. Like T cells (14), ILC2s undergo metabolic reprogramming to meet the high energy demand imposed by cell proliferation and the activation of effector functions (15, 16).

In the resting state, ILC2 utilize branched chain amino acids (BCAAs) and arginine to support mitochondrial oxidative phosphorylation (OXPHOS) to sustain homeostatic functions (17). ILC2 become highly proliferative following activation with IL-33, relying on glycolysis and mammalian target of rapamycin (mTOR) to produce type 2 cytokines (18), while continuing to fuel OXPHOS with amino acids to maintain cellular fitness and proliferation (17, 19). Metabolic reprogramming during ILC2 effector differentiation also requires increased anabolic metabolism, leading to increased lipid droplet (LD) formation and requiring fatty acid oxidation (FAO) to fuel pathogenic allergic airway inflammation (20–23). In addition, the formation of LDs is facilitated by glucose and was shown to be important to produce phospholipids that fuel ILC2 proliferation (21). Glucose was further shown to regulate the gene expression of diglyceride acyltransferase (DGAT1) and peroxisome proliferator-activated receptor gamma (PPARγ) through the mTOR pathway (21). While DGAT1 drives LD formation (21), PPARγ promotes lipid uptake through CD36 expression (24–26). The increase in free fatty acid (FFA) uptake induced by ILC2 activation (20, 23) is fueled by group V phospholipase A2 (PLA2G5)-expressing macrophages (27). In addition, PLA2G5 intrinsically impacts IL-33 release from macrophages and the expression of the FFA receptor GPR40 on ILC2 (27). Interestingly, Atg5 deficiency lowered fatty acid metabolism gene expression induced by IL-33 and impaired FAO, type 2 cytokine production and cell fitness (22), suggesting that autophagy-mediated catabolic pathways are critical to sustain ILC2 metabolism.

In addition to sustaining homeostatic functions (17), amino acid metabolism is essential for lung ILC2 activation. Arginine metabolism by arginase 1 (Arg1) is required to fuel aerobic glycolysis for ILC2 proliferation and cytokine production (28). ILC2 constitutively express high levels of multiple solute carriers, including Slc3a2, Slc7a5 and Slc7a8 (19), known to encode for large neutral amino acid transporter chains (29). Slc3a2 encodes the protein CD98 that heterodimerizes with other solute carriers to form active amino acid transporters, such as Slc7a5 and Slc7a8, that together form the surface amino acid transporters LAT1 and LAT2 (29). ILC2-intrinsic deletion of Slc7a5 and Slc7a8 impaired the proliferative and cytokine-producing capacity through tuning of mTOR signaling (19). In addition, catabolism of tryptophane (Trp) by the enzyme tryptophan hydroxylase 1 (Tph1) drives ILC2 effector functions (30). Moreover, methionine metabolism facilitates ILC2-driven inflammation through STAT3-dependent production of type 2 cytokines (31), underlining the various ways amino acid metabolism contributes to the regulation of ILC2 homeostasis, proliferation and cytokine production. Collectively, these insights highlight that fine-tuning metabolic pathways is critical for maintaining ILC2 homeostasis and regulating their effector functions, including cell fitness, proliferation and cytokine production. Here we detail a framework of experimental approaches to study key immunometabolic states of primary murine ILC2 and link them to phenotypes and functionality.

2 Materials and methods

2.1 Mice

C57BL/6J mice were originally purchased from The Jackson Laboratory (Bar Harbor, Maine, USA) and bred in-house at McGill University under specific pathogen-free conditions with ad libitum access to food and water. Experiments were conducted with adult female mice (aged 8-12 weeks) in accordance with the guidelines and policies of McGill University and the Canadian Council on Animal Care.

2.2 Isolation of bone marrow-derived group 2 innate lymphoid cells

Adult female mice were anaesthetized with 5% isoflurane (Fresenius Kabi, Catalog No. CP0406V2) and euthanized via CO_2 asphyxiation, followed by cervical dislocation as a confirmation of death. The hind legs were harvested, and the bulk of the muscles were removed with scissors to expose the leg bones. The femur and tibia bones were separated and cleaned with sterilized gauze (Fisher Scientific, Catalog No. 22-037-907) to remove any trace muscle or connective tissues, and briefly washed with 70% ethanol. Centrifugation was implemented to extract bone marrow from the femur and tibia bones. This centrifugation method began with the preparation of bone marrow extraction tubes, whereby a hole was punctured in the bottom of a 0.5 mL tube (Sarstedt, Catalog No. 72.737.002) with an 18-gauge needle (Becton Dickinson, Catalog No. 305196). These extraction tubes were sterilized by autoclave and each tube was set inside a sterile 1.5 mL collection tube (Progene, Catalog No. 87-B150-C) containing 100 µL of sterile Dulbecco's Phosphate Buffered Saline (DPBS; Cytiva, Catalog No. SH30028.02). The bones were cut at the epiphysis on both ends to expose the bone marrow, and a single bone was vertically placed inside one 0.5 mL extraction tube. The 1.5 mL tubes containing the cut bones and extraction tubes were sealed and centrifuged at 1900*g for 5 minutes at room temperature. This allowed the bone marrow to be extracted through the punctured hole and into the collection tube with DPBS. After centrifugation, the 0.5 mL tubes and hollow bones were discarded. The bone marrow was resuspended in the DPBS and transferred to a 50 mL tube (Fisher Scientific, Catalog No. 14-432-22), with a maximum of 20 bones (5 mice) per tube. Each 50 mL tube was filled to a volume of 50 mL with DPBS and centrifuged at 450*g for 5 minutes at 4°C to wash the bone marrow. The supernatant was discarded, and the bone marrow pellet was resuspended in 1 mL of Ammonium-Chloride-Potassium (ACK) lysis buffer (ThermoFisher Scientific, Catalog No. A1049201) for 20 to 30 seconds to remove red blood cells from the pellet. This reaction was neutralized by filling the tube to 50 mL with Fluorescence-Activated Cell Sorting (FACS) buffer made with 2% Fetal Bovine Serum (FBS; Wisent, Catalog No. 080150) in DPBS. The tube was centrifuged, and the pellet was washed twice with FACS buffer (450*g, 5 minutes, 4°C) to remove any trace of the lysis buffer. To prevent non-specific binding of antibodies to the fragment crystallization receptors (FcRs), the cells were blocked for 15 minutes on ice using a 1:10 dilution of in-house formulated "Fc-block" (supernatant of the 2.4G2 hybridoma producing the purified anti-mouse CD16/CD32 monoclonal antibody (mAb)) in FACS buffer. The bone marrow cells were stained with an antibody cocktail (Table 1) for 30 minutes on ice in the dark directly in the blocking solution. The stained bone marrow cells were washed twice in FACS buffer (450*g, 5 minutes, 4°C), filtered through a 70 µm pore strainer (Fisher Scientific, Catalog No. 22-363-548), and kept on ice prior to cell sorting. Bone marrow-derived ILC2 were sorted using a FACS Aria III and FACSAria Fusion (BD Biosciences) equipped with 405 nm, 488 nm, 561 nm (Fusion

TABLE 1 Group 2 Innate Lymphoid Cell (ILC2) sorting antibodies.

Marker	Company	Fluorophore	Clone	Dilution	RRID or Catalogue Number
Lineage Cocktail					
TCRα/β	eBioscience	PE	H57-597	1:200	AB_466067
TCRγ/δ	eBioscience	PE	eBioGL3	1:400	AB_465934
CD3e	eBioscience	PE	145-2C11	1:400	AB_465497
Ly-6G/Ly-6C(Gr1)	eBioscience	PE	RB6-8C5	1:500	AB_466046
CD11b	eBioscience	PE	M1/70	1:500	AB_2734870
TER-119	eBioscience	PE	TER-119	1:400	AB_466043
CD45R (B220)	eBioscience	PE	RA3-6B2	1:200	AB_465672
CD19	eBioscience	PE	eBio1D3	1:200	AB_657660
NK1.1	eBioscience	PE	PK136	1:50	AB_466051
CD5	eBioscience	PE	53-7.3	1:200	AB_465524
CD11c	eBioscience	PE	N418	1:100	AB_465553
FceR1	eBioscience	PE	MAR-1	1:100	AB_466029
ILC2$^+$ Markers & Viability					
Ly-6A/E (Sca-1)	BioLegend	Alexa Fluor 488	E13-161.7	1:200	AB_756201
CD25	eBioscience	eFluor 450	PC61.5	1:50	AB_10671550
CD117 (c-Kit)	eBioscience	APC	2B8	1:25	AB_469431
Viability	eBioscience	7-AAD	NA	1:60	00-6993-50

only) and 640 nm lasers using FACSDiva Version 6.0 (Aria III) or Version 8.0 (Fusion) based on the absence of lineage markers and the expression of ILC2 specific markers (Figure 1, Table 1).

2.3 Expansion and resting of murine bone marrow-derived group 2 innate lymphoid cells

After cell sorting, isolated ILC2s were cultured in 96-well round-bottom plates (VWR, Catalog No. CA62406-121) at 37°C in 5% CO_2 with a seeding density of $2.5x10^4$ cells per well in 200 µL of complete cell culture media (Table 2) with cytokines for expansion. These cytokines included: recombinant murine IL-2 (R&D Systems, Catalog No. 402-ML-100/CF), IL-7 (R&D Systems, Catalog No. 407-ML-200/CF), and IL-33 (R&D Systems, Catalog No. 3626-ML-010/CF) each at a concentration of 50 ng/mL and TSLP (R&D Systems, Catalog No. 555-TS-010/CF) at a concentration of 20 ng/mL. Every 2 days the cell culture was "split" whereby the cells were resuspended in the 200 µL volume, and 100 µL of the cell suspension was transferred to a new well. Each well was returned to a final volume of 200 µL by adding 100 µL of freshly prepared expansion cell culture media to facilitate proliferation. ILC2s were expanded for a maximum of three weeks, after which the cells were consolidated into 50 mL tubes and washed twice in RPMI 1640 (450*g, 5 minutes, 4°C) to remove any trace of expansion cytokines. The cells were counted and then seeded at a density of $2.5x10^4$ cells per well in 96-well round-bottom plates in 200 µL of complete cell culture media without β-mercaptoethanol (Table 2) and with 10 ng/mL each of IL-2 and IL-7. The cells incubated with these cytokines for three days at 37°C in 5% CO_2 to "rest" the cells. This 3-day period of reduced activity was necessary after 3 weeks of energy-demanding proliferation to bring the cells down to a homeostatic baseline level of metabolic activity.

2.4 Cell seeding and cytokine stimulation for experimental assays

After resting, ILC2s were consolidated into 50 mL tubes and washed twice in RPMI 1640 (450*g, 5 minutes, 4°C) to remove any trace of resting cytokines. Cells were counted and seeded at a density of $1.0x10^5$ in 100 µL of phenol red-free complete cell culture media (Table 2) either in a 96-well round-bottom plate (Sections 2.5-7, 2.10) or a Seahorse XFe96 cell culture microplate (Agilent™ Technologies, Catalog No. 103794-100; Section 2.8). Each condition for flow cytometric assays (Sections 2.5-7, 2.10)

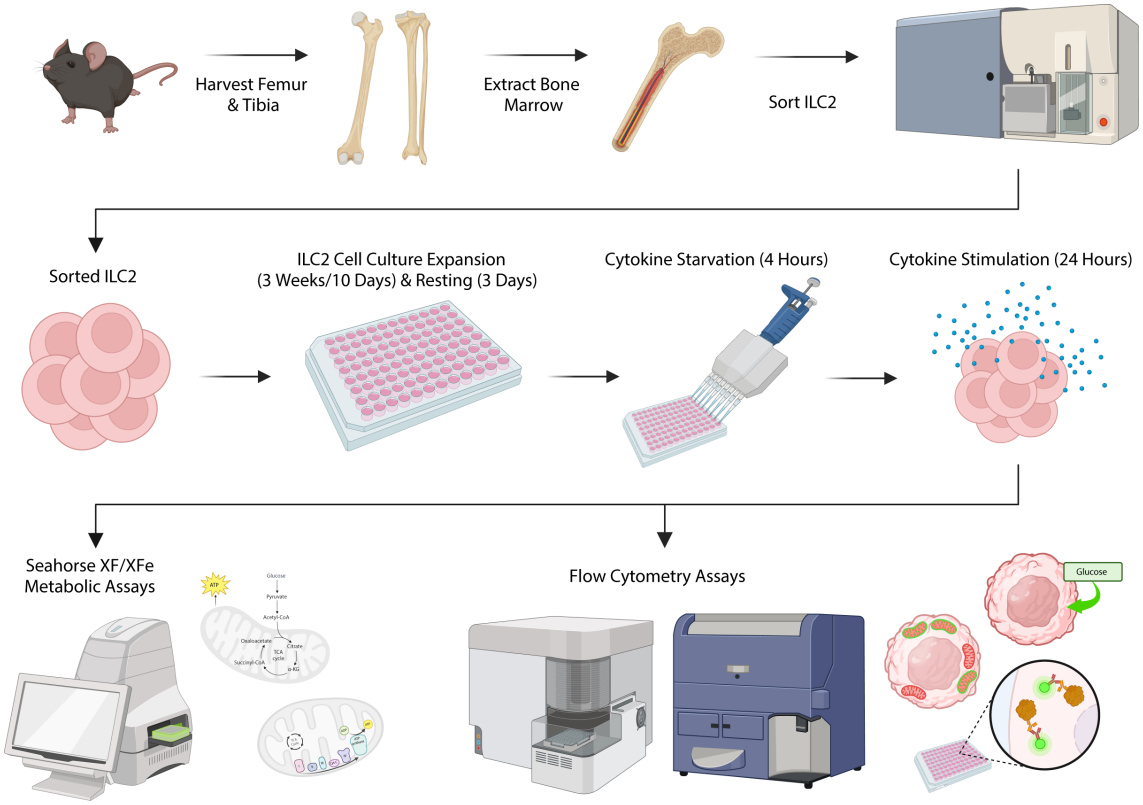

FIGURE 1
Schematic of experimental workflow. Femurs and tibias were harvested from female C57BL/6J wild-type mice and group 2 innate lymphoid cells (ILC2) were isolated from the bone marrow by flow cytometric cell sorting. ILC2 were cultured *in vitro* for expansion followed by a period of rest and cytokine starvation. ILC2 were subsequently re-stimulated with cytokines to determine metabolic activities using both flow cytometric assays and the Seahorse XF/XFe Analyzer. Created in BioRender. Deagle, R. (2025) https://BioRender.com/x72g976.

TABLE 2 Group 2 Innate Lymphoid Cell (ILC2) cell culture and assay media recipes.

Reagent	Company	Catalog Number	Final Concentration	Volume
Complete Cell Culture Media				
RPMI 1640 Medium	Cytiva	With Phenol Red SH30096.02 Phenol Red-Free SH30605.01		45 mL
Fetal Bovine Serum (FBS)	Wisent	080150	10%	5 mL
L-Glutamine (200 mM)	Cytiva	SH30034.01	2 mM	500 µL
Penicillin-Streptomycin (10,000 µg/mL)	Cytiva	SV30010	100 µg/mL	500 µL
Gentamicin (10 mg/mL)	Sigma-Aldrich	G1272	50 µg/mL	120 µL
β-Mercaptoethanol (55 mM) *Omitted for resting and experiments*	Gibco	21985023	50 µM	50 µL
Agilent™ Seahorse XF Cell Mito Stress and XF Real-Time ATP Rate Assay				
Seahorse XF DMEM Medium	Agilent	103575-100		48.5 mL
Seahorse XF Glucose (1M)	Agilent	103577-100	10 mM	500 µL
Seahorse XF Pyruvate (100 mM)	Agilent	103578-100	1 mM	500 µL
Seahorse XF Glutamine (200 mM)	Agilent	103579-100	2 mM	500 µL
Agilent™ Seahorse XF Glycolysis Stress Assay				
Seahorse XF DMEM Medium	Agilent	103575-100		49.5 mL
Seahorse XF Glucose (1 M)	Agilent	103577-100	2 mM	500 µL

were plated in triplicate and each condition for Seahorse assays (Section 2.8) were plated in quintuplicate. The ILC2s incubated for 4 hours at 37°C in 5% CO_2 without cytokines to starve the cells of cytokines, bringing them to a latent stage of activity prior to cytokine stimulation (Figure 1). The cytokine stimulation conditions for all experiments were the following: IL-2, IL-7, IL-33, IL-2+IL-33, and IL-7+IL-33. Each cytokine stimulation was prepared as a 2X concentrated solution (20 ng/mL) in phenol red-free complete cell culture media (Table 2). After cytokine starvation, 100 µL of the appropriate cytokine stimulation was added to the corresponding well for a total volume of 200 µL and a 1X concentration of cytokines (10 ng/mL). The ILC2s underwent cytokine stimulation for a period of 24 hours at 37°C in 5% CO_2 prior to all experiments. After 24 hours of cytokine stimulation, ILC2 viability was typically lowest (78-80%) when stimulated with survival cytokines alone, such as IL-7 or IL-2, whereas ILC2 viability was highest (90-96%) when stimulated with activating cytokine conditions, such as IL-7+IL-33 or IL-2+IL-33.

2.5 Glucose uptake by flow cytometry

The glucose uptake in ILC2 was measured using the glucose analog 2-(N-(7-Nitrobenz-2-oxa-1,3-diazol-4-yl)Amino)-2-Deoxyglucose (2-NBDG; ThermoFisher Scientific, Catalog No. N13195) which was stored at -20°C at a stock concentration of 10 mM (5 mg lyophilised powder in 1.46 mL dimethyl sulfoxide (DMSO)). Immediately prior to experiments, the 10 mM stock of 2-NBDG was diluted 1:100 in warm phenol red-free complete media (Table 2) to a 2X concentrated solution of 100 µM. After 24 hours of cytokine stimulation, the cells were resuspended and transferred to a conical-bottom 96-well plate (Sarstedt, Catalog No. 82.1583.001). The cells were washed twice with phenol red-free RPMI 1640 (450*g, 5 minutes, 4°C) and resuspended in 100 µL of phenol red-free complete cell culture media (Table 2). A volume of 100 µL of the 2X concentrated 2-NBDG was added to each well (excluding unstained and viability controls) for a final 1X concentration of 50 µM, and the plate incubated with the glucose analog for 30 minutes at 37°C in 5% CO_2. After incubation, the cells were washed once with phenol red-free RPMI 1640 and once with FACS buffer (450*g, 5 minutes, 4°C). The supernatant was discarded, and the cells were resuspended in 195 µL of FACS buffer prior to acquisition on the flow cytometer. Immediately before the sample was acquired on the flow cytometer, 5 µL of viability dye (7-AAD; eBioscience, Catalog No. 00-6993-50) was added to each sample (excluding the unstained control wells) and transferred to a 5 mL FACS tube (Fisher Scientific, Catalog No. 352008). Each sample was acquired using a LSRFortessa Cell Analyzer (BD Biosciences) until 20,000 events were recorded. 2-NBDG (465/540 nm) was acquired using the 488 nm laser and 7-AAD (535/617 nm) with the 561 nm laser. After sample acquisition, the files were exported in .fcs format from FACSDiva and analyzed

using FlowJo software (BD, Version 10.10.0). Debris, doublet, and dead cells (7-AAD$^+$) were excluded via flow cytometry gating. The 2-NBDG and the forward scatter were analyzed on the x- and y-axes, respectively. The reagent 2-NBDG had no adverse effect on the viability of ILC2 during this assay.

2.6 Analysis of PGC-1α expression levels by intracellular flow cytometry

Viability staining, fixation, and permeabilization. After 24 hours of cytokine stimulation, the cells were resuspended and transferred to a conical-bottom 96-well plate. The cells were washed twice with DPBS (450*g, 5 minutes, 4°C) and the supernatant was discarded. The fixable viability dye APC-eFluor780 (eBioscience, Catalog No. 65-0865) was stored at -80°C and diluted 1:1000 in DPBS. Excluding unstained controls, 50 µL of the diluted viability dye was added to each well and incubated on ice in the dark for 30 minutes. After incubation, the cells were washed twice with FACS buffer (450*g, 5 minutes, 4°C). The fixation/permeabilization solution was made during the centrifugation time, whereby the Fixation/Permeabilization Concentrate (eBioscience, Catalog No. 00-5123-43) was diluted 1:4 in Fixation/Permeabilization Dilutant (eBioscience, Catalog No. 00-5223-56). The supernatant from the cell culture plate was discarded, and 100 µL of the fixation/permeabilization solution was added to all wells and incubated on ice in the dark for 30 minutes. During incubation, the Permeabilization Buffer (10X; eBioscience, Catalog No. 00-8333-56) was diluted 1:10 in deionized water (dH_2O). The fixed and permeabilized cells were washed twice with 100 µL of the 1X permeabilization buffer (600*g, 5 minutes, 4°C) and the 2.4G2 hybridoma blocking solution was prepared during the centrifugation time as previously described (Section 2.2). The supernatant from the cell culture plate was discarded and 50 µL of blocking solution was added to all wells, followed by 15-minute incubation on ice in the dark.

Intracellular staining of PGC-1α. While incubating cells in the blocking solution, the antibody dilutions were made in 1X permeabilization buffer. The PGC-1α antibody (Proteintech, Catalog No. CL488-66369) was diluted 1:1000 from its stock concentration of 1000 µg/mL to 1 µg/mL and the IgG1 isotype control antibody (Proteintech, Catalog No. CL488-66360-1) was diluted 1:200 from its stock concentration of 200 µg/mL to 1 µg/mL. After incubation, the cell culture plate was centrifuged (600*g, 5 minutes, 4°C) and the supernatant was discarded. A volume of 100 µL of antibody dilution was added to the appropriate wells, excluding unstained controls, and incubated for 30 minutes on ice in the dark. The stained cells were washed twice with 1X permeabilization buffer (600*g, 5 minutes, 4°C) and the supernatant was discarded. The cells were resuspended in 200 µL of FACS buffer and transferred to a 5 mL FACS tube.

Flow cytometry. Each sample was acquired using an Aurora Spectral Flow Cytometer (Cytek Biosciences) until 20,000 events were recorded. The directly conjugated PGC-1α and isotype control (493/522 nm) were acquired using the 488 nm laser and APC-eFluor780 (756/785nm) with the 633 nm laser. After sample acquisition, the files were exported in .fcs format from FACSDiva (BD Biosciences) and analyzed using FlowJo software (BD Biosciences, Version 10.10.0). Debris, doublet, and dead cells (APC-eFluor780$^+$) were excluded via flow cytometry gating. The PGC-1α and the forward scatter were analyzed on the x- and y-axes, respectively.

2.7 Analysis of mitochondrial mass and membrane potential by flow cytometry

Fluorescent label preparation. Total mitochondrial mass was measured using Mitotracker™ Deep Red FM (ThermoFisher Scientific, Catalog No. M22426), which was stored at -20°C at a stock concentration of 1 mM (50 µg lyophilised powder in 91.98 µL DMSO). Mitochondrial membrane potential was measured using Tetramethylrhodamine, Methyl Ester, Perchlorate (TMRM; ThermoFisher Scientific, Catalog No. T668) which was stored at -20°C at a stock concentration of 10 mM (25 mg lyophilised powder in 5 mL DMSO). Ready-to-use TMRM aliquots were prepared at an intermediate concentration of 100 µM by diluting the stock 1:100 in DMSO and were stored at -20°C until needed for experiments. Immediately prior to experiments, the 1 mM Mitotracker™ Deep Red FM stock solution was diluted 1:10 in warm phenol red-free RPMI 1640 for an intermediate concentration of 100 µM. Both Mitotracker™ Deep Red FM and TMRM were finally diluted together 1:1000 in warm phenol red-free RPMI 1640 to a 2X concentrated solution of 100 nM for experimental conditions. Each dye was also prepared separately for single-variable controls. In addition, cell viability was measured using 4′,6-diamidino-2-phenylindole (DAPI; ThermoFisher Scientific, Catalog No. 62248) where only dead cell nuclei would be labeled. The 1 mg lyophilized stock was reconstituted in 1 mL of dH_2O to make a 1 mg/mL stock solution and was stored at 4°C. An intermediate concentration of 100 µg/mL was made by diluting DAPI 1:10 in FACS buffer immediately prior to sample acquisition.

Mitochondrial staining. After 24 hours of cytokine stimulation, the cells were resuspended and transferred to a conical-bottom 96-well plate. The cells were washed twice with phenol red-free RPMI 1640 (450*g, 5 minutes, 4°C) and resuspended in 100 µL of phenol red-free complete cell culture media (Table 2). The 2X concentrated Mitotracker™ Deep Red FM and TMRM dilution was added to each well (excluding single color and viability controls) at a volume of 100 µL for a final volume of 200 µL and a final concentration of 50 nM for each dye. The cells incubated with the dyes for 30 minutes at 37°C in 5% CO_2. This assay was optimized to use a concentration of 50 nM for each mitochondrial dye to ensure maximum viability, as overloading the cells with these dyes can create adverse effects. After incubation, the cells were washed once with phenol red-free media and once with FACS buffer (450*g, 5 minutes, 4°C). The supernatant was discarded, and the cells were resuspended in 198 µL of FACS buffer prior to acquisition on the flow cytometer.

Flow cytometry and data export. Immediately before the sample was acquired on the flow cytometer, 2 µL of the intermediate DAPI solution was added to each sample (excluding

the unstained control wells) for a final concentration of 1 µg/mL and the cell suspension was transferred to a 5 mL FACS tube. Each sample was acquired using a LSRFortessa Cell Analyzer (BD Biosciences) until 20,000 events were recorded. Mitotracker™ Deep Red FM (644/665 nm) was acquired using the 633 nm laser, TMRM (548/573 nm) with the 561 nm, and DAPI (350/470 nm) with the 405 nm laser. After sample acquisition, the files were exported in .fcs format from FACSDiva and analyzed using FlowJo software. Debris, doublet, and dead cells ($DAPI^+$) were excluded via flow cytometry gating. Mitotracker™ Deep Red FM and TMRM were analyzed on the x- and y-axes, respectively.

2.8 Agilent™ Seahorse Extracellular Flux Assay preparation

Calibration and cell culture reagents. Concurrent with the Seahorse XFe96 microplate preparation (Section 2.4), the base of the Seahorse XFe96 sensor cartridge (Agilent™ Technologies, Catalog No. 103792-100) was loaded with 200 µL of Seahorse XF Calibrant (Agilent™ Technologies, Catalog No. 100840-000) and incubated in a CO_2-free incubator at 37°C for 24 hours to hydrate the lid of the sensor cartridge. The day of the experiment, assay media for the Seahorse experiments were freshly prepared and warmed to 37°C for experiments (Table 2). The Seahorse XF Mito Stress Assay and Seahorse XF Real-Time ATP Rate Assay used the same assay media composition where Seahorse XF DMEM medium was supplemented with L-glutamine, glucose, and pyruvate (Table 2). The Seahorse XF Glycolysis Stress Assay used the Seahorse XF DMEM medium supplemented with only L-glutamine (Table 2).

Cell culture microplate. After 24 hours of cytokine stimulation, the cell culture microplate was removed from the incubator and centrifuged at 450*g for one minute at room temperature. The 24-hour old cell culture media was carefully removed from the plate to minimize cell disruption and replaced with 180 µL of the freshly prepared assay media specific to the Seahorse assay being conducted (Table 2). The cell culture microplate incubated for one hour in a CO_2-free incubator at 37°C. Incubation of both the sensor cartridge and the cell culture microplate in CO_2-free conditions permitted proper diffusion of CO_2 from the cells, medium, and plate; ensuring that all were properly de-gassed prior to running the assays.

Stock solutions. During this one-hour incubation time, the relevant assay media was used to make stock solutions of the different compounds associated with the Seahorse XF Mito Stress Test Kit (Agilent™ Technologies, Catalog No. 103015-100), the Seahorse XF Real-Time ATP Rate Assay Kit (Agilent™ Technologies, Catalog No. 103592-100), or the Seahorse XF Glycolysis Stress Test Kit (Agilent™ Technologies, Catalog No. 103020-100). The Seahorse XF Mito Stress Test Kit compounds included oligomycin, carbonyl cyanide-4 phenylhydrazone (FCCP), and rotenone + antimycin A; the Seahorse XF Real-Time ATP Rate Assay Kit included oligomycin and rotenone + antimycin A; and the Seahorse XF Glycolysis Stress Test Kit included glucose, oligomycin, and 2-Deoxy-Glucose (2-DG; Table 3). Each compound was resuspended several times by pipetting with the corresponding assay medium and were vortexed for one minute to ensure a thorough reconstitution of the compound (Table 3).

Loading concentrations. The stock solutions were used to make a 10X concentrated solution of each compound with the corresponding assay media (Table 4). Each compound solution associated with the assay being performed was loaded into a specific port in the lid of the sensor cartridge (Port A, B, C, or D), which would be at a final 1X concentration after its timed injection during the assay (Table 4, Section 2.9). Any remaining compound solutions were discarded after the ports in the sensor cartridge lid were properly loaded. The Seahorse XFe96 sensor cartridge was returned to the CO_2-free incubator until it was time to run the assay.

TABLE 3 The reconstitution volumes for each compound to generate the stock solutions from the Agilent™ Seahorse XF Cell Mito Stress Assay, Real-Time ATP Rate Assay, and Glycolysis Stress Assay Kits.

Compound	Quantity per Tube (nmol)	Reconstitution Volume (with Assay Medium)	Stock Concentration
Agilent™ Seahorse XF Cell Mito Stress Assay			
Oligomycin	63	630 µL	100 µM
FCCP	72	720 µL	100 µM
Rotenone+Antimycin A	27 (each)	540 µL	50 µM
Agilent™ Seahorse XF Real-Time ATP Rate Assay Kit			
Oligomycin	63	420 µL	150 µM
Rotenone+Antimycin A	27 (each)	540 µL	50 µM
Agilent™ Seahorse XF Glycolysis Stress Assay Kit			
Glucose	300,000	3000 µL	100 mM
Oligomycin	72	720 µL	10 µM
2-DG	1,500,000	3000 µL	500 mM

Each compound reconstitution was completed with the assay medium specific to the assay.

TABLE 4 The working concentration solutions and volumes of each compound for the Agilent™ Seahorse XF Cell Mito Stress Assay, Real-Time ATP Rate Assay, and Glycolysis Stress Assay.

Reagent	Stock Solution Volume	Assay Media Volume	Loading Concentration (10X)	Volume Added to Port	Final Concentration (1X)
Agilent™ Seahorse XF Cell Mito Stress Assay					
Oligomycin	450 µL	2550 µL	15 µM	20 µL (Port A)	1.5 µM
FCCP	600 µL	2400 µL	20 µM	22 µL (Port B)	2.0 µM
Rotenone/ Antimycin A	300 µL	2700 µL	5 µM	25 µL (Port C)	0.5 µM
Agilent™ Seahorse XF Real-Time ATP Rate Assay					
Oligomycin	450 µL	2550 µL	15 µM	20 µL (Port A)	1.5 µM
Rotenone/ Antimycin A	300 µL	2700 µL	5 µM	22 µL (Port B)	0.5 µM
Agilent™ Seahorse XF Glycolysis Stress Assay					
Glucose	3000 µL	0 µL	100 mM	20 µL (Port A)	10 mM
Oligomycin	300 µL	2700 µL	10 µM	22 µL (Port B)	1.0 µM
2-DG	3000 µL	0 µL	500 mM	25 µL (Port C)	50 mM

Each working concentration solution was made with the assay medium specific to the assay. The working concentrations were loaded into each port at a 10X concentration, achieving a 1X concentration after the timed injection during the assay runtime.

2.9 Agilent™ Seahorse Extracellular Flux Assay and data normalization

Parameter setting and calibration. The Seahorse XF/XFe Analyzer was turned on one hour prior to running the assays to stabilize. The Seahorse Wave Controller software (Agilent, Version 2.6) was opened on the computer, and the appropriate template file was selected (i.e.: Seahorse XF Cell Mito Stress Test, Glycolysis Stress Test, or Real-Time ATP Rate Assay). Under *Assay Navigation*, the option *Group Definitions* was selected and then *Groups* to create sample names. Sample names were determined based on the cytokine stimulations. A map of the conditions in the cell culture plate was generated under *Plate Map*, where wells labeled A1, A12, H1, and H12 were excluded to account for background signal. The sample names under *Group* were selected and applied to the generated plate map. A *Project Name* was created under *Run Assay* to identify the type and date of the assay, followed by *Start Run* to begin the calibration process. When the software prompted *Load Calibrant Utility Plate*, the sensor cartridge was removed from the CO_2-free incubator and placed in the Seahorse XF/XFe Analyzer by selecting *Open Tray*. The option *I'm Ready* was selected to begin calibration which lasted approximately 20 minutes.

Seahorse data acquisition. When calibration was complete, the lid of the sensor cartridge was retained by the machine, and the base of the sensor cartridge was removed from the loading tray and replaced with the base of the cell culture microplate. The well labeled A1 in the cell culture microplate was aligned with the top-left corner of the loading tray and the option *Load Cell Plate* was selected to close the loading tray. The appropriate assay was chosen in the software to begin the assay. During the runtime of the assay, the Seahorse XF/XFe Analyzer automatically performed a timed injection of the relevant compound from the corresponding port in the lid of the sensor cartridge and into the cell culture plate below. The message *Unload Sensor Cartridge* signaled that the assay was complete, and the lid of the sensor cartridge was removed from the machine. *Eject* was selected to remove the cell culture microplate from the Seahorse XF/XFe Analyzer. The prompt *Assay Complete!* appeared on screen and the file was saved for viewing results after data normalization.

Cell viability data acquisition. The cell culture microplate was immediately used for cell viability quantification via flow cytometry to perform data normalization from the Seahorse assays. A volume of 5 µL of 7-AAD viability dye was added directly to each well, the cells were resuspended and transferred to a 5 mL FACS tube. Each sample was acquired using an Aurora Spectral Flow Cytometer (Cytek Biosciences) until 20,000 events were recorded. After sample acquisition, the files were exported in .fcs format from FACSDiva (BD Biosciences) and analyzed using FlowJo software (BD Biosciences, Version 10.10.0). Debris, doublet, and dead cells (7-AAD$^+$) were excluded via flow cytometry gating and the number of live, single cells were exported as an Excel file (Microsoft Corporation, Version 16.88) in .xls format. Due to the nature of the assays interrupting metabolic processes and the length of time

required to run the experiment, cell viability was lower than prior to the beginning of the assays.

Seahorse data normalization and export. The number of live, single cells were imported to a spreadsheet under *Normalize* in the Wave software. The Seahorse assay data was normalized according to the viability data by selecting *Apply*. To generate the data output from the assay, the *Results* tab was selected, followed by selecting the file of interest. In the *Functions* tab, *Export* was selected, and an Excel document was generated for each assay by selecting either Seahorse XF Cell Mito Stress Test Report Generator, Seahorse XF Glycolysis Stress Test Report Generator, or Seahorse XF Real-Time ATP Rate Assay Report Generator. Each Excel file was reviewed, and the three most consistent technical replicates (out of the five) were chosen from the dataset and transferred to GraphPad for graph configuration and statistical analyses (Section 2.13).

2.10 Agilent™ Seahorse Extracellular Flux Assay metric calculations

The following rationale and equations were used to quantify the rate of ATP production in ILC2s for both the oxidative phosphorylation (OXPHOS) and glycolytic metabolic pathways (Section 3.8). All equations, calculations, and contextual information were provided by the *Agilent™ Seahorse XF Real-Time ATP Rate Assay Kit User Guide*.

Glycolytic ATP production rate calculation. The Agilent™ Seahorse XF Real-Time ATP Rate Assay permits the measurement of the extracellular acidification rate (ECAR), determined by the extrusion of protons (H^+) from the cells into the extracellular environment. The oxygen consumption rate (OCR) is measured simultaneously by the Seahorse XF/XFe Analyzer under basal conditions and continues to measure with each consecutive addition of mitochondrial inhibitors (oligomycin and rotenone/antimycin A). Pathway-specific information about mitochondrial or glycolytic ATP production (*mitoATP* and *glycoATP*, respectively) can be determined by transforming the ECAR and OCR data to ATP production rates (Section 3.8). In the glycolytic pathway, 2 molecules each of ATP, H^+, and lactate are produced during the conversion of one glucose molecule:

$$Glucose + 2\ \ ADP + 2\ \ Pi \rightarrow 2\ \ Lactate + 2\ \ ATP + 2\ \ H_2O + 2\ \ H^+ \quad (1)$$

Understanding the balance of Equation 1 and implementing the validated method previously described by Agilent™ (32) we can conclude, as shown in Equation 2, that the rate of ATP production in the glycolytic pathway (*glycoATP*) is equal to the Glycolytic Proton Efflux Rate (*glycoPER*):

$$glycoATP\ \ Production\ \ Rate\ \ (\ pmol\ \ ATP/min\ ) = glycoPER\ \ (\ pmol\ \ H^+/min\ ) \quad (2)$$

Mitochondrial ATP production rate calculation. To calculate the ATP production rate associated with OXPHOS in the mitochondria (Equation 3), the difference is taken between the basal OCR and the OCR that is specifically inhibited by the ATP synthase inhibitor (oligomycin; OCR_{Oligo}):

$$OCR_{ATP}\ \ (\ pmolO_2/min\ ) = OCR\ \ (\ pmolO_2/min\ ) - OCR_{Oligo}(\ pmolO_2/min\ ) \quad (3)$$

In turn, the OCR_{ATP} needs to be transformed to the rate of mitochondrial ATP production (Equation 4). A multiplication of 2 is used to convert molecules of O_2 to the number of oxygen (O) atoms consumed. This product is multiplied by the P/O ratio which represents "the number of molecules of ADP phosphorylated to ATP per atom of O reduced by an electron pair flowing through the electron transfer chain" (32). Agilent™ recommends an average value of 2.75, a standard P/O value for these calculations that was previously validated and accurately represents cell experimental conditions:

$$mitoATP\ \ Production\ \ Rate\ \ (\ pmol\ \ ATP/min\ ) = OCR_{ATP}\ \ (\ pmolO_2/min\ ) \times 2(\ pmolO/min\ ) \times P/O\ \ (\ pmol\ \ ATP/pmolO\ ) \quad (4)$$

The total cellular ATP production (Equation 5) can finally be determined as the sum of both the glycolytic (Equation 2) and the mitochondrial (Equation 4) ATP production rates:

$$ATP\ \ Production\ \ Rate\ \ (pmol\ \ ATP/min) = glycoATP\ \ Production\ \ Rate\ \ (pmol\ \ ATP/min) + mitoATP\ \ Production\ \ Rate\ \ (pmol/min) \quad (5)$$

2.11 SCENITH analysis of murine bone marrow-derived Group 2 Innate Lymphoid Cells

Single Cell ENergetic metabolism by profilIng Translation inHibition (SCENITH) analysis was performed with bone marrow-derived ILC2.

Reagent preparation. Glucose metabolism was inhibited with the glucose analog 2-Deoxy-D-Glucose (2-DG; Sigma Aldrich, Catalog No. D6134-25G) which was stored at -20°C at a stock concentration of 2 M (25 g crystalline powder in 76.14 mL dH_2O). Mitochondrial ATP synthesis was inhibited with the antibiotic oligomycin (Sigma Aldrich, Catalog No. 75351-5MG) which was stored at -20°C at a stock concentration of 1 mM (5 mg lyophilized powder in 6.32 mL dH_2O). The antibiotic puromycin (Sigma Aldrich, Catalog No. P7255-25MG) was used as a proxy for measuring protein synthesis, which was stored at -20°C at a stock concentration of 50 mg/mL (25 mg lyophilised powder in 500 µL dH_2O). Immediately prior to experiments, each of these reagents were prepared as an intermediate 4X concentrated solution in complete cell culture media (Table 2). 2-DG was prepared at a concentration of 400 mM (1:5 dilution), oligomycin at 4 µM (1:250 dilution), and puromycin at 40 µg/mL (1:1250 dilution).

Metabolic inhibition and sample preparation. After 24 hours of cytokine stimulation, the cells were resuspended and transferred to a conical-bottom 96-well plate. The plate was centrifuged (450*g, 5 minutes, 4°C) and 100 µL of media was removed from each well, excepting the control wells which only removed 50 µL. In turn, 50 µL of the 4X concentrated solutions of either 2-DG, oligomycin, or a combination of the two were added to the respective wells for a total volume of 150 µL and incubated for 30 minutes at 37°C in 5% CO_2. After incubation, 50 µL of the 4X puromycin was added to each well (excluding the negative control wells) for a final volume of 200 µL and incubated for an additional 15 minutes at the same conditions described above. The final 1X concentrations of 2-DG, oligomycin, and puromycin in the 200 µL volume were 100 mM, 1 µM, and 10 µg/mL, respectively.

Antibody staining for puromycin (protein synthesis proxy) detection. The cells were washed twice with DPBS (450*g, 5 minutes, 4°C) and then stained for viability with the fixable APC-eFluor780 dye, as described in Section 2.6. In brief, the cells incubated with the dye for 30 minutes on ice in the dark, followed by fixation, permeabilization, washes in 1X permeabilization buffer, and blocking in 2.4G2 hybridoma. The anti-puromycin antibody (Millipore-Sigma, Catalog No. MABE343-AF488) was diluted 1:1000 from its stock concentration of 0.5 mg/mL to 0.5 µg/mL. After incubation, the cell culture plate was centrifuged (600*g, 5 minutes, 4°C) and the supernatant was discarded. A volume of 100 µL of antibody dilution was added to the appropriate wells, excluding unstained controls, and incubated for 30 minutes on ice in the dark. The stained cells were washed twice with 1X permeabilization buffer (600*g, 5 minutes, 4°C) and the supernatant was discarded. The cells were resuspended in 200 µL of FACS buffer and transferred to a 5 mL FACS tube for flow cytometric acquisition.

Flow cytometry. Each sample was acquired using an Aurora Spectral Flow Cytometer (Cytek Biosciences) until 20,000 events were recorded. The directly conjugated anti-puromycin (493/522 nm) was acquired using the 488nm laser and APC-eFluor780 (756/785 nm) with the 633 nm laser. After sample acquisition, the files were exported in .fcs format from FACSDiva (BD Biosciences) and analyzed using FlowJo software (BD Biosciences, Version 10.10.0). Debris, doublet, and dead cells (APC-eFluor 780$^+$) were excluded via flow cytometry gating. Anti-puromycin and forward-scatter were analyzed on the x- and y-axes, respectively. Cell viability was slightly lower than prior to the assay due to the interruption of metabolic processes, however the short exposure time (30 minutes) to metabolic inhibition did not severely compromise ILC2 integrity.

2.12 SCENITH metabolic calculations

The puromycin fluorescence (gMFI) in the cells measured by flow cytometry represents protein synthesis, and this output changes based on the presence of inhibitors that interrupt specific ATP producing processes. Due to the energy-demanding nature of protein synthesis, these data can be interpreted in terms of ATP production. Cells treated with 2-DG (DG) represent the ATP production when glycolysis is interrupted, oligomycin (O) represents ATP production when OXPHOS is interrupted, and cells treated with both inhibitors (DGO) represent ATP production when ATP synthesis is fully inhibited. These fluorescent signals are used in combination with control (Co) samples to calculate the specific dependencies and capacities of ILC2s.

Glucose dependence. The percentage of glucose dependence quantifies how dependent are translation levels on glucose oxidation. This is calculated as the difference in protein synthesis between control cells and those treated with 2-DG, divided by the difference between control cells and complete inhibition of ATP production (Equation 6):

$$Glucose\ \ Dependence\ \ (\%) = 100 \times \left(\frac{Co - DG}{Co - DGO} \right) \quad (6)$$

Mitochondrial dependence. The percentage of mitochondrial dependence quantifies how much translation is dependent on OXPHOS, which is defined as the difference in protein synthesis between control cells and those treated with oligomycin, divided by the difference between control cells and complete inhibition of ATP production (Equation 7):

$$Mitochondrial\ \ Dependence\ \ (\%) = 100 \times \left(\frac{Co - O}{Co - DGO} \right) \quad (7)$$

Fatty acid oxidation (FAO) and amino acid oxidation (AAO) capacity. The FAO & AAO capacity is defined as the capacity to use fatty acids and amino acids as sources for ATP production in the mitochondria when glucose oxidation is inhibited, including glycolysis and glucose-derived acetyl-CoA by OXPHOS (Equation 8):

$$FAO\ \ \&\ \ AAO\ \ Capacity\ \ (\%) = 100 - (100 \times (\frac{Co - DG}{Co - DGO})) \quad (8)$$

Glycolytic capacity. The percentage of the glycolytic capacity is defined as the maximum capacity to sustain protein synthesis levels when mitochondrial OXPHOS is inhibited. Subtracting from 100 generates the value of how much ATP would be from glycolysis, without OXPHOS (Equation 9):

$$Glycolytic\ \ Capacity\ \ (\%) = 100 - (100 \times (\ \frac{Co - O}{Co - DGO}\ )) \quad (9)$$

2.13 Flow cytometric and statistical analysis

Flow cytometry analysis was performed using FlowJo software (BD, Version 10.10.0). Geometric mean fluorescence intensities (GeoMFI or gMFI) of the signals were calculated, triplicates were averaged per stimulatory condition and presented in bar graphs with all flow cytometry data represented as mean ± standard deviation (SD). Histograms and bar graphs were created using FlowJo and Prism softwares (Graphpad, Version 9) respectively. Statistical analysis was performed as ordinary one-way ANOVA and *post-hoc* Tukey's multiple comparison tests to obtain statistical significance (p-values) between experimental conditions. p-values below 0.05 were defined as statistically significant ($^*p \leq 0.05$, $^{**}p \leq 0.01$, $^{***}p \leq 0.001$, $^{****}p \leq 0.0001$).

3 Results

The fine-tuning of metabolic pathways is critical for maintaining ILC2 homeostasis and the regulation of cellular fitness and effector functions. We therefore aimed to establish a comprehensive set of rapidly applicable experimental approaches to study metabolic activities of ILC2 using flow cytometry-based assays in combination with the Seahorse Analyser (Figure 1). The applied methods here detail the level of glucose uptake, the magnitude of energy production obtained by glycolysis and oxidative phosphorylation, as well as the plasticity of ILC2 metabolic programming of these respective pathways. Furthermore, we addressed numerous facets of mitochondrial involvement in ILC2 metabolism including mitochondrial biogenesis, the total mass of mitochondria per cell, the respiration of mitochondria, and the performance of that respiration.

3.1 Determining glucose uptake by ILC2

To study the metabolic activities of ILC2, we obtained primary murine sort purified bone marrow-derived ILC2 (Figure 1, Supplementary Figure 1) that were further expanded *in vitro* as previously described (33, 34). IL-33 has been established as a key driver of ILC2 activation (35). IL-7 and IL-2 secreted by tissue-resident non-hematopoietic stromal cells as well as innate and adaptive immune cells, respectively, have been shown to act synergistically with IL-33 to induce proliferation and cytokine production (33, 36, 37). However, the effects of these cytokines (IL-2, IL-7, IL-33) alone or in synergy (IL-2+IL-33, IL-7+IL-33) as they pertain to glucose metabolism in ILC2 remain incompletely understood.

We first aimed to establish glucose uptake by ILC2 at defined steady and activation states using 2-(*N*-(7-Nitrobenz-2-oxa-1,3-diazol-4-yl)Amino)-2-Deoxyglucose (2-NBDG), a fluorescent glucose analogue (Figure 2). To investigate how activating cytokines impact glucose uptake, bone marrow-derived ILC2 were incubated with IL-7, IL-2, IL-33 alone, or in combinations of IL-7+IL-33 or IL-2+IL-33. After 24 hours of cytokine stimulation, 2-NBDG was added to the cells, incubated for 30 minutes, and subsequently analyzed by flow cytometry. Bone marrow-derived ILC2 treated with IL-7 (Figures 2A, B) or IL-2 alone (Figures 2C, D) exhibited moderate levels of exogenous glucose uptake, which considerably increased when treated in combination with IL-33. ILC2 treated with IL-33 alone displayed a higher uptake of exogenous glucose compared to IL-7 alone (Figures 2A, B), but not in regards to IL-2 alone (Figures 2C, D). In fact, the combination of IL-2+IL-33 exhibited the highest uptake of glucose compared to IL-33 or IL-2 alone (Figures 2C, D). Collectively, these observations demonstrate that ILC2 are actively acquiring exogenous glucose at steady state but were found to take up the most glucose when synergistically activated by IL-2+IL-33.

3.2 Quantification of mitochondrial biogenesis

Mitochondria are biosynthetic and bioenergetic organelles that also act as critical signaling platforms instructing decisions about cell proliferation, death, and differentiation. Mitochondria sustain immune cell phenotypes and functions, and depending on metabolic demands they can switch from being primarily catabolic ATP-generating organelles to anabolic organelles that produce the critical building blocks needed for macromolecule synthesis (38). Immune cells typically exhibit quiescent levels of metabolic activity at steady state and can shift to being highly metabolically active during the activation phase (5). This high energy demand triggers mitochondrial biogenesis to stimulate the production of more mitochondria and to replace mitochondria damaged by oxidative stress (39). The co-activator peroxisome proliferator-activated receptor gamma coactivator 1 alpha (PGC-1α) is characterized as a master regulator of mitochondrial biogenesis and oxidative metabolic pathways at both the transcriptional and post-translational levels (40). To investigate how cytokines known to drive ILC2 effector functions influence mitochondrial biogenesis, we first evaluated the expression levels of PGC-1α using intracellular flow cytometry. Bone marrow-derived ILC2 were incubated with IL-7, IL-2, IL-33 alone, or in combinations of IL-7+IL-33 or IL-2+IL-33. After 24 hours of cytokine stimulation, the cells were fixed, permeabilized, and labeled using a directly conjugated antibody for PGC-1α followed by flow cytometric analysis. ILC2 treated with IL-7 (Figures 3A, B) or IL-2 alone (Figures 3C, D) exhibited moderate levels of PGC-1α expression, which considerably increased in the presence of IL-33. There was no significant elevation in PGC-1α expression between IL-33 alone and the combination of either IL-7+IL-33 (Figures 3A, B) or IL-2+IL-33 (Figures 3C, D). However, these synergistic combinations of activating cytokines displayed higher levels of PGC-1α expression compared to IL-7 (Figure 3B) or IL-2 alone (Figures 3C, D). These data suggest that the presence of IL-33 primarily influences PGC-1α expression to drive mitochondrial biogenesis rather than relying on the synergistic activation of cytokines known to influence ILC2 effector functions.

3.3 Quantification of mitochondrial mass and active mitochondria

We next aimed to investigate mitochondrial metrics directly through the use of fluorescent functional dyes to be analyzed by flow cytometry. With the development of dyes such as MitoTracker™ Deep Red, it is possible to label all mitochondria within living cells and quantify the total mass produced by ILC2 at defined steady and activation states. MitoTracker™ Deep Red is a lipophilic carbocyanine-based dye that permeates the cell membrane to covalently bind thiol-reactive chloromethyl groups within the mitochondrial membrane, permitting all mitochondria to be fluorescently labeled (41). When glucose is acquired exogenously

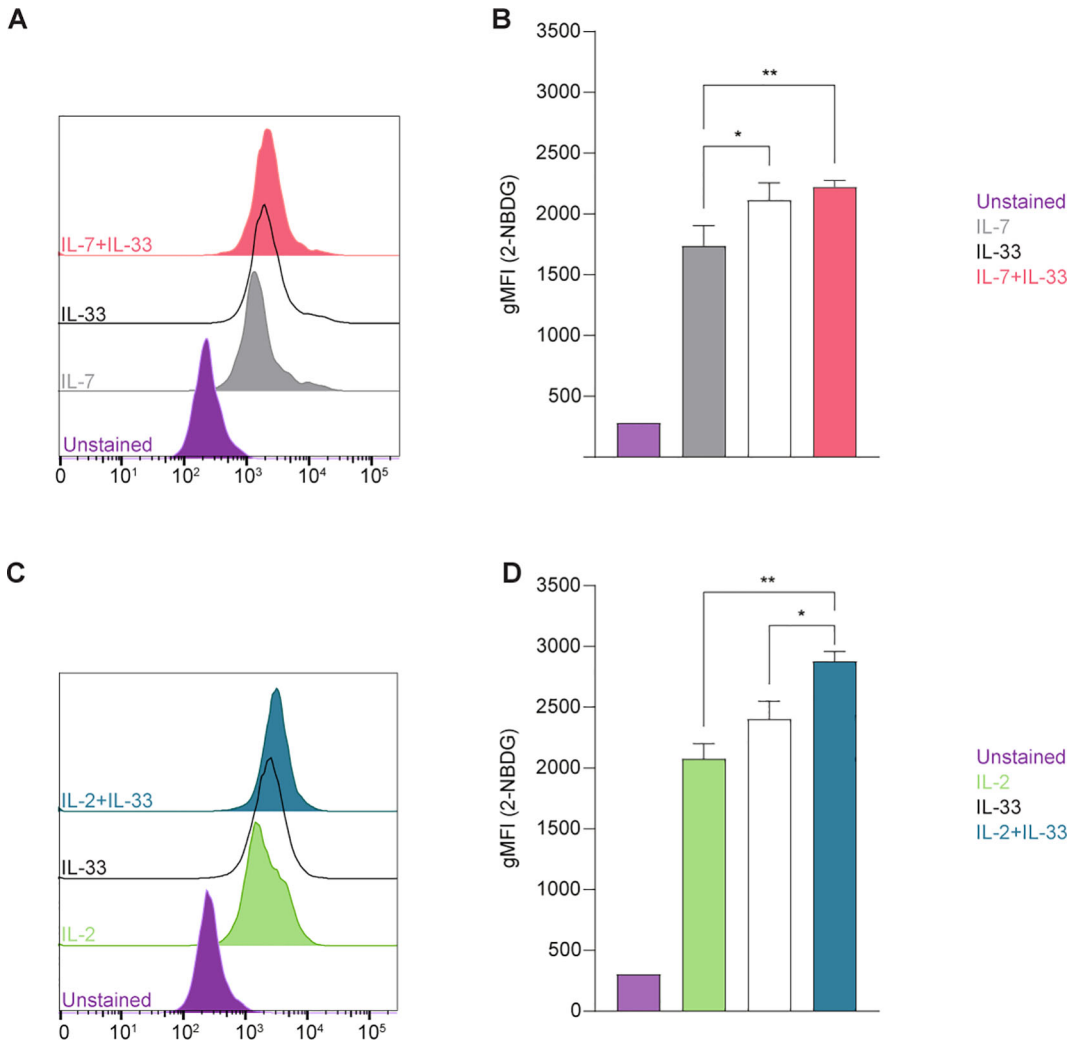

FIGURE 2
Group 2 innate lymphoid cells (ILC2) increase glucose uptake upon stimulation with activating cytokines. Bone marrow-derived group 2 innate lymphoid cells (ILC2) were stimulated with either IL-7 only, IL-33 only, or a combination of IL-7 and IL-33 **(A, B),** or IL-2 only, IL-33 only, or a combination of IL-2 and IL-33 **(C, D)**. All cytokines were applied at 10 ng/mL. 2-NBDG was added after 24 hours of cytokine stimulation and incubated for 30 minutes to assess capacity of glucose uptake by flow cytometric analysis, determining the geometric Mean Fluorescence Intensity (gMFI). ILC2 that were not incubated with 2-NBDG served as negative control (Unstained). Data reporting the treatment with IL-33 are the same for **(A-D)**. Data are shown as average ± standard deviation (SD) and are representative of three independent experiments. Statistical analysis was performed using one-way ANOVA followed by Tukey's multiple comparisons test ($p < 0.05$ = *, $p < 0.01$ = **).

by the cell, the glucose is utilized by the mitochondria either through glycolysis or oxidative phosphorylation to produce energy in the form of adenosine triphosphate (ATP). While anaerobic glycolysis generates two ATP per glucose molecule, the aerobic process of oxidative phosphorylation produces 36 molecules of ATP (42). In brief, oxidative phosphorylation utilizes the electron transport chain (ETC) to drive protons (H^+) against their concentration gradient out of the inner mitochondrial membrane space (42). This accumulation of H^+ in the intermembrane space can then flow back through the ATP-generating component of the ETC, completing the energy production cycle (43). This difference in H^+ concentration effectively creates both a pH and electrical gradient to generate a membrane potential in the mitochondria (42). This membrane potential, or polarization, can be exploited to label actively respirating mitochondria with other functional dyes, such as tetramethylrhodamine methyl (TMRM). TMRM is similar to MitoTracker™ Deep Red in that they are both lipophilic cationic dyes so they will both be drawn into mitochondria across this charged gradient, however, TMRM exhibits a low binding affinity to mitochondrial proteins and functional groups (43). Effectively, MitoTracker™ Deep Red labels all mitochondria that are present, whereas TMRM preferentially labels actively respirating mitochondria, and neither interacts with damaged mitochondrial membranes where this gradient is impaired.

To further analyze whether mitochondrial biogenesis was replacing potentially damaged mitochondria or increasing the overall mass during activation states, we optimized a flow cytometry-based protocol to rapidly quantify the total mass of mitochondria in live bone marrow-derived ILC2. To investigate how activating cytokines impact the overall mass of mitochondria

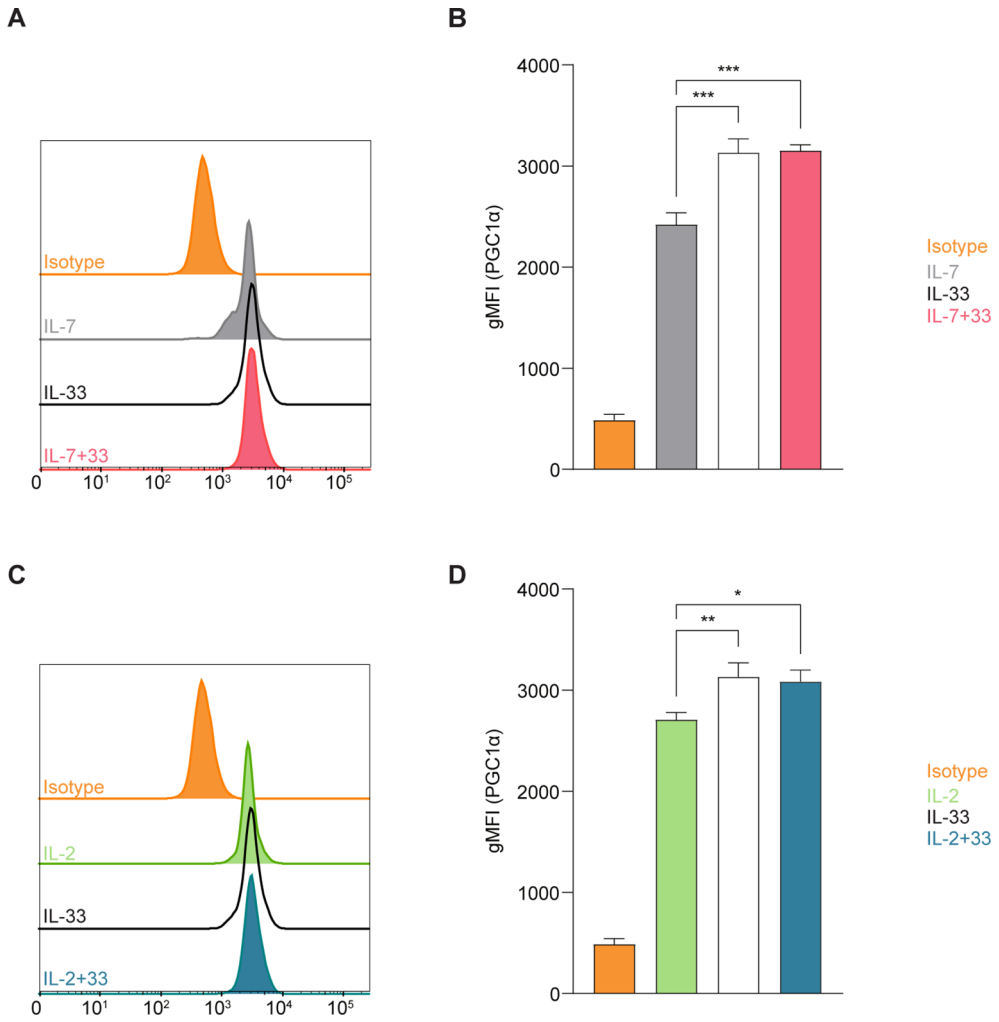

FIGURE 3
Group 2 innate lymphoid cells (ILC2) elevate expression of PGC-1a upon stimulation with activating cytokines. Bone marrow-derived group 2 innate lymphoid cells (ILC2) were stimulated with either IL-7 only, IL-33 only, or a combination of IL-7 and IL-33 **(A, B),** or IL-2 only, IL-33 only, or a combination of IL-2 and IL-33 **(C, D)**. All cytokines were applied at 10 ng/mL. After 24 hours of cytokine stimulation cells were harvested and the protein expression levels of the peroxisome proliferator–activated receptor gamma coactivator-1 alpha (PGC-1a) were assessed by intracellular flow cytometric analysis, determining the geometric Mean Fluorescence Intensity (gMFI). Isotype antibody stainings served as control (Isotype). Data reporting the treatment with IL-33 are the same for **(A-D)**. Data are shown as average ± standard deviation (SD) and are representative of three independent experiments. Statistical analysis was performed using one-way ANOVA followed by Tukey's multiple comparisons test ($p < 0.05$ = *, $p < 0.01$ = **, $p < 0.001$ = ***).

synthesized by ILC2, cells were incubated with IL-7, IL-2, IL-33 alone, or in combinations of IL-7+IL-33 or IL-2+IL-33. After 24 hours of cytokine stimulation, the mitochondrial dyes MitoTracker™ Deep Red and TMRM were added to the cells, incubated for 30 minutes, and ILC2s were subsequently analyzed by flow cytometry (Figure 4A). To investigate mitochondrial mass, we first analyzed ILC2 positive for MitoTracker™ Deep Red. ILC2 treated with IL-7 (Figure 4B) or IL-2 alone (Figure 4E) exhibited moderate levels of mitochondrial mass, which considerably increased in the presence of IL-33 alone. While there was no significant elevation in mitochondrial mass between IL-7 alone and the synergistic combination of IL-7+IL-33 (Figure 4B), there was a slight increase between IL-2 alone and IL-2+IL-33 (Figure 4E). Interestingly, the mitochondria mass decreased between IL-33 alone and IL-7+IL-33 (Figure 4B). These results suggest, similarly to the PGC-1α expression levels, that IL-33 influences the mitochondrial mass produced by ILC2 more than the synergistic effects of activating cytokines.

In addition, we sought to understand how active this mitochondrial mass was by investigating their membrane polarization as an indicator of mitochondrial respiration. To further understand how cytokines known to activate ILC2 impact mitochondrial respiration and activity, we analyzed bone marrow-derived ILC2 positive for TMRM to assess mitochondrial membrane polarization. Bone marrow-derived ILC2 treated with IL-7 (Figure 4C) or IL-2 alone (Figure 4F) exhibited low levels of membrane polarization, which considerably increased in the presence of IL-33. Furthermore, combined cytokine treatment of IL-7 +IL-33 (Figure 4C) or IL-2+IL-33 (Figure 4F) markedly increased polarization of the mitochondrial membrane compared to either IL-7, IL-2, or IL-33 alone. These observations demonstrate that ILC2 exhibit

10.3389/fimmu.2025.1545790

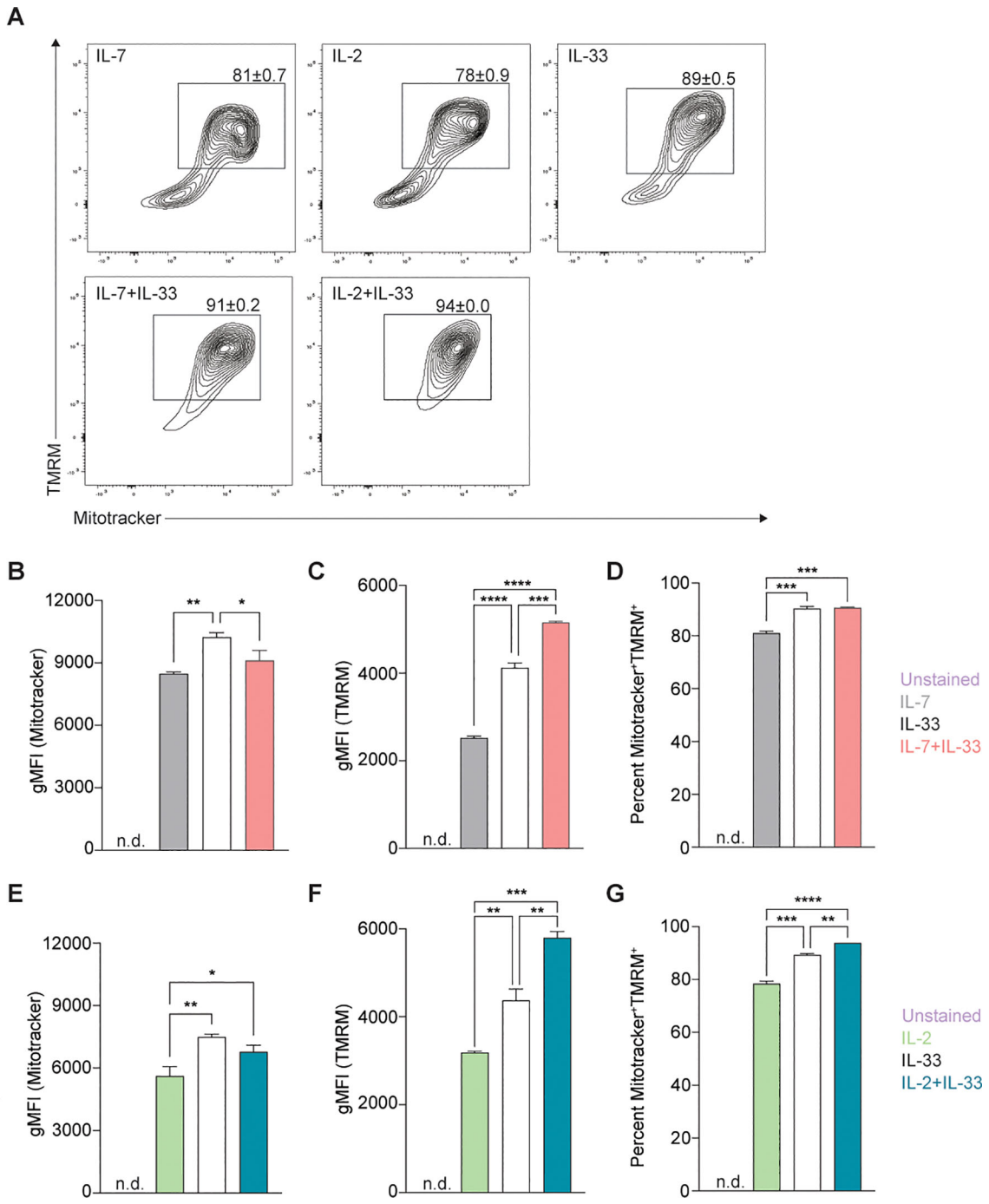

FIGURE 4
Stimulation of Group 2 innate lymphoid cells (ILC2) with activating cytokines augments mitochondrial mass and mitochondrial membrane polarization. Bone marrow-derived group 2 innate lymphoid cells (ILC2) were stimulated with either IL-7 only, IL-33 only, or a combination of IL-7 and IL-33 **(A, B-D)**, or IL-2 only, IL-33 only, or a combination of IL-2 and IL-33 **(A, E-G)**. All cytokines were applied at 10 ng/mL. After 24 hours of cytokine stimulation cells were harvested and stained with Mitotracker and TMRM to quantify by flow cytometric analysis mitochondrial mass as well as mitochondrial membrane potential, respectively. ILC2 not stained with MitoTracker and TMRM were used as negative control (Unstained). Flow cytometric contour plots are depicted in **(A)** with gates set on $TMRM^+$ (y-axis) and $MitoTracker^+$ (x-axis) double-positive populations. From gated populations geometric Mean Fluorescence Intensities (gMFI) for Mitotracker **(B, E)** and TMRM **(C, F)**, as well as frequencies of $Mitotracker^+TMRM^+$ double-positive populations **(D, G)** were determined. Data reporting the treatment with IL-33 are the same for **(A–G)**. Data are shown as average ± standard deviation (SD) and are representative of three independent experiments. Statistical analysis was performed using one-way ANOVA followed by Tukey's multiple comparisons test (*$p \leq 0.05$, **$p \leq 0.01$, ***$p \leq 0.001$, ****$p \leq 0.0001$).

low levels of mitochondrial polarization at steady state, actively increase their polarization upon treatment with IL-33, but especially when synergistically activated by IL-2+IL-33, or IL-7+IL-33.

Independent analysis of MitoTracker™ Deep Red and TMRM yielded information about the total mitochondrial mass and the total mitochondrial membrane polarization present within each cytokine stimulation, respectively. However, the information regarding what proportion of the total mitochondrial mass was actively respirating during defined steady and activation states remained unknown. Through the implementation of gating strategies (Figure 4A), we identified mitochondria that were positive for both MitoTracker™ Deep Red and TMRM to elucidate this ratio. Approximately 80% of the mitochondrial population was active in IL-7 (Figure 4D) or IL-2 alone (Figure 4G), which significantly increased to roughly 90% in the presence of IL-33. Similarly, compared to stimulations with IL-7 (Figure 4D) or IL-2 alone (Figure 4G), a marked elevation in the proportion of active mitochondria was found when ILC2 were activated by IL-7+IL-33 (Figure 4D) or IL-2+IL-33 (Figure 4G). However, while there was a significant increase in the proportion of active mitochondria between IL-33 alone and IL-2+IL-33 (Figure 4G), this was not the case when comparing stimulations of IL-33 with IL-7+IL-33 (Figure 4D). Collectively, these observations suggest that while mitochondrial mass production plateaus during peak ILC2 activation states, the mitochondrial membrane potential and overall activity increases when synergistically activated by IL-2+IL-33.

3.4 Determining cell density for Seahorse Extracellular Flux Assays

We next set out to complement flow cytometry-based assays with the Agilent™ Seahorse XF technology to assess specific inquiries about ILC2 glucose metabolism using the Mito Stress Assay, the Glycolysis Stress Test, and the Real-Time ATP assay. These approaches generate incredibly useful data that cover a myriad of metrics; however, they are also extremely sensitive assays that are heavily influenced by cell density. As such, the number of cells present in each well play a significant role in the detection of specific measurements, as well as the consistency between replicates. If the cellular confluence within the well is too dense, this will translate to measurements that are beyond the Seahorse XF/XFe Analyzer's detection range resulting in inaccurate readings. Likewise, cellular confluence that is too sparse will result in measurements too low to be within the detection threshold. The primary measurement that is acquired in the Mito Stress Assay is called the Oxygen Consumption Rate (OCR), and implements the use of four compounds that modulate and probe mitochondrial functions: oligomycin, carbonyl cyanide-4 (trifluoromethoxy) phenylhydrazone (FCCP), rotenone, and antimycin A. In brief, the basal OCR is measured before the injection of oligomycin, the maximum OCR value is measured after the injection of FCCP, and the lowest OCR is measured after the injection of rotenone and antimycin A. According to Agilent's user guide *Characterizing Your Cells: Using OCR Values to Determine Optimal Seeding Density*, a cellular confluence between 50-90% and a basal OCR range of 20-160 pmol/min is recommended for optimal results. However, these recommendations are general and not specific to ILC2. Here, we implemented the Mito Stress Assay to determine the optimal seeding density for OCR detection, even at the ILC2s highest and lowest OCR measurements across all cytokine stimulations.

We performed a titration of three different cell concentrations that were seeded and incubated for 24 hours with either IL-7, IL-2, IL-33 alone or combinations of IL-7+IL-33, as well as IL-2+IL-33. The cell seeding densities of 50,000, 75,000 or 100,000 cells per well were used in the Mito Stress Assay to obtain OCR values (Figure 5). The seeding density of 50,000 cells/well resulted in OCR values that were either not detectable or just above the detection threshold for all cytokine stimulations (Figures 5A–E, right). Similarly to 50,000 cells/well, the seeding density of 75,000 cells/well yielded OCR values that were not consistently detectable for IL-7 alone stimulations (Figure 5A, right), and were just above the detection threshold for IL-2 (Figure 5B, right), IL-33 (Figure 5C, right), IL-7+IL-33 (Figure 5D, right), and IL-2 +IL-33 treatments (Figure 5E, right). The only cell seeding density that gave OCR values consistently within the detection range across all cytokine stimulations was 100,000 cells/well. Furthermore, this seeding density was also the closest to the recommended basal OCR range of 20-160 pmol/min and presented with a post-cytokine stimulation confluency of 80% (Figures 5A–E, left). As such, 100,000 cells/well was the cell seeding density chosen for all metabolic assays conducted in this paper (Figures 5A–E, left).

3.5 Quantification of Mito Stress Assay metrics

As previously addressed in Section 3.4, the Mito Stress Assay is a metabolic assay to evaluate mitochondrial respiration and function. Mitochondrial respiration is driven by the electron transport chain (ETC); a series of five protein complexes (I, II, III, IV, V) located at the interface of the mitochondrial matrix and intermembrane space (39, 42). Through the implementation of compounds such as oligomycin, FCCP, rotenone, and antimycin A, various elements of the ETC can be manipulated to modulate mitochondrial respiration and evaluate individual metrics. The Mito Stress Assay can measure six metrics in total: basal respiration, ATP production, proton (H^+) leak, maximal respiration, spare respiratory capacity, and nonmitochondrial respiration. Each of the metrics are calculated in reference to the OCR measurements acquired by the Seahorse XF/XFe Analyzer at specific timepoints, and in response to the compound injections that disrupt or facilitate elements of mitochondrial respiration. According to the *Seahorse XF Cell Mito Stress Test Kit User Guide* the (i) basal respiration is measured first and represents the oxygen consumption required to meet the energetic demand of the cell at baseline conditions. (ii) ATP production specifically shows the amount of ATP produced by mitochondrial respiration to meet cellular energy demands. This metric is measured when oligomycin is injected to inhibit ATP synthase (complex V), subsequently

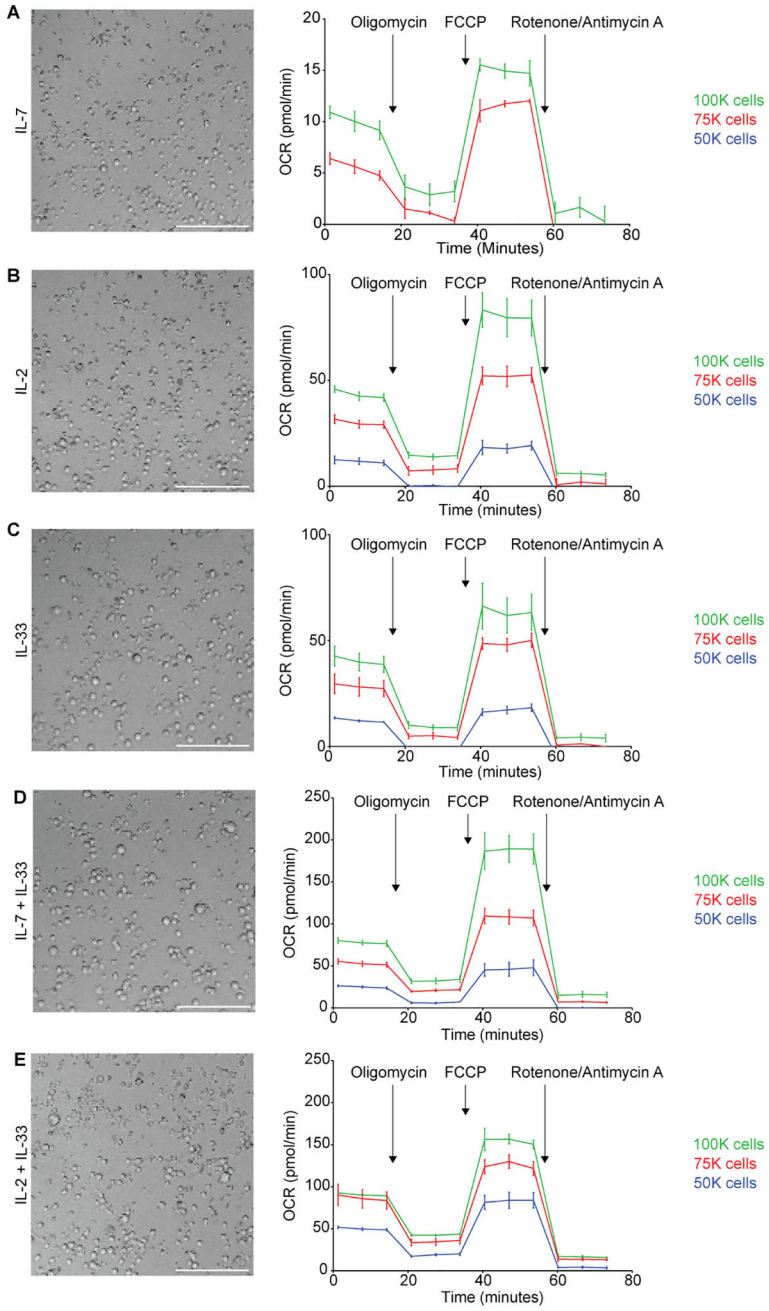

FIGURE 5
Determining cell seeding density for Seahorse metabolic assays. Bone marrow-derived group 2 innate lymphoid cells (ILC2) were seeded at three different cell densities (100.000 (100k), 75.000 (75k) or 50.000 (50k) per well) into Seahorse XFe96 microplates and stimulated with either IL-7 only **(A)**, IL-2 only **(B)**, IL-33 only **(C),** IL-7 and IL-33 **(D)**, or with IL-2 and IL-33 **(E)**. All cytokines were used at 10 ng/mL. After 24 hours of cytokine stimulation the Mito Stress Test assay was performed using the Seahorse Analyzer and oxygen consumption rates (OCR) were determined. Brightfield microscopy images of seeding densities of 100.000 cells/well are shown **(A-E)**; size bars = 150mM. Data are shown as average ± standard deviation (SD) and are representative of three independent experiments.

reducing the electron flow in the ETC and the subsequent OCR values. (iii) Proton leak can be an indicator of mitochondrial damage but can also be used mechanistically to regulate mitochondrial ATP production. This metric is the difference between the OCR values for basal respiration and ATP-linked respiration. (iv) The maximal respiration demonstrates the maximum rate of respiration that is possible for the cell to achieve and is measured after the injection of FCCP which mimics a physiological "energy demand." This compound acts as an uncoupling agent that disrupts mitochondrial membrane potential by collapsing the proton gradient, enabling the ETC to operate at maximum capacity to oxidize substrates, such as glucose. (v) The spare respiratory capacity is the cell's ability to respond to energy demands, which can be used as an indicator for cellular fitness and is calculated by subtracting the basal respiration from the maximum respiration. (vi) Finally, nonmitochondrial

respiration is the cellular respiration that continues after the mitochondrial respiration has been inhibited through the injection of rotenone and antimycin A which inhibit complexes I and III, respectively.

To further understand the intricacies of mitochondrial respiration during steady and activation states, we applied the Seahorse Mito Stress Assay for sort-purified bone marrow-derived ILC2 to evaluate their proton leakage, basal respiration, maximum

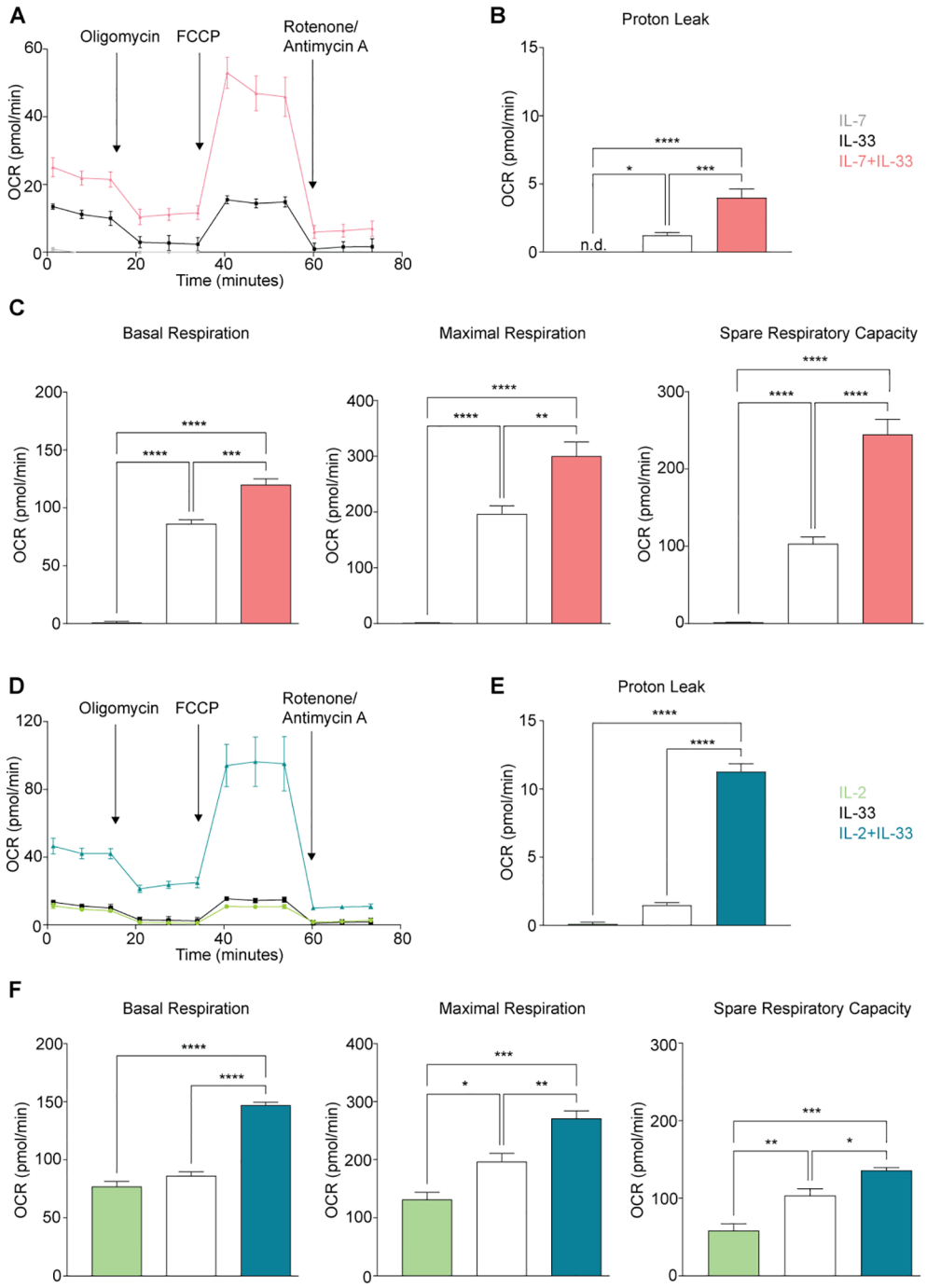

FIGURE 6
Group 2 innate lymphoid cells (ILC2) elevate oxygen consumption (OCR) rate upon stimulation with activating cytokines. Bone marrow-derived group 2 innate lymphoid cells (ILC2) were seeded into Seahorse XFe96 microplates at a cell density of 100.000 cells/well and stimulated with either IL-7 only, IL-33 only, or a combination of IL-7 and IL-33 **(A-C)**, or with IL-2 only, IL-33 only, or a combination of IL-2 and IL-33 **(D-F)**. All cytokines were used at 10 ng/mL. After 24 hours of cytokine stimulation the Mito Stress Test assay was performed using the Seahorse Analyzer and oxygen consumption rates (OCR) **(A, D)**, proton leak **(B, E)**, basal and maximal respiration as well as the spare respiratory capacities **(C, F)** were determined. Data reporting the treatment with IL-33 are the same for **(A-F)**. Data are shown as average ± standard deviation (SD) and are representative of three independent experiments. Statistical analysis was performed using one-way ANOVA followed by Tukey's multiple comparisons test (*$p \leq 0.05$, **$p \leq 0.01$, ***$p \leq 0.001$, ****$p \leq 0.0001$).

respiration, and spare respiratory capacity. ILC2 were incubated with IL-7 (Figure 6A), IL-2 (Figure 6D), IL-33 alone (Figures 6A, D), or with combinations of IL-7+IL-33 (Figure 6A) or IL-2+IL-33 (Figure 6D). After 24 hours of cytokine stimulation, ILC2 were prepped for the Mito Stress Assay (Section 2.8) and evaluated on the Seahorse XF/XFe Analyzer (Figure 6). The levels of proton leakage in ILC2 treated with IL-7 alone were lowest of all tested cytokine treatments (Figures 6B, E). There was a marked elevation in the levels of proton leakage in the presence of IL-33 alone, as well as with the combined treatment of IL-7+IL-33 (Figure 6B). Furthermore, the combined treatment of IL-2+IL-33 demonstrated remarkably higher proton leakage in comparison to IL-2 or IL-33 alone (Figure 6E). These observations demonstrate that ILC2 exhibit minimal signs of mitochondrial damage at steady state but were found to exhibit higher levels of proton leakage when synergistically activated by IL-7+IL-33, but especially with IL-2 +IL-33.

We established in Section 3.3 that activation of ILC2 results in increased fluorescence of the dye TMRM, a dye that is preferentially acquired by mitochondria in the presence of an active membrane potential. This membrane potential is generated through the ETC during oxidative phosphorylation, and indicates mitochondrial respiration is taking place. With the Mito Stress Assay, we were then able to inhibit or facilitate specific elements of the ETC to evaluate the basal respiration, maximal respiration, and the spare respiratory capacity. These three metrics evaluated in ILC2 treated with IL-7 alone presented with minute OCR levels compared to all other cytokines (Figure 6C). There was a marked elevation in OCR levels in the presence of IL-33 alone, as well as with the combined treatment of IL-7+IL-33 (Figure 6C) for basal respiration, maximal respiration, and space respiratory capacity. In contrast, ILC2 treated with IL-2 alone already exhibited moderate OCR levels in regards to these three respiratory metrics (Figure 6F). The combined treatment of IL-2+IL-33 was significantly higher in basal respiration OCR values in comparison to treatments with IL-2, as well as IL-33 alone (Figure 6F). For both the maximal respiration and the spare respiratory capacity, the OCR values in ILC2 treated with IL-2 alone were lower in comparison to all other cytokine treatments (Figure 6F). Furthermore, there was marked elevation in the OCR values in the presence of IL-33 alone, as well as with the combined treatment of IL-2+IL-33 for the maximal respiration as well as the spare respiratory capacity. Collectively, these observations demonstrate that ILC2 are utilizing mitochondrial respiration at a minimum during steady state but were found to increase their respiration most when synergistically activated by IL-7+IL-33, as well as IL-2+IL-33.

3.6 Quantification of Glycolysis Stress Test metrics

Glycolysis and oxidative phosphorylation are two major and interconnected energy producing processes in the cell. Glycolysis occurs when glucose is metabolized within the cell to generate two molecules of pyruvate, followed by a reducing reaction to form lactate as NADH and then reoxidized to make NAD^+ (44). This reoxidization occurs in both anaerobic and aerobic glycolysis, however under anaerobic conditions this process occurs in the cytoplasm via lactate dehydrogenase (44). Under aerobic conditions the NADH is first shuttled to the mitochondria and then converted to NAD^+ before participating in the ETC to generate ATP (44). In either case, the production of lactate in the cytoplasm results in the extrusion of H^+ into the extracellular medium consequently raising its pH (44). In the Glycolysis Stress Test Assay, the speed at which the extracellular medium becomes acidic due this H^+ accumulation is measured directly as the Extracellular Acidification Rate (ECAR). According to the *Seahorse XF Glycolysis Stress Test Kit User Guide*, (i) glycolysis is measured first and represents the rate of glycolysis under basal conditions. The ECAR is measured as the injected glucose at saturated levels is converted into pyruvate while producing water, CO_2, NADH, H^+, and finally ATP. (ii) The glycolytic capacity is measured after the injection of oligomycin, an ATP synthase inhibitor, effectively shutting down oxidative phosphorylation and shifting energy production entirely to glycolysis. This metric exhibits the highest ECAR measurement and serves as an indication of the cells theoretical maximum rate of glycolysis. (iii) The glycolytic reserve measures the potential or ability of a cell to respond to an energy demand and is defined as the difference between the glycolytic capacity and the glycolytic basal rate. This is measured after the injection of a glucose analogue called 2-DG that inhibits glycolysis by competitively binding the first enzyme in the glycolysis pathway, causing a decrease in the ECAR measurement, which is necessary to prove that the ECAR produced in the experiment was due to glycolysis.

To investigate how cytokines known to drive ILC2 effector functions influence glycolysis during steady and activation states, we optimized the Seahorse Glycolysis Stress Test for sort-purified bone marrow-derived ILC2 to analyze basal glycolysis, glycolytic capacity, and glycolytic reserve. To this end, ILC2 were incubated with IL-7, IL-2, IL-33 alone, or with combinations of IL-7+IL-33 or IL-2+IL-33. After 24 hours of cytokine stimulation, ILC2 were prepped for the Glycolysis Stress Test (Section 2.8) and evaluated on the Seahorse XF/XFe Analyzer (Figures 7A, B). The basal glycolytic rate (Glycolysis; left) and the glycolytic capacity (center) in ILC2 treated with IL-7 (Figure 7C) or IL-2 alone (Figure 7D) were significantly lower in comparison to all other cytokine treatments. There was a marked elevation in both metrics in the presence of IL-33 alone, as well as with the combined treatments of IL-7+IL-33 (Figure 7C) and IL-2+IL-33 (Figure 7D). In contrast, while there was no difference between IL-7 (Figure 7C) or IL-2 alone (Figure 7D) compared to IL-33 alone when measuring the glycolytic reserve values (right), the combined cytokine treatments of IL-7+IL-33 (Figure 7C) and IL-2+IL-33 (Figure 7D) were significantly higher in comparison to all other cytokine treatments. These observations demonstrate that ILC2 are utilizing glycolysis at a minimum and exhibit a low glycolytic capacity during steady state (IL-7 or IL-2 only), but were found to increase the glycolytic rate and capacity when stimulated with IL-33, and the most when synergistically activated by IL-7+IL-33, or by IL-2+IL-33.

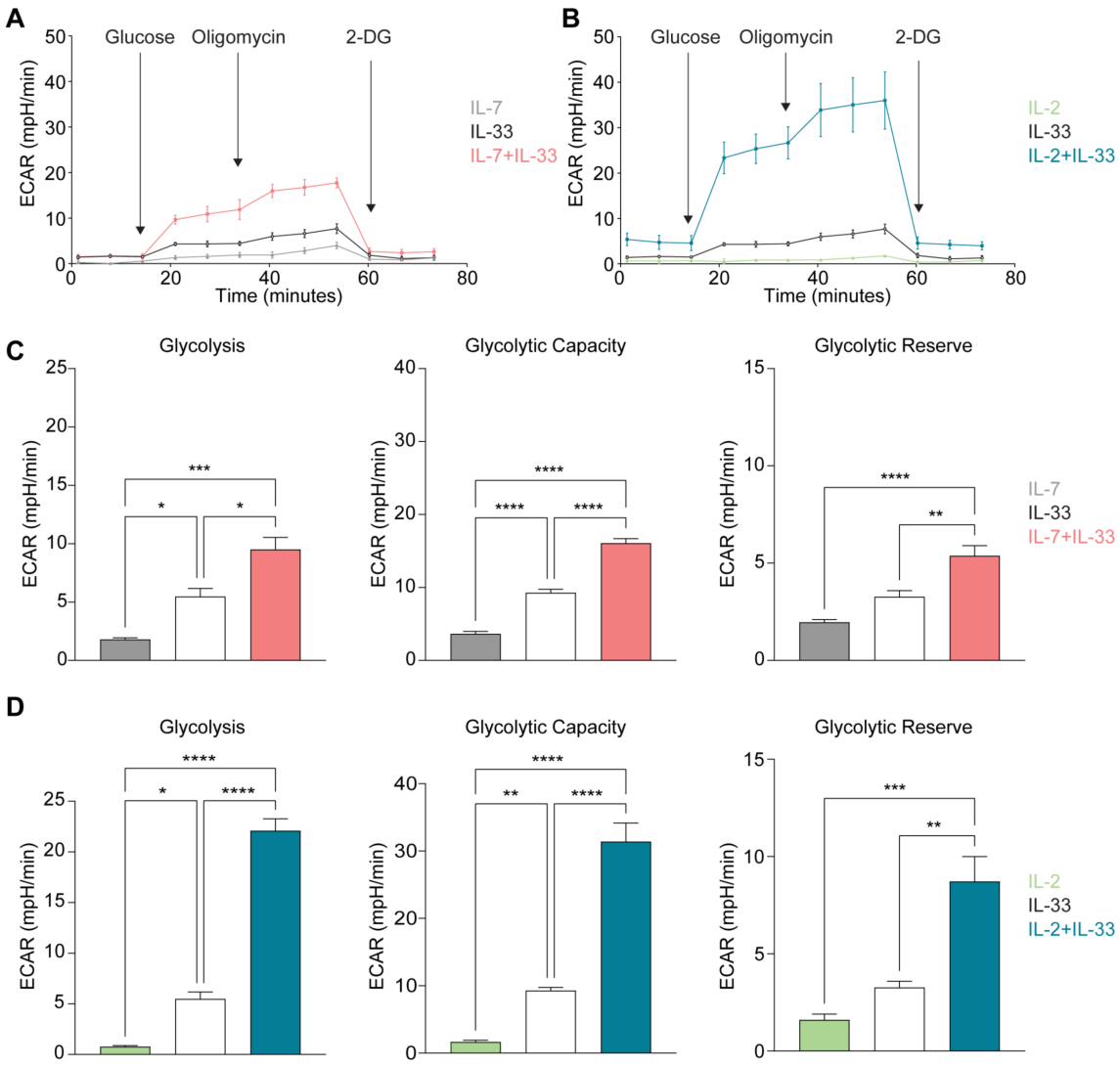

FIGURE 7
Group 2 innate lymphoid cells (ILC2) increase glycolysis upon stimulation with activating cytokines. Bone marrow-derived group 2 innate lymphoid cells (ILC2) were seeded into Seahorse XFe96 microplates at a cell density of 100.000 cells/well and stimulated with either IL-7 only, IL-33 only, or a combination of IL-7 and IL-33 **(A, C)**, or with IL-2 only, IL-33 only, or a combination of IL-2 and IL-33 **(B, D)**. All cytokines were used at 10 ng/mL. After 24 hours of cytokine stimulation the Glycolysis Stress assay was performed using the Seahorse Analyzer and extracellular acidification rates (ECAR) **(A, B)**, and the levels of glycolysis, glycolytic capacity as well as the glycolytic reserve **(C, D)** were determined (2-Deoxy-D-Glucose (2-DG)). Data reporting the treatment with IL-33 are the same for **(A - D)**. Data are shown as average ± standard deviation (SD) and are representative of three independent experiments. Statistical analysis was performed using one-way ANOVA followed by Tukey's multiple comparisons test (*p ≤ 0.05, **p ≤ 0.01, ***p ≤ 0.001, ****p ≤ 0.0001).

3.7 SCENITH analysis

We next took advantage of a recently described method referred to as Single Cell ENergetic metabolism by profilIng Translation inHibition (SCENITH), which enables us to determine metabolic dependencies and capacities in their entirety at the single-cell level. While SCENITH has been shown to be as reliable and comparable to other well-established techniques such as Seahorse, it is an especially well-suited approach to analyze rare cells like ILC2s, as SCENITH requires far fewer cells and is less dependent on cell density (45). SCENITH incorporates the detection of puromycin as its primary readout, providing a proxy measurement for global translation and protein synthesis (46). (45) The contribution of the glycolytic or OXPHOS metabolic pathways in terms of energy production can be assessed by analyzing protein synthesis in the presence of inhibitors, where glycolysis is inhibited by 2-deoxyglucose (2-DG), OXPHOS with oligomycin, or both to inhibit all energy production. Protein synthesis is an energy demanding process, therefore SCENITH equates decreased protein synthesis with the interruption of ATP production caused by the addition of these inhibitors. In all, SCENITH quantifies four metrics: glucose dependence, mitochondrial dependence, glycolytic capacity, and fatty acid oxidation (FAO) and amino acid oxidation (AAO) capacity (Section 2.12). While the total level of translation correlates with the global metabolic activity of the cells, the dependency parameters underline essential cellular pathways. In

contrast, "capacity" is the inverse of dependency, which reveals the maximum compensatory capacity to exploit alternative pathway/s when one is inhibited.

The global level of translation was low in ILC2s stimulated with IL-7 (Figures 8A, B) or IL-2 (Figures 8E, F) alone, gradually increased when treated with IL-33 alone, but protein synthesis was highest when ILC2s were stimulated with IL-7+IL-33 (Figures 8A, B) and IL-2+IL-33 (Figures 8E, F). These data also revealed that ILC2s stimulated with IL-7+IL-33 (Figure 8C) and IL-2+IL-33 (Figure 8G) exhibited a significantly lower dependence on glucose and mitochondria compared to ILC2s treated with IL-7 (Figure 8C) or IL-2 (Figure 8G) alone. ILC2s treated with IL-33 alone presented a reduced dependence on glucose and mitochondria compared to IL-7 (Figure 8C), whereas only a reduced dependence on mitochondria was observed between IL-33 treated cells and IL-2 (Figure 8G) alone. Similarly, ILC2s treated with IL-2+IL-33 (Figure 8G) exhibited an even lower dependence on glucose and mitochondria compared to IL-2 (Figure 8G), whereas only a reduced dependence on mitochondria was observed between IL-7+IL-33 treated cells and IL-33 (Figure 8G) alone. Conversely, compared to the glycolytic capacity of ILC2 treated with IL-7 (Figure 8D) or IL-2 (Figure 8H), a marked elevation was observed when cells were stimulated with IL-33, and again when stimulated with IL-7+IL-33 (Figure 8D) or IL-2 +IL-33 (Figure 8H). When evaluating the FAO & AAO capacity, ILC2s treated with IL-7 alone (Figure 8D) exhibited the lowest capacity compared to all other cytokine conditions, whereas those stimulated with IL-2+IL-33 (Figure 8H) exhibited a higher capacity compared to all other conditions. Collectively, these data demonstrate that ILC2s exhibit great metabolic flexibility in the presence of IL-33, but even more so when stimulated with the synergistic combination of activating cytokines IL-7+IL-33, as well as IL-2+IL-33.

3.8 Characterization of ATP production via Agilent™ Seahorse Real-Time ATP Rate Assay

In our final analysis step, we aimed to quantify absolute ATP production levels of ILC2 using the Agilent™ Seahorse XF ATP Real-Time rate assay, which also measures and quantifies the rate of ATP production from the glycolytic and mitochondrial system simultaneously (Section 2.10). As expected, stimulations with IL-7 (Figure 9A) or IL-2 alone (Figure 9C) yielded low ATP production rates. While treatment of ILC2 with IL-33 slightly increased ATP production, a massive elevation of energy production was observed when cells were activated with IL-7+IL-33 (Figure 9A) or IL-2+IL-33 (Figure 9C). ATP generation by ILC2 stimulated by only IL-7 was largely driven by glycolysis (Figure 9B). In contrast, IL-2 as well as IL-33-driven energy production comparably relied on OXPHOS as well as glycolysis (Figures 9B, D). Compared to the IL-33 stimulation only, glycolysis-mediated ATP production frequencies increased only slightly when ILC2 were treated with combinations of IL-7+IL-33 (Figure 9B) or IL-2+IL-33 (Figure 9D). However, the massive increase in ATP upon IL-7+IL-33 (Figure 9B) or IL-2+IL-33 (Figure 9D) stimulation, compared to IL-7, IL-2, or IL-33 only treatments, was driven by glycolysis as well as OXPHOS.

4 Discussion

ILC2 exert critical functions to ensure tissue barrier integrity, driving and reinforcing immunological protection by orchestrating innate as well as adaptive immune processes. However, when deregulated, ILC2 have been shown to contribute to the pathogenesis of several chronic inflammatory barrier disorders through the release of large quantities of type 2 signature cytokines including IL-4, IL-5 and IL-13. Although recent studies started to uncover critical components of the metabolic wiring of ILC2, many aspects remain elusive. This is largely due to the rarity of ILC2 in tissues and their limited expansion in culture posing a challenge on obtaining sufficient cell counts to carry out large-scale experiments. Moreover, there is a lack of accessibility of rapid assays to study the intricacies of metabolic pathways. Applying our recently described protocol to expand murine bone marrow-derived ILC2 (23, 33), we detail here a framework of experimental approaches to study key immunometabolic states utilizing flow cytometry, SCENITH, as well as the Seahorse platform.

We provide an in-depth protocol of how to use ILC2 for studies applying the Seahorse platform, where drug treatments can be delivered to the cells at specific targets and timepoints to further elucidate the metabolic identities of ILC2. While the information from Seahorse assays is valuable, they require special equipment as well as proprietary kits and consumables, thereby limiting the number of researchers accessing this platform due to financial and accessibility restrictions. We therefore further detail flow cytometry-based assays, including SCENITH, that can be rapidly implemented for metabolic studies of ILC2. Seahorse and SCENITH assays exhibit both a high degree of accuracy and provided complementary insights into the metabolic programming of ILC2. Comparatively, the high values for glycolytic and OXPHOS capacities in ILC2 treated with IL-7+IL-33 and IL-2+IL-33 found in Seahorse were corroborated by those found using SCENITH. In fact, the trend in values between single cytokine stimulations and synergistic cytokine treatments were consistent between the two platforms. In both Seahorse and SCENITH approaches, the IL-2 alone conditions exhibited values that were higher than the stimulations with IL-7 alone. Although overall SCENITH is more user-friendly and accessible to the research community, the Seahorse platform provides additional insights that are highly specific. As such, we would recommend that, if possible, researchers should use SCENITH to corroborate and bolster insights revealed by Seahorse.

Our applied framework of experimental approaches combining flow cytometry assays with proprietary metabolic platforms demonstrates that the utilization of glucose is markedly elevated upon cytokine-mediated activation of ILC2. In parallel, we reveal increases in mitochondrial biogenesis (PGC-1α), mitochondrial mass as well as mitochondrial membrane potential upon ILC2 activation. Our study reveals that ILC2 take up moderate levels of

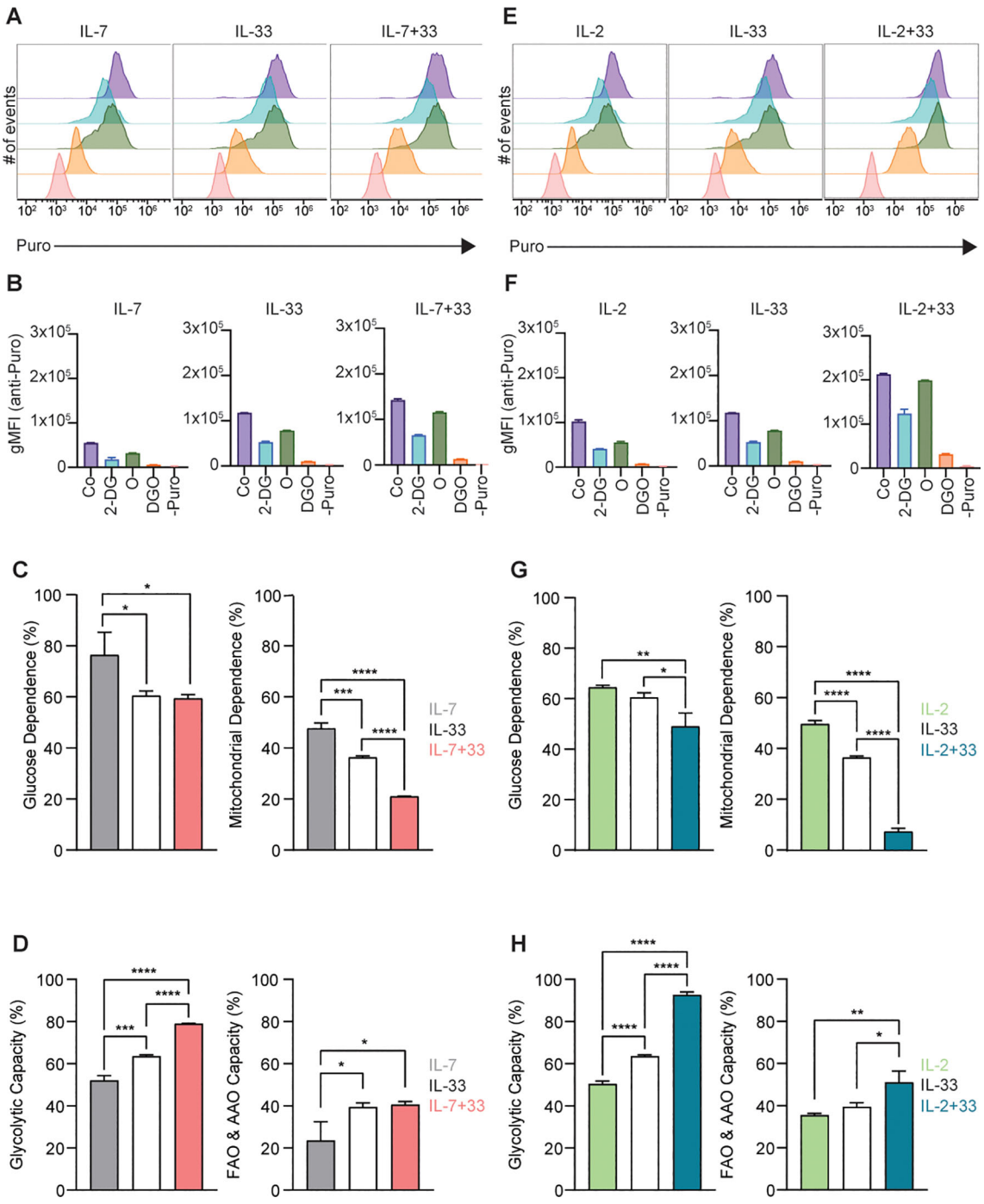

FIGURE 8
SCENITH analysis of group 2 innate lymphoid cells (ILC2). **(A-F)** SCENITH (Single Cell ENergetIc metabolism by profiling Translation inHibition) analysis was performed by stimulating bone marrow-derived group 2 innate lymphoid cells (ILC2) with either IL-7 only, IL-33 only, or a combination of IL-7 and IL-33 **(A-D),** or IL-2 only, IL-33 only, or a combination of IL-2 and IL-33 **(E-H)**. All cytokines were applied at 10 ng/mL. After 24 hours of cytokine stimulation cells were either left untreated as control (Co) or incubated with 2-Deoxy-D-Glucose (2-DG), Oligomcyin (O), or a combination of 2-DG and O (DGO) for 30 minutes. Subsequently, cells were treated for 15 minutes with puromycin followed by intracellular staining with an anti-puromycin antibody. Cells that were not treated with puromycin were used as a negative control (-Puro). ILC2 were then analyzed by flow cytometry **(A, E),** geometric mean intensities (gMFI) of the anti-puromycin staining acquired **(B, F),** and gMFI values used to determine glucose dependence and mitochondrial dependence **(C, G)**, as well as glycolytic and fatty acid oxidation (FAO) and amino acid oxidation (AAO) capacities **(D, H)**. Data reporting the treatment with IL-33 are the same for **(A-H)**. Data are shown as average ± standard deviation (SD) and are representative of three independent experiments. Statistical analysis was performed using one-way ANOVA followed by Tukey's multiple comparisons test (*$p \leq 0.05$, **$p \leq 0.01$, ***$p \leq 0.001$, ****$p \leq 0.0001$).

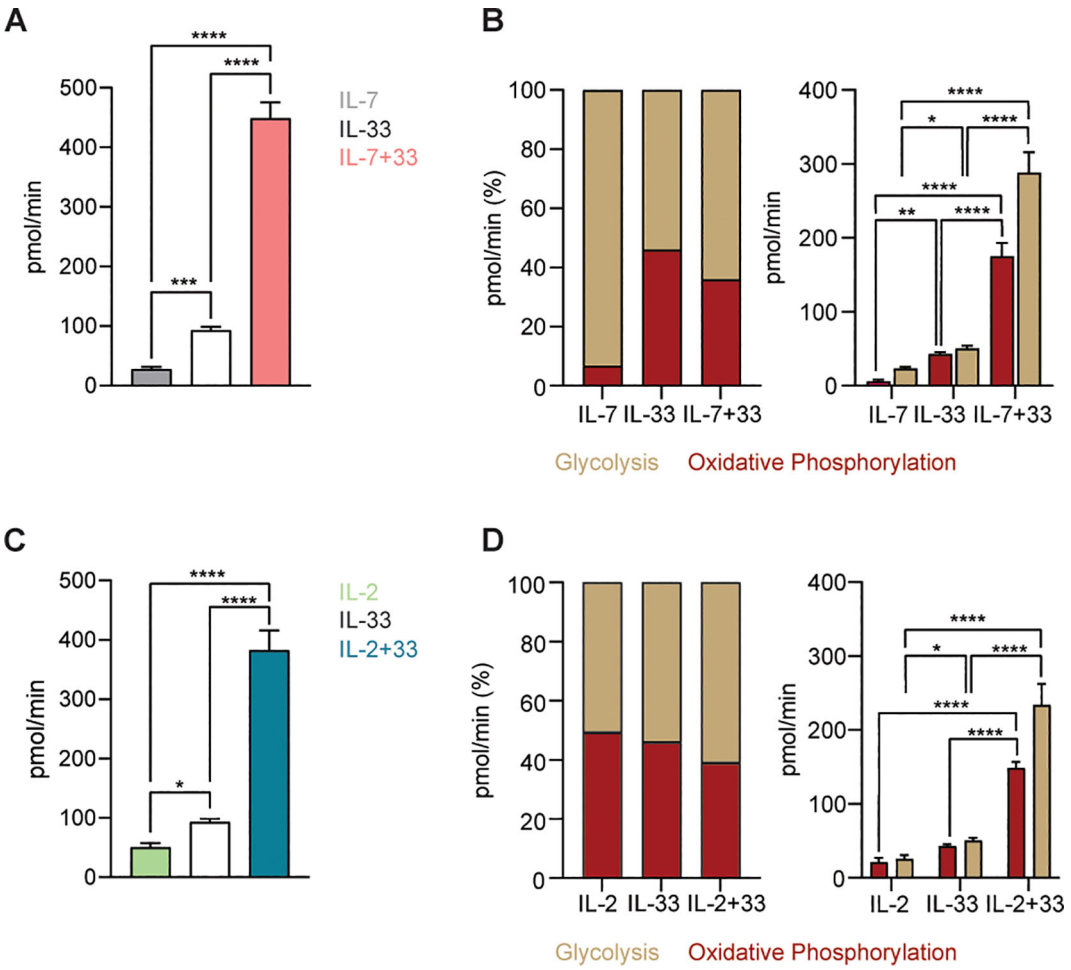

FIGURE 9
Group 2 innate lymphoid cells (ILC2) augment ATP production upon stimulation with activating cytokines. **(A-D)** To determine ATP production bone marrow-derived group 2 innate lymphoid cells (ILC2) were seeded into Seahorse XFe96 microplates at a cell density of 100.000 cells/well and stimulated with either IL-7 only, IL-33 only, or a combination of IL-7 and IL-33 **(A, B)**, or with IL-2 only, IL-33 only, or a combination of IL-2 and IL-33 **(C, D)**. All cytokines were used at 10 ng/mL. After 24 hours of cytokine stimulation the Real-Time ATP Rate assay was performed using the Seahorse Analyzer. ATP production from oxidative phosphorylation as well as glycolysis were analyzed and depicted as a proportion of 100% and as absolute values. Data reporting the treatment with IL-33 are the same for **(A-D)**. Data are shown as average ± standard deviation (SD) and are representative of three independent experiments. Statistical analysis was performed using one-way ANOVA followed by Tukey's multiple comparisons test (*p ≤ 0.05, **p ≤ 0.01, ***p ≤ 0.001, ****p ≤ 0.0001).

glucose, exhibit low levels of mitochondrial respiration, and utilize glycolysis at a minimum rate during steady state (IL-7 or IL-2 alone), but gradually increase their glucose metabolism, as well as OXPHOS, upon activation with IL-33. Interestingly, while glycolysis is not heavily utilized at steady state, the proportion of ATP produced by ILC2 is almost exclusively from glycolysis in the presence of IL-7. In contrast, IL-2 treated ILC2 consistently present with a nearly 50:50 ratio of glycolysis- and OXPHOS-mediated ATP production. Overall, mitochondrial respiration if highly elevated, with OXPHOS producing more ATP than glycolysis. In fact, IL-2 +IL-33 exhibited the highest values for mitochondrial respiration (TMRM) and basal respiration (Seahorse). Increased mitochondrial respiration is typically correlated with an increased demand for energy which can induce the production of ROS that damage mitochondrial integrity, consequently stimulating mitochondrial biogenesis. Concurrently, we observe that ILC2 treated with IL-2 +IL-33 present the highest degree of proton leak and mitochondrial respiration. The mitochondrial mass in ILC2 treated with IL-33 was higher than that of those treated with IL-7 or IL-2 alone. However, this mass decreased in the synergistic combination of these cytokines. It is possible that ILC2 treated with IL-33 increased their mitochondria production to meet the energy demand, but the increased respiration caused damage to the mitochondria and the overall mass decreased as a consequence. While PGC-1α levels as well as mitochondrial mass increased with IL-33 stimulation compared to homeostatic cytokine treatments with IL-7 or IL-2 alone, synergistic cytokine activation did not yield an elevation of values above those obtained with IL-33 only. In contrast, stimulations with IL-7+IL-33 or IL-2+IL-33 markedly elevated their mitochondrial potential, indicative of mitochondrial respiration. These findings were further complemented by Seahorse Real-Time ATP Rate analysis as well as SCENITH, revealing that synergistic activation of ILC2 with IL-7+IL-33 or IL-2+IL-33 led to markedly higher ATP production and protein

synthesis and elevated glycolytic and FAO & AAO capacities. Collectively, this demonstrates that the increase in mitochondrial potential upon synergistic activation with IL-7+IL-33 or IL-2+IL-33 translates into elevated energy production, leading to synergistic cytokine production and proliferation of ILC2 (23, 33). Interestingly, SCENITH analysis further demonstrated that ILC2 treated with IL-7+IL-33 or IL-2+IL-33 have reduced glucose and mitochondrial dependence, suggesting a high metabolic flexibility of ILC2 when activated by IL-33, but especially when primed by IL-7+IL-33, or IL-2+IL-33. Taken together, these findings indicate that metabolic substrate accessibility and availability is a main driver in the metabolic wiring of ILC2, which will need further experimental interrogation in future studies.

Data availability statement

The raw data supporting the conclusions of this article will be made available by the authors, without undue reservation.

Ethics statement

The animal study was approved by Canadian Council on Animal Care of McGill University. The study was conducted in accordance with the local legislation and institutional requirements.

Author contributions

SK: Conceptualization, Data curation, Formal analysis, Investigation, Methodology, Project administration, Visualization, Writing – original draft, Writing – review & editing. RD: Investigation, Writing – original draft, Writing – review & editing. NI: Writing – review & editing, Visualization. AE: Visualization, Writing – review & editing, Data curation, Investigation, Methodology. AR-D: Investigation, Writing – review & editing. FR: Investigation, Writing – review & editing. GB: Investigation, Writing – review & editing. SR: Writing – review & editing. JF: Writing – review & editing, Conceptualization, Funding acquisition, Project administration, Resources, Supervision.

Funding

The author(s) declare that financial support was received for the research and/or publication of this article. This work was supported by a project grant (PJT – 175173) from the Canadian Institutes of Health Research (CIHR), a Leaders Opportunity Fund infrastructure grant from the Canadian Foundation of Innovation (CFI; 38958) and a Miravo Healthcare Research Grant in Allergic Rhinitis or Urticaria by the Canadian Allergy, Asthma and Immunology Foundation (CAAIF; 3656894). NI and SK both acknowledge support of a Doctoral Training Scholarship by the Fonds de recherche du Québec – Santé (FRQS) (325991 for NI, 284343 for SK).

Acknowledgments

The authors thank Julien Leconte and Camille Stegen from the Flow Cytometry and Cell Sorting Facility (FCCF) at the Life Sciences Complex at McGill University. The FCCF acknowledges support by the Canadian Foundation for Innovation (CFI) and by the Faculty of Medicine and Health Sciences at McGill University. The authors thank Dr. Hamza Loucif for discussions. The authors further thank Dr. Daina Avizonis from the McGill Metabolomics Innovation Resource (MIR) Core Facility for excellent technical support. MIR acknowledges support from the Terry Fox Foundation, CFI, Génome Québec, and a donation from the Dr. John R. Fraser and Mrs. Clara M. Fraser Memorial Trust.

Conflict of interest

The authors declare that the research was conducted in the absence of any commercial or financial relationships that could be construed as a potential conflict of interest.

The author(s) declared that they were an editorial board member of Frontiers, at the time of submission. This had no impact on the peer review process and the final decision.

Generative AI statement

The author(s) declare that no Generative AI was used in the creation of this manuscript.

Publisher's note

Supplementary material

The Supplementary Material for this article can be found online at: https://www.frontiersin.org/articles/10.3389/fimmu.2025.1545790/full#supplementary-material

SUPPLEMENTARY FIGURE 1
Gating strategies for the isolation of murine bone marrow-derived group 2 innate lymphoid cell (ILC2). Debris and doublets were excluded and murine bone marrow-derived ILC2 precursors were defined and isolated by flow cytometric sorting as lineage-negative, c-kit^{-}Sca-1^{+}CD25^{+} cells.

References

1. Harris NL, Loke P. Recent advances in type-2-cell-mediated immunity: insights from helminth infection. *Immunity*. (2017) 47:1024–36. doi: 10.1016/j.immuni.2017.11.015

2. Molofsky AB, Locksley RM. The ins and outs of innate and adaptive type 2 immunity. *Immunity*. (2023) 56:704–22. doi: 10.1016/j.immuni.2023.03.014

3. van der Zande HJP, Zawistowska-Deniziak A, Guigas B. Immune regulation of metabolic homeostasis by helminths and their molecules. *Trends Parasitol*. (2019) 35:795–808. doi: 10.1016/j.pt.2019.07.014

4. Kedia-Mehta N, Finlay DK. Competition for nutrients and its role in controlling immune responses. *Nat Commun*. (2019) 10:2123. doi: 10.1038/s41467-019-10015-4

5. Buck MD, Sowell RT, Kaech SM, Pearce EL. Metabolic instruction of immunity. *Cell*. (2017) 169:570–86. doi: 10.1016/j.cell.2017.04.004

6. Zaiss DMW, Pearce EJ, Artis D, McKenzie ANJ, Klose CSN. Cooperation of ILC2s and T(H)2 cells in the expulsion of intestinal helminth parasites. *Nat Rev Immunol*. (2024) 24:294–302. doi: 10.1038/s41577-023-00942-1

7. Spencer SP, Wilhelm C, Yang Q, Hall JA, Bouladoux N, Boyd A, et al. Adaptation of innate lymphoid cells to a micronutrient deficiency promotes type 2 barrier immunity. *Science*. (2014) 343:432–7. doi: 10.1126/science.1247606

8. Li S, Bostick JW, Ye J, Qiu J, Zhang B, Urban JF Jr., et al. Aryl hydrocarbon receptor signaling cell intrinsically inhibits intestinal group 2 innate lymphoid cell function. *Immunity*. (2018) 49:915–28 e5. doi: 10.1016/j.immuni.2018.09.015

9. Lewis G, Wang B, Shafiei Jahani P, Hurrell BP, Banie H, Aleman Muench GR, et al. Dietary fiber-induced microbial short chain fatty acids suppress ILC2-dependent airway inflammation. *Front Immunol*. (2019) 10:2051. doi: 10.3389/fimmu.2019.02051

10. Schneider C, O'Leary CE, von Moltke J, Liang HE, Ang QY, Turnbaugh PJ, et al. A metabolite-triggered tuft cell-ILC2 circuit drives small intestinal remodeling. *Cell*. (2018) 174:271–84 e14. doi: 10.1016/j.cell.2018.05.014

11. Nadjsombati MS, McGinty JW, Lyons-Cohen MR, Jaffe JB, DiPeso L, Schneider C, et al. Detection of succinate by intestinal tuft cells triggers a type 2 innate immune circuit. *Immunity*. (2018) 49:33–41 e7. doi: 10.1016/j.immuni.2018.06.016

12. Hurrell BP, Sakano Y, Shen S, Helou DG, Li M, Shafiei-Jahani P, et al. Iron controls the development of airway hyperreactivity by regulating ILC2 metabolism and effector function. *Sci Transl Med*. (2024) 16:eadk4728. doi: 10.1126/scitranslmed.adk4728

13. Shi Z, Ohno H, Satoh-Takayama N. Dietary derived micronutrients modulate immune responses through innate lymphoid cells. *Front Immunol*. (2021) 12:670632. doi: 10.3389/fimmu.2021.670632

14. Bantug GR, Galluzzi L, Kroemer G, Hess C. The spectrum of T cell metabolism in health and disease. *Nat Rev Immunol*. (2018) 18:19–34. doi: 10.1038/nri.2017.99

15. Yu H, Jacquelot N, Belz GT. Metabolic features of innate lymphoid cells. *J Exp Med*. (2022) 219. doi: 10.1084/jem.20221140

16. Zhou L, Lin Q, Sonnenberg GF. Metabolic control of innate lymphoid cells in health and disease. *Nat Metab*. (2022) 4:1650–9. doi: 10.1038/s42255-022-00685-8

17. Surace L, Doisne JM, Croft CA, Thaller A, Escoll P, Marie S, et al. Dichotomous metabolic networks govern human ILC2 proliferation and function. *Nat Immunol*. (2021) 22:1367–74. doi: 10.1038/s41590-021-01043-8

18. Salmond RJ, Mirchandani AS, Besnard AG, Bain CC, Thomson NC, Liew FY. IL-33 induces innate lymphoid cell-mediated airway inflammation by activating mammalian target of rapamycin. *J Allergy Clin Immunol*. (2012) 130:1159–66 e6. doi: 10.1016/j.jaci.2012.05.018

19. Hodge SH, Krauss MZ, Kaymak I, King JI, Howden AJM, Panic G, et al. Amino acid availability acts as a metabolic rheostat to determine the magnitude of ILC2 responses. *J Exp Med*. (2023) 220. doi: 10.1084/jem.20221073

20. Wilhelm C, Harrison OJ, Schmitt V, Pelletier M, Spencer SP, Urban JF Jr., et al. Critical role of fatty acid metabolism in ILC2-mediated barrier protection during malnutrition and helminth infection. *J Exp Med*. (2016) 213:1409–18. doi: 10.1084/jem.20151448

21. Karagiannis F, Masouleh SK, Wunderling K, Surendar J, Schmitt V, Kazakov A, et al. Lipid-droplet formation drives pathogenic group 2 innate lymphoid cells in airway inflammation. *Immunity*. (2020) 52:620–34 e6. doi: 10.1016/j.immuni.2020.03.003

22. Galle-Treger L, Hurrell BP, Lewis G, Howard E, Jahani PS, Banie H, et al. Autophagy is critical for group 2 innate lymphoid cell metabolic homeostasis and effector function. *J Allergy Clin Immunol*. (2020) 145:502–17.e5. doi: 10.1016/j.jaci.2019.10.035

23. Roy-Dorval A, Deagle RC, Roth F, Raybaud M, Ismailova N, Krisna SS, et al. Analysis of lipid uptake, storage, and fatty acid oxidation by group 2 innate lymphoid cells. *Front Immunol*. (2024) 15:1493848. doi: 10.3389/fimmu.2024.1493848

24. Fali T, Aychek T, Ferhat M, Jouzeau JY, Busslinger M, Moulin D, et al. Metabolic regulation by PPARγ is required for IL-33-mediated activation of ILC2s in lung and adipose tissue. *Mucosal Immunol*. (2021) 14:585–93. doi: 10.1038/s41385-020-00351-w

25. Ercolano G, Gomez-Cadena A, Dumauthioz N, Vanoni G, Kreutzfeldt M, Wyss T, et al. PPARγ drives IL-33-dependent ILC2 pro-tumoral functions. *Nat Commun*. (2021) 12:2538. doi: 10.1038/s41467-021-22764-2

26. Xiao Q, He J, Lei A, Xu H, Zhang L, Zhou P, et al. PPARgamma enhances ILC2 function during allergic airway inflammation via transcription regulation of ST2. *Mucosal Immunol*. (2021) 14:468–78. doi: 10.1038/s41385-020-00339-6

27. Yamaguchi M, Samuchiwal SK, Quehenberger O, Boyce JA, Balestrieri B. Macrophages regulate lung ILC2 activation via Pla2g5-dependent mechanisms. *Mucosal Immunol*. (2018) 11:615–26. doi: 10.1038/mi.2017.99

28. Monticelli LA, Buck MD, Flamar AL, Saenz SA, Tait Wojno ED, Yudanin NA, et al. Arginase 1 is an innate lymphoid-cell-intrinsic metabolic checkpoint controlling type 2 inflammation. *Nat Immunol*. (2016) 17:656–65. doi: 10.1038/ni.3421

29. Xia R, Peng HF, Zhang X, Zhang HS. Comprehensive review of amino acid transporters as therapeutic targets. *Int J Biol Macromol*. (2024) 260:129646. doi: 10.1016/j.ijbiomac.2024.129646

30. Flamar AL, Klose CSN, Moeller JB, Mahlakoiv T, Bessman NJ, Zhang W, et al. Interleukin-33 induces the enzyme tryptophan hydroxylase 1 to promote inflammatory group 2 innate lymphoid cell-mediated immunity. *Immunity*. (2020) 52:606–19 e6. doi: 10.1016/j.immuni.2020.02.009

31. Fu L, Zhao J, Huang J, Li N, Dong X, He Y, et al. A mitochondrial STAT3-methionine metabolism axis promotes ILC2-driven allergic lung inflammation. *J Allergy Clin Immunol*. (2022) 149:2091–104. doi: 10.1016/j.jaci.2021.12.783

32. Agilent. *Quantifying Cellular ATP Production Rate Using Agilent Seahrose XF Technology*. (2018).

33. Duerr CU, McCarthy CD, Mindt BC, Rubio M, Meli AP, Pothlichet J, et al. Type I interferon restricts type 2 immunopathology through the regulation of group 2 innate lymphoid cells. *Nat Immunol*. (2016) 17:65–75. doi: 10.1038/ni.3308

34. Mindt BC, Krisna SS, Duerr CU, Mancini M, Richer L, Vidal SM, et al. The NF-kappaB transcription factor c-rel modulates group 2 innate lymphoid cell effector functions and drives allergic airway inflammation. *Front Immunol*. (2021) 12:664218. doi: 10.3389/fimmu.2021.664218

35. Topczewska PM, Rompe ZA, Jakob MO, Stamm A, Leclere PS, Preusser A, et al. ILC2 require cell-intrinsic ST2 signals to promote type 2 immune responses. *Front Immunol*. (2023) 14:1130933. doi: 10.3389/fimmu.2023.1130933

36. Sheikh A, Abraham N. Interleukin-7 receptor alpha in innate lymphoid cells: more than a marker. *Front Immunol*. (2019) 10:2897. doi: 10.3389/fimmu.2019.02897

37. Roediger B, Kyle R, Tay SS, Mitchell AJ, Bolton HA, Guy TV, et al. IL-2 is a critical regulator of group 2 innate lymphoid cell function during pulmonary inflammation. *J Allergy Clin Immunol*. (2015) 136:1653–63.e7. doi: 10.1016/j.jaci.2015.03.043

38. Weinberg SE, Sena LA, Chandel NS. Mitochondria in the regulation of innate and adaptive immunity. *Immunity*. (2015) 42:406–17. doi: 10.1016/j.immuni.2015.02.002

39. Bennett CF, Latorre-Muro P, Puigserver P. Mechanisms of mitochondrial respiratory adaptation. *Nat Rev Mol Cell Biol*. (2022) 23:817–35. doi: 10.1038/s41580-022-00506-6

40. Halling JF, Pilegaard H. PGC-1alpha-mediated regulation of mitochondrial function and physiological implications. *Appl Physiol Nutr Metab*. (2020) 45:927–36. doi: 10.1139/apnm-2020-0005

41. Clutton G, Mollan K, Hudgens M, Goonetilleke N. A reproducible, objective method using mitoTracker(R) fluorescent dyes to assess mitochondrial mass in T cells by flow cytometry. *Cytomet A*. (2019) 95:450–6. doi: 10.1002/cyto.a.23705

42. Deshpande OA, Mohiuddin SS. *Biochemistry, Oxidative Phosphorylation*. Treasure Island (FL: StatPearls (2024).

43. Perry SW, Norman JP, Barbieri J, Brown EB, Gelbard HA. Mitochondrial membrane potential probes and the proton gradient: a practical usage guide. *Biotechniques*. (2011) 50:98–115. doi: 10.2144/000113610

44. Naifeh J, Dimri M, Varacallo M. *Biochemistry, Aerobic Glycolysis*. Treasure Island (FL: StatPearls (2024).

45. Stork BA, Dean A, York B. Methodology for measuring oxidative capacity of isolated peroxisomes in the Seahorse assay. *J Biol Methods*. (2022) 9:e160. doi: 10.14440/jbm.2022.374

46. Arguello RJ, Combes AJ, Char R, Gigan JP, Baaziz AI, Bousiquot E, et al. SCENITH: A flow cytometry-based method to functionally profile energy metabolism with single-cell resolution. *Cell Metab*. (2020) 32:1063–75 e7. doi: 10.1016/j.cmet.2020.11.007

Frontiers in Immunology

Explores novel approaches and diagnoses to treat immune disorders.

The official journal of the International Union of Immunological Societies (IUIS) and the most cited in its field, leading the way for research across basic, translational and clinical immunology.

Discover the latest Research Topics

See more →

Frontiers

Avenue du Tribunal-Fédéral 34
1005 Lausanne, Switzerland
frontiersin.org

Contact us

+41 (0)21 510 17 00
frontiersin.org/about/contact